SANDIA REPORT
SAND2021-7984
Printed July 2021

Sandia National Laboratories

Performance Evaluation of Comparative Vacuum Monitoring and Piezoelectric Sensors for Structural Health Monitoring of Rotorcraft Components

Dennis P. Roach
Tom M. Rice

Prepared by
Sandia National Laboratories
Albuquerque, New Mexico
87185 and Livermore,
California 94550

Issued by Sandia National Laboratories, operated for the United States Department of Energy by National Technology & Engineering Solutions of Sandia, LLC.

Available to DOE and DOE contractors from
U.S. Department of Energy
Office of Scientific and Technical Information
P.O. Box 62
Oak Ridge, TN 37831

Telephone: (865) 576-8401
Facsimile: (865) 576-5728
E-Mail: reports@osti.gov
Online ordering: http://www.osti.gov/scitech

Available to the public from
U.S. Department of Commerce
National Technical Information Service
5301 Shawnee Rd
Alexandria, VA 22312

Telephone: (800) 553-6847
Facsimile: (703) 605-6900
E-Mail: orders@ntis.gov
Online order: https://classic.ntis.gov/help/order-methods/

SAND2021-7984
Unlimited Release
Printed June 2021

Performance Evaluation of Comparative Vacuum Monitoring and Piezoelectric Sensors for Structural Health Monitoring of Rotorcraft Components

Dennis Roach, 6600
Tom Rice, 6621
Transportation Safeguards and Surety Organization

Sandia National Laboratories
P.O. Box 5800
Albuquerque, NM 87185

ABSTRACT

The costs associated with the increasing maintenance and surveillance needs of aging structures are rising at an unexpected rate. Multi-site fatigue damage, hidden cracks in hard-to-reach locations, disbonded joints, erosion, impact, and corrosion are among the major flaws encountered in today's extensive fleet of aging aircraft and space vehicles. Aircraft maintenance and repairs represent about a quarter of a commercial fleet's operating costs. The application of Structural Health Monitoring (SHM) systems using distributed sensor networks can reduce these costs by facilitating rapid and global assessments of structural integrity. The use of in-situ sensors for real-time health monitoring can overcome inspection impediments stemming from accessibility limitations, complex geometries, and the location and depth of hidden damage. Reliable, structural health monitoring systems can automatically process data, assess structural condition, and signal the need for human intervention. The ease of monitoring an entire on-board network of distributed sensors means that structural health assessments can occur more often, allowing operators to be even more vigilant with respect to flaw onset. SHM systems also allow for condition-based maintenance practices to be substituted for the current time-based or cycle-based maintenance approach thus optimizing maintenance labor.

The Federal Aviation Administration has conducted a series of SHM validation and certification programs intended to comprehensively support the evolution and adoption of SHM practices into routine aircraft maintenance practices. This report presents one of those programs involving a Sandia Labs-aviation industry effort to move SHM into routine use for aircraft maintenance. The Airworthiness Assurance NDI Validation Center (AANC) at Sandia Labs, in conjunction with Sikorsky, Structural Monitoring Systems Ltd., Anodyne Electronics Manufacturing Corp., Acellent Technologies Inc., and the Federal Aviation Administration (FAA) carried out a trial validation and certification program to evaluate Comparative Vacuum Monitoring (CVM) and Piezoelectric Transducers (PZT) as a structural health monitoring solution to specific rotorcraft applications. Validation tasks were designed to address the SHM equipment, the health monitoring

task, the resolution required, the sensor interrogation procedures, the conditions under which the monitoring will occur, the potential inspector population, adoption of CVM and PZT systems into rotorcraft maintenance programs and the document revisions necessary to allow for their routine use as an alternate means of performing periodic structural inspections. This program addressed formal SHM technology validation and certification issues so that the full spectrum of concerns, including design, deployment, performance and certification were appropriately considered.

Sandia Labs designed, implemented, and analyzed the results from a focused and statistically-relevant experimental effort to quantify the reliability of a CVM system applied to Sikorsky S-92 fuselage frame application and a PZT system applied to an S-92 main gearbox mount beam application. The applications included both local and global damage detection assessments. All factors that affect SHM sensitivity were included in this program: flaw size, shape, orientation and location relative to the sensors, as well as operational and environmental variables. Statistical methods were applied to performance data to derive Probability of Detection (POD) values for SHM sensors in a manner that agrees with current nondestructive inspection (NDI) validation requirements and is acceptable to both the aviation industry and regulatory bodies.

The validation work completed in this program demonstrated the ability of both CVM and PZT SHM systems to detect cracks in rotorcraft components. It proved the ability to use final system response parameters to provide a Green Light/Red Light ("GO" – "NO GO") decision on the presence of damage. In additional to quantifying the performance of each SHM system for the trial applications on the S-92 platform, this study also identified specific methods that can be used to optimize damage detection, guidance on deployment scenarios that can affect performance and considerations that must be made to properly apply CVM and PZT sensors. These results support the main goal of safely integrating SHM sensors into rotorcraft maintenance programs. Additional benefits from deploying rotorcraft Health and Usage Monitoring Systems (HUMS) may be realized when structural assessment data, collected by an SHM system, is also used to detect structural damage to compliment the operational environment monitoring.

The use of in-situ sensors for health monitoring of rotorcraft structures can be a viable option for both flaw detection and maintenance planning activities. This formal SHM validation will allow aircraft manufacturers and airlines to confidently make informed decisions about the proper utilization of CVM and PZT technology. It will also streamline future regulatory actions and formal certification measures needed to assure the safe application of SHM solutions

Sandia National Laboratories is a multimission laboratory managed and operated by National Technology and Engineering Solutions of Sandia, LLC., a wholly owned subsidiary of Honeywell International, Inc., for the U.S. Department of Energy's National Nuclear Security Administration under contract DE-NA0003525.

ACKNOWLEDGEMENTS

This program was sponsored by the FAA William J. Hughes Technical Center under the direction of technical program manager Paul Swindell. Research to optimize the operation and maintenance of rotorcraft requires close interaction of multiple agencies. The adoption of Structural Health Monitoring (SHM) practices to compliment or replace traditional Nondestructive Inspection (NDI) tasks accentuated the need for these ties and the program's success hinged on close cooperation among all participants. This program was formulated by the Sandia National Laboratories Airworthiness Assurance Center (AANC) – operated by Sandia Labs for the FAA - in concert with the industry team including the FAA, Sikorsky Aircraft, Structural Monitoring Systems Ltd. (SMS), Anodyne Electronics Manufacturing Corporation (AEM) and Acellent Technologies. Program planning was also conducted with the U.S. Navy to leverage similar SHM activities and interests from this agency.

This team worked to address the full range of engineering performance assessment tasks including: validation planning, test procedures, sensor design and layout, application-specific installation drawings, inspection, Damage Tolerance Analysis, data analysis, data package preparation, and plans for the formal document revisions needed for final approval of the SHM systems for use on rotorcraft. The contributions of this team are gratefully acknowledged with key engineering work produced by the following core team members: Mark Davis, Andrew Brookhart and Eric Schenck of Sikorsky Aircraft, Trevor Lynch-Staunton of AEM, Toby Chandler and Mike Reveley of SMS, Howard Chung and Susheel Yadav of Acellent Technologies, and Paul Swindell of the FAA. Important engineering guidance and program support from the following Navy participants are gratefully acknowledged: Dave Rusk and Will Milan. The authors would also like to thank the following Sikorsky Aircraft personnel who provided programmatic support, technical guidance and worked with the team to select SHM applications and move this technology toward routine use on Sikorsky rotorcraft: Avinash Sarlashkar, Jim Cycon, Nancy Held-Sheehe, Doug Tritsch, Carlos Rios, Darryl Toni, Ralph Abreu, Preston Bates, Jeff Cheung, Ide Ehigiatoe, Elin Kaiser, Elise Baker, George Schneider, Jeffrey Schaff and Matt Watson.

The authors would like to acknowledge the following AEM participants for their engineering support and management oversight of the CVM sensor design, fabrication and quality assurance: Derrick Formosa and Brian Shaigec. Special thanks goes to Clay Newton (Sandia Labs) for his assistance in SHM validation test activities. We would also like to acknowledge Acellent Technologies participants for their engineering support and management oversight of the PZT sensor design, fabrication and quality assurance: Amrita Kumar, Irene Li and Spandan Mishra.

The contributions of other FAA participants, who provided guidance and direction on all aspects of this program, are also gratefully acknowledged. Program sponsors and contributors to program planning included Mark Freisthler, Ian Won, Greg Schneider, Walt Sippel and Michael Gorelik of the FAA Transport Aircraft Directorate. Additional guidance and oversight from other FAA offices came from: Patrick Safarian (FAA Air Transport Offices), Nancy Marsh (FAA Seattle Aircraft Certification Office), and Bill Heliker (FAA Seattle Aircraft Evaluation Group; currently Aircraft Maintenance Div).

THIS PAGE INTENTIONALLY LEFT BLANK

Performance Evaluation of Comparative Vacuum Monitoring and Piezoelectric Sensors for Structural Health Monitoring of Rotorcraft Components

TABLE OF CONTENTS

LIST OF FIGURES

LIST OF TABLES

THIS PAGE INTENTIONALLY LEFT BLANK

1. BACKGROUND ON DEPLOYING STRUCTURAL HEALTH MONITORING SOLUTIONS

The aerospace industry is striving to reduce the unit acquisition and operating costs to their customers while maintaining required safety levels. To obtain this goal, manufacturers are introducing new material, production methods and maintenance technologies. Aircraft manufacturers and maintenance companies have been evaluating new technologies such as Structural Health Monitoring (SHM) to reduce long-term maintenance costs and increase aircraft availability [1.1 – 1.5]. Though well-established design and maintenance procedures exist to detect the effect of structural fatigue, new and unexpected phenomena must be addressed by the application of advanced flaw detection methods. Similarly, innovative deployment methods must be developed to overcome a myriad of inspection impediments stemming from accessibility limitations, complex geometries, and the location and depth of hidden flaws.

Health monitoring of structures is a major concern of the engineering community. This need is even more intense in the case of aging aerospace and civil structures, many of which are operating well beyond their initial design lives. The current damage tolerance design philosophy requires that a structure be capable of sustaining small damage without failure, and that an inspection program be instituted to detect such flaws before they grow to a critical size. This damage tolerance approach recognizes the impossibility of establishing complete structural redundancy – the fail-safe design premise – and places greater emphasis on inspection to ensure safety and reliability.

Multi-site fatigue damage and hidden cracks in hard-to-reach locations are among the major flaws encountered in today's extensive fleet of aging aircraft, bridges, buildings, and civil and space transport vehicles. The costs associated with the increasing maintenance and surveillance needs of aging structures are rising at an unexpected rate. Aircraft maintenance and repairs represent about a quarter of a commercial fleet's operating costs. The application of Structural Health Monitoring (SHM) systems using distributed sensor networks can reduce these costs by facilitating rapid and global assessments of structural integrity. These systems also allow for condition-based maintenance practices to be substituted for the current time-based or cycle-based maintenance approach thus optimizing maintenance labor. Other advantages of on-board distributed sensor systems are that they can eliminate costly, and potentially damaging, disassembly, improve sensitivity by producing optimum placement of sensors with minimized deployment concerns and decrease maintenance costs by eliminating more time-consuming manual inspections. Through the use of in-situ sensors, it is possible to quickly, routinely, and remotely monitor the integrity of a structure in service. This requires the use of reliable structural health monitoring systems that can automatically process data, assess structural condition, and signal the need for specific maintenance actions.

Current aircraft maintenance operations require personnel entry into normally inaccessible or hazardous areas to perform mandated, nondestructive inspections. To gain access for these inspections, structure must be removed, sealant must be removed and restored, fuel cells must be vented to a safe condition, or other disassembly processes must be completed. These processes are not only time-consuming, but they provide the opportunity to induce damage to the structure. The use of in-situ sensors, coupled with remote interrogation, can be employed to overcome

multiple inspection impediments. Furthermore, prevention of unexpected flaw growth and structural failure can be improved if on-board health monitoring systems exist that could regularly assess structural integrity. Such systems would be able to detect incipient damage before catastrophic failures occur. The ease of monitoring an entire on-board network of distributed sensors means that structural health assessments can occur more often, allowing operators to be even more vigilant with respect to flaw onset. When accessibility issues are considered, distributed sensor systems may also represent significant time savings by eliminating the need for component tear-down and by completing large area inspections quickly.

While ad-hoc efforts to introduce SHM into routine aircraft maintenance practices are valuable in leading the way for more widespread SHM use, there is a significant need for an overarching plan that will guide near-term and long-term activities and will uniformly and comprehensively support the evolution and adoption of SHM practices. The Federal Aviation Administration is addressing these issues through a series of SHM validation programs. Overall, an SHM evaluation and deployment plan must contain input from aircraft manufacturers, regulators, operators, and research organizations so that the full spectrum of issues, ranging from design to deployment, performance and certification are appropriately considered. The SHM validation and utilization program described in this data package has produced guidelines for SHM system designers or procedures for assessing the performance of SHM systems. This program, involving an OEM, airline, national lab, SHM provider and the FAA provided information and guidance that supports the adoption of SHM practices and allows the aviation industry to make informed decisions about the proper utilization of SHM. It is also being used to assess what regulatory guidance is needed to assure the safe incorporation of SHM through formal certification programs.

1.1. SHM Definition and Benefits Derived from its Use

SHM, which is often closely associated with nondestructive inspection (NDI) but which extends beyond normal NDI activities, has been defined in a wide variety of ways. Several definitions of SHM are provided below along with a definition of NDI to provide a basis of comparison and contrast.

Nondestructive Inspection (NDI) – examination of a material to determine geometry, damage, or composition by using technology that does not affect the future usefulness of the structure. Normal attributes of NDI deployment are:

- High degree of human interaction
- Local, focused inspections
- Requires access to area of interest (applied at select intervals)

Structural Health Monitoring (SHM) is the use of in-situ, mounted or embedded sensors and associated data analysis to aid in the assessment of structural or mechanical condition or system operation including the direct detection of structural flaws. The parameters to be monitored could indicate flaws directly or they could be physical properties such as load, strain, pressure, vibration, or temperature from which damage, malfunction, mechanical problems, or the need for additional investigation can be inferred.

The replacement of our present-day manual inspections with automatic health monitoring could substantially reduce the associated life-cycle costs. Motivated by these pressing needs, considerable research efforts are currently being directed towards development of health monitoring sensors and systems. Whether the sensor network is hardwired to an accessible location within the aircraft or monitored in a remote, wireless fashion, the sensors can be interrogated in a real-time mode. However, it is anticipated that the sensors will most likely be examined at discrete intervals, probably at normal maintenance checks. Figure 1-1 depicts a notional view of a sensor network deployed on an aircraft to monitor critical sites over the entire structure. Examples of some common flaws found in aircraft structure that could be monitored using SHM systems are shown in Figure 1-2.

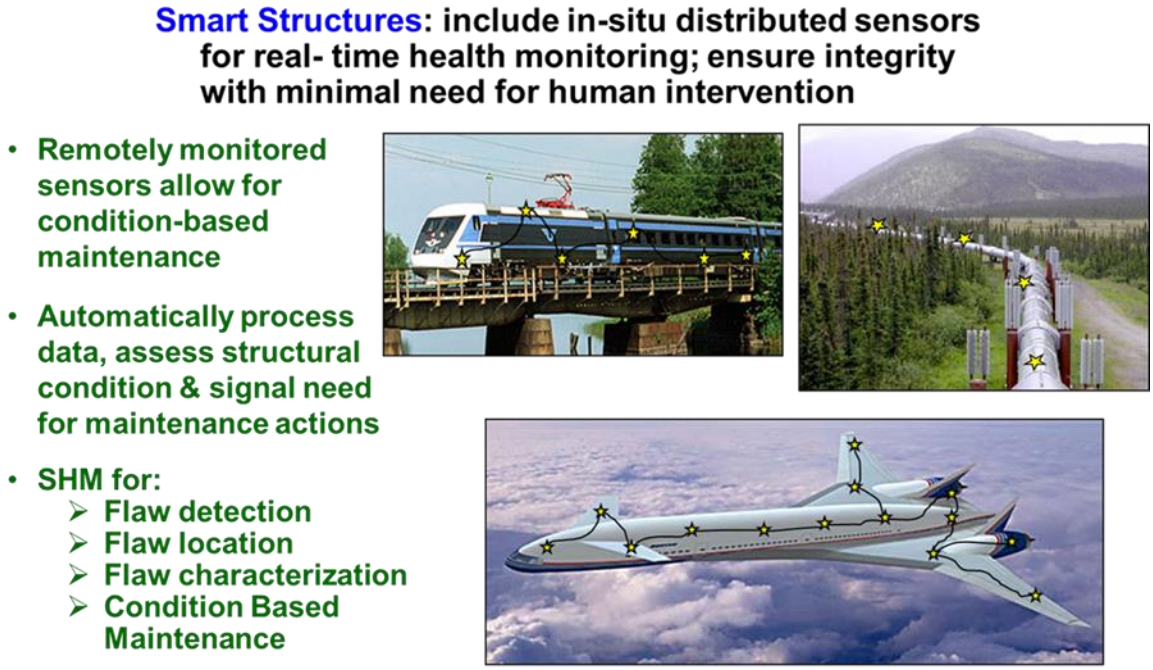

Figure 1-1. Depiction of Distributed Network of Sensors to Monitor Structural Health

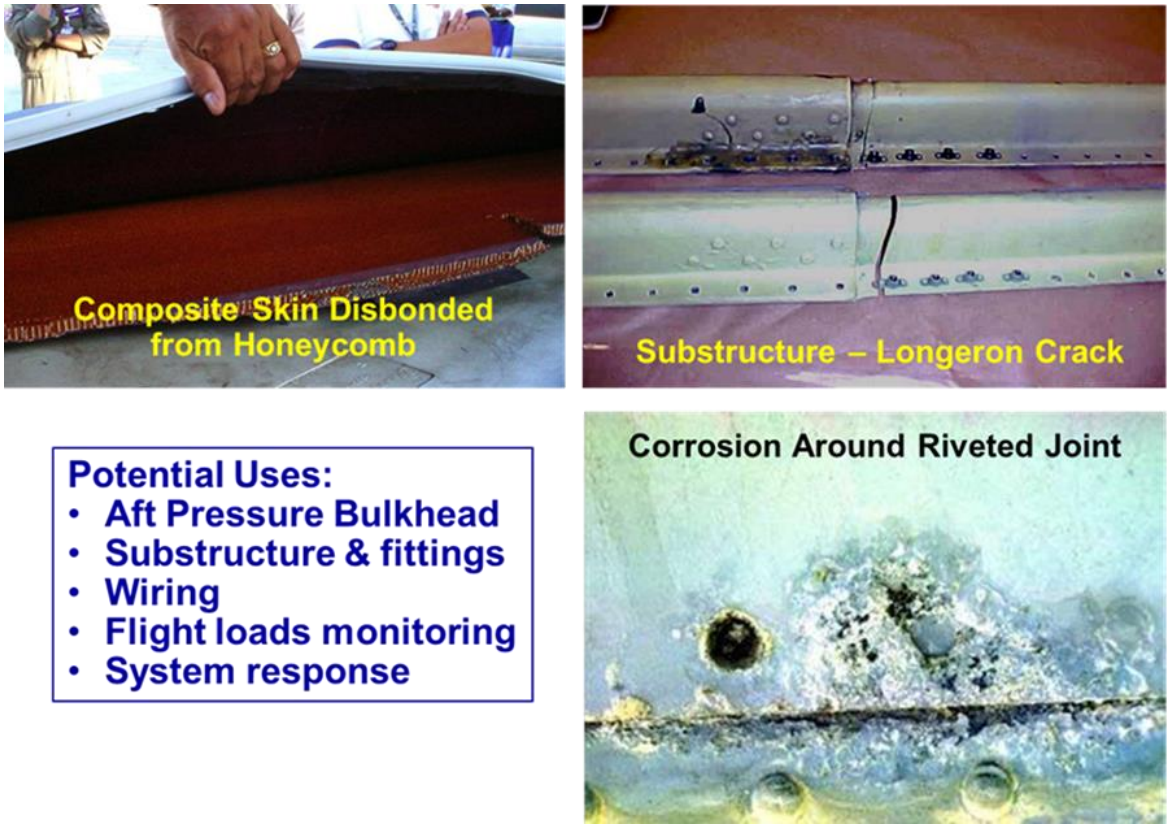

Figure 1-2. Sample Disbond, Crack and Corrosion Damage in Aircraft Structure that Could Be Monitored Using SHM Systems

A more detailed description of SHM includes:

Structural Health Monitoring (SHM) – sometimes referred to as "Smart Structures" or "Smart Systems;" involves the use of nondestructive inspection principles coupled with in-situ sensing to allow for rapid, remote, and real-time condition assessments. The sensors may record certain signatures wherein deviations from such signatures may indicate a mechanical issue which needs to be addressed. Alternately, the sensors may deterministically detect a flaw thus indicating the type of damage and location for further assessment. Such a system may be used to conduct health assessments for areas of the aircraft that have traditionally been difficult to access. SHM systems may either be used to supplement normally scheduled inspections or provide continued monitoring of a given structure.

A more succinct definition of SHM produced by the SAE Aerospace Industry Steering Committee on SHM (AISC-SHM) is:

Structural Health Monitoring (SHM) – The process of acquiring and analyzing data from on-board sensors to determine the health of a structure

There are numerous potential benefits that SHM offers regarding airplane maintenance and operation [1.1-1.11]:

Near-Term SHM Benefits

- Increased vigilance with respect to flaw onset
- Elimination of costly & potentially damaging structural disassembly
- Reduced operation and maintenance costs
- Increased availability of the aircraft fleet, by reduction of down-time after unforeseen events
- Ensure safety by identifying problems (aircraft operations, diminished structural integrity) that could threaten airworthiness
- Overcome accessibility limitations, complex geometries, depth of hidden damage
- Early flaw detection to enhance safety and allow for less drastic and less costly repairs
- Eliminate normal human factors concerns using automated, uniform deployment of SHM sensors and automated data analysis (improved sensitivity)
- Detection of blunt impact events occurring during operation
- Reduction of inspection time
- Allow for maintenance-on-demand (Condition Based Maintenance) in lieu of current time- or cycle-based maintenance practices
- Accommodate performance trend analyses and timely, possibly even pre-emptive, corrective actions.

Long Term SHM Benefits

- Optimized structural efficiency (weight savings)
- New design philosophies (SHM designed into the structure)
- In-depth assessments of operational environments to produce knowledge-based maintenance processes (Prognostic Health Management)
- Provide information to aid in-flight decisions
- Accumulate information to study performance history, automatically identify trends, and suggest corrective maintenance if necessary
- Allow for maintenance credits based on usage history and oversight provided by SHM.

In recent years, turn-key self-sufficient SHM systems have been evolved using networks of integrated sensors for the continuous monitoring, inspection and damage detection of structures to reduce labor cost and human error. Figure 1-3 summarizes some of the technology advancements that have occurred to make SHM solutions a viable alternative to traditional NDI practices. In principle, SHM in commercial airplane applications have the potential to detect structural discrepancies, determine the extent of damage, determine effects of structural usage, and eventually determine the impact on structural integrity and continued airworthiness. SHM systems can also be used to monitor loads and strain fields, or other critical environments, to better evaluate the state of the structure or mechanism.

Figure 1-4 through Figure 1-6 show the general architecture for an SHM system and how it might operate within an aircraft maintenance program. Note the use of multiple inputs to the aircraft health assessment via: 1) sensors that directly measure damage or provide pre-cursors to damage,

2) structural analyses, and 3) loads and environmental monitoring that can help guide and focus maintenance activities.

- Evolution of miniaturized sensors & supporting technology
- Design of turnkey systems with reasonable costs
- Ability to monitor new & unexpected phenomena (new inspection needs; DTA and rapid flaw growth)
- Promise for technical & economic gains more clearly defined
- OEM willingness to explore SHM merits
- Long-term prognosis -
  - Complete health assessment with network of SHM "nerves"
  - Automated data transmission (real-time monitoring; alarms)
  - Embedded sensors (MEMS)
  - Improved diagnostics using neural networks (historical data)
  - Direct ties to maintenance planning and actions
  - Reduction in life-cycle costs

Figure 1-3. Technology Advancements to Make SHM a Viable Alternative to Alternate Health Monitoring Methods

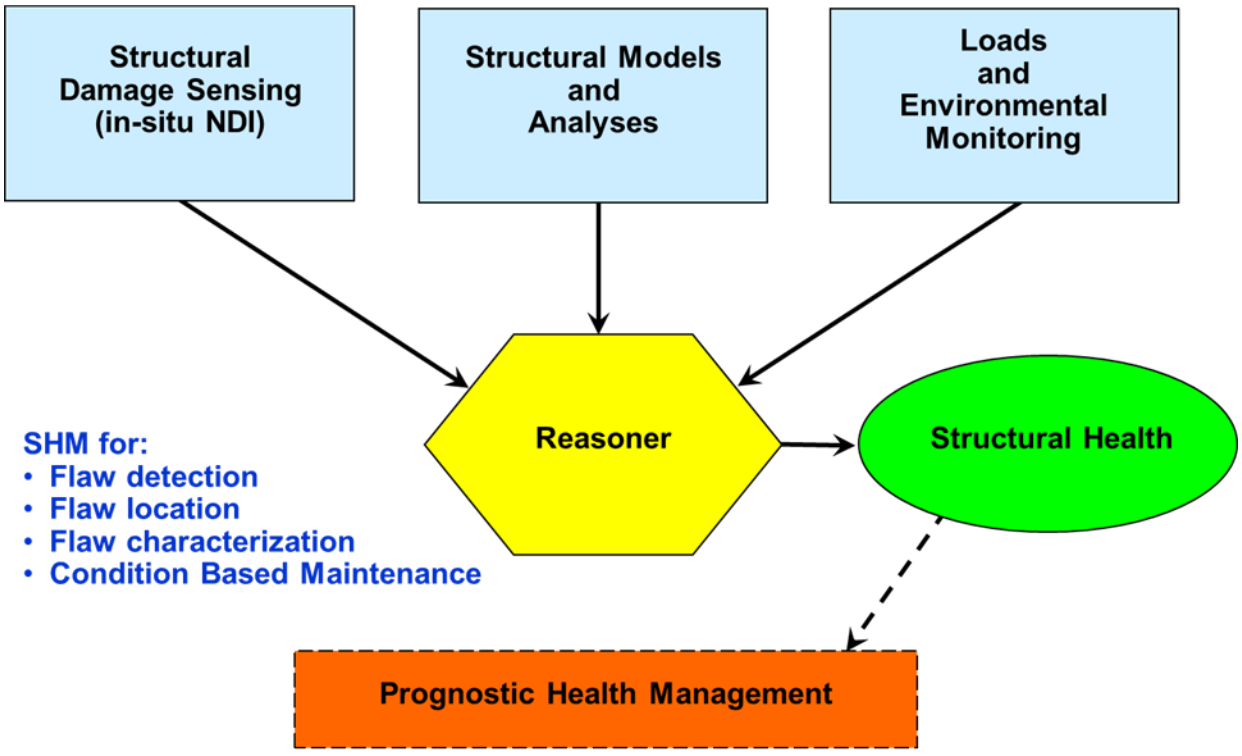

Figure 1-4. Premise of Structural Health Monitoring - Basic Operation of an SHM System within an Aircraft Maintenance Program

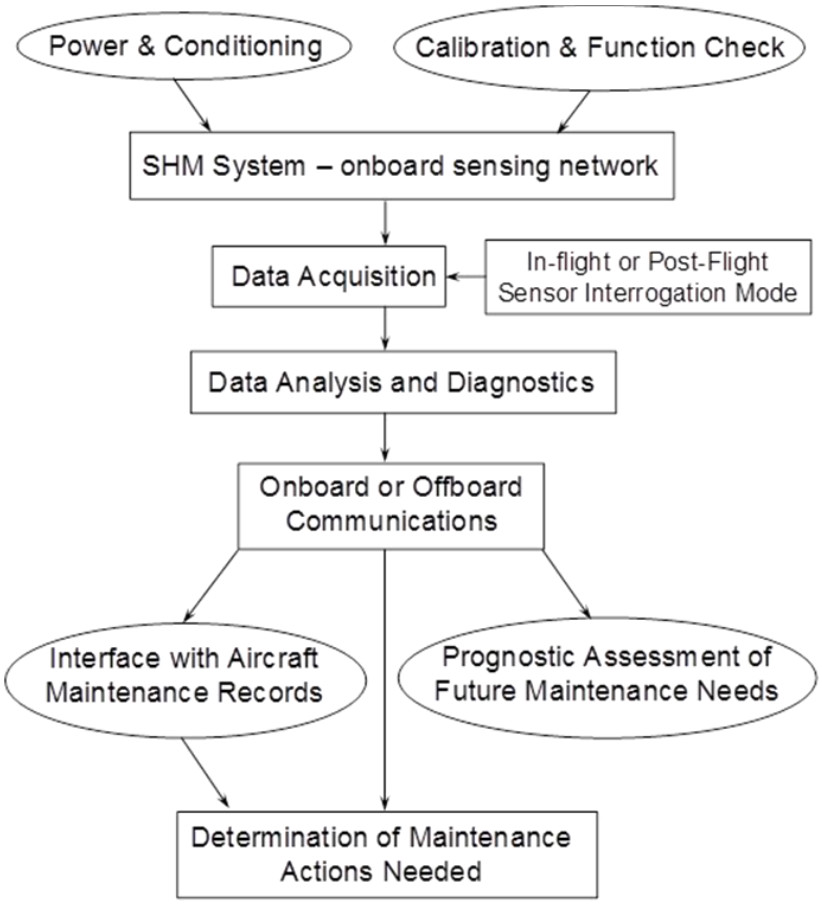

Figure 1-5. Operation of an SHM System within an Air Carrier's Maintenance Program

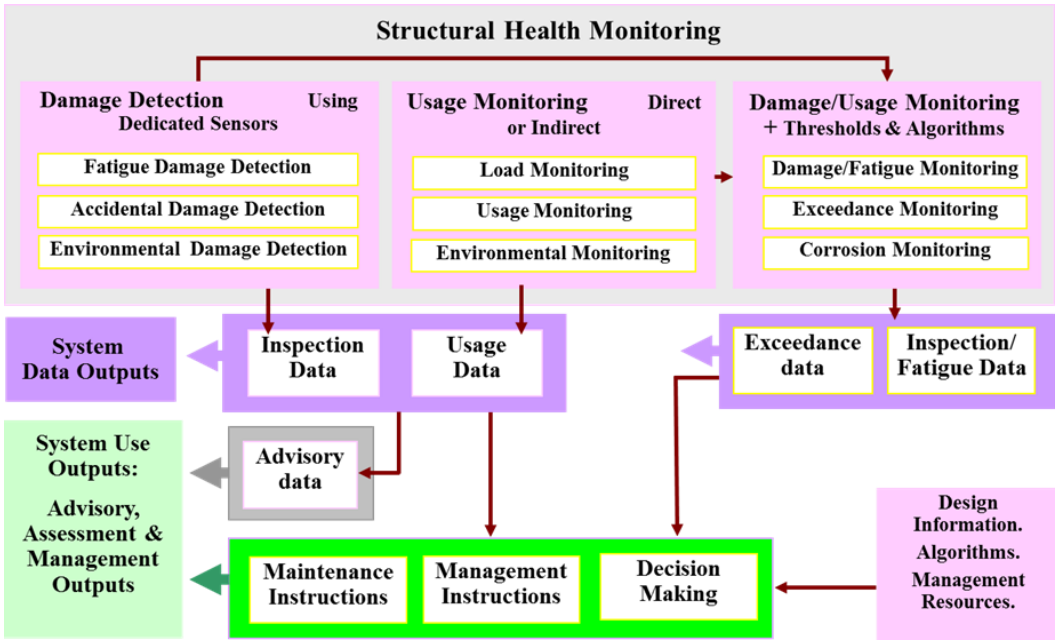

Figure 1-6. Potential Functions of SHM Systems

Figure 1-7 and Figure 1-8 show a wide range of structures from multiple industries such as oil and gas, transportation, mining, and renewable energy, where SHM solutions can address structural monitoring needs. In general, SHM sensors should be low profile, lightweight, easily mountable, durable, and reliable. To reduce human factors concerns with respect to flaw identification, the sensors should be easy to monitor with minimal need for users to conduct extensive data analysis. Figure 1-9 compares two styles of SHM sensors. The deterministic sensor can produce a signal (or change in signal) that directly indicates the presence of damage. Oftentimes, the parameter used to describe the sensor output is generally referred to as the Damage Index (DI). When the DI level exceeds a certain, predetermined threshold, the sensor is detecting damage in the structure. Other sensors may fall into the category of derivative. These type of sensors can use some well-defined structural response, such as strain, displacement or temperature to infer the presence of damage. These sensors can work equally as well as deterministic sensors for SHM applications, however, additional testing and calibration is required to properly relate their output to structural damage. Figure 1-10 provides several examples of mountable, in-situ SHM sensors.

Figure 1-7. Sample Structures Showing a Wide Range of Uses for SHM Systems (Part A)

Figure 1-8. Sample Structures Showing a Wide Range of Uses for SHM Systems (Part B)

Deterministic sensors produce direct flaw detection & flaw growth

Examples: CVM, EC, cMUT, Corrosion, Fiber Optics, PZT

Derivative sensors require calibration & produce indicators (follow-up NDI needed)

Examples: Force, Accelerometer, Temperature, Pressure, Strain

Load Cells - Load monitoring could be used for design credits (structural optimization) and/or operation credits (modify maintenance program)

Strain Sensors – Can determine excess strain levels but subsequent NDI visit is required to determine if strain readings correlate to damage

Figure 1-9. Deterministic vs. Derivative Sensors for Health Monitoring Applications

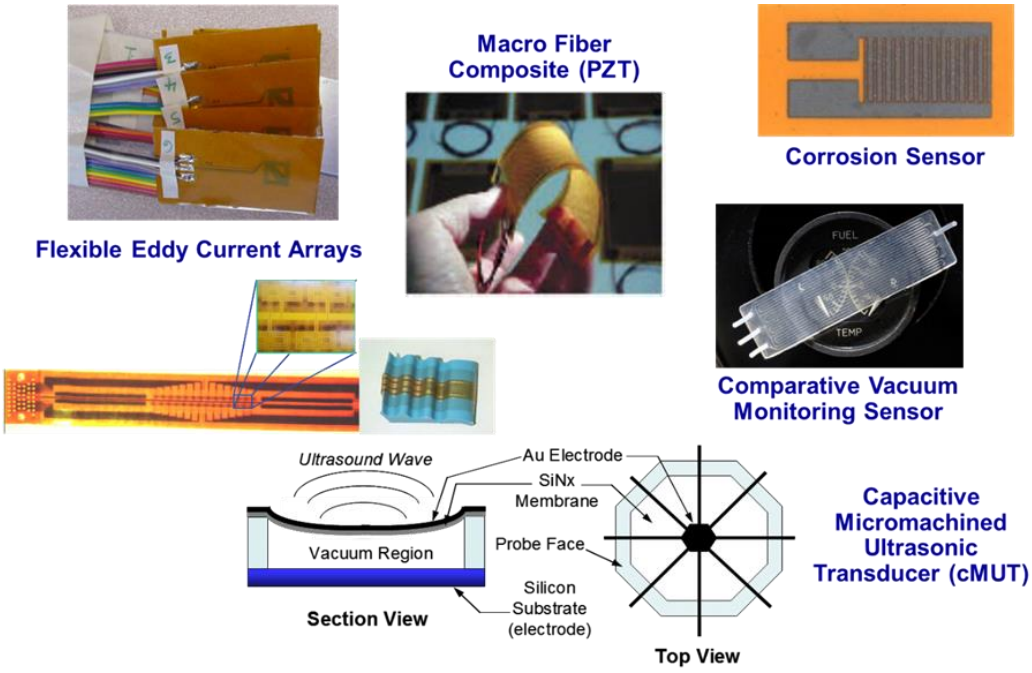

Figure 1-10. Examples of SHM Sensors

For optimum performance of the in-situ sensor-based approaches, the signal processing and damage interpretation algorithms must be tuned to the specific structural interrogation method. Initial research has highlighted the ability of various sensors to detect common flaws found in composite and metal structures with sensitivities that could exceed current flaw detection requirements, if needed. Use of SHM solutions in routine maintenance activities can only be achieved by overcoming the basic obstacles listed in Figure 1-11. Programs such as the one described here and many other evolution and validation efforts underway within the SHM community have addressed these potential roadblocks and have created an environment where the application of SHM systems is possible. Completed validation programs at the Sandia Labs AANC – conducted jointly with aircraft manufacturers and airlines – worked to integrate SHM sensors into aircraft maintenance programs. These evaluations incorporated both cost-benefit analyses, as well as statistically-derived performance reliability numbers.

Whether the sensor network is hardwired to an accessible location within the aircraft or monitored in a remote, wireless fashion, the sensors can be interrogated in a real-time mode. However, it is anticipated that in the monitoring of SHM sensors will most likely be at normal maintenance checks. The important item to note is that the ease of monitoring an entire network of distributed sensors means that structural health assessments can occur quickly and in an automated fashion [1.12 – 1.16].

- Cost of sensors and sensor systems
- Ease of use and coverage area
- Need for rapid customization of sensors
- Need for substantial business case (cost-benefit analysis) – operators must realize benefits of multi-use
- OEMs may need to own technology
- Small-scale damage must be detected in large-scale structures
- Validation activities – general performance assessments needed; reliability of SHM systems must be demonstrated
- Validation activities – field trials on operating aircraft is necessary but time consuming
- Certification – need to streamline specific applications; technical, educational and procedural initiative (OEMs, operators, regulators)
- Standardization needed for validation and certification activities
- Technology transfer and implementation requires changes in maintenance programs

Figure 1-11. Impediments and Challenges to SHM Deployment

Several SHM sensors have been demonstrated to reliably detect damage both in the laboratory environment and in commercial applications. One example of a more mature sensor that can detect cracks and structural defects is the Comparative Vacuum Monitoring (CVM) sensor. A number of organizations have been investigating and demonstrating the use of CVM as a means for inspecting certain commercial airplane applications [1.8, 1.17 - 1.22]. In the CVM applications studied to date, the CVM technology is a permanently mounted nondestructive damage detection sensor that can be queried at the same inspection intervals as the currently accepted NDT methods. The advantage of the CVM in this case is that the inspected structure only needs to be accessed once for CVM installation. Afterward, the area is inspected by remotely connecting to the CVM without need for structural teardown. This program involved a detailed investigation into CVM technology with an emphasis on a specific aircraft application and a desire to produce approved, routine use of this SHM solution.

The interest in SHM has risen dramatically in recent years. Driven by the potential for both technical and economic benefits, OEMs and airlines currently have groups of engineers engaged in developing and applying SHM solutions to aircraft monitoring needs. Figure 1-12 shows a summary of just some of the agencies that are studying the integration of SHM into routine aircraft maintenance. Figure 1-13 shows several, traditional hand-deployed NDI equipment along with the signals generated during the inspections. It highlights some of the challenges associated with signal interpretation that can be simplified using SHM systems.

Figure 1-12. Sample Organizations within the Aviation Community that are Studying the Integration of SHM into Routine Aircraft Maintenance

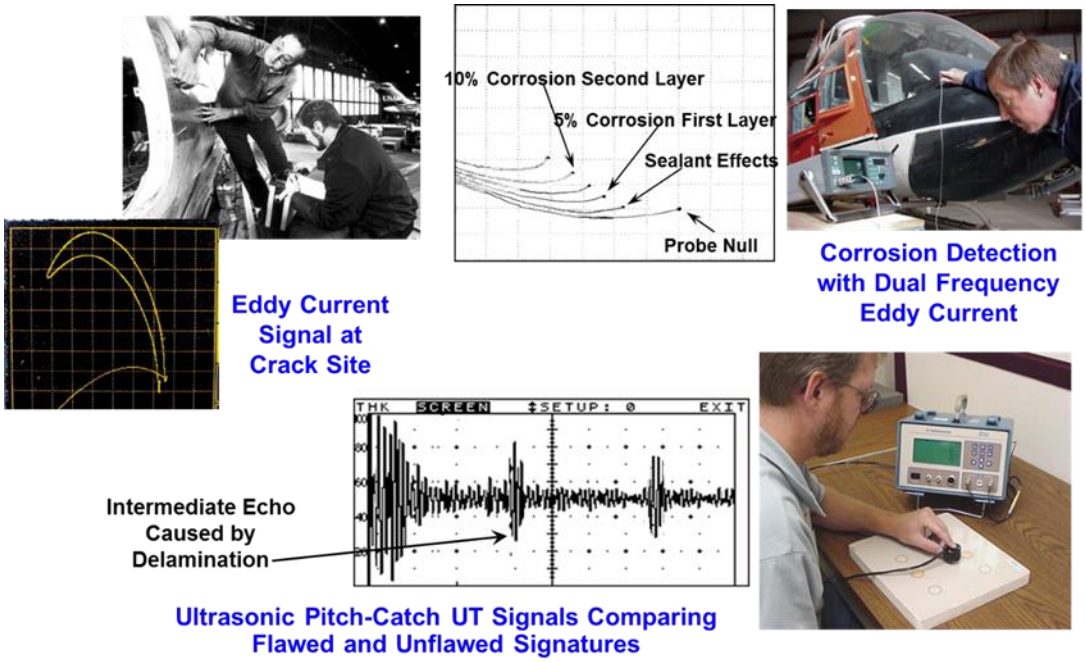

Figure 1-13. Typical A-Scan Signals Used for Flaw Detection with Hand-Held NDI Devices Highlighting Signal and Human Factors Challenges Associated with Current NDI Deployment

1.2. Industry Survey and Insight on Potential SHM Usage

An important element in developing and applying SHM solutions for the aviation industry is a clear understanding of the current status of SHM technology and the pending regulatory issues facing the aviation industry to safely adopt SHM practices. To acquire such information, the AANC used a survey to collect information on industry interest in deploying SHM solutions. The comprehensive survey, implemented with the aviation industry, determined the technology maturation level of SHM, identify integration issues, and prioritize research and development needs associated with implementing SHM on aircraft. The survey was implemented via a customized, on-line web site and was sent to persons involved in the operation, maintenance, inspection, design, construction, life extension, and regulation of aircraft as summarized in Figure 1-14. Specific emphasis was placed on structural and maintenance characteristics that may impact the operational performance of an inspection process or health monitoring system. Over 450 people responded to the survey to provide industry information on SHM deployment and utilization, validation and certification, SHM standardization, sensor evolution and operation, cost-benefit analysis, and SHM system description. The survey results were initially used by the FAA to identify and prioritize research and development needs associated with implementing SHM on aircraft.

Below are just a few results excerpted from the in-depth presentation of the overall results obtained from the SHM Industry Survey [1.23]. Overall, it was determined that there is a strong interest in SHM. Industry's main concerns with implementing SHM on aircraft are achieving a positive cost-benefit and the time to obtain approval for SHM usage. OEMs and airlines felt that research and development efforts should be focused on: global systems, sensor technology, system validation and integration, and regulatory guidance. In addition, they felt that standardization and guidelines are needed in validation, certification, and sensor design with aviation in mind.

Over 200 applications, covering all aircraft structural, engine, and systems areas, were identified. The 80 applications provided as the respondent's first selection are listed below. The main trends of potential SHM applications include: general damage detection and crack detection in structural members, corrosion detection and coating monitoring, hard landing, load monitoring, impact detection and indication, hot spot monitoring, bolt tightness monitoring, strain levels, heat damage, monitoring of fuselage door and window areas, bond monitoring, delamination in composite structures, monitoring of existing cracks, monitoring fuselage skin repairs and flaw detection in difficult-to-inspect/access areas.

Figure 1-15 shows that most respondents think SHM is a viable alternative to nondestructive testing. More than half of respondents think 5 years is a reasonable timeframe to recoup the costs of an SHM system while almost 1/3 of the respondents felt that 2 years was reasonable. Figure 1-16 shows that over 50 percent of respondents think that all primary structural areas are candidates for SHM applications: fuselage pressure bulkhead, frames, stringers, wing ribs and spars, landing gear, main attachments and skin areas. In fact, there were no aircraft regions that received insignificant responses. Aircraft systems where respondents are less interested in implementing SHM were power train and nonstructural systems.

Owners/Operators	OEMs	Regulators	Maintainers
All Nippon Airways American Airlines Austrian Air Force China Airlines Continental Airlines Delta Air Lines Federal Express Finnair Hawaiian Airlines Japan Airlines Jazz Airlines Jet Blue Airways Kalitta Air LLC NASA Qantas Airways Singapore Airlines Swiss Air United Airlines US Airways USAF US Army USCG US Navy	Airbus Astronics-Adv. Electronic Systems Avensys Inc. BAE systems Bell Helicopter Textron Boeing Bombardier Aerospace Cessna Aircraft Company Dassault Aviation EADS Military Air Systems Embraer Goodrich Honeywell Lockheed Martin Aeronautics Messier-Dowty Mistras Group, Inc Polskie Zaklady Lotnicze Sp. PZL Swidnik Rolls-Royce Corp Systems & Electronics, Inc. TecScan	Air Transport Association CAA - NL CAA - Bra EASA FAA NAVAIR NAWCAD Transport Canada (TCCA) USAF US Army USCG US Navy	Aerotechnics Inc Air New Zealand China Airlines Christchurch Engine Centre Fokker Aircraft Services B.V. Fuji Heavy Industries, Ltd. Jazz Air LTD Lufthansa Technik AG NASA Olympic Airways Services S.A. SAA Technologies SR Technics Switzerland LTD Texas Aero Engine Services Timco / GSO United Airlines USAF US Army USCG US Navy

Over 450 responses from OEMs, regulators, operators, and research organizations.

Figure 1-14. SHM Survey of Aviation Industry to Gage Interest and Range of Applications for SHM

First SHM Application Listed by Survey Respondents:

1. Overload monitoring and detection
2. Overload monitoring
3. Bolt torque monitoring
4. Debonding detection and assessment in specific areas
5. Hard /heavy landing
6. Impact damage detection
7. Airframe monitoring
8. Door hinge area
9. Corrosion detection
10. Anything that reduces operating costs
11. Key hot spots (locations that are known to develop damage and require additional inspections
12. Moisture detection in wet areas (galley, lavatory etc.)
13. Landing gear overload detection
14. Corrosion detection
15. Composite structures (delamination and other damage)
16. Areas that require disassembly for routine inspection
17. Composites

18. Monitor moisture in corrosion prone areas
19. Crack detection in structural critical areas, with the evaluation of crack length or other parameter to assess criticality
20. Leading edge composite disbond
21. Inaccessible areas that require major tear down
22. Fiber breakage and delamination in composite structures
23. Monitoring known crack locations
24. Crack growth monitoring in difficult to access regions of airframe as an AMOC to manual inspection.
25. SHM of UAV composite structures
26. Crack detection in high load areas such as door cutout
27. Wing lug attach fittings
28. Landing gear attach points
29. Impact detection
30. Propagation rates of disbond/delamination of composites
31. Around fuselage doors cutout
32. Fuselage door
33. B747
34. Repair and bonded patches
35. Corrosion prevention, detection and sizing
36. Delaminations on hidden areas of honeycomb flight control structure
37. Primary structures
38. Structural damage
39. Cracks in lap-splice joints
40. Composites damage
41. Monitoring for impact damage during aircraft operation due to bird, tree, hail strike
42. Hot spots
43. Conventional NDI replacement
44. CRJ - 559 area
45. Aging aircraft with known structural health issues
46. No access (costly access) structure
47. Corrosion detection
48. Stabilizer shim migration
49. Cracks in the airframe
50. Composite structures that may get heat damaged, inner fixed structures of thrust reverser
51. Fuselage skin
52. Aft pressure bulkhead
53. Commercial aircraft
54. Compressor and turbine blades (tip timing method)
55. Frames
56. Landing gear fittings
57. Tension bolts
58. Tail-strike indicator (already in use on A340+A380)
59. Structural cracking
60. Bonded structures monitoring
61. Rotor vibration monitoring

62. Lightning hit damage detection at the location where access is difficult (e.g. top of fuselage, vertical and horizontal stabilizers)
63. Any difficult-to-access location
64. Hard landing detection
65. Corrosion in hard to access areas in bilge
66. Structure integrity in load carrying composite structures
67. Fuselage skin
68. Heavy landing event monitoring
69. Structural fatigue
70. Closed areas with no access to either side
71. Cracks in pressure bulkheads
72. Fuselage skin crack detection
73. Frame shear angles.
74. Corrosion detection
75. Monitoring structural repairs
76. Critical bolts (hot spots) - small cracks
77. Crack detection in metallic components
78. Corrosion assessment in bays
79. Multilayer crack detection at fastener holes
80. Flight control abnormal loading

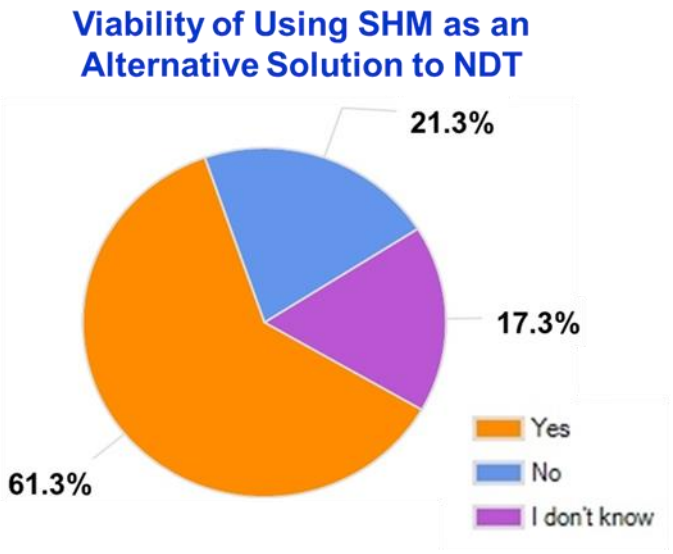

- **55% of aircraft operators, maintainers, and military personnel say that 5 years is a reasonable payback period for recouping the cost associated with using an SHM system**
- **31% say 2 years is reasonable**

Figure 1-15. Survey Results Indicating that Most Airlines are Interested in Using SHM

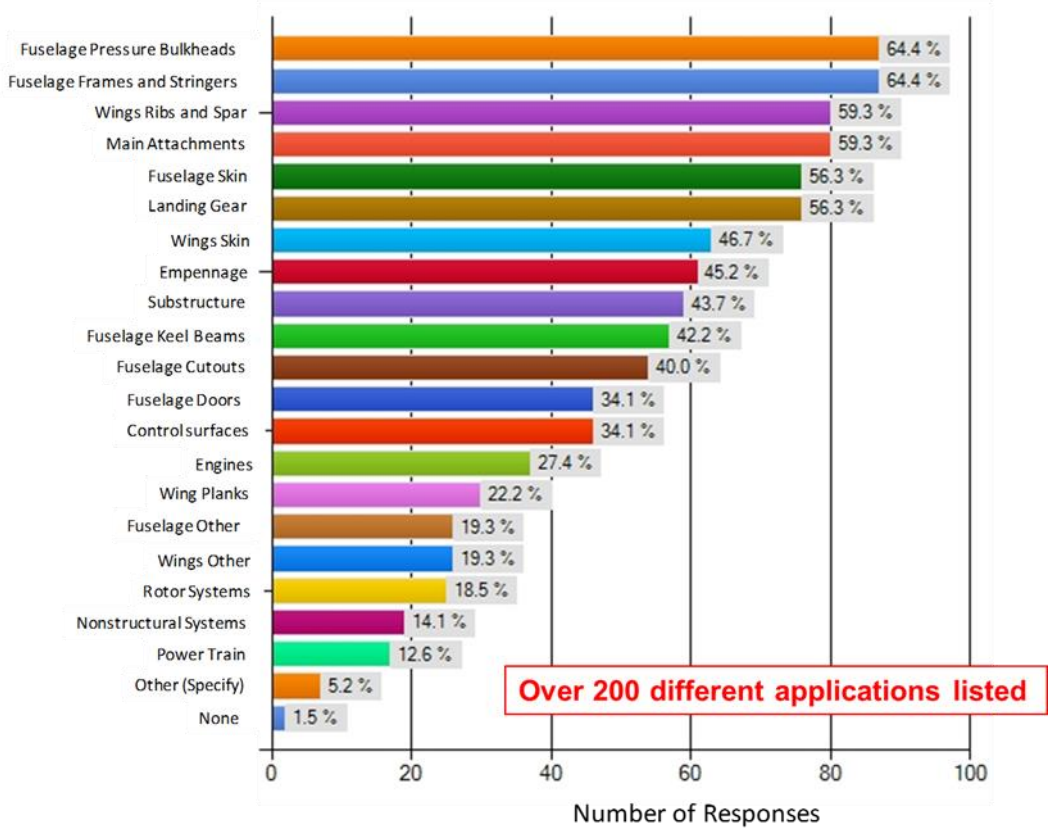

Figure 1-16. SHM Survey Result - Areas Respondents Feel SHM Solutions are Viable

Figure 1-17 summarizes the types of damage/flaws the industry is interested in detecting. It's not surprising that a large majority of the persons surveyed were interested in detecting the major damage types found on aircraft: cracks, corrosion, delaminations and disbonds. Related damage from stress risers, impact, fluid ingress, and other environments are also cited often. Damage associated with composites, exposure, mechanical malfunction and off-design conditions (e.g. ground support activities) were also listed. Overall, the potential damage and malfunctions where respondents would like to utilize SHM covered a very broad spectrum of applications with the majority of the damage types being listed by over 1/3 of the survey participants.

In the next five years, many of the systems being planned for application are local or hot spot monitoring systems. Figure 1-18 shows that 85% of those surveyed anticipate applying local systems and only 15% believe that global (wide area) SHM systems will be applied within the five year time frame. In the survey, local implies focused evaluation of specific areas that currently require local inspections; often associated with a Detailed Visual Inspection or a Special Detailed Inspection. Global implies evaluation of large areas such as control surfaces or fuselage panels; often associated with a General Visual Inspection or some wide-area NDI task

Figure 1-19 shows that the main reasons respondents are interested in SHM are associated with cost considerations (e.g. avoiding disassembly, reduction in labor hours) and safety/reliability considerations (e.g. early flaw detection, improved sensitivity). Another item of note is that almost

all of the possible reasons for using SHM were listed in over 1/3 of the survey responses. Reasons that were deemed as less important pertained to obtaining maintenance credits, design credits or weight savings, and monitoring electrical and aircraft systems. These are mostly long-term prospects for SHM so it is not surprising that these are currently of less interest to end-users.

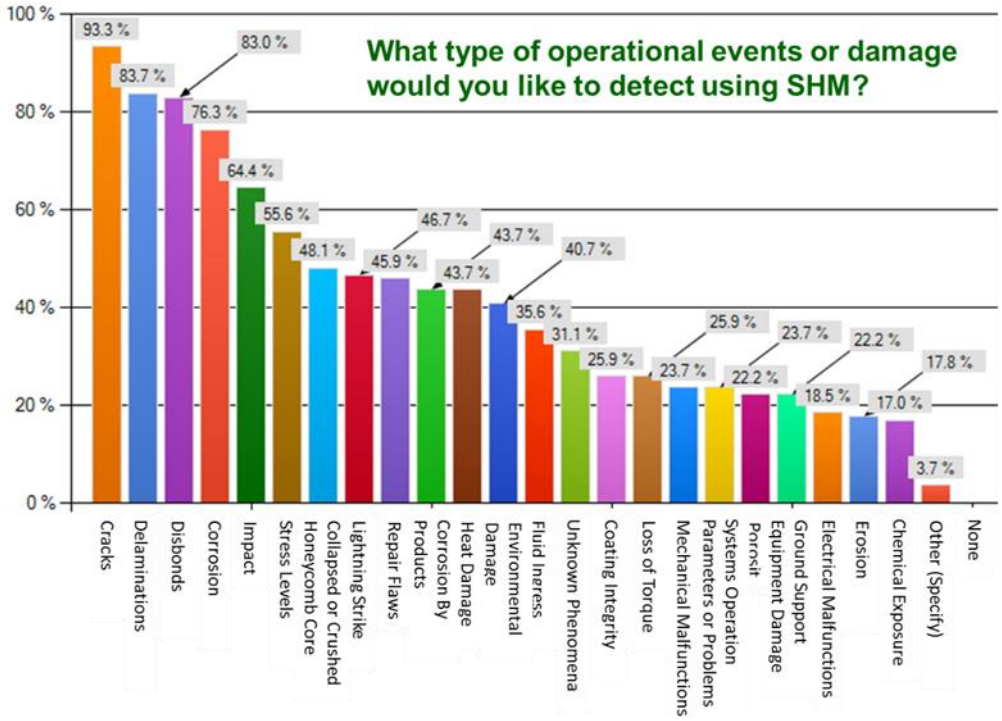

Figure 1-17. SHM Survey Results Listing the Damage that Users Would Like to Detect

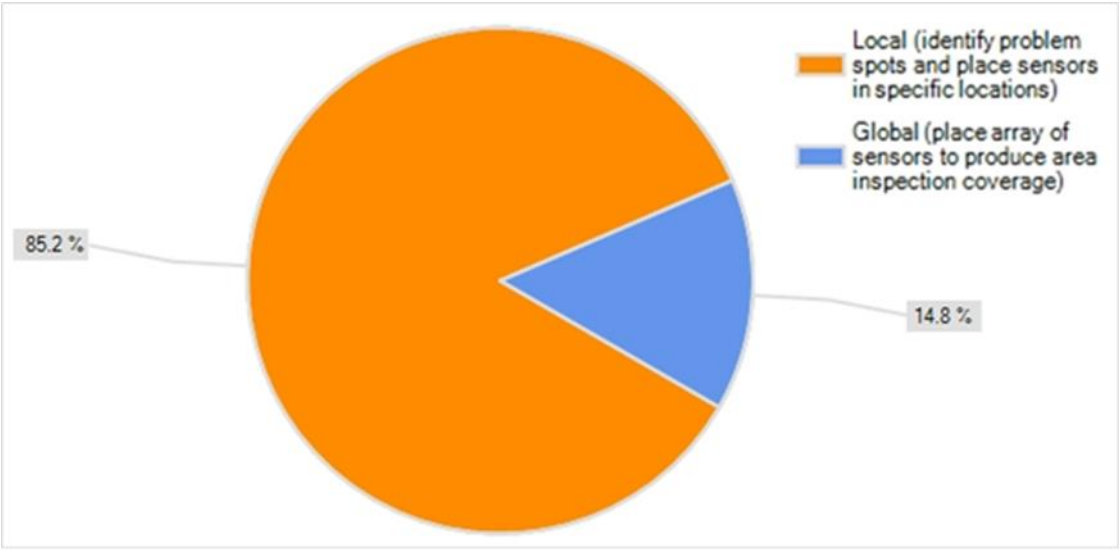

Figure 1-18. Type of SHM Expected to be Deployed in the Near-Term

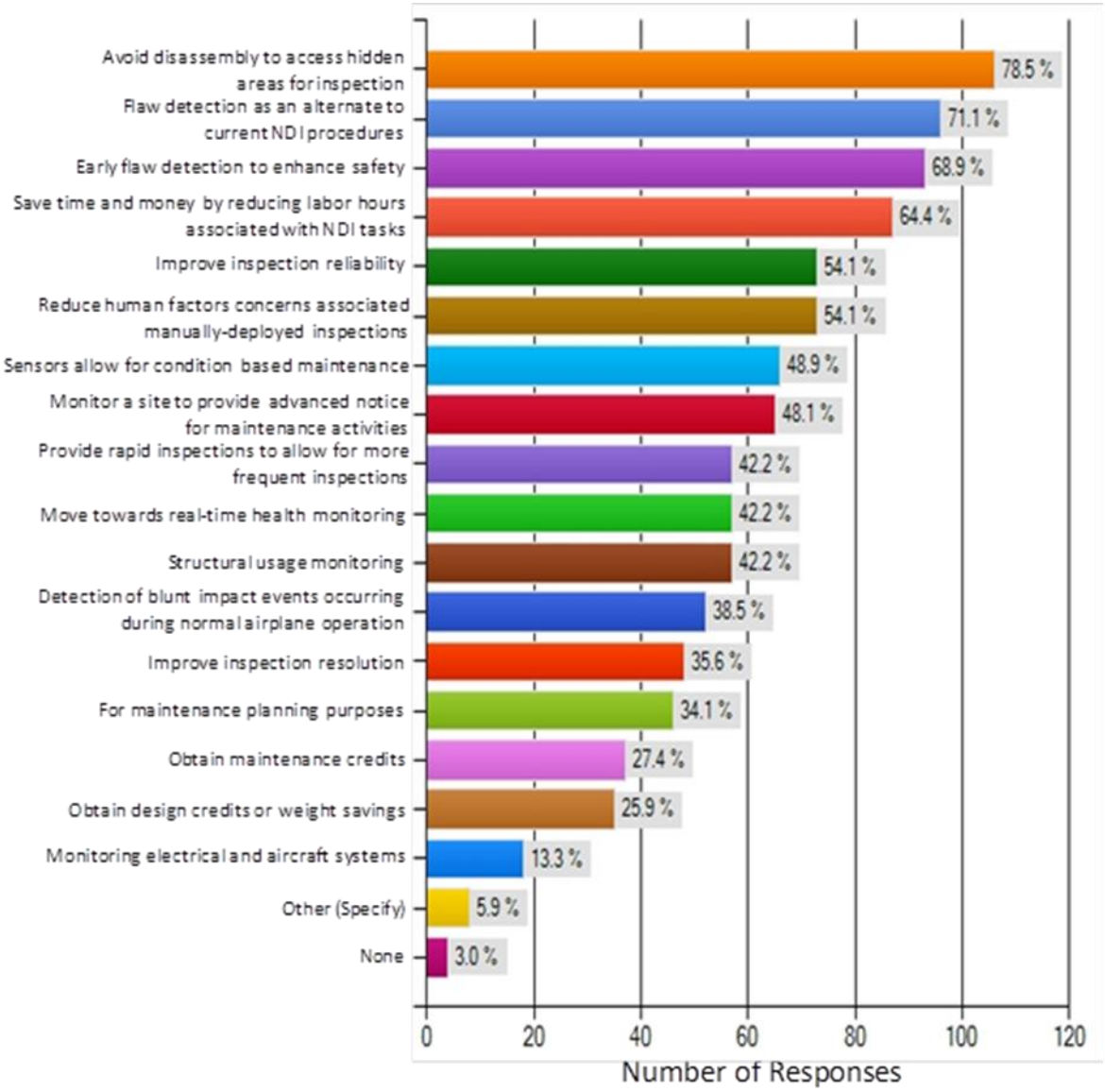

Figure 1-19. Respondents Reasons for Interest in SHM

Table 1-1 contains the prioritized list of the most important items in determining the cost-benefit of using SHM systems on an aircraft. The most important factor (52% had it as a response priority of 5) is the elimination of structural tear down to access areas to be monitored. Other items receiving at least 30% response level and a priority of 4 or 5 include: initial cost of SHM equipment, recurring cost of SHM sensors, time required for validation/qualification, time required to obtain permission for use from regulators, compliance requirements, and the frequency that the SHM system will be used.

Table 1-1. Most Important Items for Determining the Cost-Benefit of Implementing an SHM Solution

What are the most important items when considering the cost-benefit of implementing an SHM solution?(prioritize with 1 being lowest and 5 being highest priority)					
Answer Options	**1**	**2**	**3**	**4**	**5**
Initial cost of SHM equipment	4%	7%	24%	35%	30%
Recurring cost of SHM sensors	0%	10%	28%	40%	22%
Replacing existing inspections with more rapid monitoring	1%	13%	29%	31%	26%
Elimination of structural teardown to access a region to be monitored	0%	1%	21%	25%	52%
Frequency of potential SHM utilization (inspection intervals)	1%	4%	43%	31%	19%
Cost of validation	4%	6%	37%	27%	27%
Cost of qualification	3%	8%	33%	29%	26%
Time required for validation/qualification	3%	9%	32%	35%	21%
Compliance requirements – existing or future needs	0%	13%	28%	34%	24%
Time required to obtain permission for use from OEM	1%	9%	46%	28%	16%
Time required to obtain permission for use from regulators	3%	6%	32%	33%	26%
Training required for maintenance personnel	7%	27%	37%	19%	9%
Need to adjust maintenance program to accommodate SHM	7%	20%	29%	29%	16%

References

1.1. Brand, C., Boller, C., "Identification of Life-Cycle Cost Reductions in Structures with Self Diagnostic Devices," RTO AVT Specialist Meeting on Design for Low Cost Operation, February 2006.

1.2. Sun J., Chen, D., Li, C., and Yan, H., "Integration of Scheduled Structural Health Monitoring with Airline Maintenance Program Based on Risk Analysis," Journal of Risk and Reliability, Vol. 232, January 2018.

1.3. Dong, T., and Kim, N., "Cost-Effectiveness of Structural Health Monitoring in Fuselage Maintenance of the Civil Aviation Industry," Aerospace Journal, August 2018.

1.4. Sbarufatti, C., Manes, A., Giglio, M., "Application of Sensor Technologies for Local and Distributed Structural Health Monitoring," Structural Control and Health Monitoring, Volume 21, Issue 7, December 2013.

1.5. Rulli, R., Dotta, F., Prado, G., Roach, D., Rice, T., "Advancements on the Adoption of SHM Damage Detection Technologies into Embraer Aircraft Maintenance Procedures," International Workshop on Structural Health Monitoring, September 2017.

1.6. Speckmann, H., Roesner, H., "Structural Health Monitoring: A Contribution to the Intelligent Aircraft Structure," European Congress on Nondestructive Testing, September 2006.

1.7. Roach, D., Use of distributed sensor systems to monitor structural integrity in real-time, Quality, Reliability, and Maintenance in Engineering, Professional Engineering Publishing Ltd., Oxford, UK, 2004.
1.8. Roach, D., Rackow, K., "Health Monitoring of Aircraft Structures Using Distributed Sensor Systems," DoD/NASA/FAA Aging Aircraft Conference, March 2006.
1.9. Niblock, T., Mian, M., Clements, R., "Advanced Sensing, Degradation Detection, Diagnostic and Prognostic Capabilities for Structural Health Management," Stanford Int'l Workshop on Structural Health Monitoring, September 2009.
1.10. Boller, C., Chang, F-K, Yozo, F., "Encyclopedia of Structural Health Monitoring," ISBN 9780470058220, John Wiley & Sons, Ltd., 2009.
1.11. Kim, S., Frangopol, D., "Optimal Decision Making for Cost-Effective SHM Planning," International Workshop on Structural Health Monitoring, September 2019.
1.12. Roach, D., "Validation and Verification Processes to Certify SHM Solutions for Commercial Aircraft Applications," Structural Health Monitoring, DEStech Publisher, Lancaster, PA, September 2013.
1.13. Mandache, C., Genest, M., Khan M., Mrad, N., "Considerations on Structural Health Monitoring Reliability, International Workshop on Smart Materials, Structures & NDT in Aerospace, Nov 2011.
1.14. Lindgren, E., "An NDE perspective on SHM: Some Personal Observations", Aircraft Airworthiness and Sustainment Conference, April 2011.
1.15. Giurgiutiu, V., and Cuc, A., "Embedded Non-Destructive Evaluation for Structural Health Monitoring Damage Detection, and Failure Prevention," The Shock and Vibration Digest, Vol. 37, No. 2, March 2005.
1.16. Rulli, R., Dotta, F., Anchieta, P., "Flight Tests Performed by Embraer on SHM Systems," Advanced Materials Research, Vol. 764, September 2013.
1.17. Loader, C., "Durability of Continuous Vacuum Monitoring Sensor for ADF Applications," Defense Science and Technology Organization Report DSTO-CC-Q1694/01, 2004.
1.18. Roach, D., "Real Time Crack Detection Using Mountable Comparative Vacuum Monitoring Sensors," *Journal of Smart Structures and Sensors,* Vol. 5, No. 4, July 2009.
1.19. Stehmeier, H., and Speckmann, H., "Comparative Vacuum Monitoring of Fatigue Cracking in Aircraft Structures," 2nd European Workshop on Structural Health Monitoring, July 2004.
1.20. Xiachua, L., Hongfu, Z., "A New Technology of Aircraft Structural Health Monitoring," J. of Advanced Materials Research, Vol. 764, September 2013.
1.21. Roach, D., "Use of Comparative Vacuum Monitoring Sensors for Automated, Wireless Health Monitoring of Bridges and Infrastructure," Proceedings of the 9th International Conference on Bridge Maintenance, Safety and Management, July 2018.
1.22. Rulli, R., Dotta, F., Anchieta, P., "Flight Tests Performed by Embraer on SHM Systems," Advanced Materials Research, Vol. 764, September 2013.
1.23. Roach, D., Neidigk, S., Smith, B., "Utilization of Structural Health Monitoring Solutions and Recommendations for the Federal Aviation Administration's SHM Research and Development Program," Dept. of Transportation Report DOT/FAA/AR-14/92, November 2014.

THIS PAGE INTENTIONALLY LEFT BLANK

2. ROTORCRAFT SHM PROGRAM OVERVIEW

Multi-site fatigue damage, hidden cracks in hard-to-reach locations, disbonded joints, erosion, impact, and corrosion are among the major flaws encountered in today's rotorcraft structures. Rotorcraft structure is greatly influenced by the loads of the dynamic components. The cracking tends to be a result of high cycle fatigue and tends to fail in very short intervals after crack onset. Unique flaw onset, coupled with new and unexpected phenomena, have placed greater demands on the application of advanced nondestructive inspection (NDI) and health monitoring techniques. In addition, innovative deployment methods must be employed to overcome a myriad of inspection impediments stemming from accessibility limitations, complex geometries, and the location and depth of hidden damage.

A Health and Usage Monitoring System (HUMS) records the status of critical systems and components on helicopters so that the early detection of progressive defects, or indications of them, is possible and thus rectification can be achieved before they have an immediate effect on operational safety. A basic system collects some usage parameters such as take-offs, landings, engine starts and winch lifts as well as a small subset of engine and transmission health data. The most modern systems monitor the health of all significant vibrating and spinning parts such as engines, gearboxes, shafts, fans, rotor systems. The use of in-situ sensors for health monitoring of all other rotorcraft structures appears to be a viable option for both flaw detection and maintenance planning activities. Local sensors can be used to directly detect the onset of crack, corrosion, or disbond flaws. Detection of unexpected flaw growth and structural failure could be improved through the use of health monitoring systems that assess structural integrity. Reliable, structural health monitoring systems can automatically process data, assess structural condition, and signal the need for human intervention.

In order to optimize results and streamline the integration of SHM solutions for rotorcraft, this program involved collaboration between the FAA-AANC at Sandia Labs and Sikorsky Aircraft, and the U.S. Navy. The joint portion of the FAA-AANC-Sikorsky-Navy SHM research effort leveraged the ongoing Navy Airframe Risk and Reliability studies along with SHM-related R&D initiatives in many rotorcraft systems including drive systems, structures, propulsion, dynamic components, electrical and wiring, and flight control and hydraulics. This effort demonstrated several viable SHM systems utilizing proven sensors to detect representative rotorcraft structural damage and a model for the inclusion of structural health data into HUMS-based decision making processes. Efforts to move the proposed system through the certification process including Alternate Means of Compliance (AMOC), addition to Service Bulletins, and the accrual of potential maintenance credits was investigated. Activities focused on the SHM portion of HUMS while also looking at the big picture of blending SHM information with usage monitoring to produce a more informed, comprehensive rotorcraft maintenance approach.

The activities described here were completed to meet the overall objectives: 1) develop a strong background knowledge in HUMS hardware and associated integration of sensors and coordination of work tasks with industry collaborators, 2) evolve the certification process and develop SHM system validation methods through specific SHM application efforts, 3) prove SHM concepts through specimen design and lab testing, and 4) explore the integration of an SHM system into HUMS to evaluate the added structural damage feature in a HUMS system.

The initial phase of the program was dedicated to specific task and SHM application definition through more detailed interaction with Sikorsky. Case studies were reviewed (e.g. tail crack issues) to identify the benefits of SHM on rotorcraft. Mature diagnostic and prognostics systems from ongoing Structural Integrity Monitoring Systems (SIMS) efforts will be leveraged and customized for this effort. The long-term goal is focused on real-time monitoring but this program will start off with discrete sensor measurements when the aircraft is on the ground. Considerations included the accrual of maintenance credits pre-approval of SHM systems to accommodate rapid transition to industry on demand. SHM concepts addressed both hot spot (local) and wide area (global) monitoring. The second phase of the program included sensor, system and application selection. Validation testing addressed the spectrum of performance assessments requirements and included POD for health monitoring. Existing test data will be used to minimize the number of future validation tests and to demonstrate the use of an SHM performance database for more rapid SHM deployment.

Program Goal:
To mature the integration of Structural Health Monitoring (SHM) solutions for rotorcraft structures with an emphasis on their use in Health and Usage Monitoring Systems (HUMS).

Program Objectives:

1) Complete the validation process for two viable SHM system utilizing proven sensors to detect representative rotorcraft structural damage
2) Propose an end-to-end process for the inclusion of structural health data into HUMS/SHM-based decision making processes, which could be used by the OEM, operator, and regulatory agencies to approve SHM-related maintenance credits.
3) Integrate results into rotorcraft AC 29-2C, MG15 to ensure safe adoption of SHM solutions

Expected Outcome

- Demonstration of a viable SHM system utilizing proven sensors to detect representative rotorcraft structural damage
- Investigate both local SHM (individual sensor monitors expected flaw origin location) and global SHM (sensor networks monitor a region for flaw onset)
- A model for the inclusion of structural health data into HUMS-based decision making processes
- Integrate results into rotorcraft AC 29-2C, MG15 to ensure safe adoption of SHM solutions
- Documented efforts to move the proposed system through the certification process possibly including:
    - Alternate Means of Compliance (AMOC)
    - Mods to SBs/ADs; STCs
    - Investigating potential accrual of maintenance credits
- The Rotorcraft subcommittee of the SAE AISC-SHM committee plans to develop industry guidance standards for SHM use on Rotorcraft.
- Tie the SHM sensors and data collected into the HUMS system. This is a new use for HUMS and the research being performed will support this guidance.

Sensor Systems for Rotorcraft SHM Applications - The primary goal of this program is to mature the integration of Structural Health Monitoring (SHM) solutions for rotorcraft structures with an emphasis on their use in Health and Usage Monitoring Systems (HUMS). Currently HUMS sensors are primarily used to assess and record critical mechanical system performance including motors, drive trains, engines and other mechanical components. They provide data on these systems to predict mechanical health and usage. HUMS benefits have led to an increase in safety, and a reduction in flight checks and unscheduled maintenance. Additional benefits from deploying HUMS may be realized when structural assessment data, collected by an SHM system, is also collected and used to detect structural damage in addition to the operational environment monitoring.

HUMS systems usually monitor dynamic rotor conditions for things such as unusual vibrations caused by possible damage. These vibrations often cause secondary damage in the surrounding structure. It would be of interest to see if there is any correlation between cracks monitored by an SHM system and data from a HUMS system. Ultimately, condition-based maintenance practices could be substituted for the current time-based maintenance approach. Other advantages of on-board distributed sensor systems are that they can eliminate costly, and potentially damaging, disassembly, improve sensitivity by producing optimum placement of sensors and decrease maintenance costs by eliminating more time-consuming manual inspections. The key element in a Structural Health Monitoring (SHM) system is a calibration of sensor responses so that damage signatures can be clearly delineated from sensor data produced by unflawed structures.

Initial research has highlighted the ability of various sensors to detect common flaws found in composite and metal structures with sensitivities that often exceed current flaw detection requirements. These sensor systems range in maturity from laboratory-based prototypes to turnkey systems that appear ready for aircraft use. A focused validation program at the AANC, conducted jointly with rotorcraft manufacturers and operators, was conducted with the long-term goal to safely integrating SHM sensors into rotorcraft maintenance programs. This report presents a Sandia Labs-Sikorsky Aircraft effort to assess SHM for routine use on rotorcraft. This program addressed formal SHM technology validation and certification issues so that the full spectrum of concerns, including design, deployment, performance and certification were appropriately considered.

The FAA Airworthiness Assurance Center (AANC) at Sandia Labs, in conjunction with Sikorsky and the FAA, completed a study to conduct validation testing for two different SHM systems: Comparative Vacuum Monitoring and Piezoelectric Transducers. Validation tasks were designed to address the SHM equipment, the health monitoring task, the resolution required, the sensor interrogation procedures, the conditions under which the monitoring will occur, and the potential inspector population. To carry out the validation process, knowledge of aircraft maintenance practices was coupled with an unbiased, independent evaluation. Sandia Labs designed, implemented, and analyzed the results from a focused and statistically-relevant experimental effort to quantify the reliability of SHM systems as applied to potential Sikorsky applications. All factors that affect SHM sensitivity were included in this program: flaw size, shape, orientation and location relative to the sensors, operational and environmental variables and issues related to the presence of multiple flaws within a sensor network. Statistical methods were applied to performance data to derive Probability of Detection (POD) values for SHM sensors in a manner

that agrees with current nondestructive inspection (NDI) validation requirements and has been deemed acceptable to both the aviation industry and regulatory bodies in previous, similar efforts.

The costs and complexity associated with the increasing maintenance and surveillance needs of aging aircraft are rising at an unexpected rate. The application of distributed sensor systems may reduce these costs while enhancing safety. In the near future, it may be possible to quickly, routinely, and remotely monitor the integrity of a structure in service and determine its health usage. There is a need to safely and efficiently adopt reliable structural health monitoring systems that can process data, assess structural condition and provide additional information for health usage monitoring on rotorcraft. This SHM rotorcraft program was conducted to provide information and guidance that will support the safe adoption of SHM practices and also allow OEMs, regulators, and carriers to make informed decisions about the proper utilization of SHM. The activities conducted in this program demonstrated the feasibility of routine SHM usage. This formal SHM validation will allow the rotorcraft industry to confidently make informed decisions about the proper utilization of SHM. It will also streamline the regulatory actions and formal certification measures needed to assure the safe application of SHM solutions.

The FAA Advisory Circular AC-29-2C, Section MG-15, addresses airworthiness approval of Health and Usage Monitoring Systems (HUMS). The AC provides guidance for achieving airworthiness approval for installation, credit validation, and instructions for continued airworthiness (ICA) for a full range of HUMS applications. Installation includes all the equipment needed for the end-to-end application that is associated with acquiring, storing, processing, and displaying the HUMS application data, including airborne and ground-based equipment. The AC establishes an acceptable means of certifying a rotorcraft HUMS. In association with this AC, this program exercised the steps needed to certify an SHM system on rotorcraft. This includes the items listed above in concert with a Functional Hazard Assessment (FHA), a rigorous quantification of performance, evaluations of equipment installation and ground-based data acquisition, and an initial assessment of the integration of SHM into HUMS to produce Maintenance Credits. The performance validation considered the accuracy, resolution, durability, data fidelity and system repeatability. Credit validation includes evidence of effectiveness for the developed algorithms, acceptance limits, trend setting data, tests, etc., and the demonstration methods employed. A plan was also evolved to ensure continued airworthiness of the SHM components.

Most HUMS technologies focus on monitoring the conditions in terms of measurements of vibration, not structural damage, cracks, or failures. Because fatigue damage of rotorcraft components in service is a major concern, development, validation and demonstration of a system for crack detection and crack growth monitoring is critically needed. The adoption of SHM into HUMS will provide the ability to detect structural damage.

In general, SHM sensors should be low profile, lightweight, easily mountable, durable, and reliable. To reduce human factors concerns with respect to flaw identification, the sensors should be easy to monitor with minimal need for users to conduct extensive data analysis. For optimum performance of the in-situ sensor-based approaches, the signal processing and damage interpretation algorithms must be tuned to the specific structural interrogation method. Initial research has highlighted the ability of various sensors to detect common flaws found in composite

and metal structures with sensitivities that could exceed current flaw detection requirements, if needed. Completed validation programs at the Sandia Labs AANC – conducted jointly with aircraft manufacturers and airlines – worked to integrate SHM sensors into aircraft maintenance programs. These evaluations incorporated both cost-benefit analyses, as well as statistically-derived performance reliability numbers.

Several SHM sensors have been demonstrated to reliably detect damage in a laboratory environment and in a few commercial applications. One example of the more mature sensors that show promise in detecting cracks and structural defects is the Comparative Vacuum Monitoring (CVM) sensor. A number of organizations have been investigating and demonstrating the use of CVM as a means for inspecting certain commercial airplane applications [1.4, 1.6 - 1.7]. In the CVM applications studied to date, the CVM technology is a permanently mounted nondestructive damage detection technique (NDT) sensor that can be queried at the same inspection intervals as the currently accepted NDT methods. The advantage of the CVM in this case is that the inspected structure only needs to be accessed once for CVM installation. Afterward, the area is inspected by remotely connecting to the CVM without need for structural teardown. Another mature sensor and turnkey SHM system utilizes Piezoelectric Transducers (PZT) to measure the response of a structural area to a Lamb Wave (LW) interrogation. Subsequent, similar measurements compare current structural response signatures to Baseline signatures from the pristine structure to determine if damage is present. This program, conducted jointly with Sikorsky, involved a detailed investigation into CVM and PZT SHM technology. Figure 2-1 and Figure 2-2 show some sample Sikorsky aircraft and applications that were considered for this study of SHM solutions.

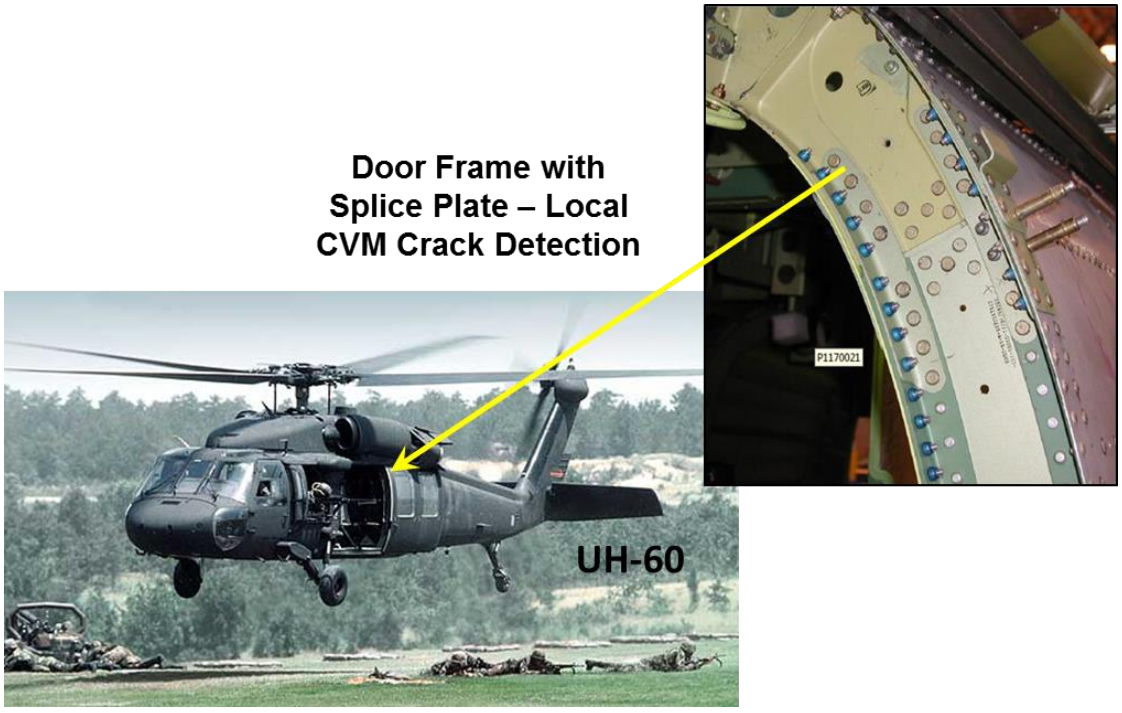

Figure 2-1. Door Frame Joint in Sikorsky UH-60 Black Hawk Helicopter

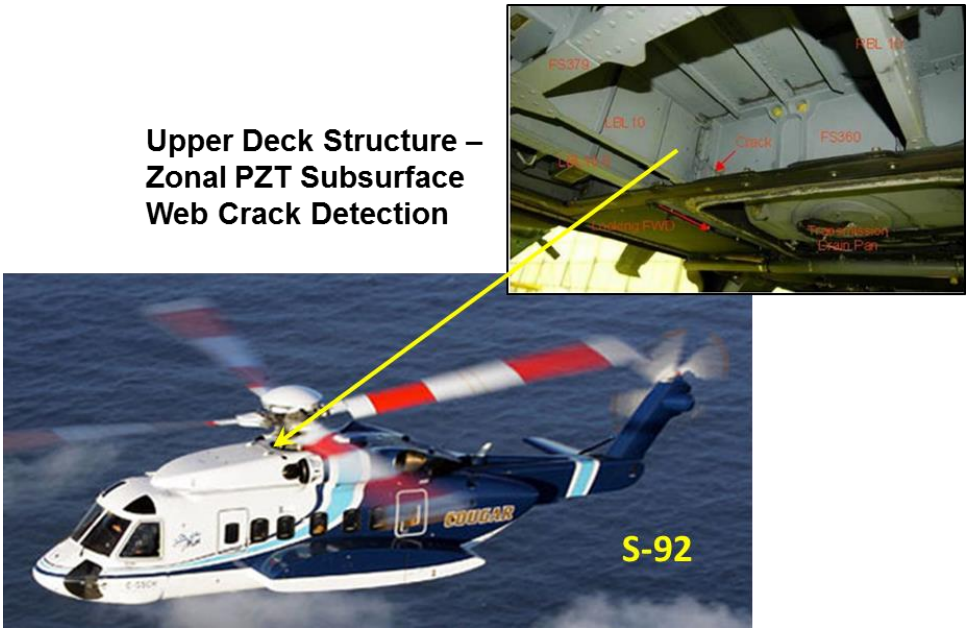

Figure 2-2. Main Upper Deck Structure on Sikorsky S-92 Helicopter

Deployment of Health Monitoring Sensor Networks – Distributed sensor networks can be deployed in any of the three approaches listed below. These options are listed in the order of increasing complexity, however, less labor is required to monitor the systems as they become more complex.

1. *In-Situ Sensors Only* – The sensors are the only items permanently installed on the structure. At the desired inspection intervals, power, signal conditioning, and data acquisition electronics are manually transported to the structure to be monitored. The sensors are linked to the monitoring electronics via a connector and flaw detection is completed by an inspector at the site.
2. *Sensor Network with In-Situ Data Acquisition* – In this system, miniature, packaged electronics are also placed in-situ with the sensor network. The electronics contains the necessary power, memory and programmable circuitry for automated data logging. The data is periodically downloaded to a laptop through manual hook-ups at the site.
3. *Sensor Network with Real-Time Data Transmission to a Remote Site* – This approach is similar to item #2 with the addition of a telemetry system that allows for continuous, wireless transmission of data to a remote site. A web site can be programmed to interrogate critical aspects of the data and use pre-set thresholds to provide continuous green light/red light information regarding the health of the structure. The web site can even be programmed to automatically send an e-mail to maintenance personnel if the condition monitoring process indicates the need for repairs or other maintenance. In this mode of operation, it may be desirable to incorporate interface electronics to condition the signals and analyze data in-situ. This eliminates the need to transmit larger raw data files.

The latter approach allows for true condition-based maintenance in lieu of maintenance checks based on time of operation. A series of expected maintenance functions will already be defined,

however, they will only be carried out as their need is established by the health monitoring system. The use of condition-based maintenance coupled with continuous on-line structural integrity monitoring could significantly reduce the cost of inspection, maintenance, and repair.

Whether the sensor network is hardwired to an accessible location within the aircraft or monitored in a remote, wireless fashion, the sensors can be interrogated in a real-time mode. However, it is anticipated that in the initial application of SHM technology, the sensors will most likely be examined at discrete intervals, probably at normal maintenance checks. The important item to note is that the ease of monitoring an entire network of distributed sensors means that structural health assessments can occur quickly and in an automated fashion.

Summary of Program Goals:

- Establish the viability of SHM methods for aircraft maintenance
- Leverage completed SHM certification efforts (data) and follow similar tasks for FAA (regulatory) approvals
- Utilize independent validation efforts to quantify the performance of SHM systems for Embraer applications
- Produce certification data package to support SHM solutions on rotorcraft

SHM Solutions Studied:

- Comparative Vacuum Monitoring (CVM)
- Piezoelectric Transducers (PZT) also referred to as Lamb Wave (LW) technology

Current SHM Technology Gaps and Project Work Plan

Gap #1: Prior efforts have not addressed complex structural assemblies with reliability approaches.

- Efforts have either been technology demonstrations on complex structures OR simpler structures with the application of minimal statistical frameworks

Project Effort:

- Adapt local framework to zonal/global component monitoring application, and perform analysis of framework for applicability to potential multi-site damage problem
- Identify critical features of zonal/global components that need addressing and define representative test articles for zonal/global framework validation

Gap #2: Explicit guidance on the use of SHM for credit application does not exist within AC-29-2C, MG-15.

- Document does not address critical items for SHM such as applicability of POD methodology, required testing, etc.

Project Effort:

- Perform mock certification approach for both local and global applications, covering application and testing requirements using project components as examples

2.1. SHM Validation Process

The Airworthiness Assurance NDI Validation Center (AANC) at Sandia Labs uses a validation approach that is designed to address the equipment, the inspection task, the resolution required, the inspection procedures, the conditions under which the inspection will occur, and the potential inspector population. To carry out the validation process, knowledge of aircraft maintenance practices must be coupled with an unbiased, independent evaluation. The AANC has designed, implemented, and analyzed the results from a wide range of statistically-relevant experimental programs to quantify the reliability of inspection methods as deployed at commercial aircraft maintenance facilities. Much of this methodology to quantify NDI performance can be adapted to the validation of SHM systems. However, it is important to recognize the unique validation and verification tasks that arise from distinct differences between SHM and NDI deployment and flaw detection. An important element in developing SHM validation processes is a clear understanding of the regulatory measures needed to adopt SHM solutions along with the knowledge of the structural and maintenance characteristics that may impact the operational performance of an SHM system.

The AANC, in conjunction with multiple partners from the aviation industry, has conducted a long-term research program to develop and validate Comparative Vacuum Monitoring (CVM) Sensors and Piezoelectric Transducers (PZT) for crack detection. CVM and PZT sensors are permanently installed to monitor critical regions of a structure. The use of in-situ sensors for health monitoring of rotorcraft structures appears to be a viable option for both flaw detection and maintenance planning activities. Local sensors can be used to directly detect the onset of crack, corrosion, or disbond flaws. Reliable, structural health monitoring systems can automatically process data, assess structural condition, and signal the need for human intervention.

This program looked at the application of SHM solutions to particular rotorcraft applications. In this case, the validation effort focused on the use of CVM sensors to detect cracks in the frame gusset of a Sikorsky S-92 aircraft and the use of PZT sensors to detect cracks in main beams representative of major component mounts such as engines. Statistical methods using One-Sided Tolerance Intervals were employed to derive Probability of Detection (POD) levels for each of the test scenarios. The result was a series of flaw detection curves that can be used to propose CVM and PZT sensors for rotorcraft crack detection. This approach produced sufficient data to certify CVM and PZT sensor performance for specific applications. Towards that end, probability of flaw detection assessments were coupled with on-aircraft flight tests in related studies to comprehensively study the performance, deployment, and long-term operation of CVM and PZT sensors on aircraft.

The primary goal of this program was to mature the integration of Structural Health Monitoring (SHM) solutions for rotorcraft structures with an emphasis on their use in Health and Usage Monitoring Systems (HUMS). This effort was undertaken to demonstrate several viable SHM systems utilizing proven sensors to detect representative rotorcraft structural damage and to provide a model for the inclusion of structural health data into HUMS-based decision making processes. Activities focused on the SHM portion of HUMS while also looking at the big picture

of blending SHM information with usage monitoring to produce a more informed, comprehensive rotorcraft maintenance approach. Efforts to move the proposed system through the certification process including Alternate Means of Compliance (AMOC), addition to Service Bulletins, and the accrual of potential maintenance credits was investigated.

Validation of Structural Health Monitoring Systems

The validation and certification process begins with the declared application intent, and a determination of the resultant criticality. The declared intent should specify whether this application is for credit (replaces required task or leads to changes in the requirements for a task) and if it adds to, replaces, or intervenes in maintenance practices or flight operations. When the declared intent is for credit, the end-to-end criticality for such an application should be determined and used as an input to establish the validation criteria. If the declared intent is for noncredit (provides additional data above and beyond required tasks), it may be certified if it can be shown that the installation of the equipment will not result in a hazard to the aircraft. Therefore, criticality describes the severity of the result of an SHM application failure or malfunction.

The program to implement SHM, and thus the validation plan, requires a clear definition of the application. There are several considerations that must be addressed when formulating this definition. These considerations include, but are not limited to, structural configuration, structural variation, usage environment, system durability requirements, configuration management, and system maintenance [2.1 – 2.7]. The SHM Validation Plan should address the following items (see Figure 2-3 through Figure 2-6):

1. Part Geometry – Engineering drawings that define specific dimensional information regarding the part or assembly, including the local structural interfaces, geometric interference, manufacturing variability and access. These drawings should define the geometry and composition of mating components and how these mating components are joined to the component under interrogation. The assembly defines the boundary conditions under which the SHM system must reliably function. The assembly configuration can affect the sensor design and placement
2. Material – The material description must include, in the case of metallic structure, the alloy type and heat treatment or temper condition, and may require a description of any surface treatments including coatings or plating and thicknesses. In addition, material details may be required for other structure located in the region of interest including fastener type and material composition.
3. Flaw Location and Orientation – A clear definition of both the expected flaw location and orientation is required. This information may be available in the form of damage tolerance analysis, and fatigue test results (subcomponent, component, or full scale).
4. Effectivity/Configuration Changes – A list of affected aircraft or systems by tail or serial number. This information should include a description of any deviations or configuration changes in component design, including variances in any of the items described above. Potential structural variability that could affect the reliability or repeatability of an SHM system should be defined. Sources of variability include but are not limited to variations in structural faying surface interfaces, coating systems, or part configuration often due in large part to production changes, repairs or deterioration of materials over time. Such an

accounting provides a level of assurance that all affected systems are inspected and that SHM processes are appropriately adjusted to compensate for known variances.

5. Access for Installation/Stay-Out Zones – Points of access for installation and repair of the SHM system must be identified. This description should include panels or doors that can be removed to facilitate system installation, description of local structure or subsystems that may hinder access, areas that can be used for cable routing or other system subcomponents, aircraft systems that may be affected by SHM hardware, and regions that cannot be used to mount SHM system subcomponents (stay-out zones).
6. SHM Performance/Capability – Provide both a goal and threshold $\boldsymbol{a}_{NDI}$ (or $\boldsymbol{L}_{NDI}$) value. The value of $\boldsymbol{a}_{NDI}$ has been established as the $\boldsymbol{a}_{90/95}$ Probability of Detection value determined statistically using appropriate methods (see Figure 2-7 through Figure 2-9). The $\boldsymbol{a}_{90/95}$ is an estimate of the crack size that will be detected 90% of the time with a statistical confidence of 95%. The goal value is the detection capability that may be very challenging to meet but would result in inspection intervals that provide an economic or maintenance benefit to the program. The goal and threshold values should be used to develop the SHM demonstration experiment. In addition, these values should be used to develop SHM interrogation intervals.
7. False Positive Rates – False positives (also known as false alarms) can present a significant economic and availability burden if not appropriately controlled as they can drive costly and intrusive structural disassembly. The maximum allowable rate of false positives can best be defined by the OEM or by operators.
8. Durability – System durability requirements, in terms of ability to operate in expected environments for specific periods without failure, should be defined. Failure rates must be sufficiently low to support the maintenance concept and provide long term monitoring without the need for invasive maintenance or repair of the monitoring system.
9. Usage Environment – The usage environment includes but is not limited to temperature profiles, humidity, fuel, hydraulic fluid or chemical exposure, strain and vibration. A definition of this environment will drive the design of environmental and durability testing and the qualification/airworthiness requirements.
10. Other Requirements – The SHM Validation Plan should clearly define other, pertinent aircraft specific requirements. These may include maximum system weight and size, power requirements, etc. Development of the Validation Plan should be closely coordinated with the appropriate aircraft system and safety engineering authority within the operator's maintenance program.

The SHM Validation Program should use a multi-phased approach that includes controlled, representative laboratory testing that will eventually lead to on-aircraft flight tests. Each phase must address various aspects of the four critical factors (detection capability, durability, installation/supportability, safety) with a successful outcome supporting a decision milestone to move to the next phase. Validation testing can consist of mounting SHM sensors to representative specimens and cyclically loading the specimens to generate and grow fatigue damage. Preliminary testing may involve the use of simulated defects (e.g. electro-discharge machined (EDM) notches, simulated disbonds/delaminations) to represent damage but should progress to use of cyclically loaded fatigue damaged specimens.

The loading spectrum used for fatigue propagation should be based on the anticipated on-aircraft load environment; however, higher load rates may be required for economy. Test specimens must be manufactured from the same material, alloy, heat treat and possess a similar microstructure as the intended application. The sample design should be sufficiently complex (contain stiffeners, fastener holes, tapers, curves, etc. as appropriate) to represent the intended application but may not require the detailed replication of aircraft structure geometry or assembly. The goal for this phase is to demonstrate the system detection capability to sense and reliably identify relevant damage on structures in a relevant environment. A relevant environment is defined as test conditions that closely simulate the load spectrum when the test coupons are exposed to an environment similar to the intended application. Conditions that may have to be simulated include vibration, temperature, pressure, and exposure to moisture or aircraft fluids (hydraulic fluids, fuel, greases). The test samples should represent the intended application in terms of pertinent geometry, material, and assembly, including boundary conditions.

SHM Validation Process Tasks

The objective of any SHM technology validation exercise is to provide quantifiable evidence that a particular inspection or maintenance methodology (equipment plus its operation) can achieve a satisfactory result. The validation process must consider the numerous factors that affect the reliability of an inspection methodology including the individual inspector/operator, his equipment, his procedures and the environment in which he is working. It also accounts for the viability of the SHM approach within the aircraft's maintenance program. The approach is based on the use of real-life Validation Assemblies which are full-scale structural assemblies containing known, realistic defects or other operational malfunctions which the SHM system is intended to monitor.

The validation process should: 1) provide a vehicle in which skills, automation of instrumentation and human error can be evaluated in an objective and quantitative manner, 2) produce a comprehensive, quantitative performance assessment of the SHM system and utilization procedure in a systematic manner, 3) provide an independent comparison between SHM solutions and alternate maintenance and monitoring methodologies, 4) optimize SHM utilization methodologies through a systematic evaluation of results obtained in laboratory and field test beds, 5) produce the necessary teaming between the airlines, aircraft manufacturers, regulators, and related SHM development and research agencies to ensure that all airworthiness concerns have been properly addressed.

The process of validating SHM techniques involves the specification of a structure with defects or containing the appropriate boundary conditions and features to allow for the assessment of whatever physical parameter the SHM system is monitoring. The validation process may involve the production of full-size sections of airframes or appropriate laboratory test samples which contain natural, fully characterized defects or realistic, engineered defects. Inspection or monitoring of these Validation Assemblies must occur under conditions identical to those of the day-to-day inspection environment. The validation process is a full-scale, realistic mockup of the daily activities of the maintenance personnel involved in the proposed SHM application. The tests performed are then independently assessed against industry standards in terms of personnel and instrument performance. In this regard, independence and objectivity are essential. Some

validation efforts may include the use of airline maintenance personnel who will perform the monitoring tasks using normal working practices and under normal working conditions (lighting, heating, noise, work shifts, etc.).

- **Declared Intent** - application is for credit (replaces task or leads to changes in the requirements for a task); criticality describes the severity of the result of an SHM application failure or malfunction
- **Usage Mode for SHM System**
  - "Hot spot" or local monitoring (S-SHM)
  - Prognostic and condition-based health monitoring (P-SHM and C-SHM) - shift to predictive and continuous monitoring will require extensive validation and successful in-service experience so that regulatory agencies and operators can acquire confidence in these SHM approaches
- **Aircraft Maintenance Practices** – change in programs; how to adopt
- **Deployment** – operational performance & repeatability
- **Regulatory Actions and Industry Acceptance** – depends on certification process (AMOC, NDT SPM, SB/AD, STC)
- Key element in an SHM system is a **calibration of sensor responses** so that damage signatures can be clearly delineated from sensor data produced by undamaged structures
- Commercial implementation of SHM needs to be proven through statistically-viable **lab performance** data and successful **field operation** data
- **Data requirements** need to be established for determining the applicability of SHM (boundaries) and to address certification requirements
- **Educational** initiatives with key players – understanding of SHM, its usage and its limitations

Figure 2-3. Considerations for Producing an SHM Validation Plan

- **Validation Process** should:
  1) provide a vehicle in which skills, instrument deployment & human error can be evaluated in an objective and quantitative manner
  2) provide an independent comparison between SHM solutions and alternate maintenance and monitoring methodologies
  3) optimize SHM utilization methodologies through a systematic evaluation of results obtained in laboratory and field test beds
  4) produce the necessary teaming between the airlines, aircraft manufacturers, regulators, and related SHM development and research agencies to ensure that all airworthiness concerns have been properly addressed
- **Validation Assemblies** – Assess technology and process; deployed under conditions identical to those of the day-to-day maintenance environment; use airline maintenance personnel who will perform the monitoring tasks using normal working practices and under normal working conditions
- **Comprehensive Evaluation** - Assess performance, training and integration into maintenance program (technical and admin)

Figure 2-4. Considerations for SHM Validation Process Tasks

- **SHM Method** - SHM solution, device, sensor spacing, data acquisition process, data analysis method, data interpretation (thresholds, S/N), use of baselines
- **Structural Configuration** – geometry, material type, number of layers, fastener types and spacing, hole geometry, assembly specifics (fit/gaps), surface condition, coating changes
- **Flaw/Damage Condition** – type, X-Y location, depth, orientation, dimensions, morphology, presence of by-products
- **Environmental Conditions** – load scenario to generate damage, impact, environment to generate damage & establish durability

Complex Structure Requires Detailed SHM Validation

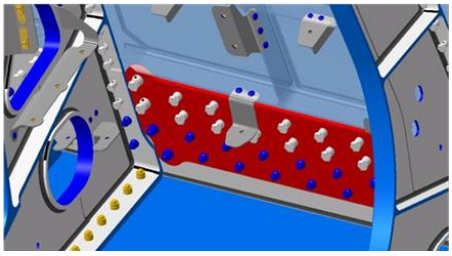

Figure 2-5. SHM Validation Process Must Account for All Factors That Can Affect Performanc

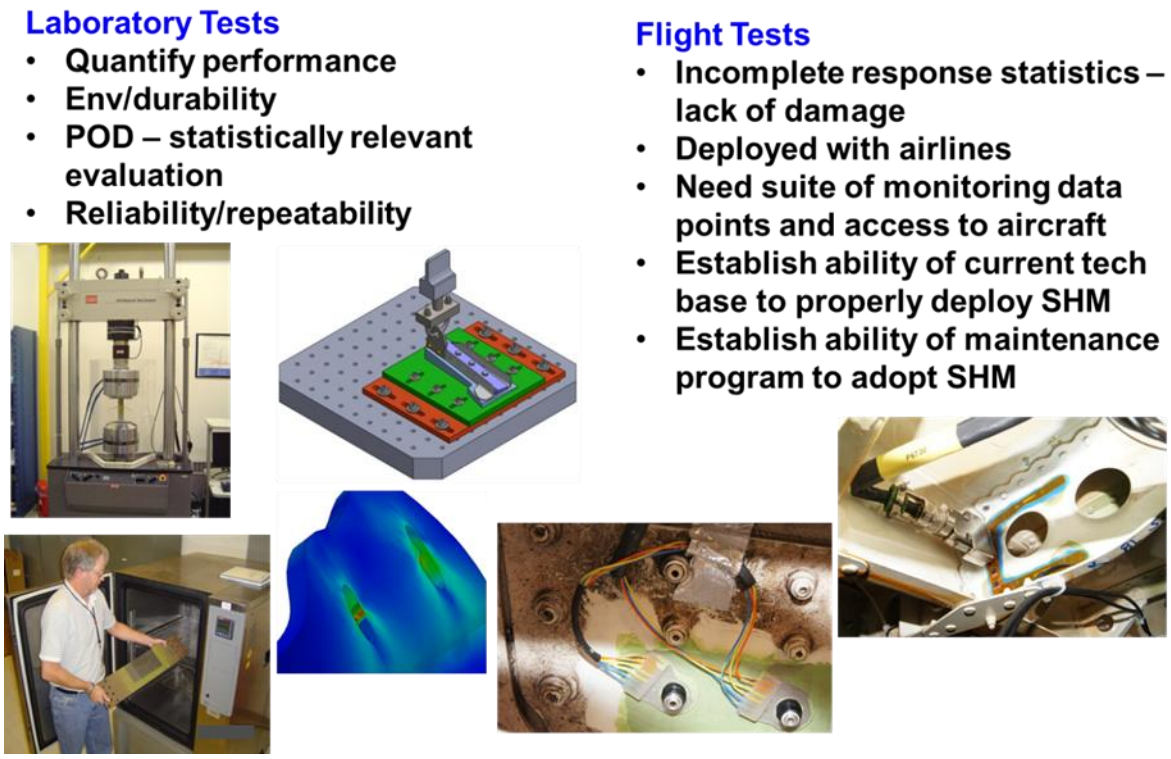

Figure 2-6. Two Major Components for Validation of SHM Capability

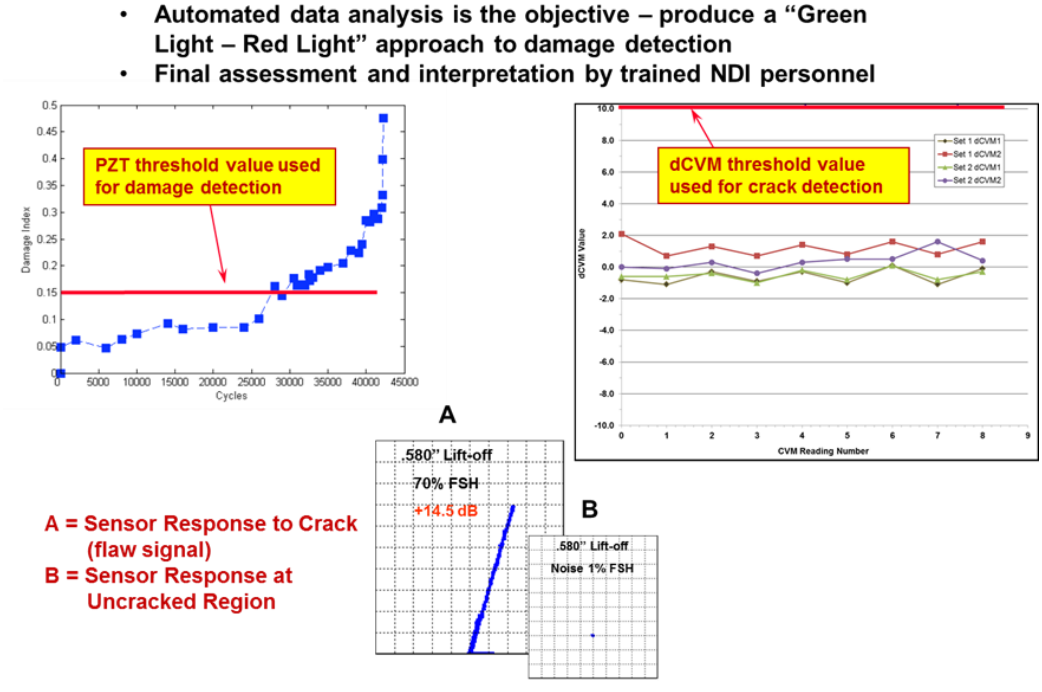

Figure 2-7. SHM Information – Importance of Establishing Damage Detection Thresholds and Minimizing Data Interpretation or Data Analysis

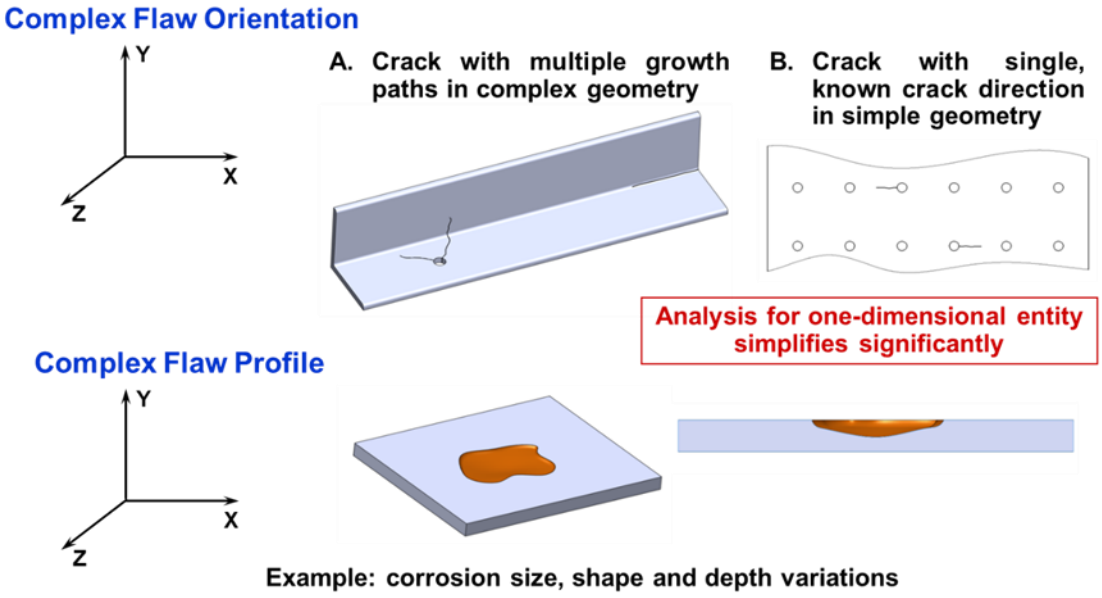

Figure 2-8. Reliability Assessment for Simple and Complex SHM Solutions

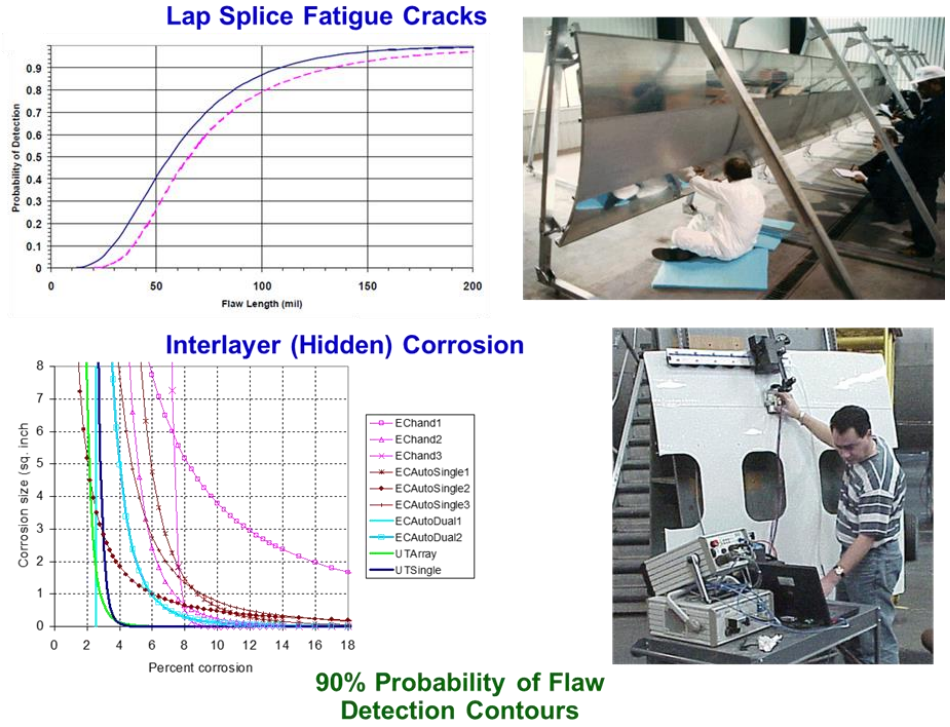

Figure 2-9. Approaches to Present NDI POD Values for Different Flaw Geometries

2.2. Comparative Vacuum Monitoring – Technology Description

Comparative Vacuum Monitoring (CVM) is a pneumatic sensor technology developed to detect the onset of cracks. CVM sensors are permanently installed to monitor critical regions of a structure. The CVM sensor is based on the principle that a steady state vacuum, maintained within a small volume, is sensitive to any leakage. A crack in the material beneath the sensor will allow leakage resulting in detection via a rise in the monitored pressure. Figure 2-10 through Figure 2-12 show top-view and side-view schematics of the self-adhesive, elastomeric sensors with fine channels etched on the adhesive face along with a sensor being tested in a lap joint panel. When the sensors are adhered to the structure under test, the fine channels and the structure itself form a manifold of galleries alternately at low vacuum and atmospheric pressure. Vacuum monitoring is applied to small galleries that are placed adjacent to the set of galleries maintained at atmospheric pressure. If a flaw is not present, the low vacuum remains stable at the base value. If a flaw develops, air will flow from the atmospheric galleries through the flaw to the vacuum galleries. The graphics show results from this crack detection monitoring and the pressure response used to indicate the presence of a crack. It is important to note that the sensor detects surface breaking cracks once they interact with the vacuum galleries. When a crack develops, it forms a leakage path between the atmospheric and vacuum galleries, producing a measurable change in the vacuum level. This change is detected by the CVM monitoring system (PM200 device) shown in Figure 2-12 and Figure 2-13. Figure 2-11 also shows a photo of a fatigue crack as it engages the first vacuum gallery of a CVM sensor. A pressure rise, corresponding to a rupture in the gallery and a leakage path to atmospheric pressure, occurs at this same time. The large increase in the pressure corresponds to crack detection as shown in the Figure 2-12 plot. One signal (blue curve) corresponds to vacuum levels produced when there is no crack indication and the other signal (red curve) occurs when a vacuum is not achievable. This latter signal is produced when the CVM detects a crack.

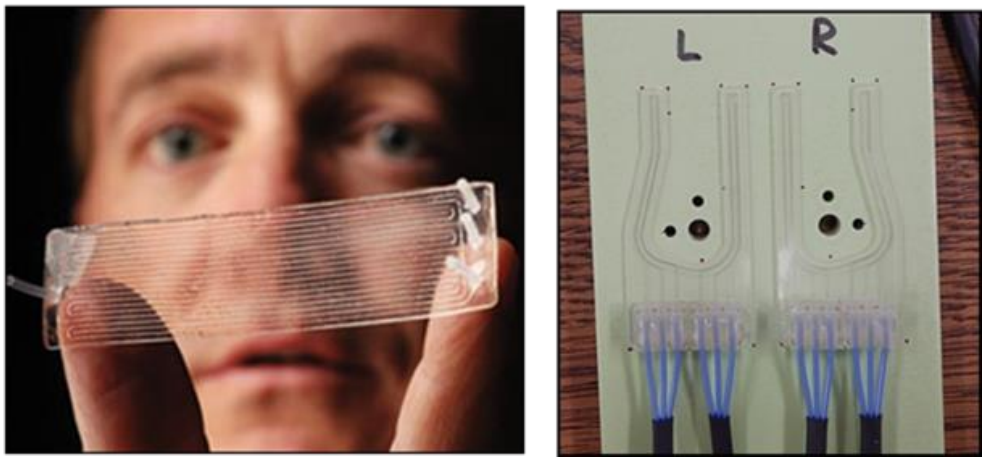

Figure 2-10. Sample Custom CVM Sensor Designs for Applications Requiring Different Monitoring Geometries

These sensors can be attached to aircraft structure in areas where crack growth is known to occur. On an OEM-established engineering interval, a reading will be taken from an easily accessible point on the aircraft. Each time a reading is taken, the system performs a self-test. This inherent fail-safe property ensures that the sensor is attached to the structure and working properly. Since the sensor physics is based on pressure measurements, there is no electrical excitation involved. This can be important in areas where electrical signals can create interference (near avionics) or where electrical connections may pose a hazard (fuel tanks). Each time a reading is taken, the system performs a self-test to ensure: 1) there is no blockage in the galleries which would affect and subsequent vacuum measurements and 2) proper adherence of the sensor to the surface it is monitoring. This initial check provides and inherent fail-safe property that ensures the sensor is attached to the structure and working properly prior to any data acquisition.

Drivers for Application of CVM Technology

- Overcome accessibility problems; sensors ducted to convenient access point
- Improve crack detection (easier & more often)
- Real-time information or more frequent, remote interrogation
- Initial focus – monitor known fatigue prone areas
- Capability to detect individual cracks at "hot spot" sites already identified for traditional NDI (e.g. eddy current, ultrasonic, X-ray, penetrant)
- Long term possibilities – distributed systems; remotely monitored sensors allow for condition-based maintenance.

Through the use of in-situ CVM sensors, it is possible to quickly, routinely, and remotely monitor the integrity of a structure in service. Prevention of unexpected flaw growth and structural failure can be improved if on-board health monitoring systems are used continuously assess structural integrity and signal the need for human intervention. Recent events have demonstrated the need to address critical infrastructure surety needs. The applications for CVM sensors can include such diverse structures as: buildings, bridges, trains and subway vehicles, mining structures, railroad cars, trucks and other heavy machinery, pressure vessels, oil recovery equipment, pipelines, steel transmission towers, ships, tanks and a wide array of military structures. This report focuses on the application of CVM technology to rotorcraft structure.

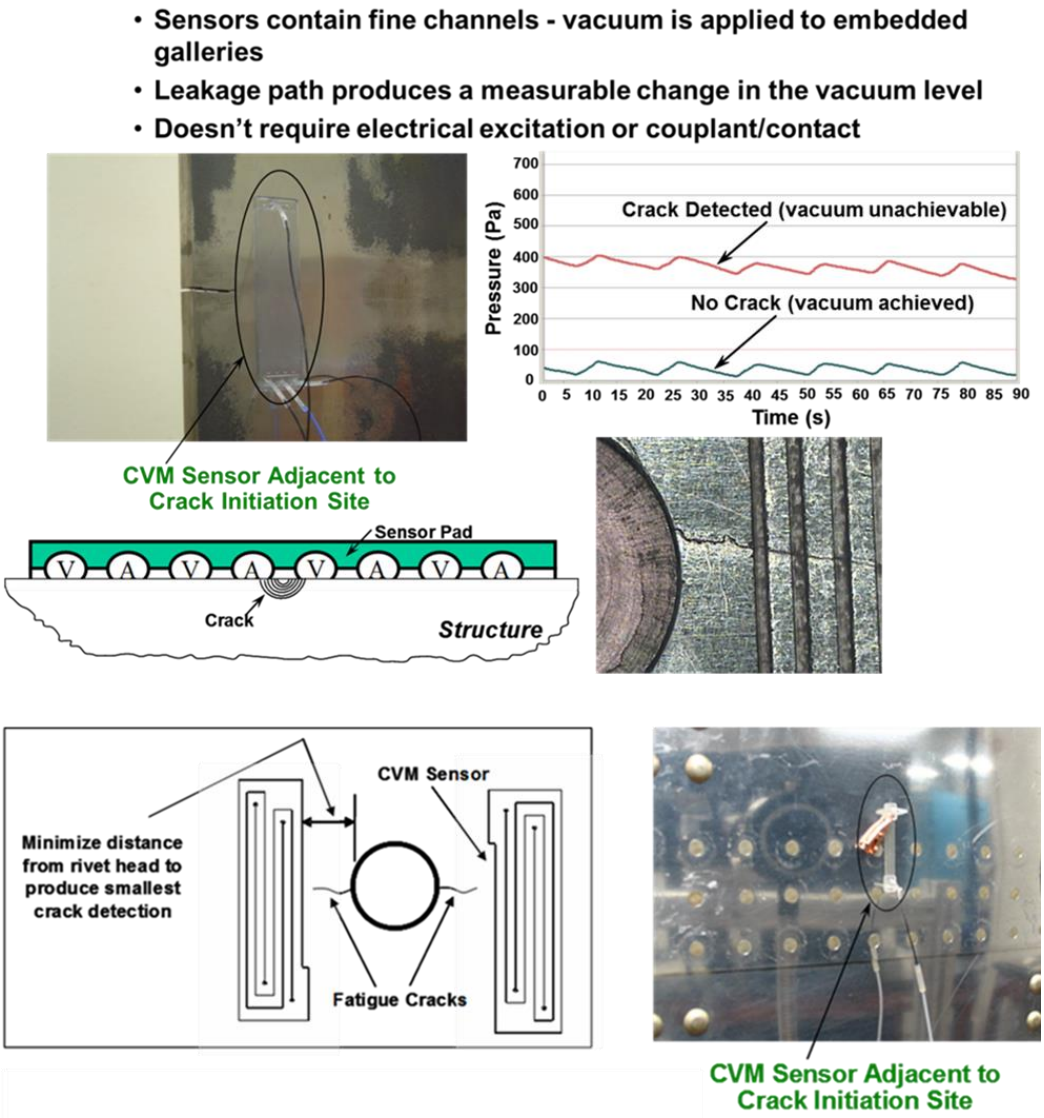

Figure 2-11. Schematic Depicting Operation of CVM Sensor with a Sensor Mounted on the Surface of an Aircraft Panel

Figure 2-12. Comparative Vacuum Monitoring System

Figure 2-13. On-Board CVM Sensor Network with Aircraft-on-Ground Connection to PM-200 Monitoring Device Using SLS Connectors

CVM Sensor Manufacture and Quality Assurance - The CVM sensor is manufactured from multiple layers of Teflon FEP sheets, where 2 to 8 sheets are laminated together with an acrylic pressure sensitive adhesive. The same adhesive is on the bottom layer and facilitates the adhesion to the aircraft. The basic production steps are:

1. Adhesive backed FEP sheet temporarily affixed to an aluminum plate.
2. The pattern for the lower base geometry layers is laser cut, then cleaned.
3. Another layer of FEP is laminated on top of the base geometry layers. This new layer is then laser cut to provide any required bias and outline, creating a partnered layer set.
4. The layers from step 3 are then stacked in proper sequence to create the desired sensor stack up.

Figure 2-14 shows a close-up of a CVM sensor which highlights the ability of the sensor to be customized to any shape and crack detection gallery layout. The photo also shows the "sensor header" region where the tubes, used for connection to the PM200 monitoring device, are interfaced with the thin galleries and built-in gallery routing within the sensor. The inner (Gallery 1) and outer (Gallery 2) galleries are also evident.

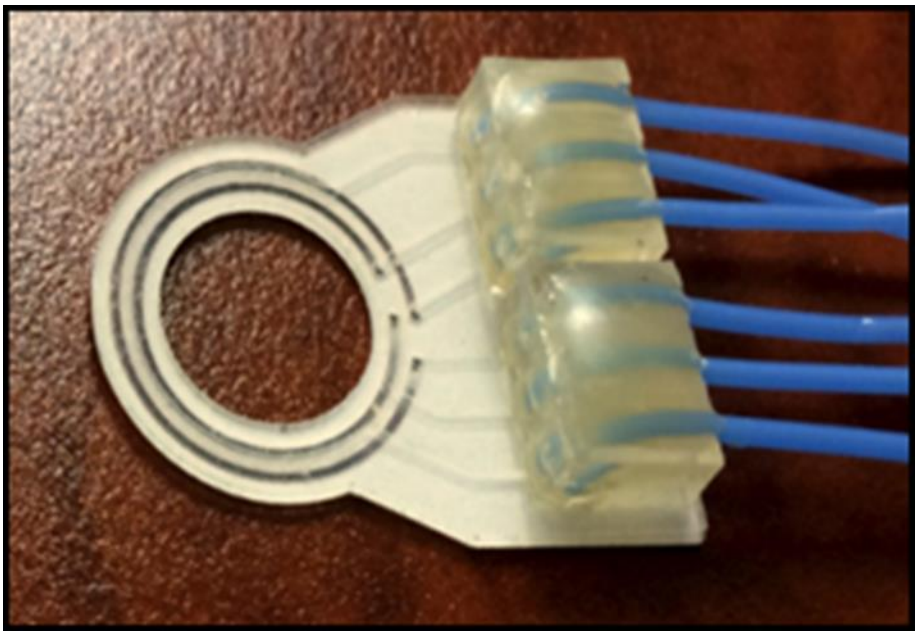

Figure 2-14. Teflon CVM Sensor and Tube Header Assembly

PM200 Instrument - The other important piece of hardware associated with CVM use, is the monitoring device known as the PM200. The PM200, shown in Figure 2-15, is a handheld battery-operated electronic instrument which uses the principles of dCVM to detect structural defects in mechanical components. The PM200 has a built-in, sensitive air flow meter. An air tank and a vacuum pump to provide the vacuum source. The partial vacuum pressure is maintained by the vacuum pump which draws air out of the tank thus lowering the air pressure inside the tank. The PM200 belongs to the Periodic Monitor class of instruments. Periodic Monitoring involves the use of a small number of test instruments (such as the PM200) to monitor the state of many sensors. That is, the state of a particular sensor is determined (i.e. inspected) periodically, perhaps in accordance with a predefined inspection schedule. When an inspection on a sensor has been completed, the instrument can be easily disconnected, transported and reconnected to another sensor. This process is repeated until all sensors have been inspected.

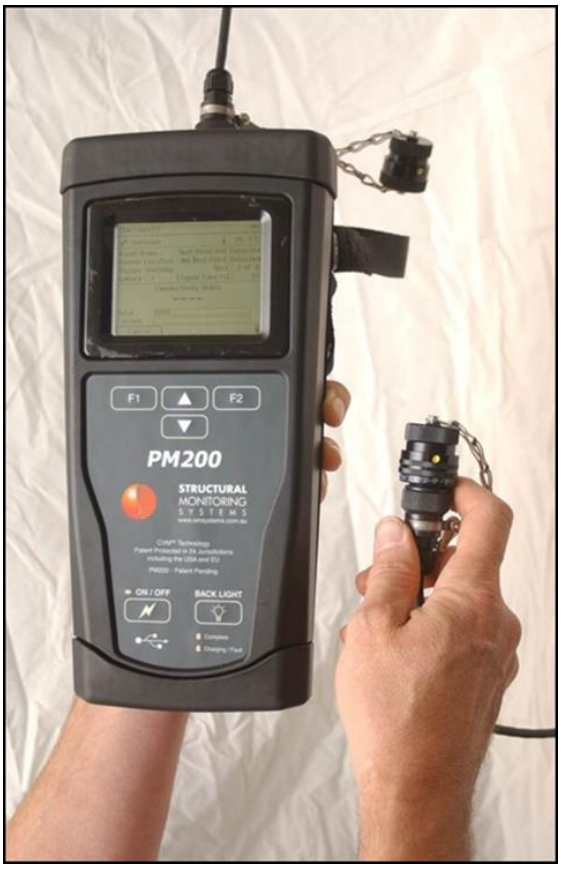

Figure 2-15. PM200 Device Used to Interrogate CVM Sensors and Perform Structural Monitoring

The end goal of the PM200 is to provide crack detection using a loss of vacuum in the sensor gallery. It does this by measuring the dCVM parameter whose value is related to the ability to pull a vacuum on the gallery. The sensors include three separate pneumatic galleries. Two of these galleries are open channels that are directly exposed to the substrate the user intends to monitor. The other gallery is the compensation gallery. It is an isolated gallery of the same physical dimensions and environmental exposure as the measurement galleries. When a measurement is made, the PM200 pulls a vacuum on the compensation gallery, as well as, one of the measurement galleries. The compensation channel is sealed and provides a clear indication of low vacuum level. A differential measurement (P1 – P2) is calculated. Thus, CVM is a measurement of air flow and dCVM is the difference between the reference Compensation Channel and the Measurement Channel:

$$\mathbf{dCVM} = CI_{(Compensation)} - CI_{(Measurement)} \quad (2.1)$$

This subtraction of the Measurement Channel from the reference Compensation Channel provides cancellation of temperature and humidity effects so it compensates for measurements at different

conditions. This approach also provides extreme sensitivity to any leakage in the galleries which, in turn, provides high Signal-to-Noise ratios for crack detection.

The SLS connectors shown in Figure 2-13 and Figure 2-15 form the completion end of the sensor leads. They are ITT Aerospace Grade connectors that contain sensor and set-up information so that each subsequent interrogation can be automatically logged into the PM200 memory. The last piece of hardware in the sensor-to-PM200 connection chain is the Snap-Click connector. The Snap-Click connector, and its use to make custom daisy-chains of CVM sensors or to mate the sensor tubes to the SLS connector, is shown in Figure 2-13 and Figure 2-16.

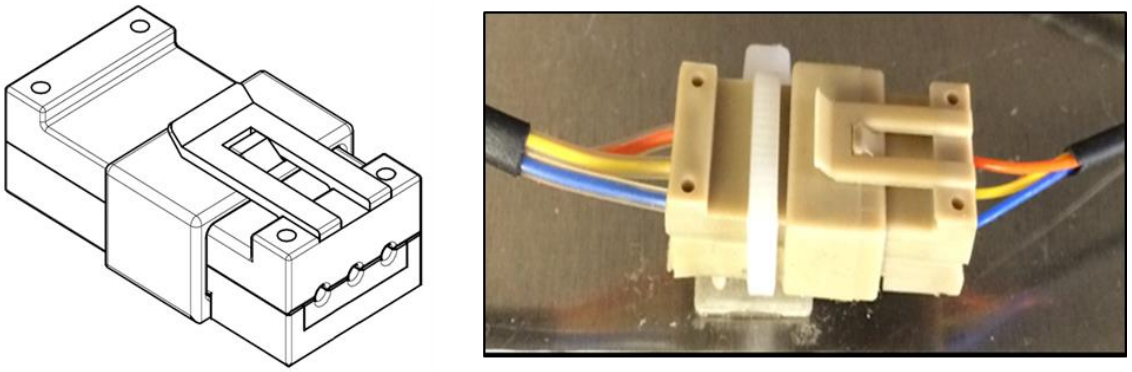

Figure 2-16. Snap-Click Pneumatic Connector

Historical Validation Testing with CVM - The Federal Aviation Administration's Airworthiness Assurance Center at Sandia Labs, in conjunction with industry (Boeing) and airline partners (Delta Air Lines), completed the first series of validation tests on the CVM system in the 2000 to 2004 timeframe in an effort to adopt Comparative Vacuum Monitoring as a standard NDI practice [2.8 - 2.10]. This prior test program produced a statistically-relevant set of crack detection levels for 0.040" to 0.100" (1.02 mm to 2.54 mm) thick panels in both the bare and primed configurations. In a subsequent program, testing was conducted at Sandia Labs, in concert with Embraer and the Agencia Nacional de Aviação Civil (ANAC) regulatory agency in Brazil, to complete validation testing of CVM sensors for a variety of potential applications on Embraer aircraft [2.11-2.12]. More recently, Sandia completed an SHM program with industry partners to produce approval for CVM use on a particular aircraft application [2.13]. In all programs, fatigue tests were completed on simulated aircraft panels to grow cracks in riveted specimens (see example in Figure 2-17) while the vacuum pressures within the various sensor galleries were simultaneously recorded. A fatigue crack was propagated until it engaged one of the vacuum galleries such that crack detection was achieved and the sensor indicated the presence of a crack by its inability to maintain a vacuum. In order to properly consider the effects of crack closure in an unloaded condition (i.e. during sensor monitoring), a crack was deemed to be detected when a permanent alarm was produced and the CVM sensor did not maintain a vacuum even if the fatigue stress was reduced to zero. The results from these validations tests are described in Ref. [2.8 – 2.13].

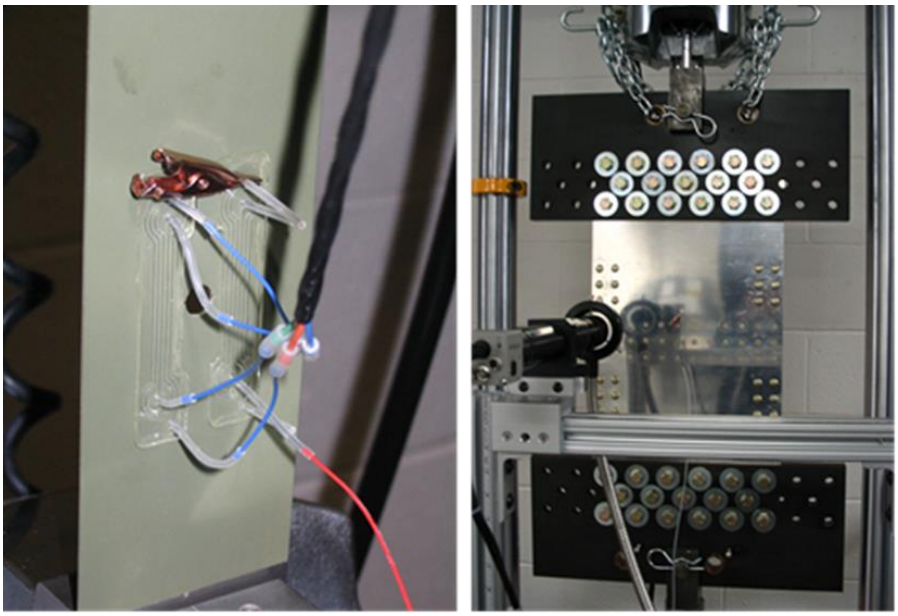

Figure 2-17. CVM Sensors Monitoring Crack Growth on Aluminum Test Specimens

Some field test functional evaluations were also completed as part of the initial FAA-industry studies on SHM utilization. In order to assess the long-term viability of CVM sensors in an actual operating environment, a series of 26 sensors were mounted on structure in four different DC-9, 757, and 767 aircraft in the Northwest Airlines and Delta Air Lines fleet. Table 2-1 summarizes the trial CVM installations on Delta and Northwest Airlines aircraft. The installations were considered "decals" because the sensors were not actually monitoring for structural damage. They were placed on low stress regions of skin and substructure in order to conduct a test of long-term response on an aircraft. Figure 2-18 shows some of the CVM installations and the monitoring process while Figure 2-19 shows typical flight test data that was acquired. The periodic testing, lasting over five years was used to study the long-term operation of the sensors in actual operating environments. This environmental durability study compliments the laboratory flaw detection testing described below as part of an overall CVM certification effort.

Table 2-1. CVM Sensors Installed on First Flight Test Program

Aircraft	Tail	Operator	Date	# Sensors	Status
DC-9	9961	NWA	Feb 04	6 (4 remaining)	2 sensors removed by NWA
DC-9	9968	NWA	Apr 05	6	3 sites
B757	669	Delta	Apr 05	8	4 sites in empennage on stringers, frames & near APB
B767	1811	Delta	Apr 05	6 (4 connected)	3 sites in empennage

Figure 2-18. Field Evaluation of CVM Sensors on Operating Aircraft

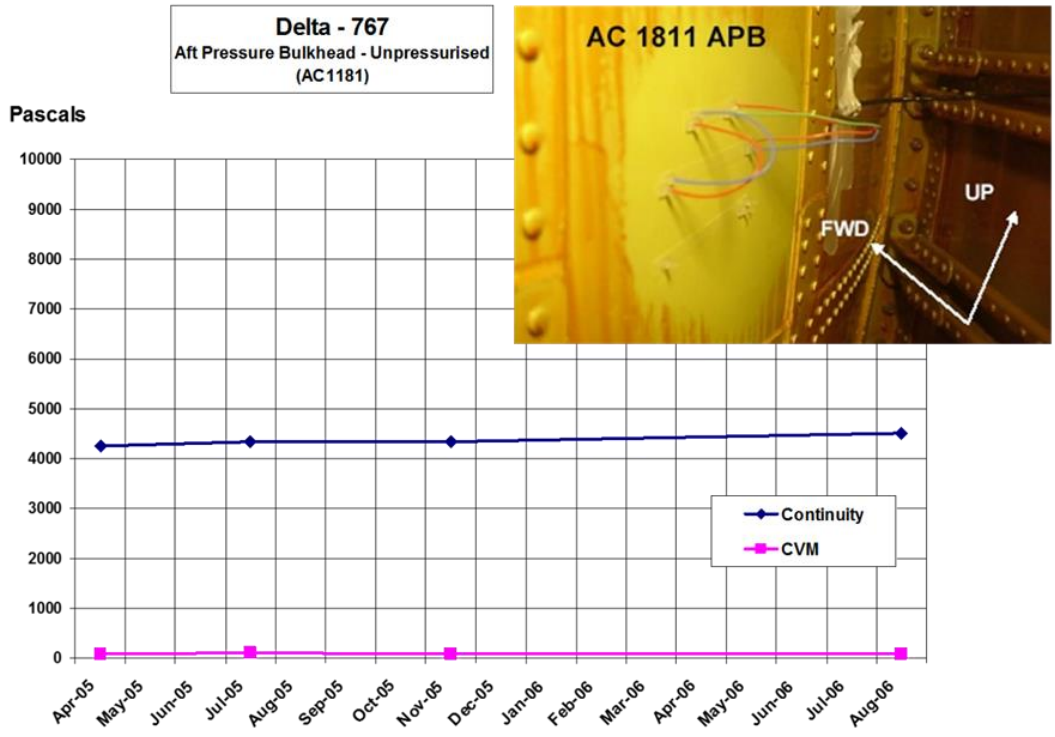

Figure 2-19. Typical Flight Test Data from CVM Sensors on Operating Aircraft

Figure 2-20 and Figure 2-21 summarize another proof-of-concept program which was driven by an actual inspection need on a commuter aircraft which involved a structure that was difficult to access. The program involved Bombardier and Transport Canada and proved the viability of the CMV system for monitoring the main engine beam in the empennage region of the CRJ aircraft platform. The initial goal of this project was to provide Bombardier and regulatory agencies with sufficient data to certify CVM sensor technology for specific aircraft applications. Probability of flaw detection assessments were coupled with on-aircraft flight tests to study the performance, deployment, and long-term operation of CVM sensors on aircraft. From a maintenance planning perspective, the objective was to eliminate access difficulties associated with this inspection and to provide an early indication of a flaw onset to properly schedule maintenance tasks. The derived benefit was a reduction in the rate of aircraft grounded after an inspection by allowing repairs to be scheduled in advance. By using CVM measurements as an alternate method of inspection (meet the inspection requirements of a Principal Structural Element), the goal was to: 1) reduce maintenance costs associated with the inspection tasks, and 2) increase threshold and repeat intervals for Fatigue Driven PSEs. Figure 2-21 shows the CVM sensor design and placement and highlights the crack detected on an operating aircraft. The lower right image is a photo of a dye penetrant inspection showing the crack engaging the CVM galleries

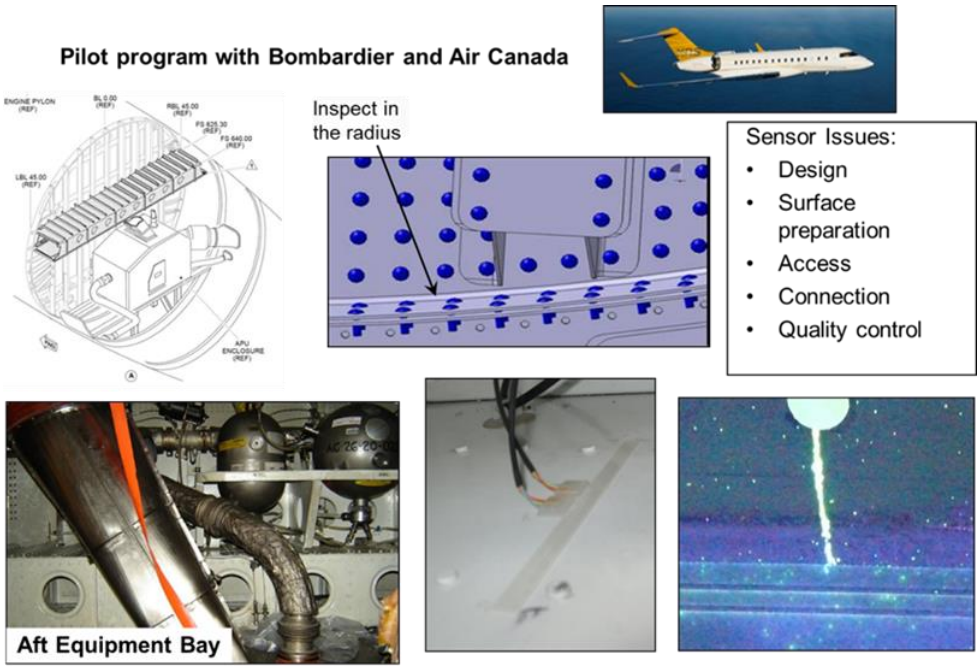

Figure 2-20. Sample Program that Produced a Successful Crack Detection by CVM Sensor on an Operating CRJ Aircraft

LHS SLS ID#1	Conducti-vity Control Gallery	Conducti-vity Gallery 1	Conducti-vity Gallery 2	CVM Gallery 1	CVM Gallery 2	Gallery 1 Status	Gallery 2 Status	Conventional NDT Result
Date	CI	CI	CI	CI	CI			
25-02-09	9300	10686	9930	2419	0.7	IF	NC	NC
26-06-09	6947	7339	7270	4276	1.1	NA	NC	NC

RHS SLS ID#2	Conducti-vity Control Gallery	Conducti-vity Gallery 1	Conducti-vity Gallery 2	CVM Gallery 1	CVM Gallery 2	Gallery 1 Status	Gallery 2 Status	Conventional NDT Result
Date	CI	CI	CI	CI	CI			
25-02-09	10192	10827	10692	0.9	1.9	NC	NC	NC
26-06-09	6702	7807	6930	2947*	12.3	C	C	C

Crack Indication**	2
No Crack Indication	4
True Positive Or False Positive	2/2 (100%)
True Negative	2/2 (100%)
False Negative	0/2 (0%)

** All galleries are considered independent

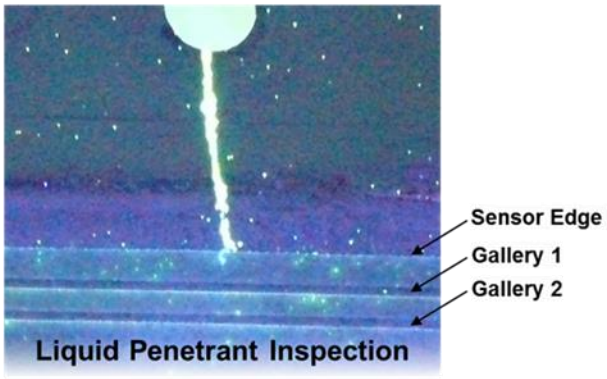

Figure 2-21. Flight Test Results from CRJ Aircraft Showing Crack Detection by CVM Sensor

Additional programs conducted to produce approval for CVM sensor use on rotorcraft and fixed wing aircraft are depicted in Figure 2-22 to Figure 2-26. Additional information on the CVM rotorcraft application shown in Figure 2-22 will be discussed in this report. Figure 2-23 shows an application of CVM sensors to detect cracks in the set of 10 Wing Box fittings on the B737 aircraft [2.13]. The goal was to move beyond the traditional prototype field testing completed in the first decade of 2000 and move into mainstream, industry-wide adoption of SHM. Towards that end, Sandia Labs, in conjunction with Boeing, Delta Air Lines, Structural Monitoring Systems Ltd., Anodyne Electronics Manufacturing Corp. and the Federal Aviation Administration (FAA) carried out a certification program to formally introduce Comparative Vacuum Monitoring (CVM) as a structural health monitoring solution to a specific aircraft wing box application. Validation tasks were designed to address the SHM equipment, the health monitoring task, the resolution required, the sensor interrogation procedures, the conditions under which the monitoring will occur, the potential inspector population, adoption of CVM into an airline maintenance program and the document revisions necessary to allow for routine use of CVM as an alternate means of performing periodic structural inspections.

Controlled, representative laboratory testing and on-aircraft flight tests addressed damage detection capability, durability, installation/supportability, and safety. The flight test series demonstrated the ability of CVM sensors to: 1) operate successfully on operating aircraft over long periods of time, 2) produce consistent data and 3) be properly installed and monitored by airline personnel. They allowed for the accumulation of over 1.5 million successful flight hours. As a result of the CVM Wing Box Fitting program and the compiled results from completed lab/flight

testing, CVM was added to the Boeing Nondestructive Testing (NDT) Manual for the 737 aircraft platform. Also, as a result of the CVM Wing Box fitting program, Boeing Service Bulletin 737-57-1309, was changed to include CVM technology as an alternate inspection method to the previously-specified visual and eddy current inspections.

Another sample application is shown in Figure 2-24 and Figure 2-25 where a network of CVM sensors are being used to monitor for crack initiation around the installation of a WiFi antennae. This activity involves the modification of a Supplemental Type Certificate to allow for CVM use on series of internal fuselage inspections which are difficult to access. The current Instructions for Continued Airworthiness require low-cycle, repeat inspection intervals on various internal structures. CVM sensors have been installed to monitor the doubler plates and substructure shown in Figure 2-24 and Figure 2-25.

Overall, the series of CVM programs outlined here provided:

- Analysis and CVM application to Multiple aircraft applications
- Completion of comprehensive performance assessments – sensitivity, reliability, durability, safety.
- Accumulation of over 50 combined years of successful operation on flying aircraft
- Formal approval from aircraft manufacturers and aviation regulators
- Allowed for routine use on aircraft
- Completion of extensive educational activities with airlines, OEMs and regulators
- Facilitated the evolution of an SHM certification process including the development of regulatory documents and advisory materials to guide the implementation of SHM systems via reliable certification programs

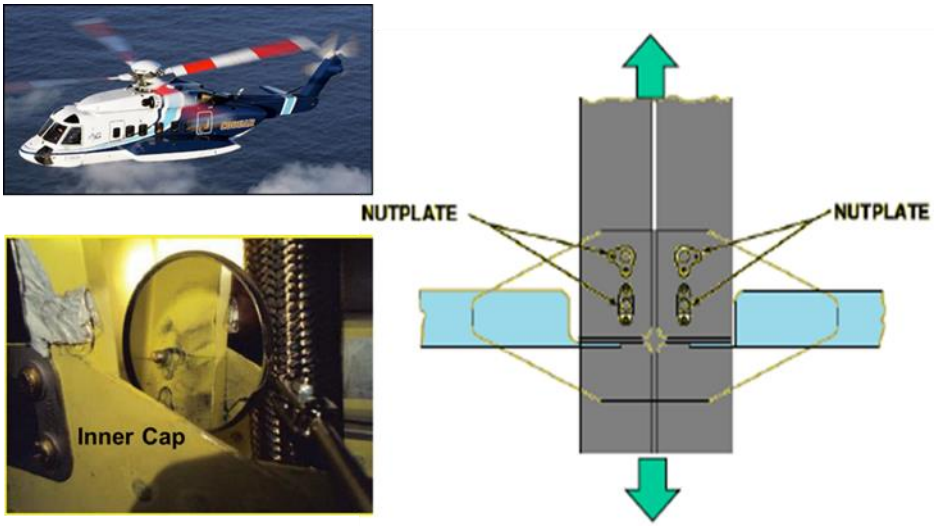

Figure 2-22. Sample Rotorcraft Application Deploying CVM System to Monitor Cracks on S-92 Frame Gusset

Figure 2-23. Sample Aircraft Application Deploying CVM System to Monitor Cracks on Wing Box Fittings

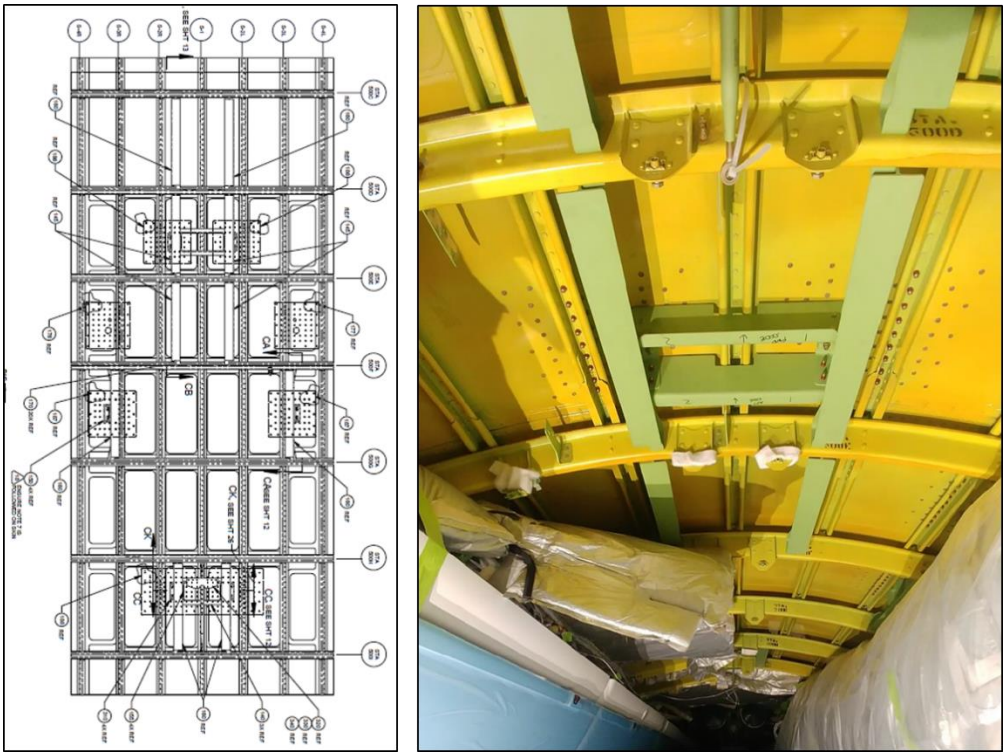

Figure 2-24: Fuselage Crown Region Where WiFi Antennae is Installed

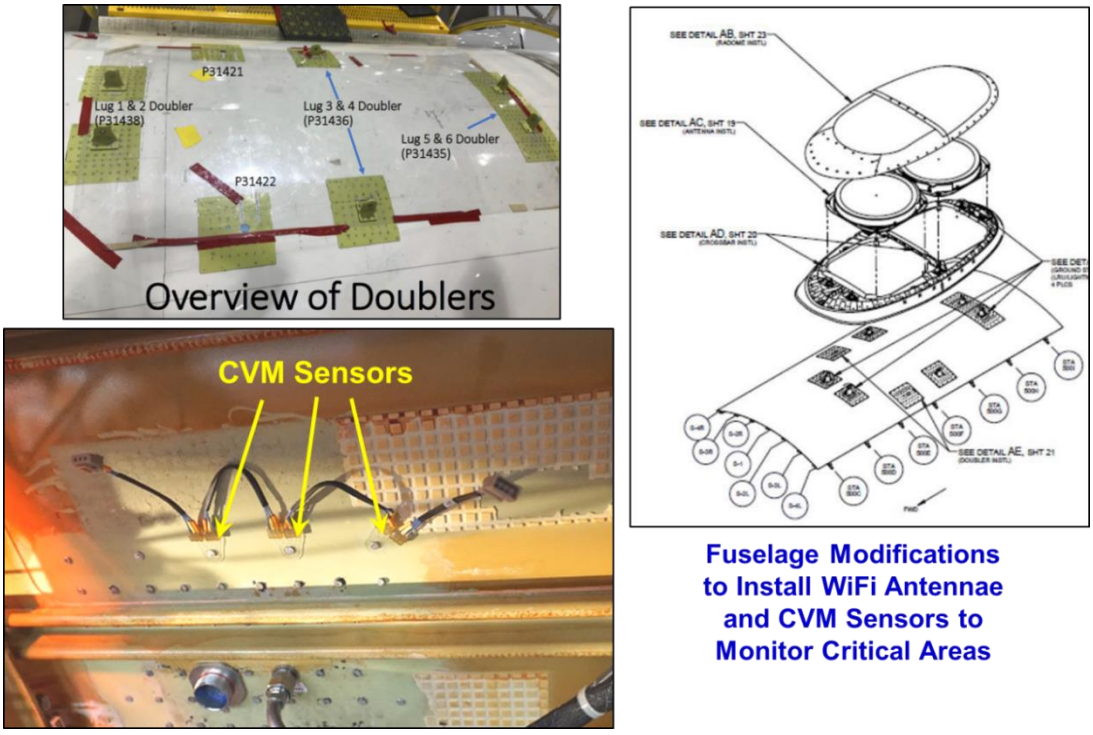

Figure 2-25: Use of CVM Sensors to Detect Cracks in Modified Fuselage Region

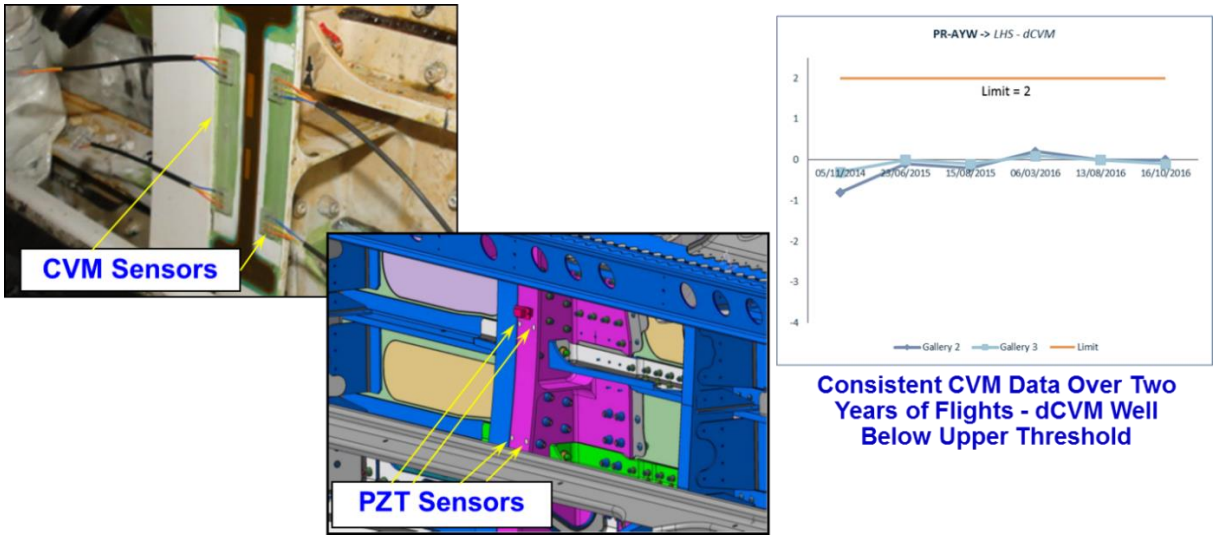

Figure 2-26: Use of CVM and PZT Sensors to Monitor Substructure Elements on Embraer Aircraft During Flight Tests

Multi-CVM Switch-Based System for Remote Bridge Monitoring – As mentioned above, SHM systems can be used to monitor a wide variety of structures that may benefit from periodic, remote inspections. A real-time monitoring system was developed for remotely interrogating a distributed array of CVM sensors [2.14]. It used a series of pressure switches that can continuously monitor

structures remotely via a wireless transmitting device. Sensors were placed in known fatigue critical locations on the bridge structure shown in Figure 2-27. If a crack breaches a CVM sensor, the pressure switch will be opened and, in turn, a message would automatically be sent to a maintenance center and any cell phone that was programmed into the firmware.

Up to 50 switches can be powered by one vacuum pump. The CVM monitoring system, shown in Figure 2-28, was mounted at a central point on the bridge structure. Multiple sensors were arranged to monitor the growth of any crack. In this design, a known crack can be monitored for a particular length when a sensor placed ahead of the crack is triggered as the crack grows. In this bridge application, known, critical locations at welded joints required periodic monitoring and their location over 100 feet from the road surface made manual on-site inspections impractical. The installed CVM monitoring system could continuously update web sites or send automated text messages or e-mails so that operators can quickly and remotely ascertain the condition of the bridge structure and determine if maintenance action is required.

Figure 2-27. Placement of CVM Sensor Network for Monitoring Critical Bridge Welds

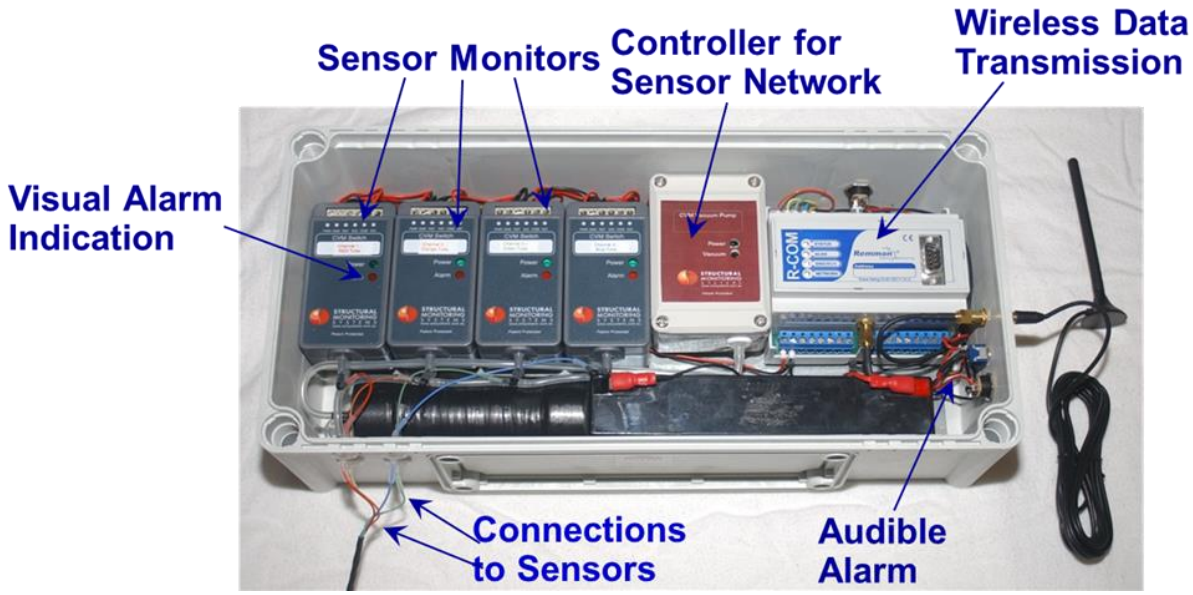

Figure 2-28. Real-Time, Remote Monitoring System for a Network of CVM Sensors

2.3. Piezoelectric Transducers – Technology Description

Piezoelectric Transducer sensors are based on active-material principles and utilize thin piezoelectric wafers of 0.125”-0.25” diameter with thicknesses of 0.010” - 0.030”. They can be easily attached to existing structures without changing the local and global structural dynamics [2.15 - 2.18]. PZT sensors can also be embedded inside composite structures to closely monitor for internal flaws. These sensors can act as both transmitters and receptors. As transmitters, piezoelectric sensors use electrical excitation to generate elastic waves in the surrounding material. As receptors, they receive elastic waves and transform them into electric signals. It is possible to install arrays of active-sensors, in which each element takes, in turn, the role of transmitter and receptor, and thus scan large structural areas using ultrasonic waves. The structural interrogation strategies using active piezoelectric sensors are twofold:

(a) For local area detection, the electro-mechanical (E/M) impedance method is applied to detect changes in the point wise structural impedance resulting from the presence and propagation of structural damage.
(b) For large area detection, wave propagation techniques using Lamb and Love waves methods are used to identify zones in the monitored area that have undergone changes in their structural integrity.

In the high-frequency E/M impedance approach, pattern recognition methods are used to compare impedance signatures taken at various time intervals and to identify damage presence and progression from the change in these signatures. In the Lamb/Love waves approach, the acousto-ultrasonic methods identifying changes in transmission velocity, phase, and additional reflections generated from the damage site are used. Both approaches can benefit from the addition of artificial intelligence neural network algorithms that can extract damage features based on a learning process. Figure 2-29 shows a sample set-up of PZT sensors on an aluminum plate and typical PZT response signals that are used in the damage detection analysis algorithms. Figure 2-30 and Figure 2-31 depict the damage detection strategy that uses the signals from various networks of piezoelectric sensors and wave propagation techniques for all paths between each actuator and receiver set.

Summary of SHM with Piezoelectric Sensor Systems

- Overcome inspection impediments - accessibility limitations, complex geometries, and the location and depth of hidden damage
- Prevention of unexpected flaw growth and structural failure – on-board health monitoring systems
- Embedded, distributed, miniature, piezoelectric (PZT) sensors – wide-area network to quickly assess the condition of a structure
- Actuation Excitation - frequency and waveform can be adjusted to optimize structural response
- Wave Reception – pitch-catch method measures changes in wave transmission (impedance)
- Wave Propagation Techniques - Lamb Wave methods are used to identify zones that have undergone significant changes in their structural consistency.

- Difference between in-service signals and original, undamaged ("Baseline) signals is used to identify structural damage
- Rapid diagnosis via portable plug-in system provides "GO" – "NO GO" decisions on area being monitored
- Artificial intelligence, neural-network algorithms are used to extract damage features based on a learning process
- Triangulation methods from time-of-flight data are used to determine the size and location of the damage

Validation Testing of Piezoelectric Sensors in Electro-Mechanical Impedance Mode - In order to evaluate this health monitoring approach, test specimens representative of aircraft lap joints were produced. The specimens contained realistic, engineered crack and corrosion flaws [2.17]. Three specimens were constructed: (1) pristine; (2) with cracks only; (3) with cracks and corrosion. The specimens were instrumented with several piezoelectric wafer active sensors, 0.25" square and 0.0075" thick. Figure 2-29 shows a set of 4 such active sensors equidistantly placed in a row at right angles to a 0.75" simulated crack (notch).

An impedance analyzer for the E/M impedance testing, and wave generator, digital oscilloscope, pulser-receiver and MHz range A/D boards for wave propagation testing were used in the experiments. Initial E/M impedance measurements were made to detect cracks at rivet locations. Figure 2-29 shows the superposed results of E/M impedance testing performed on pristine (PZT-Ref) and cracked (PZT) specimens with the same sensor arrangement as shown in Figure 2-29. As expected, the sensors further away from the crack registered less change in the E/M impedance spectrum than sensors closer to the crack. The sensor closest to the crack showed the largest change in the E/M impedance. The experimental results in Figure 2-29 clearly show the increase in impedance produced by the structural flaws. Signal optimization and system sensitivity can be achieved through strategic sensor placement, quantifying piezoelectric probe responses, and improved data analysis algorithms.

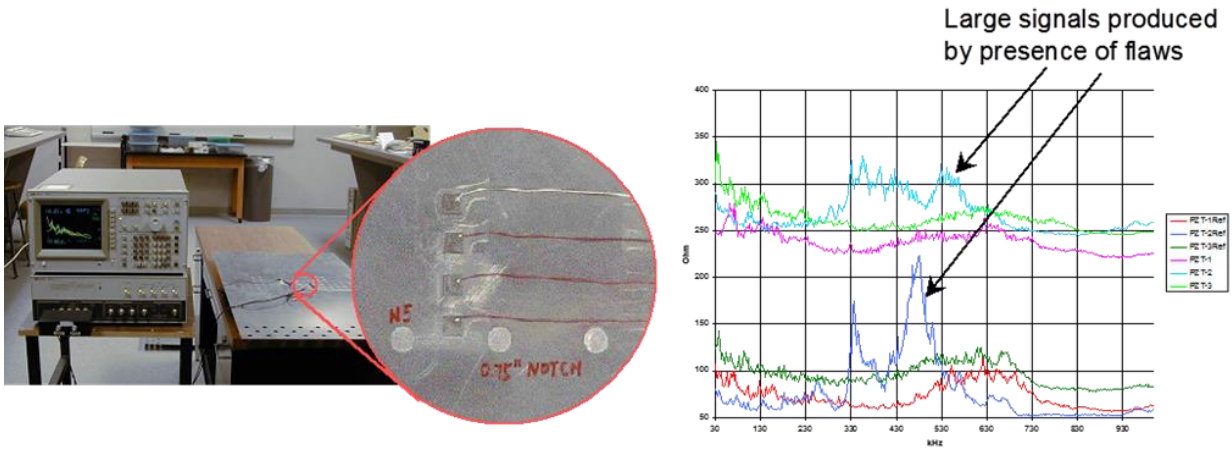

Figure 2-29. Piezoelectric Sensors on an Aircraft Panel Containing Crack and Corrosion Damage (left) and Results Obtained with the E/M Impedance Technique Using Active Sensors (right)

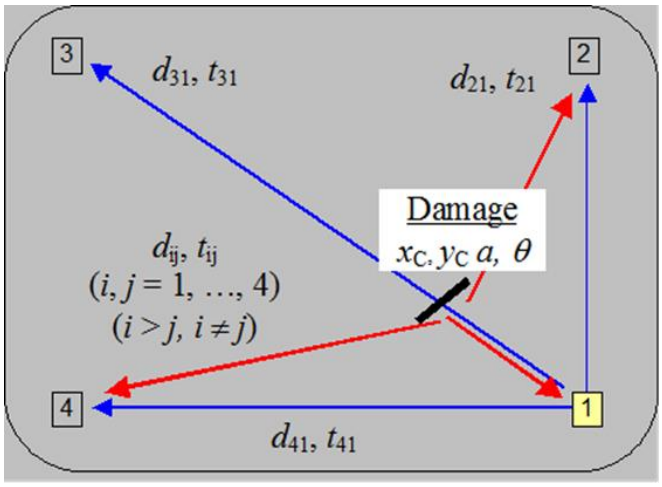

Figure 2-30. Damage Detection Strategy Using a Network of Piezoelectric Sensors and Wave Propagation Techniques for All Paths Between Each Actuator and Receiver Set

Zonal SHM with Piezoelectric Sensor Networks -

Global, or Zonal SHM, is commonly achieved using a network of widely-spaced sensors that exploit an underlying physics (e.g. disruption of wave travel) to monitor the entire area inside the sensor layout network. The use of Global SHM is commonly associated with:

- Exact flaw location may or may not be known
- Inconsistent flaw behavior
- Multi-layer, multi-component
- Could affect large area.

Examples:

- Impact damage
- Riveted joint cracking
- Corrosion

The PZT application selected for use on rotorcraft involved zonal monitoring of a series of potential fatigue crack sites on a beam structure that is representative of beams used to mount gearboxes for rotorcraft engines. Specifically, a PZT network was designed to globally monitor the aft beam used to mount the S-92 main gearbox (see Section 3.3).

Figure 2-30 and Figure 2-31 show how the signals from various networks of piezoelectric sensors and wave propagation techniques for all paths are used to detect damage. Figure 3-14 and Figure 3-15 show the specific rotorcraft gearbox mount application while Section 4.4 describes the PZT sensor layouts used to monitor this structure.

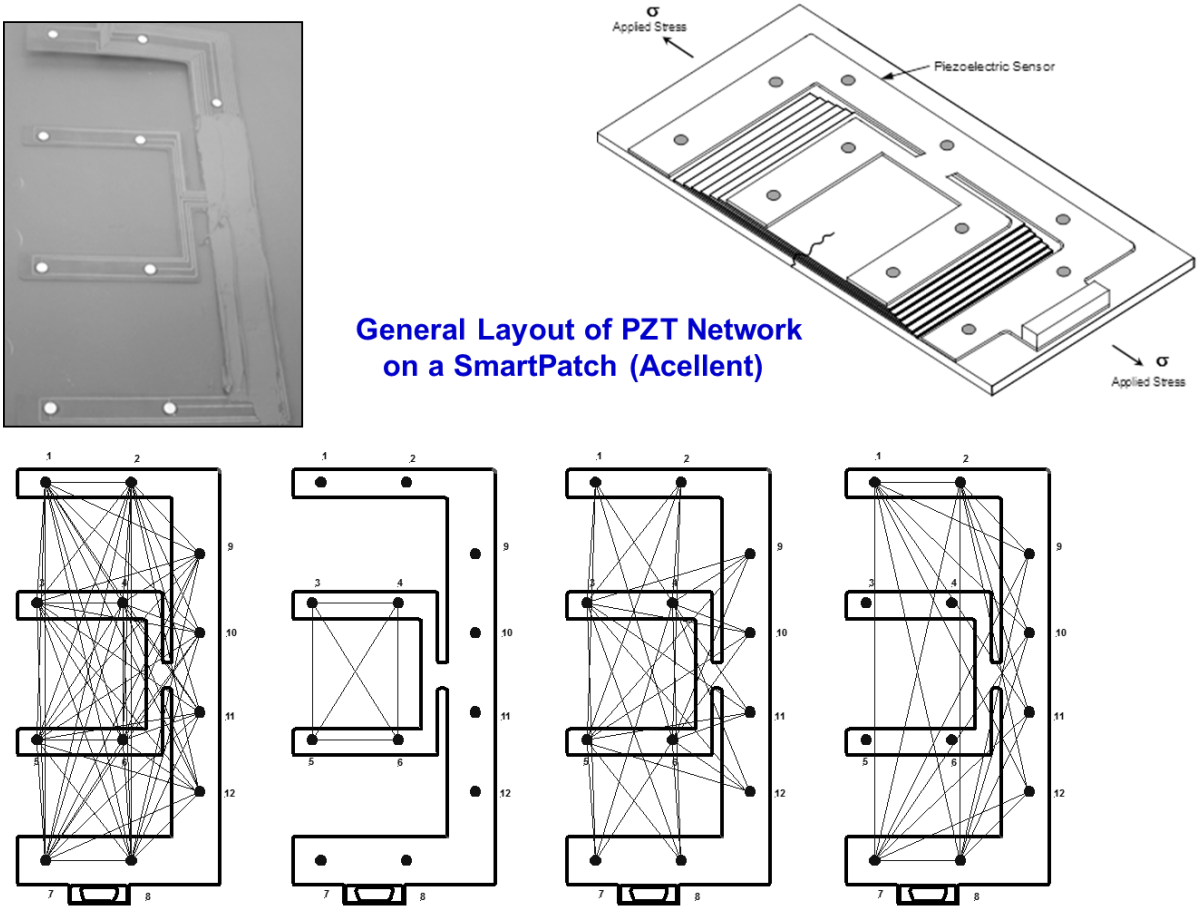

Figure 2-31. Various PZT Sensor-Receiver Paths for Global Monitoring

Mountable PZT Networks and Lamb Wave Interrogation Methods - Another structural health monitoring approach was evaluated using a built-in network of piezoelectric transducers embedded in a think dielectric carrier film [2.17]. The SHM system included the PZT network connected to portable, diagnostic hardware and software developed by Acellent Technologies, Inc. The system performs in-situ monitoring, data collection, signal processing, and real-time data interpretation to produce a two-dimensional image of the structure being interrogated. The Acellent software instructs the actuators to generate pre-selected diagnostic signals and transmit them to neighboring sensors. Multiple diagnostic wave types can be generated including 3-peak, 5-peak, and 10-peak narrow band frequency waveforms, chirp, random, and user defined excitations. The software links each sensor with its neighbors to form a web, or network, covering the structure. The system then collects the total set of responses from each of the sensor sets as each PZT takes its turn as the actuator. Changes in the Lamb Waves generated within the structure are used in concert with triangulation methods to detect the presence of structural anomalies and to determine the size and location of the flaws.

Damage Identification through Elastic Wave Propagation - The wave propagation approach uses the pitch-catch method for detecting damage in a structure. Acousto-ultrasonic methods are used

to identify changes in wave transmission. Figure 2-32 shows some of the wave motion from sensors (1) and (9) when they are used as the source of excitation for the structure. The mechanical vibration is introduced into the structure by the PZT element and travels by wave motion through the test piece at the velocity of sound, which depends on the material. If the pulses encounter a reflecting surface, some or all of the energy is reflected and monitored by adjacent PZT sensors in the network. The reflected beam, or echo, can be created by any normal (e.g. in multi-layered structures) or abnormal (flaw) interface. Figure 2-32 highlights the interaction of the UT waves with a flaw within the structure. The degree of reflection depends largely on the physical state of the materials forming the interface. Cracks, delaminations, shrinkage cavities, pores, disbonds, and other discontinuities that produce reflective interfaces can be detected. Complete reflection, partial reflection, scattering, or other detectable effects on the ultrasonic waves can be used as the basis for flaw detection.

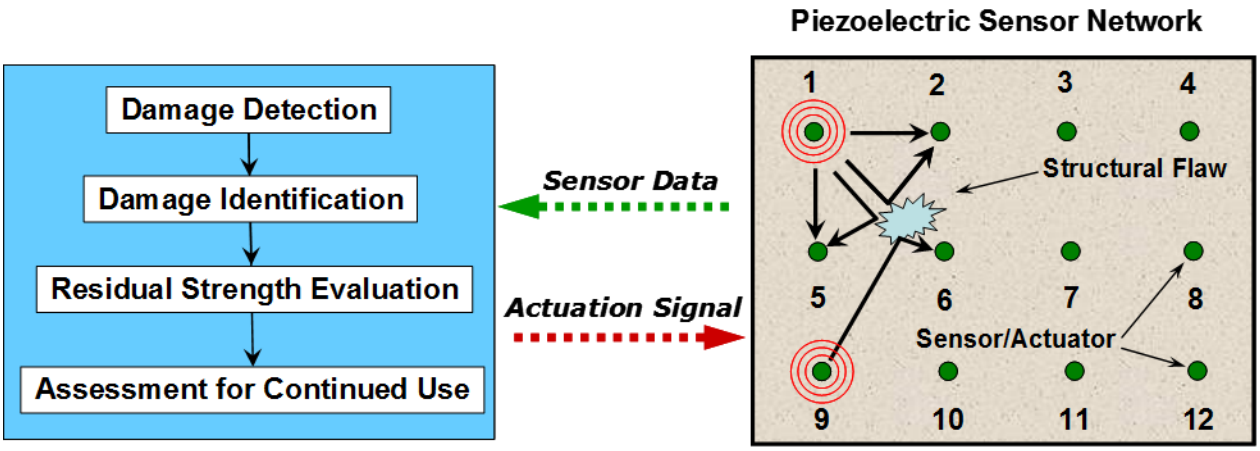

Figure 2-32. Flaw Detection Using the Wave Propagation Method

Damage Detection with PZT and Use of Damage Index Thresholds - One of the concerns with any type of in-situ sensor method for health monitoring is how to accurately classify damage in order to avoid false calls and missed flaws. It is important to determine how to accurately establish a threshold for damage identification. Calibration testing can be performed to carefully relate controlled damage onset and flaw growth to sensor response. These laboratory-based "training" exercises can utilize neural network methods to optimize the recognition of structural anomalies. Validated neural networks can continue to learn using actual field data.

In cases where lab data is limited or difficult to obtain, statistical process control in an unsupervised learning mode can be used. For instance, Ref. [2.19] proposes the use of a *Damage Index* (DI) that can be calculated using field data. The Damage Index, computed in equation (2-2), quantifies the deviation of a reconstructed signal from the original known input as a function of a signal's attenuation. The computed DI, also referred to as "*damage sensitive feature,*" can then be cast in the context of an outlier detection framework [2.20]. This allows for damage classification based on statistical analysis. The approach categorizes infinite possible system responses into a few bins (normal or extreme responses) thus allowing more accurate damage thresholds to be established. Because of the non-Gaussian nature of the feature distribution tails in the outlier detection

framework, extreme value statistics (EVS) can be employed to develop a robust and statistically confident damage classifier [2.21]. Figure 2-33 depicts how a statistically-guided damage threshold is set while Figure 2-34 shows how intelligent thresholds can be determined by using EVS and a plot of the Damage Index for a set of actuator-sensor pairs.

$$DI = 1 - \left(\int_{u_0}^{u_1} Wf_t(u, s_o)du \Big/ \int_{u_0}^{u_1} Wf_b(u, s_o)du \right) \tag{2-2}$$

where Wf_t describes the test signal's energy and Wf_b describes the baseline signal for the undamaged scenario.

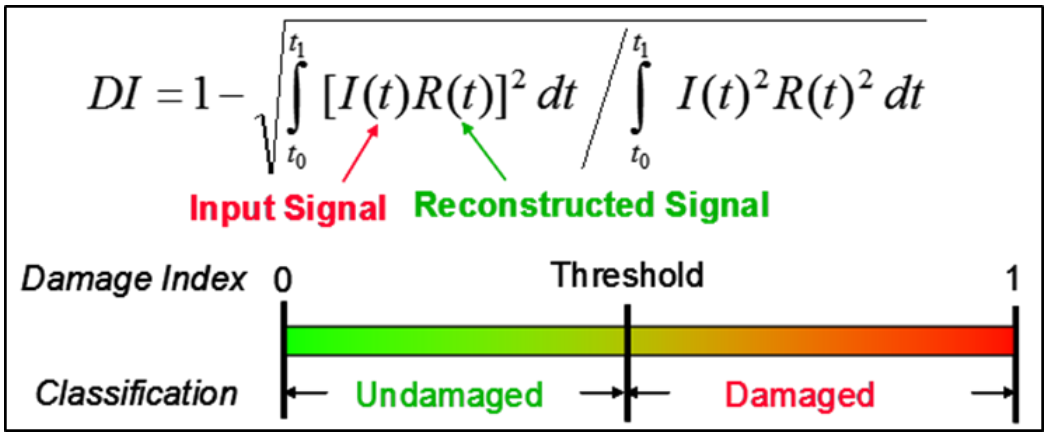

Figure 2-33. Calculation of the Damage Index Using Signal Attenuation Levels (Comparison of Input and Output Waveforms)

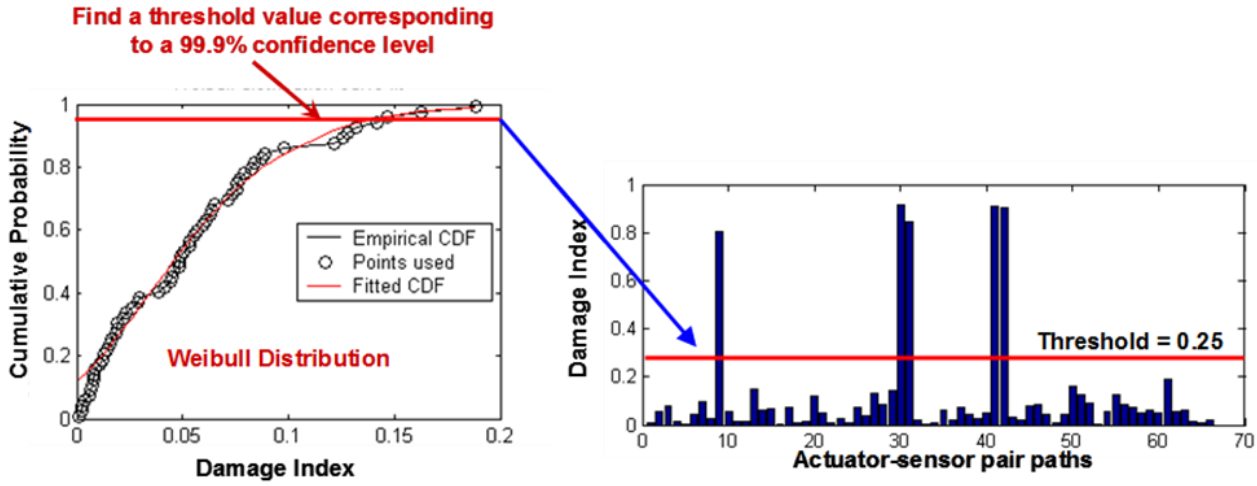

Figure 2-34. Damage Classification Using Statistical Analysis of Data to Determine Proper Damage Thresholds

Overall DI assessments can be calculated from equations (2-3) and (2-4):

$$\mathrm{DI} = \sqrt{\sum \left[Norm_{sig} - \frac{Norm_{sig} \times Ref_{sig}}{\sum Ref_{sig}^2} \times Ref_{sig} \right]^2} \tag{2-3}$$

$$Norm_{sig} = \frac{Current_{sig}}{\sqrt{\sum (Current_{sig})^2}} \tag{2-4}$$

Where $Current_{sig}$ is the current signal data and Ref_{sig} is the baseline signature data for comparison.

PZT Damage Index (DI) is calculated from the difference between current signals and Baseline signals obtained from the pristine structure. Figure 2-35 shows the comparison between two different signals obtained at different times in a structures fatigue life. The difference between these two signals, represented by the yellow curve in Figure 2-35, provides an indication of the DI and accumulation of damage or other changes in the structure.

Figure 2-35. Change in PZT Signals from their Baseline (Undamaged) Signatures are Used to Determine a Damage Index - Change in PZT Signal is Represented by Yellow Waveform

Additional discussions on the proper selection of damage detection thresholds – whether they are a Damage Index calculation or other SHM system response parameter(s) – are provided in Chapters 4, 5 and 6. One critical issue pertains to establishing such thresholds with a complete understanding of the associated noise in the system. Another criterion may involve establishing a damage detection threshold where a stable and steadily-rising SHM system response is observed. It is not uncommon for SHM systems to "temporarily" exceed a threshold, then drop below a threshold and finally move through a region of a steadily-increasing response that extends well above the threshold. Damage detection may reliably be inferred when the SHM system enters this latter stage of response. Once historical SHM system response information has been gathered for specific applications, each succeeding application of the same SHM system will be easier and more streamlined because of the expanding database of appropriate threshold settings and system response. As mentioned above, focused, calibration testing can be performed to carefully relate controlled damage onset and flaw growth to sensor response. In the early stages of such testing, before any damage is initiated, it is possible to collect SHM system response data that can be categorized as "noise." It is important to distinguish between signals that can be classified as noise and signals that correspond to damage. It may even be possible to enhance the calibration further by relating the SHM system response to actual damage size. After the source of signal noise - stemming from the structure/loading itself or something inherent in the SHM system – becomes better understood and defined, it is possible to produce better correlations between damage detection thresholds and damage presence and size. This, in turn, will lower the Probability of Detection for the SHM system. Finally, it may be possible to actually lower noise levels through enhanced data acquisition processes and further optimize POD levels.

Historical Validation Testing with PZT - In one test series, a network of PZT sensors was deployed to assess bonded joints and crack growth in a composite doubler repair installation [2.18]. Figure 2-36 shows a schematic and photos of the Boron-Epoxy laminate repair on a metal parent structure along with the set of PZTs distributed over the structure to be monitored. Note that the network of sensors/actuators is embedded in a custom polyamide film to allow for accurate placement of the network and eliminating the need for each sensor to be installed individually. The test specimen, containing engineered disbonds and a central crack, was subjected to constant-amplitude fatigue loads with maximum stresses in excess of 80% of yield levels for the ASTM A36 steel plate (thickness = 0.188").

Similar to conventional ultrasonic testing, the PZT data analysis included the following measurements: time of wave transit (or delay), path length, frequency, phase angle, amplitude, and angle of wave deflection (reflection and refraction). In this test series, the pitch-catch method studied the transmission of sound waves as they travelled from each actuator to all other receiving sensors. The sum total of received signals was then analysed to define the presence and location of flaws. In order to optimize flaw detection, a series of excitation frequencies were used: 50 KHz, 200 KHz, 350 KHz, and 500 KHz. Overall test results revealed that disbond flaws were most strongly detected with the lower, 50 KHz excitation while the crack growth was monitored best with the highest, 500 KHz excitation. Figure 2-37 shows raw PZT response data produced during the Lamb Wave interrogation method. Signal attenuations, corresponding to disbonds between the laminate and parent skin, are apparent. When all of the signals are analysed with the Acellent imaging software and flaw locations are determined by using the time base and triangulation

methods, a two dimensional image of the disbond flaws was produced. Figure 2-38 shows the engineered disbonds in the test specimen along with the image produced by the PZT sensor network. Note that both disbond flaws were clearly imaged even though one is a weak bond produced by a mold release agent and one is a complete disbond produced by a Teflon insert.

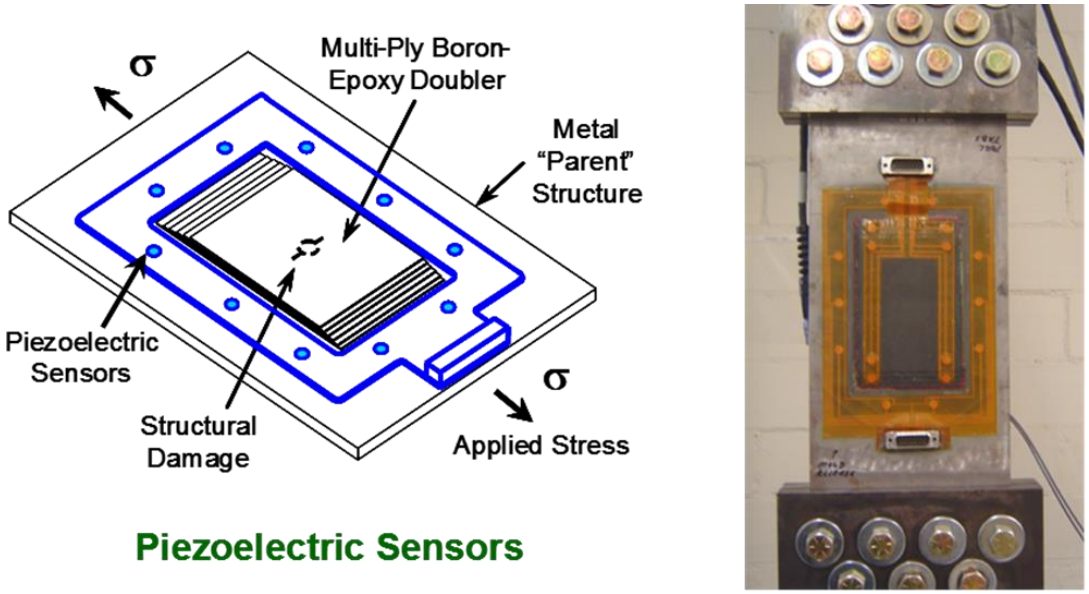

Figure 2-36. Set of Piezoelectric Sensors Used to Monitor Crack Growth and Disbonds in a Composite Doubler Bonded to a Metal Plate

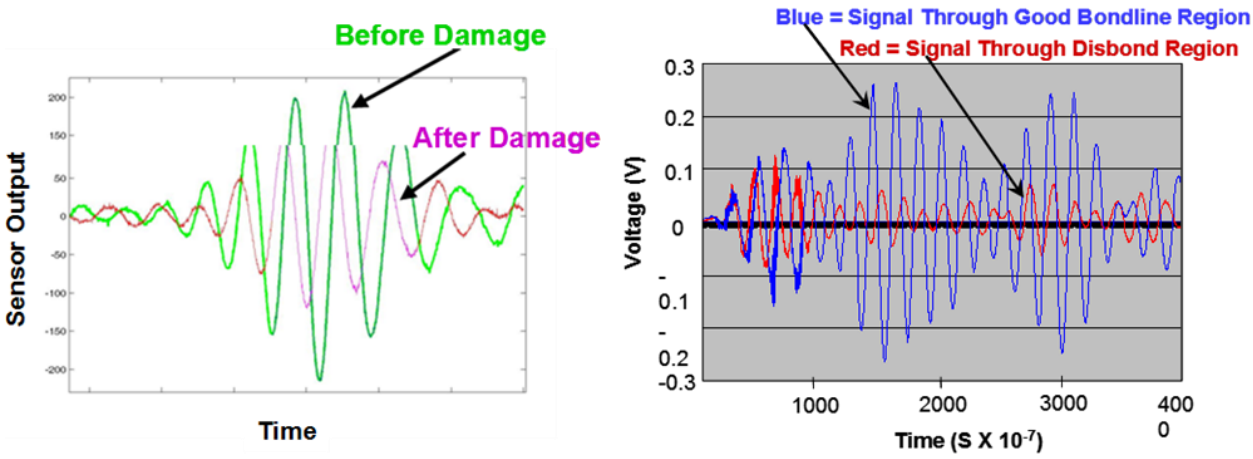

Figure 2-37. Sample Signals Observed by PZTs During 50 KHz Lamb Wave Interrogation Showing the Attenuation Corresponding to Disbonds in the Structure

Crack detection and growth was monitored using the same approach. PZT data was acquired at discrete intervals during the crack growth process. In addition, eddy current and microscopic inspections were conducted to measure the crack lengths at each cycle count. Figure 2-39 shows PZT response signals before and after crack growth occurred into the sensor path. A set of images

produced by the PZT network are shown in Figure 2-40. The crack growth (two fatigue cracks emanating from a central hole) can be clearly seen. The PZT crack growth data was analysed further to produce crack length predictions. The Acellent software contains an algorithm that allows for system learning. After inputting several crack lengths to match with the PZT data at discrete fatigue intervals, it was possible for the system to predict all subsequent crack lengths using the PZT data alone. Table 2-2 compares the crack lengths predicted by the PZT sensor network with the crack lengths determined from eddy current and microscopic measurements. The PZT predictions were all within 5% of the actual crack lengths for data taken at max load (34 kips).

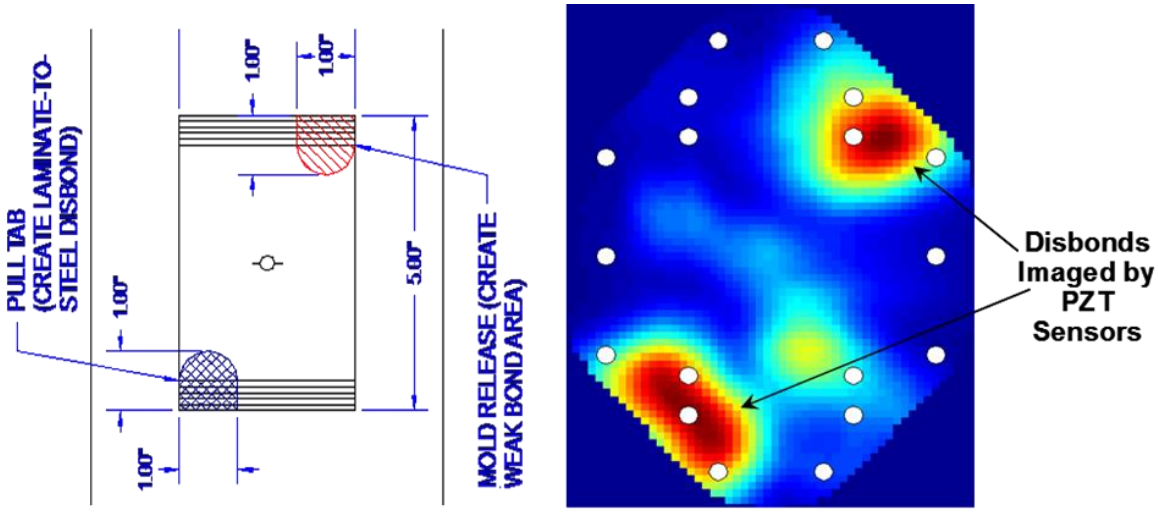

Figure 2-38. Color-Coded Image of Disbond Flaws Produced by the PZT Sensor Network

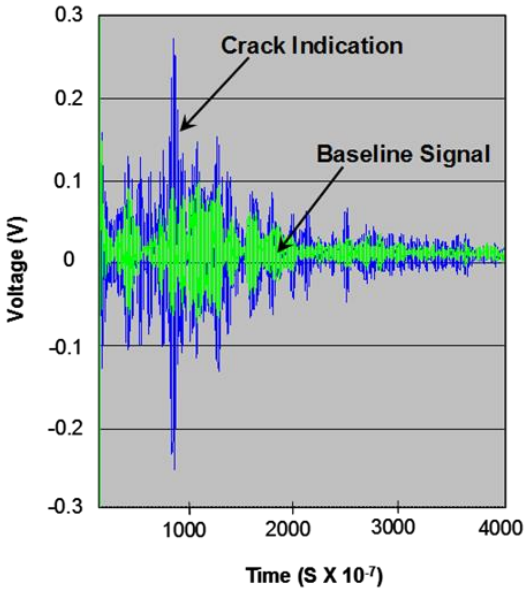

Figure 2-39. Sample PZT Signals Showing the Indication of a Fatigue Crack with a 500KHz Excitation

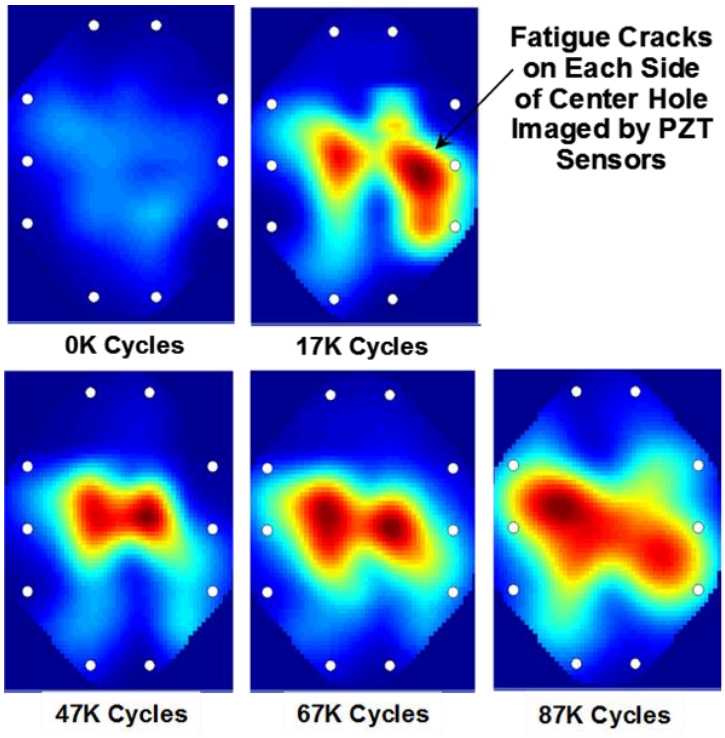

Figure 2-40. Color-Coded PZT Images Showing Crack Growth

Table 2-2. Comparison of Crack Lengths Predicted by PZT Sensors with Actual Crack Lengths Measured Using Eddy Current and Microscopic Methods

Composite Doubler with PZT Health Monitoring			
Fatigue Cycles	Measured Total Crack Length	Estimated Crack Length from PZT Sensor Data (0 lbs. load)	Estimated Crack Length from PZT Sensor Data (34 kips load)
Specimen 1 - Unflawed Composite Doubler			
0	0.00		
26,218	0.32	PZT Learning Data	PZT Learning Data
47,000	0.70	PZT Learning Data	PZT Learning Data
67,000	1.50	1.274	1.385
87,000	2.44	1.956	2.367
Specimen 2 - Composite Doubler with Disbond Flaws			
0	0.00		
19252	0.16	PZT Learning Data	PZT Learning Data
29274	0.32	PZT Learning Data	PZT Learning Data
38064	0.48	PZT Learning Data	PZT Learning Data
51576	0.80	PZT Learning Data	PZT Learning Data
60438	1.08	0.981	1.099
66439	1.34	1.35	1.349
76444	1.76	1.567	1.762
82446	2.02	1.909	2.08

Another program involved an Embraer-Sandia Labs effort to move SHM into routine use for aircraft maintenance procedures. The Federal Aviation Administration's Airworthiness Assurance Center (AANC) at Sandia Labs, in conjunction with Embraer, Azul Airlines, and Agencia Nacional de Aviação Civil (ANAC) completed a study to certify families of aircraft applications, on Embraer aircraft [2.12]. Eight target applications were identified to address both fuselage and wing inspection needs. Figure 2-41 shows several of the structures being monitored as part of the flight test portion of the program.

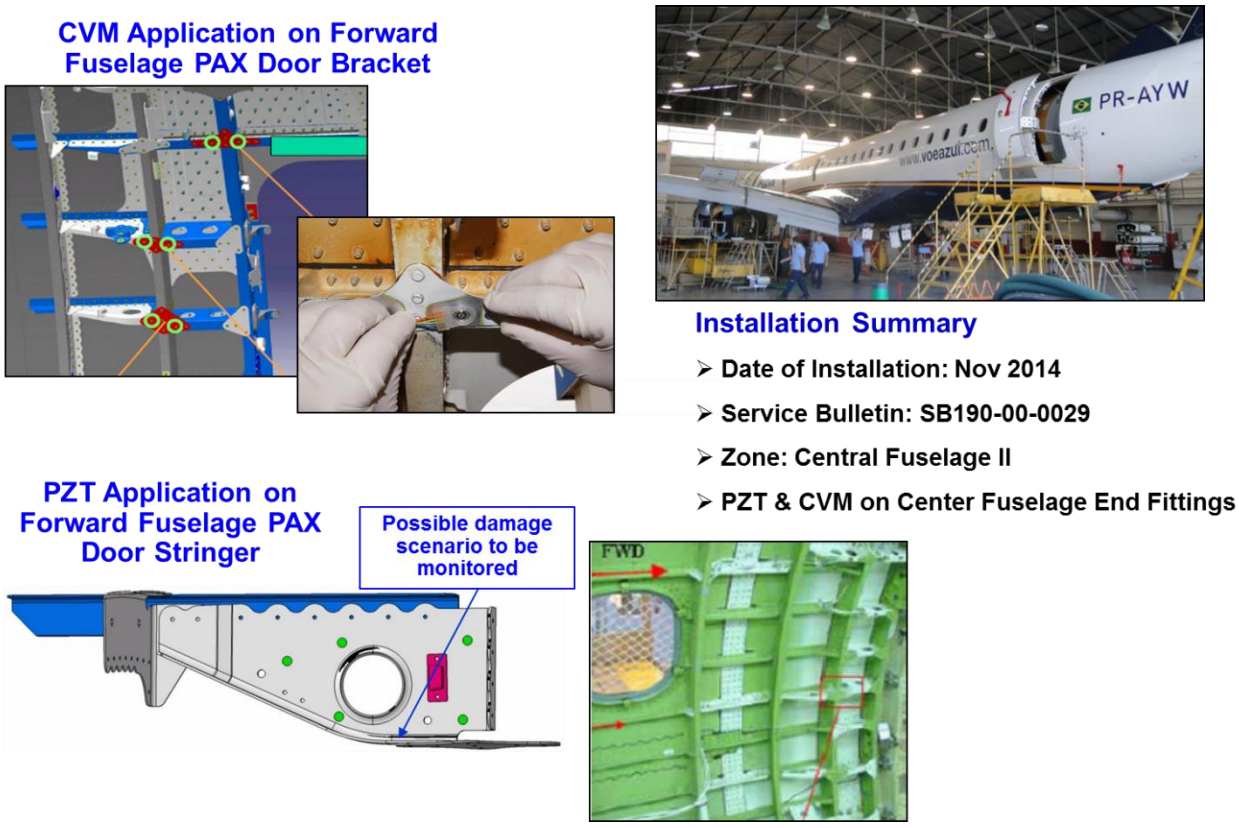

Figure 2-41. Embraer Damage Detection Applications – CVM & PZT Flight Tests – Azul Aircraft PR-AYW

A variety of other laboratory performance assessment and flight tests have been completed using the Acellent PZT system. These programs included structural response (damage detection), environmental durability (MIL-STD-810G, DO-160) and on-aircraft survivability and functionality evaluations. Figure 2-42 shows a PZT network application on a U.S. Army Bell OH-58D to monitor for cracks in the tailboom [2.22]. The current, visual inspection is required every 10 hours (or 20 hours for eddy current) of operation and takes approximately 60 minutes. Crack detection using the SHM system takes approximately 5 minutes. Figure 2-43 depicts the use of PZT sensors to monitor for corrosion in an intermediate gearbox housing on a UH-60 rotorcraft [2.23].

As part of a study into the use of SHM for Condition Based Maintenance (CBM), two SMART Layer Strips were installed on UH-60 Black Hawk as shown in Figure 2-44 [2.24]. Data was

acquired from the on-board PZT system for 72 months. The primary goal of the work was to investigate sensor reliability over a long period of time by installing SMART layer sensor networks onto a Black Hawk rotorcraft. The rotorcraft has logged 900 flight hours since the installation of SMART Layers on the rotorcraft. A total of 56 sensors were installed on the left and right sides of the tailboom. 54 out of 56 sensors are currently functioning, with the two damaged due to an installation error. There was minimal (around 5%) variation in individual impedance and capacitance values of the sensors.

Figure 2-42. PZT Application on OH-58 Tailboom

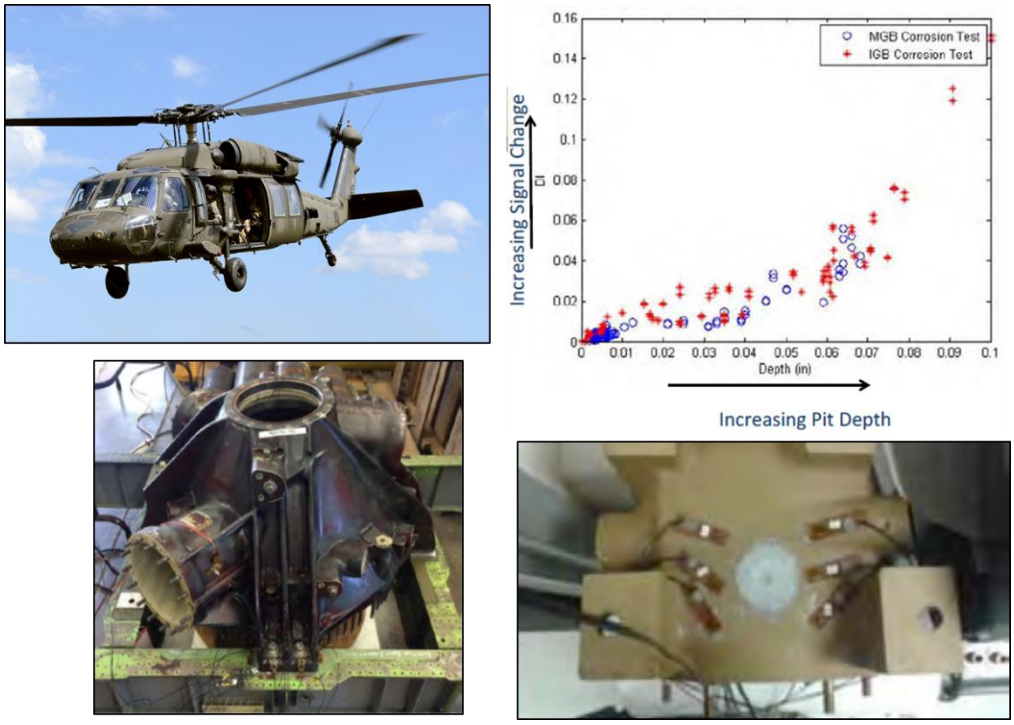

Figure 2-43. Use of PZT Sensors to Quantify Corrosion on a UH-60 Rotorcraft

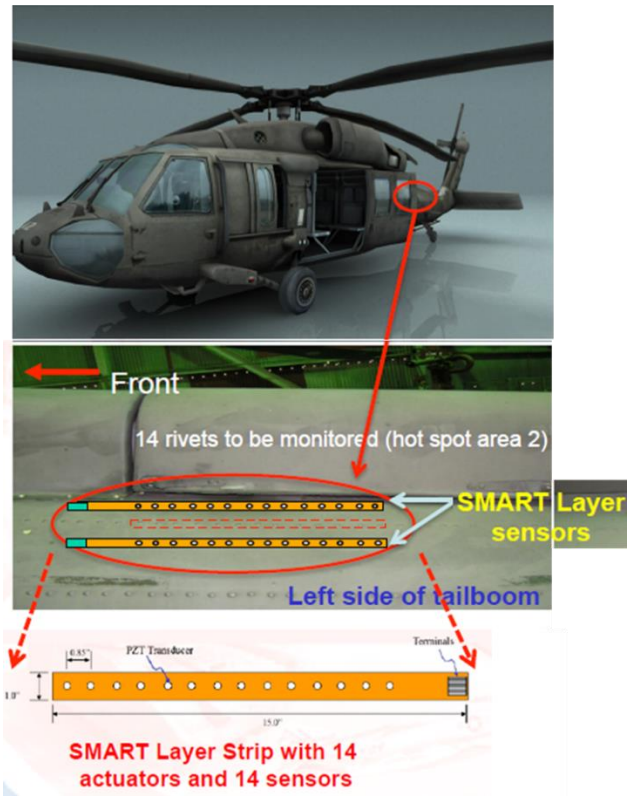

Figure 2-44. PZT Smart Layer Strips Installed to Detect Cracks in the Black Hawk Tailboom

References

2.1. SAE Aerospace Industry Steering Committee on Structural Health Monitoring, "Guidelines for Implementation of Structural Health Monitoring on Fixed Wing Aircraft," SAE Aerospace Recommended Practice ARP 6481, September 2013.

2.2. Brausch, J. and Steffes, G., "Demonstration, Qualification, and Airworthiness Certification of Structural Damage Sensing (SDS) Systems for Air Force Application," US Air Force report AFRL-RX-WP-TM-2013-0062, August 2013.

2.3. Roach, D., "Validation and Verification Processes to Certify SHM Solutions for Commercial Aircraft Applications," Structural Health Monitoring, DEStech Publisher, Lancaster, PA, September 2013.

2.4. Kessler, S.S. Certifying a structural health monitoring system: Characterizing durability, reliability and longevity. In Proceedings of the 1st International Forum on Integrated Systems Health Engineering and Management in Aerospace, November 2005.

2.5. Bockenheimer, C., Speckmann, H., "Validation, Verification and Implementation of SHM at Airbus," IWSHM Sept 2013.

2.6. Roach, D., Rice, T., "Addressing Technical and Regulatory Requirements to Deploy Structural Health Monitoring Systems on Commercial Aircraft," Proceedings of the World Congress on Aeronautical Sciences, September 2018.

2.7. SAE Aerospace Industry Steering Committee on SHM, "Guidelines for Implementation of Structural Health Monitoring on Fixed Wing Aircraft," Aerospace Recommended Practice ARP 6461, September 2013.

2.8. Piotrowski, D., Bohler, J., Melton, A., Roach, D., Rice, T., "Structural Health Monitoring of B737NG Wing Center Section Shear Fittings with Comparative Vacuum Monitoring," Airlines for America Nondestructive Testing Forum, September 2013.

2.9. Roach, D., Kollgaard, J. and Emery, S., "Application and Certification of Comparative Vacuum Monitoring Sensors for In-Situ Crack Detection", Air Transport Assoc. Nondestructive Testing Forum, October 2006.

2.10. Roach, D., "Real Time Crack Detection Using Mountable Comparative Vacuum Monitoring Sensors," *Journal of Smart Structures and Sensors,* Vol. 5, No. 4, July 2009.

2.11. Rulli, R., Dotta, F., Tamba, A., Prado, G., Roach, D., Rice, T., "Structural Health Monitoring Qualification Process and the Future of Aircraft Maintenance," Proceedings of the World Congress on Aeronautical Sciences, September 2018.

2.12. Roach, D., Rice, T., "Design and Assessment of Comparative Vacuum Monitoring and Piezoelectric Transducer Systems for Certified Use in Aircraft Structural Health Monitoring Solutions," Sandia Dept of Energy Report, SAND2017-6401, July 2017.

2.13. Roach, D., Rice, T. "Application and Certification of Comparative Vacuum Monitoring Sensors for Structural Health Monitoring of 737 Wing Box Fittings," DOE SAND2020-9184, September 2020.

2.14. Roach, D., "Use of Comparative Vacuum Monitoring Sensors for Automated, Wireless Health Monitoring of Bridges and Infrastructure," Proceedings of the 9th International Conference on Bridge Maintenance, Safety and Management, July 2018.

2.15. Lin, M., Beard, S., Kumar, A., Qing, X., Development of Structural Health Monitoring Systems Using SMART Layer Technology,“ American Society for Composites 17th Technical Conference, October 2002.
2.16. Kumar, A., Beard, S., Hannum, R. (Acellent Technology), and Roach, D. (Sandia Labs), “In-Situ Monitoring of the Integrity of Bonded Repair Patches on Civil Infrastructures,” SPIE Conference on NDE for Health Monitoring and Diagnostics, February 2006.
2.17. Giurgiutiu, V., Redmond, J., Roach, D., and Rackow, K, "Active Sensors for Health Monitoring of Aging Aerospace Structures," International Journal of Condition Monitoring and Diagnostics Engineering, February 2001.
2.18. Roach, D., DeLong, W., Rackow, K., Yepez, E., Reedy, D., White, S., “Use of Composite Materials, Health Monitoring, and Self-Healing Concepts to Refurbish Our Civil and Military Infrastructure,” Dept of Energy SAND Report SAND2007-5547, September 2007.
2.19. Sohn, H., and Park, Q., “Embedded Sensing: Lamb Wave Propagation,” Structural Health Monitoring Using Statistical Pattern Recognition, short course offered by Los Alamos National Labs, Jan. 2006.
2.20. Beard, S., Kumar, A., Qing, X., Chan, H., Zhang, C.,Ooi, T., “Practical Issues in Real-World Implementation of Structural Health Monitoring Systems”, Proceedings of SPIE on Smart Structures and Material Systems, March 2005.
2.21. Malkin, M., ”Structural Health Monitoring for Bonded Repairs: Complex Structure Testing”, Proceedings of the International Workshop on Structural Health Monitoring, Stanford University, Stanford, CA, September, 2005.
2.22. Kumar, A., “Structural Health Monitoring of Aircrafts Using Built-In Sensor Networks,” Aircraft Structural Integrity Program Conference, Dec. 2020.
2.23. Girard, W., Tucker, B., Bordick, N., Lee, S., Kumar, A., Zhang, D., Li, F., Chung, H., Beard, S., “ Flight Demonstration of a SHM System on an OH-58 Aircraft,” Int’l Workshop on SHM, Sept. 2013
2.24. Janapati, V., Chung, H., Li, F., Kumar, A., Huang, S., “Evaluation of Long-Term Flight Data from On-Board SMART Layers,” Int’l Workshop on SHM, Sept. 2015

3. ROTORCRAFT SHM APPLICATIONS SELECTED

3.1. General Test Specimen Configurations

As noted in Figure 3-1 and Figure 3-2, SHM sensor networks can be oriented to achieve "global" or wide area structural monitoring or "local," focused, small area structural health monitoring. The latter is often called "hot-spot" monitoring because the location and origin of damage onset is well known. Local SHM might be associated with crack detection arising within a known set of fasteners while global SHM might pertain to detection of impact damage anywhere within a large region of a composite aircraft component. Local SHM is often addressed using individual sensor monitoring of a specific hot-spot while global SHM is more commonly achieved using a network of widely-spaced sensors that exploit an underlying physics (e.g. disruption of wave travel) to monitor the entire area inside the sensor layout network. This program addressed both categories of SHM systems to assess the performance and merits of each while identifying important considerations when selecting SHM systems for specific applications.

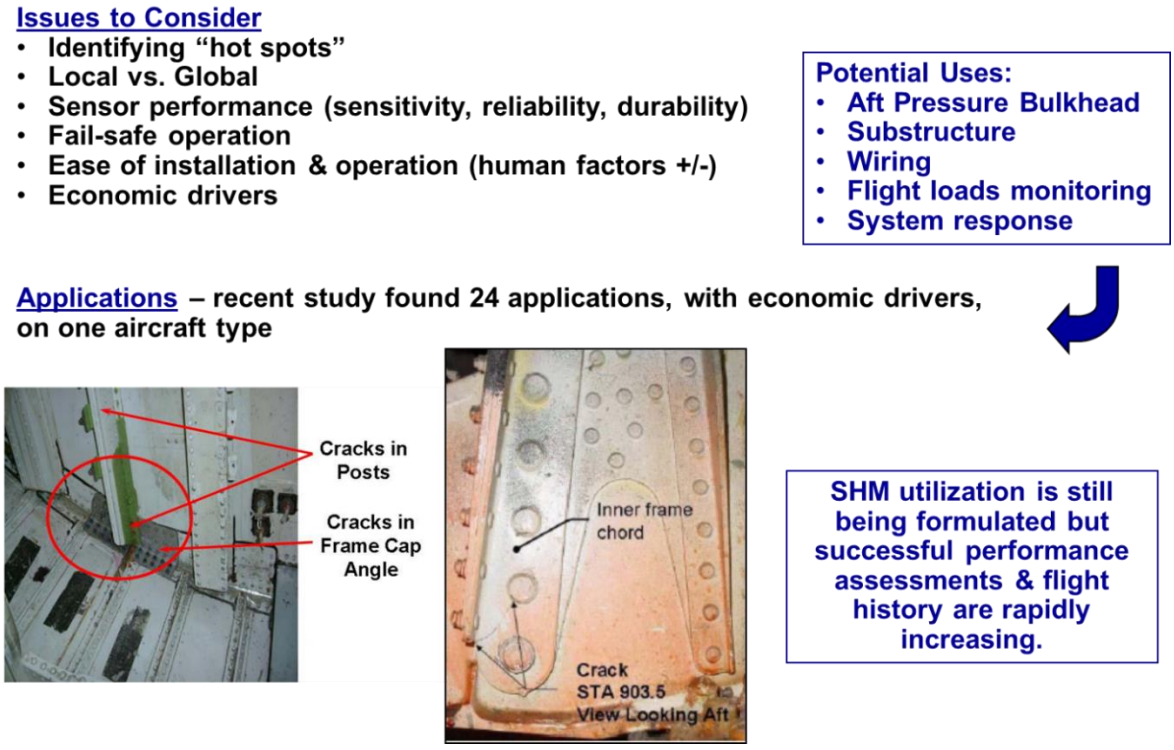

Figure 3-1. Considerations for Local Versus Global Health Monitoring

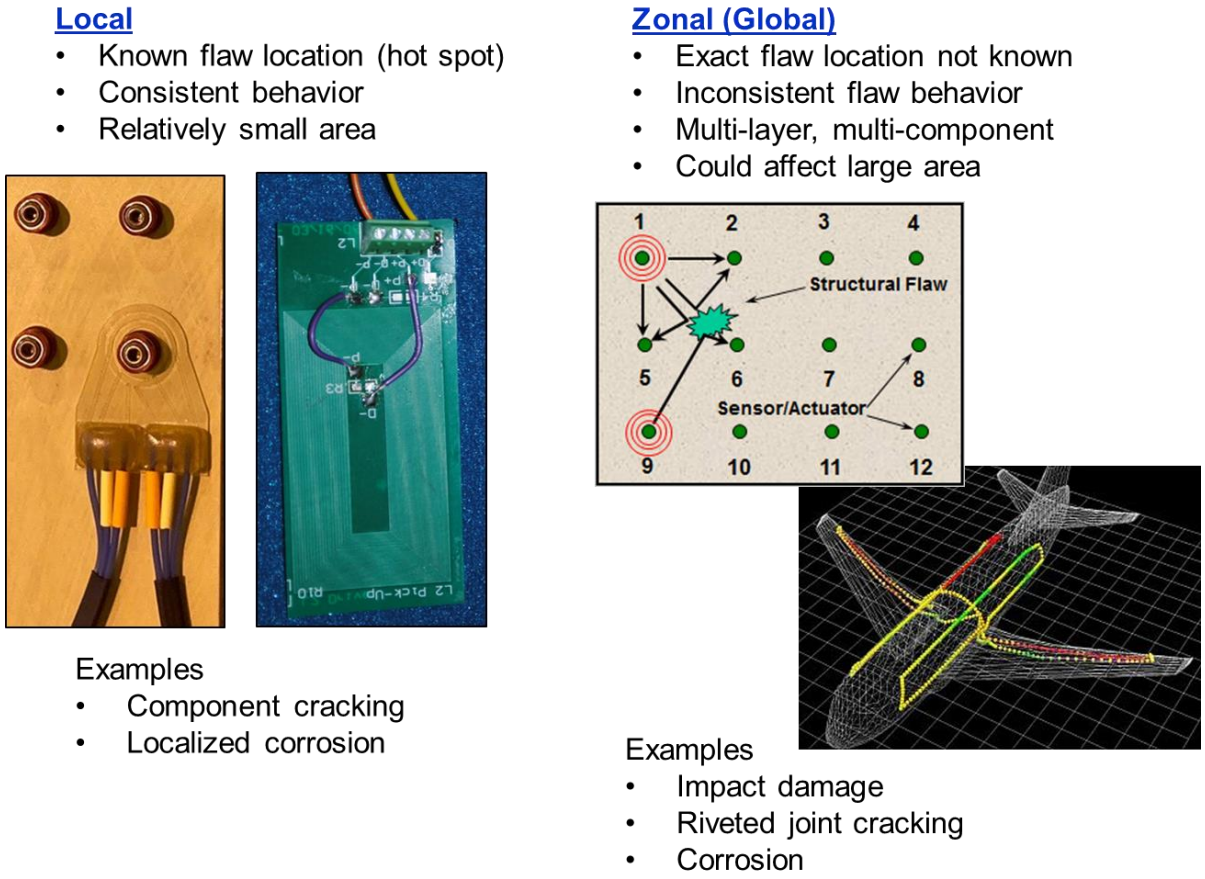

Figure 3-2. Local and Zonal Health Monitoring Approaches

3.2. CVM Rotorcraft Application – S-92 Frame Gusset

The CVM application selected for use on rotorcraft involved local, hot-spot monitoring of specific fatigue crack sites on the S-92 frame gusset. This structure has a failure history where cracking can begin at the holes associated with the fastener nutplates on the inner cap. Cracks will then grow outward to the edge of the frame.

Local (Hot Spot) Monitoring Application: S-92 Frame Gusset

- Failure History - cracking begins at nutplate/fastener plate holes on inner cap; grows outward to edge of frame
- Consistent crack behavior
- Thickness/materials are common for frame/beam caps – good extrapolation to other high-interest locations for rotorcraft SHM.

The CVM application is shown in Figure 3-3 through Figure 3-6. These figures show the gusset structure, the nutplates corresponding to the crack initiation points, the load direction used to generate the fatigue cracks, the custom CVM sensors and their placement used to monitor for the fatigue cracks.

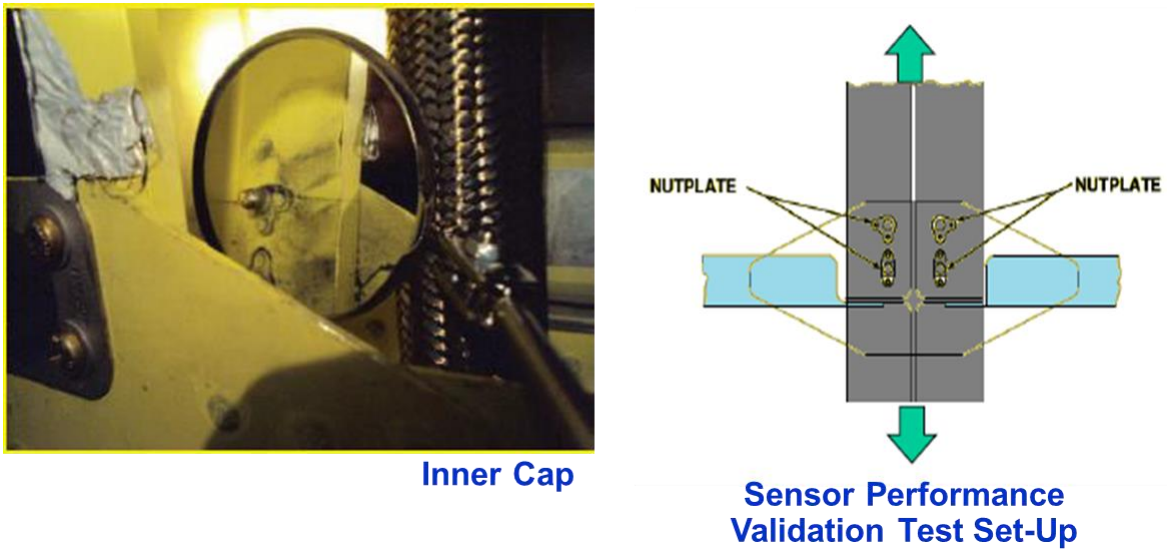

Figure 3-3. Selected Rotorcraft Application – S-92 Frame Gusset

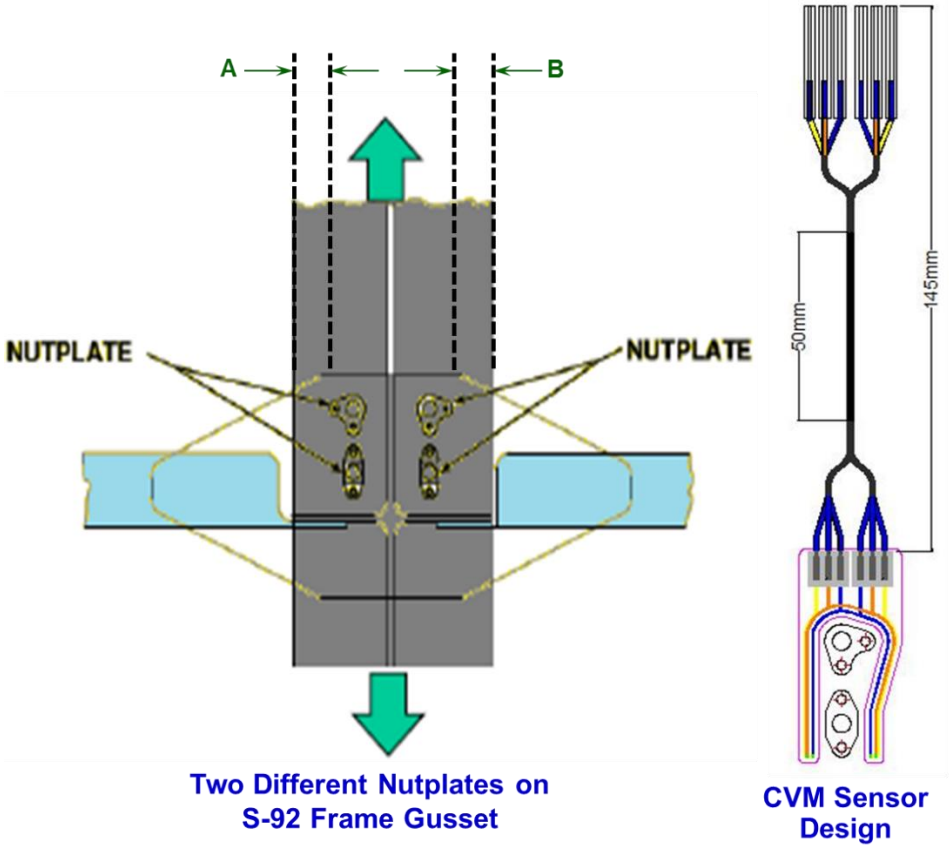

Figure 3-4. Comparative Vacuum Monitoring System - Local SHM of Cracks Emanating from Fastener and Nutplate Holes

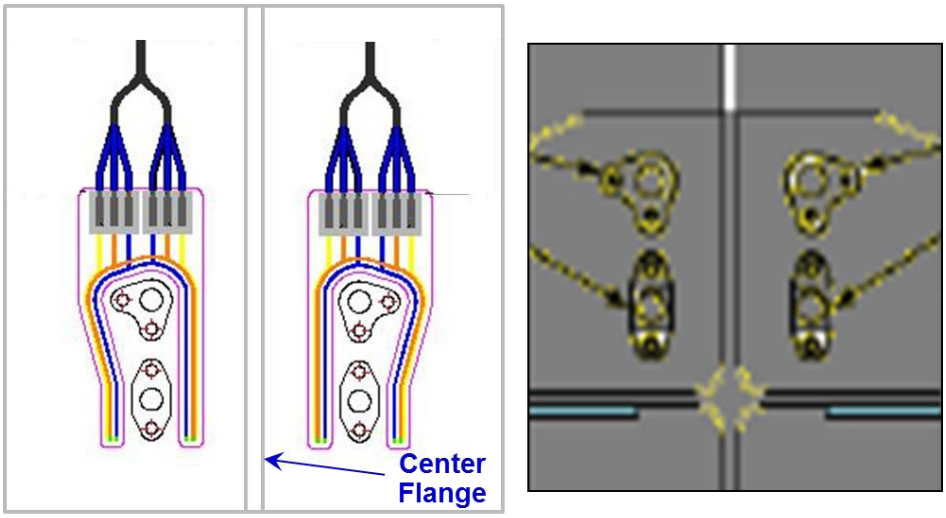

Figure 3-5. Layout of CVM Sensors on Frame Gusset Rotorcraft Structure for Crack Detection from Fastener Holes and All Nutplates

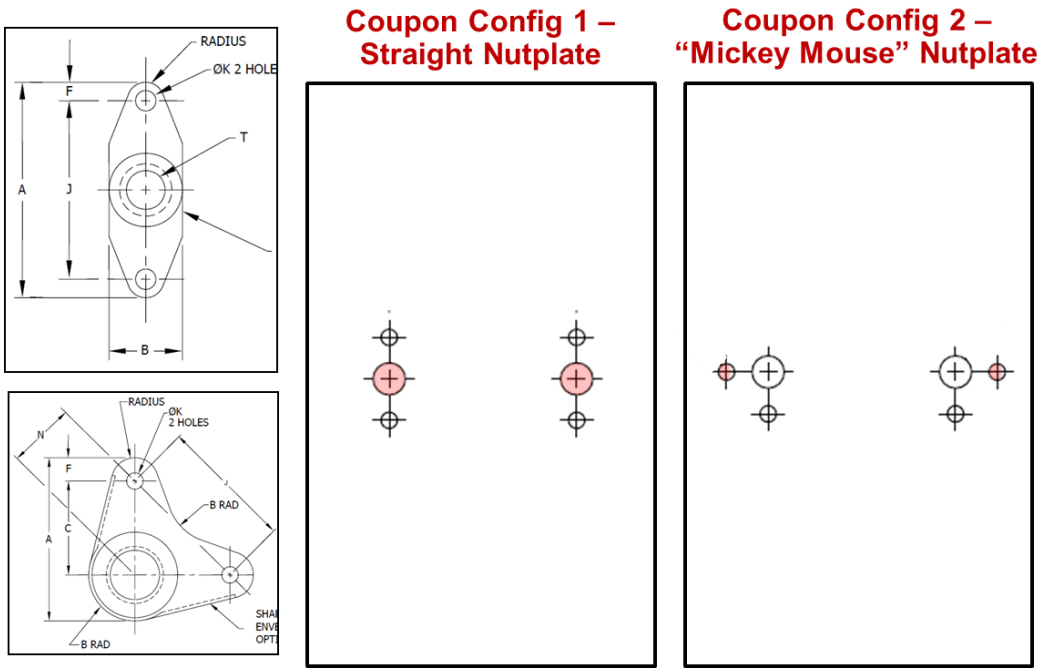

Figure 3-6. Test Specimen Designs to Evaluate CVM Crack Detection on Straight Nutplate (Config 1) and Mickey Mouse Nutplate (Config 2)

Additional details on the sensor design, the test specimens used to quantify CVM sensitivity and the separate validation testing for each of the two unique nutplates are highlighted in Figure 3-7 through Figure 3-10. The test configurations were designed in concert with Sikorsky engineers

and DER/PCP personnel so that: 1) they properly represented the geometry and crack growth scenario experienced on Sikorsky aircraft, and 2) provided validation data for a larger possible set of SHM applications. Since performance can be different for each nutplate configuration, it was decided to test separate test specimen coupons for each nutplate; one fatigue crack was initiated per nutplate. Starter notches were used to control crack propagation. This test set-up allowed for the acquisition of two data points per coupon. Each specimen was a representative 0.25" thick, made from 7075-T7351 aluminum. Figure 3-11 shows how the custom CVM sensor shapes are laser cut during production.

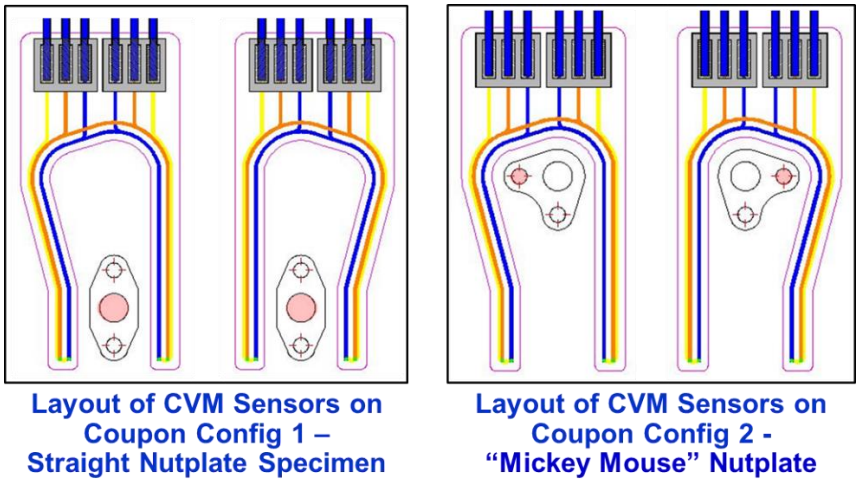

Figure 3-7. Layout of Single CVM Sensor Design on the Config1 and Config 2 Test Specimens

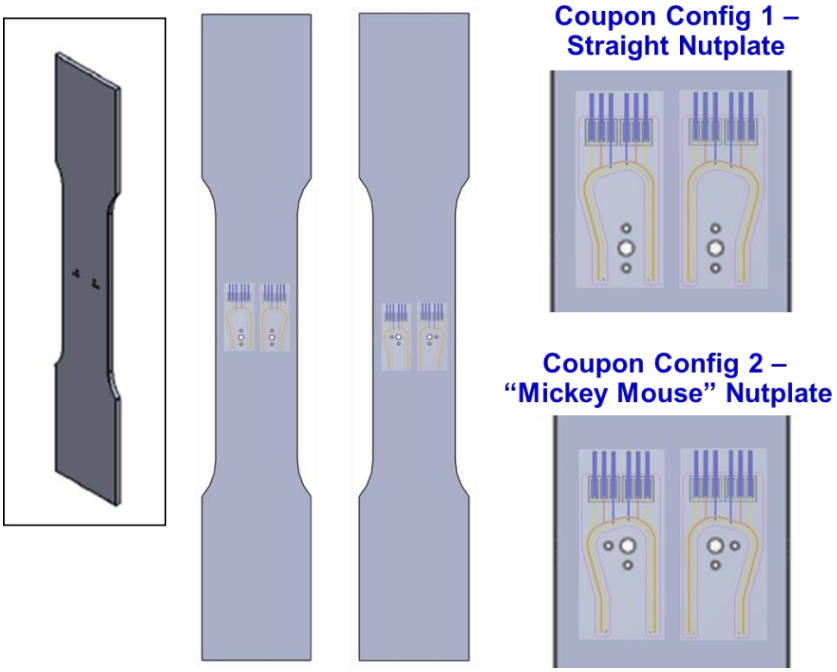

Figure 3-8. Config 1 and Config 2 Test Specimens with CVM Sensor Locations

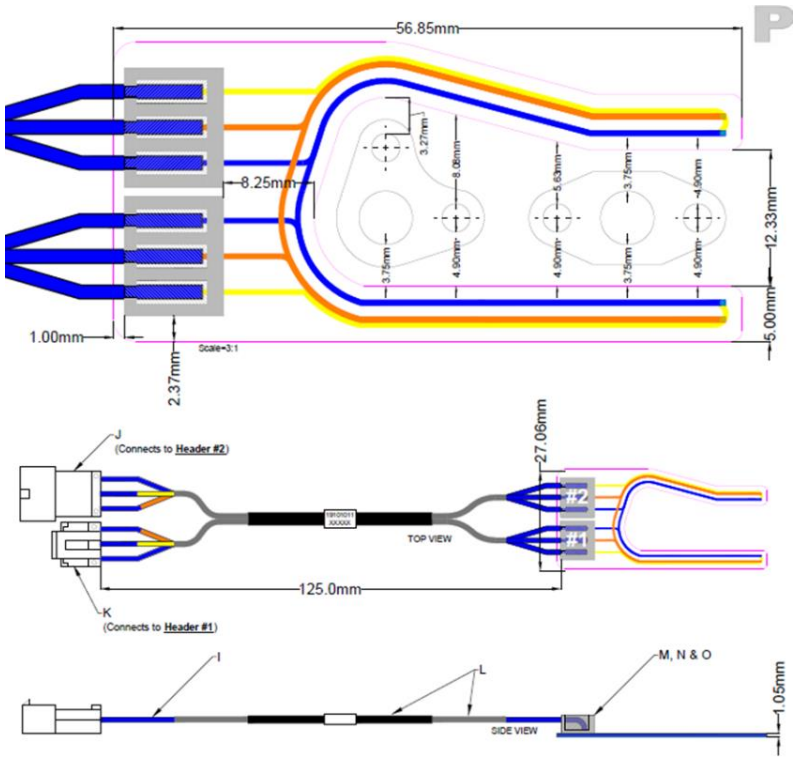

Figure 3-9. Overall CVM Sensor Dimensions with Mating to Snap-Click for Connection to PM-200 Data Acquisition Device

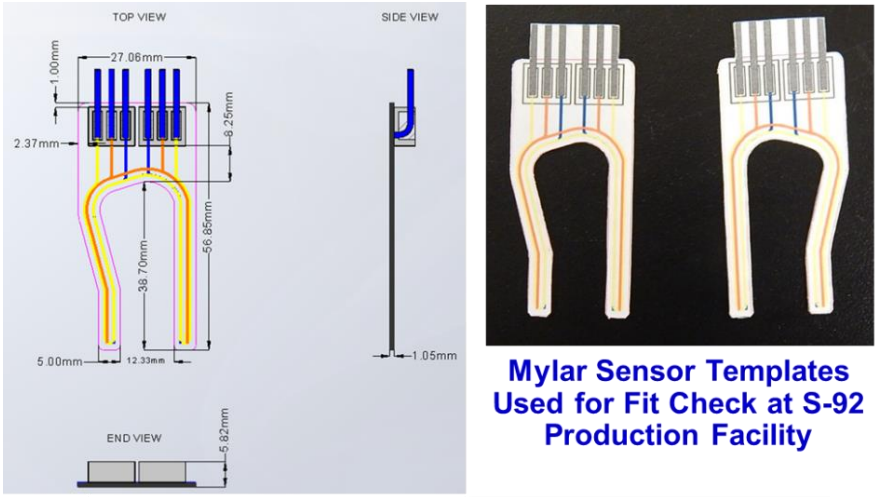

Key sensor dimensions and features					
Item	Feature	Size	Item	Feature	Size
A	Channel Pitch	1.5mm	D	Total Channel length (each)	≈195mm
B	Channel Width	0.5mm	E	Channel-edge to Channel-edge	1.00mm
C	Channel Depth	175um	F	Channel-edge to External-edge	1.25mm

Figure 3-10. CVM Sensor Dimensions and Prototype Used to Check Proper Fit on Gusset

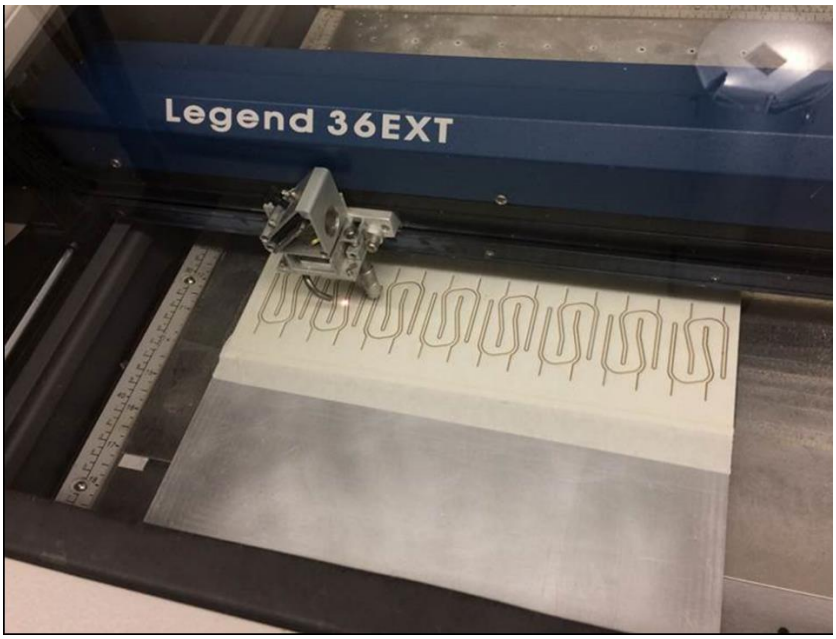

Figure 3-11. Custom CVM Sensor Production Showing Laser Cut to Produce Galleries in Teflon Sheets

3.3. PZT Rotorcraft Application – Engine Mount Beam Element

The PZT application selected for use on rotorcraft involved zonal monitoring of a series of potential fatigue crack sites on a beam structure that is representative of beams used to mount gearboxes for rotorcraft engines. Specifically, a PZT network was designed to globally monitor the aft beam used to mount the S-92 main gearbox. This structure has a failure history where cracks have been observed emanating from several fastener locations both on the frame element and the adjoining skin. It is a highly-loaded, geometrically complex region with multiple structural components and possible crack initiation locations. It is in an area that is difficult to access for conventional NDI and the high-cycle nature of the vibration and blade rotation fatigue loads can produce frequent inspection requirements (short repeat intervals). One advantage associated with the selection of this application is that such a beam is a very common structural arrangement for rotorcraft engine and gearbox mounts. Thus, the results from these validation tests could have a broad use.

The area for this PZT application is shown in Figure 3-12. These photos show the overall, reinforced crown region of the rotorcraft fuselage for the engine and gearbox mount along with a close-up of the main mount beams and potential crack sites. Figure 3-13 through Figure 3-16 provide the design details of the mount beam used in the PZT validation testing. The I-beam was fabricated from 7075-T7351 material and included features to allow for crack growth in both the web and flange holes. To better understand the effects of boundary conditions on PZT crack detection, the validation testing included interrogation of the PZT sensor networks for both open holes and holes with fasteners installed. Testing also studied any possible variations in PZT

network response for fasteners installed with different torque values (tightness). Figure 3-13 and Figure 3-14 show the beam features which serve as various crack initiation sites on the I-beam while Figure 3-15 shows a sample PZT sensor layout used to monitor for these cracks. The PZT sensor network will be described in detail in Chapters 4 and 6. Finally, Figure 3-16 shows some Finite Element Model (FEM) results which indicate high stress and potential crack initiation sites.

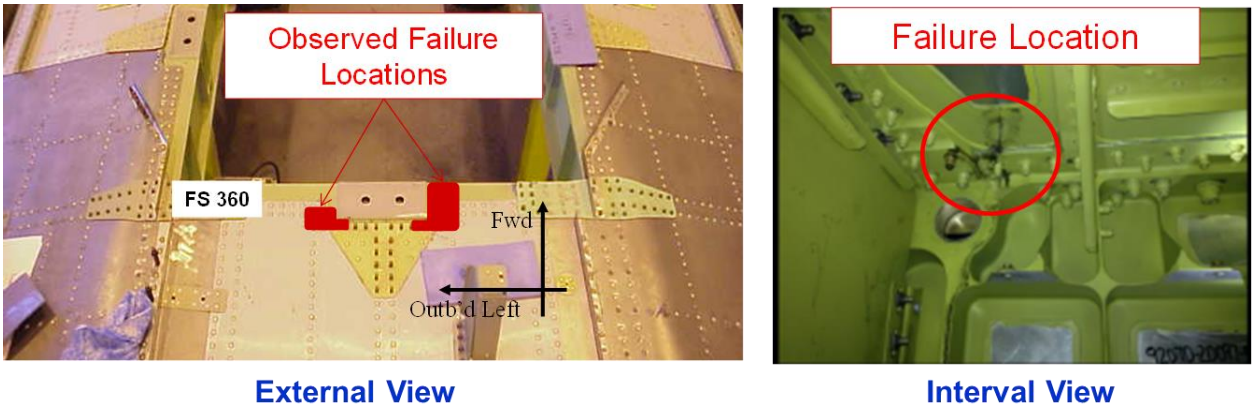

Figure 3-12. Selected Rotorcraft Application – S-92 Aft Main Gearbox Mount

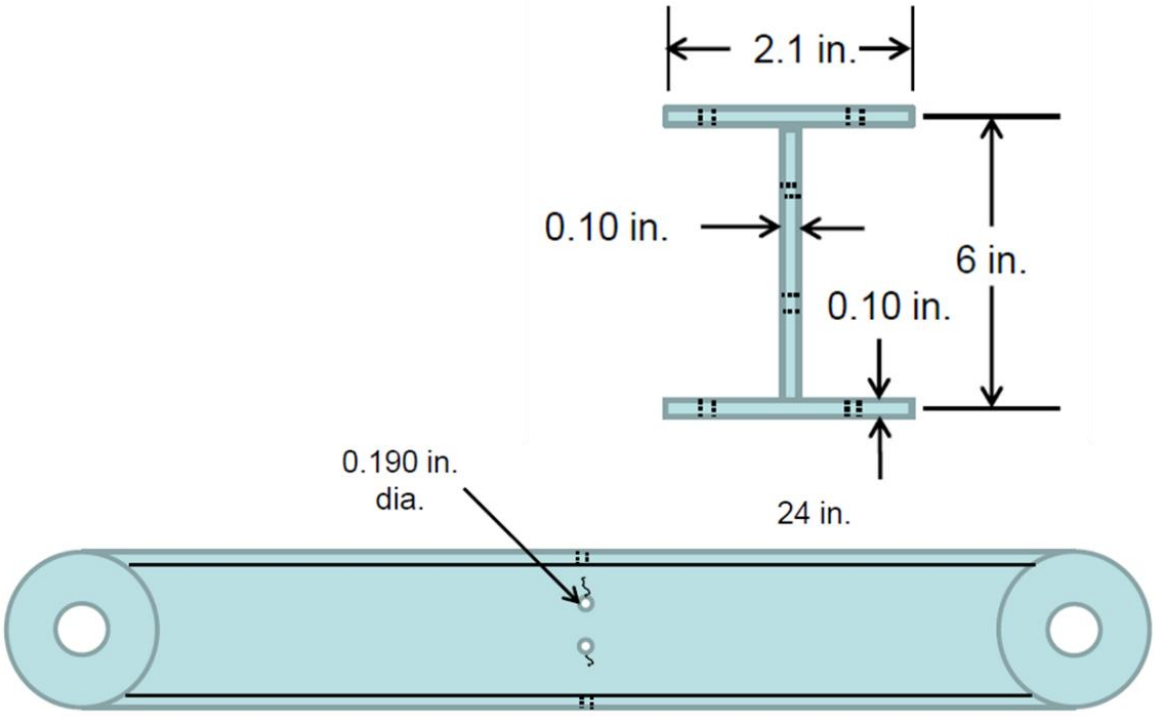

Figure 3-13. Selected Rotorcraft Application – Zonal SHM System Monitoring an I-Beam

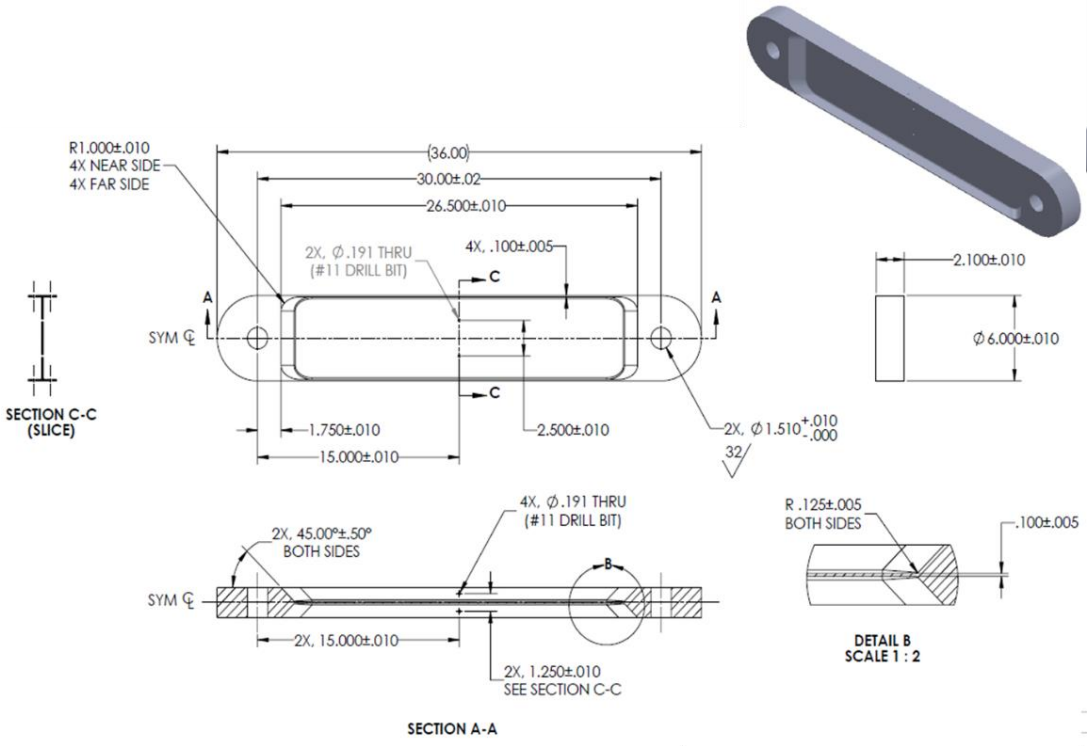

Figure 3-14. Rotorcraft I-Beam Drawing

Figure 3-15. Global PZT Crack Monitoring Application on Rotorcraft Beam

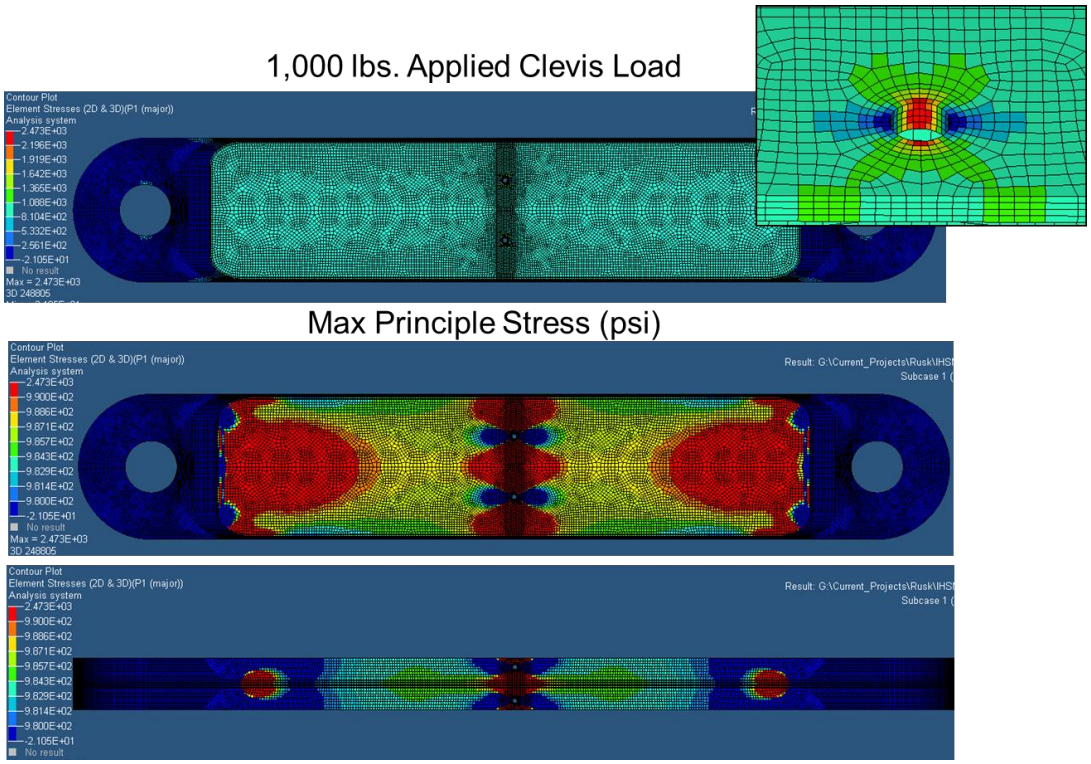

Figure 3-16. I-Beam FEM Stress Analysis

Rotorcraft Zonal SHM System Application – Monitoring a Structural Beam with PZT -

- Beam element is representative of structures and boundary conditions in rotorcraft cabin frames and bulkheads.
  - Sandia tests will monitor single cracks on each specimen in order to conduct a POD analysis [single web crack monitored by web network and single flange crack monitored by flange network to produce POD(web) and POD(flange)].
  - Amounts to one full network of all sensors to assess detection of multiple, simultaneous cracks with position/size predictions – no signal cross talk.
  - Navy tests will capture sensor performance in the presence of multiple, growing cracks [presence of signal cross talk with coupled sensor signals].
- Load/stress levels = 14 kips (14 KSI); R=0.1
- Starter notch = 0.010” to 0.015” in length
- One crack per specimen zone – set of web cracks generated for web POD and set of flange cracks generated for flange POD.
- Crack onset expected in first 5,000-10,000 cycles
- Data Acquisition (DAQ) conducted in both PZT pitch-catch and PZT pulse-echo mode
- DAQ process conducted at zero load and at various load levels to assess effects of strain field and crack closure on PZT performance.
- DAQ process conducted at room temperature and high (85^{o}F) and low (60^{o}F) temperatures to assess temperature compensation for Damage Index (DI).

    - Temperature soak will be sufficient to produce uniform temperature throughout the gauge section of the test specimen; surface temperature at time of DAQ will be recorded.
- DAQ process conducted with and without fasteners in the holes; fastener DAQ conducted to assess effects of changes in boundary conditions.
    - Bolted fastener conducted tests at 0 and 30 in-lb torque
        - Black-Oxide Alloy Steel Socket Head Cap Screw, 10-32 Thread with Low-Strength Steel Hex Nut, Zinc Plated, 10-32 Thread Size, 3/8" Wide & Steel Flat Washer; Fastener approximates size of a #10 Hi-Lock and washer approximates the OD of the Hi-Lock collar.
        - Ultimately, bolted fastener was rejected as nonrepresentative of aircraft joint. Preliminary tests revealed a wide variation in Baseline responses prior to any appearance of damage.
    - Blind rivet fastener approximates size of a #10 Hi-Lock.
- Criteria for damage detection, based on Damage Index, was determined while considering both desired POD and desire to avoid false calls.
- Eddy current inspections were conducted in-situ at each fatigue test stopping interval to determine the current length of the fatigue crack:
    - Acquired PZT signals vs. crack length for full range of "prior-to-detection" upwards through "after-crack-detection" (close to component failure).
    - Produced â vs. a data for alternate POD calculations.
- Nomenclature for crack propagation direction:
    - On Flange: inboard = toward web; outboard = toward free edge
    - On Web: inboard = toward center line; outboard = toward flange
- Three separate PZT networks were set up on: 1) web, 2) upper flange, 3) lower flange; same network on both flanges.
- One PZT network including all sensors was set up for global I-beam monitoring.

The overall goals and benefits associated with this global SHM application are:

- Realistic, but generalized, structures present various complexity and capture a range of boundary conditions (stress reapportion & reversal) on airframe structure.
- Evaluate the effects of structural complexity, boundary conditions, presence of fasteners, joint settling during fatigue, residual stresses, load shedding, temperature, load, alternate data analyses methods.
- Crack initiation points have a wide variety of geometric detail (e.g. fastener type/locations, fillet radii, cutouts, splice connections, material thickness).
- Resulting variability in boundary conditions affect wave signal propagation and response of the damage detection sensors.
- Desire to assess use of SHM to meet a zonal inspection requirement of $POD_{(90/95)}$. Establish SHM performance using same criteria as NDI - 90% POD with 95% confidence. Outcome: POD for various damage sizes with a specific set of sensor configurations on a given geometry and for specific crack origins.
- Compare different methods of determining POD for in-situ SHM: One-Sided Tolerance Interval, Hit-Miss Log Regression, a vs. a(hat); single cracks vs. multiple cracks; assess use of repeated measures from the same sensor network; demonstrate value of MAPOD combined with limited fatigue test.

- Mix: 1) multiple, concurrent cracks and associated complex SHM network responses, and 2) single, consistent crack onset with unique, distinct SHM network responses that allows for POD to be determined.
- Sandia Focus - determine POD for individual crack occurrences using a specific set of sensor configurations on a given geometry – equipment will be Acellent Scan Genie II system.
- Leverage a related Navy SHM program:
  - Utilize ties to Navy SHM program to evaluate global monitoring of a common rotorcraft beam element.
  - Navy Focus – determine PZT performance for multiple, simultaneous cracks in each test specimen to study global response of a PZT sensor network – equipment will be 6-node Metis MD7-Pro system.
  - Combine full set of Sandia and Navy PZT response tests and augment them with Model Assisted POD (MAPOD) methods to produce a complete assessment of PZT performance. Use full set of results to determine viability and value of using MAPOD to aid SHM validation.
  - Exchange of data between Navy and Sandia can be used to evaluate a fuller range of performance approaches using blind data sets.
- Demonstrate building block approach to SHM validation with accumulation of a database of performance results - allows for estimates of detection capability for structural geometries that do not conform exactly to the configurations that have been tested previously.

References

3.1. Boeing NDT Standard Practices Manual; Section 51-11-01, General Methods for Inspection of Aircraft, Release 104.00, July 20, 2011.

3.2. Boeing 737 NDT Manual, PART 5 - STRUCTURAL HEALTH MONITORING; Chapter 1: Comparative Vacuum Monitoring, 51-11-01, Center Wing Section 57-01-01.

3.3. Boeing 737 Service Bulletin, "WINGS – Center Wing Box – Front Spar Shear Fitting – Inspection, Repair and Preventive Modification," Number 737-57-1309, June 2016.

4. SHM VALIDATION METHODOLOGY – TEST SET-UP AND PROCEDURES

The overall goal of the performance evaluation testing was to quantify the sensitivity, reliability and repeatability of crack detection using PZT and CVM sensors. Simplified test configurations using representative plate structures, as well as aircraft components, were used for the flaw detection performance evaluation of both CVM and PZT sensors. Sensor crack detection performance was evaluated using statistically-valid Probability of Detection (POD) curves while sensor durability was evaluated using accelerated aging with exposure to extreme environments.

4.1. CVM Sensor Installation and Test Specimen Preparation

The test specimens and custom sensors used to quantify CVM sensitivity and the separate validation testing for each of the two unique nutplates are shown in Figure 3-7 and Figure 3-8. The test configurations were designed to properly represent the geometry, stress fields and crack growth scenario experienced on Sikorsky aircraft. Since performance can be different for each nutplate configuration, it was decided to test separate test specimen coupons for each nutplate. All components of the CVM system (see Figure 4-1), including the sensors, connectors, data acquisition equipment, data analysis software and data logging software, were evaluated in the laboratory tests.

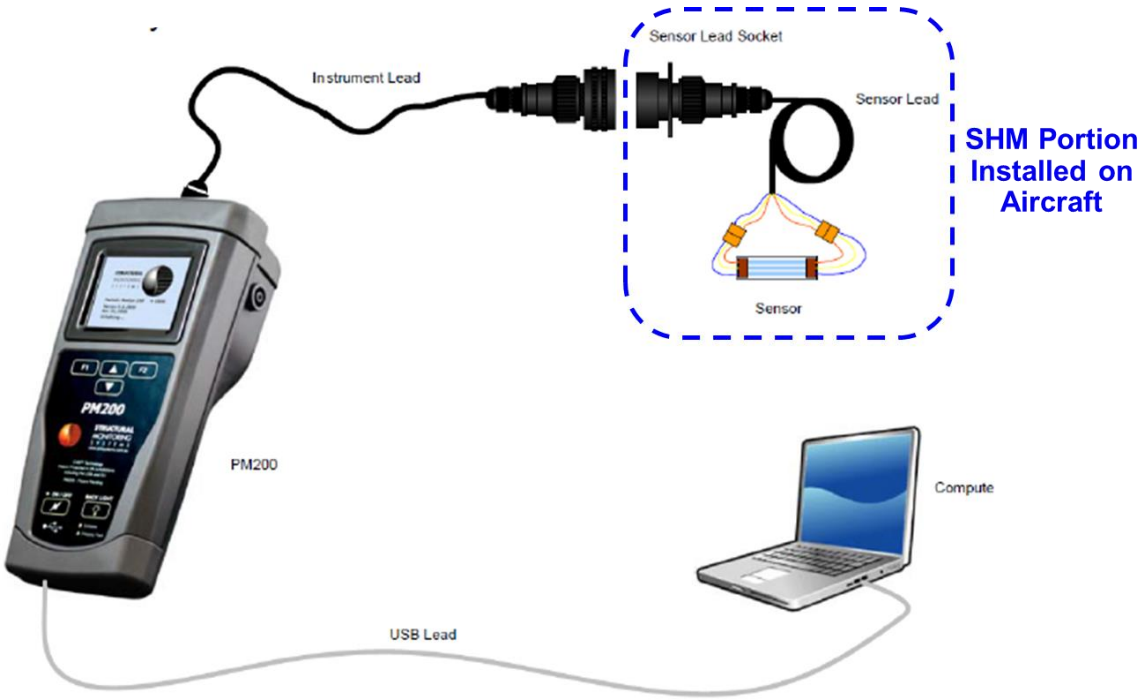

Figure 4-1. SHM Performance Validation Tests Address the Entire SHM System

CVM Sensor Installation and Fatigue Test Specimen Preparation - CVM sensor installations were completed as per SMS documents [4.1 – 4.2]. Starter notches was placed at the expected crack initiation site in each specimen using a jeweler's saw as shown in Figure 4-2. The basic steps for the surface preparation are as follows and are shown in Figure 4-3 through Figure 4-9.

1) Apply primer to test specimen.
2) Remove grease, dirt or any contaminants using a clean, lint-free cloth and Acetone or Rhodiasolve (Figure 4-4).
3) Use 600 grit sandpapers to sand the CVM installation area (Figure 4-5).
4) Clean the sanded surface again using a clean, lint-free cloth and Acetone (Figure 4-6).
5) Conduct final cleaning with deionized water.
6) Apply self-adhering sensor to the surface. Use guides (e.g. templates, surface markings, hole dowels, specialized tools) that are helpful in ensuring the accurate and repeatable placement of the sensor (Figure 4-7 and Figure 4-8).
7) Use a flat-ended spatula to press down on the sensor and produce an air-tight seal with the structure surface (Figure 4-8).
8) Allow sensor to sit for at least 15 minutes. Connect CVM sensor to PM200 unit and measure the baseline (no crack) readings for proper dCVM and continuity levels (Figure 4-9).

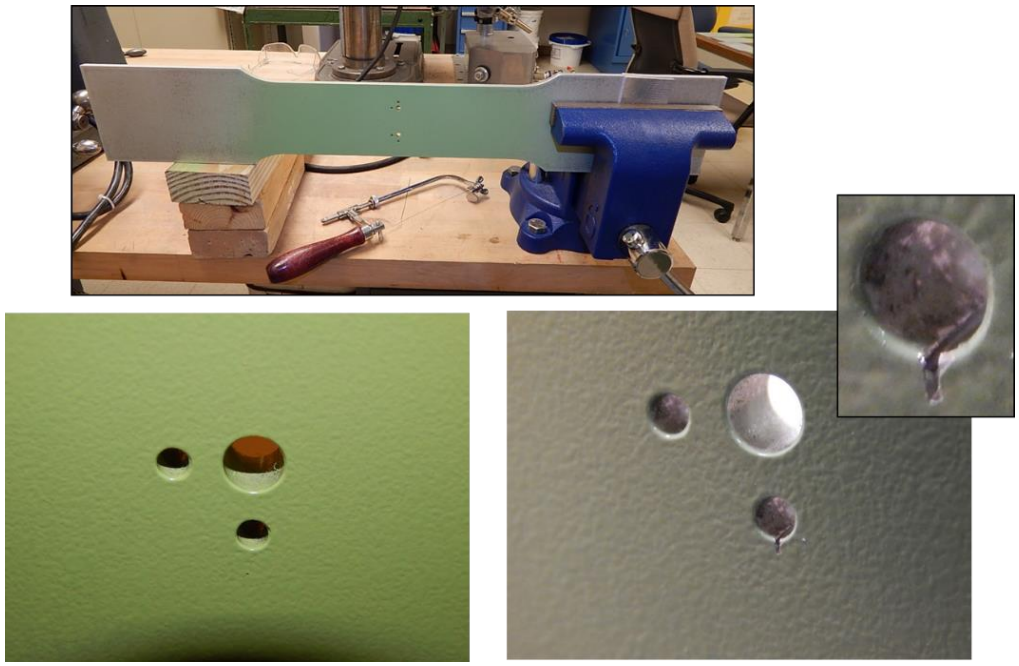

Figure 4-2. Install Small Crack Starter Notch (~ 0.020") at Crack Initiation Point

Figure 4-3. Materials Used for CVM Sensor Installation

Step 1:
Apply Acetone to a clean cloth.

Step 2:
To remove any grease, dirt, or any contaminants prior to sanding, wipe in one direction to remove solvent and dirt.

Figure 4-4. Cleaning Steps for CVM Installation

Step 3:
Using 600 grit sandpaper, sand the entire area of interest, using small circular motions.

Figure 4-5. Light Sanding of Primer Surface for CVM Installation

Step 4:
Apply Acetone using a clean cloth to remove sanded primer, as per Step 2, until all primer residue is removed.

Figure 4-6. Cleaning After Light Primer Sanding for CVM Installation

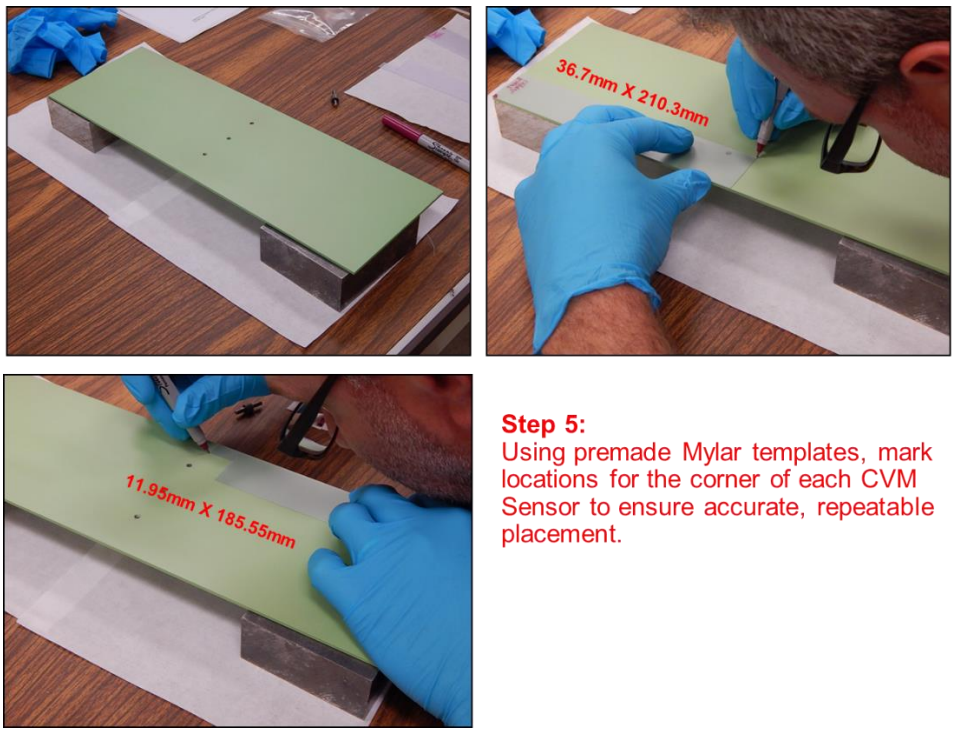

Figure 4-7. Marking Sensor Corners for Proper CVM Placement

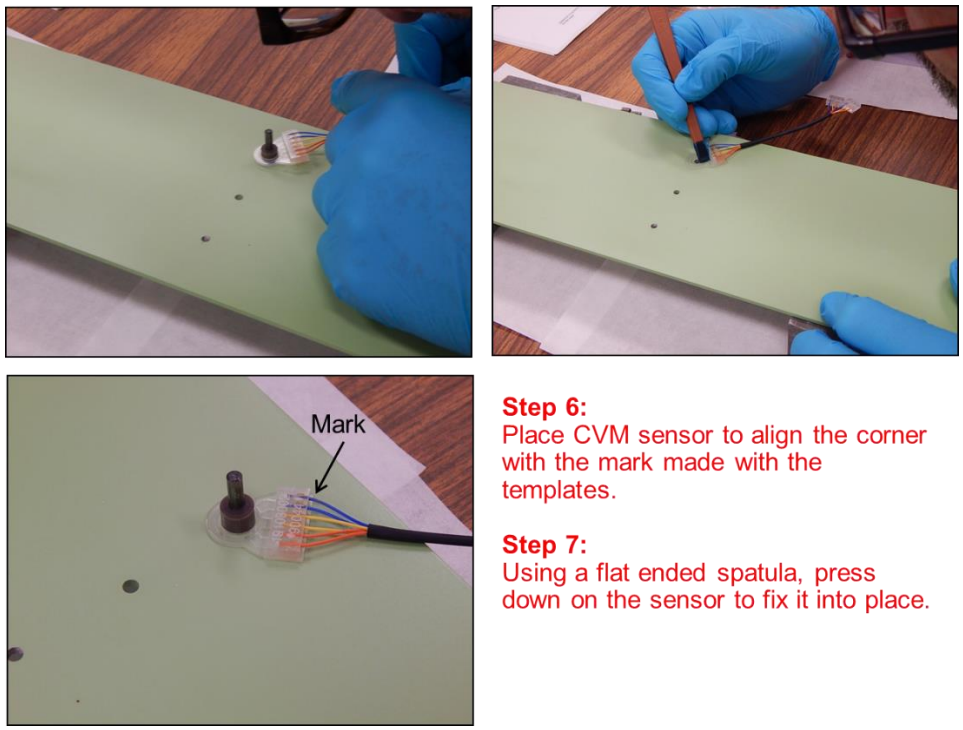

Figure 4-8. Installation of CVM Sensor and Seal with Surface

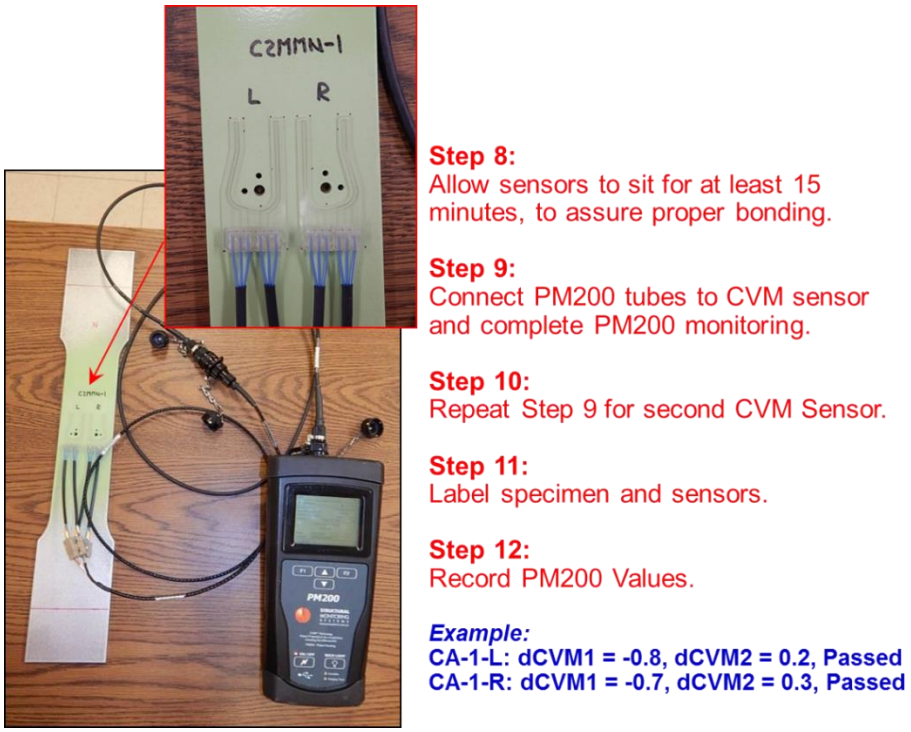

Figure 4-9. Complete Quality Assurance Check on CVM Sensor Installation

4.2. CVM Sensor Fatigue Test and Performance Evaluation Measurements

Fatigue tests were completed on the S-92 Frame Gusset test specimens using flight load spectrums while the vacuum pressures within the various sensor galleries were simultaneously recorded. A fatigue crack was propagated until it engaged one of the vacuum galleries such that crack detection was achieved and the sensor indicated the presence of a crack by its inability to maintain a vacuum. Figure 3-7 through Figure 3-10, Figure 4-10 and Figure 4-11 show various views of the Config 1 and Config 2 test specimens, the CVM sensors used to monitor for cracks stemming from any of the attachment holes, and the specimen orientation in the servo-hydraulic test machine used to apply the proper fatigue stress field.

Table 4-1 and Figure 4-12 summarize the stress calculations that were conducted to ensure the proper inclusion of tension and bending to produce representative stress levels in the gusset component. Note the use of a shim plate in the grips of the hydraulic machine to produce secondary bending in the test specimen and a representative ratio of tension and bending stresses.

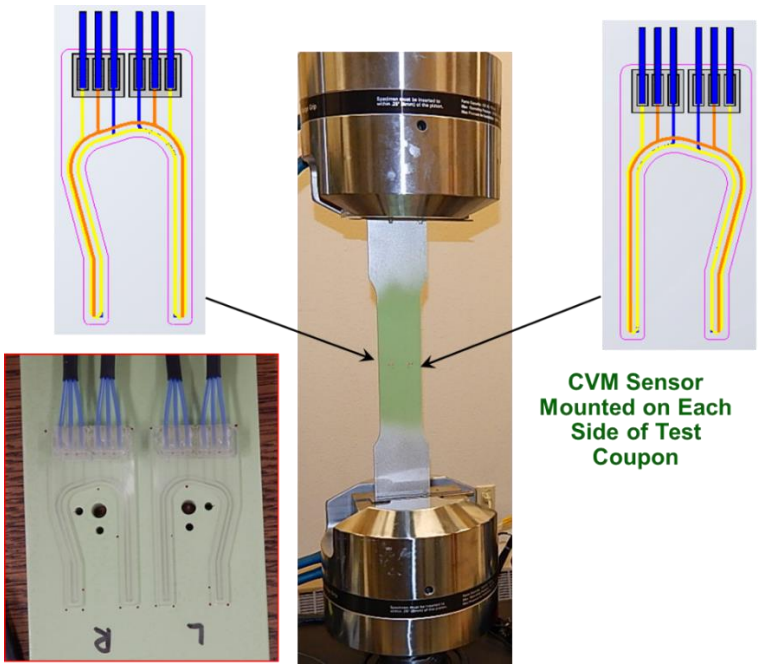

Figure 4-10. S-92 Frame Gusset Test Specimen Installed in MTS Machine for Fatigue Cycling

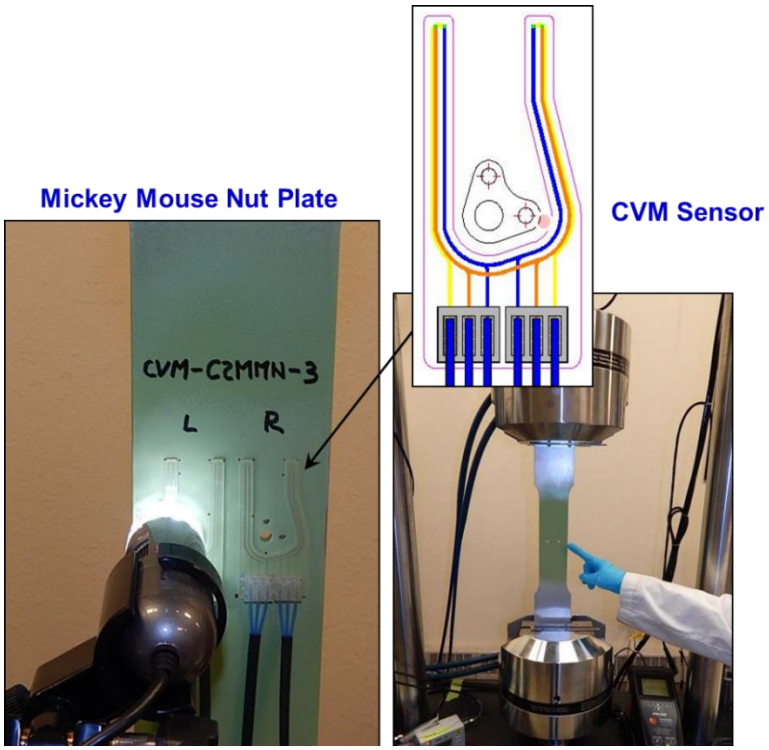

Figure 4-11. CVM Performance Testing – Fatigue of Config 2 Specimen with "Mickey Mouse" Nutplates

Table 4-1. Stress Calculations on CVM Coupon to Determine Test Set-Up for Proper Axial Tension and Secondary Bending

Parameter	Value	
Thickness	0.27	
Width	3	
Hole Width	0.584	
Cross Sectional Area	0.65232	
Applied Load	15000	Load used to produce representative stress in test specimen
Tensile Stress Goal	25000	
Area Square	0.65232	
Load	16308	
Axial Stress	22994.85	
Load	15000	
Offset	0.01	Shim plate placed on one side of specimen during machine clamping to produce representative flatwise bending in test specimen
y	0.125	
Inertia	0.003906	
Bending Stress	4800	My/Ix bending component
Max	27794.85	
R	0.1	
Min	2779.485	
Steady	15.28717	
Vib	12.50768	

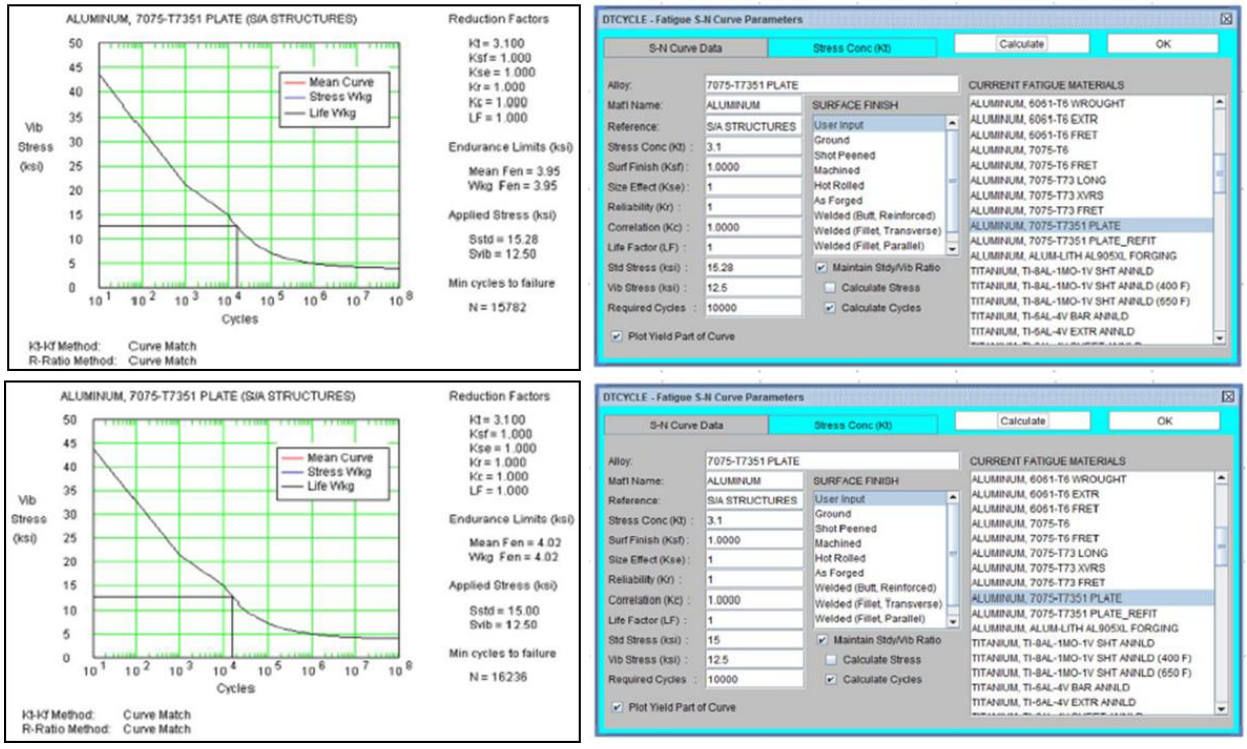

Figure 4-12. Stress Calculations on CVM Coupon to Estimate Crack Growth Under Test Loads

Fatigue and Crack Detection Data Acquisition Steps for CVM Sensor Performance Tests:

1. Load each test specimen into the 110 Kip MTS machine in accordance with the test configuration shown in Figure 4-10.
2. Set the load to produce the desired stress level that is representative of the stress levels experienced in the structure during operation. Determine and apply a suitable R ratio for the fatigue loading to establish the lower load in the fatigue tests. Apply a fatigue cycle frequency while maintaining the ability to apply the proper maximum load levels and R value.
3. Measure the distance between the rivet hole and the edge of the sensor. This distance is the Sensor Offset Distance.
4. Verify initial installation and sensor function prior to data acquisition (see Figure 4-9). Connect sensors to Kvac-4 vacuum supply device and Sim-8 gallery vacuum monitoring device as per Figure 4-13 and record the baseline Sim-8 readings for the real time sensor monitoring. Take a digital USB microscope picture of each test location (the intended crack site) prior to fatigue testing (Figure 4-14).
5. Take PM200 measurement on un-cycled test coupon to ensure proper seal between sensor and coupon. Record dCVM values and continuity vales as determined by the PM200 (see Figure 4-15).
6. Connect the Sim-8 continuous vacuum monitoring units to the MTS load machine such that the machine will automatically stop if the Sim-8 detects the initial presence of a crack (control voltage output).
7. Fatigue cycle the specimen while taking measurements with Sim-8 devices to determine the point at which the SHM sensors detect the presence of a crack. Continue this process until a sensor initial crack detection has occurred as indicated by Sim-8 real-time, dynamic reading of 12,000 to 15,000 Pa.
8. Bring the specimen to an unloaded state and use Sim-8 indications to determine if there is still an initial crack detection. Continue the fatigue cycling at very low intervals until a crack is detected by the Sim-8 device when the specimen is in an unloaded state.
9. Connect the CVM to the PM200 CVM monitoring device as shown in Figure 4-9 and determine if the PM200 is able to detect the crack. Use a dCVM reading of +/- 4.0 as the threshold for PM-200 crack detection. If the PM-200 does not detect a crack, continue to fatigue cycle the sample in small increments until the PM200 CVM system properly detects the presence of a crack when the specimen is in an unloaded state.
10. Confirm the location and presence of damage (fatigue crack), along with the crack length using conventional eddy current NDI methods and an optical microscope.
11. Record the crack lengths at CVM detection. Log any false calls where the CVM system indicates a crack detection when a crack is not actually present.
12. Continue the specimen fatigue test until a crack detection has been achieved on the second sensor.

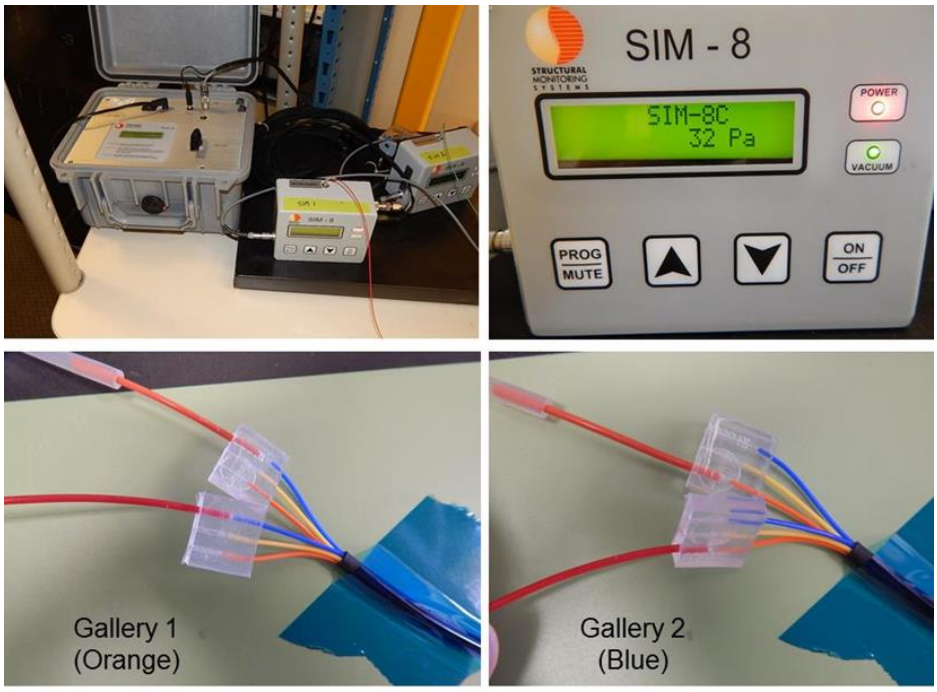

Figure 4-13. Connect CVM Sensors to Sim-8 and Kvac-4 Units for Real Time Monitoring and Measure the Baseline Value for All Galleries

Figure 4-14 to Figure 4-17 show various overall and close-up views of the CVM sensor and the galleries that monitor any crack growth from the different bolt holes. The Sim-8 devices monitor the vacuum level in each gallery in real time so that any deviations can be used to stop the fatigue tests as needed for final monitoring. The PM200 device is connected to the CVM sensor at various intervals much as it would be during monitoring (inspections) on an aircraft. Final determination of a crack detection was associated with direct readings and associated failure messages from the PM200 device.

Figure 4-16 and Figure 4-17 show different photos of fatigue cracks engaging the CVM sensors, close-up views of the micro-scales used to measure crack lengths and sample data from the CVM system. Crack length measurements, used to relate CVM response levels (dCVM) to actual crack lengths in the structure, were determined using: 1) eddy current inspections to identify the crack tip (see Figure 4-18), and 2) calibrated, high fidelity micro-scales as shown in Figure 4-19.

Figure 4-15 to Figure 4-17 show specimen testing and sample results from the crack detection tests for the straight nut plate while Figure 4-20 to Figure 4-22 show specimen testing and sample results from the crack detection tests for the "Mickey Mouse" nut plate. The data analysis used to quantify CVM performance from these tests results is described in Chapter 5.

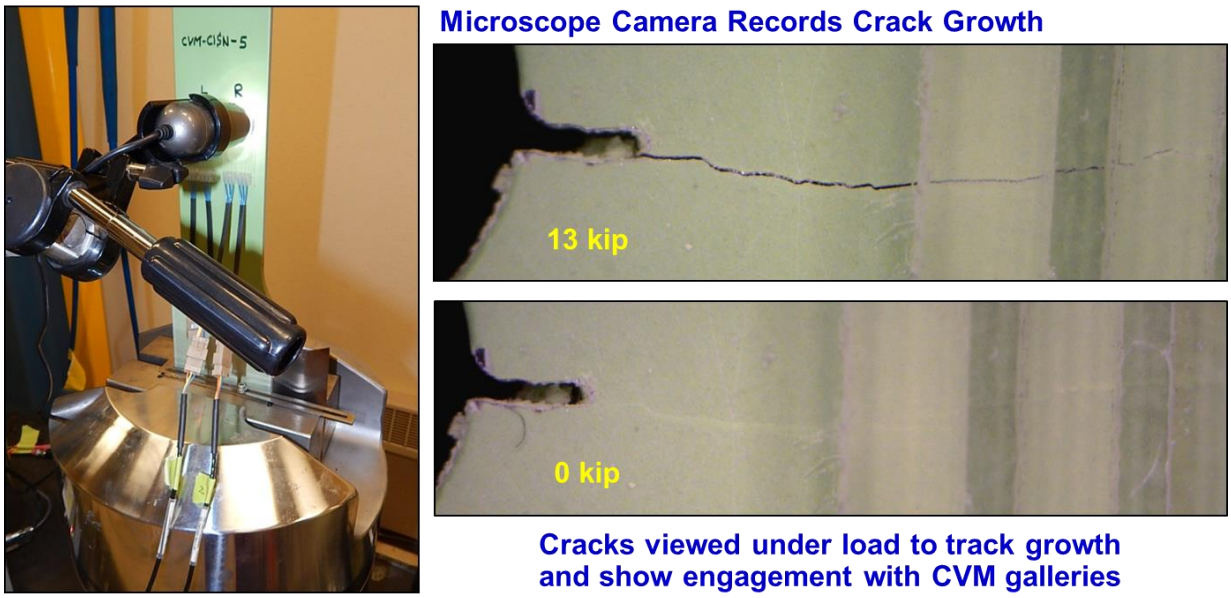

Figure 4-14. Set-Up of Microscope Camera Used to Aid Crack Length Measurements

Sikorsky Config-1 Straight Nutplate Testing (CVM)							PM200 Initial CVM Sensor Readings					
Specimen #	CVM Sensor ID	Hole Diameter D (in)	Length L (in)	Notch Length NL (in)	Distance from Hole to CVM DFH (in)	CVM Installed	Ccont	1Cont	2Cont	dCVM1 Inside Gallery	dCVM2 Outside Gallery	PM200 Screen Reading
CVM-C1SN-6	L	0.188	0.232	0.044	0.139	✓	Max CI	Max CI	Max CI	-0.6	-0.5	Passed
	R	0.188	0.234	0.046	0.149	✓	Max CI	Max CI	Max CI	-0.5	0.0	Passed

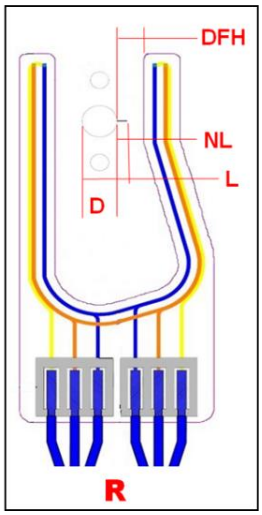

Figure 4-15. Sample Data Recorded from CVM Performance Testing - Straight Nut Plate

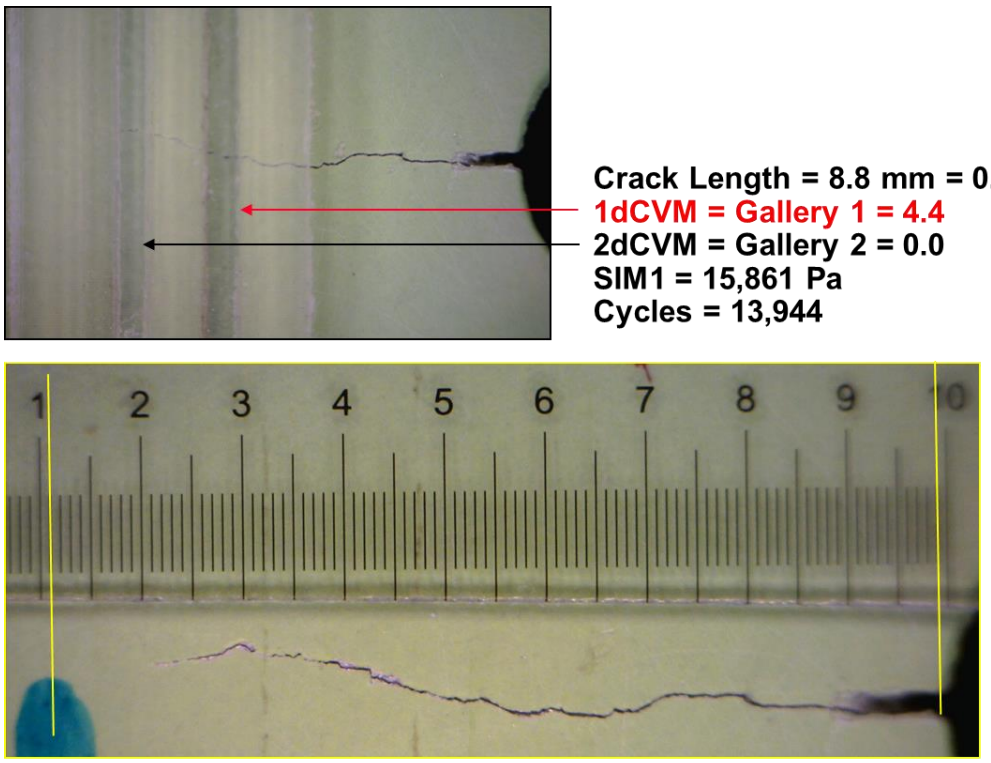

Figure 4-16. Sample Crack Growth and CVM Response Data Recorded for Each Test Specimen – Straight Nut Plate Example 1

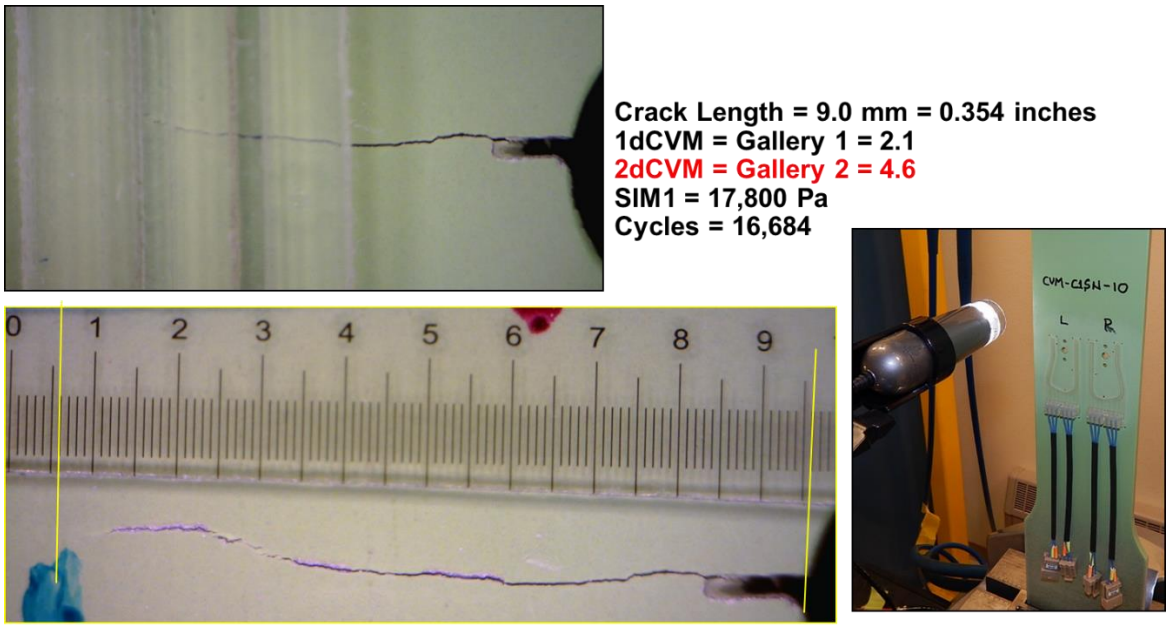

Figure 4-17. Sample Crack Growth and CVM Response Data Recorded for Each Test Specimen – Straight Nut Plate Example 2

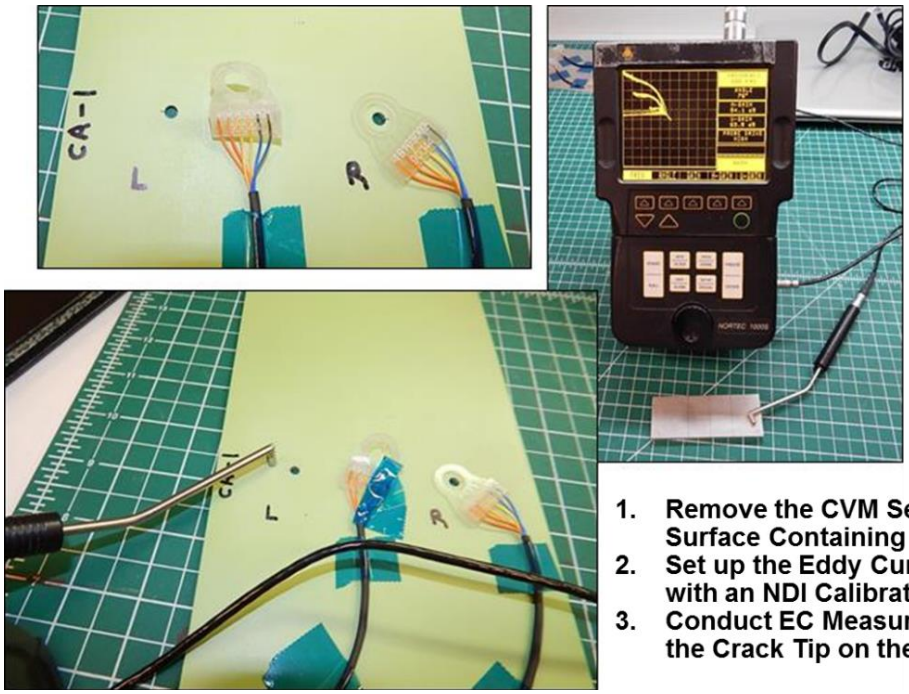

1. Remove the CVM Sensor from the Surface Containing the Crack
2. Set up the Eddy Current Equipment with an NDI Calibration Standard
3. Conduct EC Measurements and Mark the Crack Tip on the Test Specimen

Figure 4-18. Measure Length of Crack After CVM Crack Detection

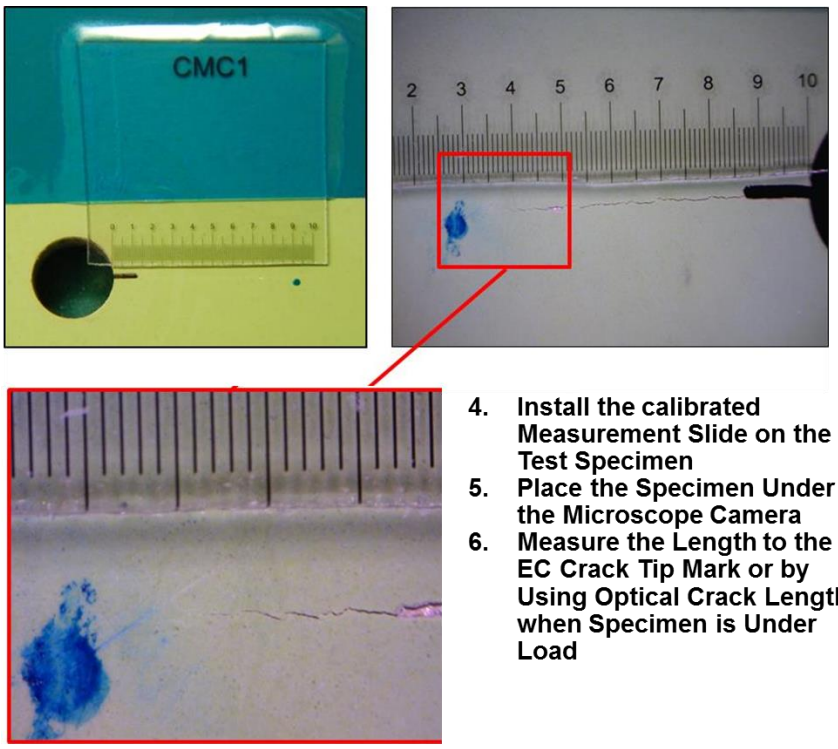

4. Install the calibrated Measurement Slide on the Test Specimen
5. Place the Specimen Under the Microscope Camera
6. Measure the Length to the EC Crack Tip Mark or by Using Optical Crack Length when Specimen is Under Load

Figure 4-19. Use of Microscope Camera and Fine Scales to Measure Crack Length at CVM Detection

Sikorsky Config-2 Mickey Mouse Nutplate Testing (CVM)							PM200 Initial CVM Sensor Readings					
Specimen #	CVM Sensor ID	Hole Diameter D (in)	Length L (in)	Notch Length NL (in)	Distance from Hole to CVM DFH (in)	CVM Installed	Ccont	1Cont	2Cont	dCVM1 Inside Gallery	dCVM2 Outside Gallery	PM200 Screen Reading
CVM-C2MMN-2	L	0.099	0.132	0.033	0.119	✓	Max Cl	Max Cl	Max Cl	-0.3	0.1	Passed
	R	0.099	0.135	0.036	0.123	✓	Max Cl	Max Cl	Max Cl	-0.3	0.0	Passed

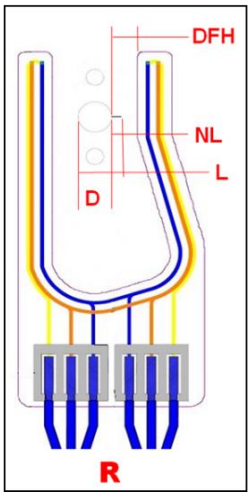

Figure 4-20. Sample Data Recorded from CVM Performance Testing – Mickey Mouse Nut Plate

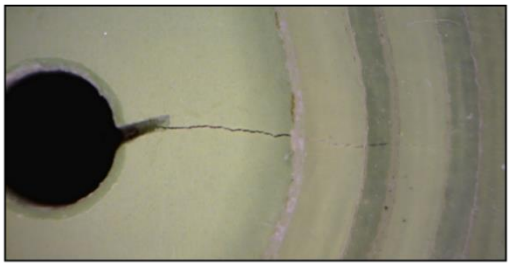

Crack Length = 6.85 mm = 0.270 in
1dCVM = Gallery 1 = 4.2
2dCVM = Gallery 2 = 1.1
SIM2 = 16,250 Pa
Cycles = 20,278

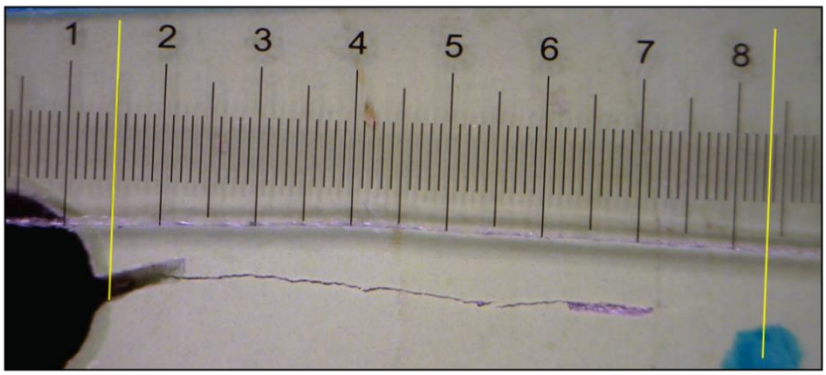

Specimen CVM-C2MMN-5, Right Sensor – Crack Measurements

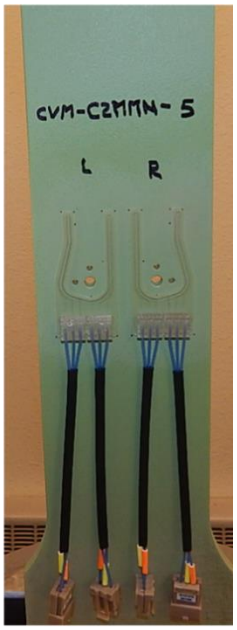

Figure 4-21. Sample Crack Growth and CVM Response Data Recorded for Each Test Specimen – Mickey Mouse Nut Plate Example 1

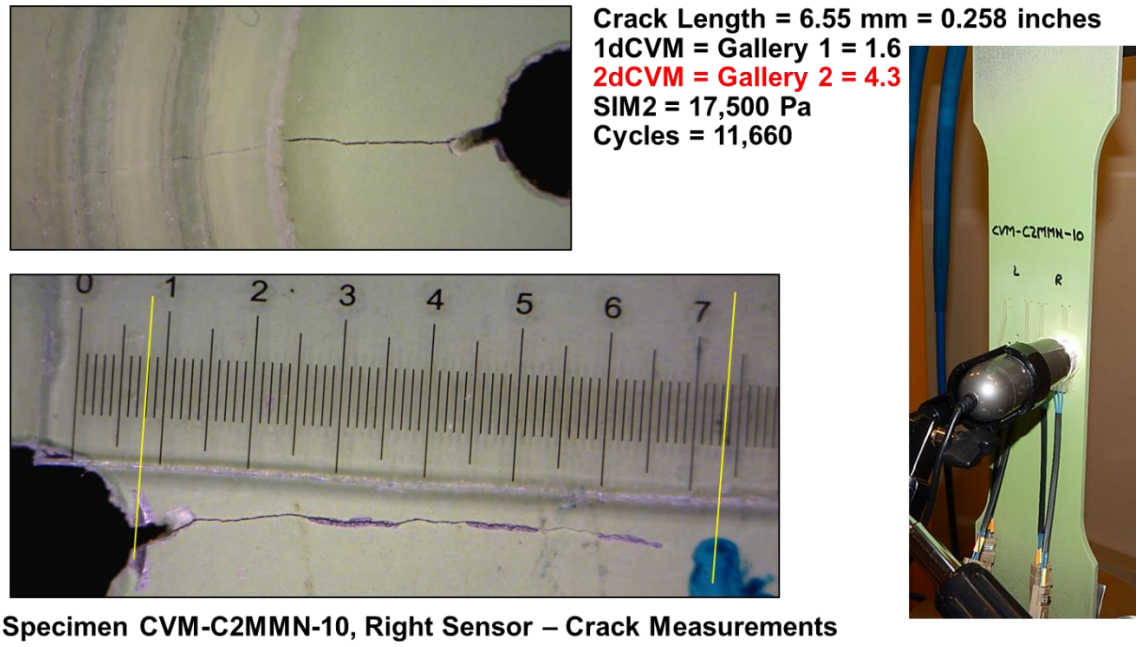

Figure 4-22. Sample Crack Growth and CVM Response Data Recorded for Each Test Specimen – Mickey Mouse Nut Plate Example 2

4.3. PZT Sensor Installation and Test Specimen Preparation

All components of the PZT system (see Figure 4-23), including the sensors, connectors, data acquisition equipment, data analysis software and data logging software, were evaluated in the laboratory tests. The test specimens and custom sensors used to quantify PZT sensitivity and conduct validation testing for the main engine/gearbox mount beam are shown in Figure 3-13 through Figure 3-15 and Figure 4-24 through Figure 4-26. The test configurations were designed to properly represent the geometry, stress fields and crack growth scenario experienced on Sikorsky aircraft.

Before sensor installation, a jeweler's saw was used to create starter notches. Notches were approximately 0.010" wide by 0.015"- 0.020" long were placed at the expected crack initiation site in each specimen using a jeweler's saw as shown in Figure 4-24. The basic steps for the surface preparation and PZT installation are as follows and are shown in Figure 4-25 through Figure 4-29.

1. Clean sensor installation surface/area with isopropanol to remove any grease or dirt prior to sanding.
2. Use 300-500 grit sandpaper, sand the installation areas and roughen the surface for bonding.
3. Clean sensor installation surface/area thoroughly with isopropanol using a clean cloth.

4. Clean the Sensor Placement Templates with isopropanol/Acetone on the side that will touch the coupons. Use Placement Templates to ensure proper positioning of PZT sensors.
5. Mark sensor installation locations with a fine Sharpie, using the placement templates (Figure 4-25 and Figure 4-26). It is important for the PZT sensor to be placed in the same location on each test coupon.
6. Before installing any sensors, electronically test each Smart Layer single PZT - Check the capacitance, as shown, making sure the sensor falls between 1.5 – 3.0 nF (see Figure 4-27).
7. Mix the Hysol EA 9320NA two part adhesive, using 100 parts A to 19 parts B. Use a scale to measure the proper amounts of each chemical, for example: 50 grams part A and 9.5 grams part B. Note: Mix enough for 1 row of sensors (5 PZT's) at a time because the adhesive starts to cure and harden after 20 minutes.
8. Clean the entire back of each sensor using isopropanol and Q-tip swabs (see Figure 4-28).
9. Apply adhesive to the back of the sensor. Do not over apply, a thin layer is fine. Also, place a little adhesive on the both sides of the connector (see Figure 4-28).
10. Place sensor on coupon. Secure it in its location and apply pressure during cure by placing Kapton tape over the sensor (see Figure 4-28). Note: sensors can slide around very easily, make sure sensor is in the correct spot before taping down.
11. Using a Q-tip remove bubbles from under the sensor. Apply slight pressure with the Q-tip on the round ceramic sensor area and move in a circular motion outward to remove the air (see Figure 4-29).
12. Cure time (from the Hysol EA 9320NA data sheet) is 5 to 7 day cure at >77°F/25°C or 1 hour cure at >180°F/82°C in an oven or under heat lamps (see Figure 4-29). PZT baseline data acquisition can occur as early as 4 days after mixing adhesive for room temperature cure.

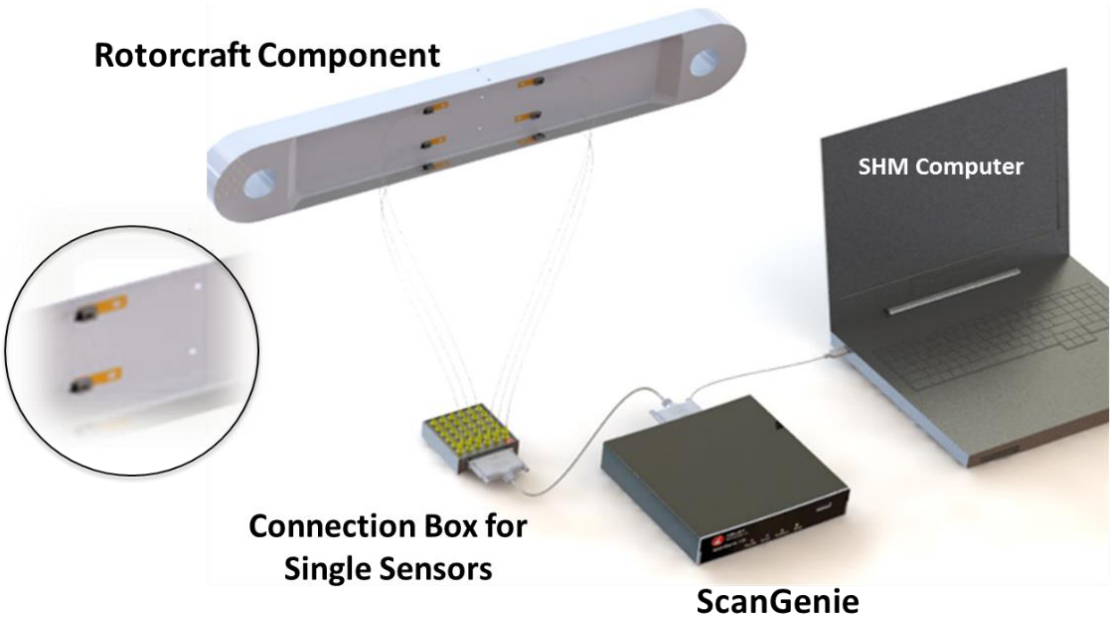

Figure 4-23. PZT System Configuration for Rotorbeam Connection to Acellent ScanGenie Equipment

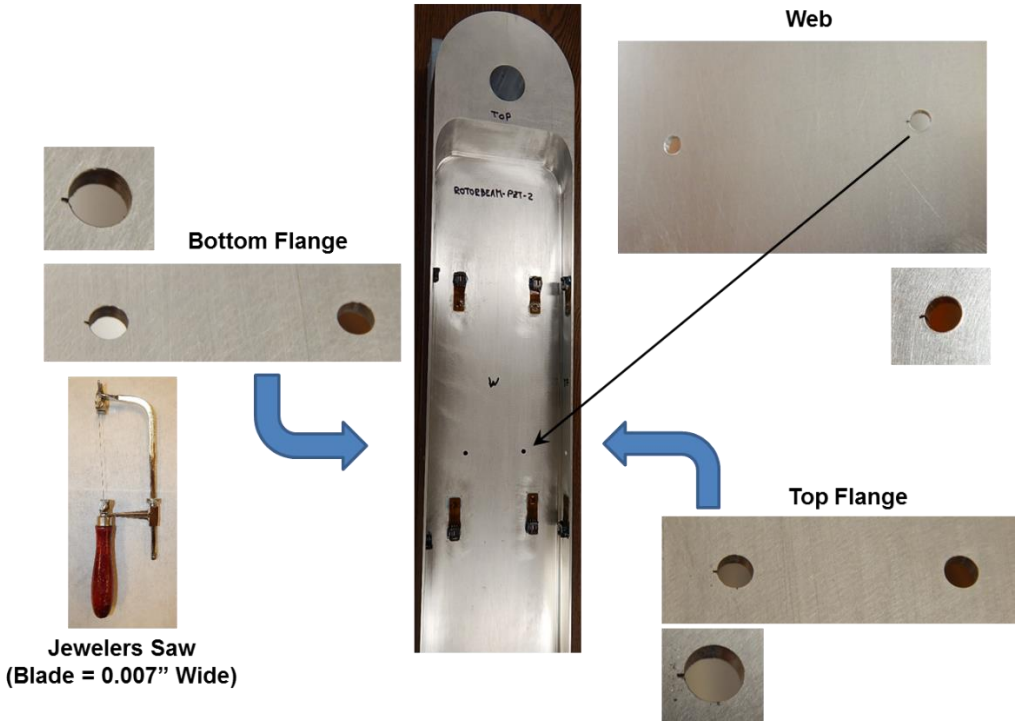

Figure 4-24. Installation of Crack Starter Notches for PZT Performance Tests

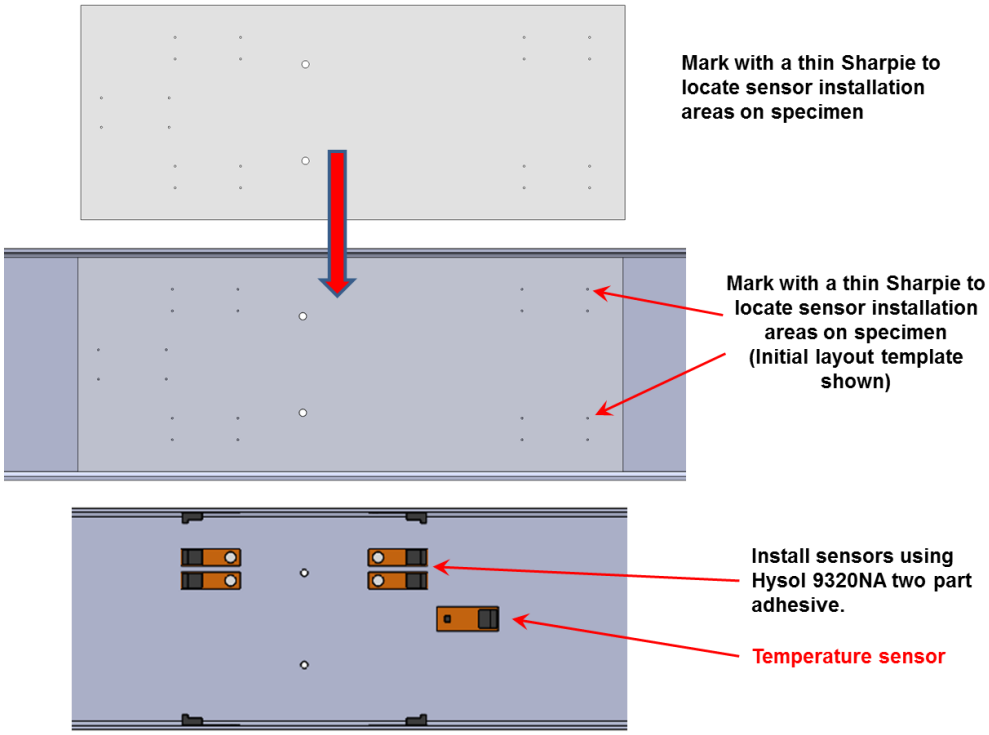

Figure 4-25. Sensor Installation Marking Template (Web) to Produce Precise Placement of PZT Sensors

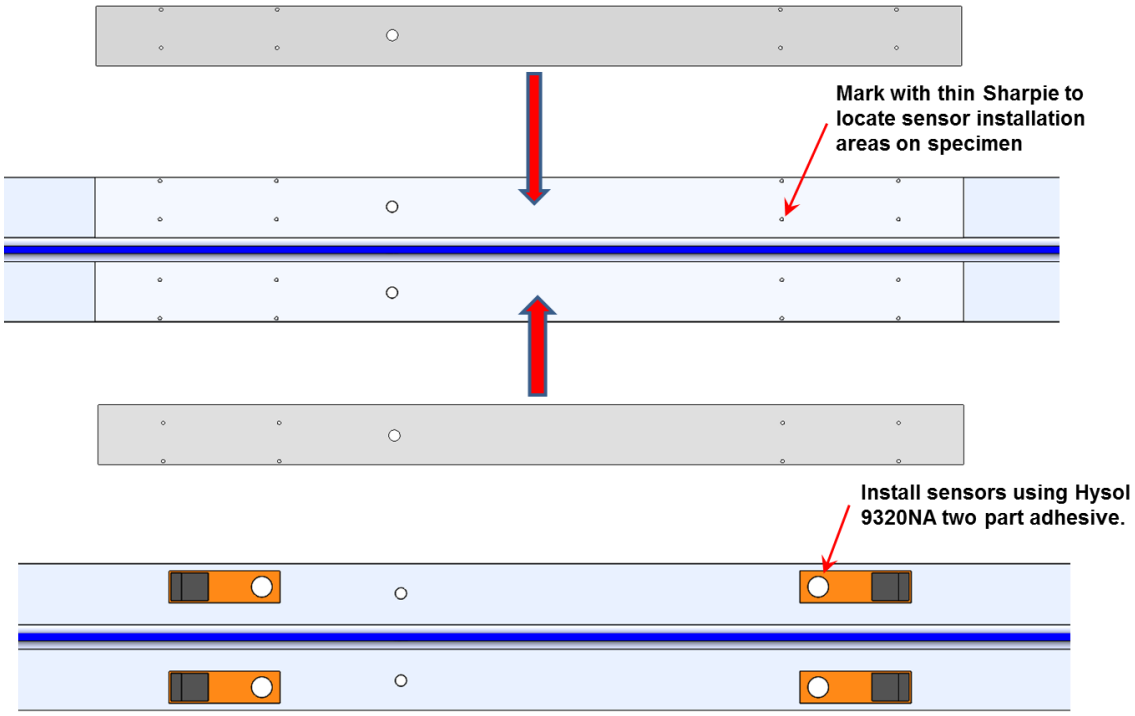

Figure 4-26. Sensor Installation Marking Template (Flange) to Produce Precise Placement of PZT Sensors

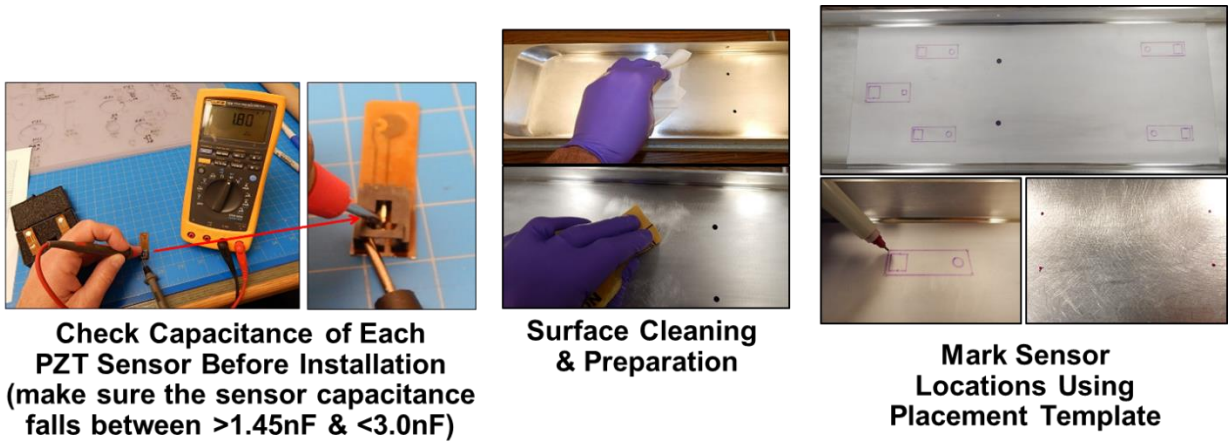

Figure 4-27. PZT Sensor Installation – Sensor Checkout and Specimen Location

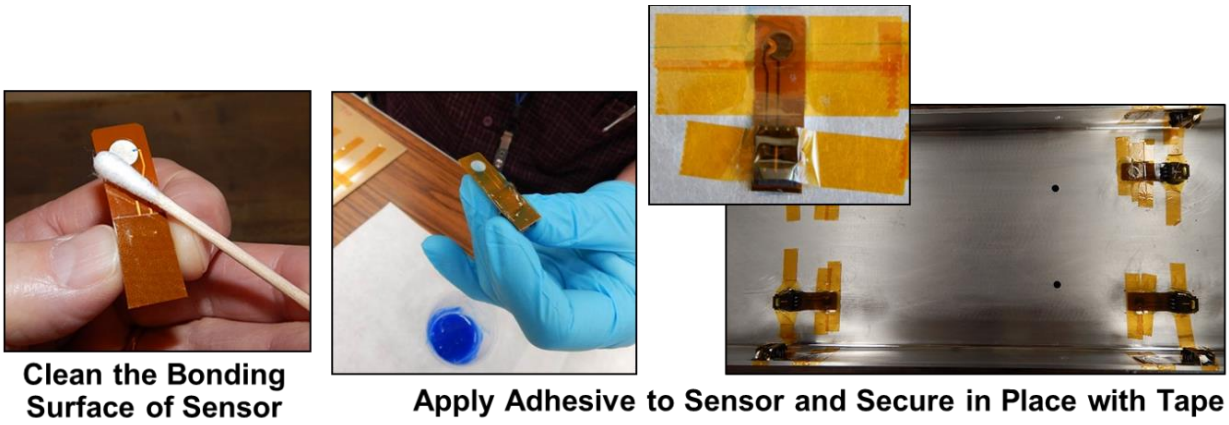

Figure 4-28. PZT Sensor Installation – Bonding Sensors in Place

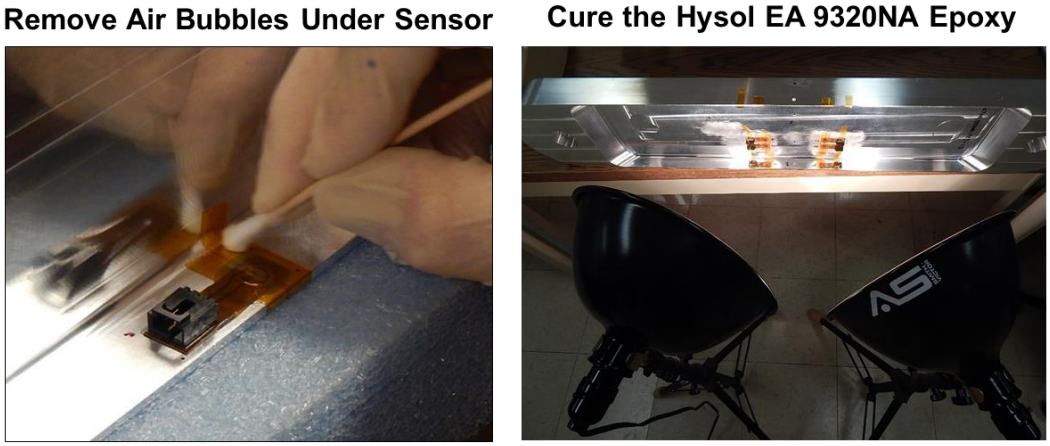

Figure 4-29. PZT Sensor Installation – Ensuring Proper Adhesive Cure

4.4. PZT Sensor Fatigue Test and Performance Evaluation Measurements

PZT Sensor Networks - As discussed in Chapter 2, PZT sensors are arranged in arrays of active-sensors, in which each element takes, in turn, the role of transmitter and receptor, and thus scan large structural areas using ultrasonic waves. The location of the sensors in the PZT network will affect both the signal path and the signal reception and, thus, the nature of the signals used to conduct SHM. PZT networks are discussed in Section 2.3 and several examples are shown in Figure 2-31 and Figure 2-32.

Figure 4-30 through Figure 4-32 show the basic PZT network used to monitor for cracks in both the web and the flanges of the rotorcraft I-beam specimen. Three zones, or network subsets, were used to monitor crack growth in the: 1) top flange (SS3), 2) web (SS2), and 3) bottom flange (SS1) of the I-beam. The most basic sensor layout is shown in Figure 4-32 where PZT sensors 1-4 are

placed to monitor the top flange, sensors 9-12 are placed to monitor the bottom flange and sensors 5-8 are placed to monitor the web region. Crack origin sites, corresponding to mounting holes in the I-beam, are also shown in these figures. Cracks were initiated for individual detection in the web, upper flange, and lower flange. These could be detected using only the network subsets in these regions. In addition, one full network including all sensors could be used to assess detection of multiple, simultaneous cracks throughout the specimen. The signal data acquisition (DAQ) was set to avoid cross-talk between adjacent cracks (i.e. signal reflection from flange cracks do not get detected by web sensors and vice versa) and to avoid mixing direct signal transmissions (e.g. Sensor 4 to Sensor 8, Sensor 6 to Sensor 7) with signals received after reflecting from adjacent structure (e.g. Sensor 5 signal traveling to lower flange and then reflecting back to Sensor 8). In some instances, the nonsymmetrical placement of the PZT sensors around the crack origin sites were used to best evaluate different modes of data acquisition. In addition to pitch-catch mode, pulse-echo mode will also be used to assess crack detection from individual sensors. Recall that pitch-catch mode involves reception of a signal by one sensor after it was transmitted by a separate sensor. Pulse-echo mode involves the transmission of a signal by one sensor and the reception of that signal by the same sensor after the signal is reflected back from any structural geometry or interface. These different DAQ modes will be described in greater detail in Chapter 6.

Several different PZT networks were deployed on the I-beam test specimen to study the effects of specific PZT positioning on overall crack detection performance. The distance of each sensor from the crack origin, the degree of symmetry in the overall layout and the number of sensors in the web network were all adjusted to produce six different PZT networks. Trial tests were conducted using each of these PZT sensor networks and one configuration was tested as the primary layout so that a larger set of consistent, statistical data could be acquired. Figure 4-33 through Figure 4-41 show the six different PZT networks listed as Configurations A, B, C, D, E and F.

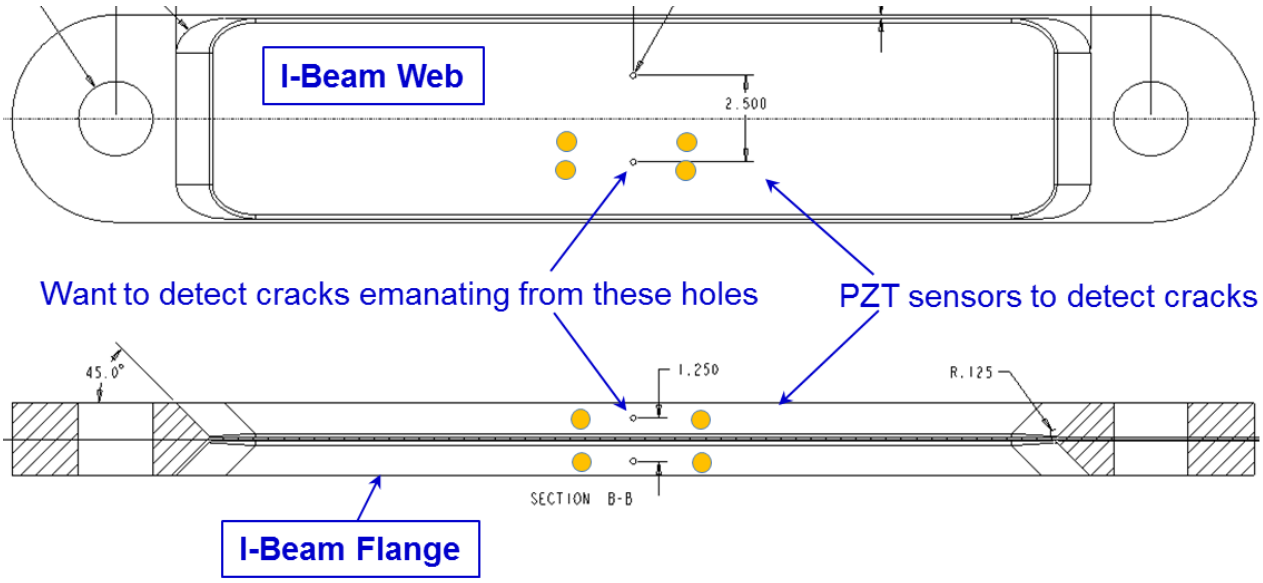

Figure 4-30. Basic PZT Sensor Layout for Rotorcraft I-Beam Specimens

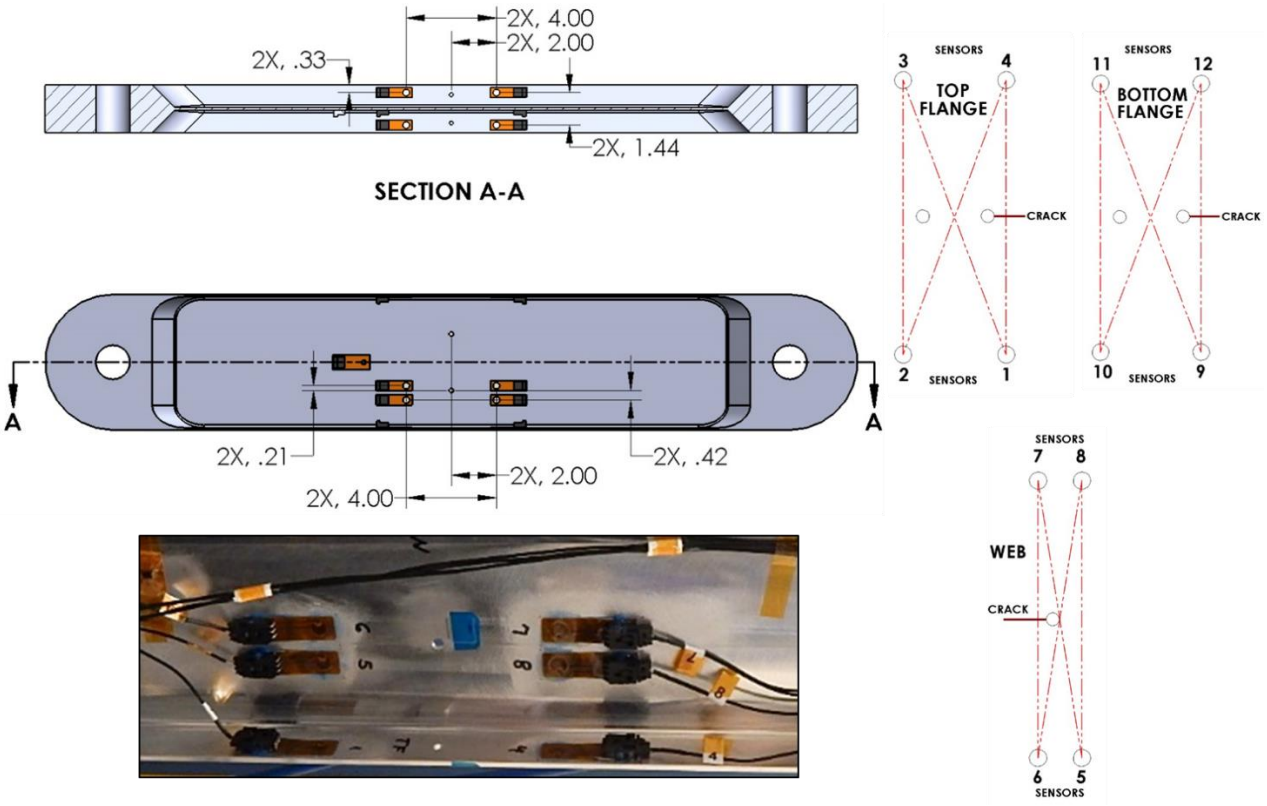

Figure 4-31. PZT Sensor Layout to Monitor for Cracks in Web and Flanges of Rotorcraft I-Beam Specimen

Sensor layout A (Figure 4-34) places two PZT sensors at 2" offsets from the crack origin and two PZT sensors at 6" offsets from the crack origin for each of the three SS1, SS2 and SS3 zones. Sensor layout B (Figure 4-35) changed the flange layouts only such that the each pair of sensors was 2" (symmetrical) from the crack origin in the flange. In sensor layout C (Figure 4-36), all three zones have symmetrically-placed sensor sets (2" on either side of crack site) plus the addition of two more sensors on the web (PZTs #13 and #14 in Figure 4-36). Sensor layout D (Figure 4-37) makes adjustments to the web zone (SS2) only by shifting sensors #6 and #7 closer to the web crack site to form a tight network with sensors #5 and #8. Sensors #13 and #14 remain in the same position as sensor layout C.

Sensor layout E (Figure 4-38 and Figure 4-39) recognizes the high probability that sensors #13 and #14 in layout D do not provide beneficial data. As a result, these sensors are removed in layout E. Two of the test specimens, RB-PZT-17F and RB-PZT-18F, had blind fasteners installed in the flange holes (i.e. not open holes as in other test specimens) so that any difference in crack detection due to the presence of tight fasteners could be determined. These specimens used sensor layout E as shown in Figure 4-39.

For sensor layout F (Figure 4-40), the sensor numbering scheme is different from the previous sensor layouts A-E. This is because the flange sensors are not included in layout F and only web cracks are monitored for these I-beam specimens. This PZT network was especially designed to

accommodate the pulse-echo mode of data acquisition. In sensor layout E, sensors #1 through #4 are arranged on the I-beam web in a similar fashion as sensors #5 through #8 on the web of sensor layout D. In addition, Figure 4-40 shows that two additional sensors, #5 and #6, are placed in the same row as sensors #3 and #4. These off-center sensors produce additional wave travel angles to be included in the pulse-echo singles for expanded sensitivity assessments. This will be discussed further in the PZT results Chapter 6. The different trial PZT networks are summarized in Figure 4-41.

Sensor layouts A, B, C and D were considered trial networks for evaluation purposes. Results from these will be presented along with comparisons to the final, best PZT network selected (Layout E for pitch-catch mode, Layout F for pulse-echo mode). Details on the three SS1, SS2 and SS3 zone subsets are presented in Figure 4-42 along with the specimen numbers representing the largest portion of the I-beam tests. Figure 4-43 through Figure 4-46 show photos and list the PZT network configuration for each of the 18 specimens tested in the PZT performance tests. Two specimens (I-beam #1 and #2) were tested using PZT network A, one specimen (#3) was tested using PZT network B, one specimen (#4) was tested using PZT network C, and one specimen (#4) was tested using PZT network D. The statistical data was acquired from the 11 specimens which were tested using PZT network E. These were specimens RB-PZT-6 through RB-PZT-12 and RB-PZT-15 through RB-PZT-18F. Finally, two specimens were tested to compare crack detection performance from the pulse-echo data acquisition mode (RB-PZT-13 and RB-PZT-14).

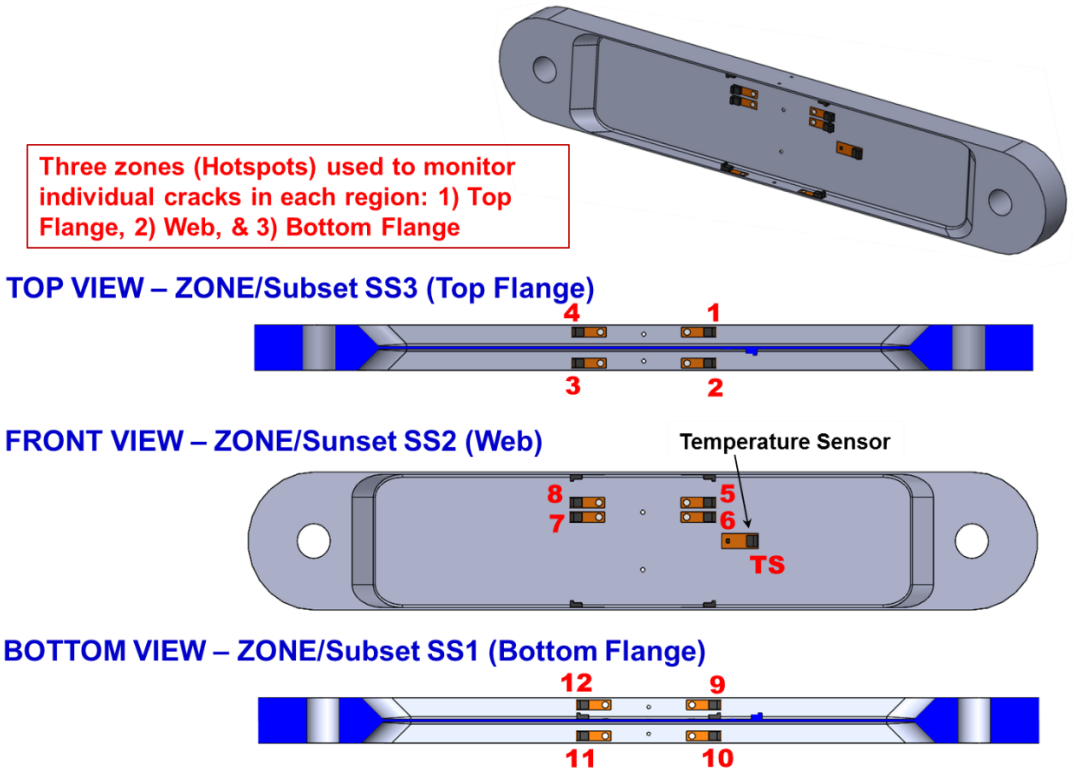

Figure 4-32. Use of Three Zones and PZT Subsets to Monitor I-Beam

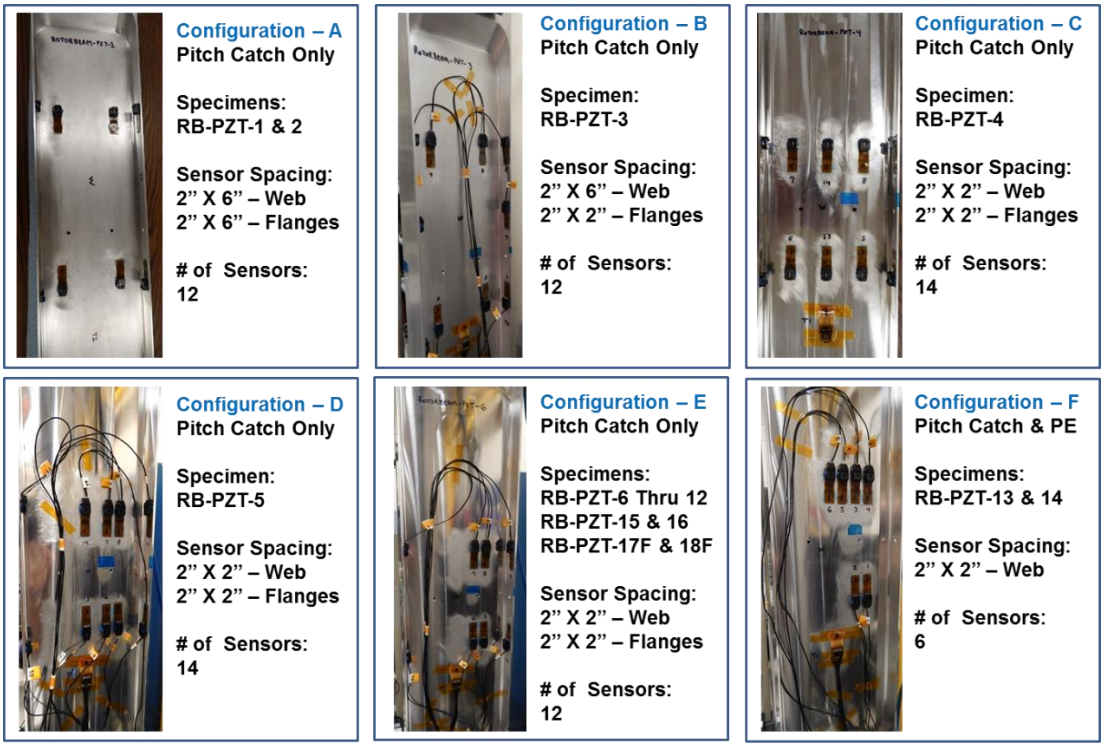

Figure 4-33. Six Different PZT Sensor Layouts Used to Study the Effects of Sensor Spacing on Crack Detection

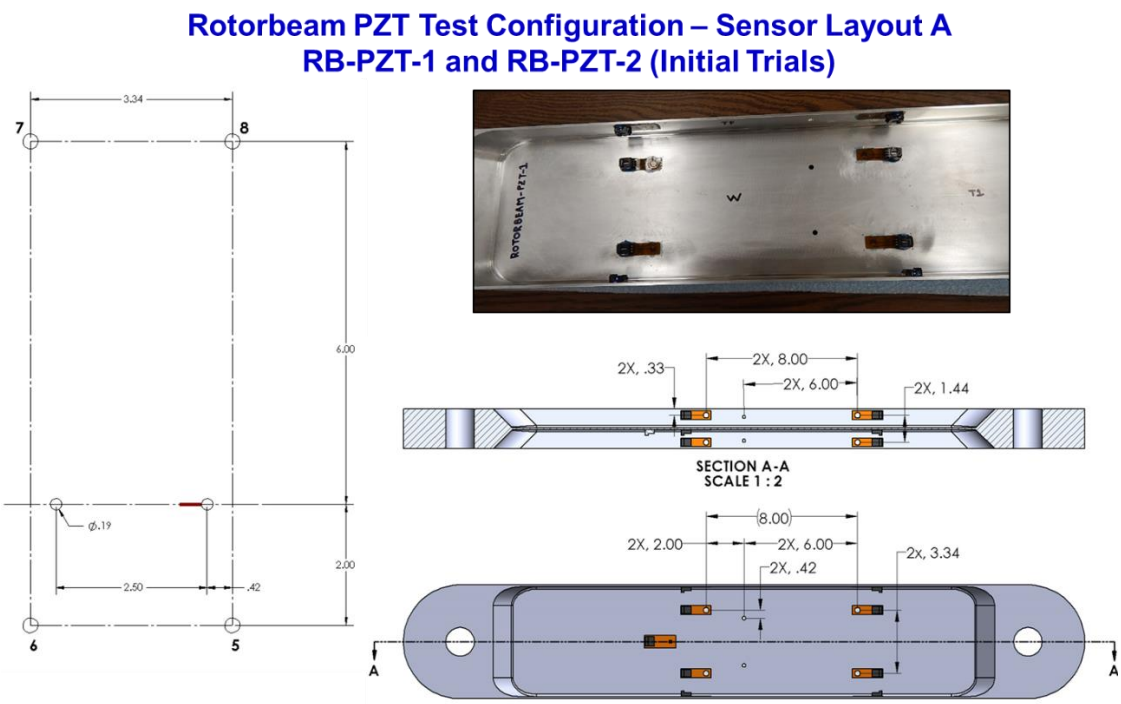

Figure 4-34. Rotorcraft I-Beam PZT Sensor Layout A

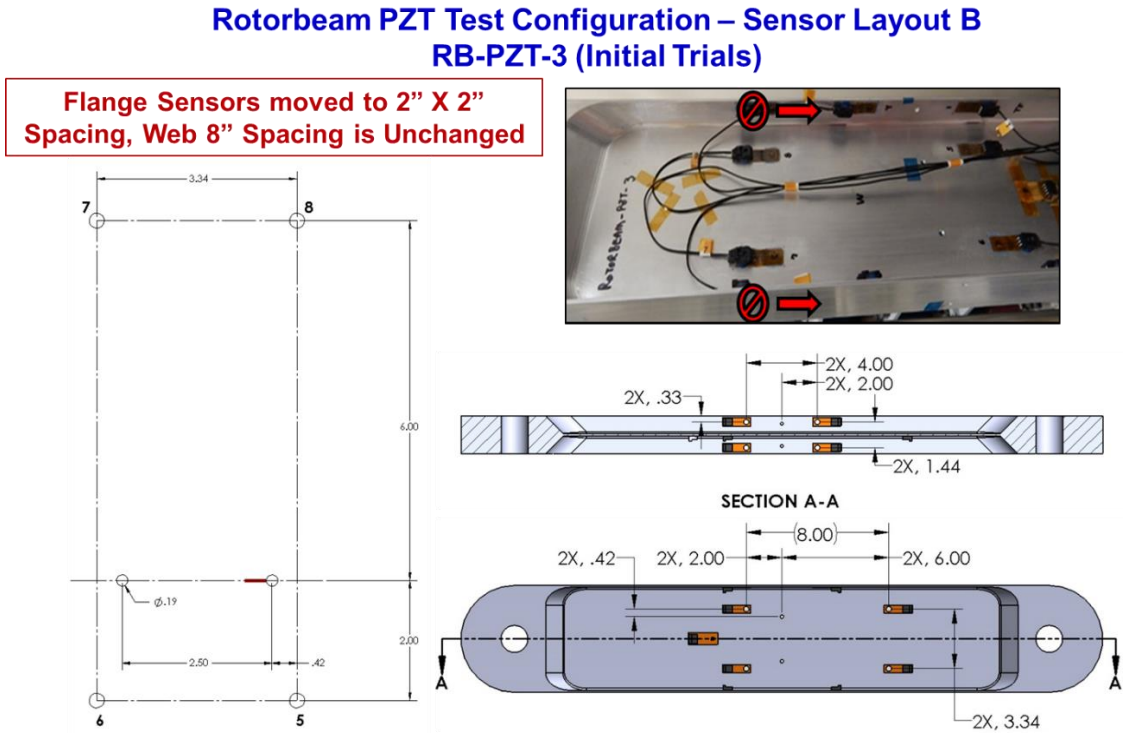

Figure 4-35. Rotorcraft I-Beam PZT Sensor Layout B

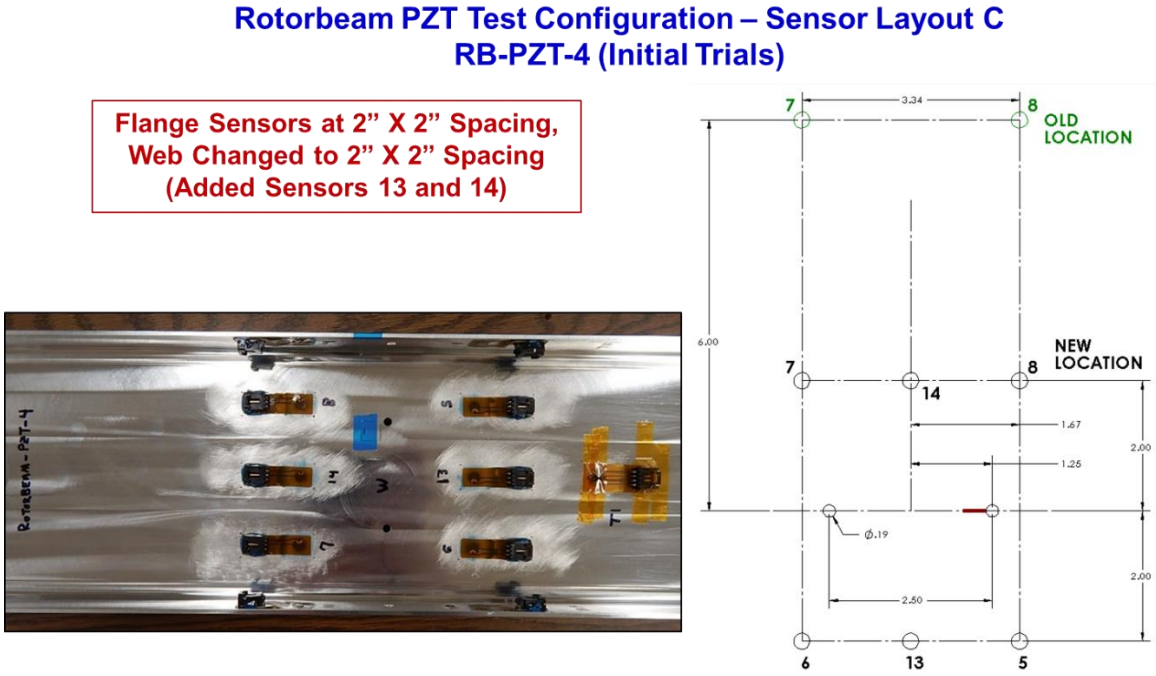

Figure 4-36. Rotorcraft I-Beam PZT Sensor Layout C

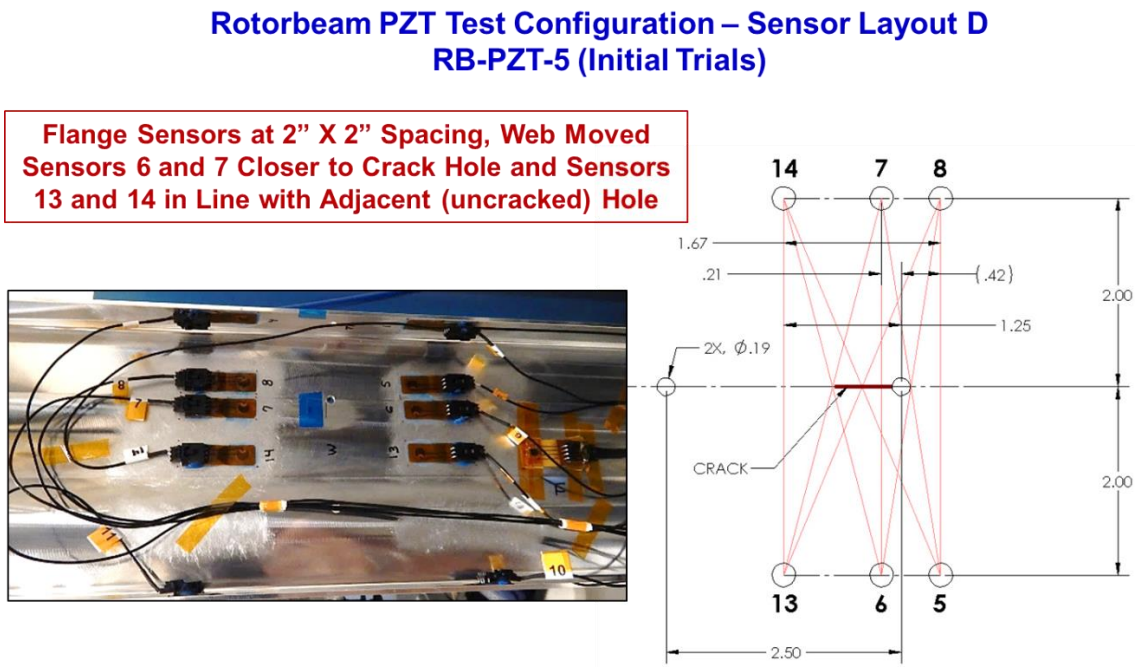

Figure 4-37. Rotorcraft I-Beam PZT Sensor Layout D

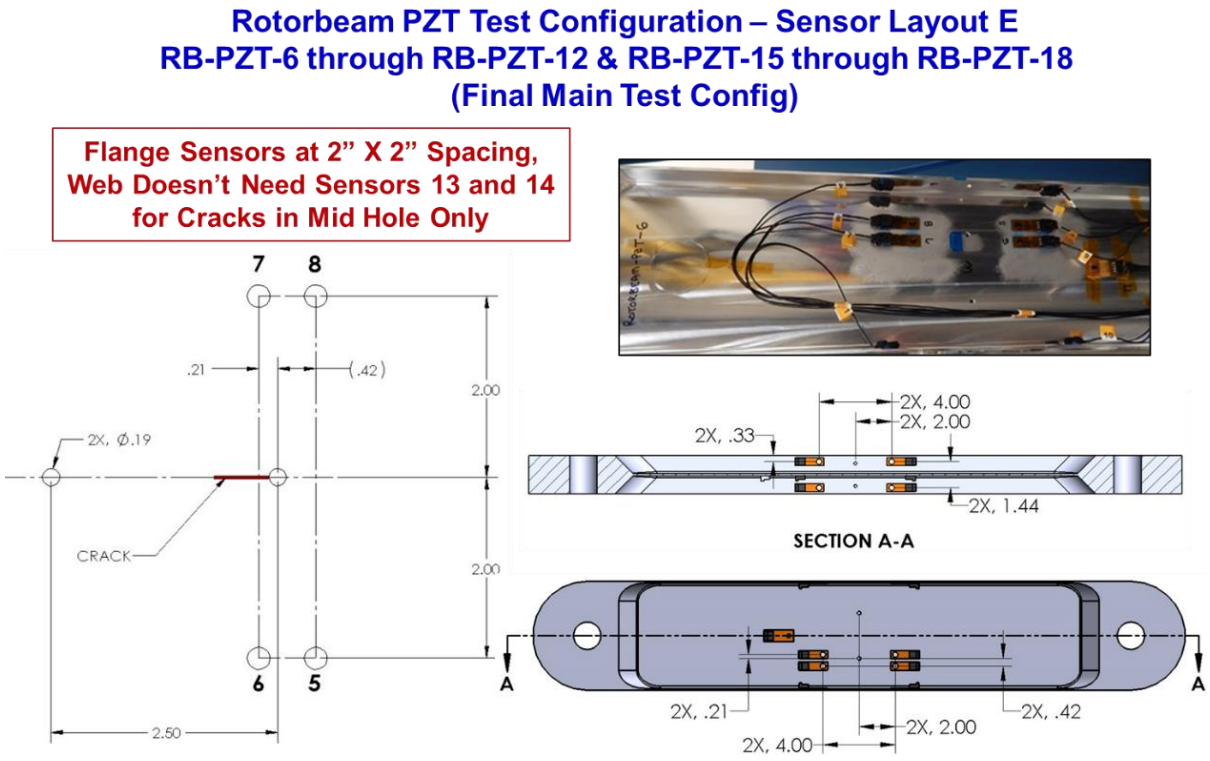

Figure 4-38. Rotorcraft I-Beam PZT Sensor Layout E

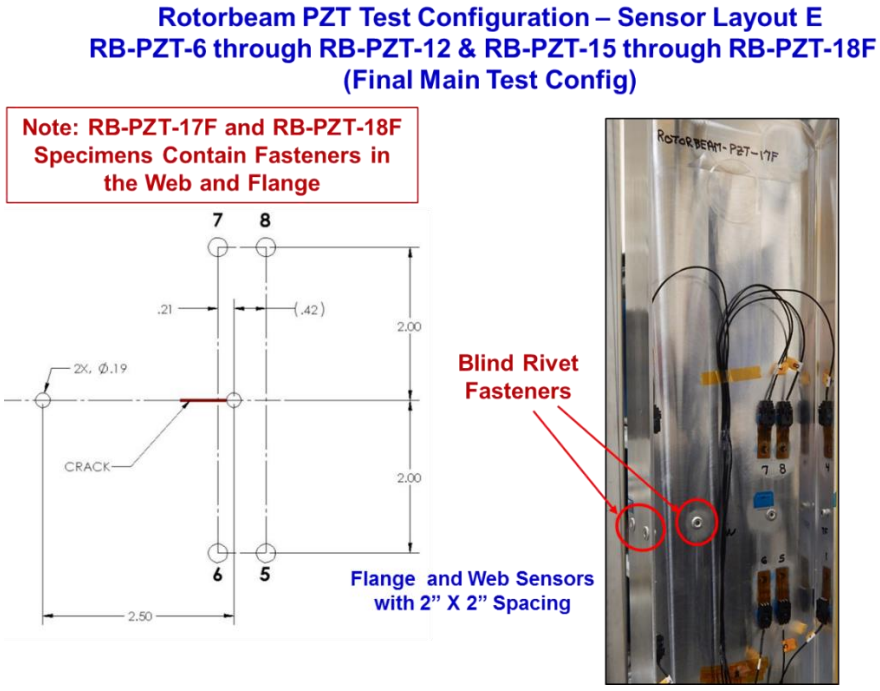

Figure 4-39. Special Case of PZT Sensor Layout E with Fasteners

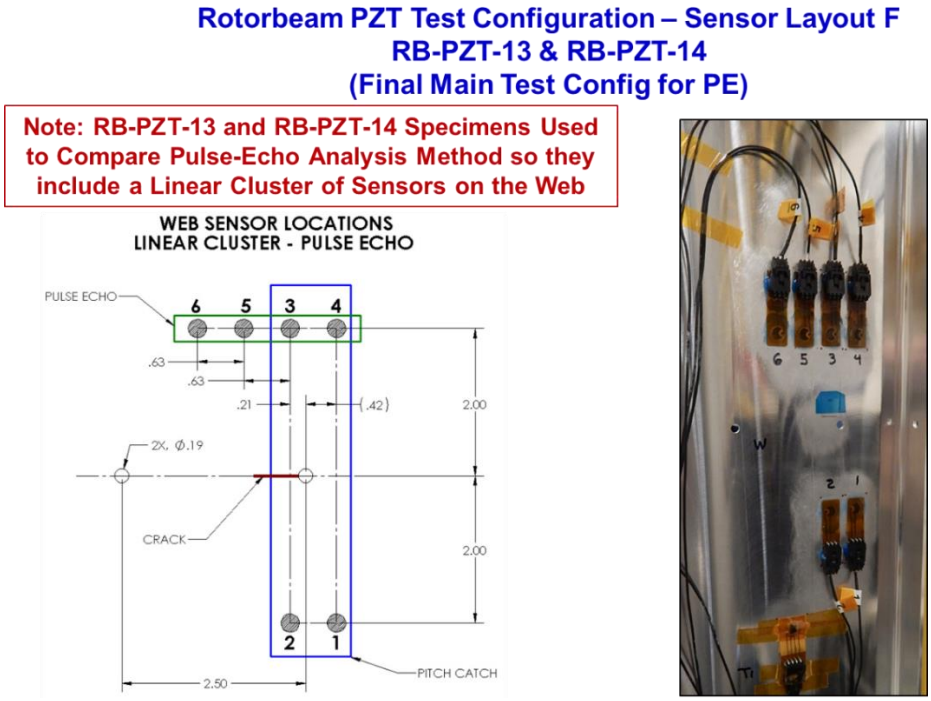

Figure 4-40. Rotorcraft I-Beam PZT Sensor Layout F

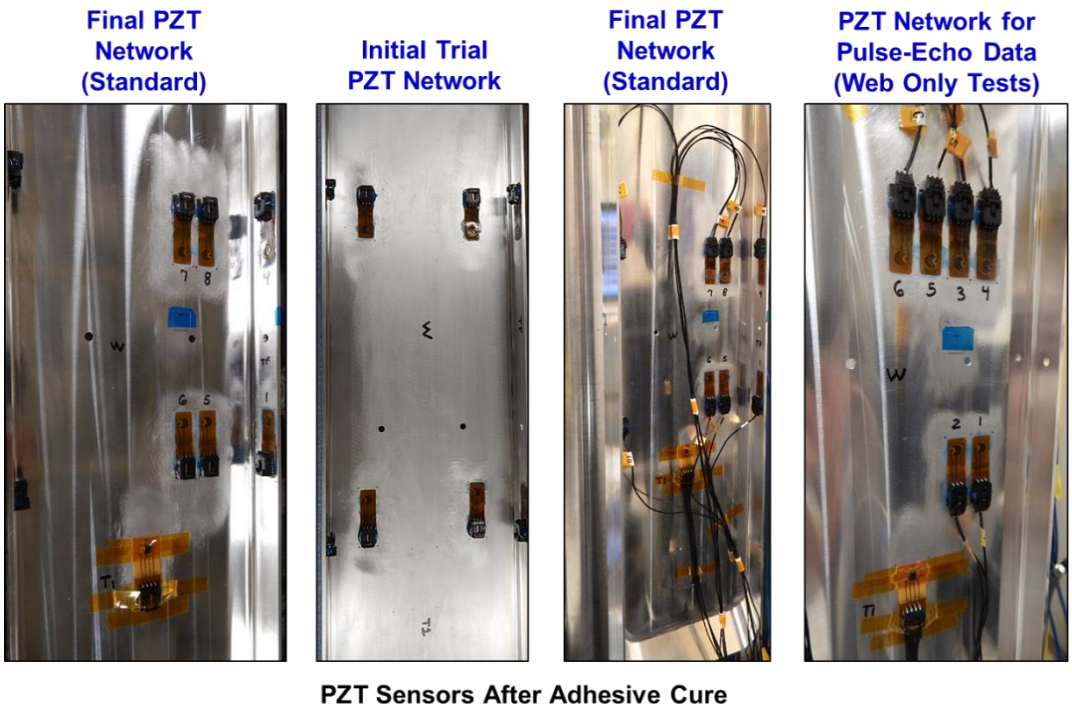

Figure 4-41. Use of Different Sensor Layouts for Complete Set of PZT Performance Tests

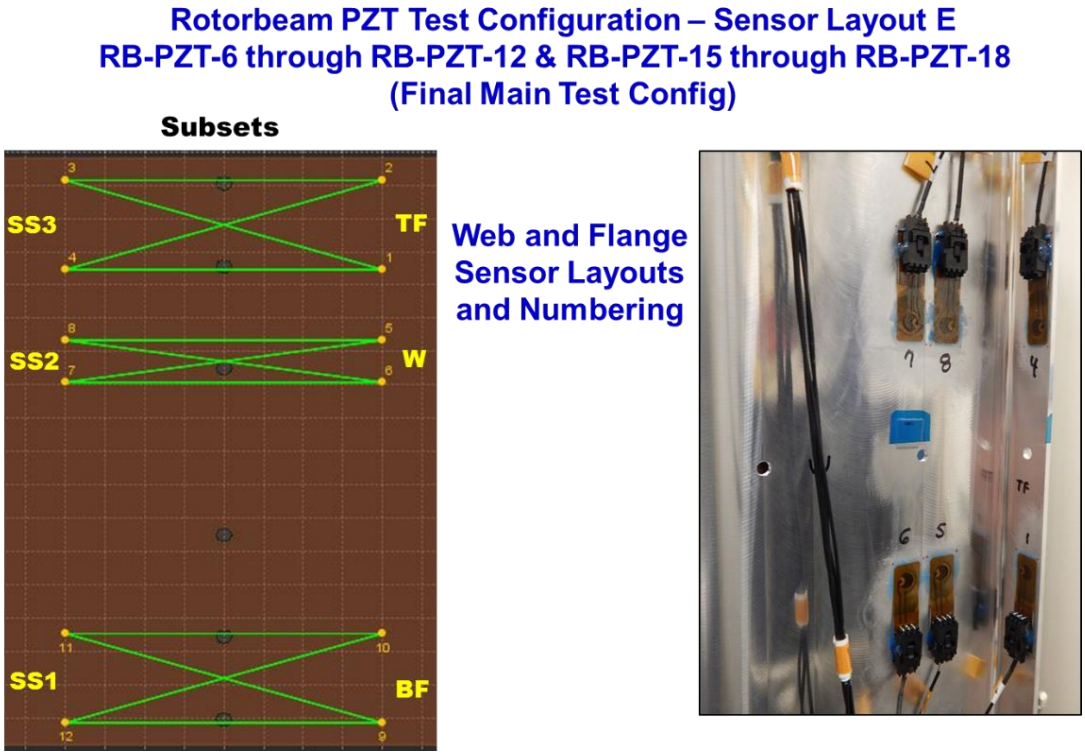

Figure 4-42. PZT Lamb Wave Paths Defined for Monitoring the Three Hot Spot Zones in PZT Configuration Layout E

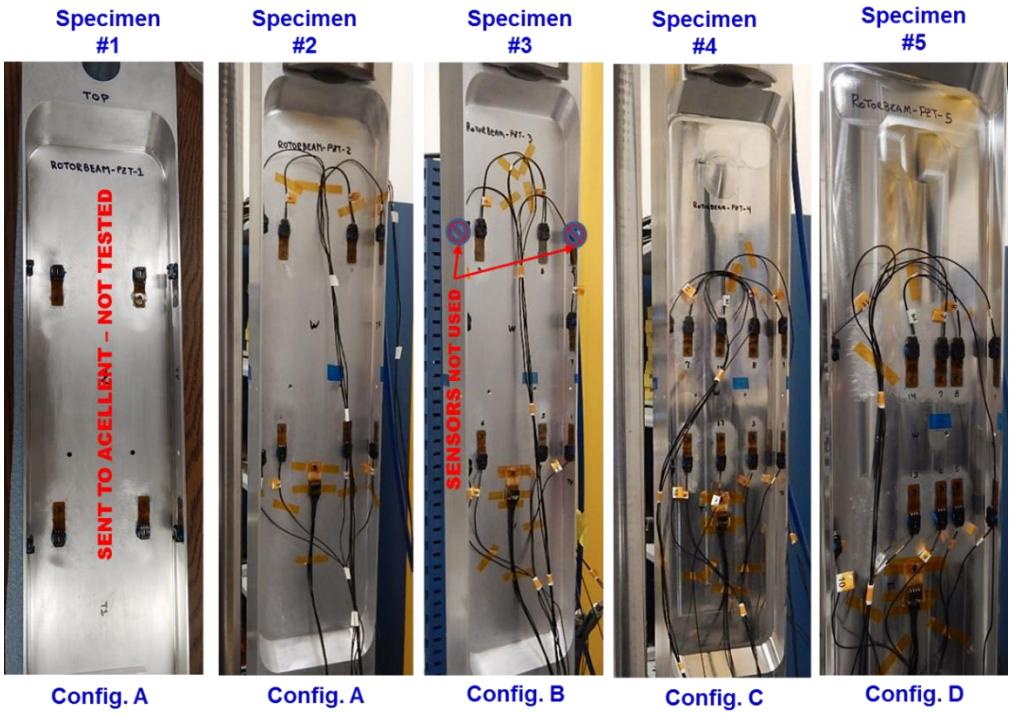

Figure 4-43. PZT Sensor Configurations Used for Specimens 1 - 5

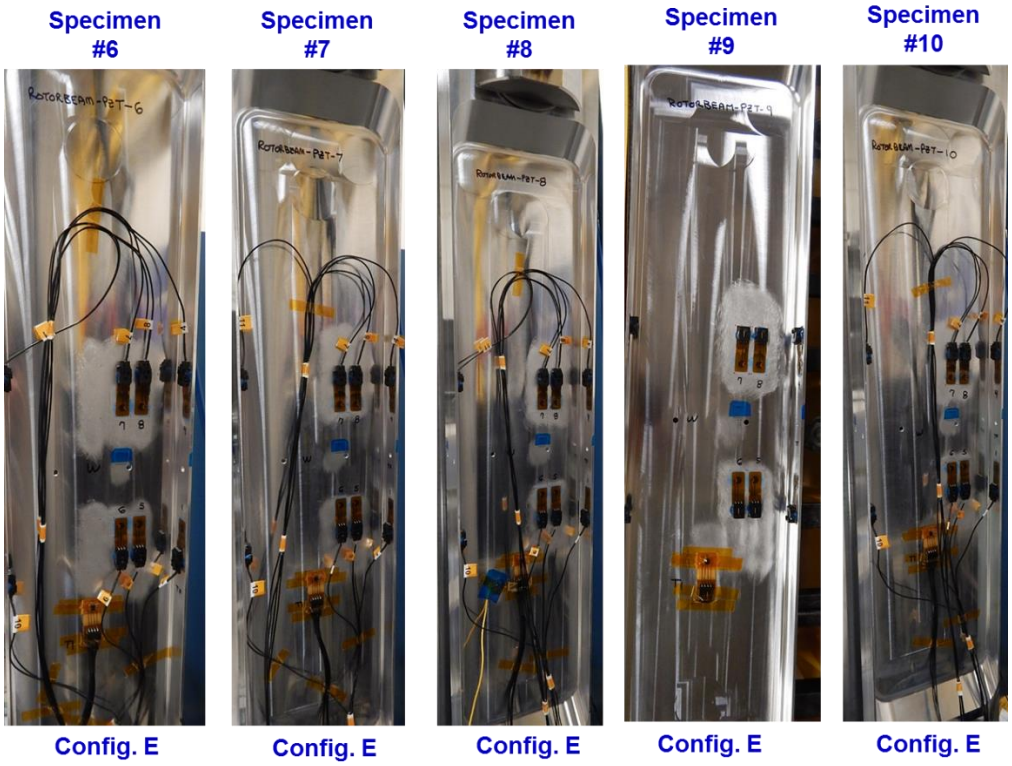

Figure 4-44. PZT Sensor Configurations Used for Specimens 6 - 10

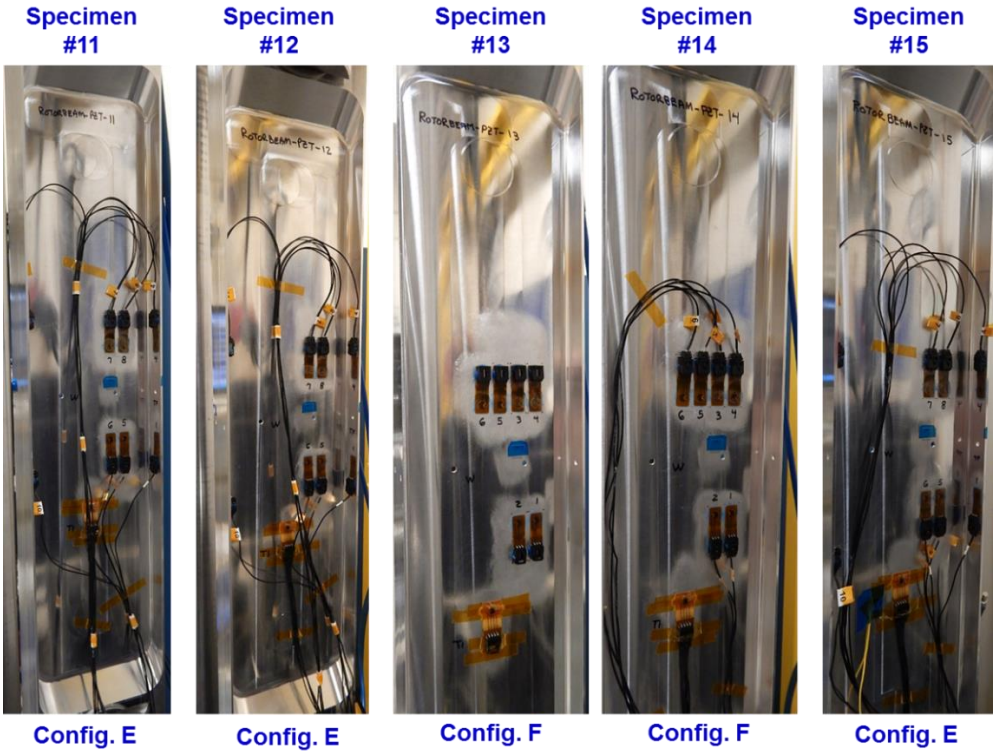

Figure 4-45. PZT Sensor Configurations Used for Specimens 11 - 15

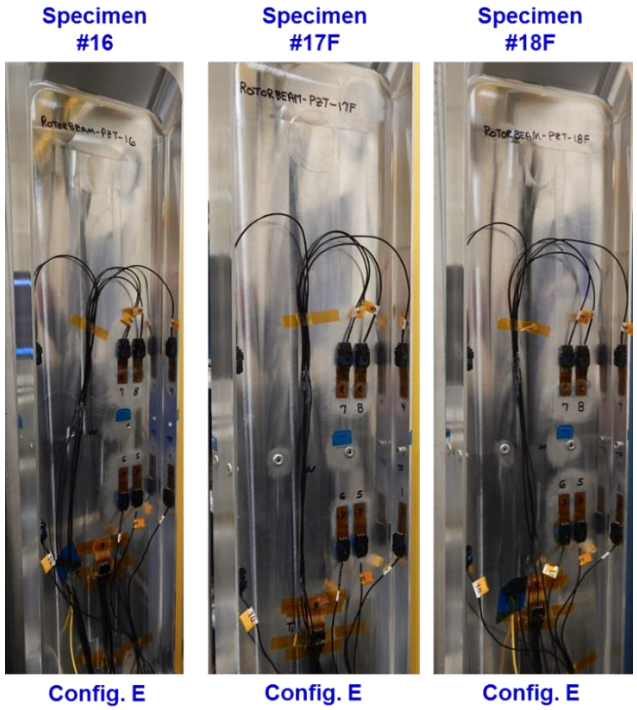

Figure 4-46. PZT Sensor Configurations Used for Specimens 16 - 18

PZT Sensor Fatigue Test Procedure - Fatigue tests were completed on the rotorcraft I-beam test specimens using flight load spectrums. The tests were periodically stopped to conduct microscopic, eddy current and PZT monitoring for crack onset and growth. A fatigue crack was propagated until, at a minimum, it was detected by the PZT system. Additional data was acquired from some of the PZT networks so that a complete response profile (Damage Index vs. crack length) could be produced. Figure 4-31, Figure 4-32 and Figure 4-47 through Figure 4-49 show various views of the rotorcraft I-beam test specimens, the PZT sensors used to monitor for cracks originating at any of the attachment holes, and the specimen orientation in the servo-hydraulic test machine used to apply the proper fatigue stress field. Figure 4-50 summarize the stress calculations that were conducted to ensure representative stress levels in the I-beam.

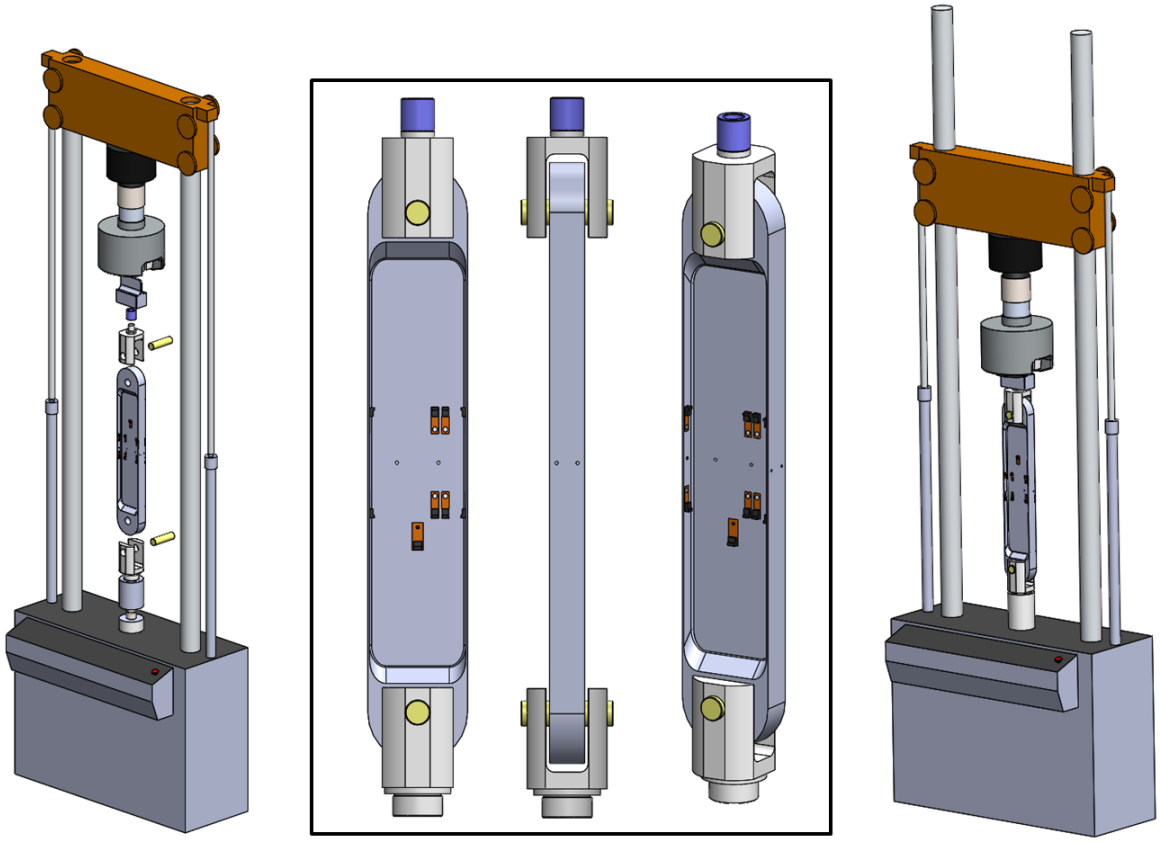

Figure 4-47. Rotorcraft I-Beam Fatigue Test Set-Up

The following steps were completed and data acquired from each I-beam specimen during the PZT performance tests:

1. Measure the capacitance of all installed PZT sensors to confirm proper function (Figure 4-49). Then, check the coupons to validate sensor and channel locations, proper pin mapping and correct wire connections. Figure 4-34 through Figure 4-40 shows the PZT sensor numbering systems that were used for each test specimen.

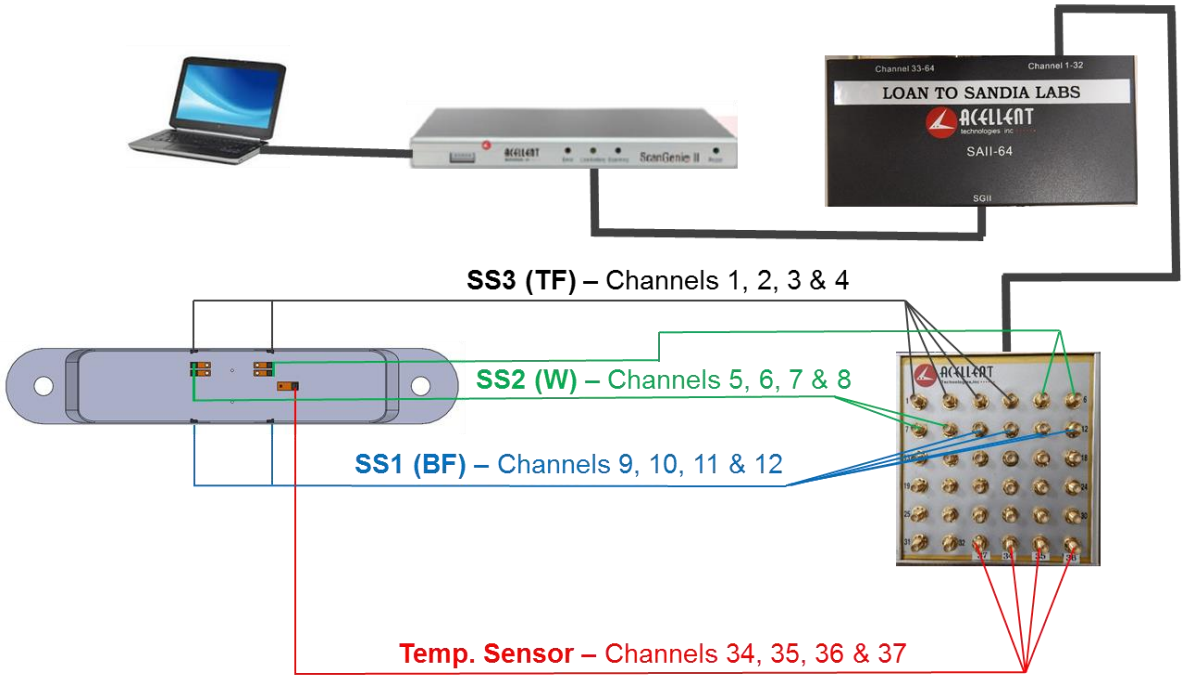

Figure 4-48. PZT Equipment Connection and Data Acquisition Layout – Three PZT Network Subsets (Zones) with a Temperature Sensor to Provide Response Compensation During DAQ

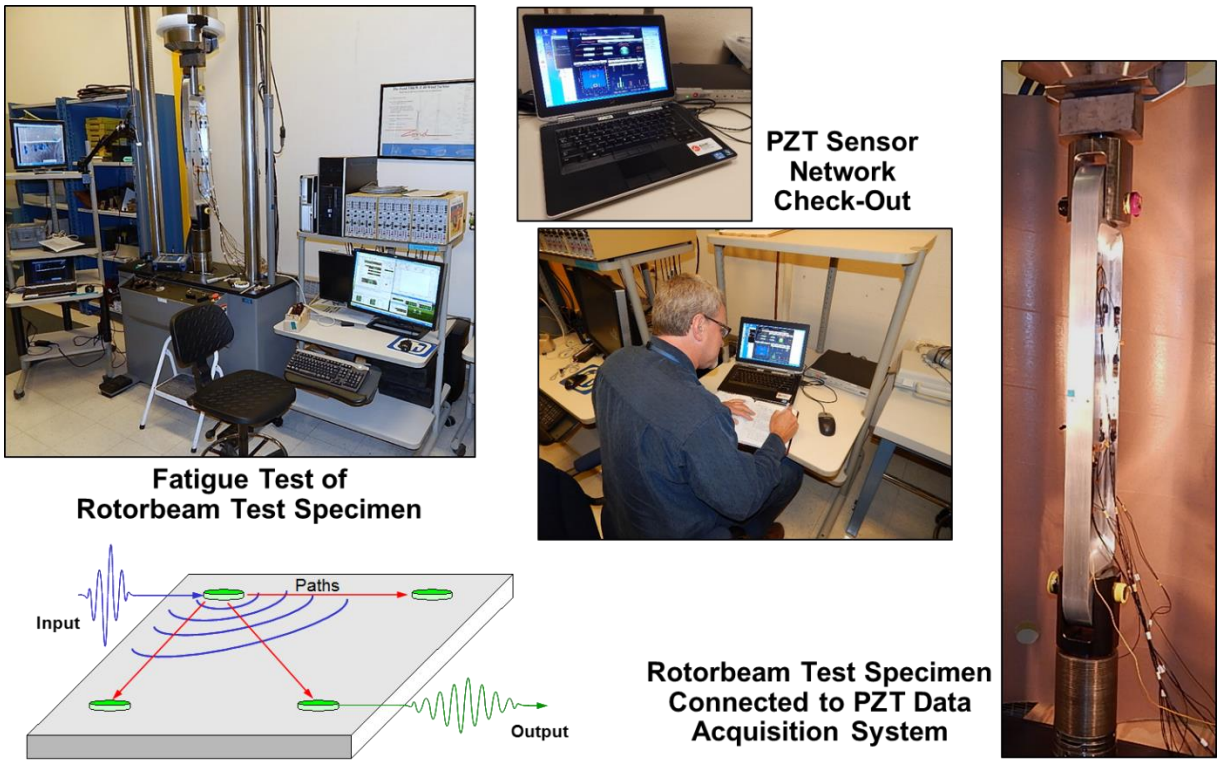

Figure 4-49. Overall Set-Up for PZT Performance Tests

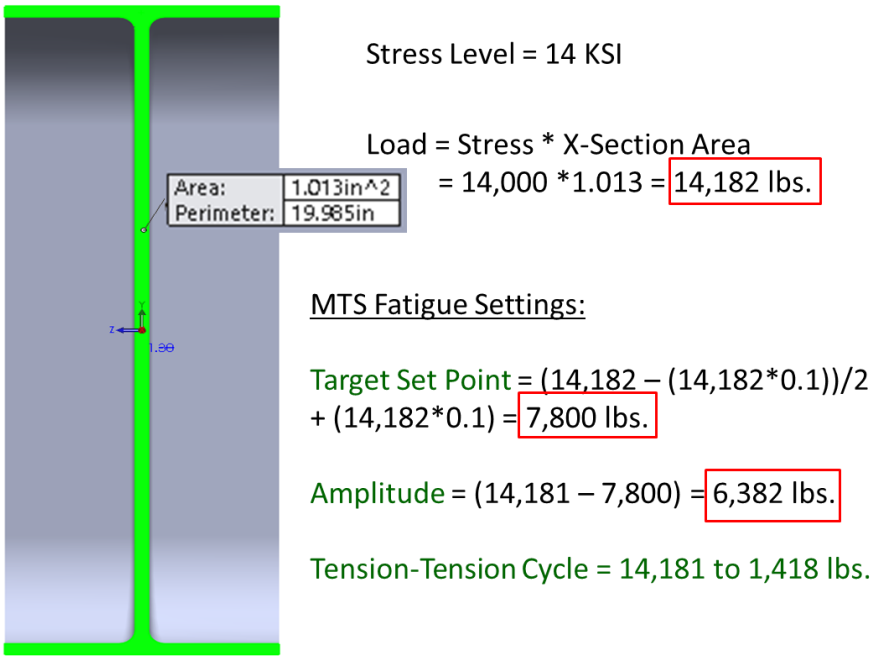

Figure 4-50. Fatigue Load Settings for Rotorcraft I-Beam

2. Create the workspace describing the PZT sensor network, sensor location layout and the array of all PZT paths using SHM Patch V2.13 software (see Figure 4-42 and Chapter 6). Configure signal paths and set up the full array of sampling frequencies (e.g. 200, 300, 400 and 500 KHz), wave type, and data acquisition using SHM Patch V2.13 software and as per the Acellent Scan Genie User's Manual. Mount the test specimen into the fatigue test machine. Conduct all data acquisition with the specimen pinned in place in the fatigue test machine to ensure repeatable boundary conditions with the load = 0 lbs (see Figure 4-48 and Figure 4-49).

3. Before initiating the fatigue test, eliminate the close horizontal paths (e.g. Paths 1-2, 3-4, 5-6, 7-8, 9-10, and 11-12 in Figure 4-42). These close horizontal paths are often tuned to the minimum excitation amplitude and minimum gain of 25V and 15dB. This means that these paths, which do not contain the critical information for crack detection, will probably reach saturation during the actual fatigue tests. Thus, these are the first paths to become saturated during testing and this can create DAQ channel tracking challenges during the fatigue tests. Conduct a general data acquisition (DAQ) of the PZT network using the Acellent DAQ software at a range of burst frequencies and choose the optimal frequency for all subsequent steps. Standard parameters for these preliminary tests are:
   - Number of Data Points: 4000
   - Sampling Rate: 24 MS/s
   - Average Number: 3
   - Burst Frequencies: e.g. 150 KHZ, 175, 200, 225, 250, 275, 300, 325 and 350 KHz
   - Amplification: 50V
   - Gain: 20 dB

4. Exercise the test specimen to loosen rivet clamping/friction and "settle" the faying surface sealant joint, if applicable. This better represents a joint that has experienced normal aircraft stress cycles. This will help avoid changes in the Damage Indices that are associated with initial changes in the sealant and associated signal transmission across the splice plate. Load the specimen for 5,000 cycles at a normal stress level of 14 KSI (14,182 lbs.), R=0.1.

5. Conduct the tuning process following Acellent documents and using the chosen interrogation frequency. Tuning will be completed on each test specimen to optimize all PZT signals. The original tuning settings (AMP and GAIN) will be close but some adjustments will need to be made on each specimen to optimize the signals. Adjust AMP and GAIN levels to optimize the PZT signals for all paths. Acquire all data with zero load on the test specimen.
    - Number of Data Points: 4000
    - Sampling Rate: 24 MS/s
    - Average Number: 3
    - Burst Frequencies: use the chosen single frequency
    - Initial Amplification: 50V; adjusted as needed to optimize signal (Amp range = 25 to 60V)
    - Initial Gain: 20 dB; then, adjusted as needed to optimize signal (Gain range = 15 to 60 dB)

6. Acquire Baseline signals from all sensors in the specimen network by conducting a Data Acquisition (DAQ) step for an array of temperatures. These will be used to allow for DAQ signal compensation calculations over a wide temperature range. Take DAQ readings at the central room temperature level of 72 to 74°F (22.2 to 23.3°C). Cool and heat the room to produce an array of temperatures. Take DAQ readings in an automated fashion every 2°C. The resulting range of temperatures will be approximately 68 to 86°F (20 to 30°C). Place foam tape over the PZT temperature sensor to ensure proper readings of the test specimen temperature. Acquire all data with zero load or 100% load on the test specimen as required for the subsequent, matching DAQ. This will produce the initial Baseline data files (no damage) used for future comparisons and, ultimately, crack detection (damage present).
    - Number of Data Points: 4000
    - Sampling Rate: 24 MS/s
    - Average Number: 3
    - Burst Frequencies: use the chosen single frequency
    - AMP and GAIN settings: are the same as those determined in the tuning process in Step (5). These AMP and GAIN settings will remain the same for the duration of the tests on each specimen.

7. Complete DAQ readings while conducting the fatigue tests. First, acquire an initial PZT data set prior to any additional fatigue cycles. Ensure that the PZT readings reveal no change in voltage levels such that initial Damage Index (DI) levels are very small numbers (less than 0.1 for all PZT paths). Take digital microscope photos of each intended crack site. Acquire all data with zero load on the test specimen.
    - Number of Data Points: 4000
    - Sampling Rate: 24 MS/s

- Average Number: 3
- Burst Frequencies: use the chosen single frequency
- AMP and GAIN settings: are the same as those determined in the tuning process in Step (5). These AMP and GAIN settings will remain the same for the duration of the tests on each specimen.

8. Conduct fatigue tests on specimen and complete DAQ readings while monitoring for crack growth. Load the specimen for sets of cycles in the 1,000 to 5,000 range – based on the history of crack growth rates for the test specimen design - at a normal stress level of 14 KSI, R=0.1. Also, conduct periodic stops based on Eddy Current (EC) crack detection and optical feedback and acquire PZT data. Take digital microscope photos of each intended crack site during various stages of the fatigue tests. Acquire PZT DAQ readings.
    - Load Levels - Use a nominal 14 KSI axial stress level. The stress and load calculations are summarized in Figure 4-50.
    - Frequency - Run the tests with max-min load ratio of R = 0.1. Thus, the loads will be a maximum of 14,182 lbs. and a minimum of 1,418 lbs. Run the fatigue cycles at a frequency of 2-4 Hz depending on the compliance of the specimen and capabilities of the load machine. With the EDM notch in place, crack initiation should occur in the 10,000 to 20,000 cycle range (+/-). Determine how much crack growth is allowable between data acquisitions and stop the tests at appropriate fatigue cycle intervals for periodic measurements.

9. Continue fatigue tests until official crack detection has been achieved as determined automatically by the Acellent Scan Genie software. Acquire PZT DAQ readings. Crack detection will be when there are one or more paths that have a DI value of greater than 0.05 as per DI threshold tests. After first crack detection has been achieved, do not eliminate subsequent saturated paths. This will provide all the data such that paths that were part of first detection are never eliminated from the DAQ process. Acquire all data with zero load on the test specimen. Set the DI threshold for crack detection for DI = 0.05. When a DI level calculated by the Acellent Scan Genie software exceeds the user-specified input of 0.05, a "STAR" appears on the image of the specimen. This will establish the point at which the PZT system first detects the crack in the test specimen. Choose the DI threshold to have some basis in conventional inspection practices which means that the signals from the damaged specimen should differ from the Baseline signals to produce a signal-to-noise (S/N) ratio of at least 3:1. Use the initial, post-tuning data to determine the "noise" level in the PZT SHM system. Then, compare this noise level with the signal level associated with crack detection to calculate the S/N ratio for each PZT network. Additional discussions on establishing a suitable DI threshold are included in Chapter 6.

10. Confirm the location and presence of damage (fatigue crack), along with the crack length using conventional eddy current NDI methods and an optical microscope (Figure 4-51). Measure the crack length at each DAQ interval using both optical and nondestructive inspection methods. Record the crack lengths at PZT detection and at any subsequent DAQ intervals. Log any false calls where the PZT system indicates a crack detection when a crack is not actually present.

- Visual-Aided Crack Measurements - Visually inspect the specimen cracks under a magnified viewing field using the optical microscope. Load the specimen to accentuate the crack opening. Use a Dino Lite Microscope USB camera combined with a set of calibrated micro-scales as shown in Figure 4-51 and Figure 4-52. When the specimen is under load (less than max fatigue levels to avoid strain hardening), it is possible to produce a large crack opening and get an accurate estimate of the crack length.
- Eddy Current Crack Measurements – Conduct EC inspections as shown in Figure 4-51. Mark the location of the crack tip and use the micro-scales to determine the crack length (Figure 4-52).

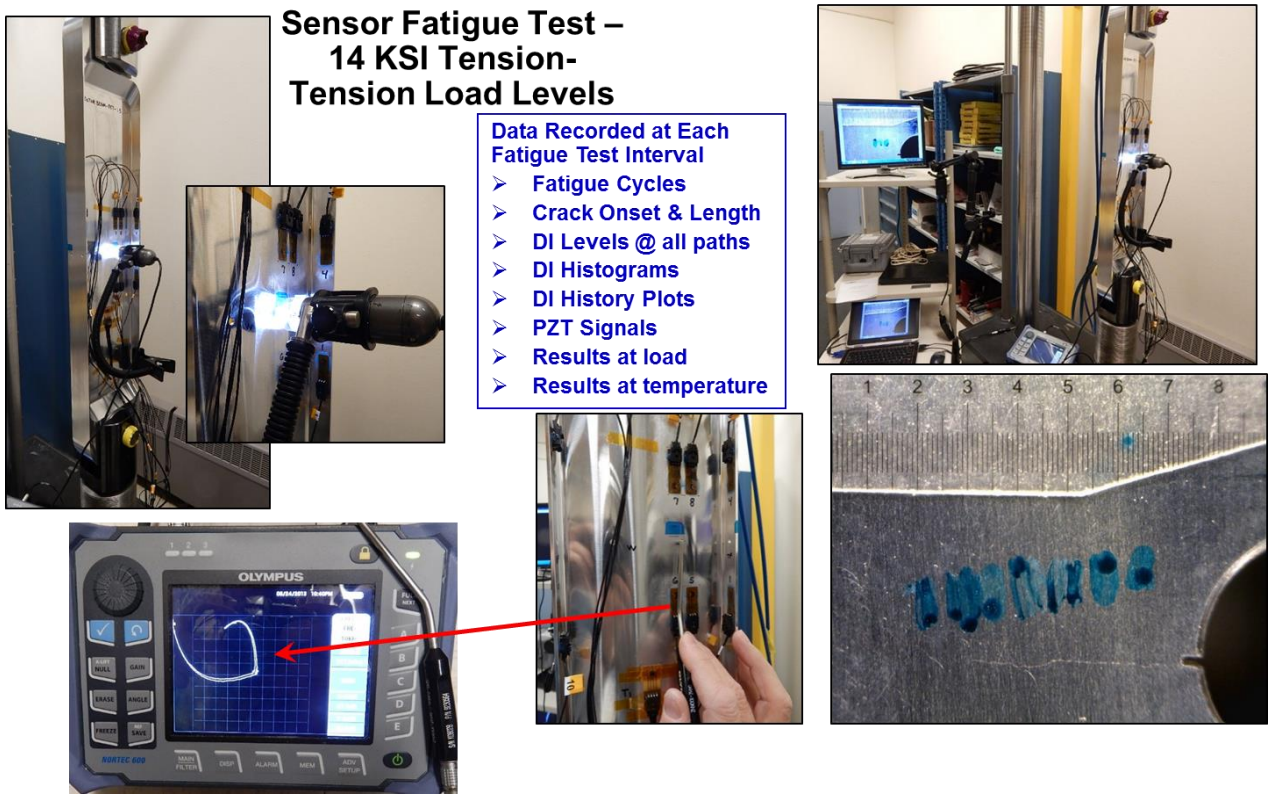

Figure 4-51. Optical Monitoring and Eddy Current Monitoring of Crack Growth

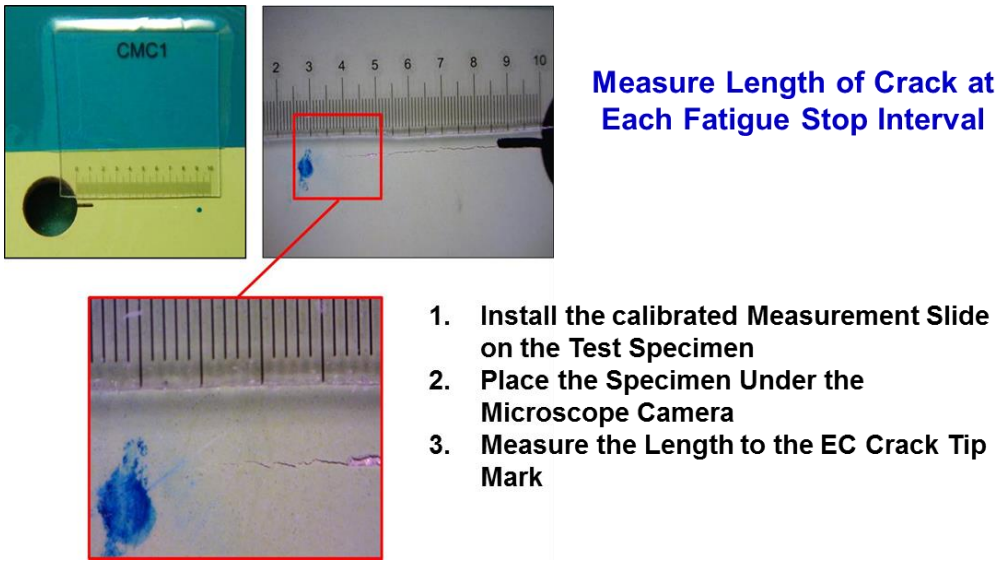

Figure 4-52. Use of Microscope Camera, Crack Tip Markings and High-Fidelity Scale to Measure Crack Length at Each Fatigue Stopping Point

11. After the Acellent software identifies a crack and the crack length has been measured, continue to fatigue the test specimen and take data at various intervals to log PZT response (and DI levels) vs. crack length. The desire is to acquire data for the crack as it increases in length in order to utilize the full set of PZT response vs. crack growth spectrum in an array of POD calculation schemes. Run a carefully-selected number of fatigue cycles and take data in an attempt to acquire data at a number of crack lengths as shown in Figure 4-53:
    - Initial crack detection (crack length = X)
    - X + 1 mm
    - X + 2 mm
    - X + 6 mm
    - X + 10 mm
    - X + 14 mm
    - The da/dN curve produced from the trial tests will be used to produce these data readings at the intervals desired.

- The permanent, unloaded Damage Detection will always be produced using all PZT data paths. Subsequent data analyses can be conducted to assess crack detection when a selected subset of sensors is used. This will allow for an assessment of PZT network sensitivity versus the density of sensors.

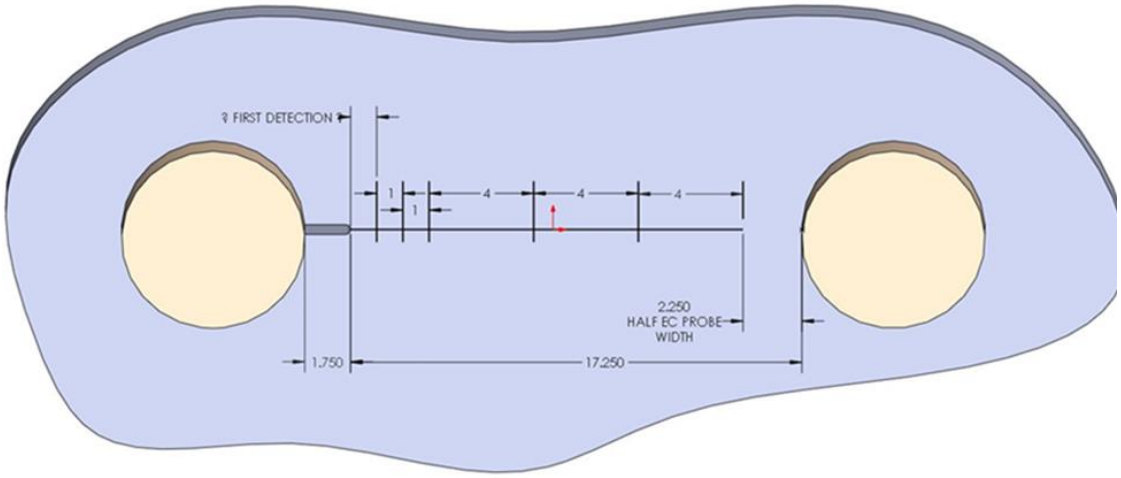

Figure 4-53. Approximate PZT Data Acquisition Points During Fatigue Testing

12. Calculate the Probability of Detection - Use the various POD analysis methods described in Section 4.6 to calculate PZT POD levels when all crack detections are included.

Data Recorded at Each Fatigue Test Interval

- Fatigue Cycles
- Crack Onset & Length
- DI Levels @ all paths
- DI Histograms
- DI History Plots
- PZT Signals
- Results at load
- Results at temperature

Summary of Testing & Data Analyses to Evaluate PZT Performance

1. PZT-1 and PZT-2: trial and calibration specimens; no real validation data; -2 assessed bolted fasteners in holes (showed high variation in DIs for bolted assembly)
2. PZT-3, -4, -5: no 500 KHz data so flange only results at RT; -3 and -4 assessed bolted fasteners in holes (showed high variation in DIs for bolted assembly)
3. PZT-6 thru PZT-12: all data for web and flange at RT
4. PZT-13 thru PZT-14: all data for web only at RT
5. PZT-15 thru PZT-16: all data for web and flange at RT
6. PZT-15 and -16: added web and flange detection at extreme hot, extreme cold
7. PZT-11 and -12: added PE mode with "Distributed Sensor Arrangement"
8. PZT-13 and -14: added PE mode with "Clustered Sensor Arrangement"
9. PZT-17F and -18F: all data for web and flange at RT with blind rivets in holes

Two additional test specimens, RB-PZT-T1 and RB-PZT-T2, were also tested. These specimens were simple flat plate coupons representing the "flange plate" of the I-beam. They contained the same PZT layout as the I-beam flange and were tested to evaluate PZT crack detection without the

compressive strains and complex boundary conditions contained in the I-beam specimen. They were also used to assess PZT response after exposure to freezing temperatures

PZT Data Goals

Produce performance assessment values for separate PZT networks concentrated on Upper Flange, Lower Flange and Web for multiple structural configurations and assess performance changes due to operating environments (see Table 4-2):

1. Unloaded with Open Holes
2. Unloaded with Blind Rivet Fasteners
3. Loaded with Open Holes (1,000 lbs and 7000 lbs)
4. Loaded with Blind Rivet Fasteners (1,000 lbs and 7000 lbs)
5. Compare results at temperature extremes to show compensation
6. Utilize pulse-echo and pitch-catch UT modes
7. Compare results from flat plates with similar dimensions to I-beam flange – assess performance without complex residual stress and boundary conditions.

Table 4-2. PZT Interrogation Configurations for Rotorcraft Zonal SHM Evaluations

Specimen Number	Tests Support Calibration	Specimen Condition During Data Acquisition									PZT Data type	
		Room Temp	Elevated Temp (85°F)	Reduced Temp (60°F)	Subfreezing Temp (-18°F)	Unloaded	Loaded (1000 lbs)	Loaded (7000 lbs)	Open Holes	Blind Rivets Installed	Pitch-Catch	Pulse-Echo
1	X	X				X			X		X	
2	X	X				X			X		X	
3	X	X				X			X		X	
4		X				X	X		X		X	
5		X				X	X		X		X	
6		X				X			X		X	
7		X				X			X		X	
8		X				X		X	X		X	
9		X				X	X	X	X		X	
10		X				X	X	X	X		X	
11		X				X	X	X	X		X	X
12		X				X	X	X	X		X	X
13		X				X	X	X	X		X	X
14		X				X	X	X	X		X	X
15		X	X	X		X	X	X	X		X	
16		X	X	X		X	X	X	X		X	
17F		X				X	X	X		X	X	
18F		X				X	X	X		X	X	
T1		X			X	X			X		X	
T2		X			X	X			X		X	

Separate baselines acquired for: 1) every 2° increment of monitoring temperature range, 2) open vs riveted hole, 3) loaded vs unloaded specimen & 4) Pulse-Echo vs Pitch-Catch DAQ modes

4.5. CVM and PZT Environmental Durability Test Procedure

When considering overall durability assessments, it is important to make sure that all operating conditions that may affect SHM system response are properly included in the test program. Application of these environments may be static or cyclic if fatigue response is an important consideration. A criteria to identify particular changes in sensor response, which involves pre- vs. post-test and intermittent measurements, is useful in assessing the SHM system's performance. Durability testing of CVM and PZT sensor systems has been addressed in a number of studies [4.3 – 4.4]. The test set-up and results are summarized in this report to properly include this critical element in any comprehensive SHM assessment. The CVM and PZT test specimens used in these studies are shown in Figure 4-54 and Figure 4-55. These specimens represent the portion of the SHM system that is flown on the aircraft as depicted in Figure 4-56. Figure 4-57 depicts all of the elements of the temperature and humidity environments along with the data acquisition points for each 9-10 day cycle. Each hot-cold-wet cycle was repeated four times to produce the full 28 days of hot-wet conditioning used in normal environmental tests. The minimum and maximum temperatures correspond to, or exceed, the DO-160 environment used to certify primer materials.

The sensors were subjected to the environmental test environment shown in Figure 4-57. First, baseline sensor data were acquired to ensure suitable sensor installation and to establish data for future comparisons after ENV exposure. Figure 4-58 shows placement of the sensors into the environmental chamber for testing. Sensor response measurements were made after each of the three environments listed above (hot-wet, cold, heat) and this process was repeated for a total of four cycles. The tests evaluated sensor ability to function after severe exposure to humidity, temperature variations, icing/freezing and heat. Results from these tests will be discussed further in Sections 5.2 and 6.4.

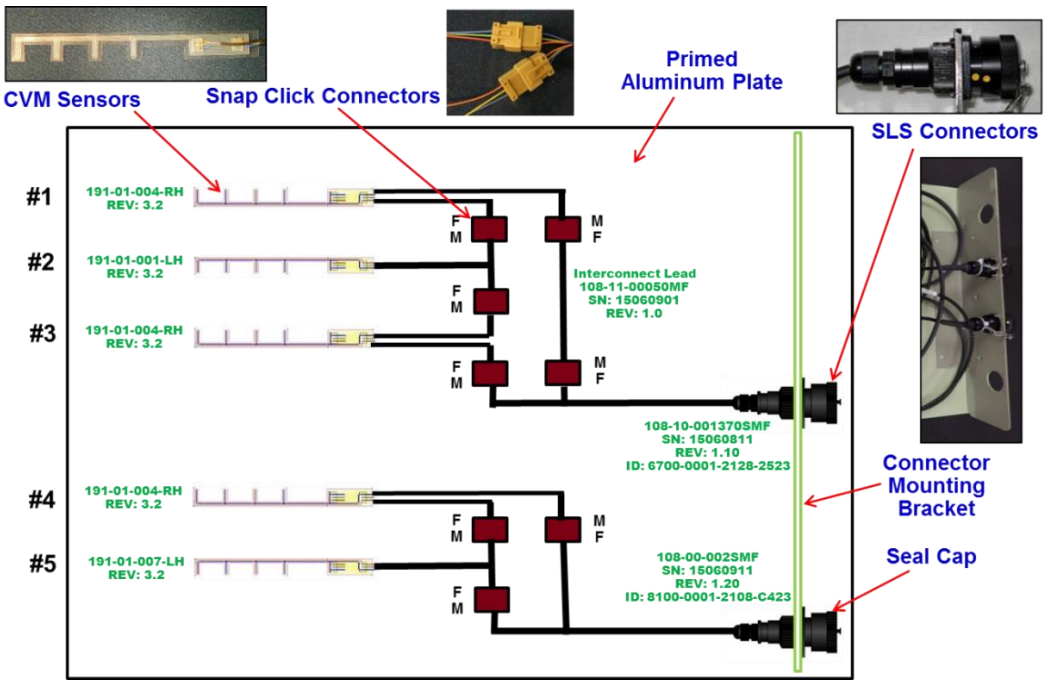

Figure 4-54. Environmental Test Configuration for CVM Sensors

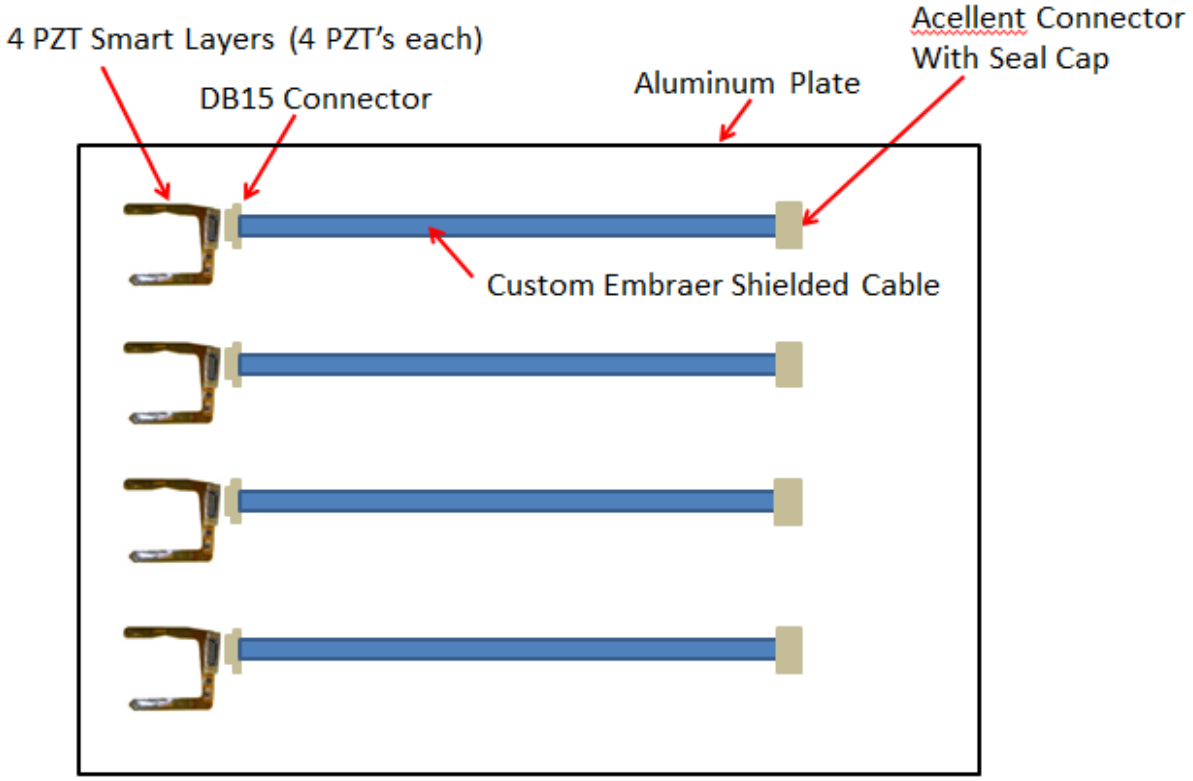

DB9 and DB15, MIL-C24308 connectors and cables were used

Figure 4-55. Environmental Test Configuration for PZT Sensors

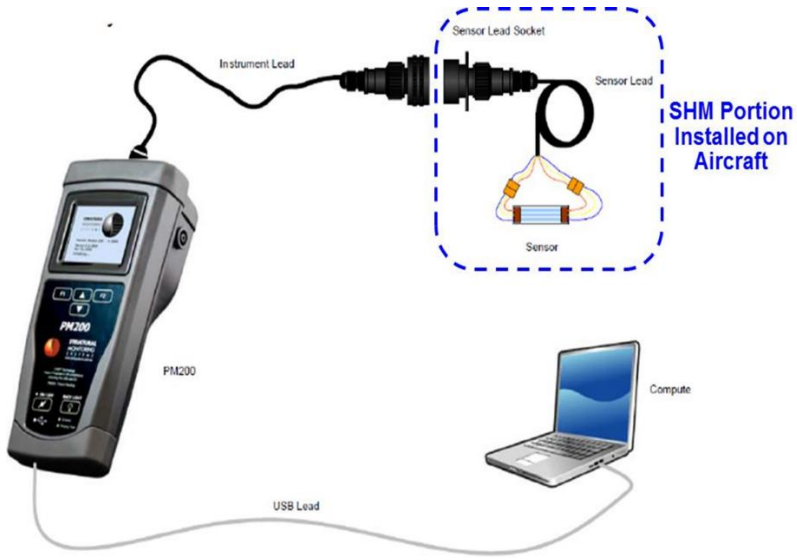

Figure 4-56. Schematic of Full CVM System Highlighting the "On-Aircraft" Portion Subjected to Durability Testing and Subsequent Monitoring

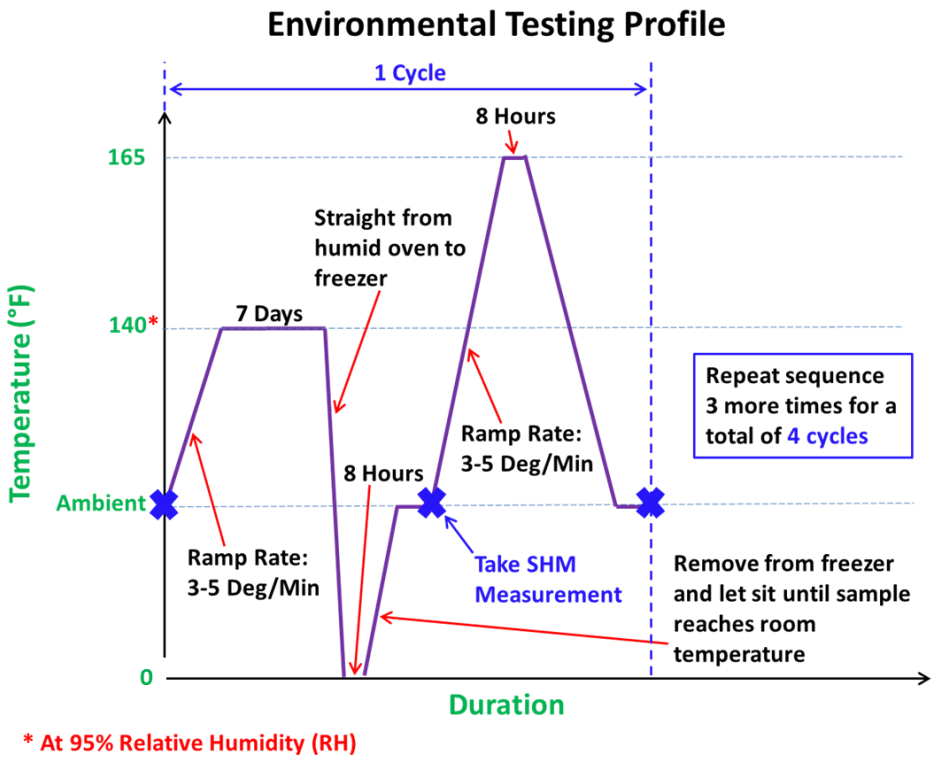

Figure 4-57. Description of Cyclic Environmental Extremes for SHM Durability Tests

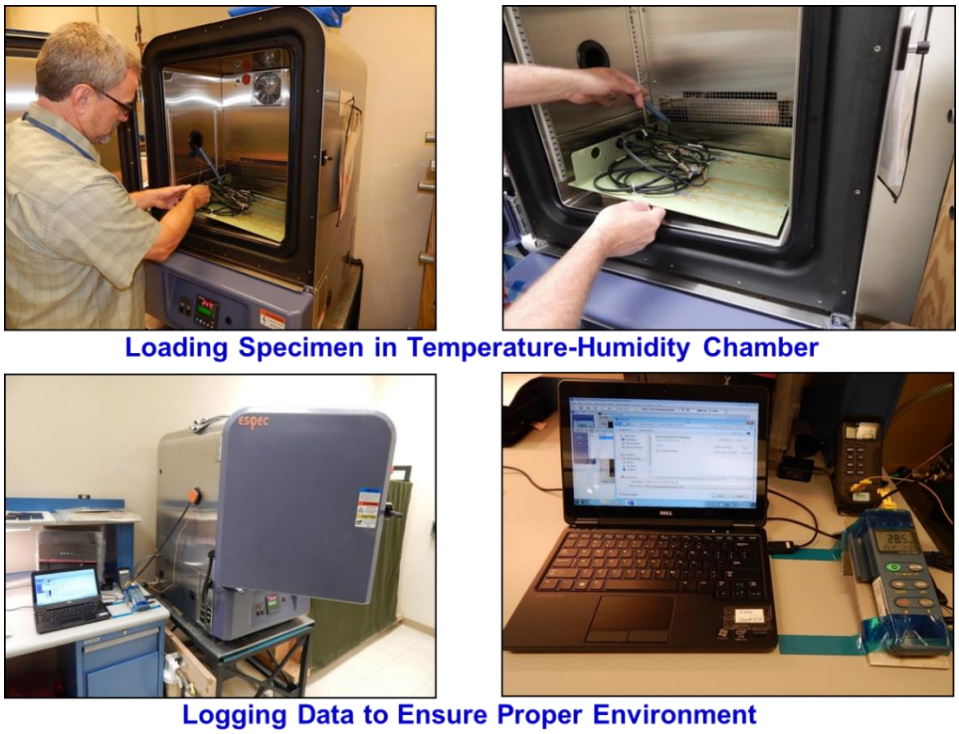

Figure 4-58. Set-Up of Durability Specimens in Environmental Test Chamber

4.6. SHM Performance Assessment Methodology

Quantifying the Reliability of SHM Systems – Oftentimes, users of any damage detection equipment, whether it is NDI or SHM devices, will want to determine the smallest flaw that can be detected with the equipment. When such devices are applied at their extreme, not all flaws of the same size will be detected. In fact, repeat inspections of the same flaw will not necessarily produce consistent hit or miss indications and different flaws of the same size may have different detection probabilities. Because of this uncertainty in the damage detection process, the capability of an NDI or SHM system is characterized in terms of the Probability of Detection (POD) as a function of the flaw size, *a*. The function *POD(a)* can be estimated through system reliability experiments on specimens containing flaws of known size. Statistical methods, such as those described in Sections 4.6.1, 4.6.2 and 4.6.3, must be used to estimate the parameters of the *POD(a)* function.

Considerations for an SHM POD Study - Some portions of the normal Probability of Detection (POD) methodology needed to quantify NDI performance can be adapted to the validation of SHM systems. However, it is important to recognize the unique validation and verification tasks that arise from distinct differences between SHM and NDI deployment and damage detection. SHM reliability calculations will depend greatly on the complexity of the structure and geometry of the damage profile. For example, corrosion damage has a widely-varying damage shape, both in the surface dimensions and in the changing depth. Contrast this with a fatigue crack that grows in a known propagation path such that the damage scenario can be described in a single parameter: crack length. In this latter case, the simplicity of such a one-dimensional entity allows for a more direct calculation of the reliability of the SHM system detecting such damage. Statistical performance assessments of damage detection sensors that are permanently mounted in a fixed position must be handled differently than similar studies using hand-held or other deployed NDI transducers that are moved along the structure being inspected. In the case of in-situ SHM sensors, the damage of interest originates, and may even propagate, into the region being monitored by the SHM sensor. Performance analyses then considers the response of the sensor or damage detection and correlates this response with the size of the damage when detected. For example, a crack in the material beneath or in the vicinity of an SHM sensor will allow for detection. The POD data could then consist of fatigue cracks that were propagated in various metal specimens with the direction of growth aligned with the mounted sensors.

Because of physical, time or cost constraints, it is often impractical to inspect an entire population. Instead, a small sample of the total population is tested and the data is used to gauge how well the entire population conforms to specifications. In traditional statistical process control, a significant number of data points are required in order to get a reasonably accurate estimate of process capability. This is because capability is usually calculated to cover a fixed multiple of standard deviations. But this percentage only holds true for larger sample sizes; that is, greater than 50. As the sample size decreases, there is greater uncertainty in knowing the true location of the mean and the true magnitude of the population variance. Therefore, the estimate of the range of values encompassing a given percentage of the population must necessarily increase to compensate. In order to maintain a reasonably accurate estimate of the capability of a process for smaller sample

sizes, it is necessary to adjust the number of multiple sample standard deviations used to define the region covering the desired proportion of the population distribution with a given confidence.

An SHM POD experiment for aerospace applications will generally consist of fixed sensors being placed on specimens which contain ultra-small starter-cracks. Then the cracks are grown in fatigue over time by applying cyclic mechanical loads to the plate. SHM signal data is taken periodically over time and related to the length of the crack at that time. Similarly, for pipeline applications, fixed sensors can be used to monitor a corrosion process where SHM signals are related to the amount of metal loss. The SHM-POD experiment should accurately simulate the actual SHM process. Again, it is important that the experiment capture relevant sources of variability. For example, the variability in cracks grown in the experiment should accurately represent the variability seen in actual cracks. The observational units in SHM POD studies will be crack/sensor combinations (where there may be an array of sensors in some applications).

In any SHM application, there will be an important consideration of how to map the SHM signal(s) into a detect/no-detect decision at each inspection opportunity (however inspection opportunity is defined), typically referred to as a damage index. The POD will then depend on the (joint) probability distribution of the inputs to that decision-making mechanism. Data from one or more SHM sensors may be mapped into one or more scalar damage indices that can be used for decision making, however, each damage index would produce separate individualized POD results. In this chapter, we will assume that the decision-making response is a scalar and that the crack length, which is known, adequately describes crack properties (i.e., truth data).

Factors Affecting Detection Sensitivity and Sources of Variability in SHM - To properly quantify POD, it is essential that all important sources of variability that could affect detection are explicitly captured. Omitting influential sources of variability in a POD study could result in overestimating the probability of detecting smaller cracks or underestimating the potential for false alarm indications.

Factors relating to damage and system properties that could affect SHM signals include:

1. Damage size, shape, and orientation (including changes in these characteristics over time). Note that this is typically the dominant source of variability in traditional NDE and it is expected that this will be true also for SHM applications.
2. Damage location relative to sensor location (including the distance between the sensor and the damage).
3. Environmental variables such as temperature and humidity.
4. Mechanical variables such as strain conditions (due to variable fuel loading, etc.).
5. Variability in sensor signal responses due to sensor-to-sensor manufacturing variability.
6. Change in the structural configuration where the sensors are located as a function of time and that could influence the SHM signal.
7. Changes in sensor performance over time due to maintenance repair, re-painting, etc.
8. Sensor aging and degradation.
9. Sensor, adhesive and other characteristics relating to installation-to-installation variability.

Then, for those factors that are not assumed to be held constant across inspections or compensated for by a calibration operation, it is essential that there be an accurate characterization of the joint

probability distribution. For example, in traditional NDE, the crack-to-crack variability arising from differences in crack morphology (different cracks with nominally the same size can have signal responses that vary) can be a source of variability and this is also expected be the case in SHM applications.

Many factors are involved in obtaining viable SHM data for POD calculations. Some of these factors depend on the SHM system itself and some depend on the type of testing, the complexity of the test article used in the assessment and the type, location, and orientation of damage being detected. Factors to be considered include, but are not limited to, determining the boundaries for the SHM system applications, producing validation tests that are representative of the actual structure, establishing proper damage detection thresholds, utilizing data with appropriate signal content compared to system noise, and data analyses methods.

Parameters to be Considered for Effect on Crack Detection - Statistical performance assessments of flaw detection sensors that are permanently mounted in a fixed position must be handled differently than similar studies using hand-held or other deployed NDI transducers that are moved along the structure being inspected. In the case of in-situ SHM sensors, the flaw of interest originates, and may even propagate, into the region being monitored by the SHM sensor. Performance analyses then considers the response of the sensor or flaw detection and correlates this response with the size of the flaw when detected.

Note: crack damage is usually repeatable, and many variables will not play a role in detection, depending on the sensor system. New variables come into play on a case-by-case basis. They must be properly controlled and uncoupled for proper performance assessments.

- SHM system side – 1) design and position of sensors relative to damage, 2) density/layout of network is applicable, 3) data analysis methods, 4) repeatability of sensor fabrication & associated response, 5) repeatability of sensor placement (assume conservative variations & assess), 6) repeatability of the sensor readout device (DAQ), 7) effects of environment (temperature, vibration, stress, chemicals) on sensor/hardware response, 8) selection of DI threshold for assigning detection (permanent, unloaded condition), 9) spatial resolution to properly capture changes associated with damage onset/growth, 10) statistics needed for sufficient data.
- Structural response side – 1) complexity of structure (layers, gaps, bushings, adjacent fasteners, hole size, nearby repairs), 2) damage onset mode & loads that generate the damage, 3) residual stress levels (crack closure), 4) stress reapportion with changing flaw profile, 5) repeatability of crack response/morphology (variations in the defect), 6) damage orientation, 7) presence of chemical by-products (e.g. aluminum oxide from corrosion), 8) presence of coatings, 8) simultaneous/multiple damage sites which could make it difficult or impossible to uncouple the SHM response for each individual damage occurrence (main affect is on testing which should include singular damage sites), 9) geometry of the monitored region (could produce signal reflections).

4.6.1. Calculating Probability of Crack Detection - Methods and Procedures for One-Sided Tolerance Interval

Use of Confidence Bounds to Calculate Specific POD Values – The Length at Detection (LaD) method for repeated inspections of cracks growing under or near fixed sensors provides a simple, statistically-valid method to compute POD for SHM applications [4.7]. This method, summarized in Figure 4-59, was originally suggested in Reference [4.8] and first applied to POD assessments of SHM systems in References [4.9 – 4.10]. This method uses only the crack-length values when cracks are first detected. Similar to other POD applications, the underlying statistical model is that there is a population of crack/sensor combinations and that the POD study is based on a sample of these crack/sensor combinations. Each crack has a length, random from crack to crack, at which the crack will be detected. Because only one observation is taken from each crack/sensor combination, the issue of dealing with the dependency of repeated measures data does not arise.

Because of the close relationship between confidence intervals for probability distribution quantiles and tail probabilities, the computation of the lower confidence bounds for POD in the LaD method, or upper bounds on the crack length associated with that POD, can also be done by using statistical methods for computing a one-sided tolerance bound, as described in Reference [4.10]. The computation of a one-sided 100(1-α)% tolerance bound to exceed at least 100p% of a normal population corresponds to the computation of a one-sided confidence bound for the 100pth percentile of the normal distribution. The one-sided tolerance bound is equal to the LaD value associated with the lower confidence limit of the POD curve at the 100pth percentile of interest. With these assumptions, there exists a distribution on the flaw lengths at which detection is first made. In this context, the probability of detection for a given flaw length is just the proportion of the flaws that have a detectable length less than that given length. That is, the reliability analysis becomes one of characterizing the distribution of damage lengths and the cumulative distribution function is analogous to a Probability of Detection (POD) curve.

In previous applications of this tolerance bound calculation, it has been termed a "One-Sided Tolerance Interval" (OSTI) because it estimates the upper bound, from the LaD distribution, which should contain 100p% of all the measurements in that LaD distribution with 100(1-α)% confidence. It should be noted that this approach evaluates the lower confidence limit of the POD curve at the single percentile value of interest. Since it is based on a sample of the entire population (*n* data points), the confidence is less than 100%. The tolerance bound calculation from a OSTI estimates the upper detection bound which should contain a certain percentage of all measurements in the population with a specified confidence, as described in Reference [4-11]. More specifically, the $a_{90/95}$ point (95% upper confidence bound on the crack size that will be detected with probability 0.90) can be obtained as an upper confidence bound on the 0.90 quantile of the LaD distribution and this is equivalent to a one-sided upper tolerance bound on the same distribution. Methods for computing this confidence (or tolerance) bound are given in Section 4.4 of Meeker, Hahn, and Escobar [4.12].

- **Interval to cover a specified proportion of a population distributed with a given confidence – related to measures of process capability**
- **One-sided Tolerance Interval – estimates the upper bound which should contain a certain percentage of all measurements in the population with a specified confidence**
- **Since it is based on a sample of the entire population (n data points), confidence is less than 100%. Thus, it includes two proportions:**
  - **Percent coverage (90%)**
  - **Degree of confidence (95%)**
- **The reliability analysis becomes one of characterizing the distribution of flaw lengths and the cumulative distribution function is analogous to a Probability of Detection (POD) curve:**

$$TI = X \pm (K_{n,\gamma,\alpha})(S) \qquad \text{[log scale calculation]}$$

- **Interested in a 1-tailed interval (utilize "+" in equation); upper limit of TI. Uncertainty in knowing the true mean and population variance requires that the estimate of the range of values encompassing a given percentage of the population must increase to compensate.**

Figure 4-59. Description of Confidence Bounds and Use of One-Sided Tolerance Interval to Determine POD for Sensor Systems in Fixed Locations

The Probability of Detection for a fixed sensor detecting a crack which is propagating in a known direction in the vicinity of the sensor can be determined using the One-Sided Tolerance Interval (OSTI) approach. The OSTI estimates the upper bound which should contain a certain percentage of all measurements in the population with a specified confidence. Since it is based on a sample of the entire population (n data points), the confidence is less than 100%. Thus, the OSTI is greatly affected by two proportions: 1) the percent coverage which is the percent of the population that falls within the specified range (normally chosen as 90%), and 2) the degree of confidence desired (normally chosen as 95%). A demonstration of this OSTI calculation specifically for SHM system response is provided in References [4.13, 4.14].

Assuming that the distribution of damage is such that the logarithm of the lengths has a Gaussian distribution, it is possible to calculate a one-sided tolerance bound for various percentile flaw sizes. To do this, it is necessary to find factors $K_{n,\gamma,\alpha}$ to determine the probability γ such that at least a proportion $(1-\alpha)$ of the distribution will be less than $X - K_{n,\gamma,\alpha}$ where X and S are estimators of the mean and the standard deviation computed from a random sample of size n. There may also be situations where the process capability is measured relative to a single-sided limit. These situations arise when a product characteristic need only meet a minimum specification limit or remain below a maximum specification limit. In this case, the desired POD value is the maximum crack length associated with the 90% POD level so an upper bound tolerance interval can be used. From the reliability analysis a cumulative distribution function is produced to provide the maximum likelihood estimation (POD). So, the tolerance interval, which represents the actual POD value for the damage of interest, can be derived from Equation 4.1:

$$T_{POD(90,\,95)} = X + (K_{n,\gamma,\alpha})(S) \qquad (4.1)$$

T = Upper tolerance bound for crack length corresponding to 90% POD with a 95% confidence
X = Mean of detection lengths
K = Tolerance factor (~ function of sample size, detection level desired and confidence level desired)
S = Standard deviation of detection lengths
n = Sample size
1- α = Detection level
ɣ = Confidence level

Using Equation 4.1, it is possible to quantify the 90% POD level (e.g. crack length) for a sensor with a desired confidence level. The value for *T* is related to the number of samples tested and the range in detection levels observed. Thus, the performance is penalized – and the resulting POD increases - if the results are obtained with only a few samples and/or if there is a high degree of variability in the results. As the number of data points increases, the K value will decrease and the POD numbers could also decrease if the mean and standard deviation remain consistent. K can be calculated as follows:

$$\boldsymbol{K = t_{n-1,\gamma}\left(\sqrt{n}\,\Phi^{-1}_{norm}(\alpha)\right)/\sqrt{n}} \tag{4.2}$$

Where,
t = non-central t-distribution with degrees of freedom n-1 and γ
Φ^{-1} = inverse CDF of a standard normal (gaussian) distribution
α = percent coverage or detection level

The data captured is that of the flaw length at the time for which the SHM sensor provided sustainable detection. R function normQuantileCI in R package StatInt is available to do the needed computation. Tables of the probability factor, K, needed to compute such tolerance bounds are also available in References [4.12, 4.15 – 4.16], and some engineering statistics textbooks. Corresponding estimation and confidence bound and confidence interval methods for the other location-scale and log-location-scale distributions are described and illustrated in Chapter 14 of Reference [4.12].

Data conditions necessary for a POD assessment using this approach are that the distribution of flaws is such that the logarithm of the lengths (strictly positive sizes) has a Gaussian distribution (log-normal distribution). The data should plot linearly on a semi-log scale (or the log values plot in a linear fashion on a linear scale) and the data should be clustered near the 50th percentile. Data conditions necessary for a POD assessment using this approach are that the distribution of flaws is such that the logarithm of the lengths (strictly positive sizes) has a Gaussian distribution (log-normal distribution). The assumption of normality can also be tested by applying the Anderson-Darling test. The Anderson-Darling test yields a P-value that can be compared to the chosen significance level to determine whether or not the assumption of normality should be rejected. The significance level, ψ, is chosen to be 0.05. Any value of P less than $\psi = 0.05$ indicates that there is sufficient evidence to reject the assumption of normality. An A-D calculation that determines a P value that is greater than 0.05 supports the assumption of a Gaussian data distribution. A normal probability plot can be created using statistical software such as Minitab®. Figure 4-60 shows two plots of sample SHM sensor crack detection data which indicates that a log-normal distribution is

a correct assumption. In addition, the Anderson-Darling test returns the required value of P > 0.05. It shuld be noted that Kolmogorov-Smirnov or Cramer-Von Mises tests can also be used to check the normality assumption.

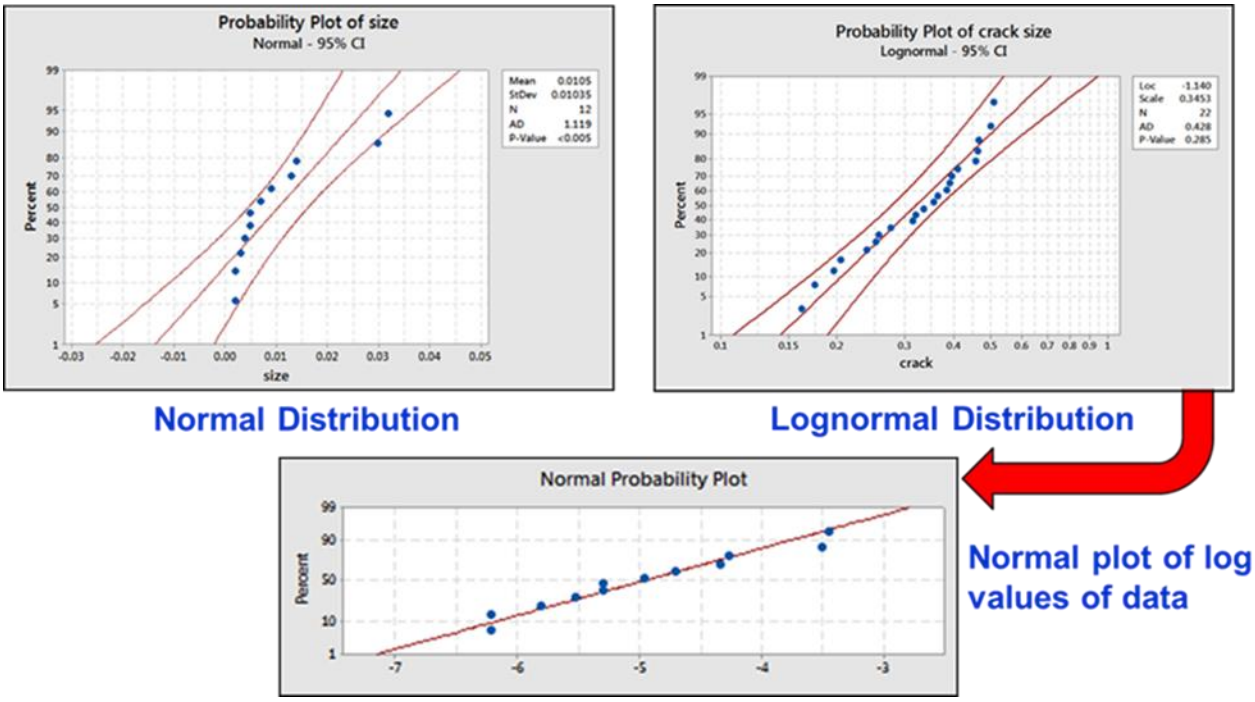

Figure 4-60. Sample Plot of SHM Data Indicating a Gaussian Distribution of Data

The discussion above shows how it is possible to calculate a one sided tolerance bound for various percentile flaw sizes - find factors $K_{n,\gamma,\alpha}$ to determine the confidence ɣ such that at least a proportion (α) of the distribution will be less than $X + (K_{n,\gamma,\alpha})S$ where X and S are estimators of the mean and the standard deviation computed from a random sample of size n. The reliability analysis becomes one of characterizing the distribution of flaw lengths and the cumulative distribution function is analogous to a Probability of Detection (POD) curve. A two-sided tolerance interval, used to indicate values at which certain compliance is met, is shown in Figure 4-61. In this case, the POD corresponds to a 1-tailed interval (utilize "+" equation 4.1) or the upper limit of tolerance interval. The uncertainty in knowing the true mean and population variance requires that the estimate of the range of values encompassing a given percentage of the population must increase to compensate. The capability of the process is determined not only by the location of the sample mean but also by the tail areas of the distribution. Recommended sampling includes the use of at least 8 data points to calculate $\boldsymbol{T}_{\mathbf{POD(90,95)}}$ to gage an entire population from a small sampling. In the case of the subject CVM and PZT testing, convergence of the POD values and the needed performance levels were used to determine the number of data points to include in the POD calculations.

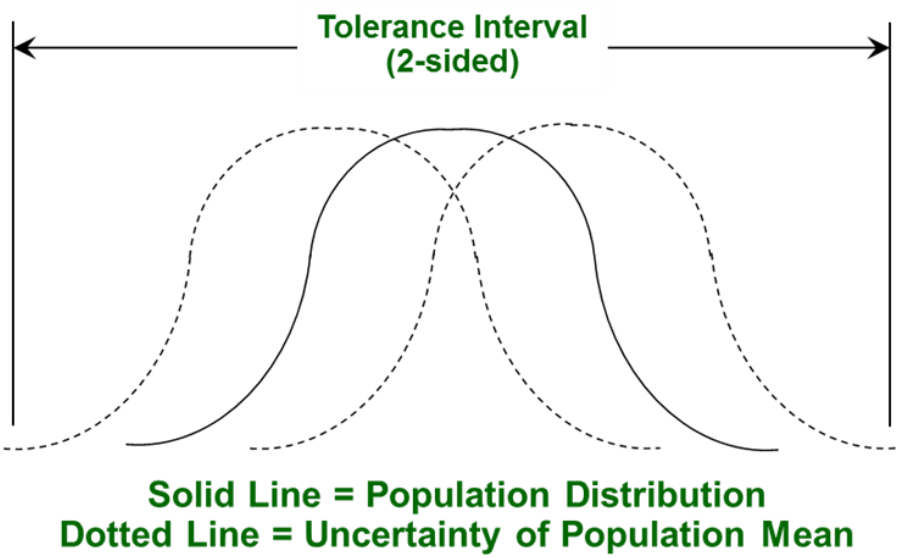

Figure 4-61. Two-Sided Tolerance Interval where the Upper Confidence Bound is Used to Describe the POD Level

Setting Appropriate Thresholds for Crack Detection – For the CVM technology, the key parameter, or Damage Index, for determining crack detection is the dCVM level measured by the PM200 device (see also Section 2.2). Preliminary testing is conducted to acquire dCVM values at different measured crack lengths for validation trending. The crack length "a" is the independent variable. So, system response tests are conducted initially to determine the all-important threshold for assigning "official crack detection." For the CVM testing, the $DI_{(threshold)} = dCVM_{(detection)} = 4.0$ was selected. This will be discussed in detail in Chapter 5. Normally the threshold level is set to provide Signal-to-Noise levels of 3 or greater (as per normal NDI rules-of-thumb) without sacrificing the sensitivity of the system or, conversely, inducing any false calls. Towards that end, the preliminary testing is used to identify any possible signal deviations during crack growth that might induce false calls and then set a threshold to stay above those levels. This has never been an issue with CVM sensors as the sensor dCVM/da plots have always been quadratically increasing plots (no up-down deviations). During the initial tests, dCVM values were acquired as the crack increased in length so that it was possible to assess where to set the threshold. The plots in Figure 4-62 show some sample data where one can place a horizontal line to determine viability of a crack detection threshold. For this data, a dCVM value = 4 was conservatively chosen as the threshold. This produced S/N ratios of 10 to over 100. For CVM sensors, and most SHM sensors in general, the chosen DI threshold will change for different applications depending on the sensor design (e.g. number of galleries and associated volume), the length of the small tubes (associated volume), component geometry and the structural response (material, crack opening, residual strains). So, the initial response tests are essential to properly setting damage detection thresholds.

For the PZT technology, a Damage Index parameter is also used to determine crack detection. These DI values are calculated within the Scan Genie software (see also Section 2.3). In a similar fashion as the CVM testing, a series of SHM system response tests were conducted to properly set the DI threshold for assigning "official crack detection." For the PZT tests, the $DI_{(threshold)} = 0.05$

was selected. This will be discussed in detail in Chapter 6. In some tests on SHM sensors, some signal reversals in DI values have been observed during early portions of the crack growth. So, in such cases, the crack detection levels (DI threshold) are set at higher DI values to avoid this gray area. As the crack continues to grow, SHM responses (DI values) tend to rapidly and continuously increase so the safe level to set DI thresholds is normally quite evident.

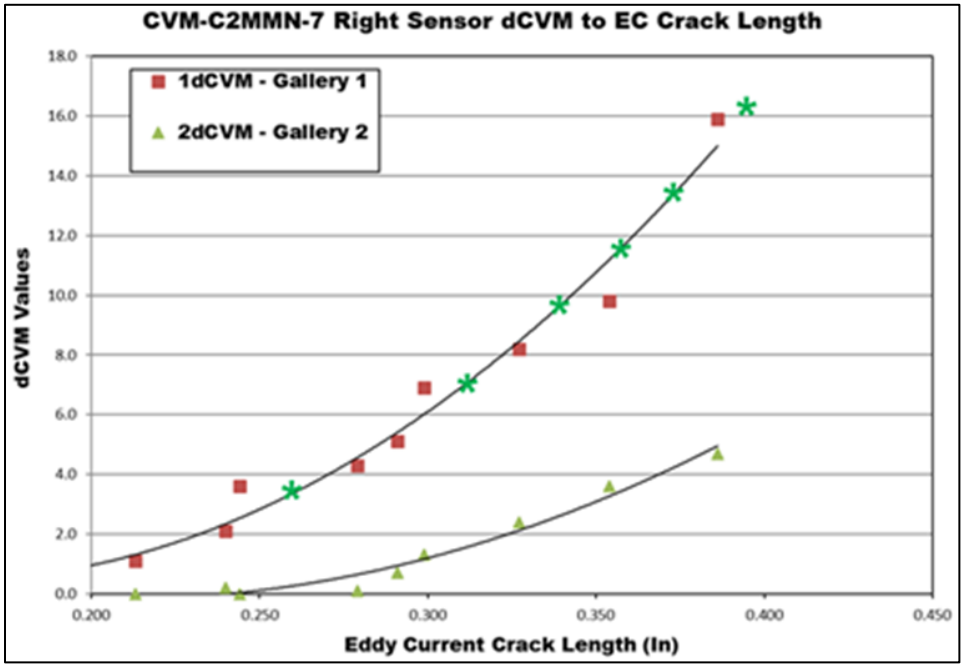

Figure 4-62. Response Relating dCVM Values to Fatigue Crack Length – Used to Establish Proper Threshold to Use for Crack Detection

The process of using thresholds to determine whether or not your inspection has detected damage is also part of the normal deployment of NDI equipment. Figure 4-63 and Figure 4-64 show several A-scan plots of data obtained from traditional pulse-echo ultrasonic inspections of different structures. In Figure 4-63, signal variations created by bondline defects or interlayer defects are highlighted and compared to signals obtained from pristine regions of the structure. Such deviations from normal signals are used to infer the presence of damage. These signal deviations must be significant enough to avoid false calls.

The graphic at the top of Figure 4-64 shows a drastic change in an ultrasonic signal where the back wall peak completely disappears due the presence of severe damage between the front and back wall. This can be contrasted with the lower signal trace in Figure 4-64 where there is only a slight reduction in the back wall peak (signal does not even drop below 40% of full screen height) due to either the small size and/or slighter severity of damage in the part. Thus, proper selection of damage thresholds – which are dependent on many factors – is crucial in the use of conventional NDI as well.

One final example of the use of conventional NDI for detecting cracks is shown in the eddy current (EC) signals in Figure 4-65. The sample signals show the use of baseline (unflawed signals) and

also highlight the possible variations in EC signals that are caused by factors other than the presence of damage, such as joint conductivity. On a case-by-case-basis, such signal variations must be considered when determining equipment settings for inspections and for identifying clear damage in the structure. Similarly, variations in SHM signals from a range of undamaged components being monitored, must be considered when setting the $DI_{(threshold)}$ corresponding to damage detection.

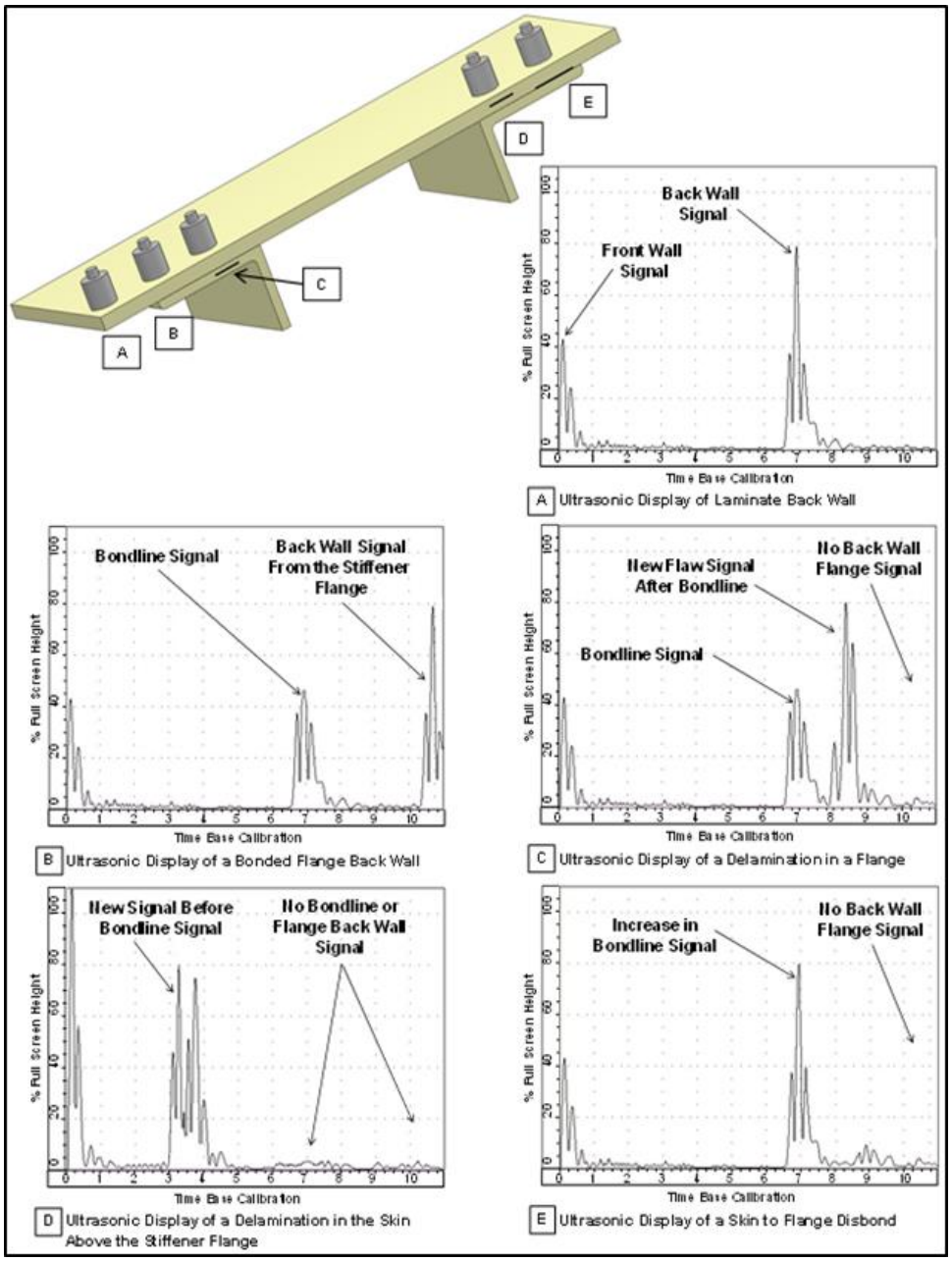

Figure 4-63. Delamination Indications at Different Structure Thicknesses for Secondarily Bonded Substructures

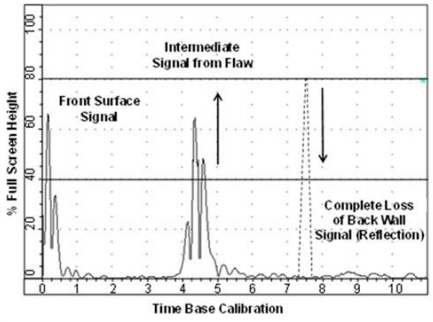

Intermediate Peak and Reduction of
Back Wall Signal Indicating a Flaw

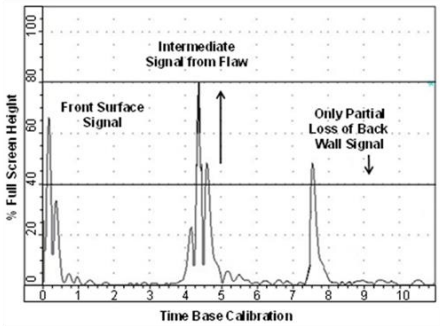

Intermediate Peak with Only a Partial Reduction in
Back Wall Signal that May Indicate a Small Flaw

Figure 4-64. Plots from PE-UT Inspections Showing the Use of Thresholds to Ascertain Damage Detection

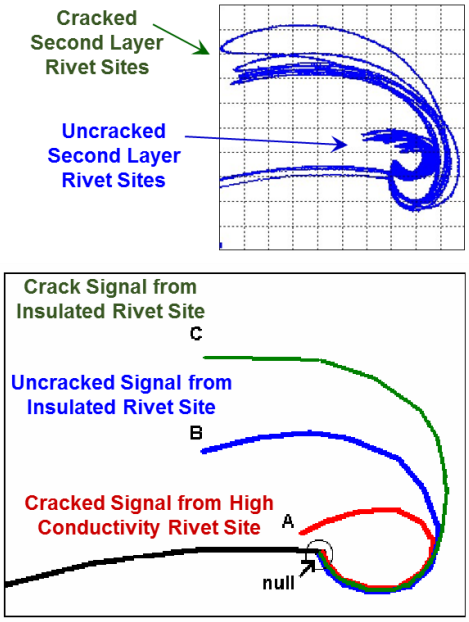

Figure 4-65. Variations in Eddy Current Signals Due to Presence of Damage or Other Conductivity Variations in the Structure

Sample Application of OSTI to POD Study Based on Comparative Vacuum Monitoring (CVM) Sensors - Comparative Vacuum Monitoring (CVM) sensors provide a method to detect cracks in structures when the sensors are adhered to the structure under test. When a crack develops, it forms a leakage path between the atmospheric and vacuum galleries, producing a measurable change in the vacuum level. This change is detected by the CVM monitoring system. In the sample performance tests discussed here, a CVM sensor was mounted adjacent to a 5mm edge notch on a series of 600 x 40 X 2mm Al-Li coupons as shown in Figure 4-66. The CVM sensor used a 20mm L crack intercept region with two 0.32mm W sensing galleries to produce the crack detection response. Each test specimen was subjected to tension-tension cyclic loading to initiate and grow natural fatigue cracks. Vacuum levels (Damage Index = dCVM level) were measured every 1,000 cycles and a calibration exercise was used to determine the dCVM value corresponding to sensor crack detection. Figure 4-67 shows plots of the CVM data from the subject test series that reveals that the Damage Index, or dCVM value, increases exponentially in crack length.

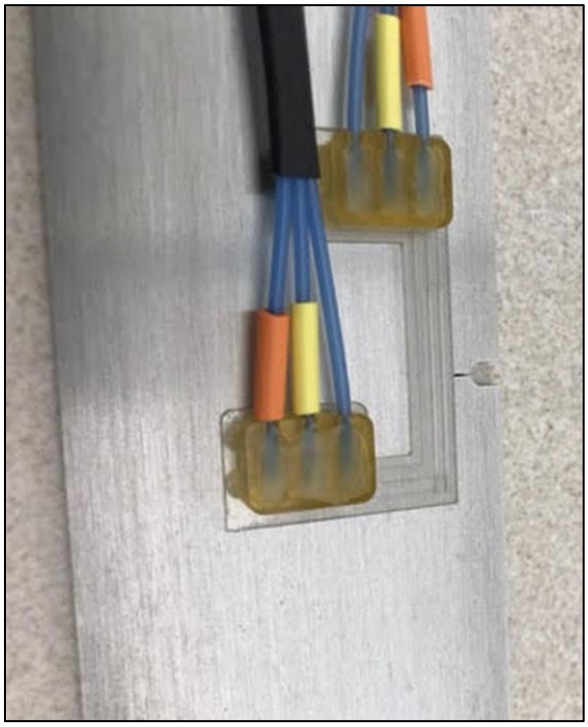

Figure 4-66. CVM Sensor Being Tested on Al-Li Coupon

The crack detection threshold of 1.5 is superimposed on the response data in Figure 4-67 to demonstrate how detection and corresponding crack length are achieved. Table 4-3 summarizes the results from the CVM performance testing described above for one specimen. It shows the changing damage detection parameter (dCVM) as the crack grows along with a highlighted level when the dCVM value exceeds the established threshold of dCVM = 1.5 for crack detection. For the example shown of Specimen 6, the crack length at CVM sensor detection is 0.08".

Table 4-4 shows the set of data from all test specimens where only the crack lengths at CVM detection are listed. That is, the crack length listed corresponding to the dCVM value that exceeded the chosen threshold (i.e. crack detection). Since the OSTI calculation is performed in the log domain, the log values are also listed in this table. These crack lengths, which are the actual values measured during testing and not an extrapolated value down to the exact threshold level, were input in the OSTI calculation equation (4.1). The value for the tolerance factor, K, is a function of sample size, detection level desired and confidence level desired. For the data shown, the number of data points is 11, the desired POD level is 90% and the desired confidence level is 95%. The methods described above can be used to determine this K value. The resulting $POD_{(90/95)}$ = 3.35 mm (0.132"). The tabulated detection values listed in Table 4-4 indicate an average crack detection value of 1.85 mm (0.073") with a standard deviation of 0.47 mm (0.018"), however, as a rough comparison, the statistical POD calculation produces a higher value due to the limited number of data points and the standard deviation in those data points [4.17 – 4.18].

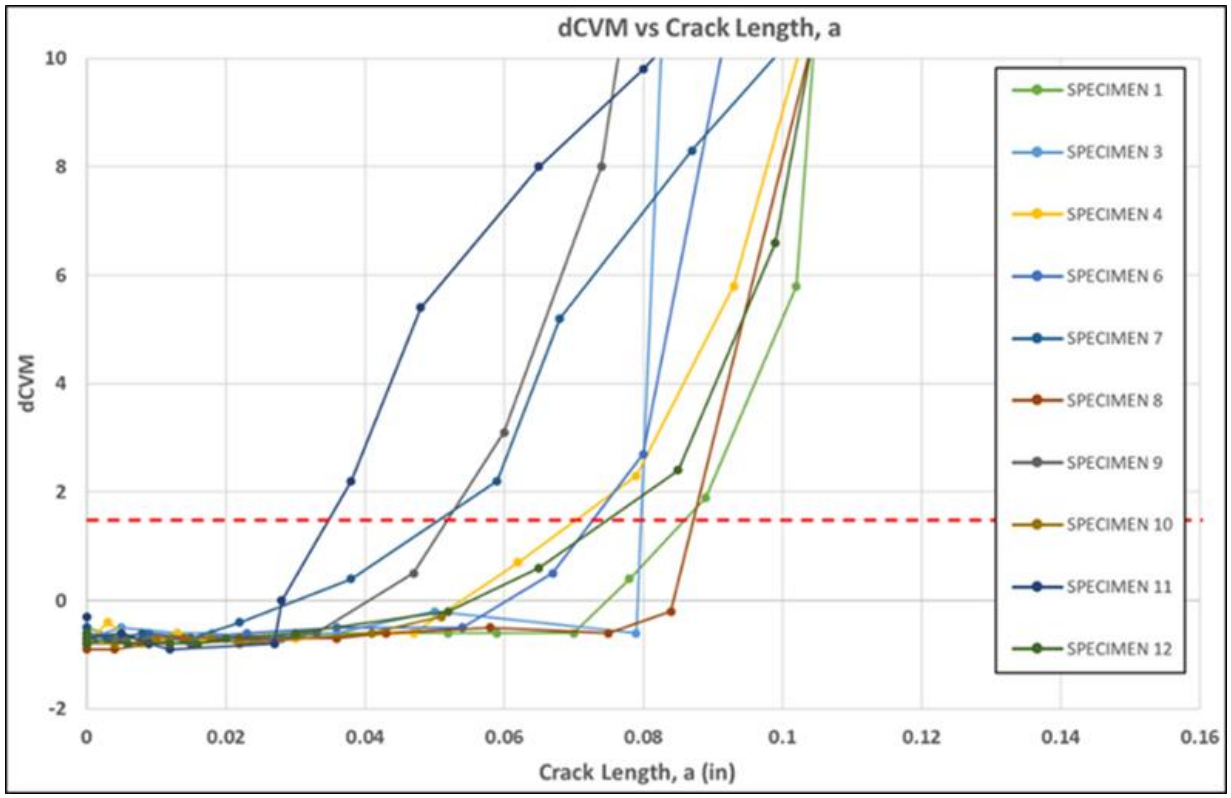

Figure 4-67. Responses from Series of CVM Sensors (dCVM) Monitoring Specimen Crack Growth During Fatigue Tests

Table 4-3. CVM Crack Detection Using Established Damage Threshold

SPECIMEN 6		
Cycles	Crack Length	Gallery 1 dCVM
0	0	-0.7
1000	0	-0.7
2000	0	-0.7
3000	0	-0.7
4000	0	-0.6
5000	0.003	-0.7
6000	0.009	-0.6
7000	0.015	-0.7
8000	0.023	-0.6
9500	0.036	-0.5
11000	0.054	-0.5
12500	0.067	0.5
14000	0.08	2.7
15500	0.093	11.2
17000	0.102	25.9
18500	0.12	72
19500	0.148	169.6

Table 4-4. Summary of CVM Crack Detection Levels for Each Al-Li Test Specimen

Specimen	Damage Index (dCVM) Level	Crack Length at CVM Detection a (in)	Log of Crack Length at CVM Detection a (in)
1	1.9	0.089	-1.051
2	1.7	0.061	-1.215
3	25.0	0.090	-1.046
4	2.3	0.079	-1.102
5	1.6	0.059	-1.229
6	2.7	0.080	-1.097
7	2.2	0.059	-1.229
8	6.5	0.100	-1.000
9	3.1	0.060	-1.222
11	2.2	0.038	-1.420
12	2.4	0.085	-1.071

4.6.2. *Calculating Probability of Crack Detection - Methods and Procedures for the Hit-Miss Log Regression Method (Mil-HDBK-1823)*

The Hit-Miss POD analysis method requires the use of approximately 50 independent data points from 50 different crack sites. In order to create a comparison that relates the POD calculated from the OSTI method to traditional POD assessments, the data from the POD testing described above was applied in a Hit-Miss POD analysis. Some extrapolation of the CVM and PZT crack detection data was necessary to produce sufficient data using only ~ 20 independent crack detection tests. Repeated measures data are used in these calculations which do not account for possible crack-to-crack variations that may exist in different specimens. Since this data involves an assumption that is not statistically valid, it must be stressed that the exercise of conducting the Hit-Miss POD calculations is for illustrative purposes only and not for any certification of SHM performance. The extrapolated data is merely used here to produce simple comparisons with the POD methodology used in Mil-Hnbk-1823. This approach will also be highlighted in the results sections of this report so that these comparisons are presented in the proper light.

Traditional methods for calculating POD values from NDI tests are described in Reference [4.19]. One of these methods is called the Hit-Miss or Log-Regression analysis. In this model, the *POD(a)* function is defined as the proportion of all cracks of size *a* that will be detected in a particular application of an SHM or NDI system. Analysis of data from reliability testing indicates that the *POD(a)* function can be reasonably modeled using the log normal distribution function or a Log Regression analysis. Thus, if the SHM system can produce output (detection) that can be reduced to a binary response, a Log-Regression (*hit/miss)* analysis can be used [4.19]. The conditional probability of a randomly selected crack population having detection probability of p and being detected at the inspection is given by $p\, f_a(p)$. The unconditional probability of a randomly selected crack from the population being detected is the sum of the conditional probabilities over the range of p, that is:

$$\text{POD(a)} = \int_0^1 p\, f_a(p) dp \tag{4.3}$$

The Log Regression *Hit/Miss* POD model is used to analyze binary (detect/no detect) data using the following underlying mathematical relationship between POD and crack size:

$$\text{POD(a)} = \frac{\exp[\alpha + \beta[ln(a)]}{1 + \exp[\alpha + \beta[ln(a)]} \tag{4.4}$$

A brief overview of the Hit-Miss method follows:

- Early attempts to quantify probability of detection, POD, considered the number, n, of cracks detected, divided by the total number, N, of cracks inspected, to be a reasonable assessment of system inspection capability, POD = n/N. This resulted in a single number for the entire range of crack sizes. Grouping specimens this way improved the resolution in crack size, but the resolution in POD suffers because there were fewer specimens in each range and many factors influence the probability of detecting any one given flaw.

- If the SHM system can produce output (detection) that can be reduced to a binary response, a *hit/miss* analysis can be used (*Hit/Miss* POD model).
- A perfect inspection produces a step function, as shown in Figure 4-68, with POD = 1 for $a > a_{crit}$ and POD = 0 when $a < a_{crit}$. It is *not* a POD(a) = constant = 1 because an inspection that finds everything is useless since it cannot discriminate between an actual crack and a benign microstructural artifact, an edge, or a surface blemish.

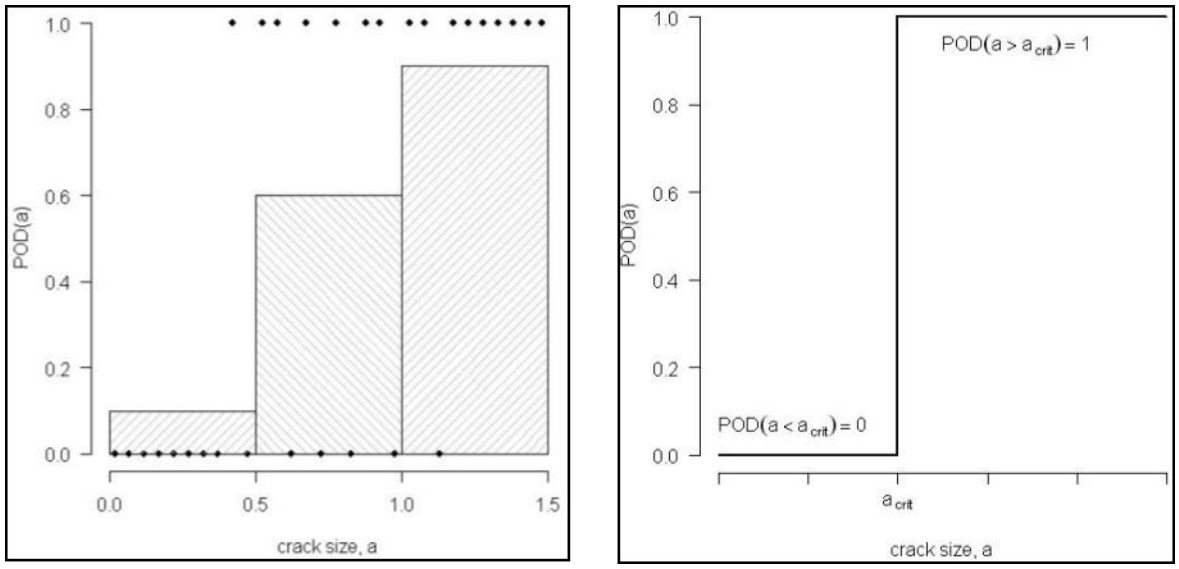

Figure 4-68. Comparison of Initial Simple POD (n/N) with a Step Function from a Perfect Inspection

- An efficient use of the binary (*hit/miss*) data is to produce an underlying mathematical relationship between POD and size.
- Logistic Regression ***Hit/Miss* POD model** is used to analyze binary (detect/no detect) data:

$$ln[POD(a)/(1-POD(a))] = \alpha + \beta[ln(a)] \quad (4.5)$$

Where,

a = crack length

α and β are estimated by maximum likelihood estimates.

- Assumption is that there is no variation in equipment or procedures.
- Assumption is that all critical factors are controlled in the testing so there is no need for additional φ function to describe other factors on the RHS of the log regression formula.
- Each flaw is either detected or not detected so the best estimate for POD(a) is either 0 or 1. A range of flaw sizes are used to determine the α and β that maximize the likelihood of the particular sequence of 0's (misses) and 1's (detects) that were observed. Figure 4-69 shows a typical POD curve determined by the Hit-Miss analysis.

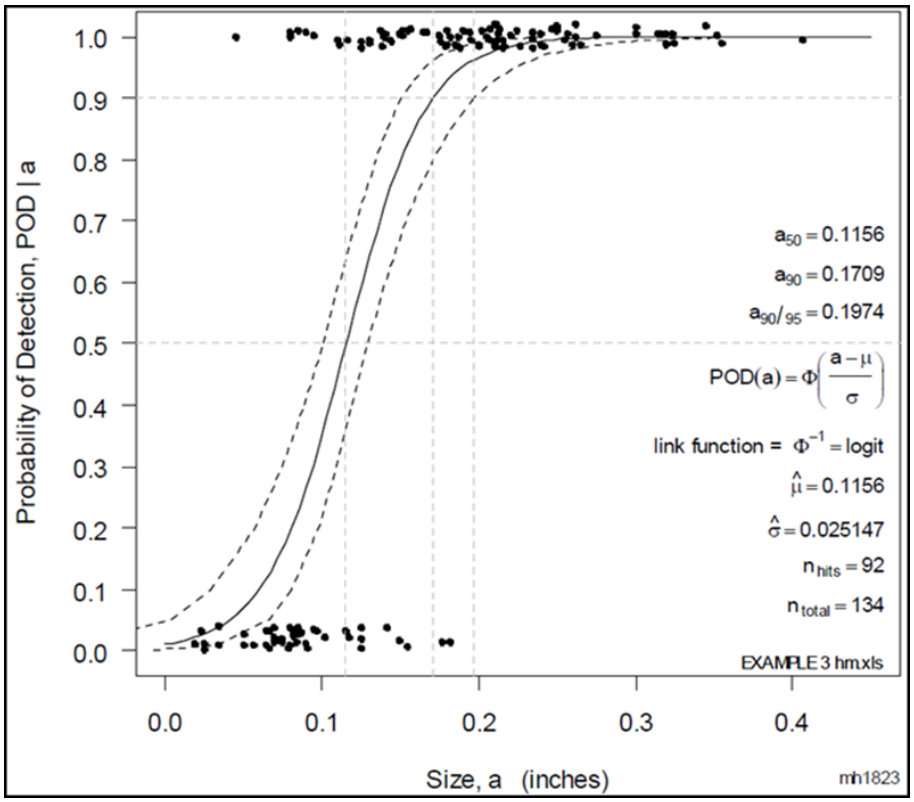

Figure 4-69. Construction of POD Curve from Hit (1) and-Miss (0) Inspection Data

Damage Detection with SHM Signals – The important aspect of SHM damage detection relates to determining how the SHM signal gets translated into flaw detection. From a simple sensor standpoint, SHM is very analogous to NDI where the set of signals represent first a baseline, corresponding to a pristine structure, and later a deviation from the baseline, possibly corresponding to a damaged structure. This deviation is used to infer the presence of a flaw. Depending on the equipment and the type of inspection being conducted, the guidance on how to delineate a flaw may differ but it is normally rooted in some desired signal-to-noise ratio which has been determined to produce the best POD while minimizing false calls. Some transducer/sensor signals may provide a more direct measure of damage (e.g. abnormal reflection peak that is absent in a pristine part) and some may be secondary and require extensive calibration (e.g. change in strain level created by nearby damage). These are more sensitivity issues which affect POD assessments but still follow the process of using deviations in signal signatures to identify flaws. Similarly, Damage Indices or other parameters based on the sum total of signals received may aid sensitivity but should not change the process for quantifying performance. Quantifying SHM performance using the Log Regression Method only requires that the signal deviation can be reduced to produce a simple detection (hit) or no-detection (miss). Thus, the mapping of SHM signals to flaw detection is key. It is possible to lower damage detection threshold in both NDI and SHM in order to improve POD, possibly at the expense of increasing false calls. However, the normal rule of thumb is that it is best to maintain a signal-to-noise ratio

of at least 3 to avoid misinterpretation of data that may stem from normal (undamaged) deviations in the structural response or SHM signals.

With the above hit-miss data description in mind, it is important to highlight a few differences in how this final, binary data is produced. For example, when deploying scanning NDI methods (e.g. pulse-echo ultrasonics on an X-Y motion gantry), it is possible to set gates during data acquisition based on the amplitude and/or time-of-flight information where the presence or absence or change in signals creates a variation in the resulting color-coded image. Such changes are used to identify a flaw. This is similar to an SHM threshold. However, in the case of NDI, it is possible for the inspector to revisit the potential damage location (or the data corresponding to the potential damage location) and conduct additional evaluations to further convince himself that damage is actually present. Even hand-held NDI deployment allows for multiple passes of the NDI transducer around the same area in question and each time may involve transducer motion from a slightly different direction. This type of human feedback loop is missing in SHM as SHM methods utilize automated data acquisition and analysis to arrive at a final hit-miss assessment. This highlights the fixed nature of SHM deployment where a well-designed SHM sensor network aims to properly model these different paths to adequately capture the necessary signal variations for analysis. So, the success in applying the Log Regression Method lies in the ability of the SHM system to produce acceptable binary data. Thus, the POD testing must accommodate all of the key variations within the set of POD specimens using statistical distribution. Such variations include flaw type, size, orientation, depth and location within the sensor coverage area.

Comparison of OSTI with Hit-Miss POD Analysis - As mentioned above, the Hit-Miss requires the use of approximately 50 independent data points from 50 different crack sites. In order to create a comparison that relates the POD calculated from the OSTI method to traditional POD assessments, the data from the POD testing described above was applied in a Hit-Miss POD analysis. Some extrapolation of the CVM and PZT crack detection data was necessary to produce sufficient data from the reduced-order, independent crack detection tests. A Gaussian distribution of hit-miss data was compiled using crack CVM detection length from each test augmented by assumed, missed crack detections below the actual CVM detection level and assumed, hit crack detections at lengths above the actual CVM detection level. Thus, it must be stressed that the exercise of conducting the Hit-Miss POD calculations is carried out here for simple comparisons to the methodology used in Mil-Hnbk-1823. Following is a description on the use of this resulting data set in the Hit-Miss POD assessments:

- Normal NDI POD values are calculated using only independent data points. This includes an independent distribution of seeded cracks where unique signals at detection are logged (one reading on each target), the test series accounts for operator-to-operator (sensor-to-sensor) variability, and the array of specimens is sufficiently large to account for crack-to-crack variability.
- Log-Regression (hit-miss) Model – For the SHM data, there were approximately 20 independent tests (cracks). In the case of the CVM data, the corresponding 65 hit-miss data points were acquired from these 20 tests and thus, not all independent. Additional extrapolated data at extremes (very small & very large cracks) were used to populate a complete POD curve.
- In the Hit-Miss assessment conducted with the limited SHM response data, the calculations are carried out with the assumption that each data point is independent and is produced by

a separate crack (separate specimen). This is not the case because the Hit-Miss analysis presented here took credit for the additional, extrapolated data as if it were independent data points (Mil-HDBK-1823 calculation).

  - If the sensors, their location, the cracks, and the sensor response is consistent enough that the assumed data is representative (additional tests produced independent data that is equivalent to the repeated measures assumed data), then the resulting "hit-miss" calculations are close to the truth.
  - If the actual responses – should many additional tests be conducted – lack consistency (deviate significantly from the assumed response), then the Hit-Miss calculations will have a much larger deviation from the truth.
  - Results obtained in the significant test set from multiple years of CVM performance testing [4.10 – 4.14, 4.17 – 4.18] gives us confidence in the extrapolations listed here and used in the "hit-miss" calculations. The assumption of consistent, additional data, based on the existing set of 20 data points, is a justified assumption but only for comparison purposes.

- Repeated measures data (multiple data points from a single crack profile and SHM response) are used in these calculations; this is an assumption that is not statistically valid. It does not account for possible crack-to-crack variations from different specimens.
- However, these results are for illustrative purposes only and not for any certification of performance. The results calculated from this hit-miss analysis are for general comparisons only.
- *Certification results are to be taken only from the OSTI method already presented above*.

4.6.3. Calculating Probability of Crack Detection - Methods and Procedures for the â vs a POD Model (Mil-HDBK-1823)

The â vs a POD analysis method requires the use of approximately 30 independent data points from 30 different crack sites. In order to create a comparison that relates the POD calculated from the OSTI method to traditional POD assessments, the data from the POD testing described above was applied in a â vs a POD analysis. Some extrapolation of the CVM and PZT crack detection data was necessary to produce sufficient data using only ~ 20 independent crack detection tests. Repeated measures data are used in these calculations which do not account for possible crack-to-crack variations that may exist in different specimens. Since this data involves an assumption that is not statistically valid, it must be stressed that the exercise of conducting the â vs a POD calculations is for illustrative purposes only and not for any certification of SHM performance. The extrapolated data is merely used here to produce simple comparisons with the POD methodology used in Mil-Hnbk-1823. This approach will also be highlighted in the results sections of this report so that these comparisons are presented in the proper light.

When the crack or other flaw decision is made on the basis of a recorded response, â, to the inspection stimulus, the data are known as *â* vs *a* inspection results and a different POD(a) analysis is available [4.20]. A general example of â versus a data from a capability demonstration is presented in Figure 4-70 while Figure 4-62, from the damage threshold discussion above, shows a specific *â* vs *a* example for the SHM performance program described in this report. It shows the

CVM system response (dCVM values) as a function of the damage parameter (crack length). When the inspection response is greater than a pre-set detection threshold, a crack is indicated for the site. In a capability demonstration, the minimum signal threshold is set as low as possible with respect to noise. Detection thresholds are set to yield a desired $a_{(90/95)}$ value with an acceptable rate of false call indications. False calls are crack indications at sites with no known cracks. These can be the result of noise or large responses from insignificant cracks. However, they can also result from anomalies that do not impair structural integrity.

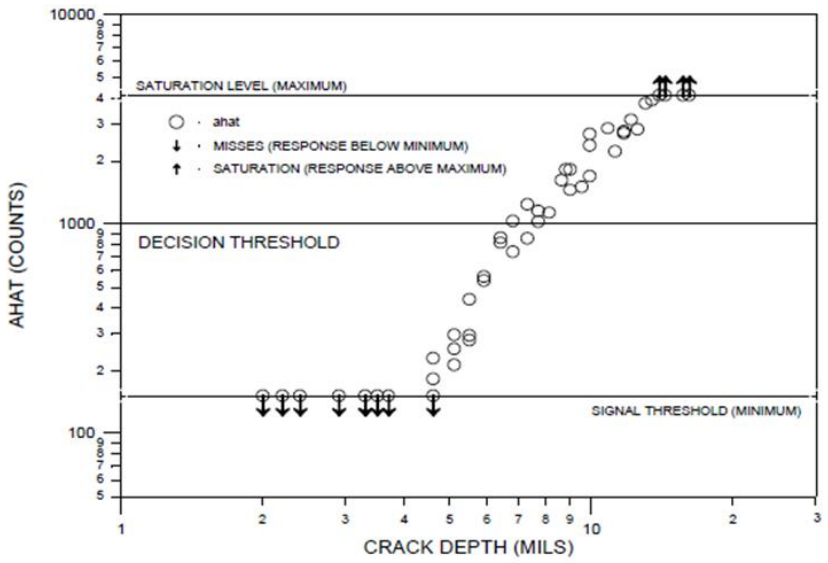

Figure 4-70. Sample *â vs a Data Showing a Damage Detection (Decision) Threshold*

â vs. a Probability of Detection Model - The recorded signal response, *â*, provides more information for analysis than a simple crack or no crack decision of a hit/miss inspection response. The *â* vs *a* POD model is derived from the correlation of the *â* versus a data and the assumptions concerning the POD(a) model can be tested using the signal response data. Further, the pattern of *â* responses can indicate an acceptable range of extrapolation for assessing performance. Therefore, the range of crack sizes in the experiment is not as critical in an *â* vs *a* analysis as in a hit/miss analysis. For example, if the decision threshold in Figure 4-70 was set at 1000 counts, only the cracks with depths between about 6 and 10 mils would provide information that contributes to the estimate of the POD(a) function. The larger and smaller cracks are always found or missed and would have provided little information about the POD(a) function in a hit/miss analysis. In the *â* analysis, however, all of the recorded *â* values provide information concerning the relation between signal response and crack size. The parameters of the POD(a) function are derived from the distribution of *â* values about the median response for cracks of size *a*.

Because of the added information in the *â* data, a valid characterization of the POD(a) function with confidence bounds can be obtained with fewer cracks than are required for the hit/miss analysis. It is recommended that at least 30 cracks be available for demonstrations whose results can be recorded in *â* vs *a* form. Increasing the number of cracks increases the precision of estimates. Perhaps, more importantly, increasing the number of cracks provides a broader

population of the different types of cracks that the inspection will address. Therefore, the demonstration specimen test set should contain as many cracked sites as economically feasible.

For the $\hat{a}$ vs a model, the POD(a) is the probability (shown by the shaded region under the probability density) that a signal, (â, "ahat") will be larger than the decision threshold. Figure 4-71 shows POD plotted on the same size axis as the "$\hat{a}$ *vs.* a" line. Note the correspondences at POD = 0.1, 0.5, and 0.9 with the respective shaded probability densities. The solid black line is defined as truth. In reality the truth would be unknown and is to be inferred from the behavior of the data. The solid black "data" points are observations of signal responses for a given damage size. Sometimes they are "censored." Censored observations are shown as open symbols. The "data" are generated and a censored regression is performed to produce the most likely model to have given rise to those observations. That is the blue line in Figure 4-71. Also shown are the confidence bounds and prediction bounds (inner and outer dotted lines, respectively). Sometimes the blue line (the model) is very close to the "truth." In reality we only get to see one collection of data, and from that data we must estimate the most likely model for the unseen and unknown and unknowable "truth," and produce its confidence bound that includes the true a_{90} at least 95 times in every 100 similar experiments (95% confidence bound).

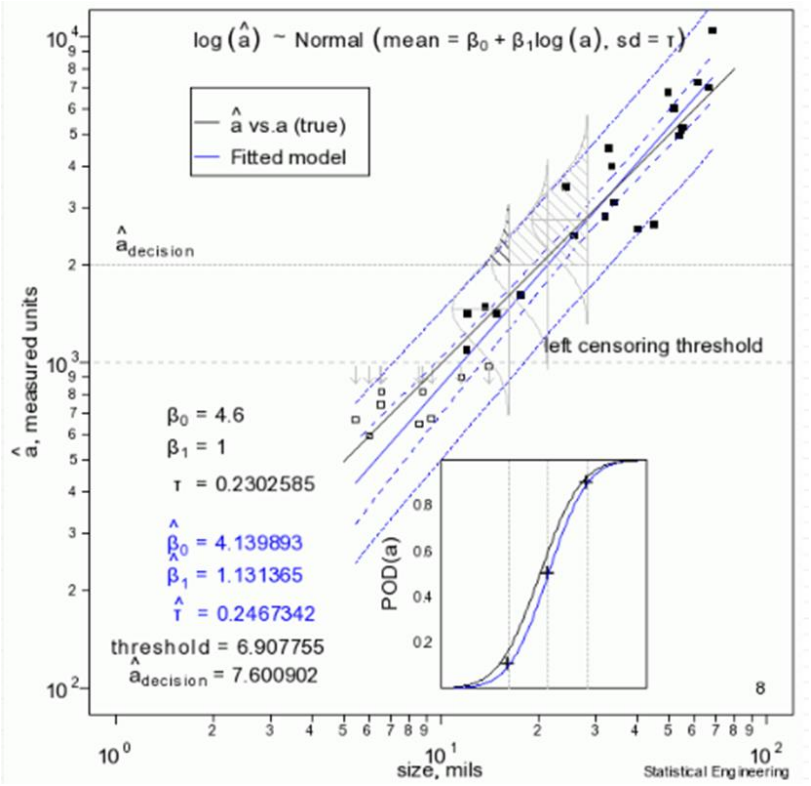

Figure 4-71. Inspection System Response vs Damage Size Showing Variability in Signals and Construction of Probability Estimates

Given SHM or NDI data generated through a controlled experiment, a generalized linear model is commonly used to determine the typical size crack than can be detected with a given probability under standard operation of the health monitoring system.

- The SHM system must produce output for damage detection that can be reduced to a quantitative signal, $\hat{a}$, corresponding to actual damage a, where $\hat{a}$ is the measured response of the SHM system to a given flaw size, a.
- Use of a critical SHM system response can contain more information, and the amplitude, $\hat{a}$, of the output makes it possible to extract other POD(a) estimates that could have narrower confidence bounds.
- POD(a) depends on a reasonable $\hat{a}$ *vs* a model - data plot of $\hat{a}$ *vs log(a)* should reveal a linear relationship (see Figure 4-72). It describes the expected response, $\hat{a}$, at any given size, a. Notice that it provides a reasonable summary of the data – the line is straight; the data are straight. The scatter is consistent and not wider at one end or the other.
- The â (y-axis) versus "a" (x-axis) data may be transformed using logarithm function along appropriate axes, if needed, to create linear correlation around the decision threshold, $\hat{a}_{(decision)}$.
- It is essential to consider the S/N ratio which includes the scatter in the results (note similarity in OSTI) when determining the detection threshold.

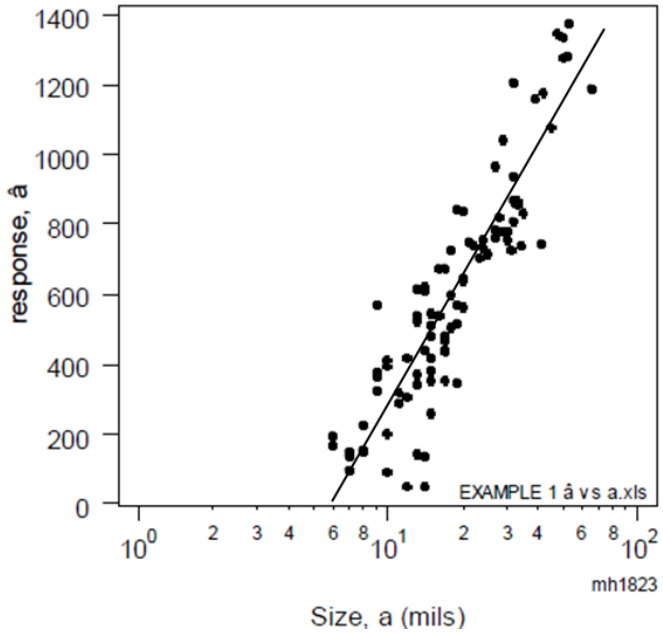

Figure 4-72. Expected Linear Response in *â vs log(a)* to Produce Probability Estimates on Detection of Damage of a Particular Type and Size

In general, NDI and SHM systems make detect/no detect decisions by interpreting its response to a health monitoring task. This response is a recordable metric, $\hat{a}$, that is related to the flaw size. For SHM systems, this is normally some kind of Damage Index. Damage detection decisions are made by comparing the magnitude of $\hat{a}$ to the decision threshold value, $\hat{a}_{(decision)}$. The $\hat{a}$ versus flaw size analysis is a method of estimating the POD(a) function based on the correlation between $\hat{a}$ and flaws of known size, a. The general formulation of the $\hat{a}$ versus a model is expressed as:

$$\hat{a} = f(a) + \delta \tag{4.6}$$

Where $f(a)$ represents the average (or median) response to a crack of size a and δ represents the sum of all the random effects that makes the inspection of a particular crack of size a different from the average of all cracks of size a. In principle, any f(a) and distribution of δ that fit the observations can be used. However, if f(a) is linear in a,

$$\hat{a} = B_0 + B_1 a + \delta \tag{4.7}$$

And δ is normally distributed with constant standard deviation, σ_δ, then the resulting POD(a) function is a cumulative normal distribution function. Monotonic transformations of $\hat{a}$ or a can be analyzed in this framework. In fact, the model has been shown to fit a large number of cases in which a logarithmic transformation of both a and $\hat{a}$ was applied. As an example consider the formulation of the $\hat{a}$ vs a analysis that has been used in the evaluation of the automated eddy current inspection systems. The relation between $\hat{a}$ and a is expressed in terms of the natural logarithms of $\hat{a}$ and a.

$$ln\,\hat{a} = B_0 + B_1 \bullet ln\,a + \delta \tag{4.8}$$

Where δ is Normal (0, σ_δ). For a decision threshold of $\hat{a}_{(decision)}$,

$$POD(a) = \Phi\left[\frac{ln\,a - \mu}{\sigma}\right] \tag{4.9}$$

Where $\Phi(z)$ is the cumulative standard normal distribution function and

$$\mu = \frac{ln\,\hat{a}_{dec} - B_0}{B_1} \tag{4.10}$$

$$\sigma = \sigma_\delta / B_1 \tag{4.11}$$

The calculation is illustrated in Figure 4-71. The parameters of the $\hat{a}$ vs a model (B_0, B_1, and σ_δ) are estimated from the data of the demonstration specimens. The probability density function of the ln($\hat{a}$) values for a 13 mil crack depth is illustrated in the Figure 4-73. The decision threshold in the example is set at $\hat{a}_{(decision)}$ = 165. The POD for a randomly selected 13 mil crack would be the proportion of all 13 mil cracks that would have an $\hat{a}$ value greater than 165 (i.e. the area under the curve above 165). In this example, the decision threshold was selected so that POD(13) = 0.90. The estimate of the POD(a) function and its 95 percent confidence bound for the decision threshold of 165 counts is presented in Figure 4-73. It might be noted that when all cracks have a recorded response between the signal minimum and maximum, the maximum likelihood estimates are identical with those obtained from a standard regression (least squares) analysis. However, when crack response is below the signal minimum or above the maximum (saturation level of the recorder), more sophisticated calculations are required to obtain parameter estimates and the

confidence bound. Complete details of the maximum likelihood calculations and more discussion of the $\hat{a}$ versus a analysis can be found in references [4.19 – 4.21].

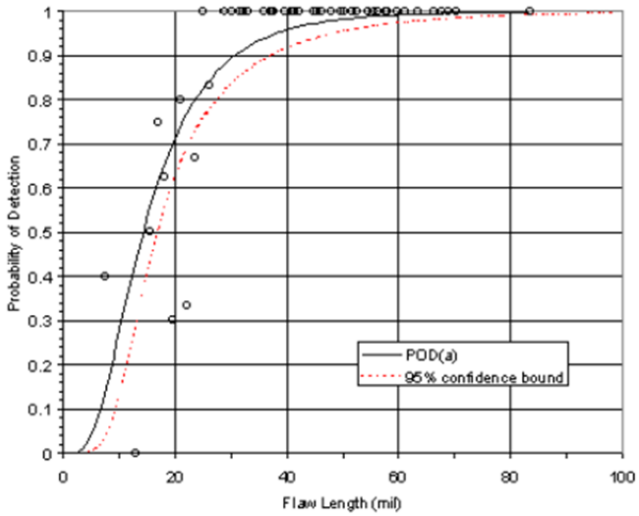

Figure 4-73. POD(*a*) Function with 95 Percent Confidence Bound for an Example *â* versus *a* Analysis

If the *â vs log(a)* relation is not linear, it may be possible to use other transformations of either the signal response or the crack size and the above analysis can be applied using the different transformation. The inverse transformation of the results provides the answers in the correct units. Data sets have been observed in which no transformation was required and the fit was made directly to *â* vs *a* data (i.e. without the logarithmic transform). It should be noted that extreme caution must be exercised when extrapolating the results beyond the range of crack sizes in the data. The POD Version 3 normally assumes a logarithmic transform.

Comparison of OSTI with *â vs. a* POD Model – The *â vs a* POD from NDI data is composed of all independent data. An independent distribution of seeded cracks (for the range of damage size desired) are used to acquire signals at detection (one reading on each target); account for operator-to-operator (sensor-to-sensor) variability and account for crack-to-crack variability. This approach produces a fully-populated ***â vs a*** response curve for the NDI method of interest. Deployment of the experiment with multiple inspectors, produces a series of *â vs a* response curves which are used to produce the overall POD assessment for a particular NDI method. In the case of the SHM analysis conducted here, the *â vs a* Model is constructed using multiple *â* data points (SHM response levels) from a single, growing crack. The use of similar data sets from a series of test specimens produces the set of *â vs a* response curves needed to calculate the POD for the SHM system.

The *â vs a* POD analysis method requires the use of completely independent data points (~ 30) from different crack sites. In order to create a comparison that relates the POD calculated from the OSTI method to traditional POD assessments, the data from the POD testing described above was applied in a *â vs a* POD model. Use of a whole set of *â* crack response data from each CVM

and PZT test specimen was necessary to produce a sufficient set of *â vs a* response curves from only ~ 20 independent crack detection tests. Thus, it must be stressed that the exercise of conducting the *â vs a* POD calculations is carried out here for simple comparisons to the methodology used in Mil-Hnbk-1823. Following are some considerations when using the *â vs a* methodology with the 20 specimens tested in the SHM testing.

- The *â vs a* POD analysis presented in this report takes credit for all data as independent data points (Mil-HDBK-1823 calculation). Thus, the confidence interval is artificially reduced.
- If the sensors, their location, the cracks, and the sensor response is consistent enough that the assumed data is representative (additional tests produced independent data that is equivalent to the repeated measures assumed data), then the *â vs a* POD results are close to the truth.
- If the actual responses – should many additional tests be conducted – exhibit deviations and lack consistency (deviate significantly from the assumed response), then the *â vs a* POD results will have much larger deviation from the truth.
- Repeated Measures Data is needed for SHM assessments – unless an extremely large number of independent tests are performed - as all data from a single specimen is repeated data (same sensor, same growing crack)
- Normal NDI POD values are calculated using only independent data points. This includes an independent distribution of seeded cracks where unique signals at detection are logged (one reading on each target), the test series accounts for operator-to-operator (sensor-to-sensor) variability, and the array of specimens is sufficiently large to account for crack-to-crack variability.
- Repeated measures data (multiple data points from a single crack profile and SHM response) are used in these calculations; this is an assumption that is not statistically valid. It does not account for possible crack-to-crack variations from different specimens.
- However, these results are for illustrative purposes only and not for any certification of performance. The results calculated from this *â vs a* POD analysis are for general comparisons only.
- *Certification results are to be taken only from the OSTI method already presented above*.

References

4.1. SMS Technical Document, "Introduction to Comparative Vacuum Monitoring – Users Manual," Doc. 000758MNm Rev. 2.

4.2. SMS Technical Document, "Surface Preparation and Installation Procedure for CVM Sensors," Doc. SMS-AP-WI-AME1 and SMS-AO-WI-4.2, Feb 2020.

4.3. Roach, D., Rice, T., "Design and Assessment of Comparative Vacuum Monitoring and Piezoelectric Transducer Systems for Certified Use in Aircraft Structural Health Monitoring Solutions," Sandia Dept of Energy Report, SAND2017-6401, July 2017.

4.4. Roach, D., Rice, T. "Application and Certification of Comparative Vacuum Monitoring Sensors for Structural Health Monitoring of 737 Wing Box Fittings," DOE SAND2020-9184, September 2020.

4.5. Roach, D., Rice, T., Rulli, R., Dotta, F., "Adoption of SHM Systems to Address Families of Aircraft Integrity Checks," Airlines for America Nondestructive Testing Forum, September 2017.
4.6. Rulli, R., Dotta, F., Roach, D., Rice, T., "Advancements on the Adoption of SHM Damage Detection Technologies into Embraer Aircraft Maintenance Procedures," Int'l Workshop on Structural Health Monitoring, September 2017.
4.7. Meeker, W., Roach, D., Kessler, S., "Statistical Methods for Probability of Detection in Structural Health Monitoring," Journal of Structural Health Monitoring, Issue TBD.
4.8. Spencer, F., "Confidence Intervals and Probability of Detection for Fixed Transducer Locations," Internal Sandia Labs memo, September 25, 2006.
4.9. Roach, D., DeLong, W., Rackow, K., Yepez, E., Reedy, D., White, S., "Use of Composite Materials, Health Monitoring, and Self-Healing Concepts to Refurbish Our Civil and Military Infrastructure," Department of Energy Report SAND2007-5547, September 2007
4.10. Roach, D., "Real Time Crack Detection Using Mountable Comparative Vacuum Monitoring Sensors," *Journal of Smart Structures and Sensors*, Vol. 5, July 2009.
4.11. Roach, D., Rice, T., Piotrowski, D., Bohler, J., Melton, A., "Paving the Path to Certification of Structural Health Monitoring Solutions in Aviation," Airlines for America Nondestructive Testing Forum, September 2013.
4.12. Meeker, W.Q., Hahn, G.J., and Escobar, L.A., *Statistical Intervals: A Guide for Practitioners and Researchers*, Second Edition. John Wiley and Sons, Inc., 2017.
4.13. Roach, D., Rice, T., "Use of On-Board Sensors to Improve Crack Onset Monitoring in Aircraft Structures," The Scientific World Journal, August 2013
4.14. Roach, D., "Use of Comparative Vacuum Monitoring Sensors for Automated, Wireless Health Monitoring of Bridges and Infrastructure," *Proceedings of the 9th International Conference on Bridge Maintenance, Safety and Management*, July 2018.
4.15. Owen, D.B., "Factors for One-Sided Tolerance Limits and for Variables Sampling Plans," Dept of Energy report SAND-SCR-607, March 1963.
4.16. Krishnamoorthy, K. and T. Mathew (2009). *Statistical Tolerance Regions: Theory, Applications, and Computation*. John Wiley & Sons, Inc, 2009.
4.17. Roach, D., Rice, T., "Calculating Probability of Detection for SHM Systems Using One-Sided Tolerance Intervals," First Int'l SHM Reliability Workshop, SAE, April 2015.
4.18. Roach, D., "Automated Health Monitoring of Rail Cars and Railroad Bridges Using Embedded Sensors," Int'l Conference on Structural Health Monitoring for Rail Systems, Qingdao, China, October 2016.
4.19. Annis, C., et.al., 2007, "Nondestructive Evaluation System Reliability Assessment", MIL-HDBK-1823, US Air Force DOD, February 2007.
4.20. Miedlar, P., Berens, A., Gunderson, A., Gallagher, J., "USAF Damage Tolerant Design Handbook: Guidelines for the Analysis and Design of Damage Tolerant Aircraft Structures," AFRL-VA-WP-TR-2003-3002, United States Air Force, Wright-Patterson Air Force Base, Jan. 2002.
4.21. Berens, A., "Probability of Detection (POD) Analysis for the Advanced Retirement for Cause (RFC)/Engine Structural Integrity Program (ENSIP) Nondestructive Evaluation (NDE) System Development, Volume 1 – POD Development," AFRL-ML-WP-TR-2001-4010, Air Force Research Laboratory, Wright-Patterson Air Force Base, Jan. 2000.

THIS PAGE INTENTIONALLY LEFT BLANK

5. CVM PERFORMANCE ASSESSMENT

5.1. CVM Crack Detection

5.1.1. Validation Process for CVM Structural Health Monitoring System

This SHM technology validation exercise was designed to produce quantifiable evidence that the CVM inspection method (equipment plus its operation) can produce the required inspection results. The validation process considered the numerous factors that affect the reliability of CVM including the individual inspector/operator, his equipment, his procedures and the environment in which he is working. With the rotorcraft gusset application in mind, it was possible to complete the performance testing using representative Validation Assemblies containing realistic defects that the SHM system is intended to monitor. Key considerations included structural configuration (geometry and material), flaw location and orientation, structural variation, installation and usage environment, SHM performance requirements ($\boldsymbol{L_{NDI}}$), and the ability to assess false positive rates. Validation testing consisted of mounting SHM sensors to representative specimens and cyclically loading the specimens to generate and grow fatigue damage as described in Chapter 4.

The test program carried out to support CVM use on rotorcraft structures followed the same process as the Ref. [5-2] program which resulted in approval for CVM use to monitor for cracks in the Wing Box fittings on Boeing 737 aircraft. A fatigue crack was propagated in a representative structure subjected to realistic flight loads until it engaged one of the vacuum galleries such that crack detection was achieved and the sensor indicated the presence of a crack by its inability to maintain a vacuum. Statistical methods using the One-Sided Tolerance Interval method were employed to derive Probability of Detection (POD) levels for CVM sensors. The result is a series of flaw detection curves that can be used to propose CVM sensors for specific rotorcraft components. Additional data pertaining to CVM sensor durability and operation during flight testing had been acquired in multiple, related programs. This data is summarized in this report for completeness.

5.1.2. CVM Performance on Rotorcraft Gusset Test Specimen

A description of the rotorcraft application, the frame gusset test specimens, the CVM sensors for the two nutplate configurations, the instrumentation test-setup, and SHM crack monitoring are provided in Sections 3.2, 4.1 and 4.2. The associated POD analysis methods are described in Section 4.6. Fatigue tests were completed on the frame gussets using flight load spectrums while the vacuum pressures within the various CVM sensor galleries were simultaneously recorded. Several trial tests were conducted to determine the optimum CVM damage detection threshold using the process described in Section 4.6. This allowed for a proper translation of the dCVM signal into official flaw detection. These tests determined that a dCVM value of 4.0 provides a proper threshold for the crack detection decision. The PM-200 monitoring device was programmed to produce a crack detection alarm when the dCVM value reached 4.0 or greater.

Fatigue tests were halted at regular intervals and when any indications from the real-time Sim-8 monitoring equipment indicated that the CVM sensors had changed response due to cracks engaging the galleries. The PM200 device was then connected to the CVM sensor as it would be during monitoring (inspections) on an aircraft. Final determination of a crack detection was associated with direct dCVM readings and associated failure messages from the PM200 device. In order to properly consider the effects of crack closure in an unloaded condition (i.e. during sensor monitoring), a crack was deemed to be detected when a permanent alarm was produced and the CVM sensor did not maintain a vacuum even if the fatigue stress was reduced to zero.

A detailed explanation of the components in the total crack length and the method used to determine the total crack length at CVM detection is presented in Figure 5-1. The critical measurement is the excursion of the crack into the CVM sensor (crack length under the sensor). The distance from the crack origin to the edge of the sensor can then be added to determine the total crack length at detection. This approach allows for the distance from the crack origin to the edge of the sensor to be a variable that can be adjusted to accommodate the expected placement variations in the CVM sensor. Worst case conditions can be used when calculating the final POD level such that the final performance assessment is arrived at in a conservative manner.

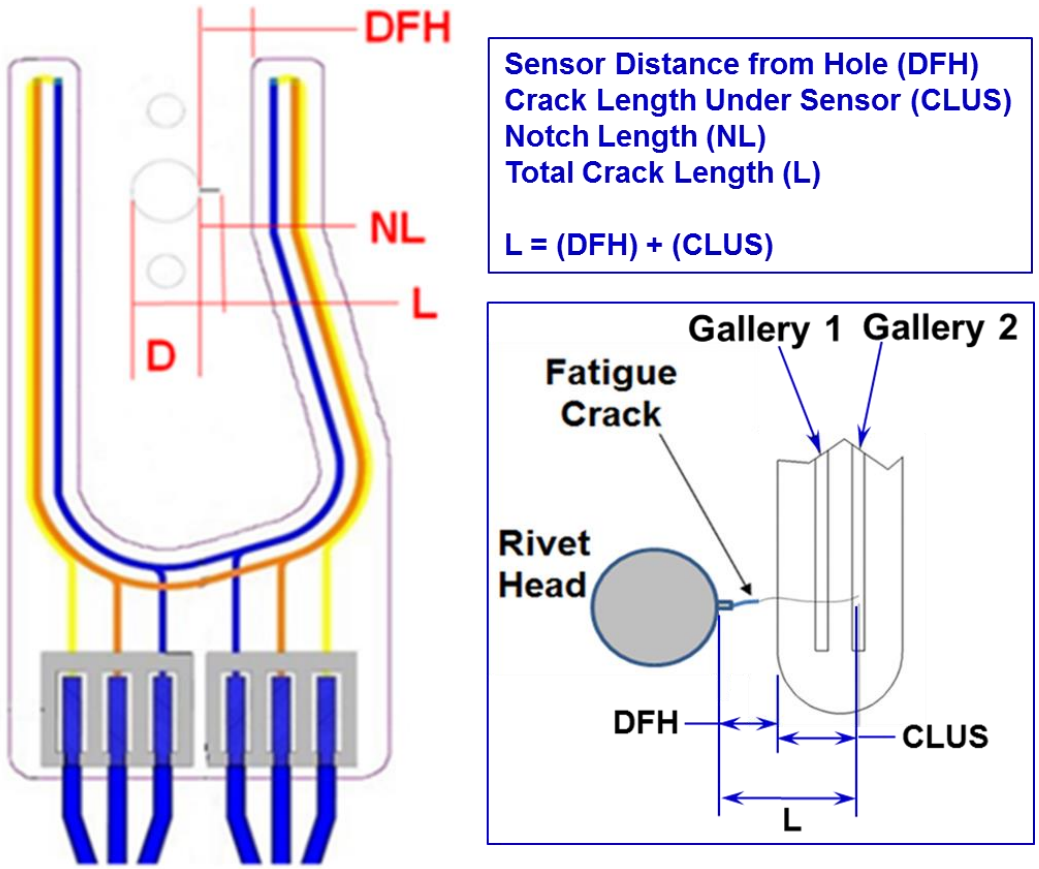

Figure 5-1. Components of Total Crack Length for POD Analysis – Sensor Distance from Hole Plus Crack Length Under Sensor

Overall, the CVM performance results are presented as follows: 1) POD assessment using multiple analyses methods for CVM sensors detecting cracks originating from the straight nut plate on the rotorcraft frame, 2) POD assessment using multiple analyses methods for CVM sensors detecting cracks originating from the Mickey Mouse nut plate on the rotorcraft frame, and 3) POD assessment using multiple analyses methods for CVM sensors detecting cracks originating from the both nut plate types on the rotorcraft frame.

Straight Nutplate

Table 5-1 summarizes the CVM crack detection performance for sensors designed and mounted to monitor the "straight" nutplate on the rotorcraft gusset frame as shown in Figure 3-5 through Figure 3-8. In this case, crack detection was achieved when the crack engaged the first gallery to provide the path to atmosphere. The average total crack length at detection, which includes the sensor offset from the crack origin was 0.319". The crack lengths under the sensor at detection ranged from 0.102" to 0.323" while the total crack lengths, including the sensor distance from the hole shown in Figure 5-1, ranged from 0.248" to 0.474". Table 5-1 also lists the corresponding dCVM values at crack detection so that the critical CVM system response can be noted and corresponding S/N values can be calculated. This data acquired from CVM fatigue tests were used to calculate the 90% POD level for CVM crack detection on the Frame Gusset subjected to tension-bending fatigue loading described above. Figure 5-2 shows a typical plot of the SIM-8 values during fatigue testing vs. the fatigue cycles (i.e. crack growth). The rising SIM-8 pressure values in the CVM gallery indicate crack growth and provides precursor information to final, permanent crack detection by the PM-200 device.

One-Sided Tolerance Interval POD Method - From a simple sensor standpoint, SHM is very analogous to NDI where the set of signals represent first a baseline, corresponding to a pristine structure, and later a deviation from the baseline, possibly corresponding to a damaged structure. This deviation is used to infer the presence of a flaw. Depending on the equipment and the type of inspection being conducted, the guidance on how to delineate a flaw may differ but it is normally rooted in some desired signal-to-noise ratio which has been determined to produce the best POD while minimizing false calls. As noted above, the dCVM threshold corresponding the CVM crack detection was set to 4.0.

The 19 data points listed in Table 5-1, were used in the OSTI method described in Section 4.6 to calculate the POD performance. Table 5-2 summarizes the OSTI calculations. The reliability calculations include a corresponding magnitude of the K (probability) factor that is related to the number of data points acquired, the desired probability desired (90%) and the desired confidence level (95%). Also, the OSTI calculations include a parameter that amounts to an increase in POD as the Standard Deviation of the data increases. As a result, while most of the crack detection levels were less than 0.350", the overall $POD_{90/95}$ value for CVM crack detection from the straight nutplate was calculated to be 0.447". The K value shown corresponds to the desired γ (confidence level) of 95%. As the number of data points increases, the K value will decrease and the POD numbers could also decrease. There were no False Calls associated with these tests where the CVM sensor indicated the presence of a crack when actually none was present. In over 400 fatigue

tests conducted using CVM sensors there have been no false calls produced by the sensors in any of the tests.

Table 5-1. CVM Crack Detection Performance in Straight Nutplate on Rotorcraft Gusset

Sikorsky Config-1 Straight Nutplate CVM Performance Tests								
Specimen No.	CVM Sensor ID	Fatique Cycles at permanent CVM Crack Detection	Sensor Distance from Hole (in)	Crack Length Under Sensor at CVM Detection a (in)	Total Crack Length (in)	Dynamic SIM-8 Reading Gallery 1 (Pa)	PM200 Reading (1dCVM)	PM200 Reading (2dCVM)
CVM-C1SN-1	Left	14,383	0.139	0.213	0.352	17401	4.3	3.3
CVM-C1SN-1	Right	13,026	0.139	0.102	0.241	12650	5.1	0.7
CVM-C1SN-2	Left	12,802	0.137	0.111	0.248	13402	4.1	1.3
CVM-C1SN-2	Right	14,652	0.152	0.112	0.264	14111	4.4	0.5
CVM-C1SN-3	Left	12,616	0.127	0.157	0.284	16044	4.4	2.1
CVM-C1SN-3	Right	15,417	0.142	0.149	0.291	15640	5	2.5
CVM-C1SN-4	Left	12,438	0.132	0.163	0.295	16303	4.2	2.5
CVM-C1SN-4	Right	Equip Problems - No Data						
CVM-C1SN-5	Left	16,302	0.144	0.206	0.350	n/a	0.5	4.2
CVM-C1SN-5	Right	21,668	0.150	0.216	0.366	18187	2.4	4.4
CVM-C1SN-6	Left	16,491	0.139	0.148	0.287	17694	1.5	4.2
CVM-C1SN-6	Right	13,944	0.149	0.197	0.346	15861	4.4	0
CVM-C1SN-7	Left	13,561	0.140	0.179	0.319	16765	2.7	5
CVM-C1SN-7	Right	17,364	0.151	0.323	0.474	18748	4.2	3.2
CVM-C1SN-8	Left	9,712	0.131	0.125	0.256	13000	4.1	0.1
CVM-C1SN-8	Right	11,234	0.145	0.135	0.280	15300	4.2	0.6
CVM-C1SN-9	Left	15546	0.154	0.163	0.317	16380	4.2	1.8
CVM-C1SN-9	Right	16,617	0.141	0.213	0.354	17754	4.2	0.7
CVM-C1SN-10	Left	16,684	0.133	0.221	0.354	17800	2.1	4.6
CVM-C1SN-10	Right	15,387	0.136	0.240	0.376	18240	4.4	4.3

Avg CVM Detection	0.178
CVM Detect Std Dev	0.055
Avg Dist From CVM Edge to Hole Edge	0.141

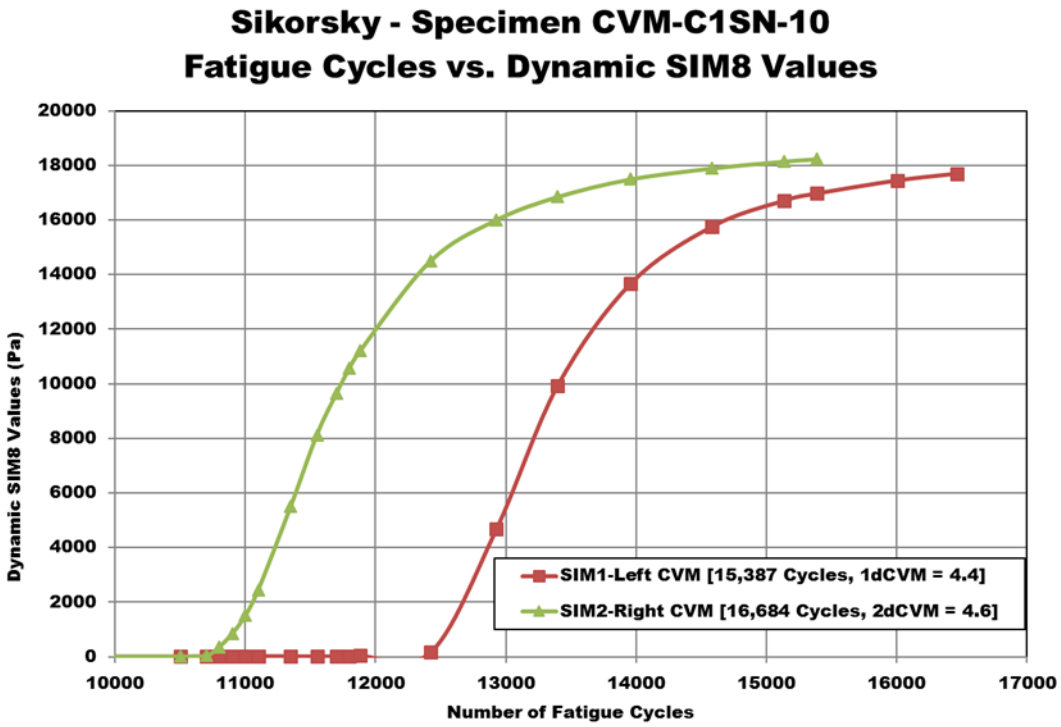

Figure 5-2. Relationship Between Dynamic SIM-8 Values vs. Fatigue Cycles (Crack Growth) – Straight Nutplate

Table 5-2. POD for CVM Monitoring Straight Nutplate Cracks - Determined Using the One-Sided Tolerance Interval Method Applied to the CVM Gusset Response Data

CVM Crack Detection Data

Distance from Hole to Sensor Edge	Total Crack Length a (in)	Crack Length Under Sensor at CVM Detection a (in)	Log of Crack Length at CVM Detection a (ln)
0.139	0.241	0.102	-0.991399828
0.139	0.352	0.213	-0.671620397
0.152	0.264	0.112	-0.950781977
0.137	0.248	0.111	-0.954677021
0.142	0.291	0.149	-0.826813732
0.127	0.284	0.157	-0.804100348
0.132	0.295	0.163	-0.787812396
0.15	0.366	0.216	-0.665546249
0.144	0.350	0.206	-0.68613278
0.139	0.287	0.148	-0.829738285
0.149	0.346	0.197	-0.705533774
0.140	0.319	0.179	-0.747146969
0.151	0.474	0.323	-0.490797478
0.131	0.256	0.125	-0.903089987
0.145	0.280	0.135	-0.869666232
0.154	0.317	0.163	-0.787812396
0.141	0.354	0.213	-0.671620397
0.133	0.354	0.221	-0.655607726
0.136	0.376	0.240	-0.619788758

Avg CVM Detection	**0.178**
CVM Detect Std Dev	**0.055**
Avg Dist From CVM Edge to Hole Edge	**0.141**

Statistic Estimates on Log Scale

Statistic	Value (in.)	Value in Linear Scale
Mean (X)	-0.769	0.178
Stnd Deviation (S)	0.130729317	0.054601962

POD Detection Levels
(ɣ = 95%, n = 19)

Flaw Size: POD = X + K(S) =	0.306

Overall POD (with sensor offset) = 0.447”

Hit-Miss Log Regression POD Method - Quantifying SHM performance using the Log Regression Method only requires that the signal deviation can be reduced to produce a simple detection (hit) or no-detection (miss). Thus, the mapping of SHM signals to flaw detection is key. It is possible to lower damage detection threshold in both NDI and SHM to improve POD, possibly at the expense of increasing false calls. So, the success in applying the Log Regression Method lies in the ability of the SHM system to produce acceptable binary data. Thus, the POD testing must accommodate all of the key variations within the set of POD specimens using statistical distribution. Such variations include flaw type, size, orientation, depth and location within the sensor coverage area.

The 19 data points listed in Table 5-1, were used in the Hit-Miss POD method described in Section 4.6 to calculate the POD performance. However, additional data points were extrapolated from each specimen using the same dCVM threshold of 4.0 to determine crack detection. For each specimen, additional data points were acquired by selecting crack lengths below dCVM = 4.0 (i.e. below detection) to correspond to "Misses" and crack lengths above dCVM = 4.0 (i.e. above detection) to correspond to "Hits." Note that the Hit-Miss Method requires the use of approximately 50 independent data points from 50 different crack sites. To create a comparison that relates the POD calculated from the OSTI method to traditional POD assessments, the data from the POD testing described above was applied in a Hit-Miss POD analysis. Some extrapolation of the CVM crack detection data was necessary to produce sufficient data from the reduced-order, 19 independent crack detection tests. Additional extrapolated data at extremes (very small & very large cracks) were used to populate a complete the Hit-Miss POD curve. A Gaussian distribution of hit-miss data was compiled using crack CVM detection lengths from each test augmented by assumed, missed crack detections below the actual CVM detection level and assumed, hit crack detections at lengths above the actual CVM detection level. Thus, it must be stressed that the exercise of conducting the Hit-Miss POD calculations is carried out here for simple comparisons to the methodology used in Mil-Hnbk-1823.

Figure 5-3 summarizes the results for each individual test specimen where the hit-miss data surrounding the CVM crack detection has been extrapolated from the raw test data. The Hit-Miss Log Regression POD method was used to calculate the individual and compiled POD values. The total set of data from the individual $POD_{(90/95)}$ values were compiled into an overall performance calculation to produce an overall $POD_{(90/95)}$ value of 0.275" for the crack length under the sensor. When this is added to the average sensor offset (Distance from Hole) of 0.141", the total crack length $POD_{(90/95)}$ = 0.416" which can be used for comparison to the OSTI $POD_{(90/95)}$ value of 0.447". These results from the Hit-miss POD method, which represents traditional POD analyses, compare well with the OSTI method (within 6.7%). The OSTI $POD_{(90/95)}$ level is higher and thus, more conservative for assessing performance.

In this Hit-Miss assessment conducted with the limited SHM response data, the calculations are carried out with the assumption that each data point is independent and is produced by a separate crack (separate specimen). This is not the case because the Hit-Miss analysis presented here took credit for the additional, extrapolated data as if it were independent data points (Mil-HDBK-1823 calculation). If the sensor response is consistent enough that the assumed data is representative (additional tests produced independent data that is equivalent to the repeated measures assumed data), then the resulting "hit-miss" calculations are close to the truth. Results obtained in the

significant test set from multiple years of CVM performance testing [4-10 – 4-14, 4-17 – 4-18] gives us confidence in the extrapolations listed here and used in the "hit-miss" calculations. Repeated measures data (multiple data points from a single crack profile and SHM response) are used in these calculations which is an assumption that is not statistically valid. It does not account for possible crack-to-crack variations from different specimens. Thus, these results are for illustrative, comparison purposes only and not for any certification of performance. *Certification results are to be taken only from the OSTI method already presented in this Section*.

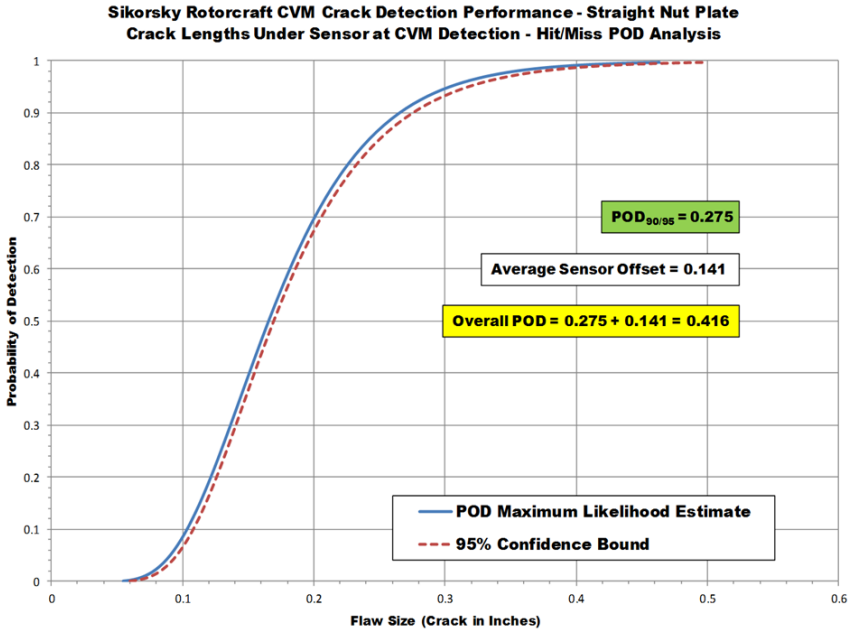

Sikorsky Straight Nut Plate Individual CVM Sensor Performance Tests Hit/Miss POD Values			
Specimen No.	CVM Sensor ID	Eddy Current Crack Length at CVM (In)	$POD_{90/95}$
CVM-C1SN-1	Left	0.213	0.217
CVM-C1SN-1	Right	0.102	0.105
CVM-C1SN-2	Left	0.111	0.114
CVM-C1SN-2	Right	0.112	0.115
CVM-C1SN-3	Left	0.157	0.160
CVM-C1SN-3	Right	0.149	0.152
CVM-C1SN-4	Left	0.163	0.166
CVM-C1SN-5	Left	0.206	0.210
CVM-C1SN-5	Right	0.216	0.220
CVM-C1SN-6	Left	0.148	0.151
CVM-C1SN-6	Right	0.197	0.200
CVM-C1SN-7	Left	0.179	0.182
CVM-C1SN-7	Right	0.323	0.327
CVM-C1SN-8	Left	0.125	0.128
CVM-C1SN-8	Right	0.135	0.139
CVM-C1SN-9	Left	0.163	0.166
CVM-C1SN-9	Right	0.213	0.217
CVM-C1SN-10	Left	0.221	0.225
CVM-C1SN-10	Right	0.240	0.244
Cumulative			0.275

Figure 5-3. POD for CVM Monitoring Straight Nutplate Cracks - Determined Using the Hit-Miss Analysis Method Applied to the CVM Gusset Response Data and Extrapolated Results

Mickey Mouse Nutplate

Table 5-3 summarizes the CVM crack detection performance for sensors designed and mounted to monitor the "Mickey Mouse" nutplate on the rotorcraft gusset frame as shown in Figure 3-5 through Figure 3-8. In this case, crack detection was achieved when the crack engaged the first gallery to provide the path to atmosphere. The average total crack length at detection, which includes the sensor offset from the crack origin was 0.299". The crack lengths under the sensor at detection ranged from 0.111" to 0.314" while the total crack lengths, including the sensor distance from the hole shown in Figure 5-1, ranged from 0.217" to 0.409". Table 5-3 also lists the corresponding dCVM values at crack detection so that the critical CVM system response can be noted and corresponding S/N values can be calculated. This data acquired from CVM fatigue tests were used to calculate the 90% POD level for CVM crack detection on the Frame Gusset subjected to tension-bending fatigue loading described above. Figure 5-4 shows a sample plot of the SIM-8 values during fatigue testing vs. the fatigue cycles (i.e. crack growth). The rising SIM-8 pressure

values in the CVM gallery indicate crack growth and provides precursor information to final, permanent crack detection by the PM-200 device. Figure 5-5 shows typical crack growth vs. fatigue cycles (da/dN) for cracks emanating from the nutplate holes in the Mickey Mouse nutplate configuration.

Table 5-3. CVM Crack Detection Performance in Mickey Mouse Nutplate on Rotorcraft Frame

Sikorsky Config-2 Mickey Mouse Nutplate CVM Performance Tests								
Specimen No.	CVM Sensor ID	Fatique Cycles at permanent CVM Crack Detection	Sensor Distance from Hole (in)	Crack Length Under Sensor at CVM Detection a (in)	Total Crack Length (in)	Dynamic SIM-8 Reading Gallery 1 (Pa)	PM200 Reading (1dCVM)	PM200 Reading (2dCVM)
CVM-C2MMN-1	Left	17,404	0.130	0.138	0.268	15330	4.2	1.4
CVM-C2MMN-1	Right	17,906	0.106	0.111	0.217	13424	4.5	1.7
CVM-C2MMN-2	Left	23,099	0.119	0.180	0.299	17100	4.2	3.1
CVM-C2MMN-2	Right	20,514	0.123	0.125	0.248	17100	4.1	0.2
CVM-C2MMN-3	Left	20,128	0.113	0.135	0.248	14600	4.2	1.2
CVM-C2MMN-3	Right	26,483	0.140	0.242	0.382	18350	5.2	3.7
CVM-C2MMN-4	Left	22,888	0.096	0.278	0.374	18600	7.3	6.4
CVM-C2MMN-4	Right	Specimen Broke - No Data						
CVM-C2MMN-5	Left	23,078	0.101	0.220	0.321	17650	4.1	1.7
CVM-C2MMN-5	Right	20,278	0.124	0.146	0.270	16250	4.2	1.1
CVM-C2MMN-6	Left	14,962	0.097	0.129	0.226	11300	4.4	0.5
CVM-C2MMN-6	Right	14,485	0.106	0.181	0.287	16800	4.2	3
CVM-C2MMN-7	Left	19,979	0.100	0.221	0.321	17600	2.9	6.5
CVM-C2MMN-7	Right	18,827	0.110	0.169	0.279	15000	4.3	0.1
CVM-C2MMN-8	Left	13,057	0.112	0.168	0.280	15500	4.2	0
CVM-C2MMN-8	Right	15,725	0.095	0.314	0.409	18280	4.9	3.7
CVM-C2MMN-9	Left	15590	0.127	0.198	0.325	17400	4.1	1.5
CVM-C2MMN-9	Right	15,316	0.114	0.219	0.333	17350	4.5	3.9
CVM-C2MMN-10	Left	12,877	0.134	0.193	0.327	17550	4.5	2.5
CVM-C2MMN-10	Right	11,660	0.081	0.177	0.258	17500	1.6	4.3

Avg CVM Detection	0.187
CVM Detect Std Dev	0.053
Avg Dist From CVM Edge to Hole Edge	0.112

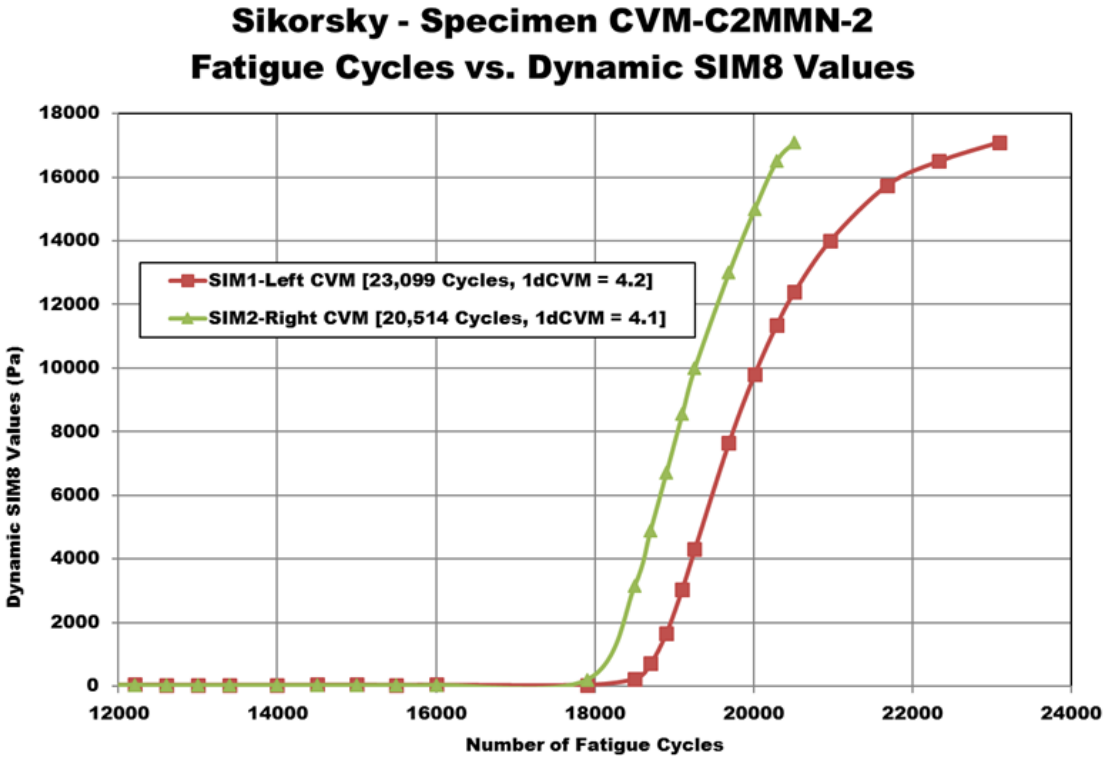

Figure 5-4. Relation Between Dynamic SIM-8 Values vs. Fatigue Cycles (Crack Growth) – Mickey Mouse Nutplate

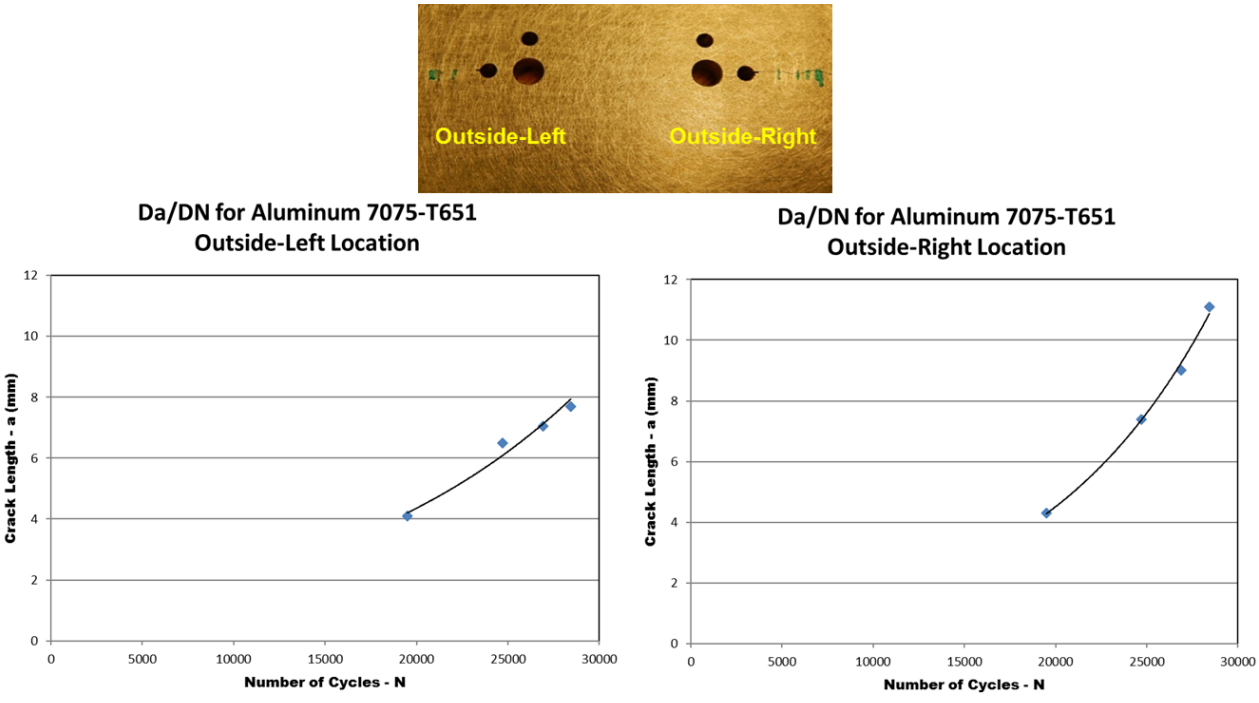

Figure 5-5. Sample da/dN Curves for Cracks Emanating from the Mickey Mouse Nutplates

One-Sided Tolerance Interval POD Method - The 19 data points listed in Table 5-3, were used in the OSTI method described in Section 4.6 to calculate the POD performance. Table 5-4 summarizes the OSTI calculations. The reliability calculations include a corresponding magnitude of the K (probability) factor that is related to the number of data points acquired, the desired probability desired (90%) and the desired confidence level (95%). Also, the OSTI calculations include a parameter that amounts to an increase in POD as the Standard Deviation of the data increases. As a result, while most of the crack detection levels were less than 0.350", the overall $POD_{90/95}$ value for CVM crack detection from the Mickey Mouse nutplate was calculated to be 0.422". The K value shown corresponds to the desired ɣ (confidence level) of 95%. As the number of data points increases, the K value will decrease and the POD numbers could also decrease. There were no False Calls associated with these tests where the CVM sensor indicated the presence of a crack when actually none was present.

Table 5-4. POD for CVM Monitoring Mickey Mouse Nutplate Cracks - Determined Using the One-Sided Tolerance Interval Method Applied to the CVM Gusset Response Data

CVM Crack Detection Data

Distance from Hole to Sensor Edge	Total Crack Length a (in)	Crack Length Under Sensor at CVM Detection a (in)	Log of Crack Length at CVM Detection a (In)
0.13	0.268	0.138	-0.860120914
0.106	0.217	0.111	-0.954677021
0.119	0.299	0.180	-0.744727495
0.123	0.248	0.125	-0.903089987
0.113	0.248	0.135	-0.869666232
0.14	0.382	0.242	-0.616184634
0.096	0.374	0.278	-0.555955204
0.101	0.321	0.220	-0.657577319
0.124	0.270	0.146	-0.835647144
0.097	0.226	0.129	-0.88941029
0.106	0.287	0.181	-0.742321425
0.100	0.321	0.221	-0.655607726
0.110	0.279	0.169	-0.772113295
0.112	0.280	0.168	-0.774690718
0.095	0.409	0.314	-0.503070352
0.127	0.325	0.198	-0.70333481
0.114	0.333	0.219	-0.659555885
0.134	0.327	0.193	-0.714442691
0.081	0.258	0.177	-0.752026734

Average Crack Length at CVM Detection =	**0.187**
Standard Deviation of CVM Detection =	**0.053**
Average Dist From CVM Edge to Hole Edge =	**0.112**

Statistic Estimates on Log Scale

Statistic	Value (in.)	Value in Linear Scale
Mean (X)	-0.745	0.187
Stnd Deviation (S)	0.121325291	0.05348766

POD Detection Levels (ɣ = 95%, n = 19)

Flaw Size: POD = X + K(S) =	0.310

Overall POD (with sensor offset) = 0.422"

Hit-Miss Log Regression POD Method - The 19 data points listed in Table 5-3, were used in the Hit-Miss POD method described in Section 4.6 to calculate the POD performance. However, additional data points were extrapolated from some specimens using the same dCVM threshold of 4.0 to determine crack detection. Since the Hit-Miss Method requires the use of approximately 50 independent data points from 50 different crack sites, it was necessary to produce additional CVM crack detection data from the 19 independent crack detection tests. Three coupons were tested such that crack lengths were measured before and after permanent crack detection. This provided a mechanical trends analysis to relate dCVM values to fatigue crack lengths and to determine a set

of Hit-Miss (detect – no detect) data points based on whether or not the dCVM values were above (hit) or below (miss) the selected crack detection threshold. For these specimens, additional data points were acquired by selecting crack lengths below dCVM = 4.0 (i.e. below detection) to correspond to "Misses" and crack lengths above dCVM = 4.0 (i.e. above detection) to correspond to "Hits."

Table 5-5 through Table 5-7 list the results from this additional data mining from six different cracks on specimens CVM-C2MMN-7, CVM-C2MMN-8 and CVM-C2MMN-9. Hit-Miss data were acquired using crack CVM detection length from these specimens along with missed crack detections (lengths) below dCVM detection level of 4.0 and hit crack detections (lengths) above the dCVM detection level. When these results were compiled with the crack detection results from the remaining CVM-C2MMN specimens, 65 hit/miss data points as listed in Table 5-8 were produced. This hit (1) and miss (0) data is plotted in Figure 5-6.

Table 5-5. dCVM and Crack Length Data for Hit-Miss Assessment – CVM-C2MMN-7

CVM-C2MMN-7 Left Sensor						CVM-C2MMN-7 Right Sensor					
Cycles	Dynamic SIM1 (Pa)	1dCVM	2dCVM	Visual Total Crack Length Front (In)	EC Total Crack Length Back (In)	Cycles	Dynamic SIM2 (Pa)	1dCVM	2dCVM	Visual Total Crack Length Front (In)	EC Total Crack Length - Back (In)
16,311	12,000	0.4	1.5	0.191	0.181	16,311	3,624	0.3	0.0	0.189	0.169
16,864	14,000	0.9	1.7	0.204	0.220	16,864	7,566	1.1	0.0	0.193	0.213
17,583	15,500	1.4	2.7	0.210	0.252	17,583	11,630	2.1	0.2	0.207	0.240
18,356	16,500	1.8	3.5	0.236	0.283	18,356	14,123	3.6	0.0	0.224	0.244
18,827	16,913	2.4	2.8	0.250	0.295	18,827	15,000	4.3	0.1	0.234	0.279
19,307	17,250	2.5	2.8	0.256	0.295	19,307	15,778	5.1	0.7	0.240	0.291
19,979	17,600	2.9	6.5	0.259	0.321	19,979	16,604	6.9	1.3	0.254	0.299
20,983	17,958	3.5	3.5	0.307	0.343	20,983	17,329	8.2	2.4	0.287	0.327
21,992	18,230	4.2	3.6	0.338	0.372	21,992	17,782	9.8	3.6	0.311	0.354
23,328	18,596	12.4	9.0	0.376	0.406	23,328	18,244	15.9	4.7	0.349	0.386

❖dCVM Corresponding to Permanent Crack Detection is Highlighted (dCVM > 4.0)

Table 5-6. dCVM and Crack Length Data for Hit-Miss Assessment – CVM-C2MMN-8

CVM-C2MMN-8 Left Sensor						CVM-C2MMN-8 Right Sensor					
Cycles	Dynamic SIM1 (Pa)	1dCVM	2dCVM	Visual Total Crack Length Front (In)	EC Total Crack Length Back (In)	Cycles	Dynamic SIM2 (Pa)	1dCVM	2dCVM	Visual Total Crack Length Front (In)	EC Total Crack Length - Back (In)
10,857	2,506	-0.2	0.1	0.175	0.224	10,857	14,000	1.2	0.5	0.188	0.252
11,733	10,105	1.3	0.1	0.201	0.248	11,733	16,000	1.7	1.2	0.205	0.274
12,679	14,470	3.4	0.0	0.224	0.276	12,679	17,000	2.5	1.6	0.231	0.305
13,057	15,500	4.2	0.0	0.228	0.280	13,057	17,243	2.7	1.7	0.235	0.317
13,969	16,808	6.4	0.3	0.258	0.319	13,969	17,750	3.4	2.8	0.278	0.341
15,039	17,763	8.4	1.3	0.299	0.354	15,039	18,100	3.7	2.8	0.298	0.370
15,725	18,357	25.2	3.6	0.307	0.374	15,725	18,280	4.9	3.7	0.321	0.409

❖dCVM Corresponding to Permanent Crack Detection is Highlighted (dCVM > 4.0)

Table 5-7. dCVM and Crack Length Data for Hit-Miss Assessment – CVM-C2MMN-9

CVM-C2MMN-9 Left Sensor						CVM-C2MMN-9 Right Sensor					
Cycles	Dynamic SIM1 (Pa)	1dCVM	2dCVM	Visual Total Crack Length Front (In)	EC Total Crack Length Back (In)	Cycles	Dynamic SIM2 (Pa)	1dCVM	2dCVM	Visual Total Crack Length Front (In)	EC Total Crack Length - Back (In)
12,561	5,094	0.1	-0.1	0.196	0.238	12,561	12,000	1.3	2.4	0.212	0.228
13,048	10,003	0.5	0.0	0.214	0.258	13,048	14,000	1.9	1.6	0.222	0.256
13,920	14,684	2.0	0.0	0.239	0.276	13,920	16,000	2.8	1.6	0.234	0.280
14,878	16,750	3.1	0.6	0.269	0.309	14,878	17,000	3.6	3.7	0.248	0.319
15,316	17,154	3.7	1.2	0.281	0.313	15,316	17,350	4.5	3.9	0.271	0.333
15,590	17,400	4.1	1.5	0.292	0.325	15,590	17,491	4.6	4.5	0.281	0.346
16,640	17,885	6.1	2.8	0.324	0.360	16,640	17,937	6.0	6.6	0.311	0.370
17,624	18,230	9.8	4.7	0.357	0.400	17,624	18,220	8.0	7.3	0.354	0.404
18,585	18,884	185.0	104.0	0.430	0.437	18,585	18,572	21.0	11.7	0.417	0.439

❖dCVM Corresponding to Permanent Crack Detection is Highlighted (dCVM > 4.0)

Table 5-8. Actual Test Hit/Miss Data Acquired from 19 Sensors (65 data points)

Sikorsky Mickey Mouse Nut Plate CVM Sensor Performance Tests		
Specimen	Eddy Current Crack Length at CVM (in)	Hit (1) or Miss (0)
CVM-C2MMN-1-L	0.138	1
CVM-C2MMN-1-R	0.111	1
CVM-C2MMN-2-L	0.180	1
CVM-C2MMN-2-R	0.125	1
CVM-C2MMN-3-L	0.135	1
CVM-C2MMN-3-R	0.242	1
CVM-C2MMN-4-L	0.278	1
CVM-C2MMN-5-L	0.220	1
CVM-C2MMN-5-R	0.146	1
CVM-C2MMN-6-L	0.129	1
CVM-C2MMN-6-R	0.181	1
CVM-C2MMN-7-L	0.081	0
CVM-C2MMN-7-L	0.120	0
CVM-C2MMN-7-L	0.152	0
CVM-C2MMN-7-L	0.183	0
CVM-C2MMN-7-L	0.195	0
CVM-C2MMN-7-L	0.195	0
CVM-C2MMN-7-L	0.221	0
CVM-C2MMN-7-L	0.243	0
CVM-C2MMN-7-L	0.272	1
CVM-C2MMN-7-L	0.306	1
CVM-C2MMN-7-R	0.059	0

Sikorsky Mickey Mouse Nut Plate CVM Sensor Performance Tests		
Specimen	Eddy Current Crack Length at CVM (in)	Hit (1) or Miss (0)
CVM-C2MMN-7-R	0.103	0
CVM-C2MMN-7-R	0.130	0
CVM-C2MMN-7-R	0.134	0
CVM-C2MMN-7-R	0.169	1
CVM-C2MMN-7-R	0.181	1
CVM-C2MMN-7-R	0.189	1
CVM-C2MMN-7-R	0.217	1
CVM-C2MMN-7-R	0.244	1
CVM-C2MMN-7-R	0.276	1
CVM-C2MMN-8-L	0.112	0
CVM-C2MMN-8-L	0.136	0
CVM-C2MMN-8-L	0.164	0
CVM-C2MMN-8-L	0.168	1
CVM-C2MMN-8-L	0.207	1
CVM-C2MMN-8-L	0.242	1
CVM-C2MMN-8-L	0.262	1
CVM-C2MMN-8-R	0.157	0
CVM-C2MMN-8-R	0.179	0
CVM-C2MMN-8-R	0.210	0
CVM-C2MMN-8-R	0.222	0
CVM-C2MMN-8-R	0.246	0
CVM-C2MMN-8-R	0.275	0

Sikorsky Mickey Mouse Nut Plate CVM Sensor Performance Tests		
Specimen	Eddy Current Crack Length at CVM (in)	Hit (1) or Miss (0)
CVM-C2MMN-8-R	0.314	1
CVM-C2MMN-9-L	0.111	0
CVM-C2MMN-9-L	0.131	0
CVM-C2MMN-9-L	0.149	0
CVM-C2MMN-9-L	0.182	0
CVM-C2MMN-9-L	0.186	0
CVM-C2MMN-9-L	0.198	1
CVM-C2MMN-9-L	0.233	1
CVM-C2MMN-9-L	0.273	1
CVM-C2MMN-9-L	0.310	1
CVM-C2MMN-9-R	0.114	0
CVM-C2MMN-9-R	0.142	0
CVM-C2MMN-9-R	0.166	0
CVM-C2MMN-9-R	0.205	0
CVM-C2MMN-9-R	0.219	1
CVM-C2MMN-9-R	0.232	1
CVM-C2MMN-9-R	0.256	1
CVM-C2MMN-9-R	0.290	1
CVM-C2MMN-9-R	0.325	1
CVM-C2MMN-10-L	0.193	1
CVM-C2MMN-10-R	0.177	1

The Hit-Miss Log Regression POD method was applied to these 65 data points to calculate the overall $POD_{(90/95)}$ value of 0.286" for the crack length under the sensor. When this is added to the average sensor offset (Distance from Hole) of 0.112", the total crack length $POD_{(90/95)}$ = 0.398" which can be used for comparison to the OSTI $POD_{(90/95)}$ value of 0.422" as shown in Figure 5-7. These results from the Hit-miss POD method, which represents traditional POD analyses, compare well with the OSTI method (within 5.7%). The OSTI $POD_{(90/95)}$ level is higher and thus, more conservative for assessing performance.

Again, it must be stressed that the exercise of conducting the Hit-Miss POD calculations is carried out here for simple comparisons to the methodology used in Mil-Hnbk-1823. Repeated measures data (multiple data points from a single crack profile and SHM response) are used in these calculations which is an assumption that is not statistically valid. It does not account for possible crack-to-crack variations from different specimens. Thus, these results are for illustrative, comparison purposes only and not for any certification of performance. *Certification results are to be taken only from the OSTI method already presented in this Section*.

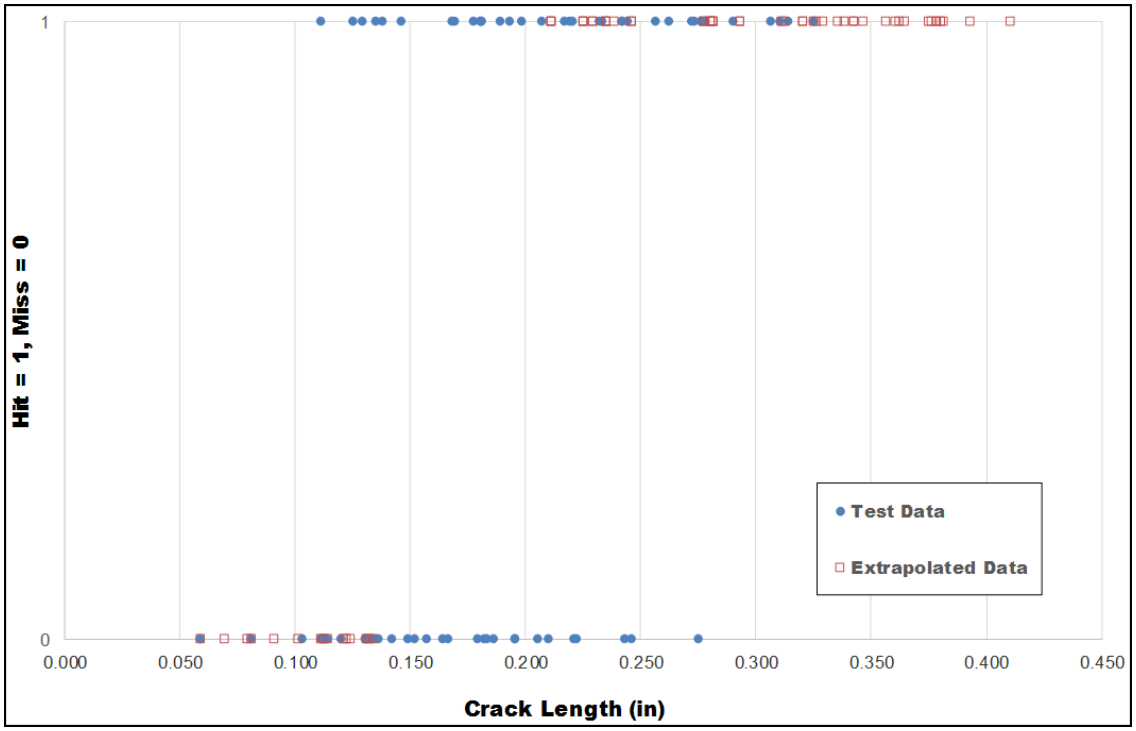

Figure 5-6. Plot of CVM Hit-Miss Crack Detection Data from Mickey Mouse Nutplate on Gusset

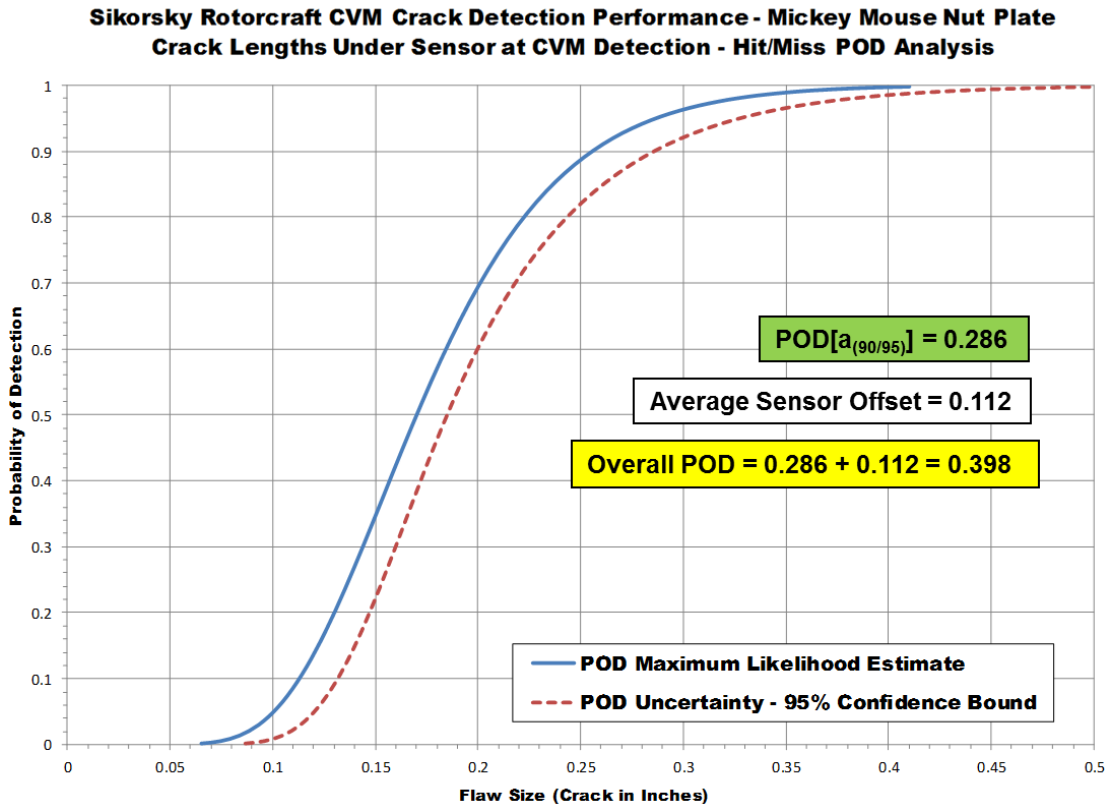

Figure 5-7. POD for CVM Monitoring Straight Nutplate Cracks - Determined Using the Hit-Miss Analysis Method Applied to the CVM Gusset Response Data and Extrapolated Results

â vs a POD Method - When the crack or other flaw decision is made on the basis of a recorded response, â, to the inspection stimulus, the data are known as *â* vs *a* inspection results and a different POD(a) analysis can performed as described in Section 4.6. Figure 4-62 shows a specific *â* vs *a* example for the CVM performance program described in this report. It shows the CVM system response *â* (dCVM values) as a function of the damage parameter *a* (crack length). When the inspection response is greater than or equal to the selected dCVM detection threshold of 4.0, a crack is indicated for the site. The *â* versus flaw size analysis is a method of estimating the POD(*a*) function based on the correlation between *â* and flaws of known size, *a*.

Because of the added information in the *â* data, a valid characterization of the POD(a) function with confidence bounds can be obtained with fewer cracks than are required for the hit/miss analysis. It is recommended that at least 30 cracks be available for demonstrations whose results can be recorded in *â* vs *a* form. The *â vs a* POD analysis method requires the use of completely independent data points (~ 30) from different crack sites. In order to apply the â vs. a method for determining POD, it is necessary to acquire data relating the response of the SHM system (â = dCVM) to the corresponding crack length (a). Three coupons were tested such that crack lengths were measured before and after permanent crack detection. This provided a mechanical trends analysis to relate dCVM values to fatigue crack lengths and create a set of â vs. a (sensor response vs. crack length) data points for use in the â vs. a POD Method.

Figure 5-8 through Figure 5-10 show the *â vs a* response curves from six different cracks on specimens CVM-C2MMN-7, CVM-C2MMN-8 and CVM-C2MMN-9. Figure 5-11 shows that the resulting set of 52 *â vs a* data points plot linearly on the log-log scale thus ensuring the proper response relationship for the *â vs a* POD Method.

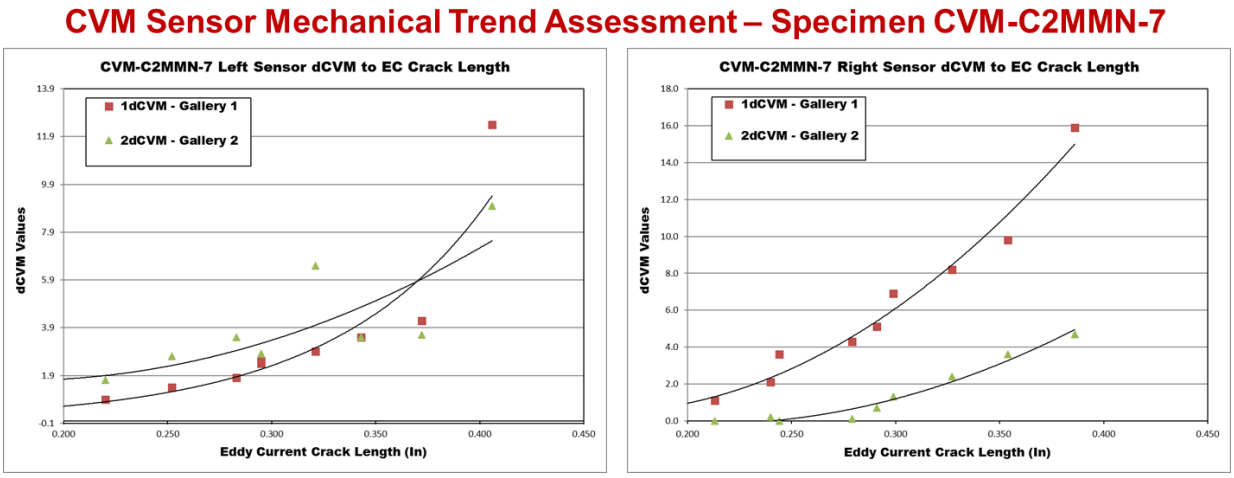

Figure 5-8. CVM Sensor Response as Function of Crack Length – CVM-C2MMN-7

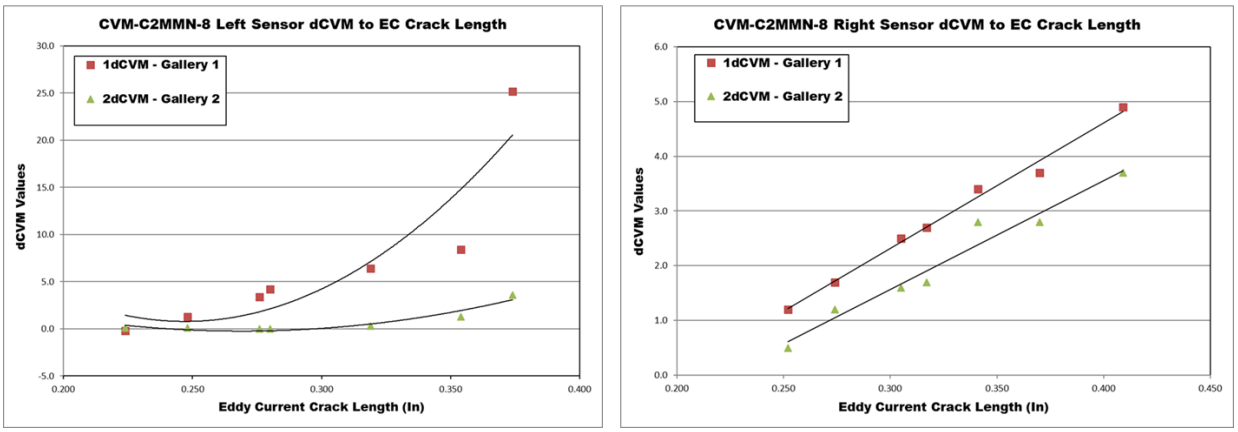

Figure 5-9. CVM Sensor Response as Function of Crack Length – CVM-C2MMN-8

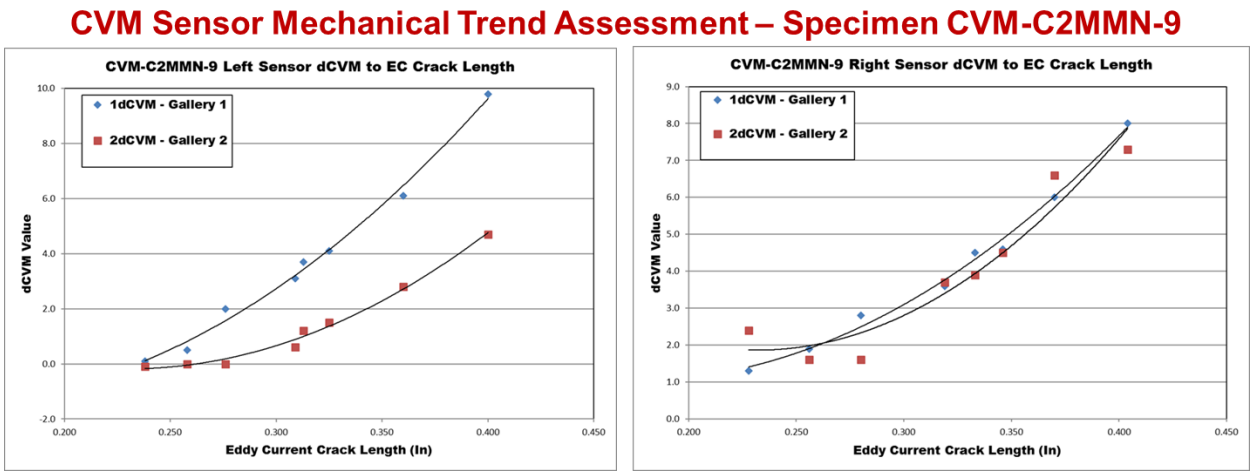

Figure 5-10. CVM Sensor Response as Function of Crack Length – CVM-C2MMN-9

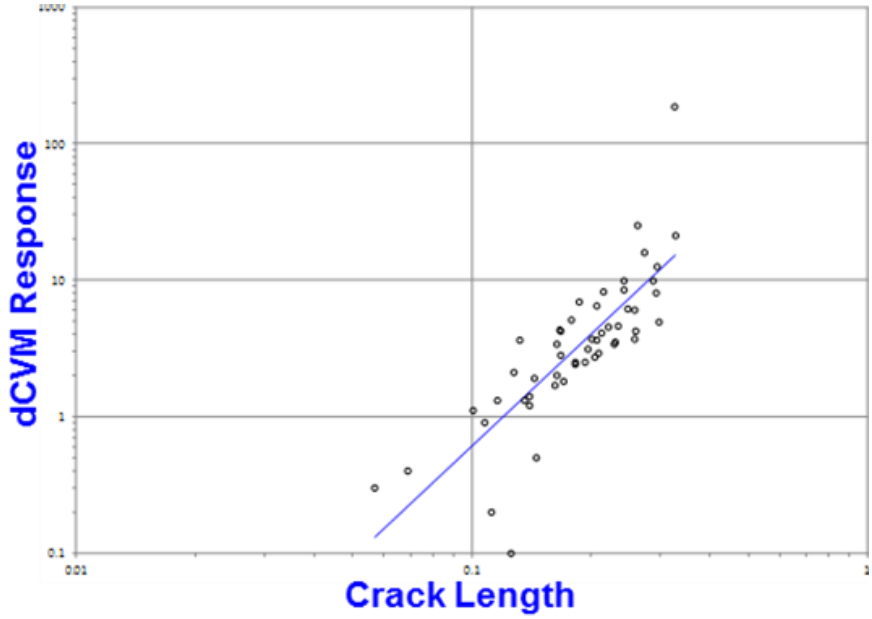

Figure 5-11. Linear Response of *a vs â* Data on a Log-Log Scale – Actual 52 Data Points

The *â vs a* POD Method was applied to these 52 data points to calculate the overall $POD_{(90/95)}$ value of 0.343" for the crack length under the sensor. When this is added to the average sensor offset (Distance from Hole) of 0.112", the total crack length $POD_{(90/95)}$ = 0.455" which can be used for comparison to the OSTI $POD_{(90/95)}$ value of 0.422" as shown in Figure 5-12. These results from the *â vs a* POD Method, which represents traditional POD analyses, compare well with the OSTI method (within 7.8%).

One advantage of using the *â vs a* POD Method is that this approach can use the response data to infer the performance of the subject SHM system when different decision thresholds are used to

detect the damage. Figure 5-13 plots the $POD_{(90/95)}$ values that would be generated from different decision thresholds. For example, an increase in the dCVM detection threshold from 4 to 7 would increase the $POD_{(90/95)}$ value to 0.577" (0.465" under sensor + 0.112" sensor offset). A decrease in the dCVM detection threshold from 4 to 2 would decrease the $POD_{(90/95)}$ value to 0.342" (0.230" under sensor + 0.112" sensor offset). Of course, any reduction in the damage detection threshold must be conducted in light of any possible changes in the Probability of False Calls

Generation of the larger set of *â* crack response data from the 19 CVM cracks tested was necessary to produce a sufficient set of *â vs a* response curves from only 19 independent crack detection tests. It should be noted that these data points are not independent data points and are only used here to provide a basis of comparison between the OSTI and Mil-Hndk-1823 *â vs a* POD Method for calculating POD level. Thus, these results are for illustrative, comparison purposes only and not for any certification of performance. *Certification results are to be taken only from the OSTI method already presented in this Section.*

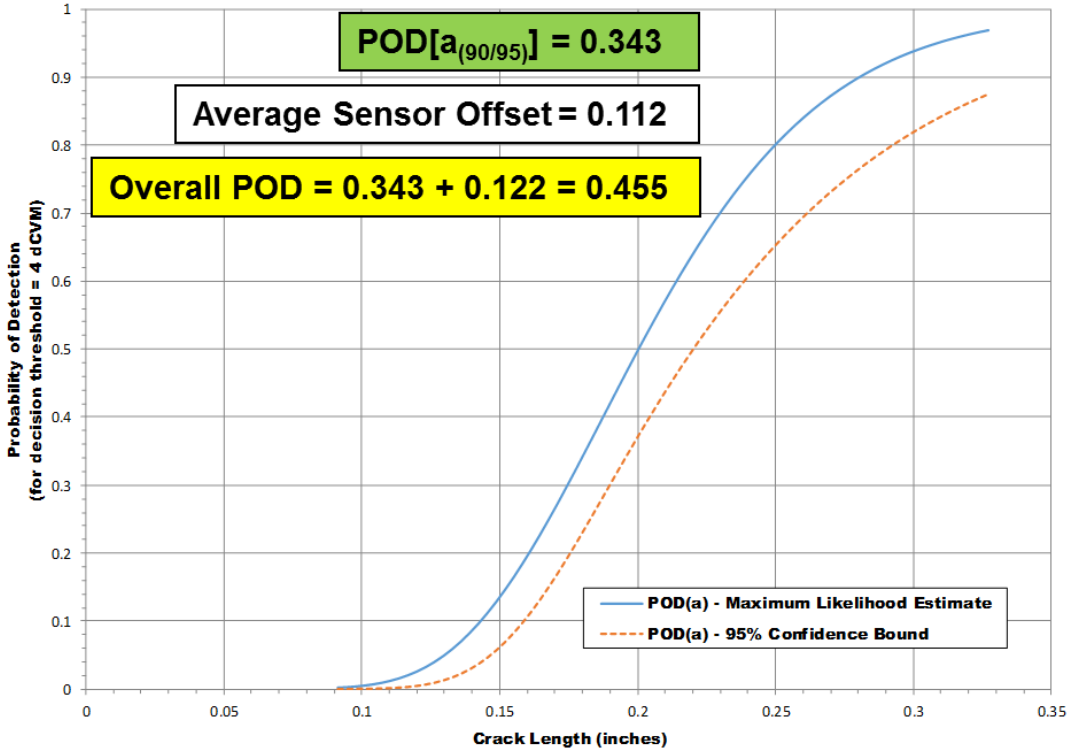

Figure 5-12. POD for CVM Monitoring Mickey Mouse Nutplate Cracks - Determined Using the *a vs â* Method Applied to the CVM Gusset Response Data – Actual 52 Data Points

Next, the mechanical trends that were measured to relate dCVM values to fatigue crack lengths and create a set of â vs. a (sensor response vs. crack length) data points was revisited. Additional dCVM vs Crack Length data points were acquired by interpolating between the measured points in Figure 5-8 through Figure 5-10. Figure 5-14 shows that the resulting set of 52 *â vs a* data points,

plus the additional 32 data points generated, plot linearly on the log-log scale thus ensuring the proper response relationship for the *â vs a* POD Method.

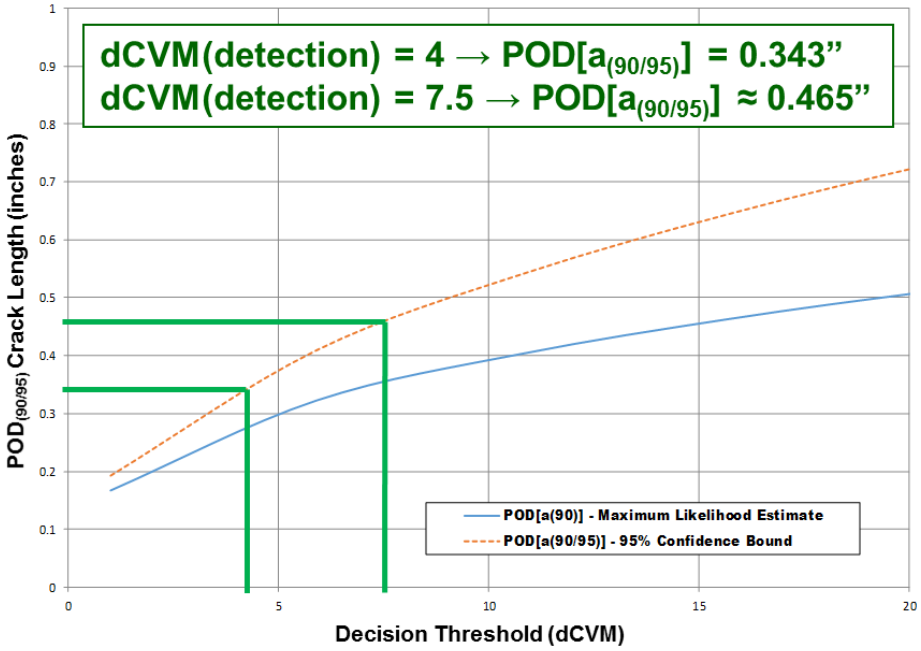

Figure 5-13. Estimated $POD_{(90/95)}$ Values for Different â Decision Thresholds (a vs. â method) – Actual 52 Data Points

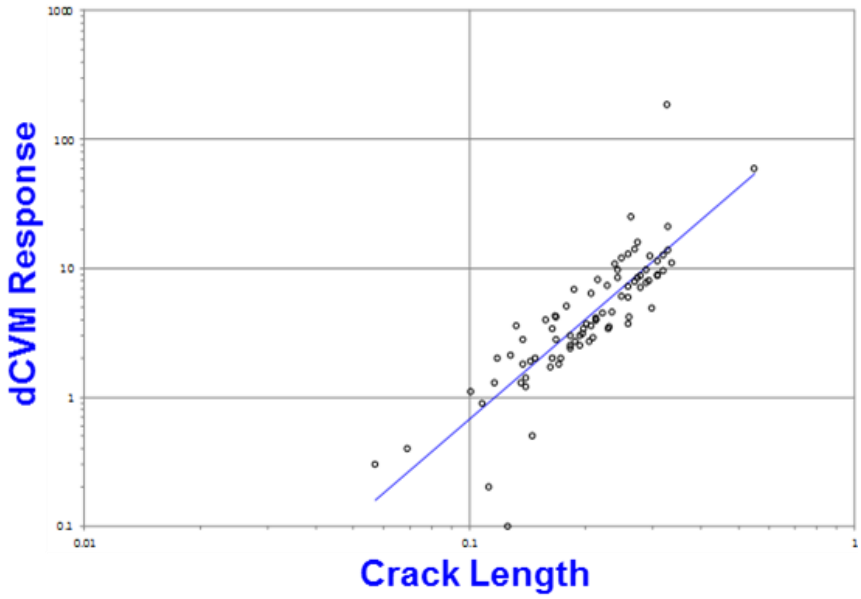

Figure 5-14. Check on Linear Response of *a vs â* Data on a Log-Log Scale – Actual 52 Data Points Plus Additional 32 Extrapolated Data Points

The *â vs a* POD Method was applied to these 84 data points to calculate the overall $POD_{(90/95)}$ value of 0.300" for the crack length under the sensor. When this is added to the average sensor offset (Distance from Hole) of 0.112", the total crack length $POD_{(90/95)}$ = 0.412" which can be used for comparison to the OSTI $POD_{(90/95)}$ value of 0.422" as shown in Figure 5-15. These results from the *â vs a* POD Method, which represents traditional POD analyses, compare well with the OSTI method (within 2.4%). The increase in data points to a total of 82 improves the confidence levels and makes the 95% confidence bound plot closer to the POD Maximum Likelihood Estimate (solid line in Figure 5-15). Thus, there are several factors included in the reduction in POD with the additional 32 data points. Again, this reiterates that such calculations only provide general comparisons between the OSTI and *â vs a* POD Method. Finally, Figure 5-16 provides an overall comparison between the $POD_{(90/95)}$ values as calculated by the OSTI, Hit-Miss and *â vs a* POD Methods. Although these values are close, one would expect that, with sufficient independent specimen testing, all three methods would converge to a similar number. *For the purposes of this program with a specific Sikorsky application, the CVM performance certification results are to be taken only from the OSTI method only.*

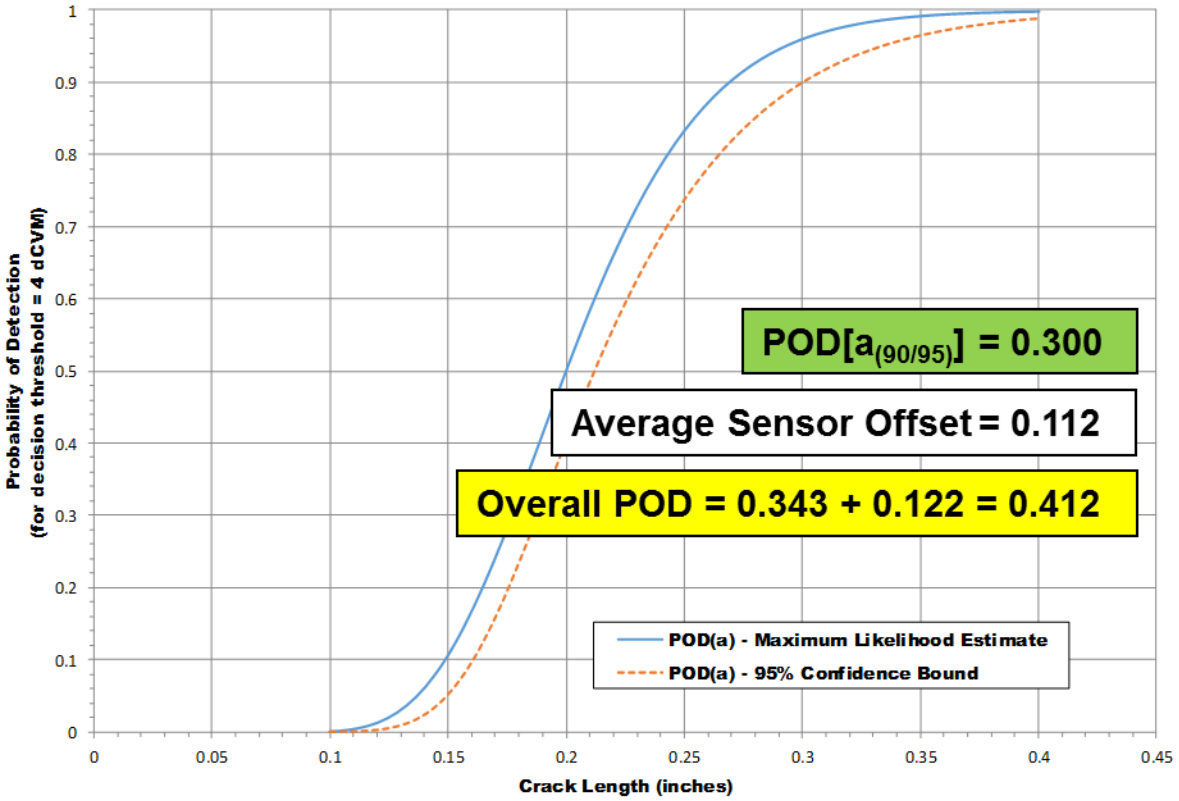

Figure 5-15. POD for CVM Monitoring Mickey Mouse Nutplate Cracks - Determined Using the *a vs â* Method from Actual 52 Data Points Plus Additional 32 Extrapolated Data Points

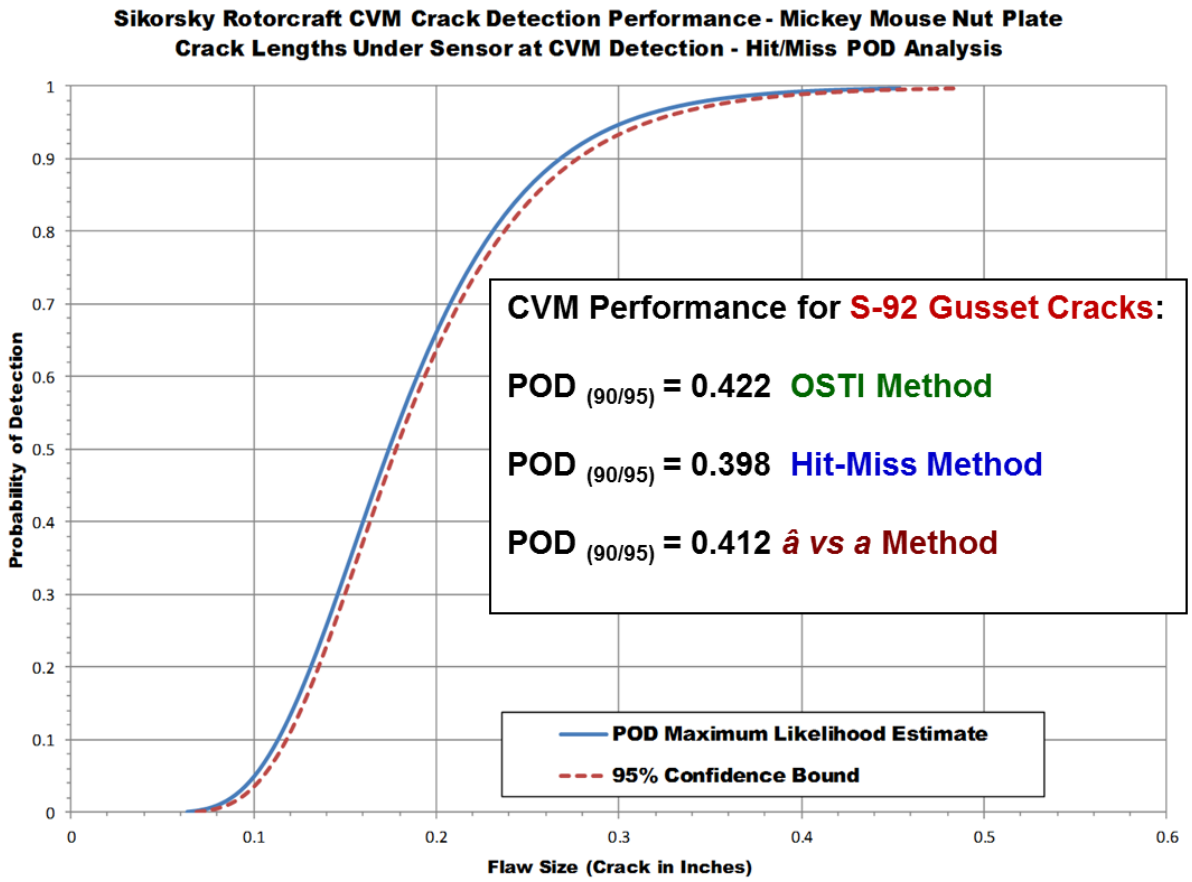

Figure 5-16. CVM Performance Testing Results – Comparison of OSTI, Hit-Miss, and a vs. â Methodologies for MM Nutplate on S-92 Frame Gusset

All Nutplates

Table 5-9 presents the full set of CVM crack detection data when data for the 38 cracks monitored on both the straight and Mickey Mouse nutplate specimens. When the data from all nutplates are combined into one analysis, the resulting OSTI calculations are presented in Table 5-9. The K (probability) factor is reduced because of the larger number of data points (38) from both nutplates. As a result, the overall POD for any cracks associated with the S-92 Frame Gusset is reduced slightly. Also, the average total crack length at detection of 0.309" (including the sensor offset) is closer to the overall $POD_{(90/95)}$ value for CVM crack detection from the all nutplates which was calculated to be 0.412". There were no False Calls associated with any of the nutplate tests.

Note that the combined data produces 38 independent data points which is much closer to the desired 50 independent data points used in the Hit-Miss POD Method. Similar data extrapolation techniques as those described above were used to produce the additional 12 data points. The Hit-Miss Log Regression POD method was applied to these 50 data points to calculate the overall $POD_{(90/95)}$ value of 0.274" for the crack length under the sensor. When this is added to the average sensor offset (Distance from Hole) of 0.127", the total crack length $POD_{(90/95)}$ = 0.401" as shown

in Figure 5-17. These results from the Hit-Miss POD Method for the straight, Mickey Mouse and combined set of nutplates are intercompared in Figure 5-18. All POD levels are quite similar.

Final, overall $POD_{(90/95)}$ values from the OSTI, Hit-Miss and *â vs a* POD Methods for each of straight, Mickey Mouse and combined set of nutplates are intercompared in Table 5-10. All three methods produced similar results even though the Hit-Miss and *â vs a* POD Methods required the use of some assumed, extrapolated data. If the assumed data is representative (additional tests produced independent data that is equivalent to the repeated measures assumed data) as is indicated by the extensive database of CVM testing, then the resulting Hit-Miss and *â vs a* calculations are close to the truth. *In any case, the CVM performance certification results will only be taken from the OSTI results.* In addition, the final performance assessment may include some level of conservative enveloping to assign overall CVM crack detection performance for the S-92 Frame Gusset application.

Table 5-9. POD for CVM Monitoring All Nutplate Cracks on S-92 Frame Gusset – Determined Using the One-Sided Tolerance Interval Method

CVM Crack Detection Data

Distance from Hole to Sensor Edge	Total Crack Length a (in)	Crack Length Under Sensor at CVM Detection a (in)	Log of Crack Length at CVM Detection a (ln)
0.139	0.241	0.102	-0.991399828
0.139	0.352	0.213	-0.671620397
0.152	0.264	0.112	-0.950781977
0.137	0.248	0.111	-0.954677021
0.142	0.291	0.149	-0.826813732
0.127	0.284	0.157	-0.804100348
0.132	0.295	0.163	-0.787812396
0.15	0.366	0.216	-0.665546249
0.144	0.350	0.206	-0.68613278
0.139	0.287	0.148	-0.829738285
0.149	0.346	0.197	-0.705533774
0.140	0.319	0.179	-0.747146969
0.151	0.474	0.323	-0.490797478
0.131	0.256	0.125	-0.903089987
0.145	0.280	0.135	-0.869666232
0.154	0.317	0.163	-0.787812396
0.141	0.354	0.213	-0.671620397
0.133	0.354	0.221	-0.655607726
0.136	0.376	0.240	-0.619788758
0.13	0.268	0.138	-0.860120914
0.106	0.217	0.111	-0.954677021
0.119	0.299	0.180	-0.744727495
0.123	0.248	0.125	-0.903089987
0.113	0.248	0.135	-0.869666232
0.14	0.382	0.242	-0.616184634
0.096	0.374	0.278	-0.555955204
0.101	0.321	0.220	-0.657577319
0.124	0.270	0.146	-0.835647144
0.097	0.226	0.129	-0.88941029
0.106	0.287	0.181	-0.742321425
0.100	0.321	0.221	-0.655607726
0.110	0.279	0.169	-0.772113295
0.112	0.280	0.168	-0.774690718
0.095	0.409	0.314	-0.503070352
0.127	0.325	0.198	-0.70333481
0.114	0.333	0.219	-0.659555885
0.134	0.327	0.193	-0.714442691
0.081	0.258	0.177	-0.752026734

Average Crack Length at CVM Detection =	**0.182**
Standard Deviation of CVM Detection =	**0.054**
Average Dist From CVM Edge to Hole Edge =	**0.127**

Statistic Estimates on Log Scale

Statistic	Value (in.)	Value in Linear Scale
Mean (X)	-0.757	0.182
Stnd Deviation (S)	0.1249907	0.053507

POD Detection Levels
(ɣ = 95%, n = 38)

Flaw Size: POD = X + K(S) =	0.286

POD for CVM Monitoring of Cracks in S-92 Frame Gusset

Overall POD (with sensor offset) = 0.412”

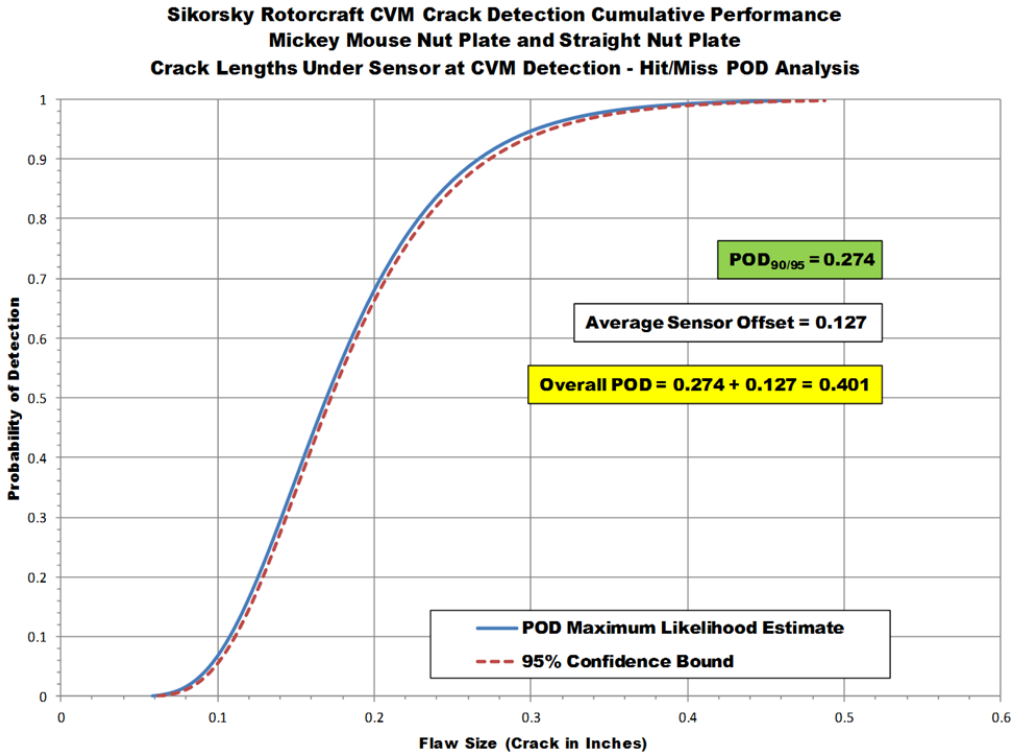

Figure 5-17. POD for CVM Monitoring All Nutplate Cracks on S-92 Frame Gusset – Determined Using the Hit-Miss Method

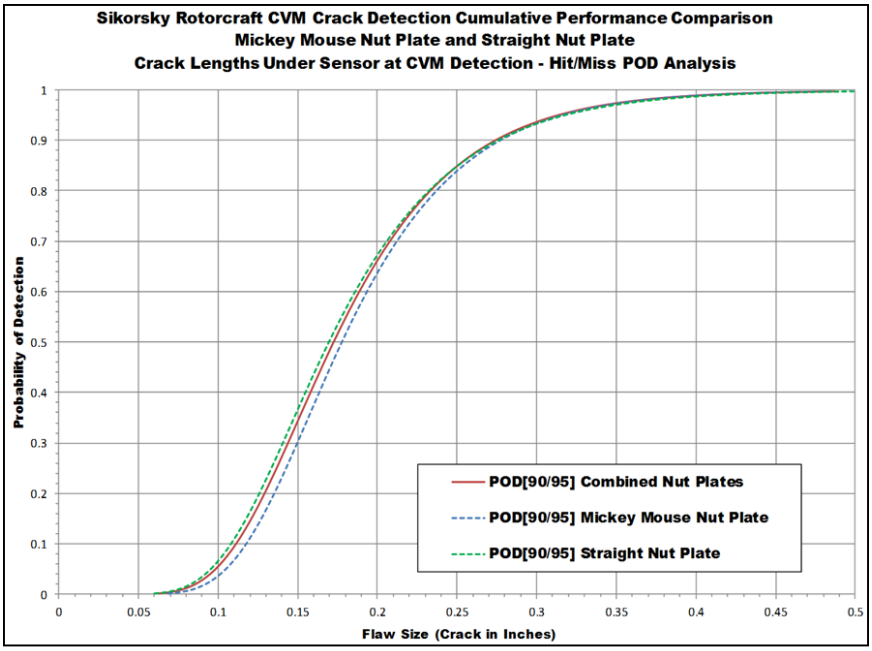

Note: sensor offset values (distance from crack origin to sensor engagement) must be added to POD levels plotted above)

Figure 5-18. Comparison of POD Levels for Each Nutplate and Overall Combined for CVM Crack Detection in Rotorcraft Frame Gusset

Table 5-10. Comparison of CVM $POD_{(90/95)}$ Values for Different Conditions and Analysis Methods

CVM Performance for Straight Nutplate:

$POD_{(90/95)}$ = 0.447 OSTI method

$POD_{(90/95)}$ = 0.416 Hit-Miss method

CVM Performance for Mickey Mouse Nutplate:

$POD_{(90/95)}$ = 0.422 OSTI method

$POD_{(90/95)}$ = 0.398 Hit-Miss method

$POD_{(90/95)}$ = 0.412 *â vs a* Method

Overall CVM Performance for Both Nutplates:

$POD_{(90/95)}$ = 0.412 OSTI method

$POD_{(90/95)}$ = 0.401 Hit-Miss method

5.2. Durability Assessments - Environmental Testing of CVM and PZT Sensors

In addition to the crack detection performance data, it is also important to conduct tests to evaluate the environmental durability of the SHM system. It is an indispensable step to carry out validation tests for any SHM systems under operational environments before it becomes an application-ready product. This testing is meant to establish the durability level of the sensors so that operators can ensure that it is deploying something that will sustain operations over a long period of time and not be a major inconvenience during subsequent maintenance. Structural health monitoring systems often experience harsh environments which can, even in the absence of damage, create varying, nonlinear and nonstationary behaviors. These response changes must be understood and either mitigated or incorporated into any damage detection algorithms to avoid any reduction in the performance of the SHM system. When considering overall durability assessments, it is important to make sure that all operating conditions that may affect SHM system response are properly included in the test program. This has been recommended in numerous SHM performance processes and demonstrated in studies on specific SHM sensor systems [5.2 – 5.3]. The overall goal is to assess the topics of durability, reliability, and longevity and to develop and apply a suitable criteria to properly assess SHM system performance in representative operating environments. Environmental tests may include, for example, temperature extremes, humidity, fluid susceptibility, altitude, mechanical connections, structural strain and component vibration.

5.2.1. Extreme Environment Cycling

Durability testing of CVM has been addressed in a number of studies [5.4 - 5.5]. A companion FAA program completed its own set of tests to comprehensively and independently add to this referenced database and arrive at a proper conclusion about the operation of CVM sensors over long periods of time [5.1]. The results from that assessment are summarized here. There are existing standards that address testing for the durability of commercial and military aircraft components [5.6] and these were utilized in the CVM durability testing described here. The environmental conditioning tests are described in Section 4.5 and consisted of the following elements:

1) Hot-Wet Conditioning (55°C ± 3°C and 95% ± 3% RH) - 28 days, monitor every 7 days.
2) Cold/Freeze/Icing - (8 hours @ -18°C) followed by monitoring after each freeze cycle.
3) Heat Exposure (8 hours @ 74°C) - followed by monitoring after each extreme heat exposure.

The CVM sensors were monitored during the time periods indicated in Figure 4-57. Recall that the sensors were installed on undamaged structure and the status of that structure did not change during the course of the 40 days of environmental testing. Thus, the optimal results would be for the CVM sensors to function properly and also produce consistently low dCVM values (i.e. no crack detected) over the entire time of the tests. Results from CVM readings during the Environmental Durability tests indicate that:

- Sensor readings during 40 day environmental tests remained small compared to the threshold level required for crack detection (see Figure 5-19)
- dCVM values ranged +/- 2.0 while the crack detection threshold was set for dCVM = 10.0
- Good durability of CVM system; no degradation
- Signal-to-noise (S/N) for crack detection is a minimum of 5 (most exceeded 20 in fatigue tests)
- Desired S/N for normal NDI operations is a minimum of 3.

Similarly, there should be no change in the status of the galleries over the course of the durability testing. Continuity checks are conducted by the PM200 device to ensure that each gallery has proper flow and is not blocked or otherwise restricted in any way. This test must be passed before any crack detection readings are acquired. Regardless of the status of the structure (damaged or undamaged), the optimal results would be for the CVM sensors to provide consistently high continuity (flow rate) values over the entire time of the tests. Results from CVM readings during the Environmental Durability tests indicate that:

- Sensor continuity measures for possible gallery blockage. During 40 day environmental tests, continuity remained large indicating proper sensor functioning and no blockage in the galleries (see Figure 5-20).
- Continuity values ranged 6,000 to 12,000; minimum levels allowed were Cont = 2,000.
- Good durability of CVM system; no degradation.

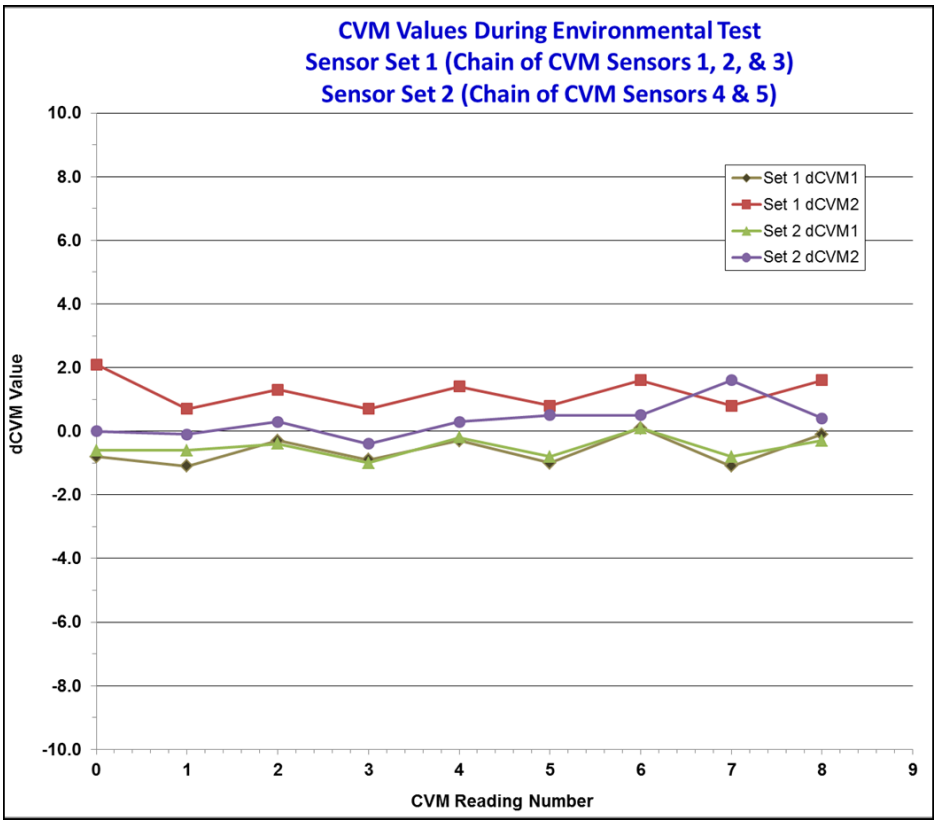

Figure 5-19. CVM Sensor Readings Remain Unchanged During Environmental Test

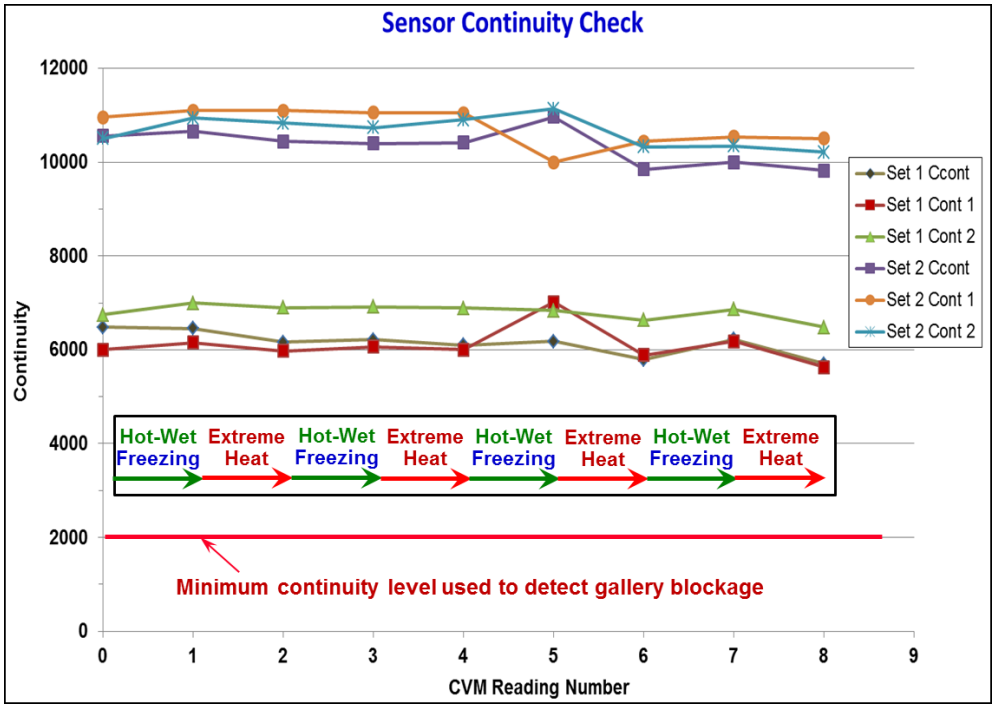

Figure 5-20. CVM Sensor Continuity Levels Remain Unchanged During Environmental Tests

The data above corresponds to the sensor groupings of Set 1= CVM1, CVM2, CVM3 and Set 2= CVM4, CVM5 as they are grouped on the 737 Wing Box fittings. Data was also acquired to show that the individual sensors maintained consistent dCVM and continuity readings before and after 40 day environmental tests. Figure 5-21 and Figure 5-22 show that there was no change in either the dCVM or continuity values and thus, no effect of 4 cycles of extreme hot-wet-cold-heat environment on CVM performance.

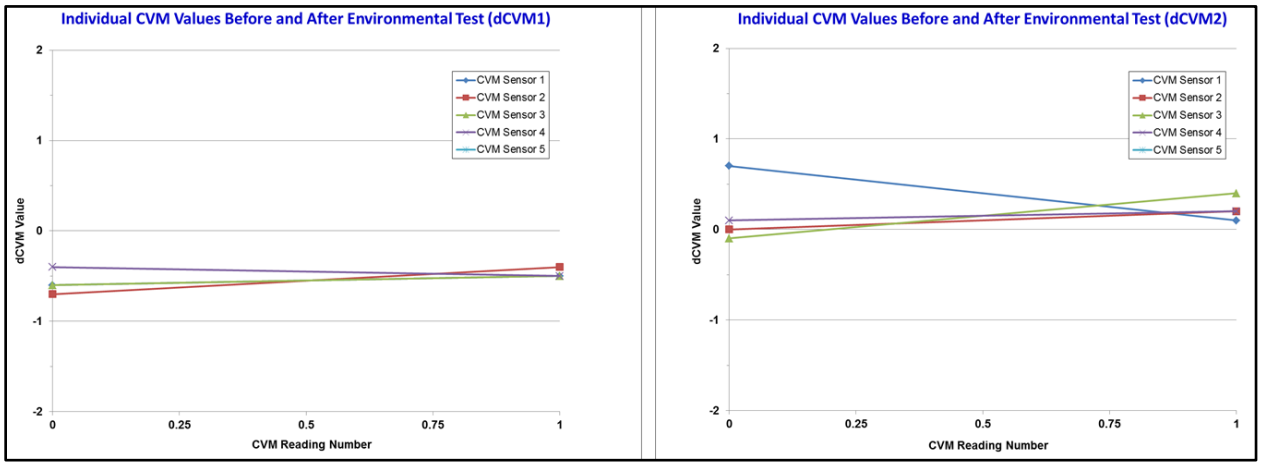

Figure 5-21. Individual CVM Sensor Readings Remain Unchanged

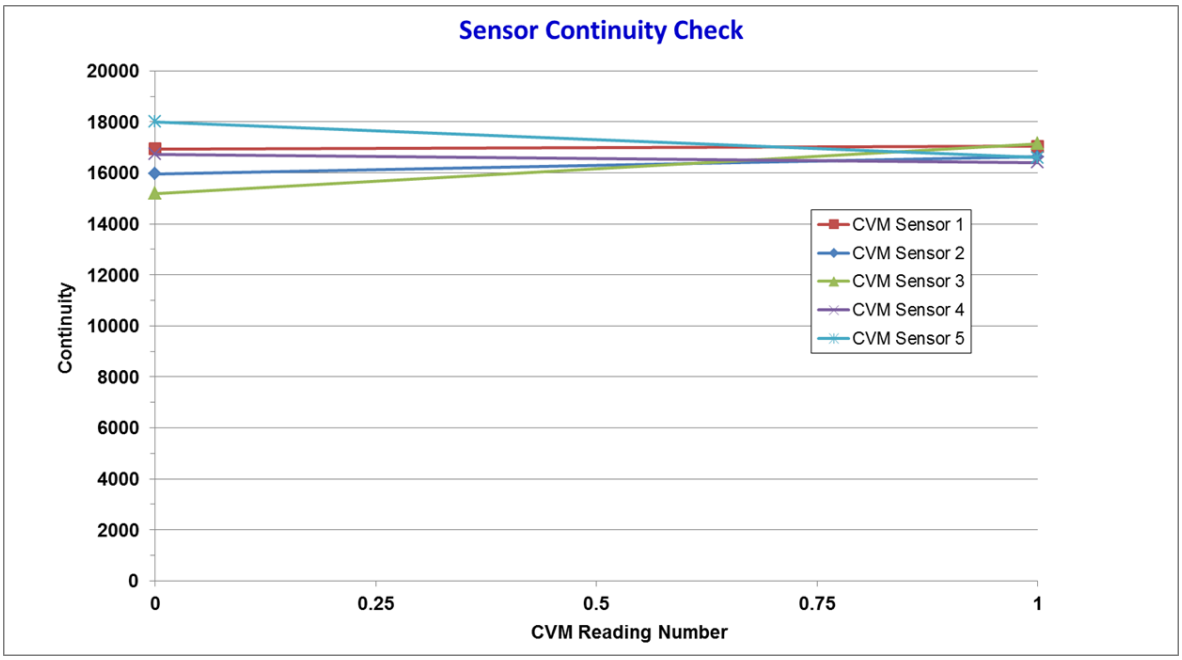

Figure 5-22. Individual CVM Continuity Readings Remain Unchanged

5.2.2. Exposure to Corrosion Inhibiting Compounds

Effect of Corrosion Inhibiting Compounds on CVM POD Performance - A focused study was also conducted to assess the effects of exposure to other materials that may exist in aircraft structures [5.1]. Specifically, in these tests CVM sensors were exposed to an array of Corrosion Inhibiting Compounds (CIC) to assess any effect on sensor performance. The objective was to provide confidence in the ability of CVM sensors to function properly and detect cracks even in the presence of CICs during crack growth. The test set-ups produced extreme exposure levels for conservative assessments. One of the key assumptions was that a small crack exists in the structure such that it is currently not detectable by CVM but could possibly allow for CIC ingress.

The test specimens were composed of a 2.5" wide plate with a doubler plate riveted to the back (material = 7075-T6). Figure 5-23 shows the test specimen design. Two rows of rivets were used to connect the two plates, however, the upper rivet row was only the single center hole to ensure controlled crack growth at this hole with the highest center stress. The single rivet also provided more space for additional CVM sensor placement as the cracks grew so that more data could be acquired from each specimen. CIC had access to the CVM sensors via wicking into the joint and along a rivet shank. No sealant was placed in the faying surface between the parent plate and the doubler to allow for maximum CIC ingress. Fatigue cracks were initiated in the specimen from the starter notches in the upper rivet hole. Cracks were propagated to a length of 0.050" or slightly longer but kept to a length that might exist prior to CVM crack detection. CIC was applied in normal application spray fashion and was applied to the front and back side of the test specimens. Fatigue loads were applied to grow the crack until permanent alarm (crack detection) was achieved by the CVM sensor. Figure 5-24 shows the application of the CIC to produce a permanent elastomeric coating on the primer surface.

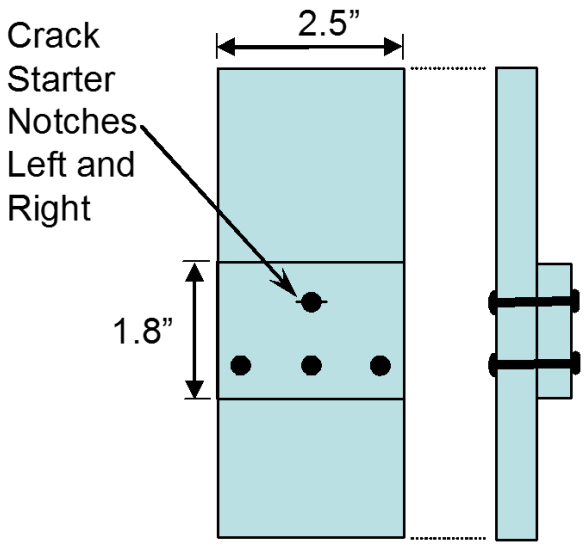

Figure 5-23. Schematic of Test Specimen used to Assess CIC Affects on CVM Operation

Figure 5-24. Application of CIC Compounds (Corban-35 and AV-8) to Test Specimens Prior to Fatigue Crack Growth

Crack Detection Results with and without CIC:

- After the application of the CIC to the cracked specimens, it was observed that no CIC was drawn into CVM galleries. Related to this, the galleries did not experience any blockage during the CIC testing.
- The crack detection results from all test specimens are summarized in Table 5-11 and Table 5-12 for Corban-35 and AV-8 CIC liquids, respectively. POD levels determined from testing with and without CIC:

$POD_{(90/95)}$ = 0.011" without CIC (16 data points)
$POD_{(90/95)}$ = 0.013" with Corban-35 CIC in place (10 data points)
$POD_{(90/95)}$ = 0.018" with AV-8 CIC in place (6 data points)
$POD_{(90/95)}$ = 0.015" with any CIC in place (16 data points)

Since this POD variation is within experimental deviations, the conclusion is that there is no appreciable difference in CVM crack detection performance (POD) with or without the presence of CIC. CIC did not affect normal CVM operation.

Table 5-11. CVM Performance in the Presence of CIC Compounds (Corban 35)

CVM Results without CIC Present			
Panel	Fastener Crack Site	Number of Fatigue Cycles	Crack Length at CVM Detection (growth after install in inches)
1	1-L	3400	0.009
1	1-R	2400	0.011
1	2-L	6200	0.013
1	2-R	6000	0.014
1	3-L	6702	0.015
1	3-R	6702	0.004
2	1-R	3200	0.010
2	2-R	4850	0.006
2	3-L	5450	0.014
2	3-R	5450	0.018
3	1-L	3725	0.012
3	1-R	2925	0.006
3	2-L	4800	0.004
3	2-R	4600	0.008
3	3-L	5325	0.016
3	3-R	5230	0.005
Average Crack Length			0.011

Description: 0.040" thick panel (primer surface)

7075-T6 Alum.

CVM Results in Presence of CIC (Corban-35 CIC)		
Panel	Sensor	Lag (inch)
3C	1-R	0.012
4C	1-L	0.016
3C	2-R	0.010
4C	2-L	0.009
4C	3-L	0.019
3C	3-R	0.012
3C	4-R	0.026
4C	4-L	0.013
2C	1-L	0.010
2C	2-L	0.006
Average Crack Length		0.013

Table 5-12. CVM Performance in the Presence of CIC Compounds (AV-8)

CVM Results without CIC Present			
Panel	Fastener Crack Site	Number of Fatigue Cycles	Crack Length at CVM Detection (growth after install in inches)
1	1-L	3400	0.009
1	1-R	2400	0.011
1	2-L	6200	0.013
1	2-R	6000	0.014
1	3-L	6702	0.015
1	3-R	6702	0.004
2	1-R	3200	0.010
2	2-R	4850	0.006
2	3-L	5450	0.014
2	3-R	5450	0.018
3	1-L	3725	0.012
3	1-R	2925	0.006
3	2-L	4800	0.004
3	2-R	4600	0.008
3	3-L	5325	0.016
3	3-R	5230	0.005
Average Crack Length			0.011

Description: 0.040" thick panel (primer surface)

7075-T6 Alum.

CVM Results in Presence of CIC (AV-8 CIC)		
Panel	Sensor	Lag (inch)
1D	1-L	0.007
1D	2-L	0.014
2D	1-R	0.030
2D	2-R	0.020
2D	3-R	0.017
2D	4-R	0.018
Average Crack Length		0.018

Overview of Effects of CIC on CVM - It should be noted that while no wicking of CIC or otherwise adverse effects of CIC on CVM performance were noted, any wicking of a liquid or other obstruction such as dust particles into a CVM sensor will result in blockage of the galleries. In such cases, the sensor will fail the initial positive flow test prior to any acquisition of data. The PM200 device will indicate a failure in this positive flow measurement (Continuity level too low) and the sensor will need to be revisited – and possibly replaced – before any crack detection data can be acquired. Thus, blockage in the sensor galleries will produce a fail-safe action and not result in the acquisition of erroneous data.

In the case of CIC application over CVM sensors, it was determined that CIC coatings can be safely applied two hours after CVM sensor installation. However, in the event that a CIC – or any other liquid application around CVM sensors – is applied such that it affects the adhesive between the sensor and the surface it is monitoring, the vacuum readings (dCVM values) will be affected and revealed during the PM200 monitoring process. This will indicate that the sensor needs to be checked. Once again, this result will correspond to a fail-safe response and a reinstallation of the sensor before any erroneous data or false calls are recorded.

5.3. CVM Flight Test Results

A number of different flight test series, several of them still underway, have been conducted with CVM sensors. These flight test series are conducted to assess the performance of CVM sensors on operating aircraft. The first test series, conducted during the first decade of 2000, placed CVM sensors in regions that were not expected to experience any cracking. For this reason, the flight tests were considered CVM installations in "decal mode" (i.e. no damage). The purpose of this initial test series was to explore general installation, operation and monitoring of CVM sensors by airline personnel while also assessing the durability of the sensors when exposed to real flight conditions. Different sensor designs were installed in various aircraft regions without any particular application in mind. The second test series, summarized here and discussed in detail in Ref. [5-1], was conducted in association with the 737 Wing Box fitting program. CVM sensors, designed to monitor the actual Wing Box fitting, were installed on the set of ten Wing Box fittings, on seven different 737 aircraft that were operating in the Delta Air Lines fleet. Overall, these flight tests allowed for the accumulation of over 1.5 million successful flight hours of CVM operation. In general, flight tests provide critical information about the long-term performance, reliability, durability and continued airworthiness of flying components

Flight Test of CVM Sensors for Wing Box Fitting Application - The SHM certification and integration activity for the 737 Wing Box fitting included both controlled laboratory-based testing and field testing. In addition to the lab performance tests described above, a set of 68 sensors were mounted on Wing Box fittings in seven different B-737 aircraft in the Delta Air Lines fleet. The sensors were monitored every 90 days for over four years, producing over 1,200 sensor response data points. These flight tests demonstrated the successful, long-term operation of the CVM sensors in actual operating environments.

Important topics to study during the flight tests included: 1) complete SHM indoctrination and training for Delta personnel (ranging from management to A&P mechanics) in all pertinent departments such as engineering, maintenance, NDI, supply and logistics, 2) formal modifications to integrate SHM into airline maintenance programs (hardware specifications, installation procedures, operation processes, inspection process, continued airworthiness instruction), and 3) Assess aircraft maintenance depots' ability to safely adopt SHM and the FAA support needed to ensure airworthiness.

A total of 10 sensors were used to monitor the 10 Wing Box fittings in each 737 aircraft. Several sensors on each side of the aircraft were connected in series (daisy-chained) to single SLS connectors. The ten sensors were daisy-chained into sets of 2 and 3 (left side of wing box) and sets of 2 and 3 (right side of wing box) such that they could be monitored by 4 SLS connectors. Figure 5-25 and Figure 5-26 provide an overview of the CVM installations on the Wing Box fittings

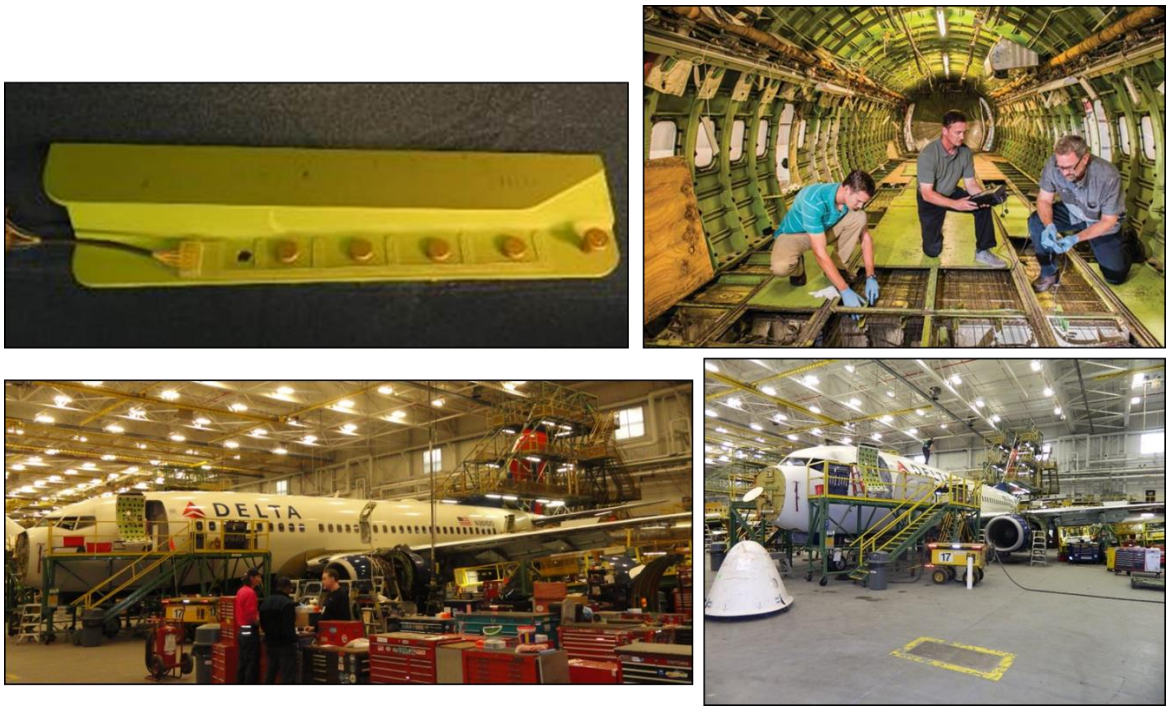

Figure 5-25. Overview of CVM Sensor Installations on Wing Box Fittings at Delta Facility

Subsequent monitoring of the CVM sensors was conducted during an overnight stay of the aircraft at the Atlanta airport. Rapid sensor interrogation with minimum access time allowed the inspections to be completed at the airport gate during overnight parking. After the aircraft arrived at its gate from its final flight of the night, Delta personnel from the Delta-Atlanta maintenance facility (Delta Tech Ops) performed the CVM data acquisition. The basic steps in the CVM monitoring process are shown in Figure 5-27 and Figure 5-28 and include:

1) Complete routine calibration of PM200 equipment before acquiring any data.

2) Access the SLS connectors from the forward baggage compartment.
3) Connect to each SLS connector and acquire CVM data on PM200 device.
4) Log all results. Data is stored on PM200 for future plotting and comparisons for desired data trending. System responds with "Green Light" – "Red Light" message to indicate any cracks that are detected. Aircraft is available for its next flight.

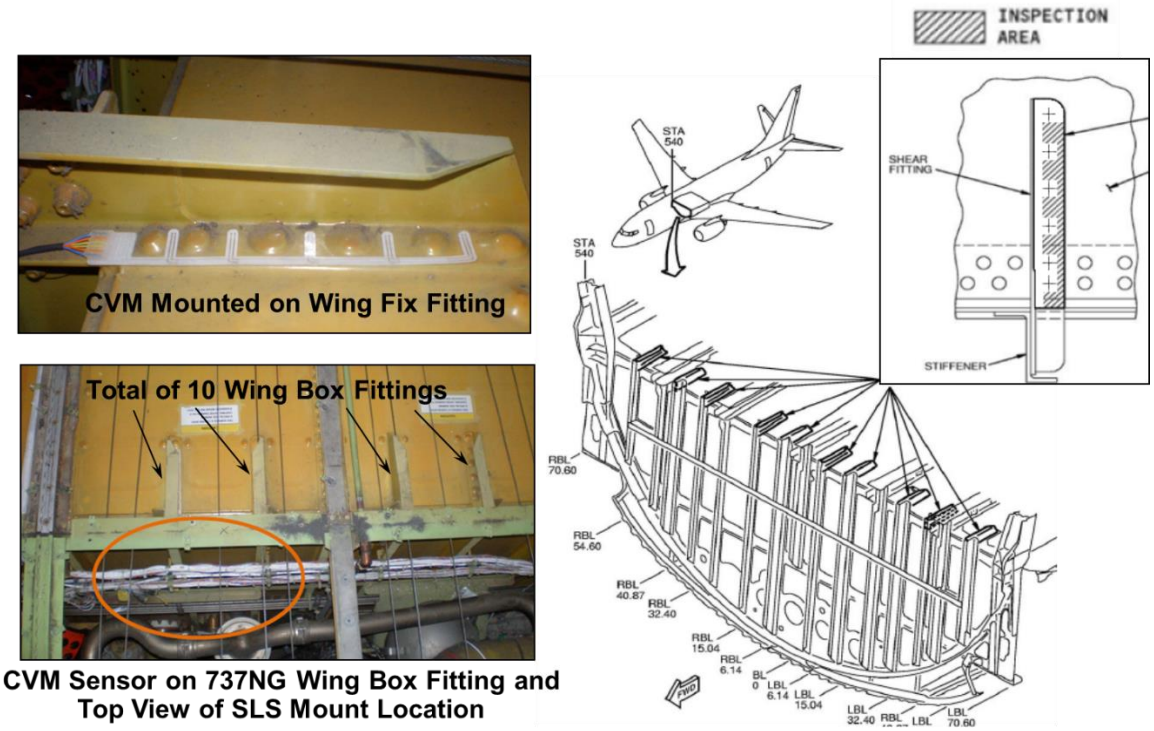

Figure 5-26. 737 Wing Box Area – Location of Ten Fittings and CVM Sensor to Monitor for Cracks in the Inspection Area Highlighted

Sample results from the first two years of operation for the seven Delta aircraft are presented in Figure 5-29 (A/C #3602) and Figure 5-30 (A/C #3603). Note that in all cases the dCVM levels should be low (for no crack detection; threshold for crack detection was determined to be 10). In all cases, the dCVM values were less than 2 (i.e. no crack detection). In addition to the low dCVM (no cracks present) readings, the data was observed to be repeatable and consistent during the monitoring period. While the initial goal was to acquire 18 months of operational data from the seven sensor networks, Delta Air Lines continued to monitor these aircraft for additional months. Several examples of extended data results are also presented here. Figure 5-31 and Figure 5-32 show additional CVM data points for aircraft 3601 and 3605, respectively. The 90 day inspection cycles for obtaining CVM data was continued so each data point represents approximately 90 days of operation. Thus, the 22 to 23 data points in these figures represent almost 6 years of proper CVM sensor operation on the 737 Wing Box fitting installations.

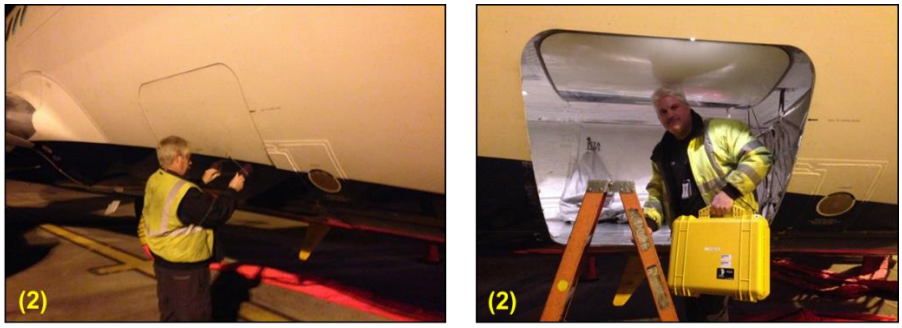

Figure 5-27. Monitoring CVM Sensors on 737NG Center Wing Box Fittings – Access to SLS Connectors through Forward Baggage Compartment

Figure 5-28. Monitoring CVM Sensors on 737NG Center Wing Box Fittings – Connecting to SLS Connectors and Acquiring Data on PM200 Monitoring Device

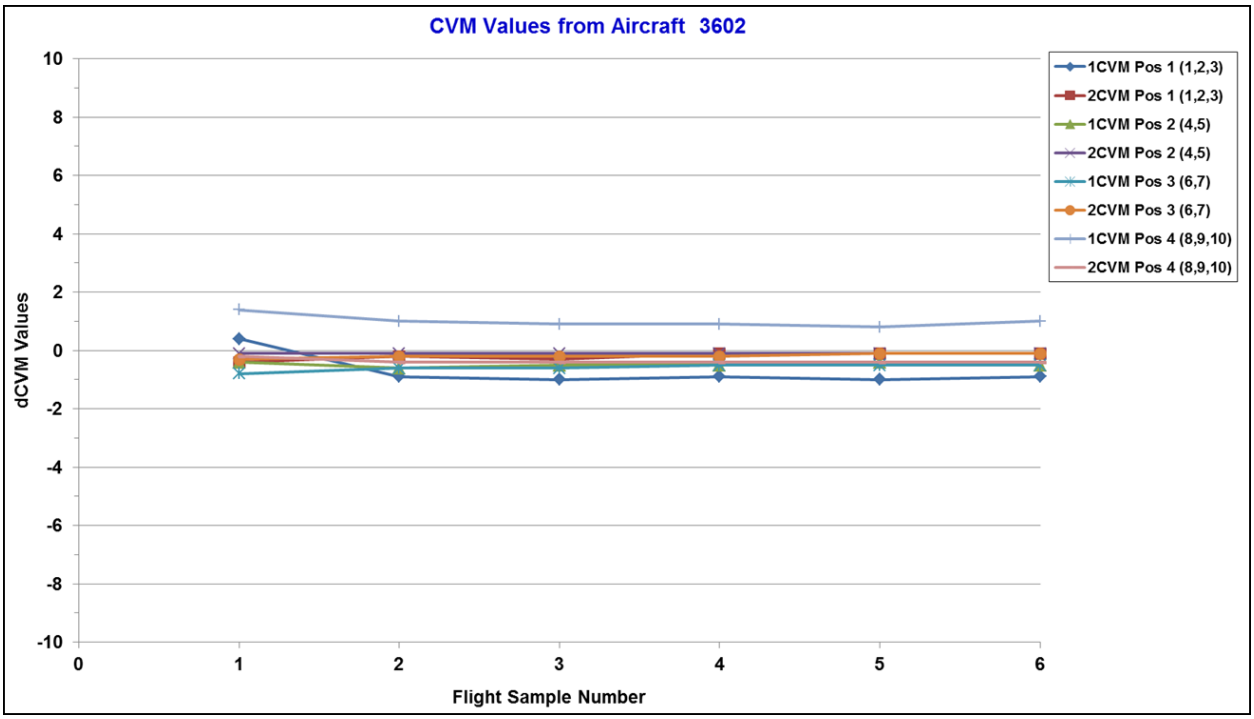

Figure 5-29. CVM Sensor dCVM Check for Delta Air Lines Aircraft 3602

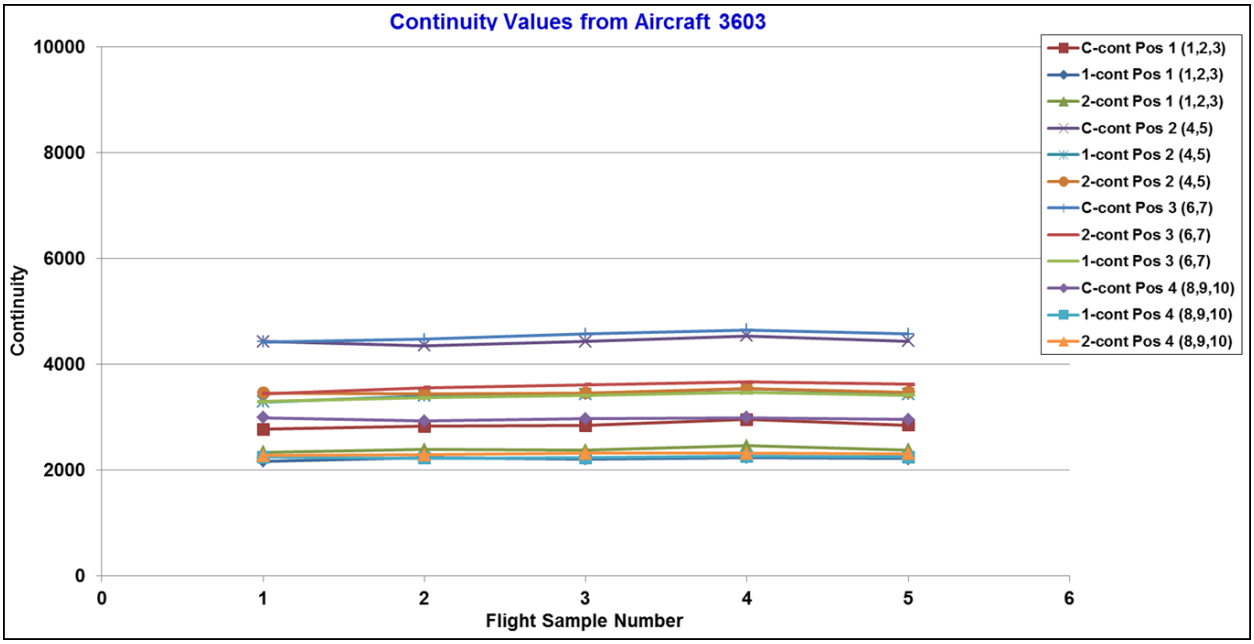

Figure 5-30. CVM Sensor dCVM Check for Delta Air Lines Aircraft 3603

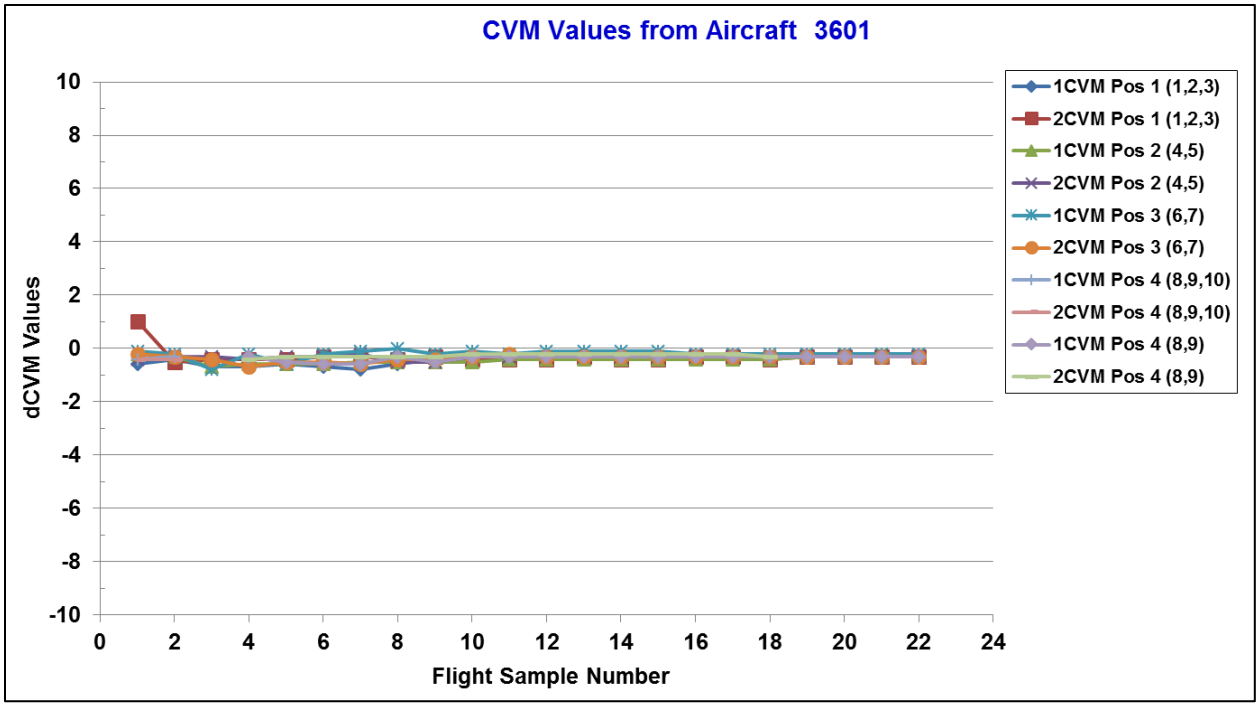

Figure 5-31. Long Term CVM Sensor dCVM Check for Delta Air Lines Aircraft 3601

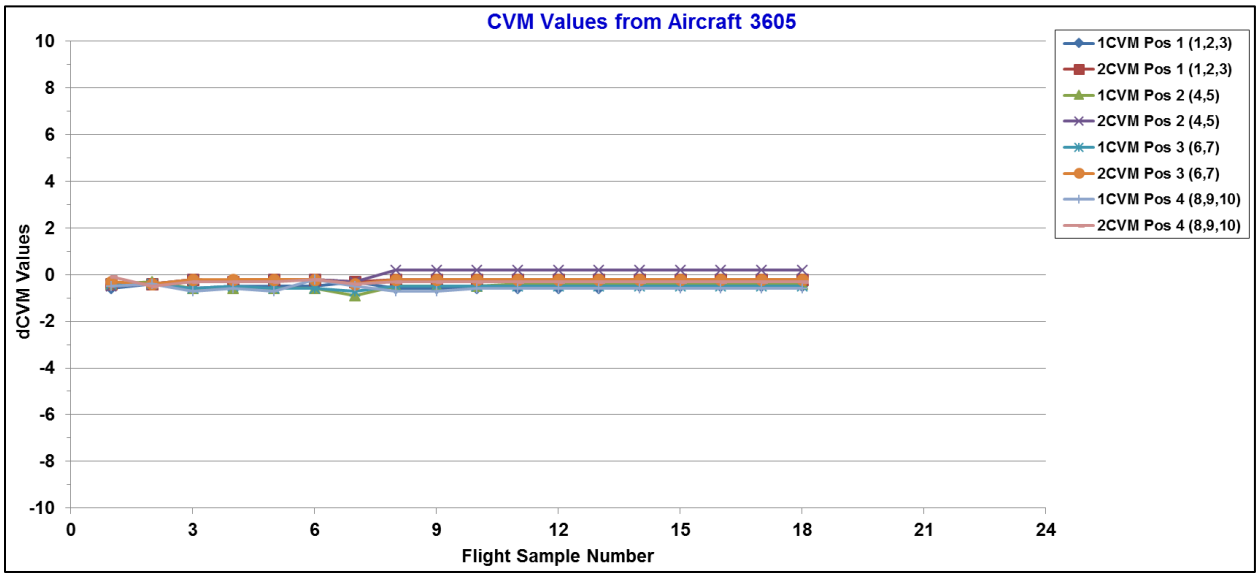

Figure 5-32. Long Term CVM Sensor dCVM Check for Delta Air Lines Aircraft 3605

Section 5.3 presents the results from 90 CVM sensor installations which were monitored for 5 years on 14 commercial aircraft. Data from the monitored sensors showed that, in all cases, the continuity numbers maintained the desired high levels while the dCVM levels remained in the low numbers associated with no crack detection. These flight test programs resulted in the

accumulation of over 1.5 million hours of successful operation (representing 50 combined years of operation on flying aircraft) and the acquisition of over 3,000 sensor monitoring data points. Two different flight test series were conducted to explore general installation, operation and monitoring of CVM sensors by airline personnel while also assessing the durability of the sensors when exposed to real flight conditions.

References

5-1 Roach, D., Rice, T., "Application and Certification of Comparative Vacuum Monitoring Sensors for Structural Health Monitoring of 737 Wing Box Fittings," Dept of Energy SAND2020-9184, September 2020.

5-2 Hong, J., Cao, L., Laflamme, S., Dodson, J., "Robust Variable Input Observer for Structural Health Monitoring of Systems Experiencing Harsh Extreme Environments," International Workshop on Structural Health Monitoring, September 2017.

5-3 Wang, Z., Cai, J., Li, J., Liu, M., "A Validation Study for a New SHM Technology Under Operational Environment," Annual Reliability and Maintainability Symposium, January 2014.

5-4 Chambers, J., "Durability Testing of an Aircraft Structural Health Monitoring System," Masters Thesis, Dept. of Aeronautics and Astronautics, Massachusetts Institute of Technology, 2006.

5-5 Loader, C., "Durability of Continuous Vacuum Monitoring Sensor for ADF Applications," Defense Science and Technology Organization Report DSTO-CC-Q1694/01, 2004.

5-6 Radio Technical Commission for Aeronautics, "Environmental Conditions and Test Procedures for Airborne Equipment," DO160G, December 2014.

6. PZT PERFORMANCE ASSESSMENT

6.1. PZT Crack Detection

The PZT structural health monitoring approach was evaluated using in-situ networks of piezoelectric transducers as described in Section 2.3. The SHM system included the PZT network connected to portable, diagnostic hardware and software developed by Acellent Technologies, Inc. The system performs in-situ monitoring, data collection, signal processing, and real-time data interpretation to produce a two-dimensional image of the structure being interrogated. The Acellent software instructs the actuators to generate pre-selected diagnostic signals and transmit them to neighboring sensors. The wave propagation approach used both the pitch-catch and pulse-echo method for detecting damage in a structure. Changes in the Lamb Waves generated within the structure are used in concert with triangulation methods to detect the presence of structural anomalies and to determine the size and location of the flaws. Cracks, delaminations, shrinkage cavities, pores, disbonds, and other discontinuities that produce reflective interfaces can be detected. Complete reflection, partial reflection, scattering, or other detectable effects on the ultrasonic waves can be used as the basis for flaw detection.

6.1.1. Validation Process for PZT Structural Health Monitoring System

Crack detection was achieved on the Rotorcraft Beam Specimens described in Section 3.3 using the PZT SHM system and the data acquired at discrete intervals during the crack growth process. The test and data acquisition process were described in Section 4.4. Overall, the PZT system was set up to detect the fatigue cracks using the following methodology.

Damage Detection with PZT and Use of Damage Index Thresholds –

- Must accurately classify damage - optimize detection & minimize false calls
- Desire to simplify damage detection and location using a single parameter and associated graphics from the sum total of all wave transmission signals
- Want to provide Green Light/Red Light ("GO" – "NO GO") decisions on the presence of damage
- Baseline – undamaged structure; normal structural settling must be accommodated to avoid false calls; initial fatigue of fasteners or bond lines in joints
- PZT Damage Index (DI) is a damage classification method based on a statistical analysis of sensor-actuator pairs (paths) that quantifies changes in wave travel (compare current waveform set with "Baseline" signals from a pristine structure). Figure 2-35 and Figure 6-1 show the comparison between two different signals obtained at different times in a structures fatigue life. The difference between these two signals provides an indication of the DI and accumulation of damage or other changes in the structure.
- Damage "threshold" is determined by calibration of network response and the physics of the wave propagation changes for each monitoring scenario – referred to as "training" the PZT SHM system

- Signal-to-Noise Ratio – damage signal is much more severe than normal fretting and wear of joints in complex structures.
- The Damage Index, computed in equation (2-2) and shown pictorially in Figure 6-2, quantifies the deviation of a reconstructed signal from the original known input as a function of a signal's attenuation. The computed DI, also referred to as "*damage sensitive feature,*" can then be cast in the context of an outlier detection framework. This allows for damage classification based on statistical analysis.
- Figure 2-33 depicts how a statistically-guided damage threshold is set while Figure 2-34 shows how intelligent thresholds can be determined by using a plot of the Damage Index for a set of actuator-sensor pairs.

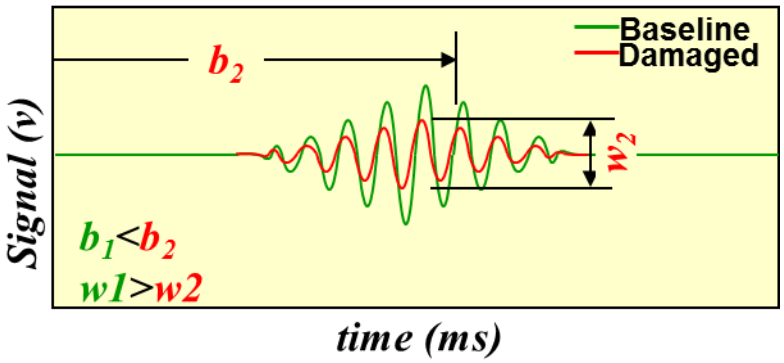

Figure 6-1. Change in PZT Response Signal Used to Detect Damage

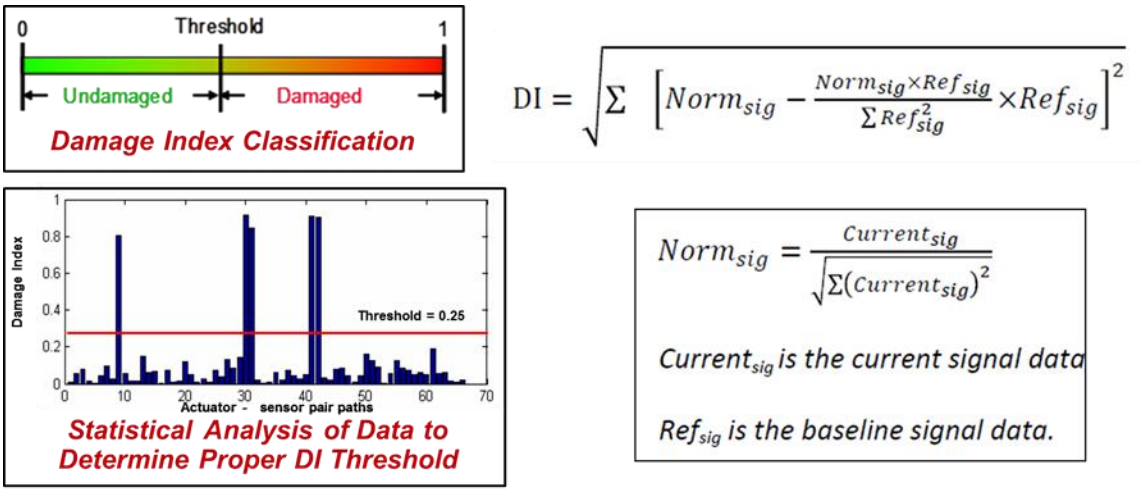

Figure 6-2. Damage Classification and DI Threshold Setting Using Statistical Analysis of Data

Figure 6-3 provides schematics of both the pitch-catch and pulse-echo mode for detecting damage in a structure. In the pitch-catch mode of sensor interrogation, a single sensor acts as a transmitter and all other sensors in the network act as wave receivers to produce the set of paths shown in

Figure 6-3. The sum total of received signals are then analyzed to define the presence and location of flaws. In the pitch-catch mode, a single sensor acts as both the transmitter and receiver at the same time to produce the series of reflective signal paths shown in Figure 6-3. To optimize flaw detection, a series of excitation frequencies were used: 200 KHz, 250 KHz, 300 KHz, 350 KHz, and 500 KHz. The DI threshold was set to 0.05 with the desire for producing suitable crack detection while also minimizing concern for producing false calls.

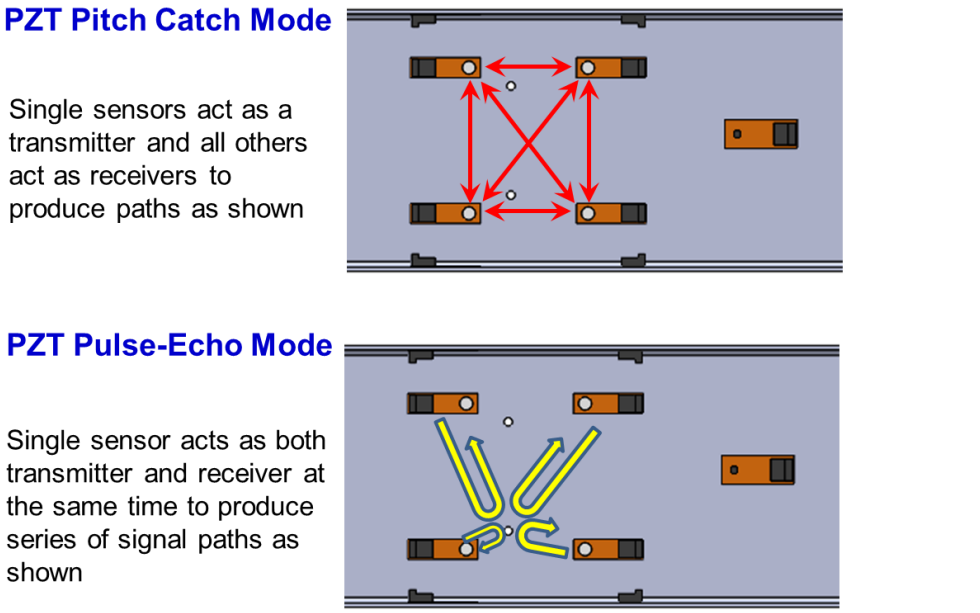

Figure 6-3. PZT Interrogation Modes for Damage Detection

Figure 6-4 shows raw PZT response data produced during the Lamb Wave interrogation method. It also shows two similar signals produced by different but symmetrical paths. Figure 6-5 shows PZT response signals before and after crack growth occurred into the sensor path. It compares two different signals obtained at different times in a structures fatigue life. The difference between these two signals, represented by the yellow curve in Figure 6-5, provides an indication of the DI and accumulation of damage or other changes in the structure. The crack growth can be clearly seen.

One of the concerns with any type of in-situ sensor method for health monitoring is how to accurately classify damage to avoid false calls and missed flaws. It is important to determine how to accurately establish a threshold for damage identification. Calibration testing can be performed to carefully relate controlled damage onset and flaw growth to sensor response. These laboratory-based "training" exercises can utilize neural network methods to optimize the recognition of structural anomalies. The Damage Index, computed using the method discussed in Section 2.3, quantifies the deviation of a reconstructed signal from the original known input as a function of a

signal's attenuation. PZT Damage Index (DI) is calculated from the difference between current signals and Baseline signals obtained from the pristine structure.

Figure 6-4. Check of PZT Signal Quality – Pitch-Catch Mode on Rotorcraft Beam Top Flange

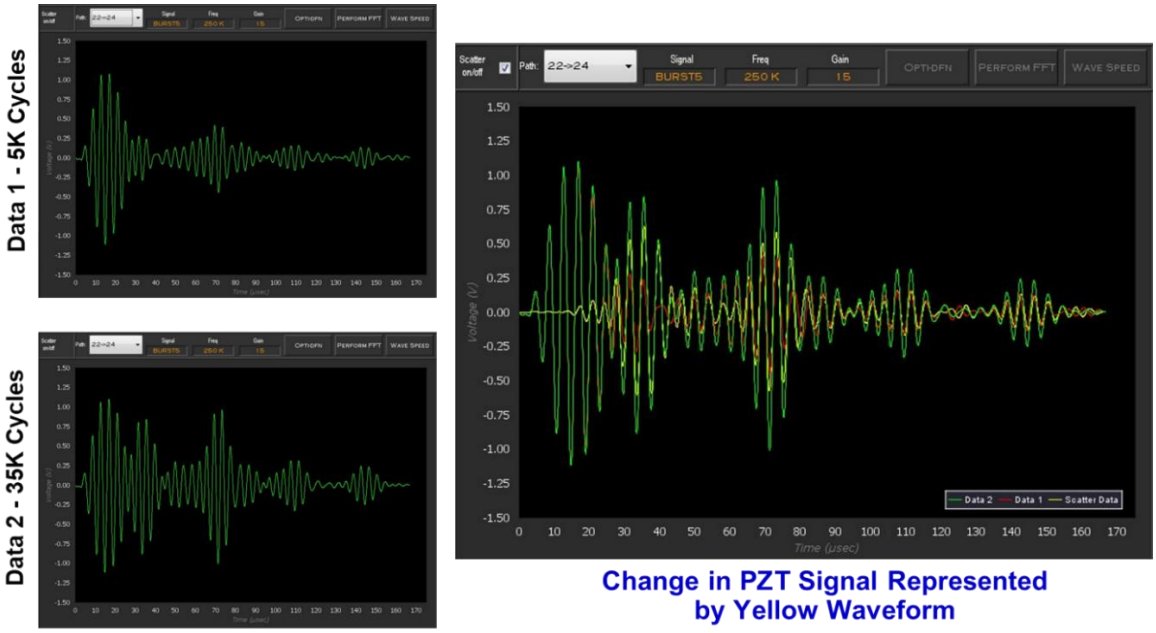

Figure 6-5. PZT Damage Index – Calculated from Difference Between Current Signals and Baseline Signals

A related criterion may involve establishing a damage detection threshold where a stable and steadily-rising SHM system response is observed. It is not uncommon for SHM systems to "temporarily" exceed a threshold, then drop below a threshold and finally move through a region of a steadily-increasing response that extends well above the threshold. Damage detection may

reliably be inferred when the SHM system enters this latter stage of response. Figure 6-6 and Figure 6-7 show two plots relating the calculated DI to the corresponding crack length. Figure 6-6 shows a continuously-increasing DI value with a damage detection threshold selected at an inflection point in the curve where the DI is increasing at a rapid rate compared to crack growth. The DI plot in Figure 6-7 is slightly different in that, prior to the onset of rapid DI increase (approximately at data point 8), there is minimal increase, and even a slight decrease, in the DI experienced. The selected DI for this data should be beyond such up-and-down DI fluctuations. The horizontal red line in Figure 6-7 shows that the selected threshold of DI=0.05 is well into the rapidly increasing range of the PZT network response. When all of the signals are analyzed with the Acellent imaging software and flaw locations are determined by using the time base and triangulation methods, a two dimensional image of the crack can be produced and this is shown on left side of Figure 6-7 superimposed over the PZT sensor layout.

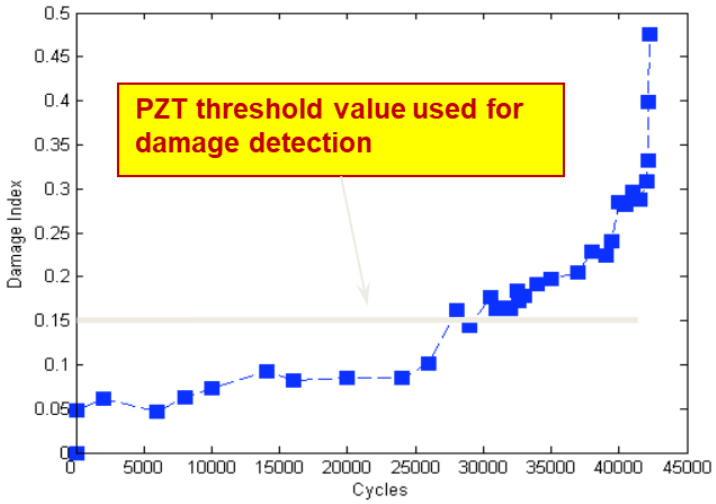

Figure 6-6. SHM Information – Setting Damage Threshold for Clear Detection and No False Calls

Figure 6-8 and Figure 6-9 show DI histograms indicating the number of paths below the DI(threshold), represented by green bars, and the number of paths that exceed the DI(threshold), represented by red bars. The actual DI(threshold) is also shown by a yellow bar at the DI = 0.05 level. The increase in DI is apparent as the crack grows (see fatigue cycles listed). The official criteria for damage detection can include a single path exceeding the DI(threshold) or more than one path exceeding the DI(threshold). Preliminary tests were used to establish a suitable threshold for the Damage Index (DI) to create the necessary sensitivity for damage detection without producing false calls. Figure 6-10 shows multiple forms of data calculated by the Acellent PZT system. These include the PZT network paths, DI vs crack growth plot, the DI histogram and the two-dimensional image of the PZT region. The presence of damage within the network is evident by the darker square in the center of this latter image.

Figure 6-11 and Figure 6-12 compare DI vs crack growth plots for different specimens and show how this DI varies initially but clearly rises to exceed the DI(threshold) line shown at the DI = 0.05 level on the plots. Note the specimens RB-PZT-9, -12, and -15 show some fluctuations and

reversal in DI levels early in the crack growth while specimen RB-PZT-11 has an ever-increasing DI level. In both cases, the DI(threshold) line is shown to be well above any of these fluctuations.

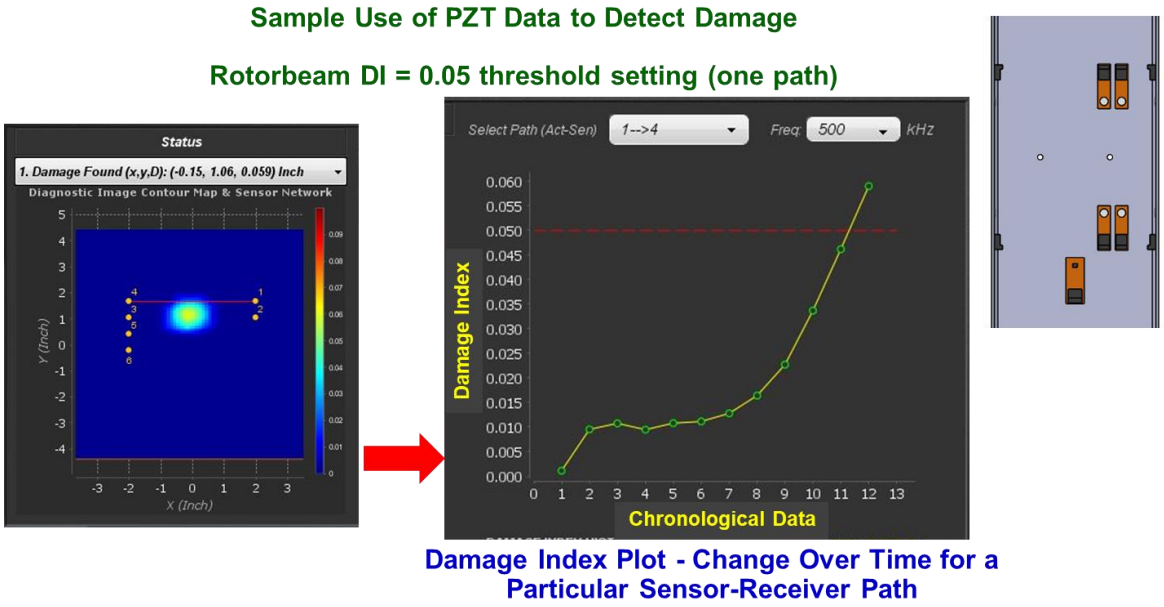

Figure 6-7. PZT Damage Index – Threshold Exceedance and Number of Paths Above Threshold = Damage Detection

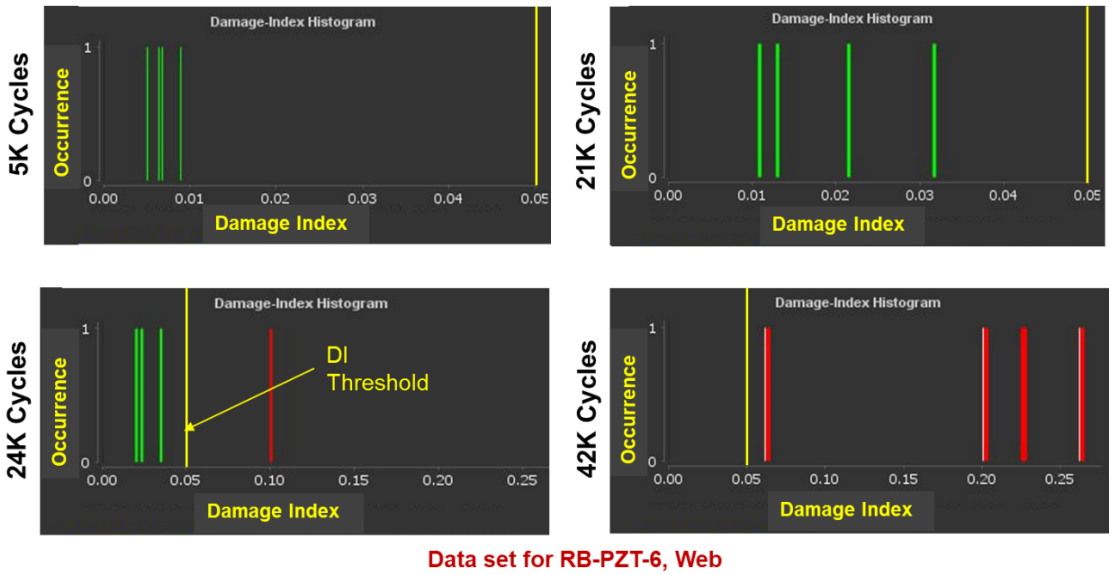

Figure 6-8. "Green Light" (Below)-"Red Light" (Above) Plots of DI Levels Indicating the Number of Paths Above and Below the Selected DI Damage Threshold for Different Fatigue Crack Lengths (RB-PZT-6 Web)

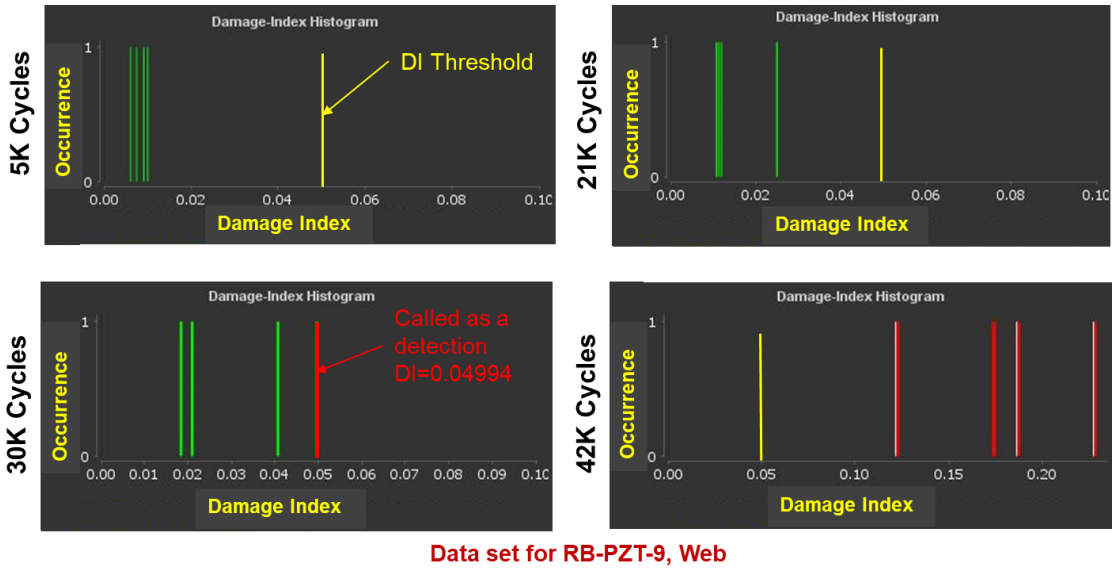

Figure 6-9. "Green Light" (Below)-"Red Light" (Above) Plots of DI Levels Indicating the Number of Paths Above and Below the Selected DI Damage Threshold for Different Fatigue Crack Lengths (RB-PZT-9 Web)

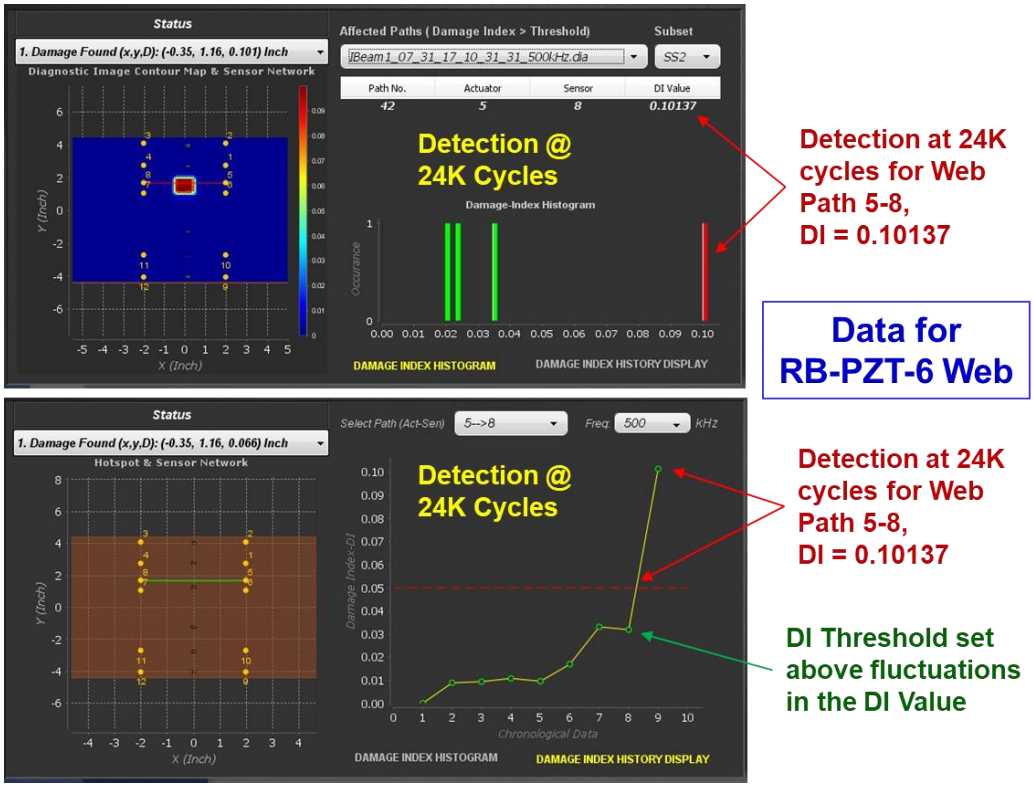

Figure 6-10. DI Histogram Indicating Threshold Exceedance and DI Level Plot Over the Crack Growth and Detection in Specimen RB-PZT-6 Web

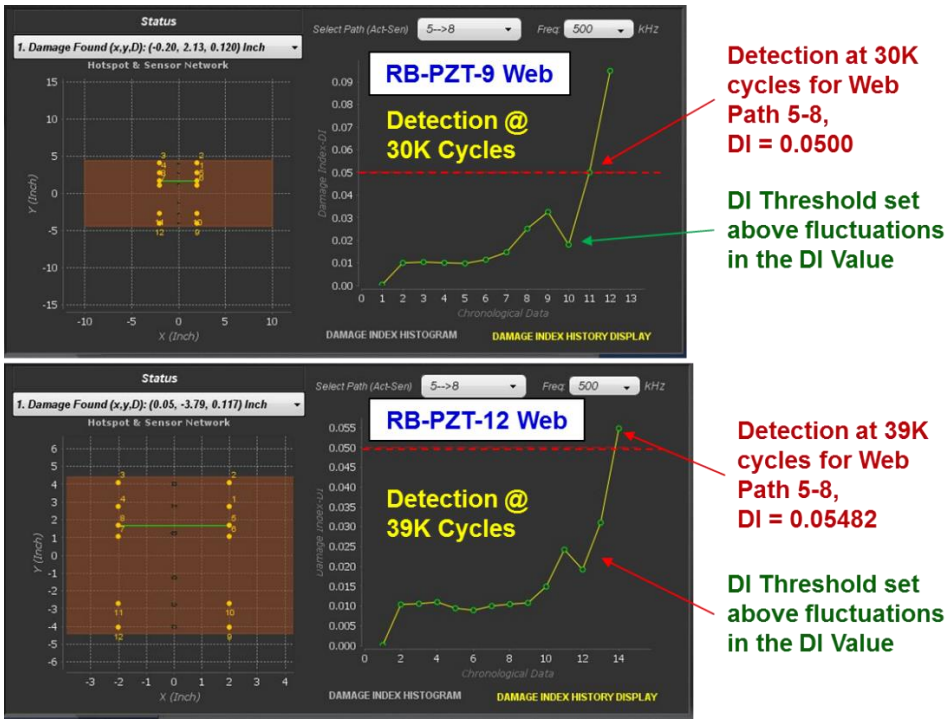

Figure 6-11. DI vs Crack Growth Indicating Threshold Exceedance and Crack Detection in Specimen RB-PZT-9 Web (Top) and RB-PZT-12 Web (Bottom)

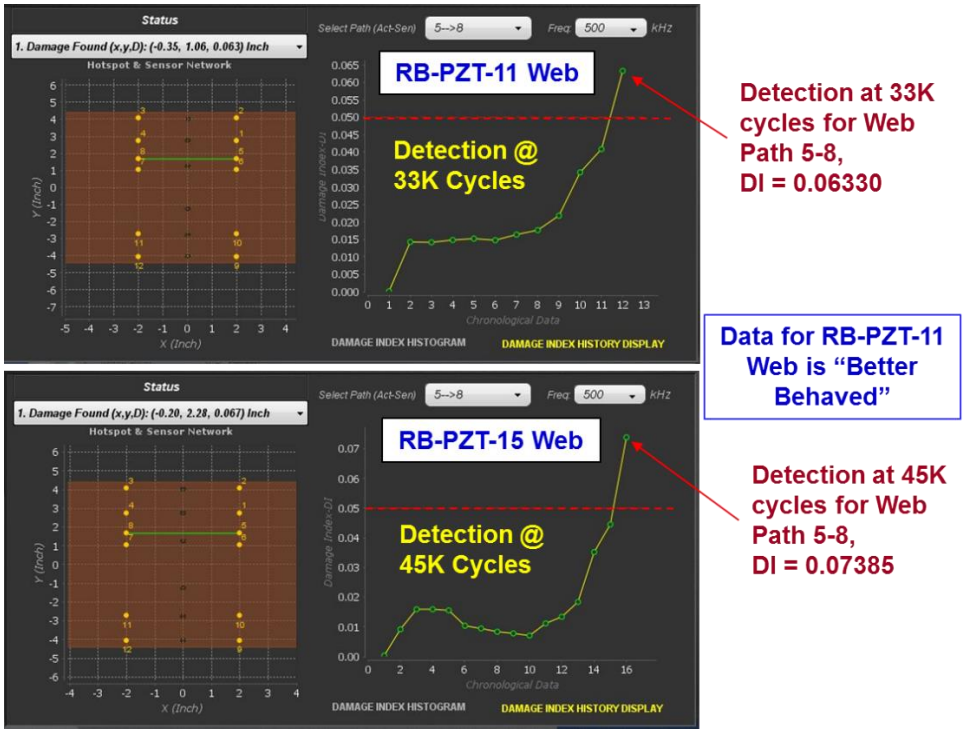

Figure 6-12. DI vs Crack Growth Indicating Threshold Exceedance and Crack Detection in Specimen RB-PZT-11 Web (Top) and RB-PZT-15 Web (Bottom)

6.1.2. PZT Performance on Rotorcraft Beam Element Specimen

Figure 6-13 shows the DI progression and crack detection with schematics of network paths for both the pitch-catch and pulse-echo modes of data acquisition. Figure 6-14 highlights the use of DI levels and data triangulation (wave time of flight information) to produce images that indicate damage growth with increasing fatigue cycles. Figure 6-13 and Figure 6-14 pertain to specimen RB-PZT-13 while Figure 6-15 and Figure 6-16 relate similar information for specimen RB-PZT-14. Damage progression, indicated by both DI histograms and color-coded images, is shown in Figure 6-17 (RB-PZT-10 web), Figure 6-18 and Figure 6-19 (RB-PZT-11 web), and Figure 6-20 and Figure 6-21 (RB-PZT-18 flange). These results show typical increases in DI values and increase in the number of paths exceeding the set threshold value as the crack increases in length.

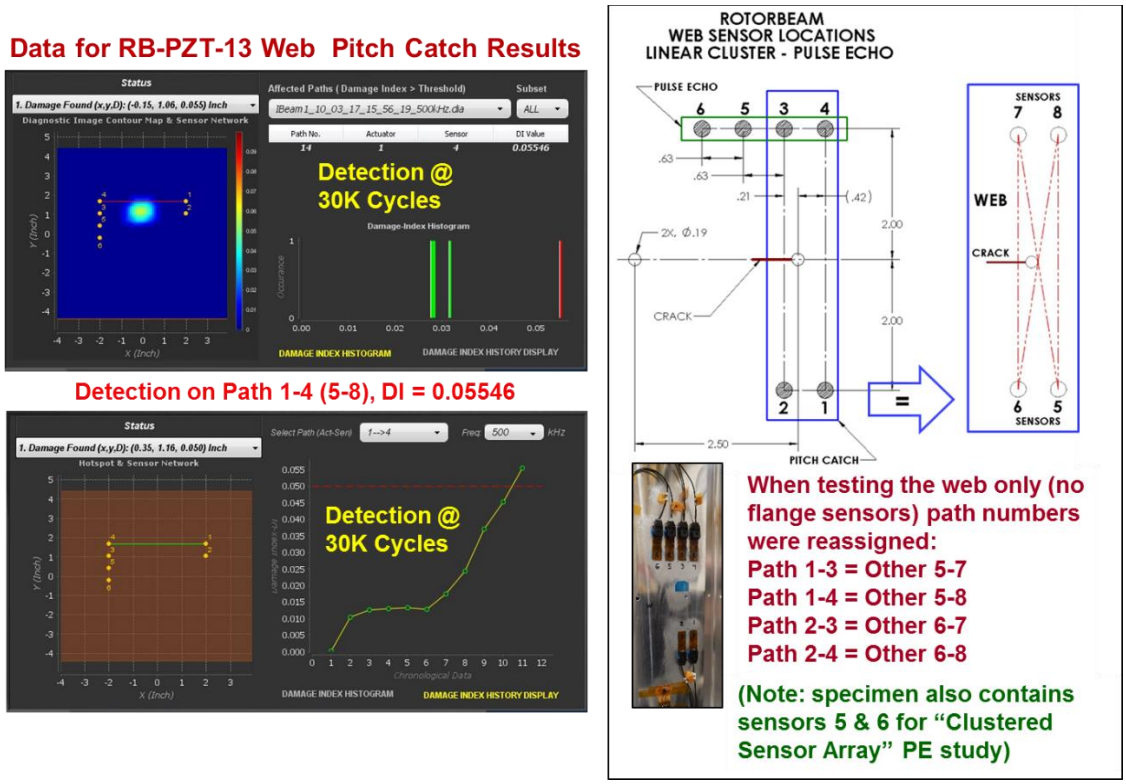

Figure 6-13. Plot of DI Progression and Associated DI Histogram for a Particular PZT Path Showing Crack Detection in the Rotorbeam Web (RB-PZT-13)

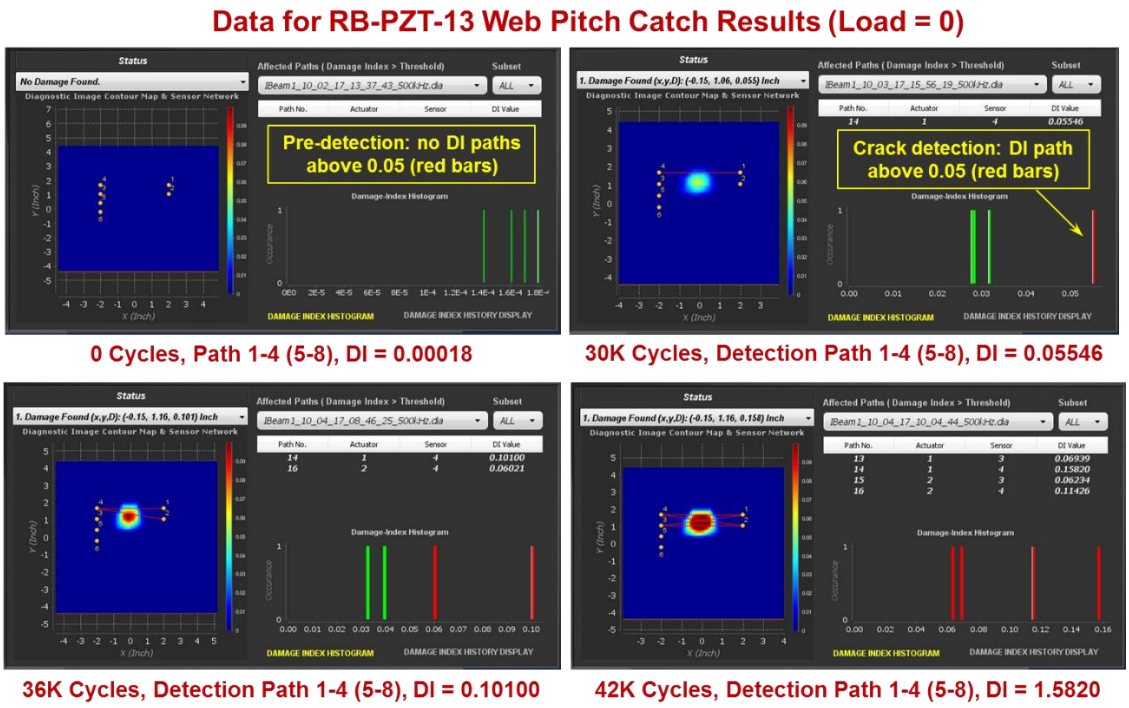

Figure 6-14. Increasing Damage Index and Number of Paths Exceeding Threshold as Crack Growth Progresses (RB-PZT-13)

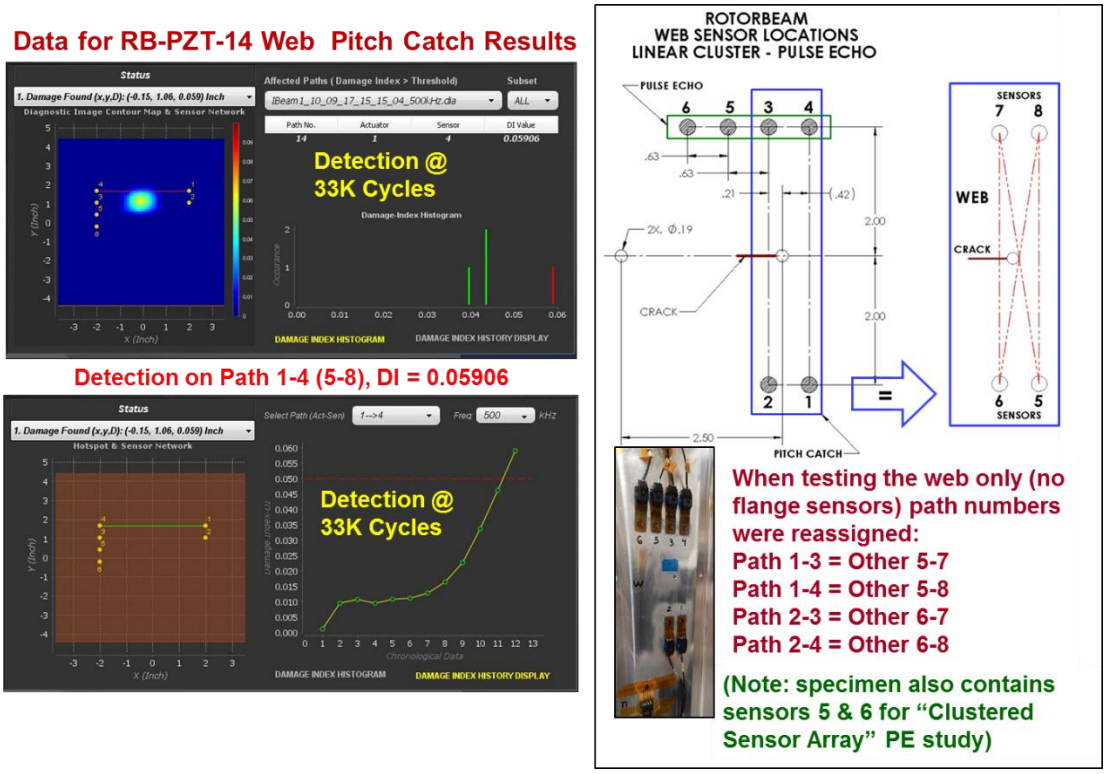

Figure 6-15. Plot of DI Progression and Associated DI Histogram for a Particular PZT Path Showing Crack Detection in the Rotorbeam Web (RB-PZT-14)

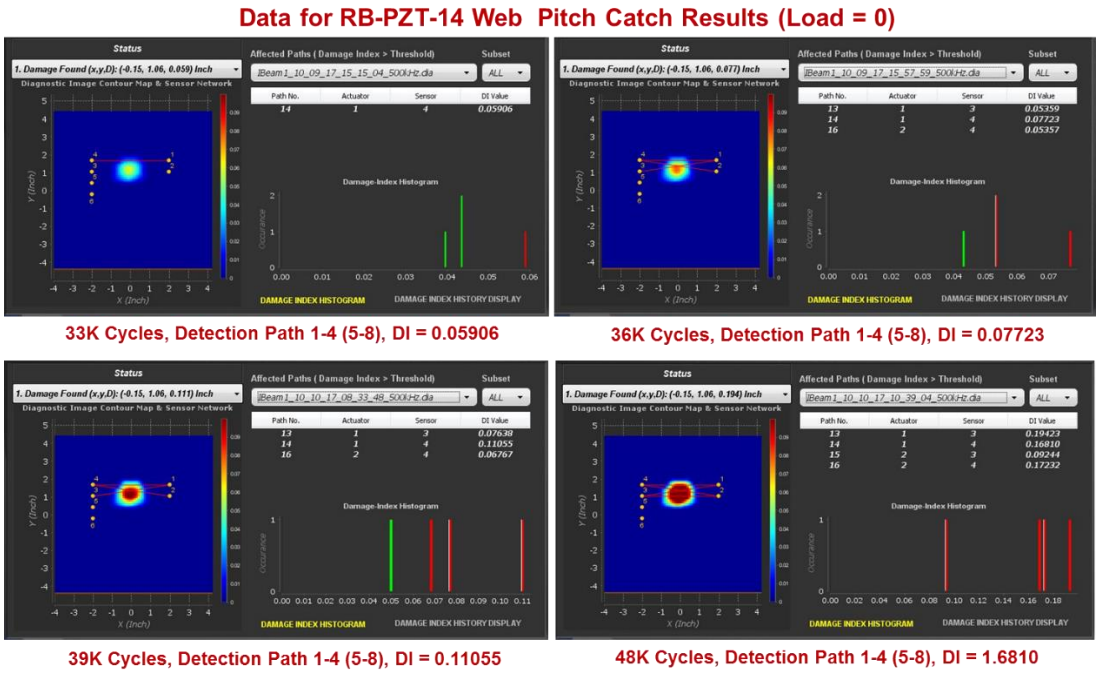

Figure 6-16. Increasing Damage Index and Number of Paths Exceeding Threshold as Crack Growth Progresses (RB-PZT-14)

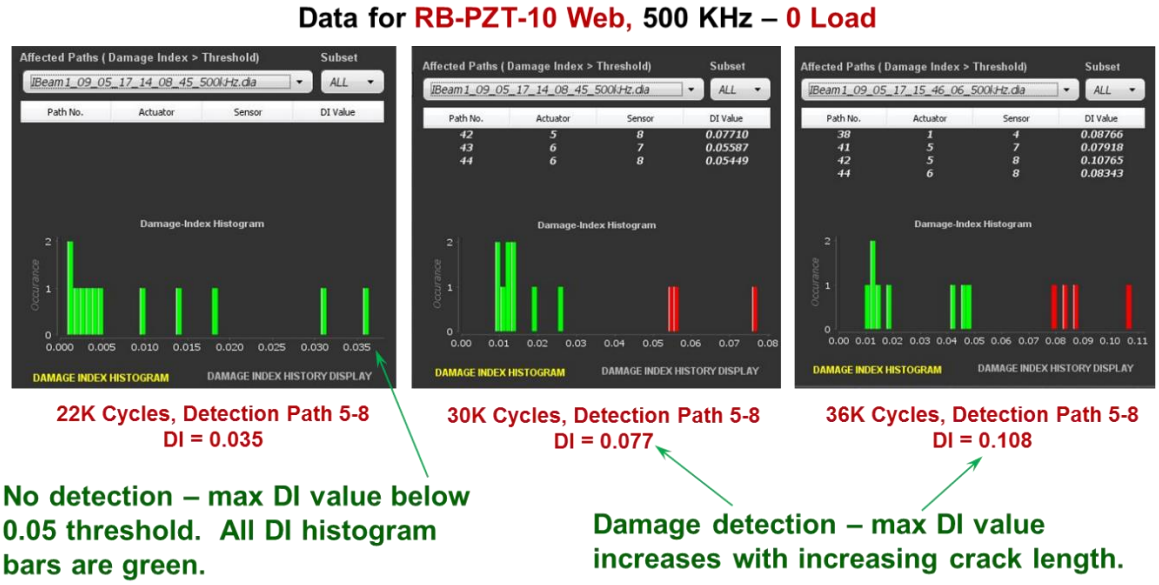

Figure 6-17. PZT DI Values Indicating Damage Progression in RB-PZT-10 Rotorbeam Web

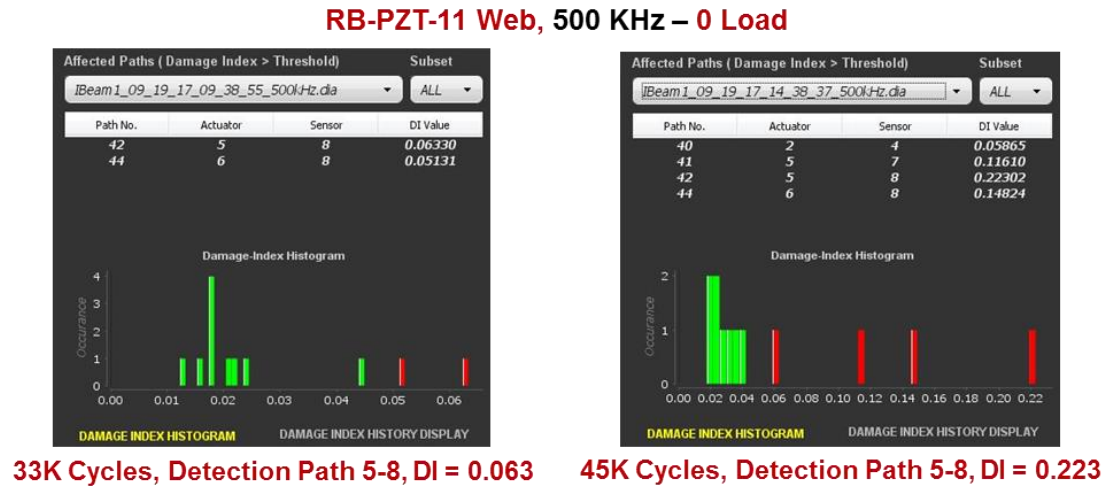

Figure 6-18. PZT DI Values Indicating Damage Progression in RB-PZT-11 Rotorbeam Web

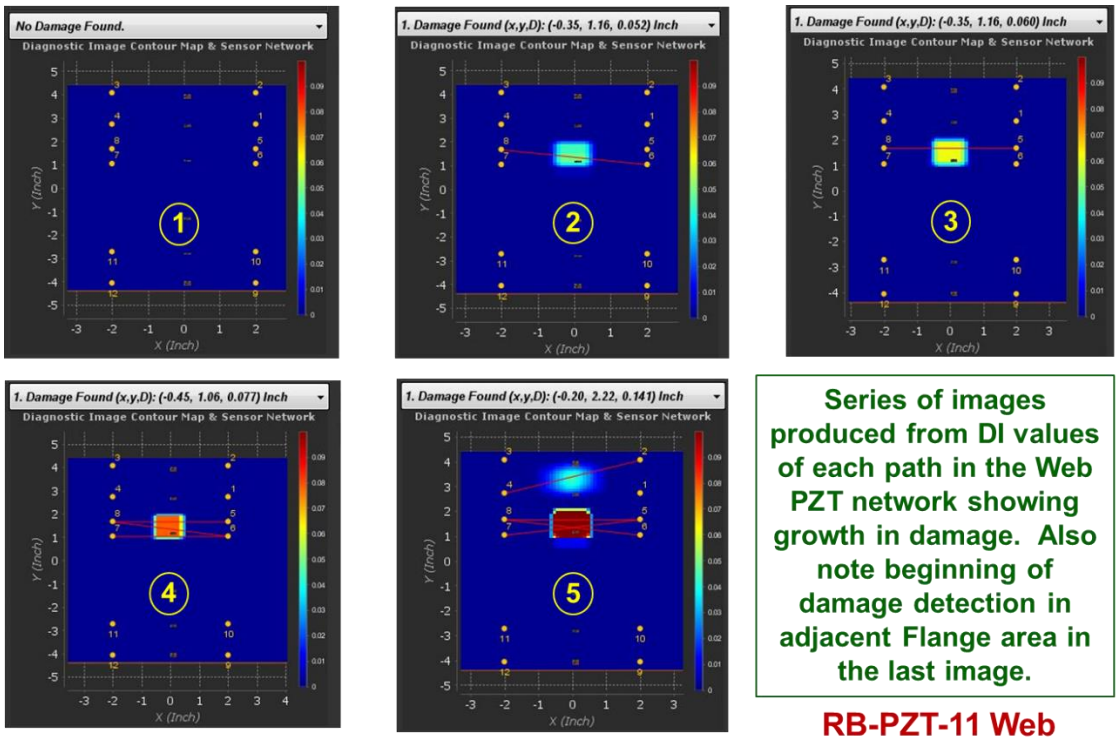

Figure 6-19. PZT Imaging of Damage Progression in Rotorbeam Web (RB-PZT-11)

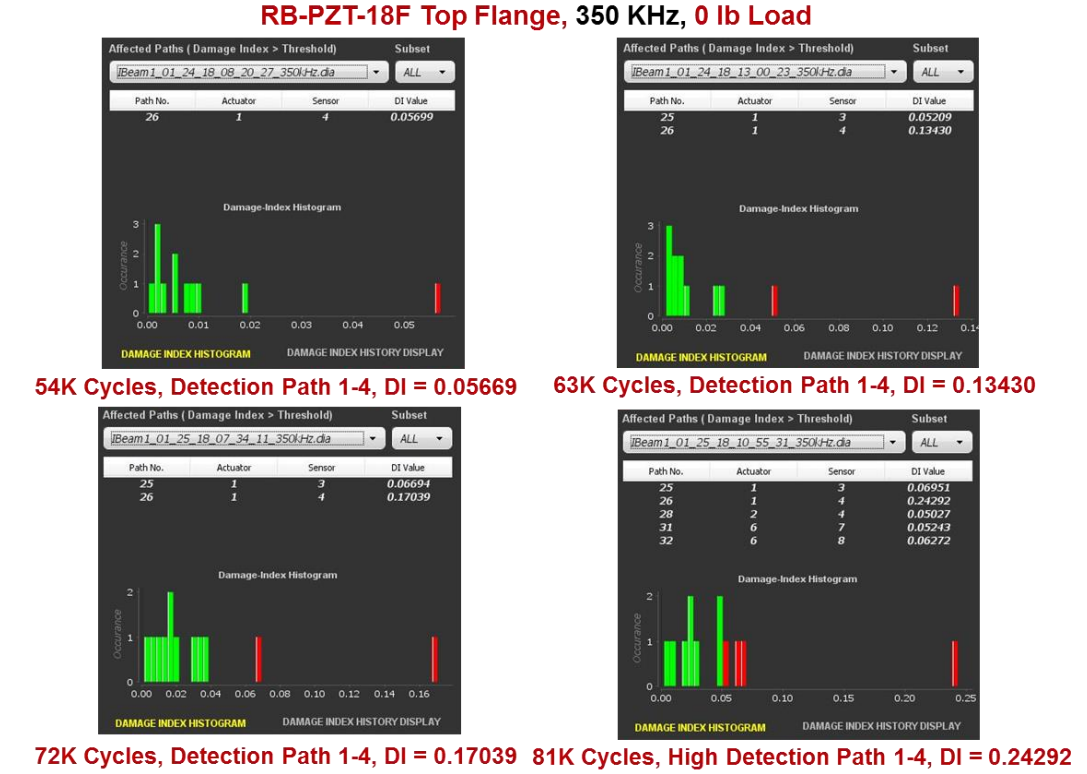

Figure 6-20. PZT DI Values Indicating Damage Progression in Rotorbeam Flange (RB-PZT-18F)

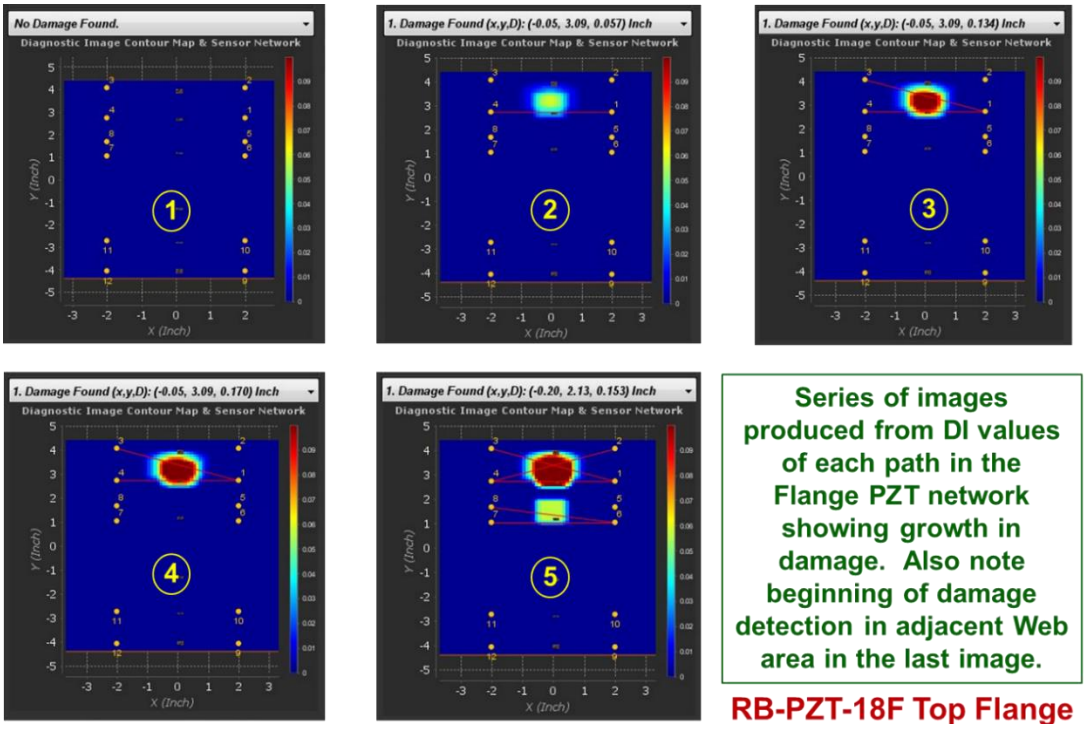

Figure 6-21. PZT Imaging of Damage Progression in Rotorbeam Flange (RB-PZT-18F)

Figure 6-22 and Figure 6-23 show the typical DI histogram and two-dimensional image of damage. They also show the sensor layout and the damage image superimposed over its actual location on the Rotorbeam web and flanges. The size and degree of color contrast associated with the damage region is proportional to the magnitude of the DI and the number of DI paths exceeding the DI(threshold).

Figure 6-24 through Figure 6-26 show examples of the DI progression, damage plots and PZT signal changes that occur during crack growth for specimens RB-PZT-6, RB-PZT-13 and RB-PZT-16, respectively. Notice that the change in PZT signals compared to the pristine condition baseline, represented by the yellow "Scatter Data" signals in the PZT response graph on the left of each figure, becomes greater as the damage progresses. As the fatigue cycles increase, the crack grows in length, the DI levels increase and the Scatter Data plots become larger. This data display provides additional insights into the damage detection approach and capabilities of the PZT SHM method and the particular data analysis deployed in the Acellent Scan Genie system.

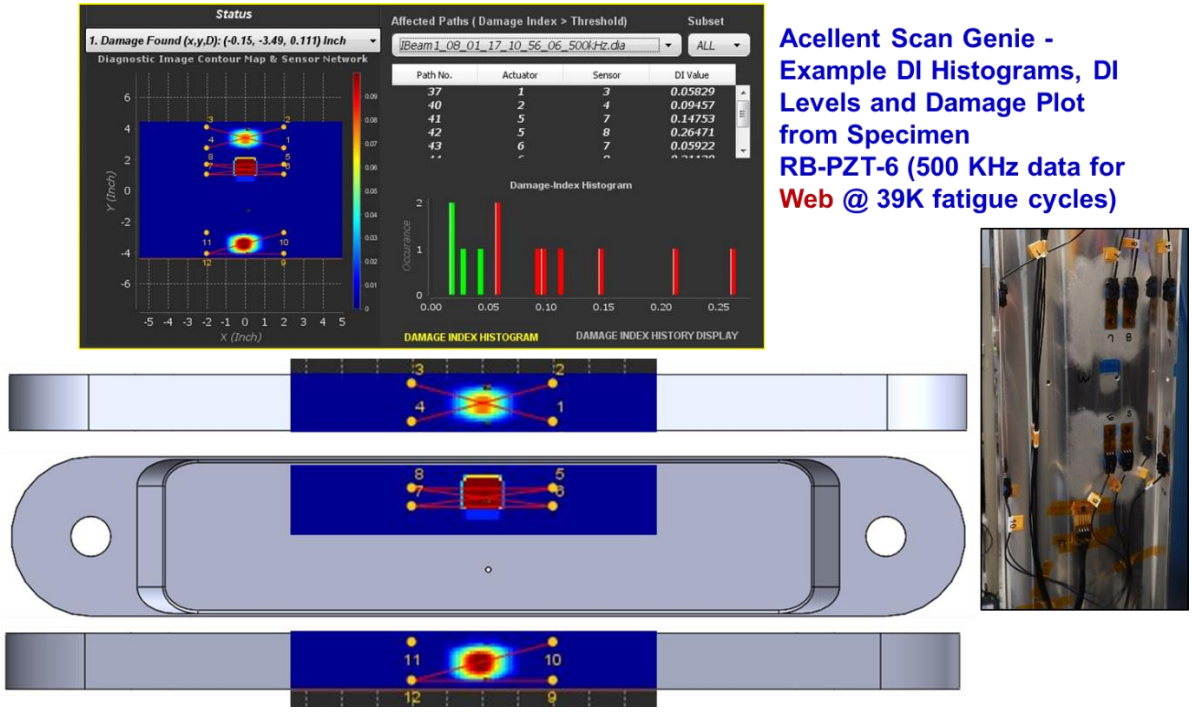

Figure 6-22. Summary of ScanGenie PZT System Output at Damage Detection – Sensor Network, DI Levels and Damage Imaging (RB-PZT-6; 500 KHz data)

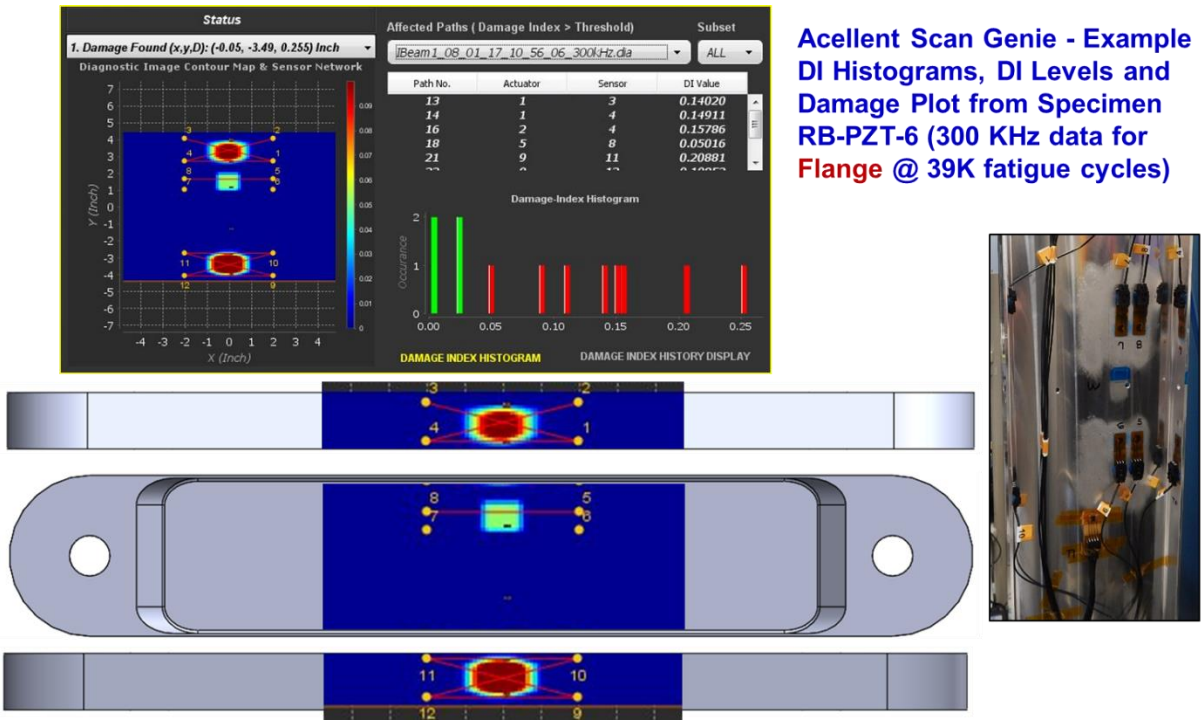

Figure 6-23. Summary of ScanGenie PZT System Output at Damage Detection – Sensor Network, DI Levels and Damage Imaging (RB-PZT-6; 300 KHz data)

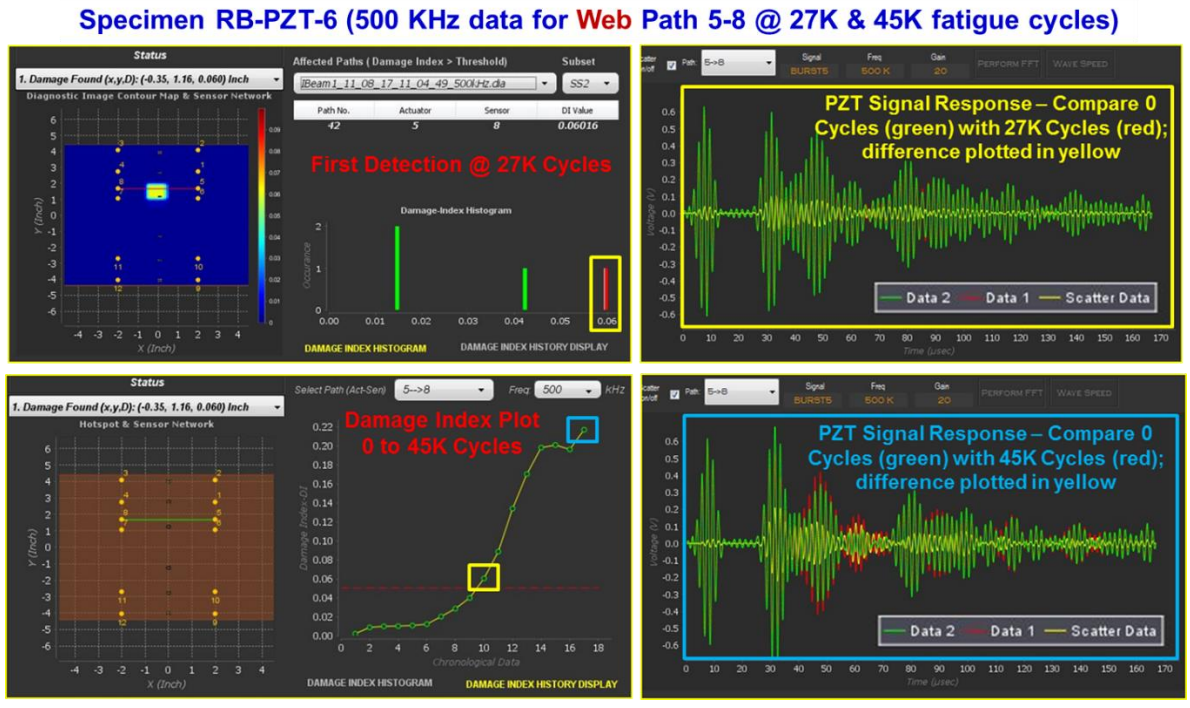

Figure 6-24. PZT Signals, DI Histograms, DI Levels and Damage Plot - Specimen RB-PZT-6

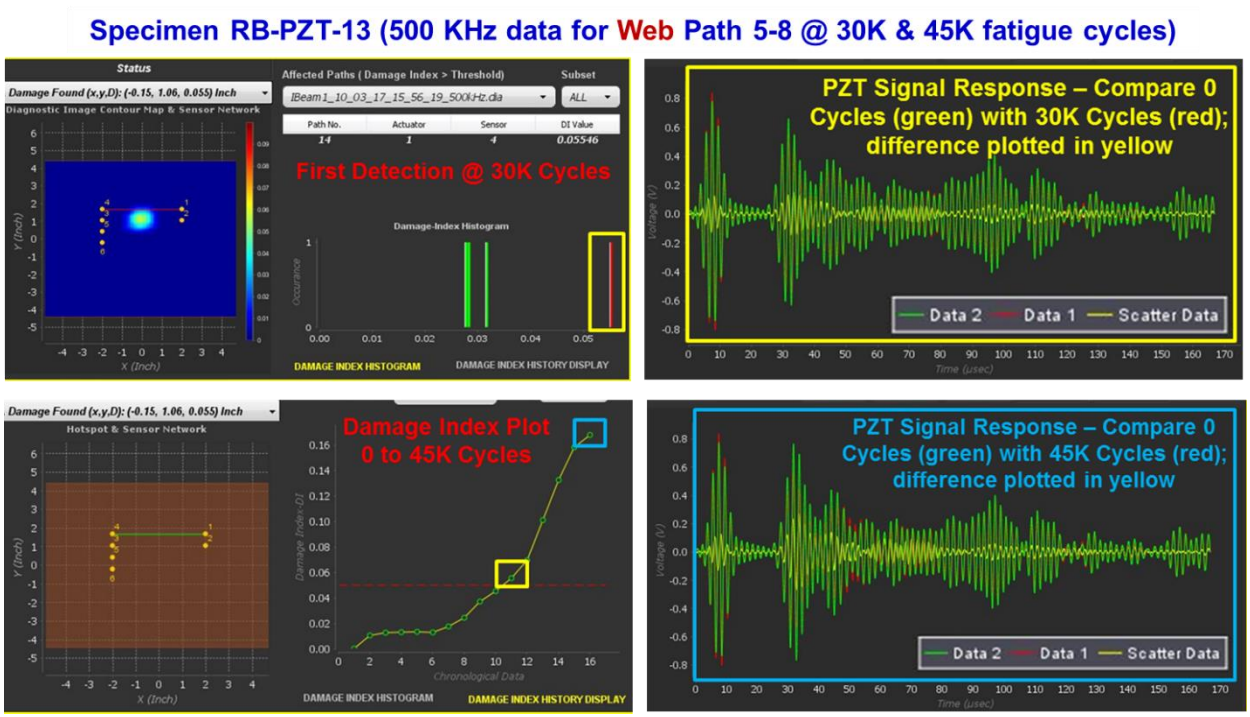

Figure 6-25. PZT System Output at Damage Detection – DI Progression and PZT Signal Changes in Specimen RB-PZT-13

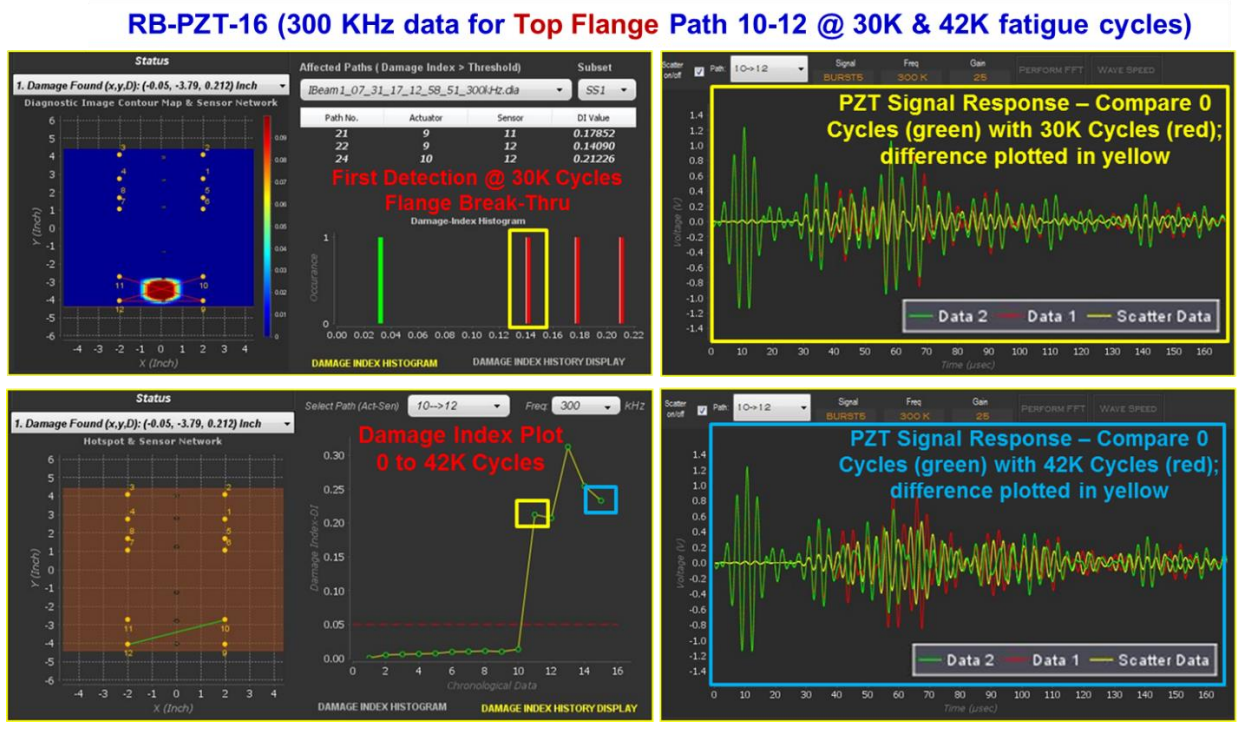

Figure 6-26. PZT System Output at Damage Detection – DI Progression and PZT Signal Changes in Specimen RB-PZT-16

Figure 6-27 through Figure 6-29 show the effects of overall structural integrity on the PZT sensor response. For singular cracks, the DI values are predominantly rapidly increasing and quite uniform (Figure 6-29). As additional cracks originate, well beyond initial crack detection, stresses are reapportioned and specimen deformation changes. Thus, the DI for different paths can be affected (Figure 6-27 and Figure 6-28). The example of specimen RB-PZT-16 in Figure 6-27 shows that when the Top Flange started growing a crack on the opposite side of the hole (39K cycles), the DI value flattened for Path 5-8 and increased dramatically for Top Flange Path 1-4. This example also shows that crack detection occurred on the Web at 27K cycles and on the Top Flange at 33K cycles.

Figure 6-30 through Figure 6-32 provide additional examples of constantly-increasing DI tracking from optimum paths with minimum noise levels. Some stress reapportion, due to multiple crack onset or extremely large cracks, and DI changes due to stress field changes are sometimes observed well above the initial crack detection threshold. Figure 6-33 through Figure 6-35 provide additional views of typical crack growth and crack length measurements in the test specimens. Figure 6-36 shows typical crack growth curves so that it is possible to relate da/dN data to the PZT DI response data.

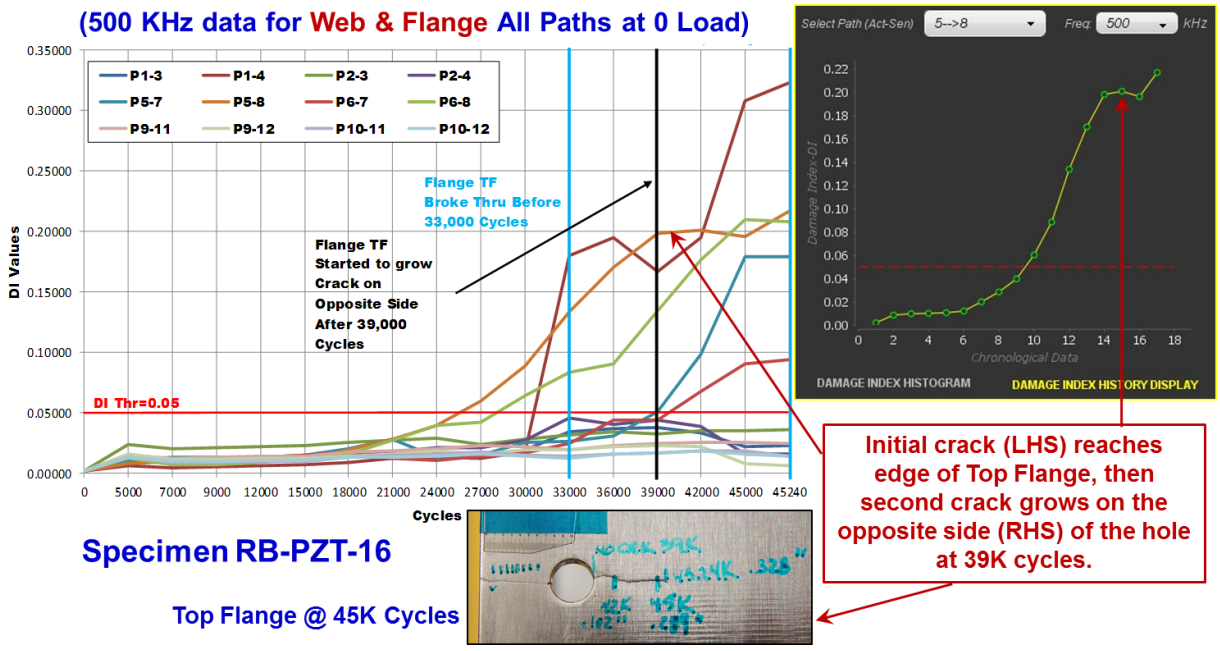

Figure 6-27. Non-Uniform Change in Damage Index Due to Stress Reapportion

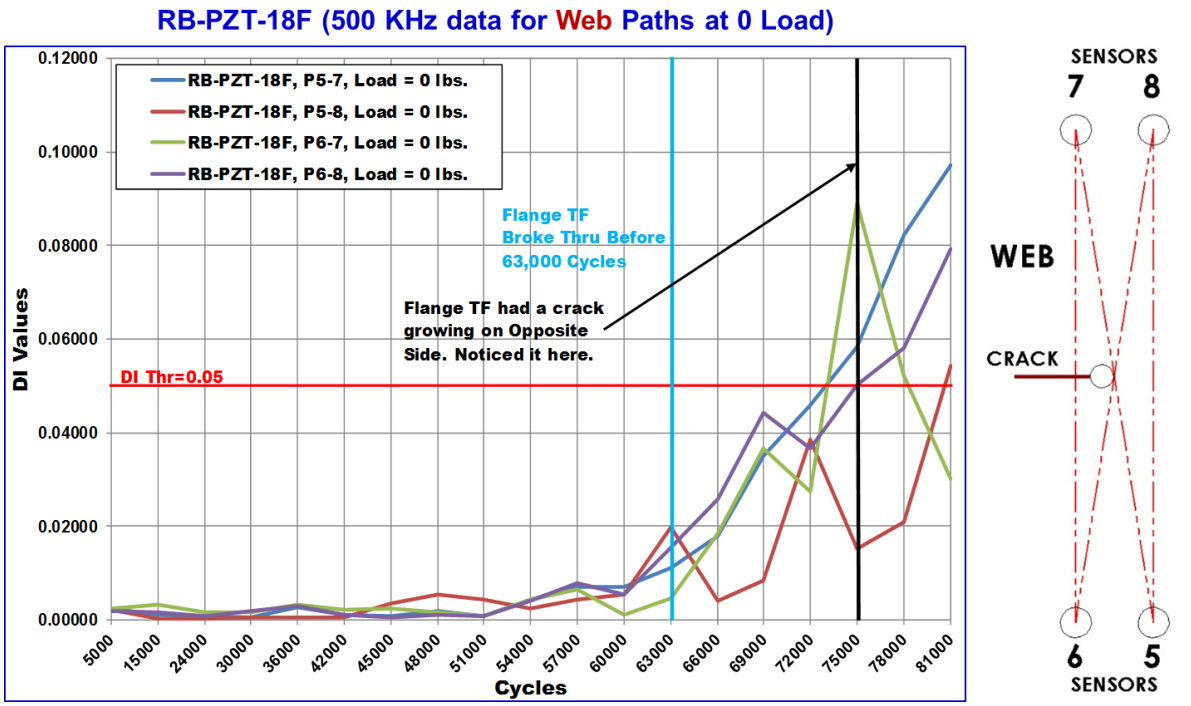

Figure 6-28. Establishing Proper Damage Index Level to Assign as "Crack Detected"

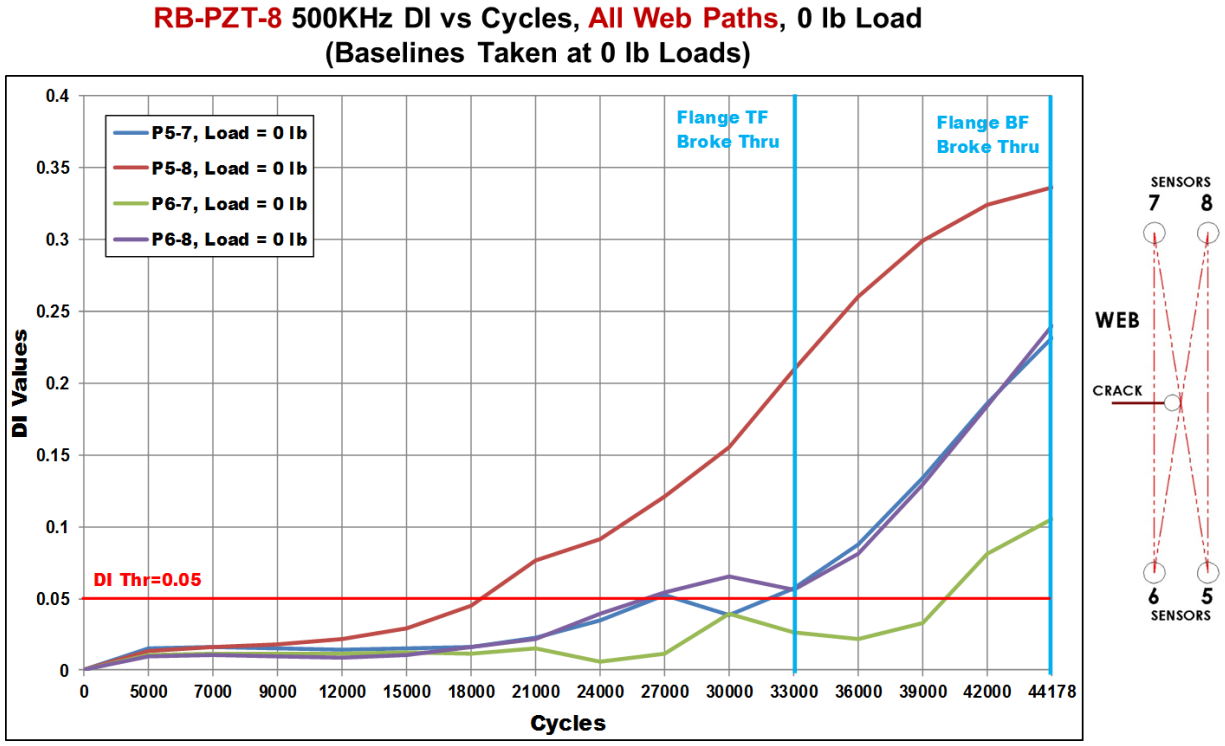

Figure 6-29. DI Progression in Web for PZT Crack Detection in RB-PZT-8 Unloaded Structure

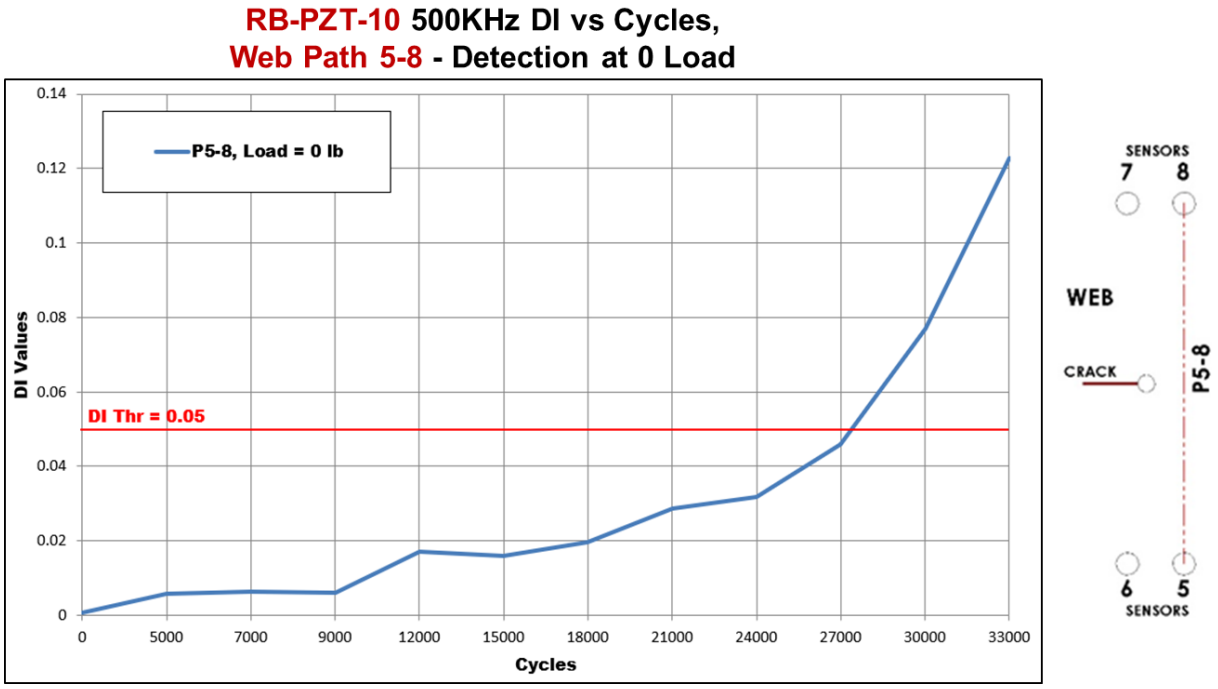

Figure 6-30. DI Progression in Web for PZT Crack Detection in RB-PZT-10 Unloaded Structure

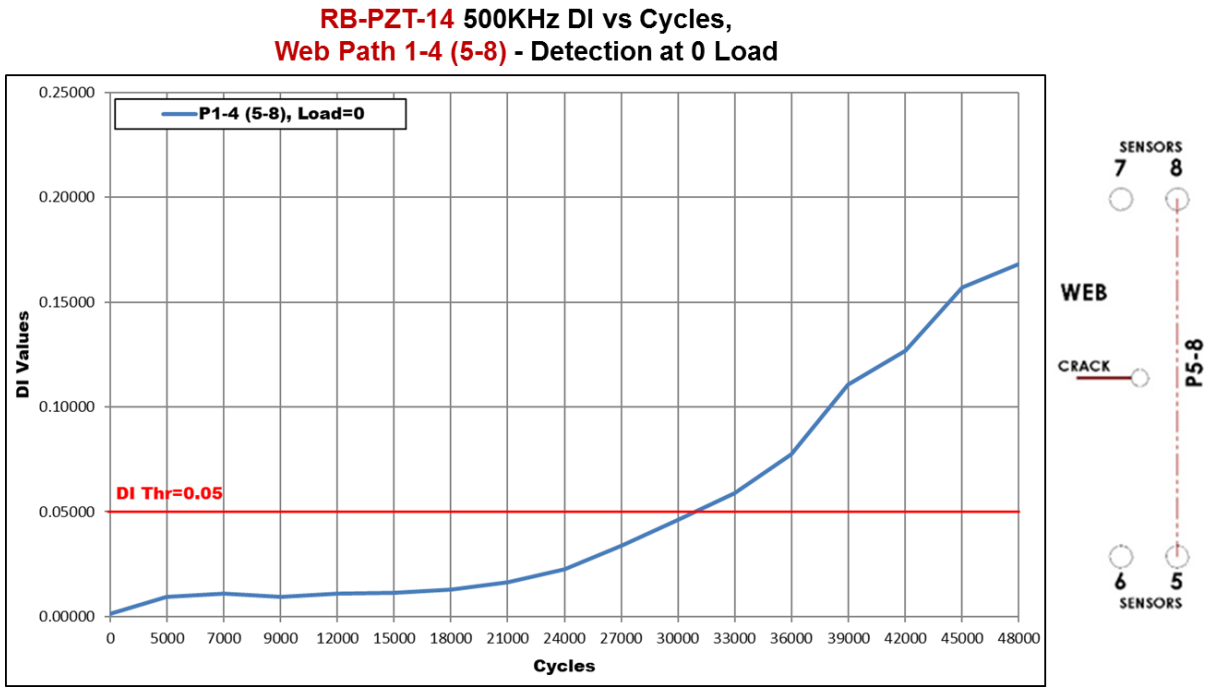

Figure 6-31. DI Progression in Web for PZT Crack Detection in RB-PZT-14 Unloaded Structure

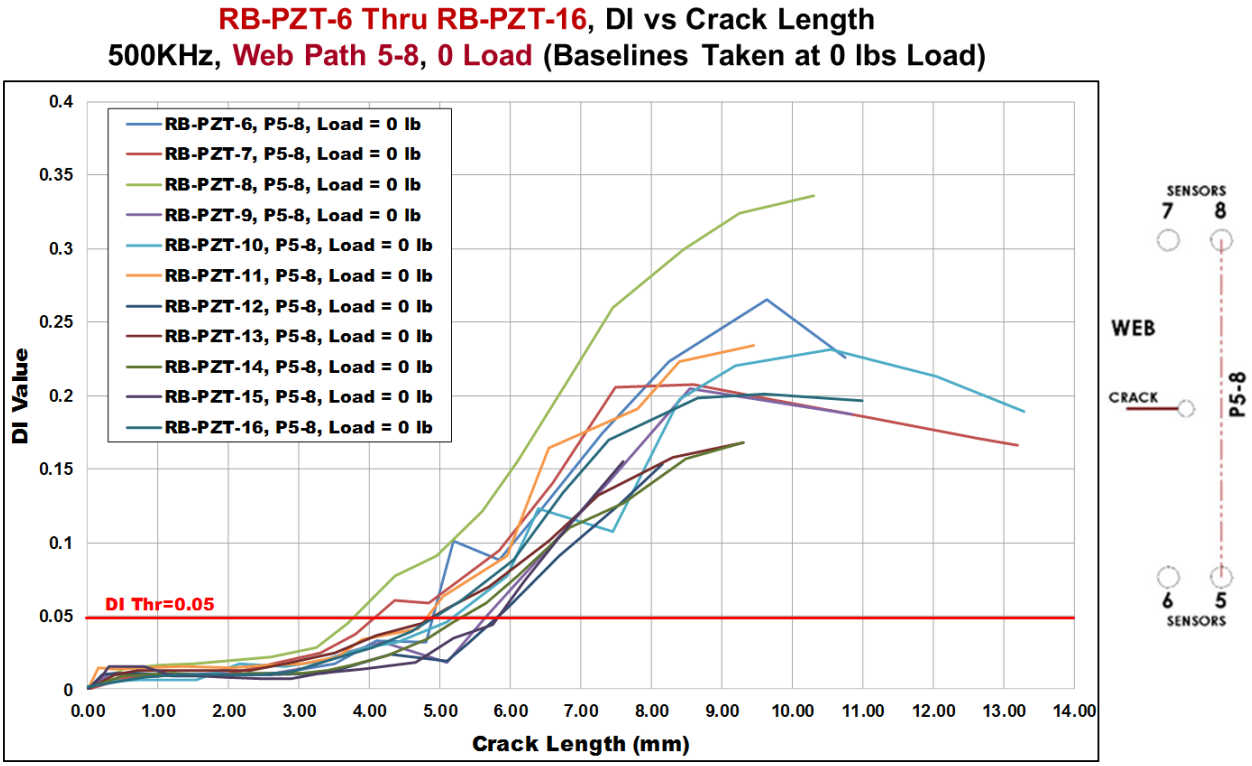

Figure 6-32. DI Progression in Web for PZT Crack Detection in RB-PZT-16 Unloaded Structure

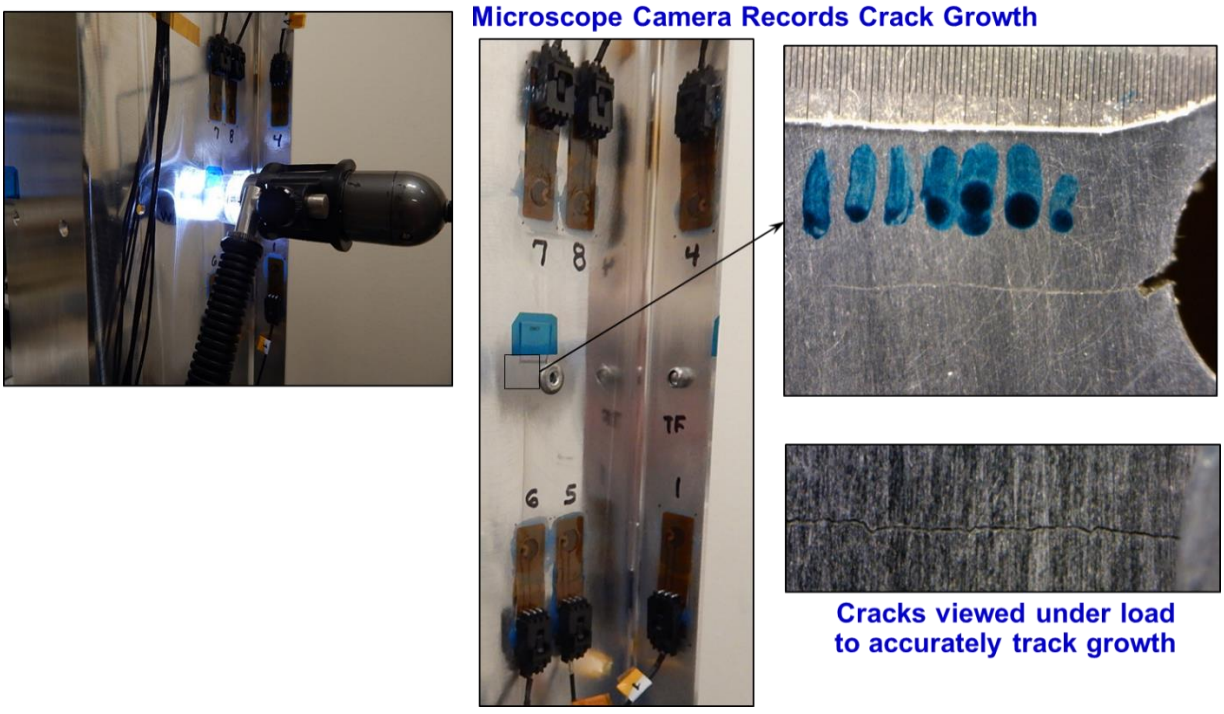

Figure 6-33. Use of Microscope Camera and Scales to Measure Crack Length in Specimens

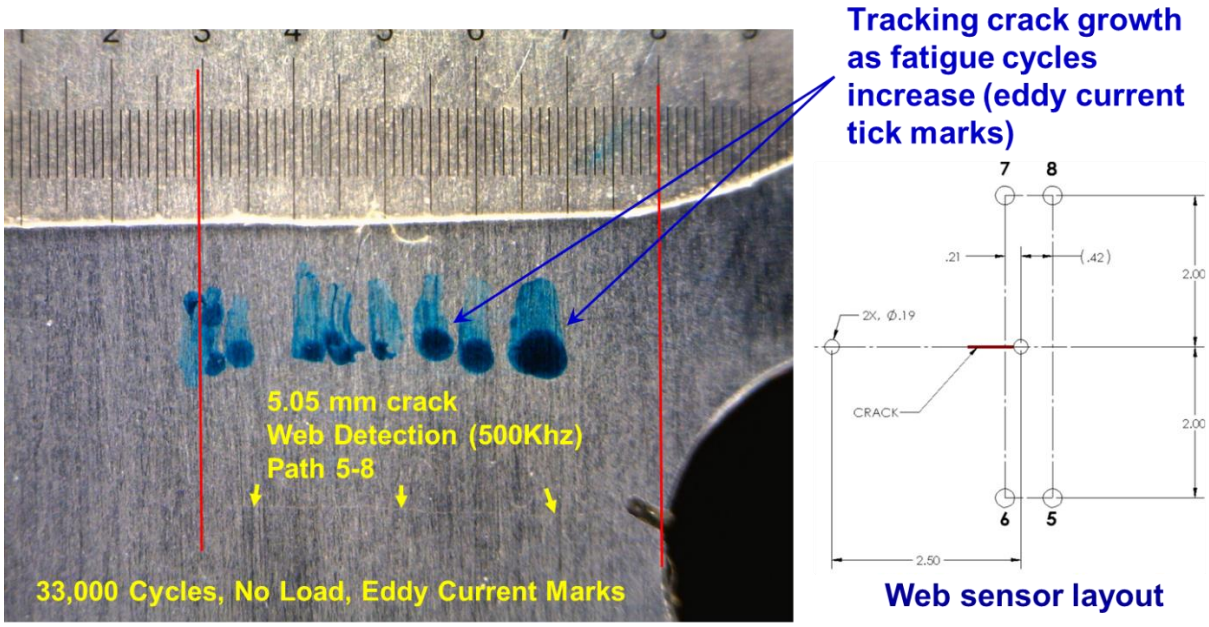

Figure 6-34. Determining Crack Length at PZT Detection & Beyond

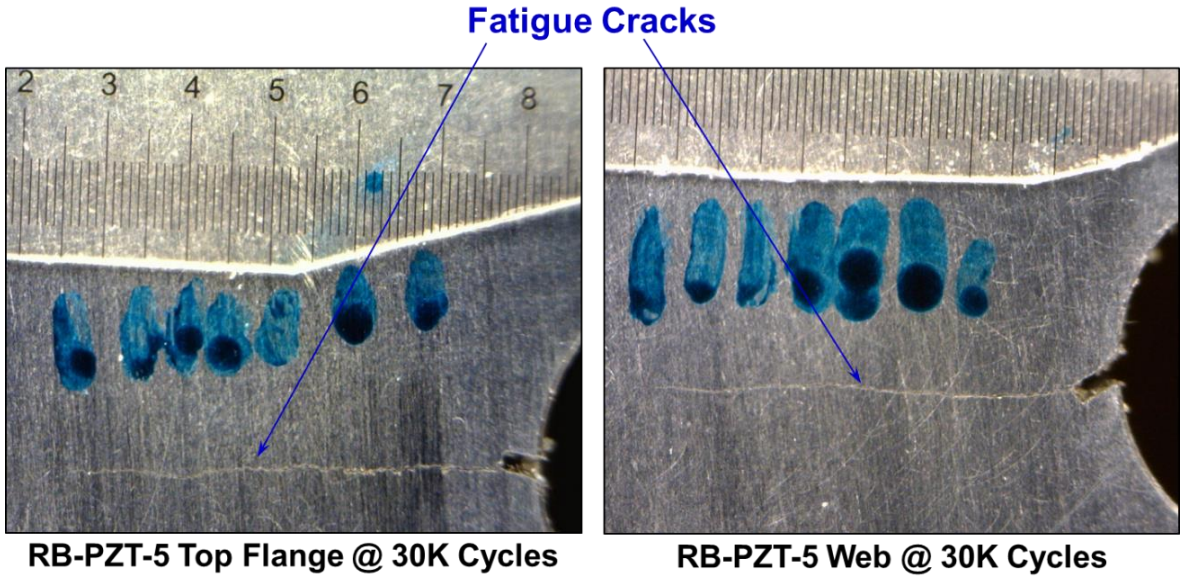

Figure 6-35. PZT Crack Detection and Measurements Recorded

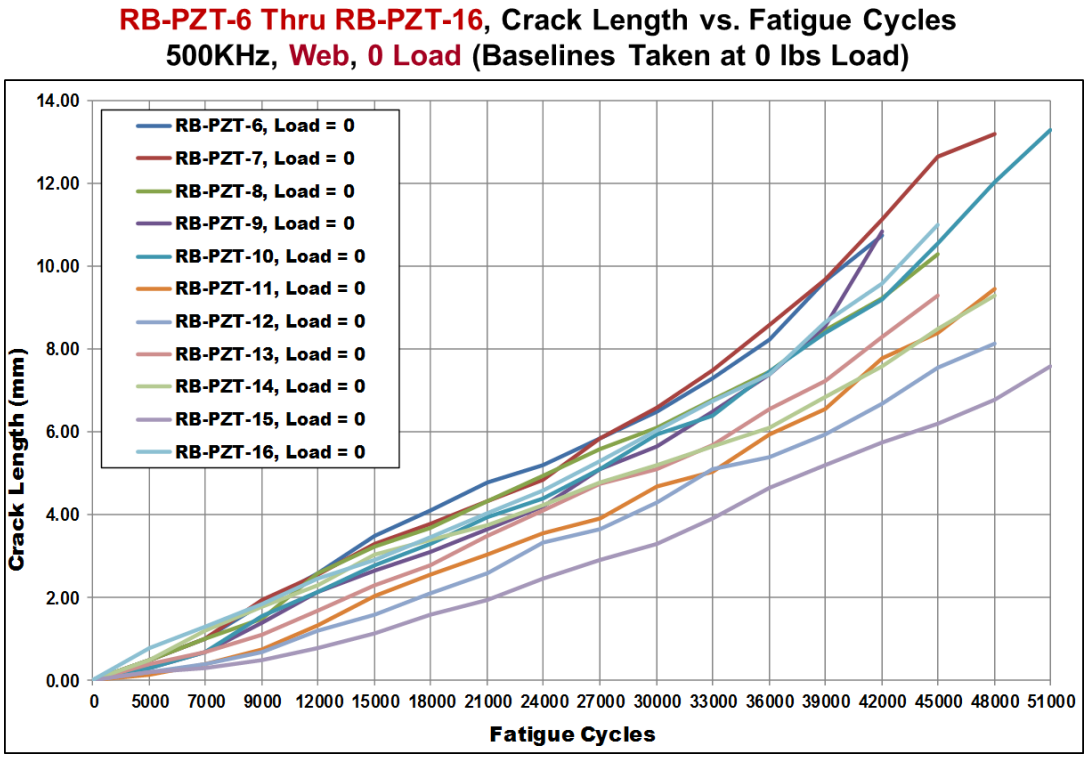

Figure 6-36. da/dN Crack Growth in Web for PZT Crack Detection in an Unloaded Structure

6.1.2.1. PZT Results for Open Holes with Cracks

Rotorbeam Web Region

When all of the damage detection considerations, data acquisition and criteria were incorporated into each fatigue test, a set of crack detections was produced for the web region on all Rotorbeam test specimens. All monitoring was performed on an unloaded structure to obtain Baseline data which was then compared to later data following the application of various fatigue cycles. All data was obtained from the structure in unloaded condition. Table 6-1 shows the resulting set of data that relates the number of fatigue cycles at PZT crack detection to the corresponding crack length in the web of the Rotorbeam structure. It also lists the DI paths that exceeded the threshold of 0.05. Note DI levels in excess of threshold value of 0.05 include second and third paths for detection to highlight the sensitivity of the different paths in the network for specific crack detection. The results were very consistent with an average crack detection of 0.21" (5.33 mm) and a Standard Deviation of only 0.024" (0.61 mm). All results correspond to crack growth originating from open holes.

One-Sided Tolerance Interval POD Method - The 11 data points listed for open-hole crack detection in the web of the Rotorbeam in Table 6-1 were used in the OSTI method described in Section 4.6 to calculate the POD performance. Table 6-2 summarizes the OSTI calculations.

Table 6-1. PZT Crack Detection in Unloaded Rotorbeam Web

PZT Performance in Web of Rotorbeam - Crack Length and Damage Index at Initial Crack Detection in Unloaded Specimens (0 Load at Data Acquisition & Baseline Determined at 0 Load)									
Specimen #	Fatigue Cycles at Detection	Crack Length at Detection mm (in)	Damage Detection Freq. (KHz)	First Path Detecting Crack	DI Value of First Path	Second Path Detecting Crack (if applicable)	DI Value of Second Path	Third Path Detecting Crack (if applicable)	DI Value of Third Path
RB-PZT-6	24,000	5.20 (0.205)	500	5-8	0.10137	N/A	N/A	N/A	N/A
RB-PZT-7	21,000	4.35 (0.171)	500	5-8	0.06055	N/A	N/A	N/A	N/A
RB-PZT-8	21,000	4.35 (0.171)	500	5-8	0.07666	N/A	N/A	N/A	N/A
RB-PZT-9	30,000	5.65 (0.222)	500	5-8	0.04994	N/A	N/A	N/A	N/A
RB-PZT-10	30,000	5.95 (0.234)	500	5-8	0.07710	6-7	0.05587	6-8	0.05449
RB-PZT-11	33,000	5.05 (0.199)	500	5-8	0.06330	6-8	0.05131	N/A	N/A
RB-PZT-12	39,000	5.95 (0.234)	500	5-8	0.05482	N/A	N/A	N/A	N/A
RB-PZT-13	30,000	5.10 (0.201)	500	5-8	0.05546	N/A	N/A	N/A	N/A
RB-PZT-14	33,000	5.65 (0.222)	500	5-8	0.05906	N/A	N/A	N/A	N/A
RB-PZT-15	45,000	6.20 (0.244)	500	5-8	0.07385	N/A	N/A	N/A	N/A
RB-PZT-16	27,000	5.30 (0.209)	500	5-8	0.06016	N/A	N/A	N/A	N/A
RB-PZT-17F	66,000	5.00 (0.197)	500	6-8	0.05186	N/A	N/A	N/A	N/A
RB-PZT-18F	75,000	6.05 (0.238)	500	5-7	0.05831	6-7	0.08897	6-8	0.05031

Table 6-2. POD Calculations Using One-Sided Tolerance Interval from PZT Response Data on Rotorbeam Web (unloaded)

PZT Crack Detection Data in Web

Crack Length at PZT Detection a (in)	Log of Crack Length at PZT Detection a (in)
0.205	-0.688246
0.171	-0.767004
0.171	-0.767004
0.222	-0.653647
0.234	-0.630784
0.199	-0.701147
0.234	-0.630784
0.201	-0.696804
0.222	-0.653647
0.244	-0.612610
0.209	-0.679854

PZT Crack Detection in Web for Unloaded Open Holes

Statistic Estimates in Log & Linear Scales

Statistic	Value in Log Scale	Value in Linear Scale
Mean (X)	-0.680139	0.210
Stnd Deviation (S)	0.051683	0.024219

POD Detection Levels (γ = 95%, n = 11)

	POD in inches	POD in mm
Flaw Size: POD = X + K(S) =	0.274	6.95

Web Open Hole Data: Crack Length at PZT Detection = 6.95 mm (0.274")

The reliability calculations include a corresponding magnitude of the K (probability) factor that is related to the number of data points acquired, the desired probability desired (90%) and the desired confidence level (95%). Also, the OSTI calculations include a parameter that amounts to an increase in POD as the Standard Deviation of the data increases. As a result, while all of the crack detection levels were less than 0.250", the overall $POD_{90/95}$ value for PZT crack detection from the Rotorbeam web was calculated to be 0.274" (6.95 mm). The K value shown corresponds to the desired γ (confidence level) of 95%. As the number of data points increases, the K value will

decrease and the POD numbers could also decrease. There were no False Calls associated with these tests where the PZT sensor indicated the presence of a crack when actually none was present.

Rotorbeam Flange Region

Table 6-3 shows the data that relates the number of fatigue cycles at PZT crack detection to the corresponding crack length in the flange of the Rotorbeam structure. It also lists the DI paths that exceeded the threshold of 0.05. Note DI levels in excess of threshold value of 0.05 include second and third paths for detection to highlight the sensitivity of the different paths in the network for specific crack detection. The results were very consistent with an average crack detection of 0.328" (8.33 mm) and a Standard Deviation of only 0.007" (0.18 mm). All results correspond to crack growth originating from open holes.

Table 6-3. PZT Crack Detection in Unloaded Rotorbeam Flange

PZT Performance in Flange of Rotorbeam - Crack Length and Damage Index at Initial Crack Detection in Unloaded Specimens (0 Load at Data Acquisition & Baseline Determined at 0 Load)									
Specimen #	Fatigue Cycles at Detection	Crack Length at Detection mm (in)	Damage Detection Freq. (KHz)	First Path Detecting Crack	DI Value of First Path	Second Path Detecting Crack (if applicable)	DI Value of Second Path	Third Path Detecting Crack (if applicable)	DI Value of Third Path
RB-PZT-3	32,000	7.50 (0.295)	300	10-12	0.07624				
	34,000	8.38 (0.330)	300	1-3	0.19733	2-4	0.08786	1-4	0.07561
RB-PZT-4	41,171	8.38 (0.330)	300	9-12	0.19223	9-11	0.12979	10-12	0.11605
	36,000	8.38 (0.330)	300	1-3	0.29197	2-4	0.24104	2-4	0.07513
RB-PZT-5	39,000	8.38 (0.330)	300	9-11	0.06720	10-12	0.06052		
	36,000	8.38 (0.330)	300	2-4	0.26156	1-4	0.13454	1-3	0.07285
RB-PZT-6	30,000	8.38 (0.330)	300	10-12	0.21226	9-11	0.17852	9-12	0.14090
	38,800	8.38 (0.330)	300	2-4	0.15786	1-4	0.14911	1-3	0.14020
RB-PZT-7	46,288	8.38 (0.330)	300	9-11	0.06963				
	33,000	8.38 (0.330)	300	1-3	0.32527	2-4	0.15403	1-4	0.11566
RB-PZT-8	44,178	8.38 (0.330)	300	10-12	0.07309	9-11	0.06783		
	33,000	8.38 (0.330)	300	1-3	0.07382	2-4	0.07201	1-4	0.06262
RB-PZT-9	44,645	8.38 (0.330)	300	9-12	0.10479	10-12	0.09991	9-11	0.05990
	30,000	8.38 (0.330)	300	1-3	0.37177	1-4	0.22275	2-4	0.22247
RB-PZT-10	33,000	8.38 (0.330)	300	2-4	0.20244	1-3	0.19483	1-4	0.15079
RB-PZT-11	48,359	8.38 (0.330)	300	10-12	0.08661	9-11	0.07823	9-12	0.06818
	39,000	8.38 (0.330)	300	1-4	0.11759	2-4	0.11667	1-3	0.07667
RB-PZT-12	36,000	8.38 (0.330)	300	9-11	0.30302	10-12	0.18816	9-12	0.10918
	42,000	8.38 (0.330)	300	2-4	0.14539	1-3	0.12329	1-4	0.10638
RB-PZT-15	45,000	8.38 (0.330)	300	1-3	0.17531	1-4	0.12028	2-4	0.11232
RB-PZT-16	45,240	8.38 (0.330)	300	9-11	0.05113				
	33,000	8.38 (0.330)	300	2-4	0.22765	1-3	0.20327	1-4	0.14762
RB-PZT-17F	68,076	8.38 (0.330)	300	1-4	0.29948	2-4	0.12731	1-3	0.11407
RB-PZT-18F	60,000	7.75 (0.305)	350	1-4	0.08509				

The 22 data points listed for open-hole crack detection in the flange of the Rotorbeam in Table 6-1 were used in the OSTI method described in Section 4.6 to calculate the POD performance. Table 6-2 summarizes the OSTI calculations. The reliability calculations include a corresponding magnitude of the K (probability) factor that is related to the number of data points acquired, the desired probability desired (90%) and the desired confidence level (95%). As a result of calculating the POD(90/95) level with 22 data points, the POD level was higher than the average crack detection. While all of the crack detection levels were less than 0.340", the overall $POD_{90/95}$

value for PZT crack detection from the Rotorbeam flange was calculated to be 0.343" (8.72 mm). The K value shown corresponds to the desired ɣ (confidence level) of 95%. As the number of data points increases, the K value will decrease and the POD numbers could also decrease. There were no False Calls associated with these tests where the PZT sensor indicated the presence of a crack when actually none was present.

Table 6-4. POD Calculations Using One-Sided Tolerance Interval from PZT Response Data on Rotorbeam Flange (unloaded)

PZT Crack Detection Data in Flange (all open holes)

Crack Length at PZT Detection a (in)	Log of Crack Length at PZT Detection a (ln)
0.295	-0.530178
0.33	-0.481486
0.33	-0.481486
0.33	-0.481486
0.33	-0.481486
0.33	-0.481486
0.33	-0.481486
0.33	-0.481486
0.33	-0.481486
0.33	-0.481486
0.33	-0.481486
0.33	-0.481486
0.33	-0.481486
0.33	-0.481486
0.33	-0.481486
0.33	-0.481486
0.33	-0.481486
0.33	-0.481486
0.33	-0.481486
0.33	-0.481486
0.33	-0.481486
0.33	-0.481486
0.33	-0.481486

PZT Crack Detection in Flange for Unloaded Open Holes

Statistic Estimates in Log & Linear Scales

Statistic	Value in Log Scale	Value in Linear Scale
Mean (X)	-0.483699	0.328
Stnd Deviation (S)	0.010381	0.007462

POD Detection Levels (ɣ = 95%, n = 22)

	POD in inches	POD in mm
Flaw Size: POD = X + K(S) =	0.343	8.72

Flange Open Hole Data: Crack Length at PZT Detection = 8.72 mm (0.343")

A summary of the overall PZT performance assessment for Rotorbeam crack detection in the web and flange regions is as follows:

- Only one crack in a single direction was used to assess each PZT network. This ensures a single, independent variable (length) to allow for the OSTI calculation.
- All crack detections used a conservative DI threshold. Data suggests that slightly lower DI values could be used for detection so additional sensitivity is possible. Thus, the crack detection lengths recorded were conservative values.
- Signal-to-noise ratios, compare sensor readings without any cracks to those produced after crack is generated in the structure:
  - Initial Baseline (pristine) DI range = 0.0005 to 0.001
  - Final crack detection readings are DI = 0.05 to 0.40 → S/N > 100. Normal inspection procedures require that the S/N > 3 so this result proves that the PZT system is producing a very strong crack indication.
- Crack detection requirement can be referenced to performance → Final POD $_{(90,95)}$ for PZT on Rotorbeam:
  - PZT Performance for Web POD $_{(90/95)}$ = 0.274"
  - PZT Performance for Flange POD $_{(90/95)}$ = 0.343"

6.1.2.2. PZT Results for Cracked Holes with Rivets Installed

Rotorbeam Web and Flange Regions

The results from the specimens containing riveted holes were then added to the OSTI calculations to evaluate the effects of rivet presence on the crack detection within a PZT sensor network. Specimens with an "F" in the name (RB-PZT-17F and RB-PZT-18F) indicate tests conducted with a fastener in the web and flange holes. Table 6-1 and Table 6-3 include these results for the web and flange regions, respectively. Table 6-5 and Table 6-6 summarize the corresponding OSTI POD calculations. There was essentially no change in the POD levels. For the web region, the average crack detection for open holes 0.210" (5.33 mm) and the average crack detection for riveted holes 0.218" (5.54). These results vary by only 3.7%. For the flange region, the average crack detection for open holes 0.328" (8.33 mm) and the average crack detection for riveted holes 0.318" (8.06 mm). These results vary by only 3.1%. For both the web region and the flange region, there is almost no difference in PZT crack detection between open and riveted holes. These results indicate that there is very little effect of rivet presence on the performance of the PZT sensor network.

Table 6-5. POD Calculations Using One-Sided Tolerance Interval from PZT Response Data on Riveted Rotorbeam Web (unloaded)

PZT Crack Detection Data in Web

Crack Length at PZT Detection a (in)	Log of Crack Length at PZT Detection a (in)
0.205	-0.688246
0.171	-0.767004
0.171	-0.767004
0.222	-0.653647
0.234	-0.630784
0.199	-0.701147
0.234	-0.630784
0.201	-0.696804
0.222	-0.653647
0.244	-0.612610
0.209	-0.679854
0.197	-0.705534
0.238	-0.623423

PZT Crack Detection in Web for Unloaded Open and Riveted Holes

Statistic Estimates in Log & Linear Scales

Statistic	Value in Log Scale	Value in Linear Scale
Mean (X)	-0.677730	0.211
Stnd Deviation (S)	0.050413	0.023799

POD Detection Levels (γ = 95%, n = 13)

	POD in inches	POD in mm
Flaw Size: POD = X + K(S) =	0.270	6.85

Web Open Hole Data: Crack Length at PZT Detection = 6.95 mm

Web Open/Riveted Hole Data: Crack Length at PZT Detection = 6.85 mm

Table 6-6. POD Calculations Using One-Sided Tolerance Interval from PZT Response Data on Riveted Rotorbeam Flange (unloaded)

PZT Crack Detection Data in Flange (open holes & riveted holes)

Crack Length at PZT Detection a (in)	Log of Crack Length at PZT Detection a (ln)
0.295	-0.530178
0.33	-0.481486
0.33	-0.481486
0.33	-0.481486
0.33	-0.481486
0.33	-0.481486
0.33	-0.481486
0.33	-0.481486
0.33	-0.481486
0.33	-0.481486
0.33	-0.481486
0.33	-0.481486
0.33	-0.481486
0.33	-0.481486
0.33	-0.481486
0.33	-0.481486
0.33	-0.481486
0.33	-0.481486
0.33	-0.481486
0.33	-0.481486
0.33	-0.481486
0.33	-0.481486
0.33	-0.481486
0.33	-0.481486
0.305	-0.515700

PZT Crack Detection in Flange for Unloaded Open and Riveted Holes

Statistic Estimates in Log & Linear Scales

Statistic	Value in Log Scale	Value in Linear Scale
Mean (X)	-0.484940	0.328
Stnd Deviation (S)	0.011897	0.008597

POD Detection Levels (γ = 95%, n = 24)

	POD in inches	POD in mm
Flaw Size: POD = X + K(S) =	0.344	8.75

Flange Open Hole Data: Crack Length at PZT Detection = 8.72 mm (0.343")

Flange Open/Riveted Hole Data: Crack Length at PZT Detection = 8.75 mm (0.344")

6.1.2.3. PZT Performance - Comparison of PODs Calculated from Different Analysis Methods

Multiple coupons were tested such that crack lengths were measured before and after crack detection. This provided a mechanical trends analysis to relate Damage Index (DI) values to fatigue crack lengths. This data allows for trend data to be used for reliability assessments. This trend data was used to produce Hit-Miss and $\hat{a}$ vs a data for comparison POD calculations

Rotorbeam Web Region

Hit-Miss Log Regression POD Method - Quantifying SHM performance using the Log Regression Method only requires that the signal deviation can be reduced to produce a simple detection (hit) or no-detection (miss). Thus, the mapping of SHM signals to flaw detection is key. The 13 crack detection data points from the 13 different specimens listed in Table 6-1 were used in the Hit-Miss POD method described in Section 4.6 to calculate the POD performance. However, additional data points were extrapolated from each specimen using the same PZT DI threshold of 0.05 to determine crack detection. For each specimen, additional data points were acquired by selecting crack lengths below DI=0.05 (i.e. below detection) to correspond to "Misses" and crack lengths above DI=0.05 (i.e. above detection) to correspond to "Hits." Note that the Hit-Miss Method requires the use of approximately 50 independent data points from 50 different crack sites. To create a comparison that relates the POD calculated from the OSTI method to traditional POD

assessments, the data from the POD testing described above was applied in a Hit-Miss POD analysis.

Some extrapolation of the PZT crack detection data was necessary to produce sufficient data from the reduced-order, 13 independent crack detection tests. Additional extrapolated data at extremes (very small & very large cracks) were used to populate a complete the Hit-Miss POD curve. Hit-Miss data for the web region of the Rotorbeam specimen was compiled using crack PZT detection lengths from each test along with missed crack detections (lengths) below PZT detection level & hit crack detections (lengths) above the PZT detection level of DI=0.05. Using this approach, actual Hit/Miss data was acquired from 13 PZT networks to produce195 data points. However, as mentioned above, these 195 data points were not independent since multiple data points were acquired from each specimen. Table 6-7 through Table 6-10 summarize the results for each individual test specimen where the hit-miss data surrounding the PZT crack detection has been extrapolated from the raw test data. This hit (1) and miss (0) data is plotted in Figure 6-37.

Table 6-7. Sample PZT Data Set Showing DI Levels Before and After Crack Detection

Specimen and Detection Path	Cycles	DI Value	Crack Length (mm)	Detection DI=>0.05
RB-PZT-6 Sensor Path 5-8	0	0.00013	0.00	0
	5,000	0.00896	0.50	0
	7,000	0.00947	1.00	0
	9,000	0.01089	1.85	0
	12,000	0.00963	2.60	0
	15,000	0.01699	3.50	0
	18,000	0.03313	4.10	0
	21,000	0.03192	4.80	0
	24,000	0.10137	5.20	1
	27,000	0.08826	5.85	1
	30,000	0.12691	6.50	1
	33,000	0.17409	7.30	1
	36,000	0.22255	8.25	1
	38,800	0.26471	9.65	1
	42,000	0.22615	10.75	1

Initial PZT crack detection

DI Corresponding to Crack Detection is DI ≥ 0.05

The Hit-Miss Log Regression POD method was used to calculate the $POD_{(90/95)}$ value for the PZT system applied in the network indicated on the Rotorbeam web region. The total set of 95 data points from the individual $POD_{(90/95)}$ values were compiled into an overall performance calculation to produce an overall $POD_{(90/95)}$ value of 0.245" (6.23 mm). This can be used for comparison to the OSTI $POD_{(90/95)}$ value of 0.270" (6.85 mm) as shown in Figure 6-38. These results from the Hit-miss POD method, which represents traditional POD analyses, compare well with the OSTI method (within 9.3%). The OSTI $POD_{(90/95)}$ level is higher and thus, more conservative for assessing performance.

Table 6-8. Damage Index Values Over Full Web Crack Growth – RB-PZT-7 to RB-PZT-10

Specimen and Detection Path	Cycles	DI Value	Crack Length (mm)	Detection DI=>0.05
RB-PZT-7 Sensor Path 5-8	0	0.00022	0.00	0
	5,000	0.00734	0.50	0
	7,000	0.0093	1.00	0
	9,000	0.01039	1.95	0
	12,000	0.01627	2.55	0
	15,000	0.0252	3.30	0
	18,000	0.03758	3.80	0
	21,000	0.06055	4.35	1
	24,000	0.05845	4.85	1
	27,000	0.09424	5.85	1
	30,000	0.14025	6.60	1
	33,000	0.20521	7.50	1
	36,000	0.2076	8.60	1
	39,000	0.19686	9.70	1
	42,000	0.18396	11.15	1
	45,000	0.17094	12.65	1
	46,288	0.16634	13.2	1
RB-PZT-8 Sensor Path 5-8	0	0.00023	0.00	0
	5,000	0.01345	0.50	0
	7,000	0.01661	1.00	0
	9,000	0.01778	1.50	0
	12,000	0.02197	2.60	0
	15,000	0.0288	3.25	0
	18,000	0.0449	3.70	0
	21,000	0.07666	4.35	1
	24,000	0.09093	4.95	1
	27,000	0.1212	5.60	1
	30,000	0.15524	6.10	1
	33,000	0.20938	6.80	1
	36,000	0.25965	7.45	1
	38,800	0.29921	8.45	1
	42,000	0.32357	9.25	1
	44,178	0.33557	10.30	1

Specimen and Detection Path	Cycles	DI Value	Crack Length (mm)	Detection DI=>0.05
RB-PZT-9 Sensor Path 5-8	0	0.00036	0.00	0
	5,000	0.01000	0.30	0
	7,000	0.01036	0.70	0
	9,000	0.01003	1.40	0
	12,000	0.00976	2.15	0
	15,000	0.01140	2.65	0
	18,000	0.01467	3.10	0
	21,000	0.02513	3.65	0
	24,000	0.03250	4.20	0
	27,000	0.01799	5.10	0
	30,000	0.04994	5.65	1
	33,000	0.09484	6.50	1
	36,000	0.14173	7.40	1
	40,000	0.20458	8.55	1
	44,645	0.18697	10.85	1
RB-PZT-10 Sensor Path 5-8	0	0.00065	0.00	0
	5,000	0.00593	0.30	0
	7,000	0.00640	0.70	0
	9,000	0.00621	1.55	0
	12,000	0.01699	2.15	0
	15,000	0.01584	2.80	0
	18,000	0.01966	3.30	0
	21,000	0.02869	3.95	0
	24,000	0.03175	4.40	0
	27,000	0.04587	5.10	0
	30,000	0.07710	5.95	1
	33,000	0.12265	6.40	1
	36,000	0.10765	7.45	1
	39,000	0.19692	8.40	1
	42,000	0.22056	9.2	1
	45000	0.23158	10.55	1
	48000	0.21248	12.05	1
	50526	0.18911	13.3	1

Figure 6-38 summarizes the Rotorbeam PZT Testing for: 1) the web region, 2) cumulative Hit/Miss POD curve, 3) unloaded open and riveted holes, 4) detection at any frequency, 5) - specimens in unloaded state, and 6) DI threshold =0.05. Note the proximity of the 95% Confidence Bound to the Max Likelihood Estimate is affected by the number of assumed, independent data points. Thus, this approximation is highly dependent on the consistency of the assumed, extrapolated (independent) data points. Figure 6-39 shows the results from the Hit-Miss POD Method for specimens with and without fasteners. The $POD_{(90/95)}$ values are essentially the same showing that fasteners had no effect on PZT crack detection in the Rotorbeam web.

In this Hit-Miss assessment conducted with the limited SHM response data, the calculations are carried out with the assumption that each data point is independent and is produced by a separate crack (separate specimen). This is not the case because the Hit-Miss analysis presented here took credit for the additional, extrapolated data as if it were independent data points (Mil-HDBK-1823 calculation). If the sensor response is consistent enough that the assumed data is representative (additional tests produced independent data that is equivalent to the repeated measures assumed data), then the resulting "hit-miss" calculations are close to the truth. Repeated measures data (multiple data points from a single crack profile and SHM response) are used in these calculations which is an assumption that is not statistically valid. It does not account for possible crack-to-crack variations from different specimens. Thus, these results are for illustrative, comparison purposes only and not for any certification of performance. *Certification results are to be taken only from the OSTI method already presented in this Section*.

Table 6-9. Damage Index Values Over Full Web Crack Growth – RB-PZT-11 to RB-PZT-14

Specimen and Detection Path	Cycles	DI Value	Crack Length (mm)	Detection DI=>0.05
RB-PZT-11 Sensor Path 5-8	0	0.00010	0.00	0
	5,000	0.01424	0.15	0
	7,000	0.01415	0.40	0
	9,000	0.01482	0.75	0
	12,000	0.01521	1.35	0
	15,000	0.01476	2.05	0
	18,000	0.01637	2.55	0
	21,000	0.01765	3.05	0
	24,000	0.02180	3.55	0
	27,000	0.03421	3.90	0
	30,000	0.04087	4.70	0
	33,000	0.06330	5.05	1
	36,000	0.09075	5.95	1
	39,000	0.16397	6.55	1
	42,000	0.19091	7.8	1
	45,000	0.22302	8.4	1
	48,359	0.23438	9.45	1
RB-PZT-12 Sensor Path 5-8	0	0.00007	0.00	0
	5,000	0.01037	0.20	0
	7,000	0.01055	0.40	0
	9,000	0.01096	0.70	0
	12,000	0.00941	1.20	0
	15,000	0.00890	1.60	0
	18,000	0.00997	2.10	0
	21,000	0.01043	2.60	0
	24,000	0.01077	3.35	0
	27,000	0.01487	3.65	0
	30,000	0.02420	4.30	0
	33,000	0.01918	5.10	0
	36,000	0.03101	5.40	0
	39,000	0.05482	5.95	1
	42,000	0.09051	6.7	1
	45,000	0.12597	7.55	1
	48,000	0.15348	8.15	1

Specimen and Detection Path	Cycles	DI Value	Crack Length (mm)	Detection DI=>0.05
RB-PZT-13 Sensor Path 5-8	0	0.00018	0.00	0
	5,000	0.01043	0.40	0
	7,000	0.01261	0.70	0
	9,000	0.01300	1.10	0
	12,000	0.01329	1.70	0
	15,000	0.01280	2.30	0
	18,000	0.01749	2.80	0
	21,000	0.02434	3.50	0
	24,000	0.03706	4.10	0
	27,000	0.04524	4.75	0
	30,000	0.05546	5.10	1
	33,000	0.06944	5.70	1
	36,000	0.10100	6.55	1
	39,000	0.13248	7.25	1
	42,000	0.15820	8.3	1
	45,000	0.16789	9.3	1
RB-PZT-14 Sensor Path 5-8	0	0.00117	0.00	0
	5,000	0.00958	0.50	0
	7,000	0.01080	1.20	0
	9,000	0.00952	1.80	0
	12,000	0.01084	2.30	0
	15,000	0.01119	3.05	0
	18,000	0.01283	3.40	0
	21,000	0.01645	3.75	0
	24,000	0.02275	4.25	0
	27,000	0.03374	4.80	0
	30,000	0.04624	5.20	1
	33,000	0.05906	5.65	1
	36,000	0.07723	6.10	1
	39,000	0.11055	6.85	1
	42,000	0.12688	7.6	1
	45,000	0.1568	8.5	1
	48000	0.1681	9.3	1

Table 6-10. Damage Index Values Over Full Web Crack Growth – RB-PZT-15 to RB-PZT-18

Specimen and Detection Path	Cycles	DI Value	Crack Length (mm)	Detection DI=>0.05
RB-PZT-15 Sensor Path 5-8	0	0.00032	0.00	0
	5,000	0.00917	0.20	0
	7,000	0.01590	0.30	0
	9,000	0.01592	0.50	0
	12,000	0.01554	0.80	0
	15,000	0.01036	1.15	0
	18,000	0.00943	1.60	0
	21,000	0.00836	1.95	0
	24,000	0.00779	2.45	0
	27,000	0.00705	2.90	0
	30,000	0.01115	3.30	0
	33,000	0.01339	3.90	0
	36,000	0.01839	4.65	0
	39,000	0.03518	5.20	0
	42,000	0.04449	5.75	0
	45,000	0.07385	6.20	1
	51,000	0.15512	7.60	1
RB-PZT-16 Sensor Path 5-8	0	0.00189	0.00	0
	5,000	0.00850	0.80	0
	7,000	0.00969	1.30	0
	9,000	0.00994	1.85	0
	12,000	0.01051	2.45	0
	15,000	0.01198	2.90	0
	18,000	0.01989	3.45	0
	21,000	0.02834	4.05	0
	24,000	0.03955	4.60	0
	27,000	0.06016	5.30	1
	30,000	0.08834	6.05	1
	33,000	0.13364	6.75	1
	36,000	0.16998	7.40	1
	39,000	0.19786	8.65	1
	42,000	0.20061	9.60	1
	45,000	0.19599	11.00	1

Specimen and Detection Path	Cycles	DI Value	Crack Length (mm)	Detection DI=>0.05
RB-PZT-17F Sensor Path 6-8	48,000	0.00325	1.30	0
	51,000	0.00677	2.70	0
	54,000	0.01072	3.00	0
	57,000	0.01905	3.60	0
	60,000	0.03260	4.00	0
	63,000	0.03634	4.30	0
	66000	0.05186	5.00	1
	69000	0.06714	5.50	1
RB-PZT-18F Sensor Path 6-7	63,000	0.00469	3.40	0
	66,000	0.01848	4.30	0
	69,000	0.03655	4.95	0
	72,000	0.02730	5.55	0
	75,000	0.08897	6.05	1
	78,000	0.05210	6.70	1

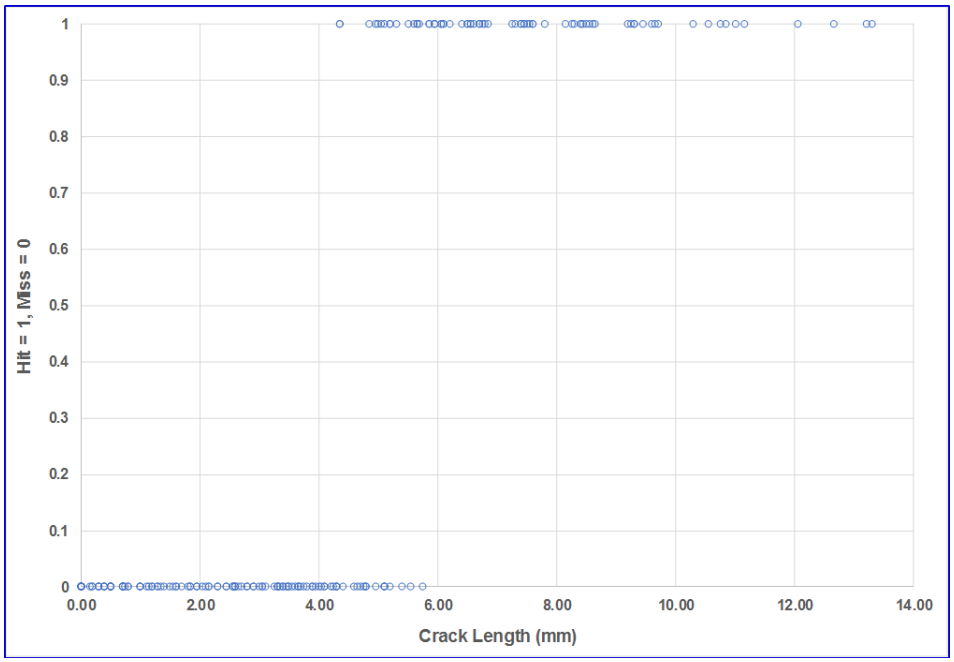

Figure 6-37. Plot of the 195 Non-independent Hit-Miss Data Points from Crack Growth in the Web of the Thirteen PZT Specimens

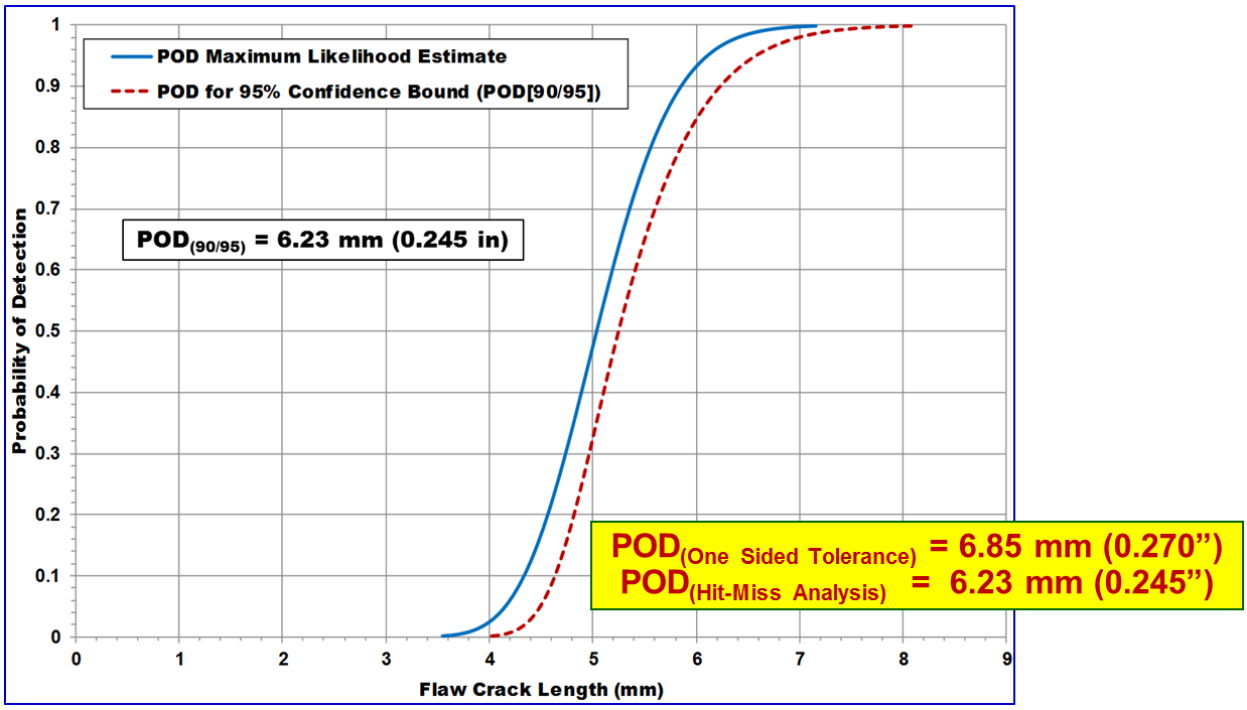

Figure 6-38. Cumulative Hit/Miss POD(90/95) Curve Generated from Repeated Measures Data from Rotorbeam PZT Testing – Web Region

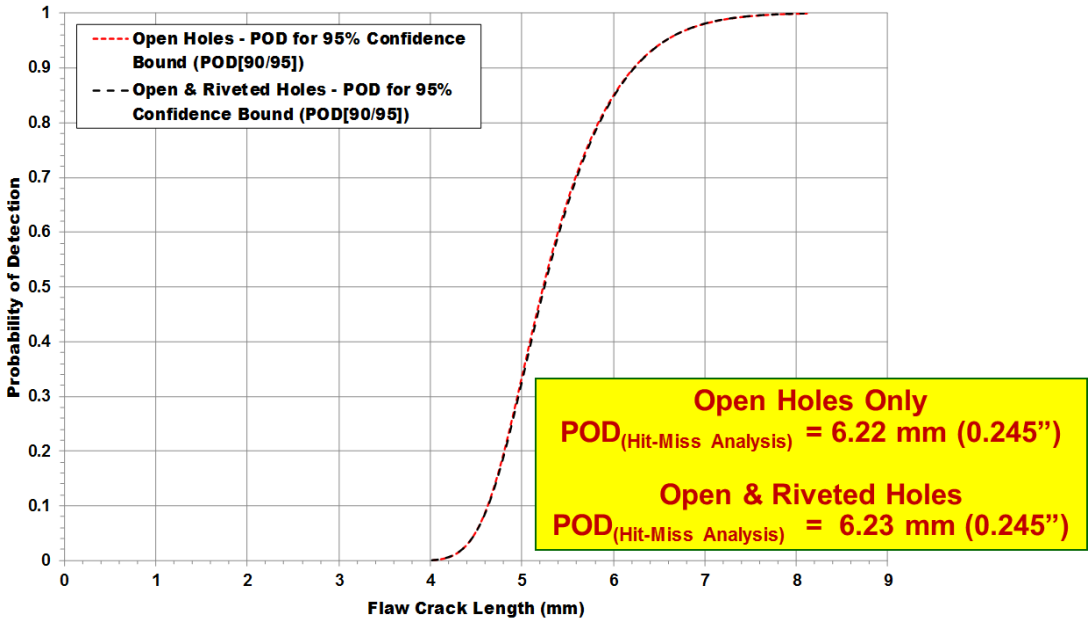

Figure 6-39. Comparison of Hit/Miss POD(90/95) Values Showing that Fasteners had No Effect on Crack Detection – Rotorbeam Web

Rotorbeam Flange Region

Hit-Miss Log Regression POD Method - A similar approach was taken for the data in the Rotorbeam flange region. Note that the Hit-Miss Method requires the use of approximately 50 independent data points from 50 different crack sites. To create a comparison that relates the POD calculated from the OSTI method to traditional POD assessments, the data from the POD testing described above was applied in a Hit-Miss POD analysis. Some extrapolation of the PZT crack detection data was necessary to produce sufficient data from the reduced-order, 24 independent crack detection tests. For each specimen, additional hit-miss data for the flange region of the Rotorbeam specimen were acquired by selecting crack lengths below DI=0.05 (i.e. below detection) to correspond to "Misses" and crack lengths above DI=0.05 (i.e. above detection) to correspond to "Hits." Using this approach, actual Hit/Miss data was acquired from 24 PZT specimens (321 data points). However, as mentioned above, these 321 data points were not independent since multiple data points were acquired from each specimen. Table 6-11 through Table 6-13 summarize the results for each individual test specimen where the hit-miss data surrounding the PZT crack detection has been extrapolated from the raw test data. This hit (1) and miss (0) data is plotted in Figure 6-40.

The Hit-Miss Log Regression POD method was used to calculate the $POD_{(90/95)}$ value for the PZT system applied in the network indicated on the Rotorbeam flange region. The total set of 321 data points into an overall performance calculation to produce a $POD_{(90/95)}$ value of 0.329" (8.35 mm). This can be used for comparison to the OSTI $POD_{(90/95)}$ value of 0.344" (8.75 mm) as shown in Figure 6-41. These results from the Hit-Miss POD Method, which represents traditional POD analyses, compare well with the OSTI method (within 4.4%). The OSTI $POD_{(90/95)}$ level is higher and thus, more conservative for assessing performance.

Table 6-11. Non-Independent Hit-Miss Data from Flange Crack Growth – RB-PZT-3 to RB-PZT-11 (Upper Flange = Path 1-3,1-4 2-4; Lower Flange = Path 9-11, 9-12, 10-12)

Specimen & Detection Path	Cycles	Crack Length (mm)	Detection DI=>0.05
RB-PZT-3 Sensor Path 1-3	11,000	0.00	0
	14,000	2.50	0
	16,000	3.05	0
	18,000	3.80	0
	20,000	4.25	0
	22,000	4.25	0
	24,000	4.70	0
	26,000	5.25	0
	28,000	5.65	0
	30,000	6.10	0
	32,000	6.85	0
	34,000	8.38	1
RB-PZT-4 Sensor Path 1-3	0	0.00	0
	5,000	0.00	0
	7,000	0.00	0
	9,000	1.00	0
	12,000	2.20	0
	15,000	3.05	0
	18,000	3.65	0
	21,000	4.30	0
	24,000	5.15	0
	27,000	5.85	0
	30,000	6.55	0
	33,000	7.20	0
	36,000	8.38	1
RB-PZT-5 Sensor Path 2-4	0	0.00	0
	5,000	0.45	0
	7,000	0.90	0
	9,000	1.45	0
	12,000	2.35	0
	15,000	3.20	0
	18,000	3.85	0
	21,000	4.35	0
	24,000	4.85	0
	27,000	5.60	0
	30,000	6.55	0
	33,000	7.45	0
	36,000	8.38	1
RB-PZT-6 Sensor Path 2-4	0	0.00	0
	5,000	0.50	0
	7,000	1.00	0
	9,000	1.50	0
	12,000	1.80	0
	15,000	2.80	0
	18,000	3.35	0
	21,000	3.90	0
	24,000	4.45	0
	27,000	4.95	0
	30,000	5.50	0
	33,000	6.15	0
	36,000	6.9	0
	38,800	8.38	1
RB-PZT-7 Sensor Path 1-3	0	0.00	0
	5,000	0.50	0
	7,000	1.00	0
	9,000	1.70	0
	12,000	2.45	0
	15,000	3.20	0
	18,000	3.80	0
	21,000	4.50	0
	24,000	5.15	0
	27,000	6.20	0
	30,000	7.05	0
	33,000	8.38	1
RB-PZT-8 Sensor Path 1-3	0	0.00	0
	5,000	0.50	0
	7,000	1.00	0
	9,000	1.90	0
	12,000	2.70	0
	15,000	3.60	0
	18,000	4.10	0
	21,000	4.80	0
	24,000	5.40	0
	27,000	6.00	0
	30,000	6.70	0
	33,000	8.38	1
RB-PZT-9 Sensor Path 1-3	0	0.00	0
	5,000	0.30	0
	7,000	0.80	0
	9,000	1.95	0
	12,000	2.65	0
	15,000	3.20	0
	18,000	3.80	0
	21,000	4.65	0
	24,000	5.40	0
	27,400	6.60	0
	30,000	8.38	1
RB-PZT-10 Sensor Path 2-4	0	0.00	0
	5,000	0.30	0
	7,000	0.60	0
	9,000	1.05	0
	12,000	2.30	0
	15,000	3.10	0
	18,000	3.80	0
	21,000	4.45	0
	24,000	4.95	0
	27,000	5.70	0
	30,000	6.65	0
	33,000	8.38	1
RB-PZT-11 Sensor Path 1-4	0	0.00	0
	5,000	0.20	0
	7,000	0.50	0
	9,000	0.90	0
	12,000	1.55	0
	15,000	2.40	0
	18,000	3.10	0
	21,000	3.80	0
	24,000	4.45	0
	27,000	5.20	0
	30,000	6.00	0
	33,000	6.50	0
	36,000	7.1	0
	39,000	8.38	1

Table 6-12. Non-Independent Hit-Miss Data from Flange Crack Growth – RB-PZT-12 to RB-PZT-18 (Upper Flange = Path 1-3,1-4 2-4; Lower Flange = Path 9-11, 9-12, 10-12)

Specimen & Detection Path	Cycles	Crack Length (mm)	Detection DI=>0.05
RB-PZT-12 Sensor Path 2-4	0	0.00	0
	5,000	0.30	0
	7,000	0.60	0
	9,000	1.00	0
	12,000	1.60	0
	15,000	2.25	0
	18,000	2.95	0
	21,000	3.40	0
	24,000	3.80	0
	27,000	4.15	0
	30,000	4.80	0
	33,000	5.40	0
	36,000	5.85	0
	39,000	7.25	0
	42,000	8.38	1
RB-PZT-15 Sensor Path 1-3	0	0.00	0
	5,000	0.30	0
	7,000	0.60	0
	9,000	1.00	0
	12,000	1.40	0
	15,000	1.85	0
	18,000	2.60	0
	21,000	3.15	0
	24,000	3.50	0
	27,000	4.00	0
	30,000	4.50	0
	33,000	5.10	0
	36,000	5.5	0
	39,000	6.15	0
	42,000	6.9	0
RB-PZT-16 Sensor Path 2-4	0	0.00	0
	5,000	0.60	0
	7,000	1.00	0
	9,000	1.55	0
	12,000	2.40	0
	15,000	3.20	0
	18,000	3.95	0
	21,000	4.50	0
	24,000	5.10	0
	27,000	5.80	0
	30,000	6.70	0
	33,000	8.38	1
RB-PZT-17F Sensor Path 1-4	42,000	1.20	0
	45,000	2.10	0
	48,000	3.8	0
	51,000	4.35	0
	54,000	5	0
	57000	5.45	0
	60000	6.1	0
	63000	6.55	0
	66000	7.05	0
	69000	8.38	1
RB-PZT-18F Sensor Path 1-4	36,000	3.00	0
	42,000	3.60	0
	45,000	4.2	0
	48,000	4.9	0
	51,000	5.55	0
	54000	6.7	0
	57000	7.3	0
	60000	7.75	0
	63000	8.38	1
RB-PZT-3 Sensor Path 10-12	11,000	0.00	0
	14,000	2.50	0
	16,000	3.25	0
	18,000	3.80	0
	20,000	4.40	0
	22,000	4.80	0
	24,000	5.05	0
	26,000	5.60	0
	28,000	6.00	0
	30,000	6.65	0
	32,000	7.50	1
	34,000	8.38	1
RB-PZT-4 Sensor Path 9-12	7,000	0.00	0
	9,000	1.00	0
	12,000	1.95	0
	15,000	2.80	0
	18,000	3.45	0
	21,000	3.70	0
	24,000	3.70	0
	27,000	4.35	0
	30,000	5.05	0
	33,000	5.05	0
	36,000	5.75	0
	39,000	6.5	0
	42,000	6.5	0
	45,000	6.5	0
	47,171	8.38	1
RB-PZT-5 Sensor Path 9-11	0	0.00	0
	5,000	0.50	0
	7,000	1.00	0
	9,000	1.50	0
	12,000	2.05	0
	15,000	2.50	0
	18,000	3.25	0
	21,000	3.80	0
	24,000	4.30	0
	27,000	5.00	0
	30,000	5.75	0
	33,000	6.40	0
	36,000	7.65	0
	39,000	8.38	1
RB-PZT-6 Sensor Path 10-12	0	0.00	0
	5,000	0.50	0
	7,000	1.00	0
	9,000	2.20	0
	12,000	2.85	0
	15,000	3.55	0
	18,000	4.20	0
	21,000	5.00	0
	24,000	5.90	0
	27,000	6.70	0
	30,000	8.38	1

Table 6-13. Non-Independent Hit-Miss Data from Flange Crack Growth – RB-PZT-7 to RB-PZT-16 (Upper Flange = Path 1-3,1-4 2-4; Lower Flange = Path 9-11, 9-12, 10-12)

Specimen & Detection Path	Cycles	Crack Length (mm)	Detection DI=>0.05
RB-PZT-7 Sensor Path 9-11	0	0.00	0
	5,000	0.25	0
	7,000	0.50	0
	9,000	1.00	0
	12,000	1.50	0
	15,000	2.00	0
	18,000	2.85	0
	21,000	3.15	0
	24,000	3.75	0
	27,000	3.75	0
	30,000	4.40	0
	33,000	4.75	0
	36,000	5.3	0
	39,000	5.9	0
	42,000	6.45	0
	45000	7.45	0
	46288	8.38	1
RB-PZT-8 Sensor Path 10-12	0	0.00	0
	5,000	0.25	0
	7,000	0.50	0
	9,000	0.85	0
	12,000	1.80	0
	15,000	2.45	0
	18,000	2.95	0
	21,000	3.55	0
	24,000	4.15	0
	27,000	4.15	0
	30,000	4.70	0
	33,000	5.25	0
	36,000	5.70	0
	39,000	6.15	0
	42,000	7.10	0
	44,178	8.38	1
RB-PZT-9 Sensor Path 9-12	0	0.00	0
	5,000	0.30	0
	7,000	0.60	0
	9,000	0.95	0
	12,000	2.05	0
	15,000	2.70	0
	18,000	3.20	0
	21,000	3.75	0
	24,000	4.10	0
	27,400	4.65	0
	30,000	4.65	0
	33,000	5.40	0
	36,000	5.95	0
	40,000	6.75	0
	44,645	8.38	1

Specimen & Detection Path	Cycles	Crack Length (mm)	Detection DI=>0.05
RB-PZT-11 Sensor Path 10-12	0	0.00	0
	5,000	0.10	0
	7,000	0.20	0
	9,000	0.40	0
	12,000	0.70	0
	15,000	1.20	0
	18,000	2.00	0
	21,000	2.55	0
	24,000	2.95	0
	27,000	3.50	0
	30,000	4.20	0
	33,000	4.65	0
	36,000	4.95	0
	39,000	5.5	0
	42,000	6.1	0
	45000	6.9	0
	48359	8.38	1
RB-PZT-12 Sensor Path 9-11	0	0.00	0
	5,000	0.40	0
	7,000	0.70	0
	9,000	1.20	0
	12,000	1.90	0
	15,000	2.80	0
	18,000	3.40	0
	21,000	4.05	0
	24,000	4.80	0
	27,000	5.50	0
	30,000	6.40	0
	33,000	7.35	0
	36,000	8.38	1
RB-PZT-16 Sensor Path 9-11	0	0.00	0
	5,000	0.60	0
	7,000	1.00	0
	9,000	1.40	0
	12,000	2.00	0
	15,000	2.55	0
	18,000	2.90	0
	21,000	3.30	0
	24,000	3.55	0
	27,000	4.20	0
	30,000	4.60	0
	33,000	5.20	0
	36,000	5.8	0
	39,000	6.4	0
	42,000	7.35	0
	45000	7.85	0
	45240	8.38	1

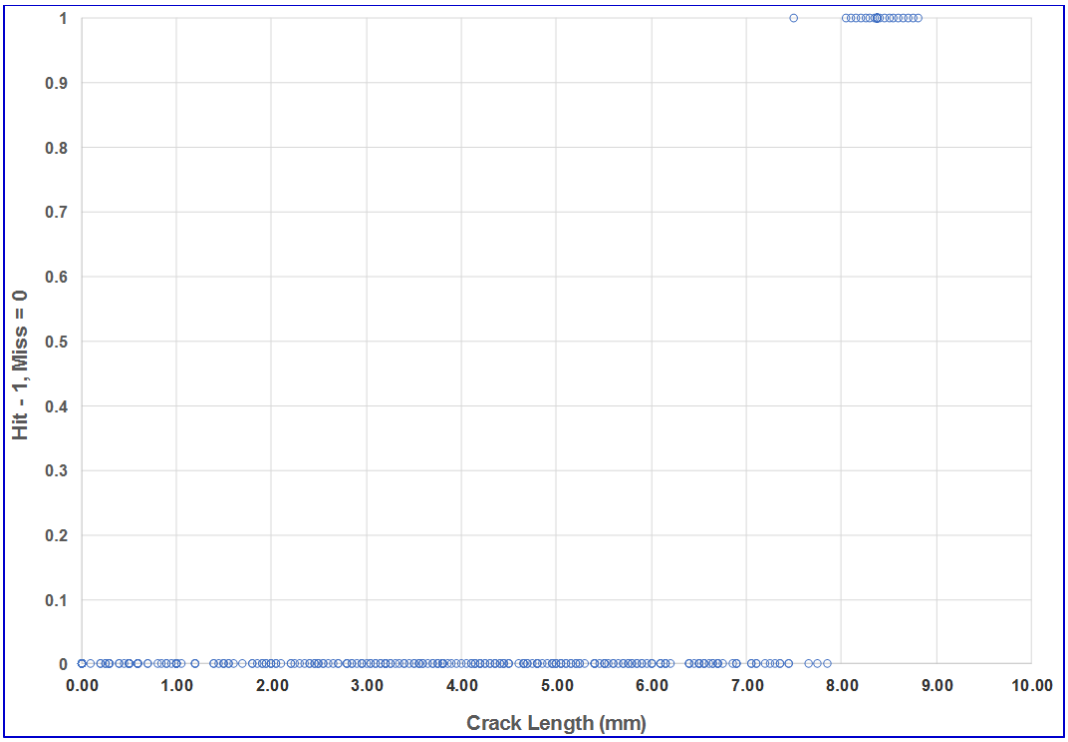

Figure 6-40. Plot of the 321 Non-independent Hit-Miss Data Points from Crack Growth in the Upper and Lower Flange of the Thirteen PZT Specimens

Figure 6-41 summarizes the Rotorbeam PZT Testing for: 1) the flange region, 2) cumulative Hit/Miss POD curve, 3) unloaded open and riveted holes, 4) detection at any frequency, 5) - specimens in unloaded state, and 6) DI threshold =0.05. Note the proximity of the 95% Confidence Bound to the Max Likelihood Estimate is affected by the number of assumed, independent data points. Thus, this approximation is highly dependent on the consistency of the assumed, extrapolated (independent) data points. Figure 6-39 through Figure 6-42 shows the results from the Hit-Miss POD Method for specimens with and without fasteners. The $POD_{(90/95)}$ curves are essentially the same showing that fasteners had no effect on PZT crack detection in the Rotorbeam flange.

In this Hit-Miss assessment conducted with the limited SHM response data, the calculations are carried out with the assumption that each data point is independent and is produced by a separate crack (separate specimen). This is not the case because the Hit-Miss analysis presented here took credit for the additional, extrapolated data as if it were independent data points (Mil-HDBK-1823 calculation). If the sensor response is consistent enough that the assumed data is representative (additional tests produced independent data that is equivalent to the repeated measures assumed data), then the resulting "hit-miss" calculations are close to the truth. Repeated measures data (multiple data points from a single crack profile and SHM response) are used in these calculations which is an assumption that is not statistically valid. It does not account for possible crack-to-crack variations from different specimens. Thus, these results are for illustrative, comparison purposes only and not for any certification of performance. *Certification results are to be taken only from the OSTI method already presented in this Section*.

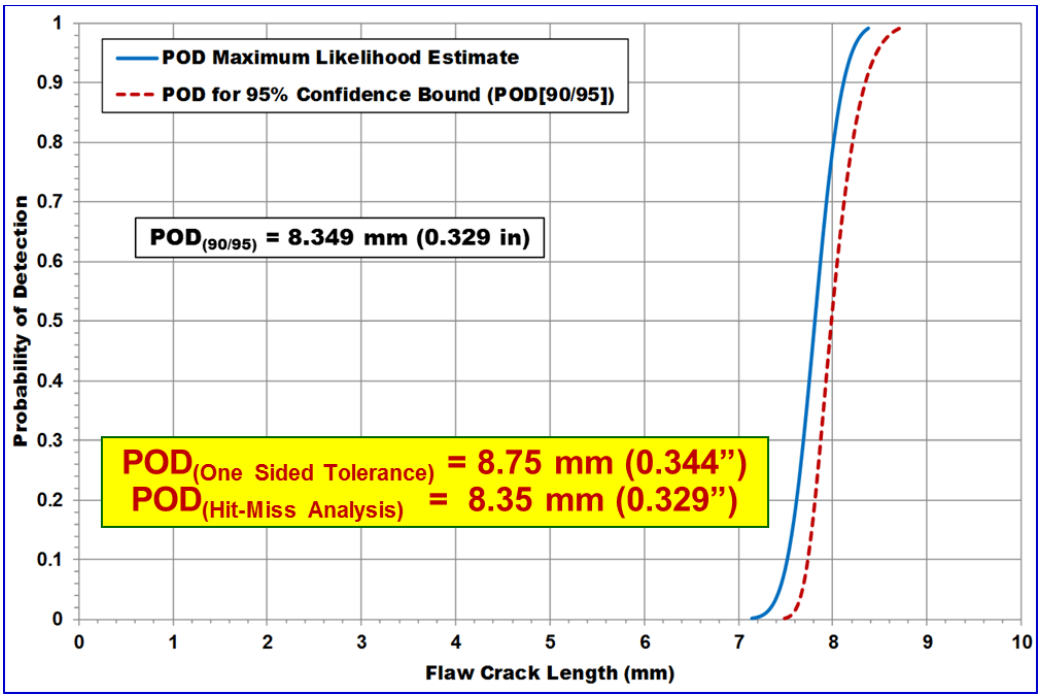

Figure 6-41. Cumulative Hit/Miss POD(90/95) Curve Generated from Repeated Measures Data from Rotorbeam PZT Testing – Flange Region

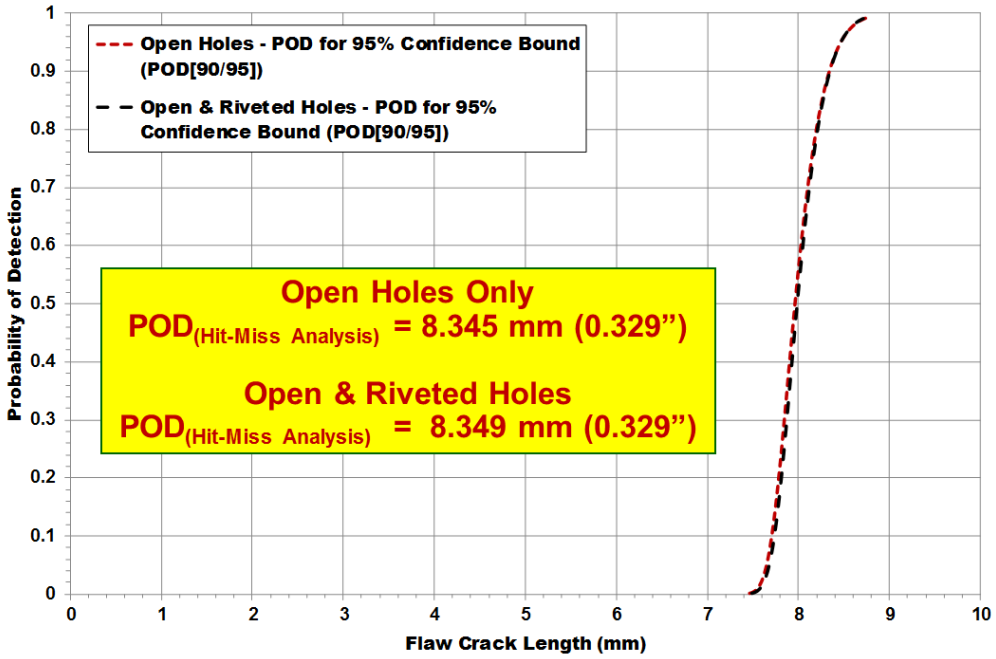

Figure 6-42. Comparison of Hit/Miss POD(90/95) Values Showing that Fasteners had No Effect on Crack Detection – Rotorbeam Flange

â vs a POD Method - When the crack or other flaw decision is made on the basis of a recorded response, â, to the inspection stimulus, the data are known as *â* vs *a* inspection results and a different POD(a) analysis can performed as described in Section 4.6. For the Rotorbeam application, this data took the form of PZT system response *â* (DI values) as a function of the damage parameter *a* (crack length). When the inspection response is greater than or equal to the selected DI detection threshold of 0.05, a crack is indicated for the site. Because of the added information in the *â* data, a valid characterization of the POD(a) function with confidence bounds can be obtained with fewer cracks than are required for the hit/miss analysis. It is recommended that at least 30 cracks be available for demonstrations whose results can be recorded in *â* vs *a* form. The *â vs a* POD analysis method requires the use of completely independent data points (~ 30) from different crack sites. To apply the â vs. a method for determining POD, it is necessary to acquire data relating the response of the SHM system (â = DI) to the corresponding crack length (a). Multiple Rotorbeam specimens were tested such that crack lengths and corresponding DI levels were measured before and after permanent crack detection in the web region.

When the crack or other flaw decision is made on the basis of a recorded response, â, to the inspection stimulus, the data are known as *â* vs *a* inspection results and a different POD(a) analysis can be performed as described in Section 4.6. For the Rotorbeam application, this data took the form of PZT system response *â* (DI values) as a function of the damage parameter *a* (crack length). When the inspection response is greater than or equal to the selected DI detection threshold of 0,05, a crack is indicated for the site. Because of the added information in the *â* data, a valid characterization of the POD(a) function with confidence bounds can be obtained with fewer cracks than are required for the hit/miss analysis. It is recommended that at least 30 cracks be available for demonstrations whose results can be recorded in *â* vs *a* form. The *â vs a* POD analysis method requires the use of completely independent data points (~ 30) from different crack sites. To apply the â vs. a method for determining POD, it is necessary to acquire data relating the response of the SHM system (â = DI) to the corresponding crack length (a). Multiple Rotorbeam specimens were tested such that crack lengths and corresponding DI levels were measured before and after permanent crack detection. This provided a mechanical trends analysis to relate PZT values to fatigue crack lengths and create a set of â vs. a (sensor response vs. crack length) data points for use in the â vs. a POD Method. Enough data points were acquired to achieve convergence in a vs. â POD analysis.

Figure 6-43 and Figure 6-44 show samples of the basic da/dN crack growth data that was generated, along with the DI vs crack length (*â* vs. *a)* information. Table 6-14 and Table 6-15 list the entire set of *DI vs a* data that was acquired from all specimen tests. Sample data from Table 6-14 and Table 6-15 are plotted in Figure 6-45 and Figure 6-46 to demonstrate the typical PZT response data on the Rotorbeam for the web and flange region, respectively. Note the relation between these DI trend curves and the chosen DI(threshold) of 0.05. Figure 6-47 shows that the resulting set of 195 *â vs a* data points plot linearly on the log-log scale thus ensuring the proper response relationship for the *â vs a* POD Method.

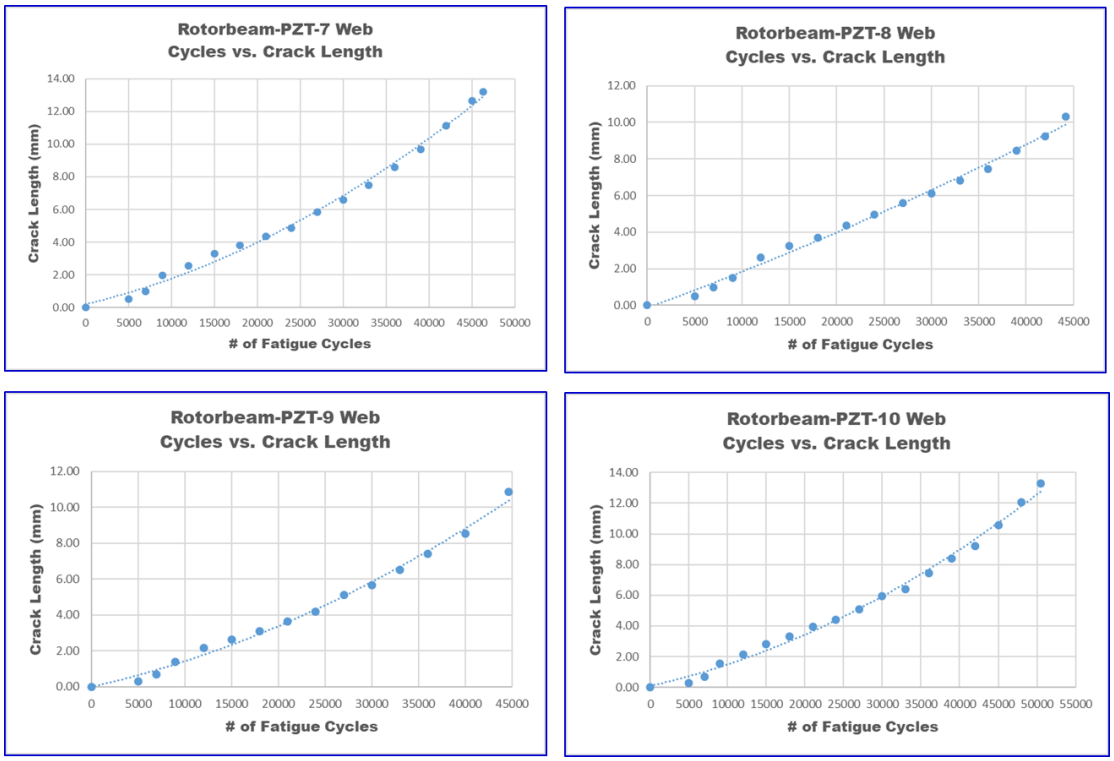

Figure 6-43. Fatigue Crack Growth in Rotorbeam Web Used for DI Trend Assessments

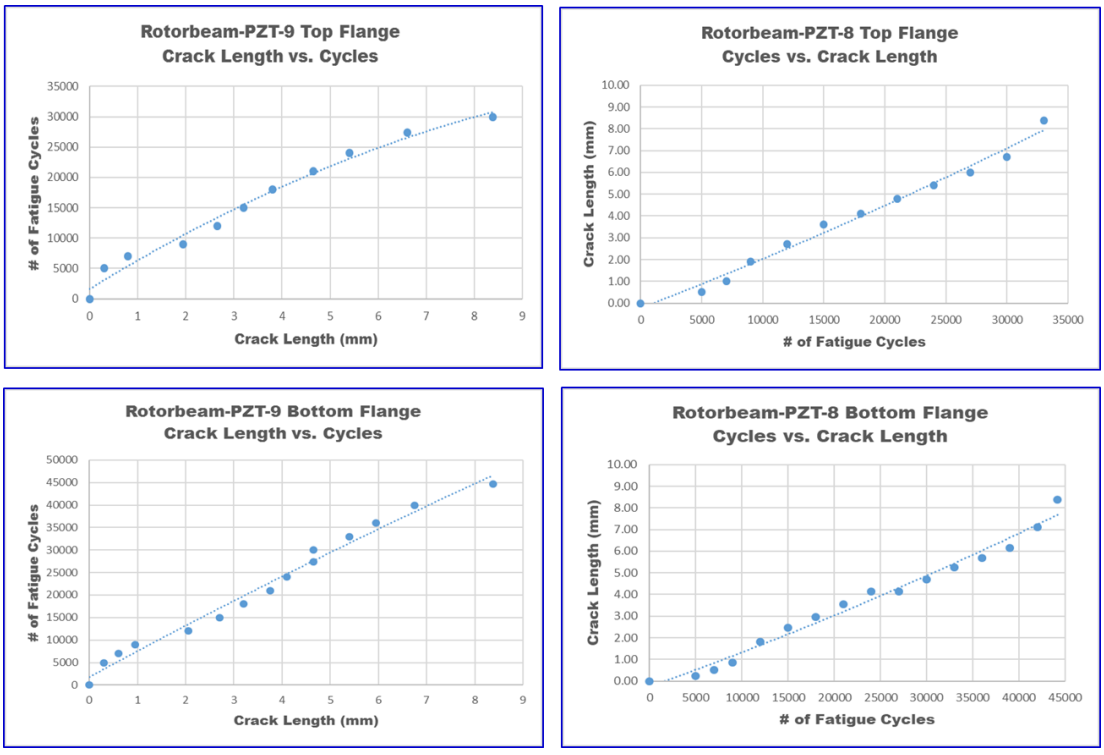

Figure 6-44. Fatigue Crack Growth in Rotorbeam Flange Used for DI Trend Assessments

Table 6-14. DI Values from Web Crack Growth for *â vs a* Analysis – RB-PZT-6 to RB-PZT-11

Specimen and Detection Path	DI Value	Crack Length (mm)
RB-PZT-6 Sensor Path 5-8	0.00013	0.00
	0.00896	0.50
	0.00947	1.00
	0.01089	1.85
	0.00963	2.60
	0.01699	3.50
	0.03313	4.10
	0.03192	4.80
	0.10137	5.20
	0.08826	5.85
	0.12691	6.50
	0.17409	7.30
	0.22255	8.25
	0.26471	9.65
	0.22615	10.75
RB-PZT-7 Sensor Path 5-8	0.00022	0.00
	0.00734	0.50
	0.0093	1.00
	0.01039	1.95
	0.01627	2.55
	0.0252	3.30
	0.03758	3.80
	0.06055	4.35
	0.05845	4.85
	0.09424	5.85
	0.14025	6.60
	0.20521	7.50
	0.2076	8.60
	0.19686	9.70
	0.18396	11.15
	0.17094	12.65
	0.16634	13.2

Specimen and Detection Path	DI Value	Crack Length (mm)
RB-PZT-8 Sensor Path 5-8	0.00023	0.00
	0.01345	0.50
	0.01661	1.00
	0.01778	1.50
	0.02197	2.60
	0.0288	3.25
	0.0449	3.70
	0.07666	4.35
	0.09093	4.95
	0.1212	5.60
	0.15524	6.10
	0.20938	6.80
	0.25965	7.45
	0.29921	8.45
	0.32357	9.25
	0.33557	10.30
RB-PZT-9 Sensor Path 5-8	0.00036	0.00
	0.01000	0.30
	0.01036	0.70
	0.01003	1.40
	0.00976	2.15
	0.01140	2.65
	0.01467	3.10
	0.02513	3.65
	0.03250	4.20
	0.01799	5.10
	0.04994	5.65
	0.09484	6.50
	0.14173	7.40
	0.20458	8.55
	0.18697	10.85

Specimen and Detection Path	DI Value	Crack Length (mm)
RB-PZT-10 Sensor Path 5-8	0.00065	0.00
	0.00593	0.30
	0.00640	0.70
	0.00621	1.55
	0.01699	2.15
	0.01584	2.80
	0.01966	3.30
	0.02869	3.95
	0.03175	4.40
	0.04587	5.10
	0.07710	5.95
	0.12265	6.40
	0.10765	7.45
	0.19692	8.40
	0.22056	9.2
	0.23158	10.55
	0.21248	12.05
	0.18911	13.3
RB-PZT-11 Sensor Path 5-8	0.00010	0.00
	0.01424	0.15
	0.01415	0.40
	0.01482	0.75
	0.01521	1.35
	0.01476	2.05
	0.01637	2.55
	0.01765	3.05
	0.02180	3.55
	0.03421	3.90
	0.04087	4.70
	0.06330	5.05
	0.09075	5.95
	0.16397	6.55
	0.19091	7.8
	0.22302	8.4
	0.23438	9.45

Table 6-15. DI Values from Web Crack Growth for *â vs a* Analysis – RB-PZT-12 to RB-PZT-18

Specimen and Detection Path	DI Value	Crack Length (mm)
RB-PZT-12 Sensor Path 5-8	0.00007	0.00
	0.01037	0.20
	0.01055	0.40
	0.01096	0.70
	0.00941	1.20
	0.00890	1.60
	0.00997	2.10
	0.01043	2.60
	0.01077	3.35
	0.01487	3.65
	0.02420	4.30
	0.01918	5.10
	0.03101	5.40
	0.05482	5.95
	0.09051	6.7
	0.12597	7.55
	0.15348	8.15
RB-PZT-13 Sensor Path 5-8	0.00018	0.00
	0.01043	0.40
	0.01261	0.70
	0.01300	1.10
	0.01329	1.70
	0.01280	2.30
	0.01749	2.80
	0.02434	3.50
	0.03706	4.10
	0.04524	4.75
	0.05546	5.10
	0.06944	5.70
	0.10100	6.55
	0.13248	7.25
	0.15820	8.3
	0.16789	9.3

Specimen and Detection Path	DI Value	Crack Length (mm)
RB-PZT-14 Sensor Path 5-8	0.00117	0.00
	0.00958	0.50
	0.01080	1.20
	0.00952	1.80
	0.01084	2.30
	0.01119	3.05
	0.01283	3.40
	0.01645	3.75
	0.02275	4.25
	0.03374	4.80
	0.04624	5.20
	0.05906	5.65
	0.07723	6.10
	0.11055	6.85
	0.12688	7.6
	0.1568	8.5
	0.1681	9.3
RB-PZT-15 Sensor Path 5-8	0.00032	0.00
	0.00917	0.20
	0.01590	0.30
	0.01592	0.50
	0.01554	0.80
	0.01036	1.15
	0.00943	1.60
	0.00836	1.95
	0.00779	2.45
	0.00705	2.90
	0.01115	3.30
	0.01339	3.90
	0.01839	4.65
	0.03518	5.20
	0.04449	5.75
	0.07385	6.20
	0.15512	7.60

Specimen and Detection Path	DI Value	Crack Length (mm)
RB-PZT-16 Sensor Path 5-8	0.00189	0.00
	0.00850	0.80
	0.00969	1.30
	0.00994	1.85
	0.01051	2.45
	0.01198	2.90
	0.01989	3.45
	0.02834	4.05
	0.03955	4.60
	0.06016	5.30
	0.08834	6.05
	0.13364	6.75
	0.16998	7.40
	0.19786	8.65
	0.20061	9.60
	0.19599	11.00
RB-PZT-17F Sensor Path 6-8	0.00325	1.30
	0.00677	2.70
	0.01072	3.00
	0.01905	3.60
	0.03260	4.00
	0.03634	4.30
	0.05186	5.00
	0.06714	5.50
RB-PZT-18F Sensor Path 6-7	0.00469	3.40
	0.01848	4.30
	0.03655	4.95
	0.02730	5.55
	0.08897	6.05
	0.05210	6.70

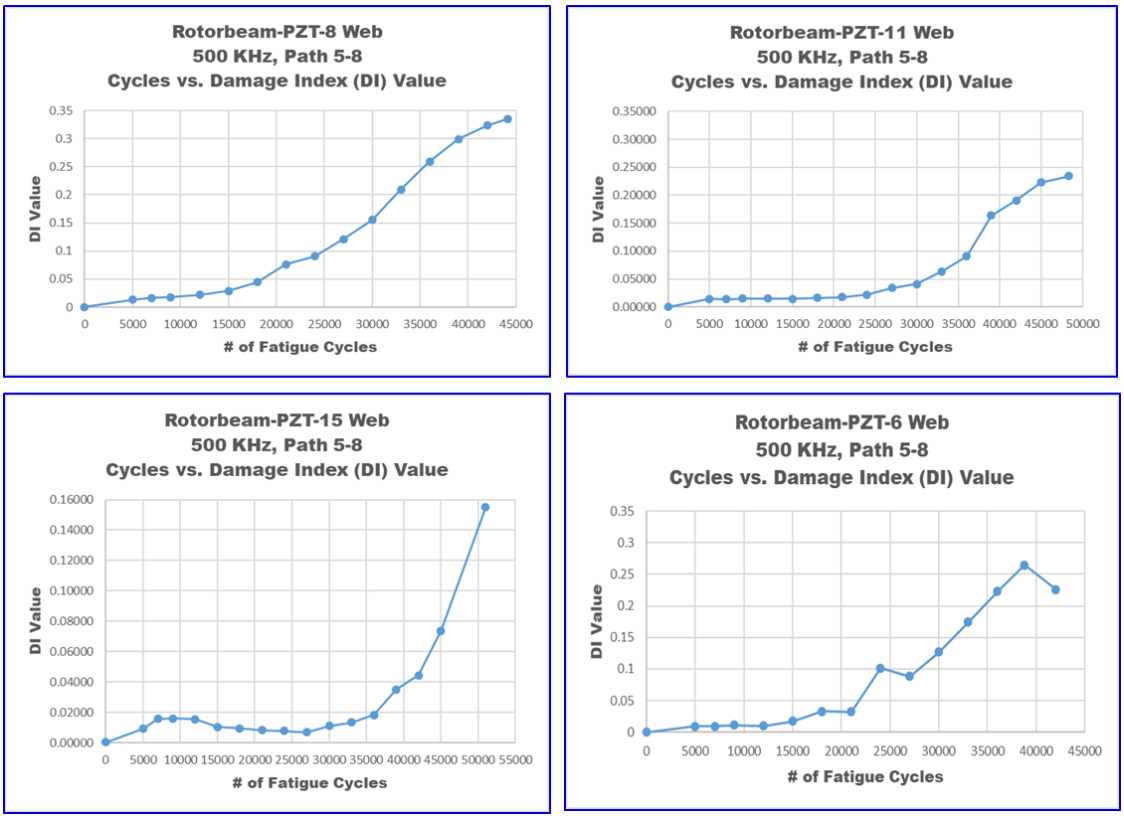

Figure 6-45. Damage Index (DI) Response with Increasing Crack Growth – Sample Set 1

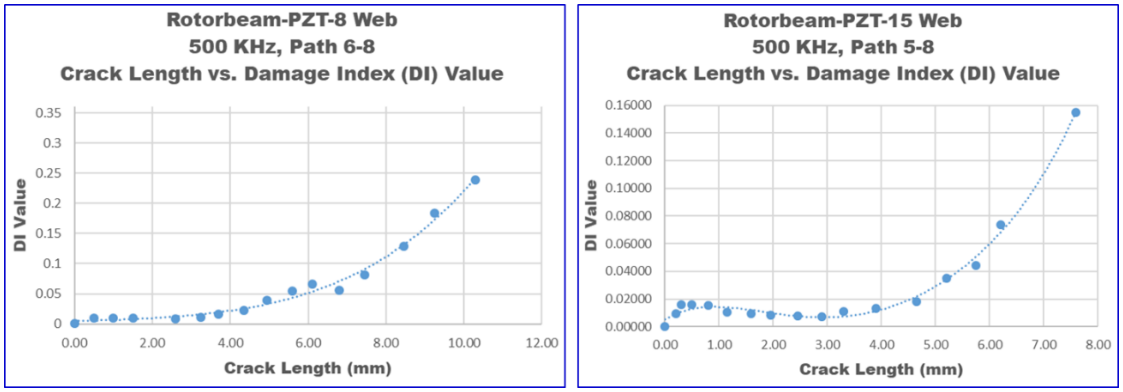

Figure 6-46. Damage Index (DI) Response with Increasing Crack Growth – Sample Set 2

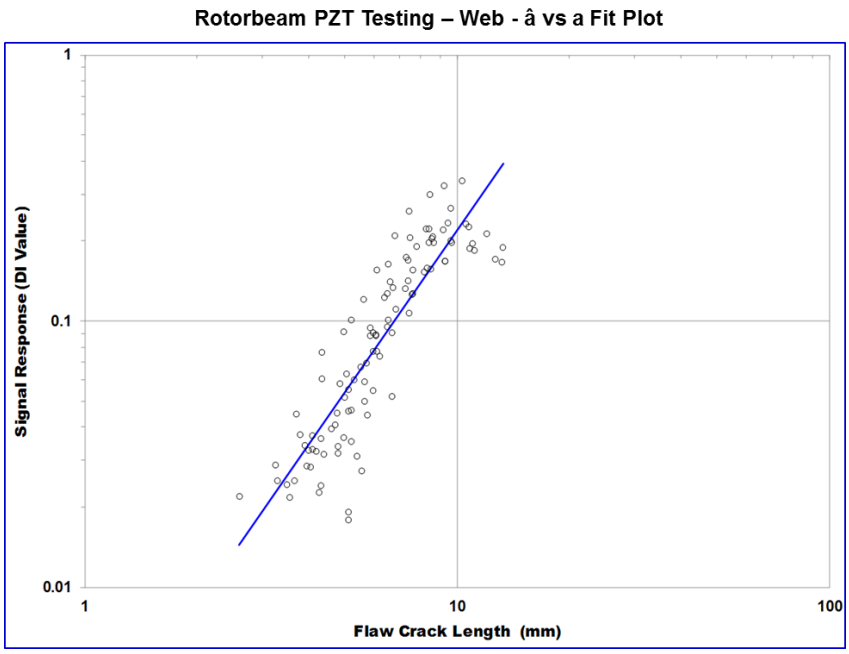

Figure 6-47. Plot of All *â vs. a* Data (DI vs Crack Length) for Web POD Analysis

The *â vs a* POD Method was applied to these 195 data points to calculate the overall $POD_{(90/95)}$ value of 0.256" (6.51 mm) for the crack length in the web region of the Rotorbeam. This can compared to the OSTI $POD_{(90/95)}$ value of 0.270" (6.85 mm) as shown in Figure 6-48. These results from the *â vs a* POD Method, which represents traditional POD analyses, compare well with the OSTI method (within 5.2%).

One advantage of using the *â vs a* POD Method is that this approach can use the response data to infer the performance of the subject SHM system when different decision thresholds are used to detect the damage. Figure 6-49 plots the $POD_{(90/95)}$ values that would be generated from different decision thresholds which allows the user to understand the changes in POD levels associated with a corresponding change in the DI damage detection threshold. For example, an increase in the DI detection threshold from 0.05 to 0.075 would increase the $POD_{(90/95)}$ value from 0.256" to 0.315". A decrease in the DI detection threshold from 0.05 to 0.025 would decrease the $POD_{(90/95)}$ value to 0.177". Of course, any reduction in the damage detection threshold must be conducted in light of any possible changes in the Probability of False Calls

Generation of the larger set of *â* crack response data from the PZT cracks tested was necessary to produce a sufficient set of *â vs a* response curves from only 22 independent crack detection tests. It should be noted that these data points are not independent data points and are only used here to provide a basis of comparison between the OSTI and Mil-Hndk-1823 *â vs a* POD Method for calculating POD level. Thus, these results are for illustrative, comparison purposes only and not for any certification of performance. *Certification results are to be taken only from the OSTI method already presented in this Section.*

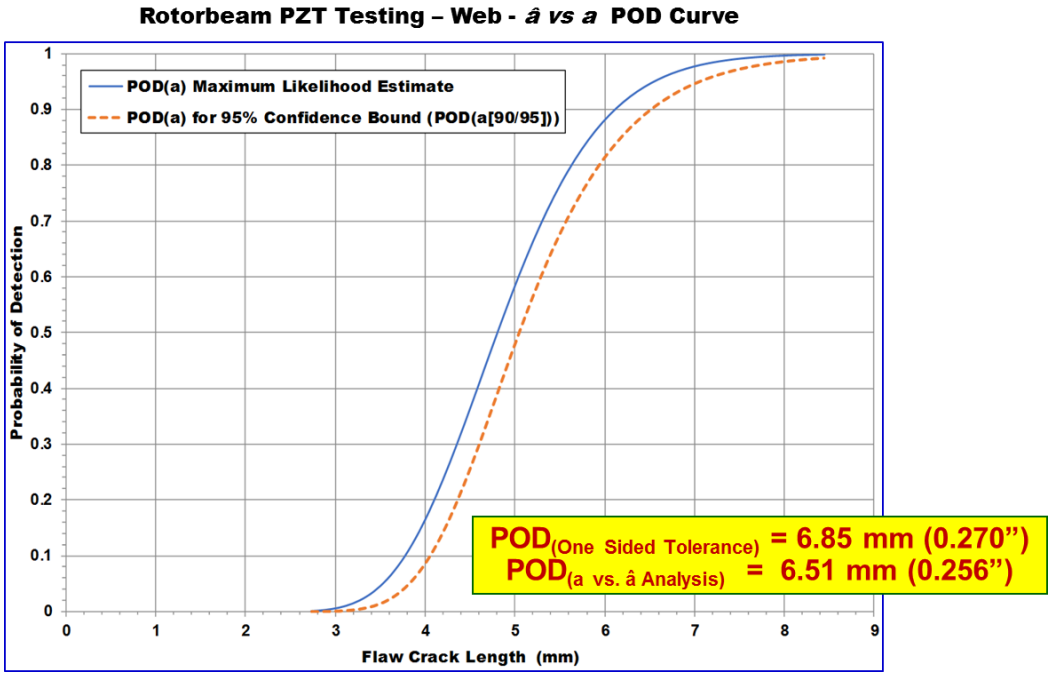

Figure 6-48. Cumulative *â vs. a* POD(90/95) Curve Generated from Repeated Measures Data from Rotorbeam PZT Testing – Web Region

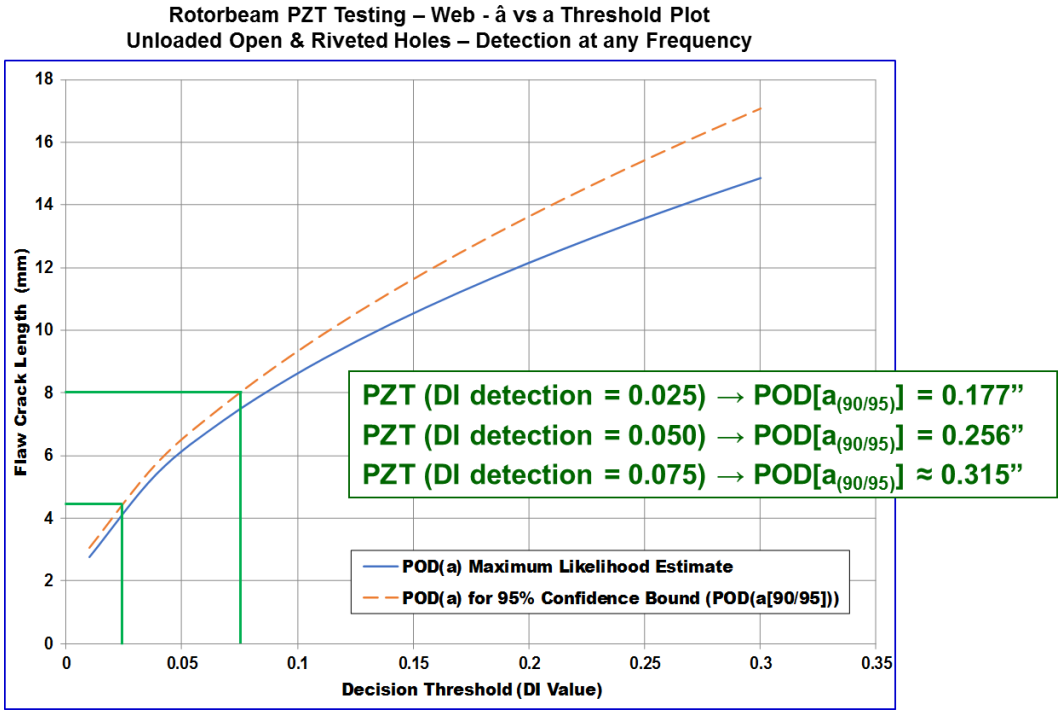

Figure 6-49. Estimated *a vs. â* $POD_{(90/95)}$ Values for the Web Crack Detection with Different Detection Thresholds

Comparison of PODs Calculated Using *OSTI, Hit-Miss & â vs a* POD Analyses Models - These results from the *Hit-Miss POD Method* and *â vs a POD Method*, which represent traditional POD analyses, compare well with the OSTI method. The increase in data points via use of repeated measures data artificially improves the confidence levels since these are not independent data points. This, in turn, makes the 95% confidence bound plot closer to the POD Maximum Likelihood Estimate (solid line in Figure 6-48). Thus, there are several factors included in the reduction in POD with the additional data points. Again, this reiterates that such calculations only provide general comparisons between the OSTI, *Hit-Miss POD Method* and the *â vs a POD Method*. Figure 6-50 provides an overall comparison between the $POD_{(90/95)}$ values as calculated by the OSTI, Hit-Miss and *â vs a* POD Methods as applied to crack detection in the web region. Figure 6-51 provides an overall comparison between the $POD_{(90/95)}$ values as calculated by the OSTI and Hit-Miss POD Methods as applied to crack detection in the flange region. Although these values are close, one would expect that, with sufficient independent specimen testing, all three methods would converge to a similar number. *For the purposes of this program with a specific Sikorsky application, the PZT performance certification results will only be taken from the OSTI results.*

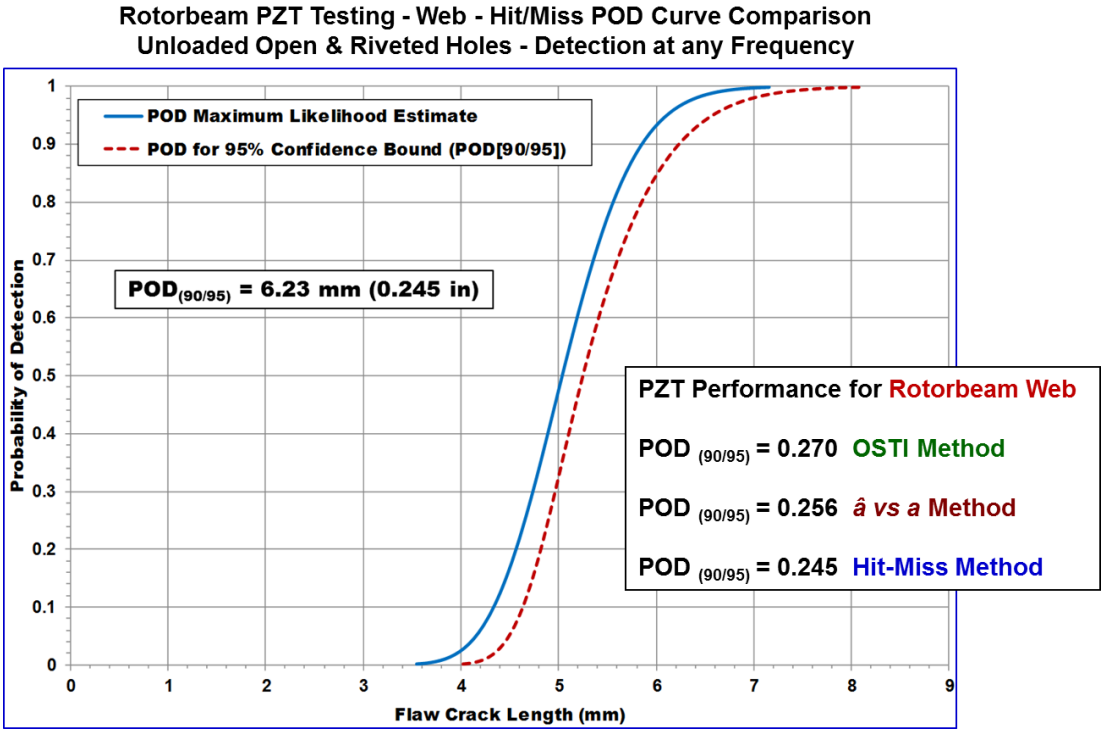

Figure 6-50. Web PZT Performance Testing Results – Comparison of OSTI, Hit-Miss, and a vs. â Methodologies

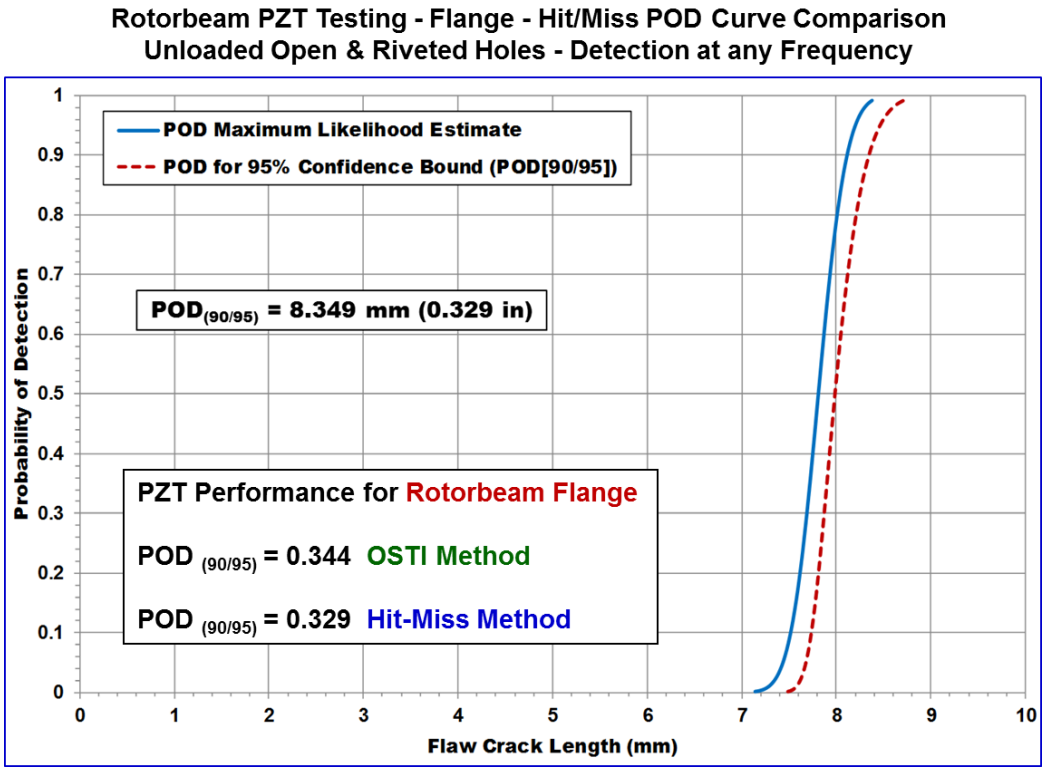

Figure 6-51. Flange PZT Performance Testing Results – Comparison of OSTI and Hit-Miss Methodologies

6.2. Effects of Structural Design and Stress Fields on PZT Performance

6.2.1. Crack Detection in Loaded vs. Unloaded Components

If the PZT networks are monitored while the structure is under load, it may be possible to improve the performance of the SHM system. This depends on the both the magnitude of the load (stress) and the direction of the stress. Tension loads, for example, tend to open a fatigue crack and increase the magnitude of the PZT signals (increase DI). Compression loads, on the other hand, may tighten the fatigue crack opening and decrease the DI levels. Torsional and bending loads can have either effect depending on the geometry of the component and the resulting direction of the local strain at the fatigue crack. In addition, load reapportionment and load shedding can occur as damage grows in a component. This can change the stress fields in a structure and change how the structure responds to load when it already has some damage. These factors must all be considered whenever deciding to monitor an SHM system while a structure is under load (e.g. monitoring during flight). In this test series, the Rotorbeam test specimen was placed under uniaxial tension during regular fatigue cycle intervals and data was acquired from the same PZT network are various tension load levels. The load levels corresponded to unloaded (0 load; results presented in Section 6.1), lightly loaded (1,000 lb) and medium loaded (7,000 lb) and highly-

loaded (14,000 lb) tension conditions. The light and medium loads produce stresses that are well below the yield stress level for this material while the high loads produce stresses that are approximately 2/3 of yield stress levels. It should be emphasized that any data acquired at elevated loads must be compared to baseline data acquired at those same loads. Otherwise, changes in PZT signals due to the change in stress levels along (i.e. no damage present) may be erroneously associated with damage detection.

Figure 6-52 provides an example from a straightforward effect of tension load on a web crack. The three curves compare the DI vs. fatigue cycles (i.e. crack length) for similar, critical paths (Web Path 5-8). Both the medium load of 7,000 lbs. and the high load of 14,000 lbs. produce an increase in the PZT response and a more rapidly-increasing DI curve. As a result, the damage detection occurs at 21,000 cycles for 0 load, 12,000 cycles for 7,000 lb load and 9,000 cycles for 14,000 lb load. In addition, these curves show that a crack in the flange that reaches the outer edge (through-crack) does not affect the DI curve for an unloaded configuration but it does create a decrease in the DI levels for the loaded configurations. This is caused by the resultant load shedding, torsion and crack closure in the web that is created by adjacent damage in the flange. Similar results showing improvements in damage detection in the web region as a result of applying tension loads to the Rotorbeam specimens can be seen in Figure 6-53 (RB-PZT-8, Path 5-7, 500 KHz data), Figure 6-54 (RB-PZT-8, Path 6-8, 500 KHz data), Figure 6-55 (RB-PZT-11, Path 5-8, 250 KHz data), Figure 6-56 (RB-PZT-10, Path 5-8, 500 KHz data), Figure 6-57 (RB-PZT-11, Path 5-8, 500 KHz data), Figure 6-58 (RB-PZT-12, Path 5-8, 500 KHz data), Figure 6-59 (RB-PZT-13, Path 5-8, 500 KHz data), and Figure 6-60 (RB-PZT-14, Path 5-8, 500 KHz data).

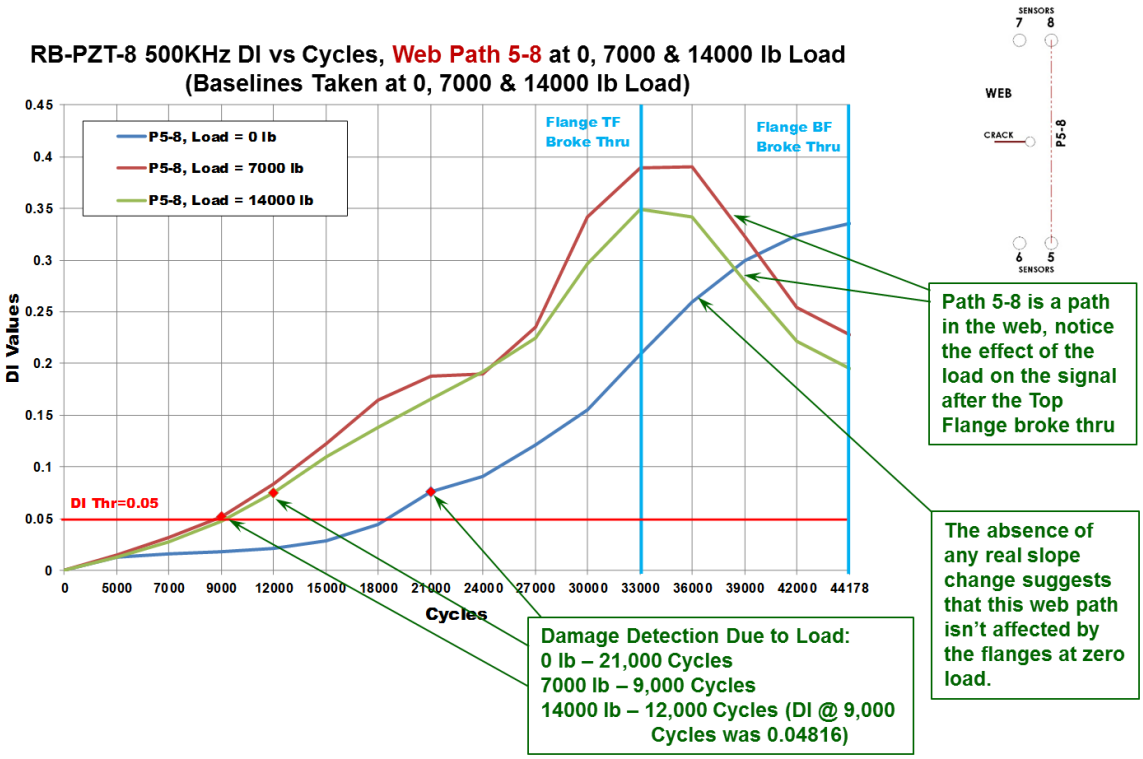

Figure 6-52. Effects of Stress Levels on Web Crack Detection - RB-PZT-8 (Path 5-8)

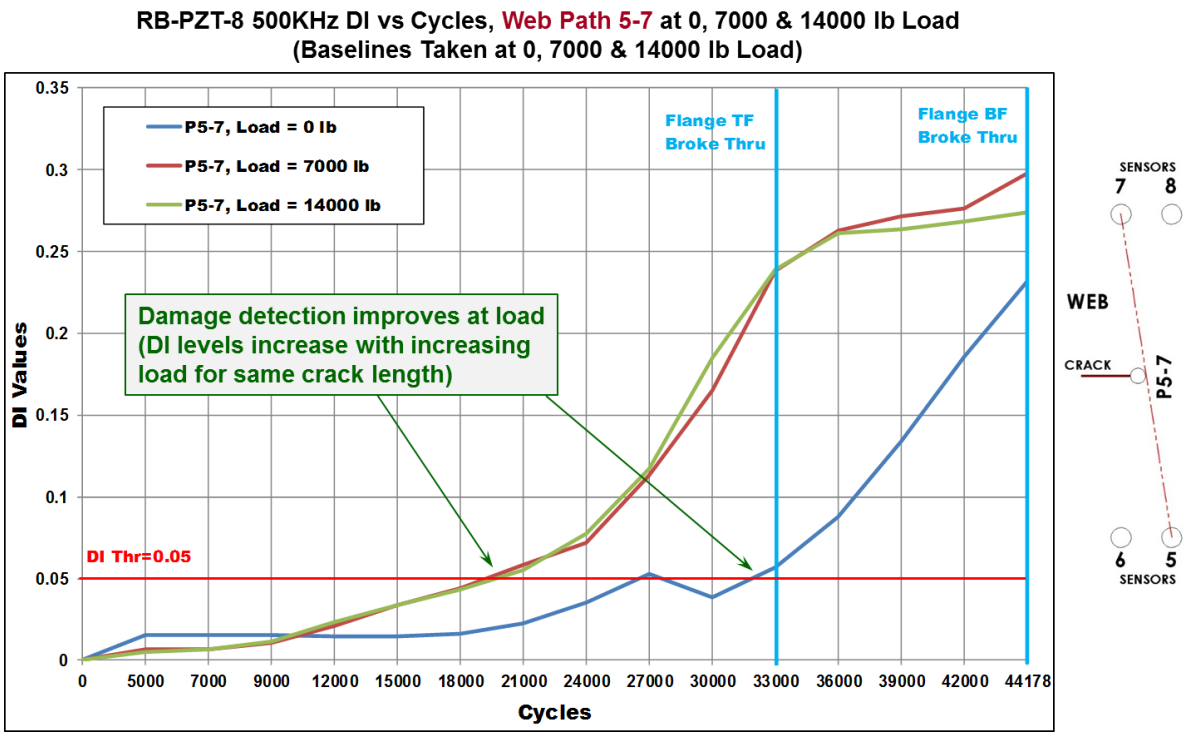

Figure 6-53. Effects of Stress Levels on Web Crack Detection - RB-PZT-8 (Path 5-7)

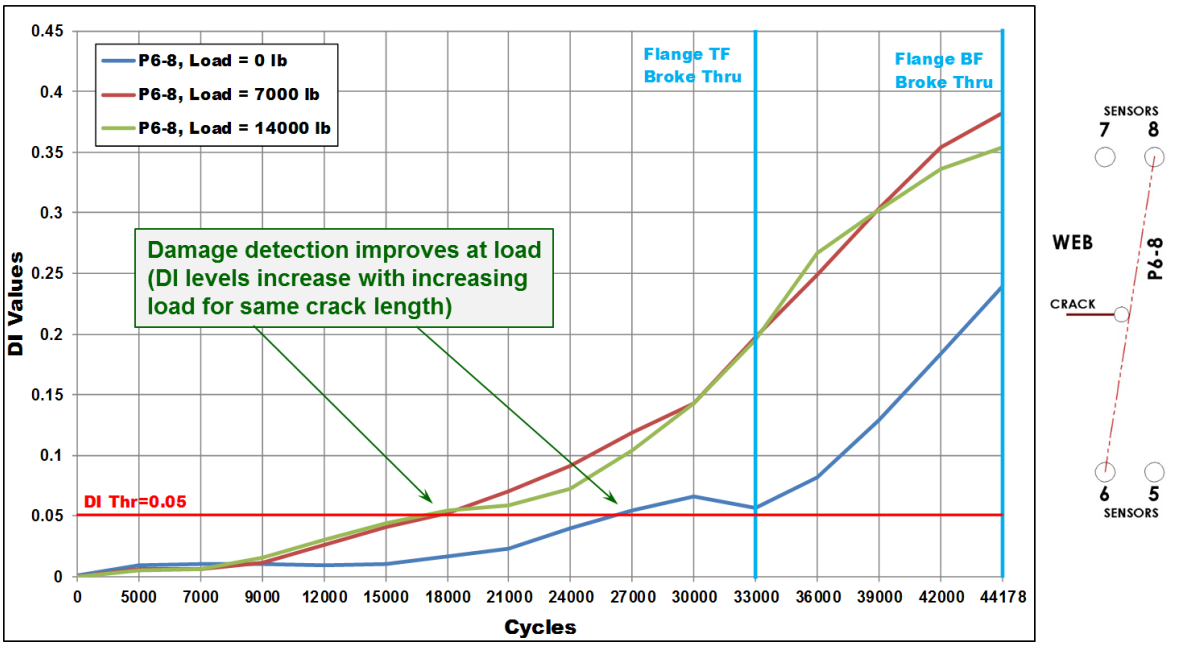

Figure 6-54. Effects of Stress Levels on Web Crack Detection - RB-PZT-8 (Path 6-8)

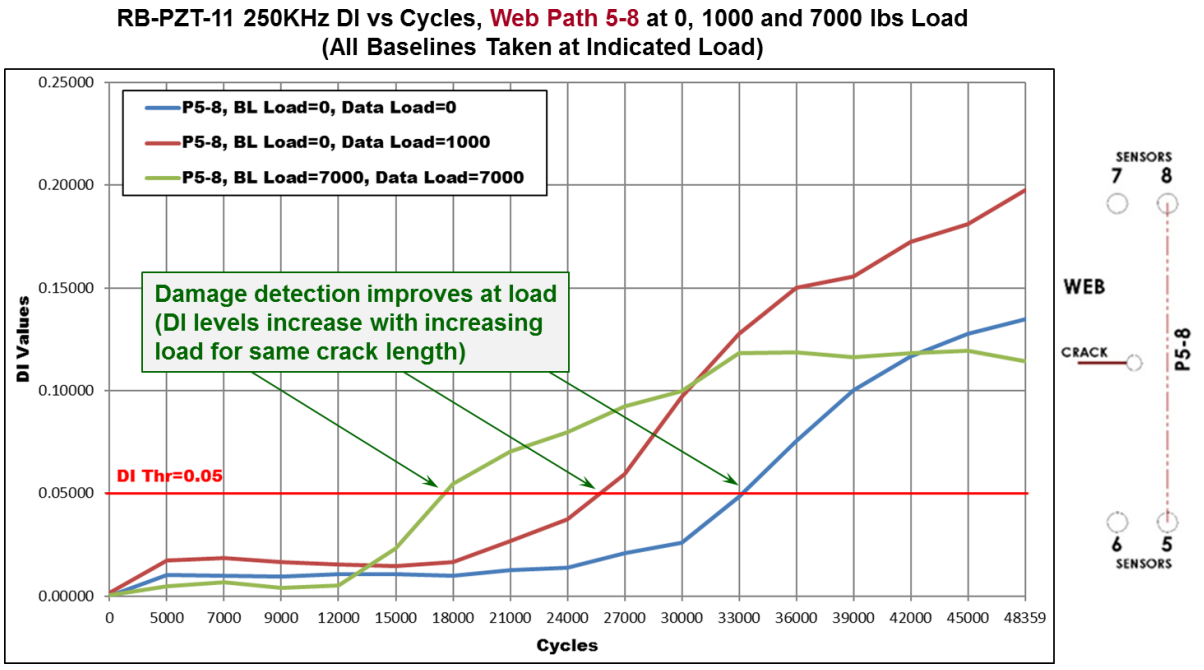

Figure 6-55. Effects of Stress Levels on Web Crack Detection - RB-PZT-9 (Path 5-8)

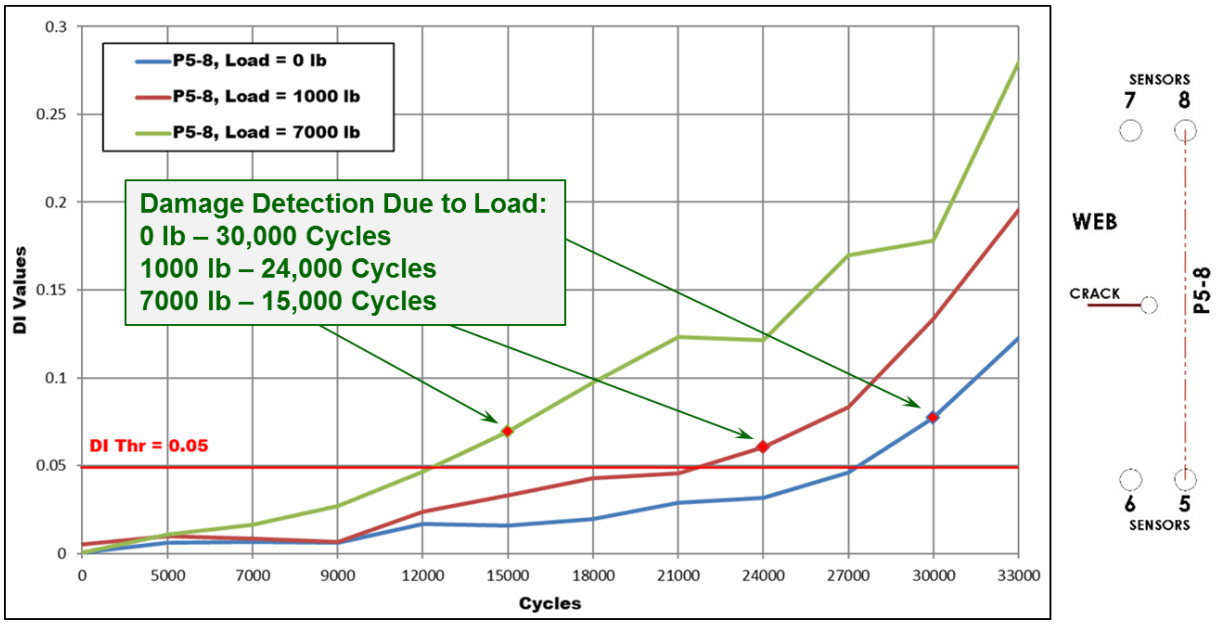

Figure 6-56. Effects of Stress Levels on Web Crack Detection - RB-PZT-10 (Path 5-8)

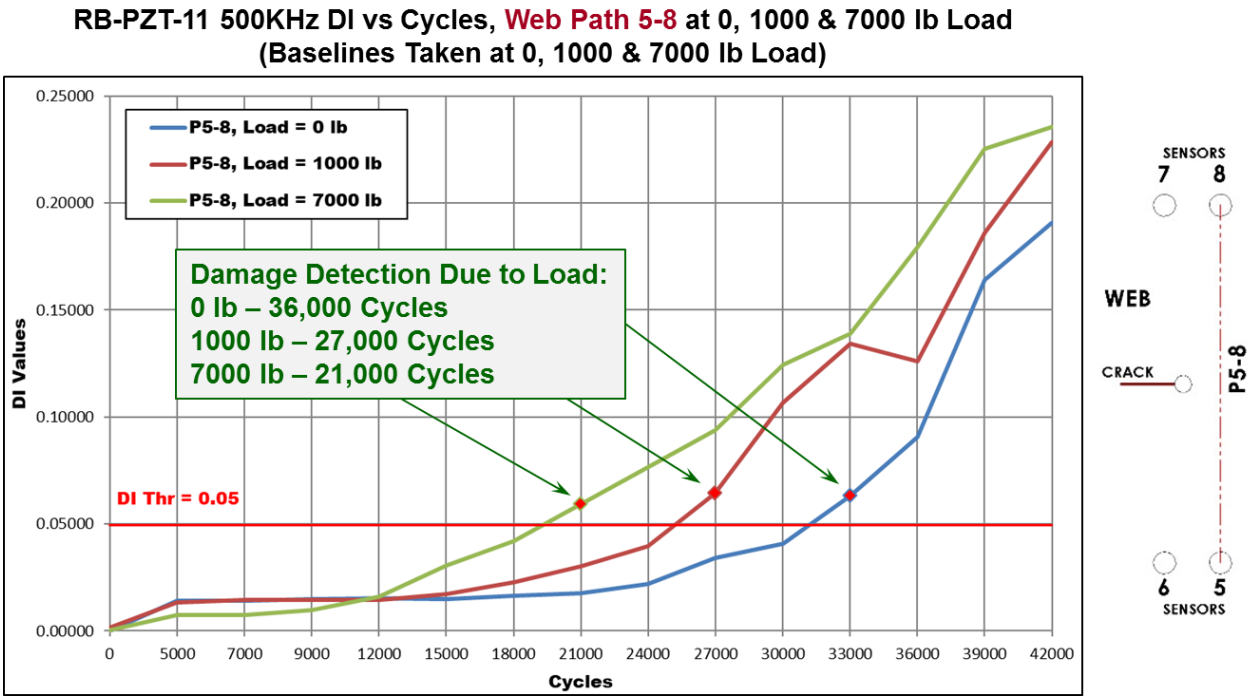

Figure 6-57. Effects of Stress Levels on Web Crack Detection - RB-PZT-11 (Path 5-8)

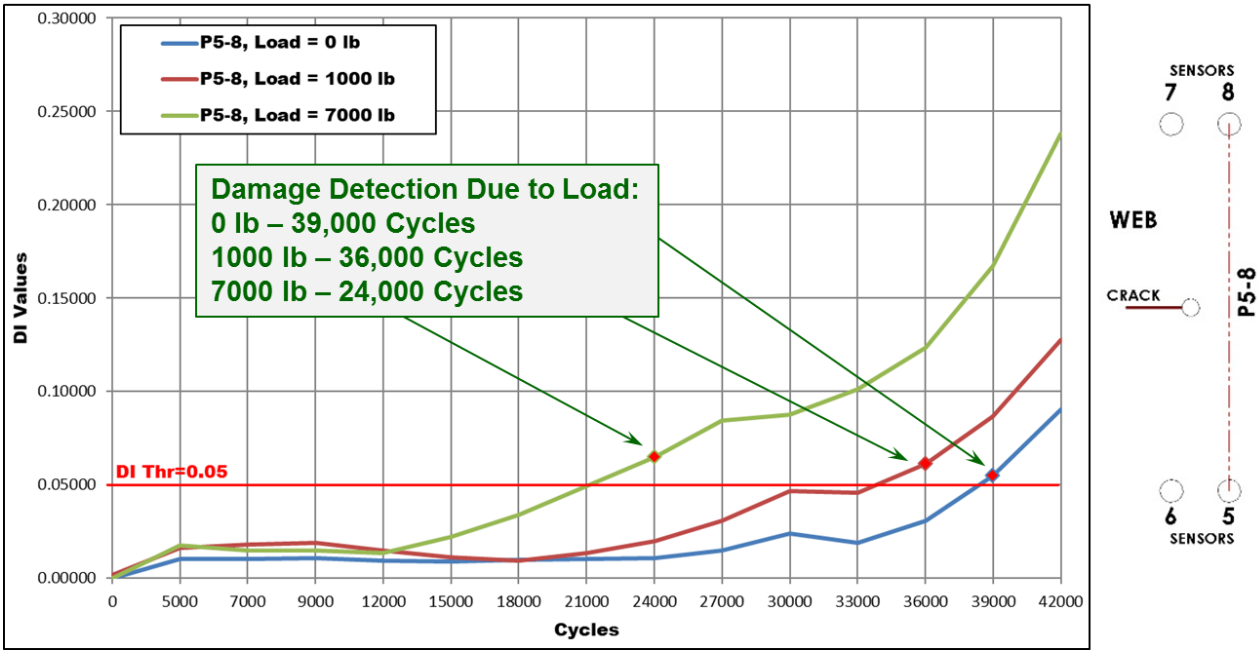

Figure 6-58. Effects of Stress Levels on Web Crack Detection - RB-PZT-12 (Path 5-8)

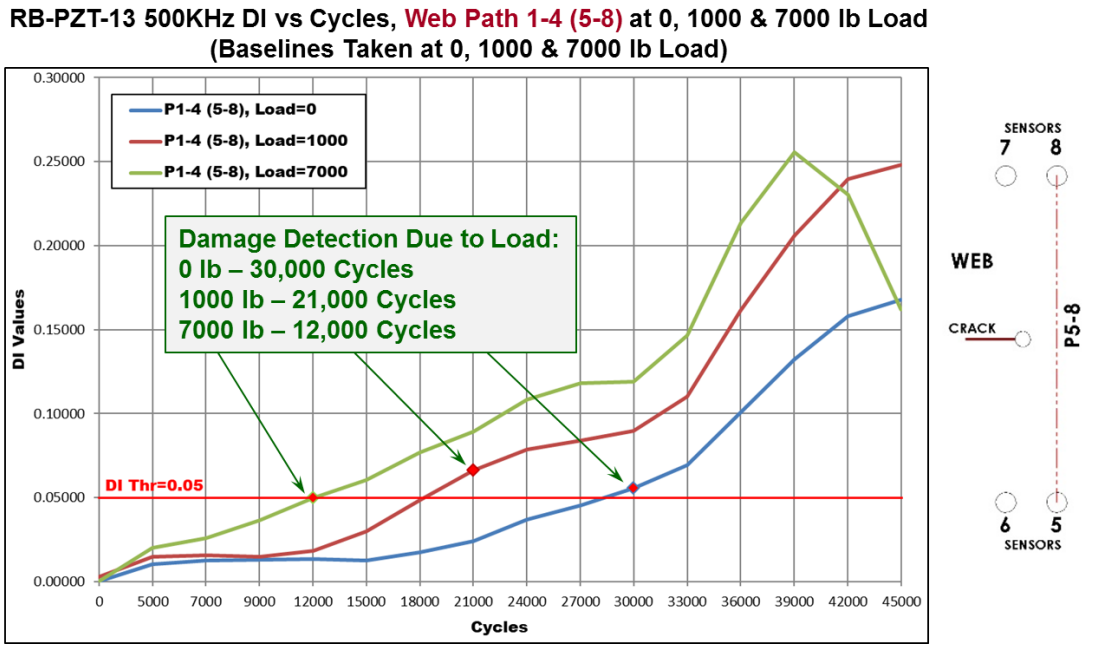

Figure 6-59. Effects of Stress Levels on Web Crack Detection - RB-PZT-13 (Path 5-8)

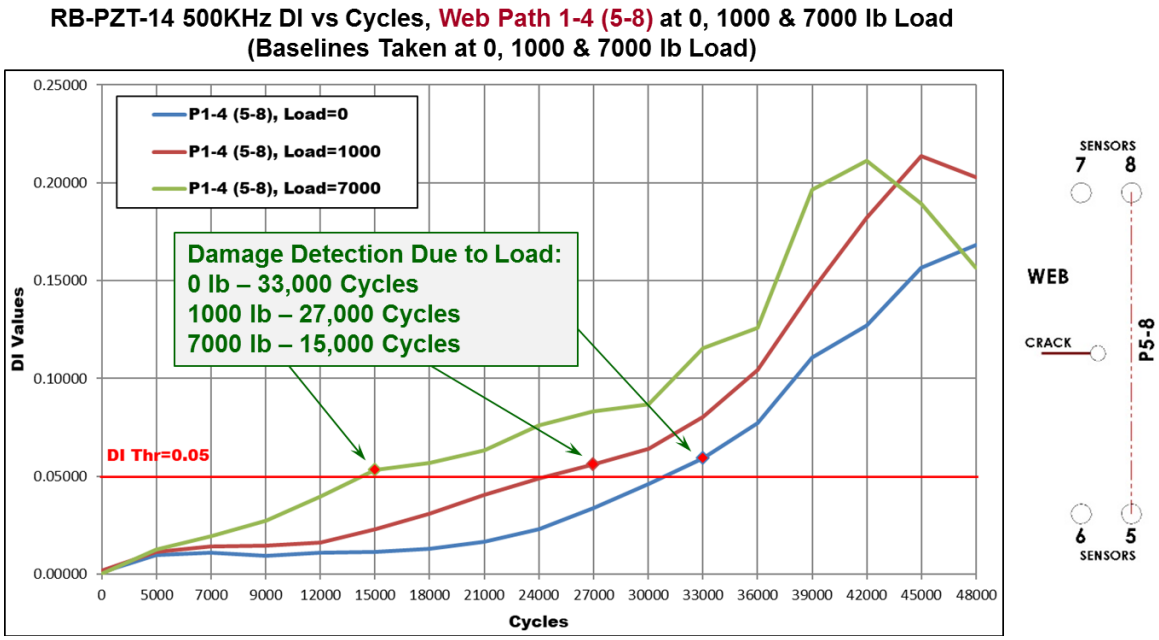

Figure 6-60. Effects of Stress Levels on Web Crack Detection - RB-PZT-14 (Path 5-8)

Overall improvement in damage detection corresponding to a shift of all DI plots to the left is shown in Figure 6-61. This provides a comparison of how DI threshold crossing occurs at lower cycles when the specimen is under a crack-opening type of stress. Note the shift to the left in all 5-8 paths when the specimen is placed under a tension load such that the stresses produce an

opening in the crack. Thus, the DI threshold is exceeded earlier in the fatigue test and smaller cracks are detected. Figure 6-62 (RB-PZT-18F, Web, Path 5-7, 500 KHz) shows the change in DI curves with increasing load when a fastener is in the hole where the crack originates. Similar improvements in damage detection are observed as the tension load is increased. If a tight fastener is in place, the degree of effect from loading may be decreased. This is due to the gripping effect of the fastener which may lessen the effect of the load on any crack opening or closing.

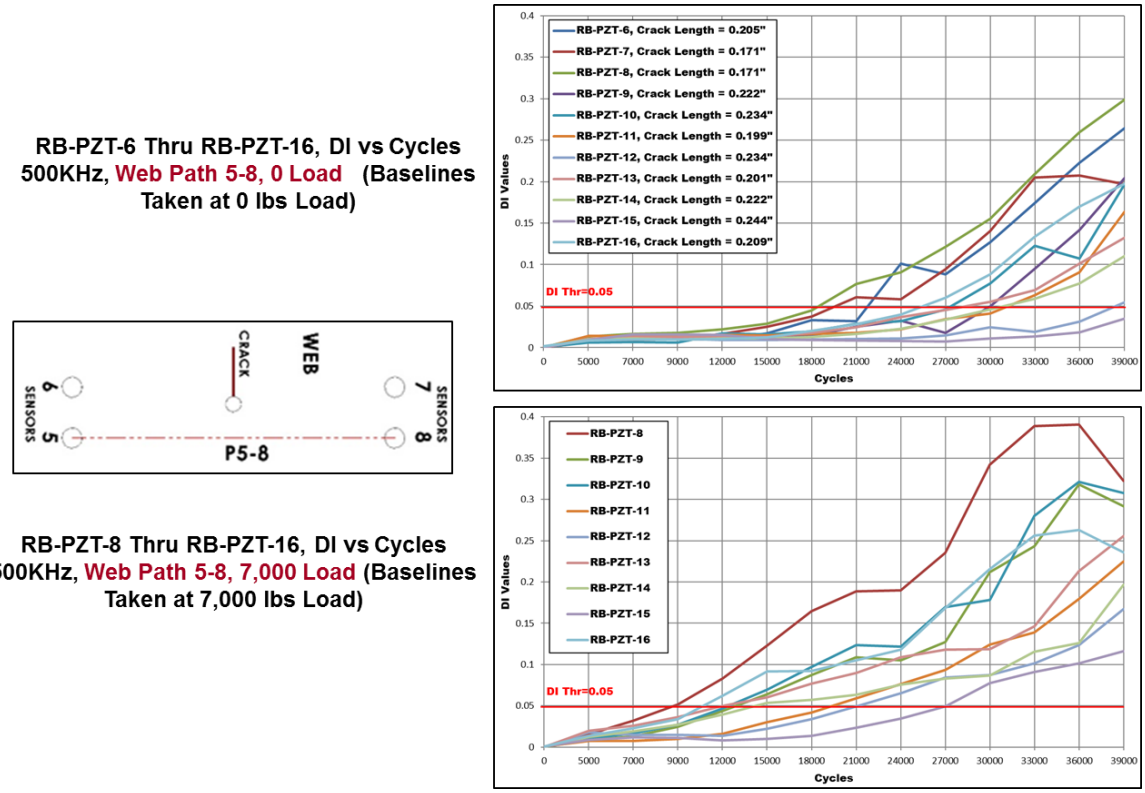

Figure 6-61. Comparison of DI Values from All Specimens Showing Effects of Loading on PZT Web Crack Detection

As noted above, load reapportionment/shedding can occur as damage grows in a component. This can change the stress fields in a structure and change how the structure responds to load when it already has some damage. Torsional and bending loads can have either a positive or negative effect on crack opening depending on the geometry of the component and the resulting direction of the local strain at the fatigue crack. Figure 6-63 provides microscopic images of a fatigue crack and highlights a unique situation with the flanges in the Rotorbeam specimen. The set of photos show cracks in the top and bottom flanges where the top flange one goes into tension (crack opening) and the bottom flange goes into compression (crack closure) due to the torsional loads induced by the non-symmetrical damage (i.e. crack in upper portion of the web and longer crack on one flange). This demonstrates that the type of stress, related to load direction, damage location and component geometry, is critical in determining whether this stress state improves or hinders crack detection. Certain crack growth and load shedding (reapportion) created torsion in the Rotorbeam and showed how complex stress regimes can change PZT responses depending on the

specific structural configuration. Figure 6-64 and Figure 6-65 show the improvement in damage detection that occurs in the top flange of the Rotorbeam as the load at PZT monitoring is increased.

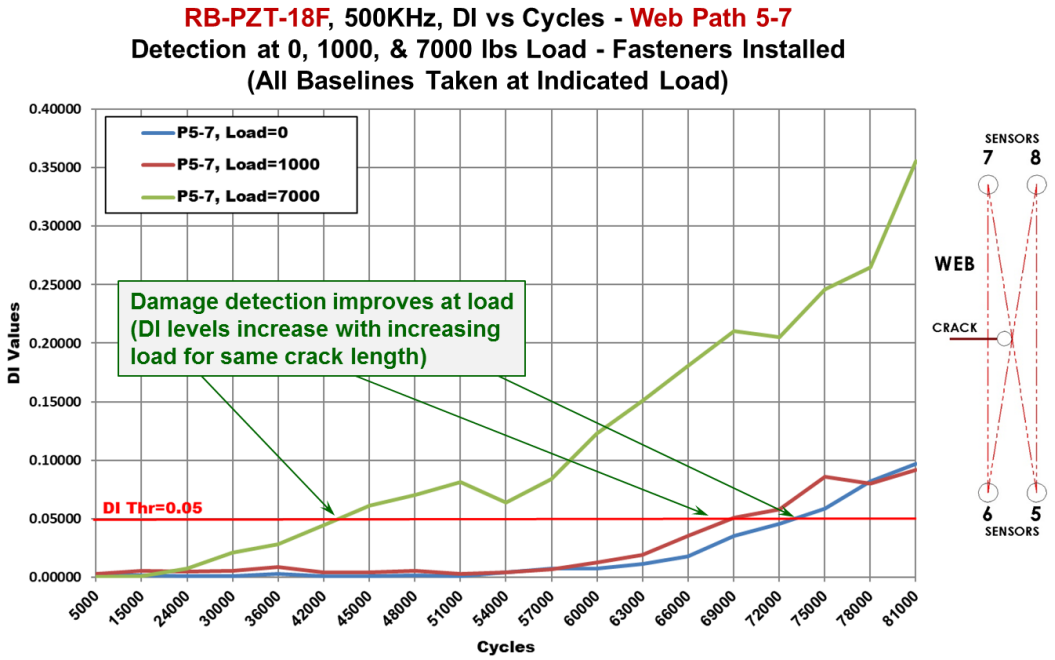

Figure 6-62. Effects of Stress Levels on Web Crack Detection - RB-PZT-18F (Path 5-7)

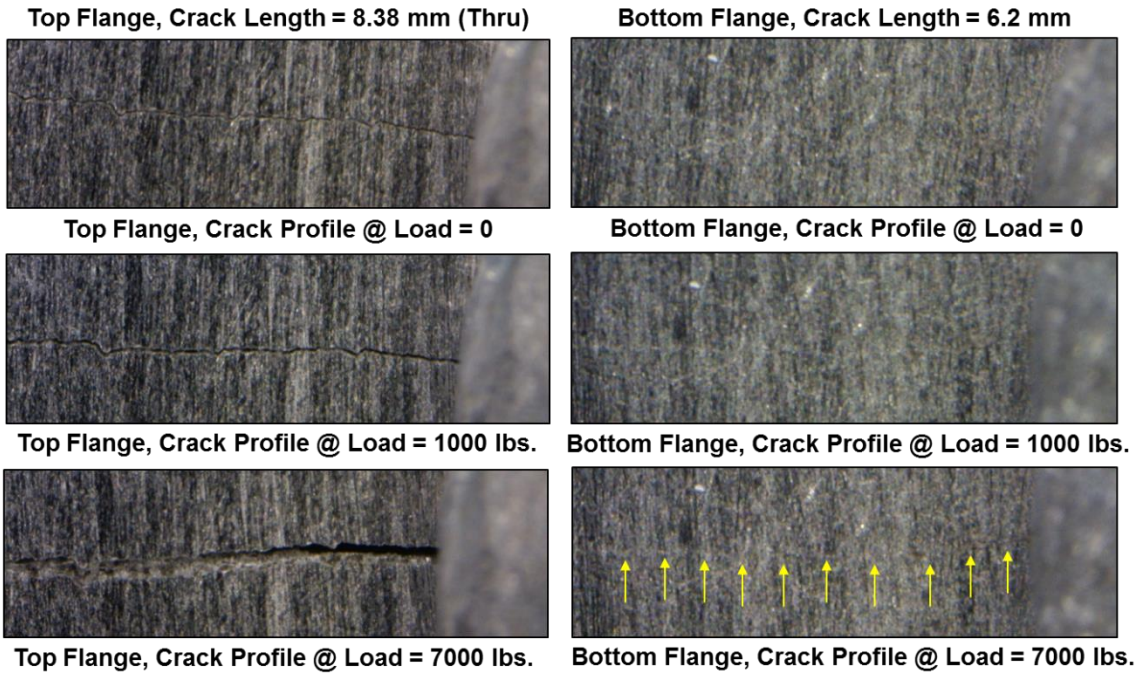

Figure 6-63. Crack Opening and Closure Comparison in Flanges Showing Opposite Effects of Load on Crack Morphology and PZT Crack Detection

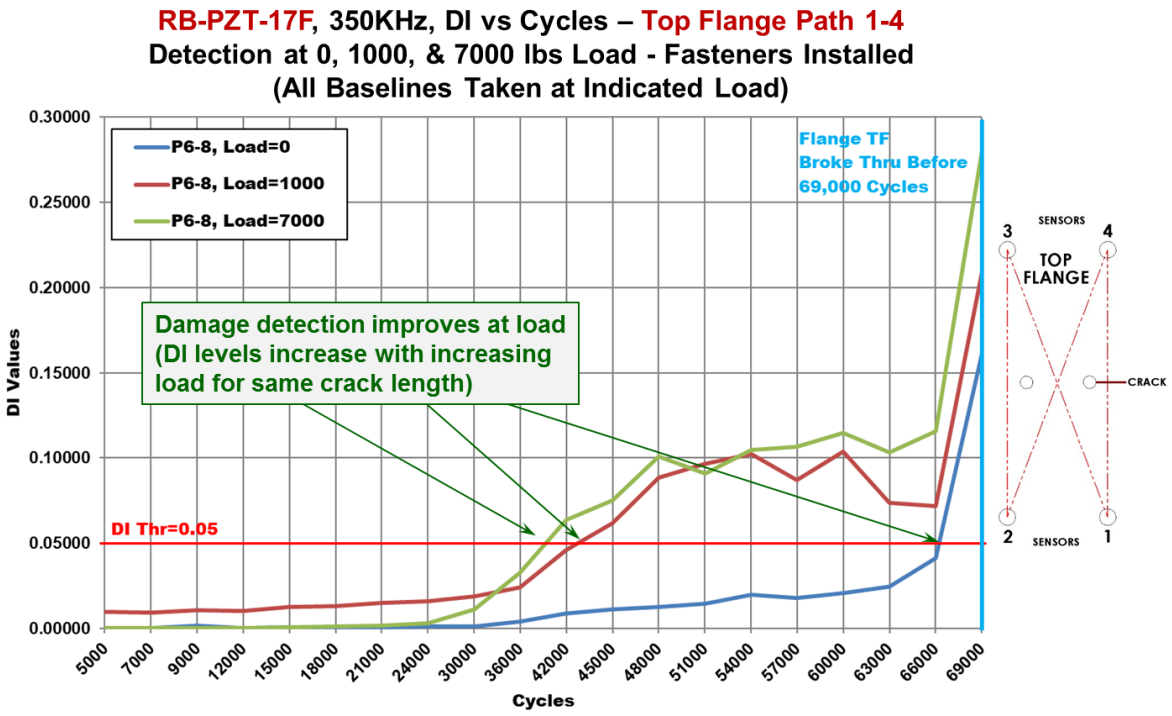

Figure 6-64. Effects of Stress Levels on Flange Crack Detection - RB-PZT-17F (Path 1-4)

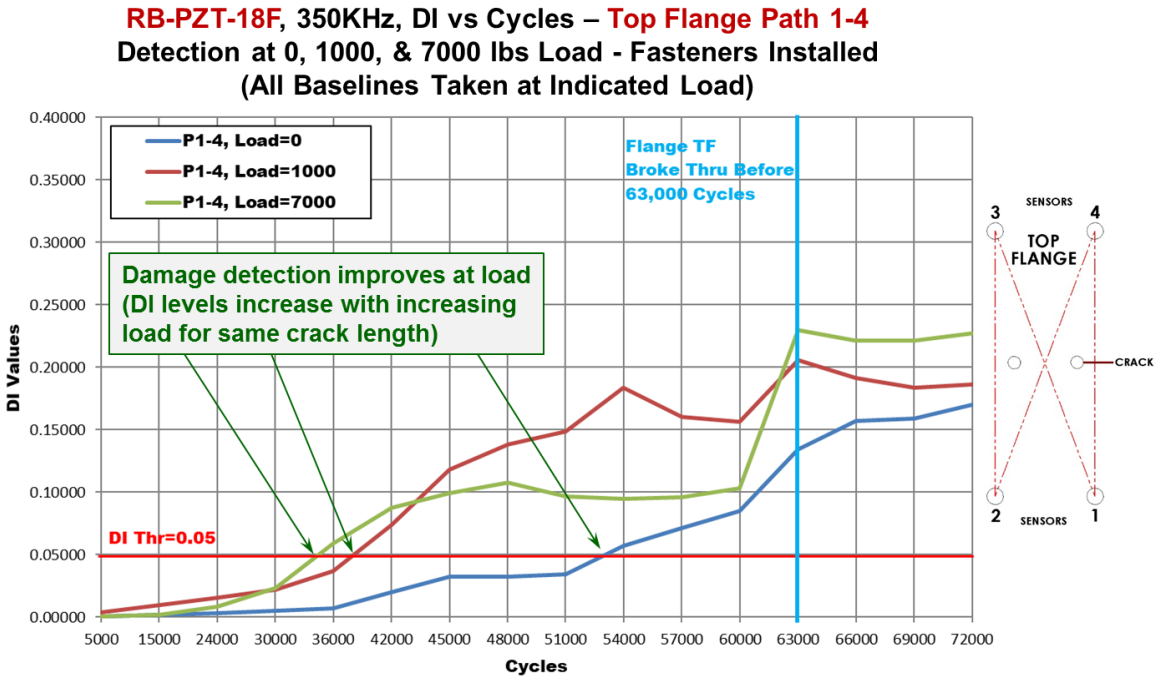

Figure 6-65. Effects of Stress Levels on Flange Crack Detection - RB-PZT-18F (Path 1-4)

Table 6-16 provides a summary of PZT crack detection in the Rotorbeam web and highlights the specific improvements in crack detection as the tension load is increased. It shows a consistent reduction in crack length at PZT detection as the structural loads increase. Note that such performance improvements can be reversed if increased loads results in overall stress redistribution in a complex joint and regions reverse from tension into compression (see Figure 6-63). The improvement in web crack detection (decrease in crack length) with increasing tension load is shown graphically in Figure 6-66. Crack detection improvements of up to 75% were observed.

Table 6-16. Comparison of PZT Crack Detection in Web Under Different Loads

PZT Performance in Web of Rotorbeam - Crack Length and Damage Index at Initial Crack Detection (Comparison of Crack Detection in Loaded & Unloaded Structures)							
Specimen #	Load at Data Acquisition (lbs)	Load Used to Determine Baseline (lbs)	Fatigue Cycles at Detection	Crack Length at Detection (in)	Damage Detection Freq. (KHz)	First Path Detecting Crack	DI Value of First Path
RB-PZT-9	0	0	30,000	0.222	500	5-8	0.04994
RB-PZT-9-500	500	0	27,440	0.201	500	5-8	0.06846
RB-PZT-9-1000	1000	0	24,000	0.165	500	5-8	0.06152
RB-PZT-9-7000	7000	7000	15,000	0.104	500	5-8	0.06371
RB-PZT-10	0	0	30,000	0.234	500	5-8	0.07710
RB-PZT-10-1000	1000	0	24,000	0.173	500	5-8	0.06027
RB-PZT-10-7000	7000	7000	15,000	0.110	500	5-8	0.06922
RB-PZT-11	0	0	33,000	0.199	500	5-8	0.06330
RB-PZT-11-1000	1000	0	27,000	0.154	500	5-8	0.06443
RB-PZT-11-7000	7000	7000	18,000	0.100	250	5-8	0.05453
RB-PZT-12	0	0	39,000	0.234	500	5-8	0.05482
RB-PZT-12-1000	1000	0	36,000	0.213	500	5-8	0.06144
RB-PZT-12-7000	7000	7000	24,000	0.132	500	5-8	0.06496
RB-PZT-13	0	0	30,000	0.201	500	5-8	0.05546
RB-PZT-13-1000	1000	0	21,000	0.138	500	5-8	0.06630
RB-PZT-13-7000	7000	7000	12,000	0.067	500	5-8	0.05002
RB-PZT-14	0	0	33,000	0.222	500	5-8	0.05906
RB-PZT-14-1000	1000	0	21,000	0.148	300	5-8	0.05493
RB-PZT-14-7000	7000	7000	12,000	0.091	300	5-8	0.07720
RB-PZT-15	0	0	45,000	0.244	500	5-8	0.07385
RB-PZT-15-1000	1000	0	39,000	0.205	500	5-8	0.05611
RB-PZT-15-7000	7000	7000	30,000	0.130	500	5-8	0.07725
RB-PZT-16	0	0	27,000	0.209	500	5-8	0.06016
RB-PZT-16-1000	1000	0	21,000	0.159	500	5-8	0.06785
RB-PZT-16-7000	7000	7000	12,000	0.096	500	5-8	0.06230
RB-PZT-17F	0	0	66,000	0.197	500	6-8	0.05186
RB-PZT-17F-1000	1000	0	60,000	0.157	500	6-8	0.05300
RB-PZT-17F-7000	7000	7000	57,000	0.142	350	5-8	0.05238
RB-PZT-18F	0	0	75,000	0.238	500	5-7	0.05831
RB-PZT-18F-1000	1000	0	69,000	0.195	500	5-7	0.05084
RB-PZT-18F-7000	7000	7000	42,000	0.060	500	5-8	0.05701

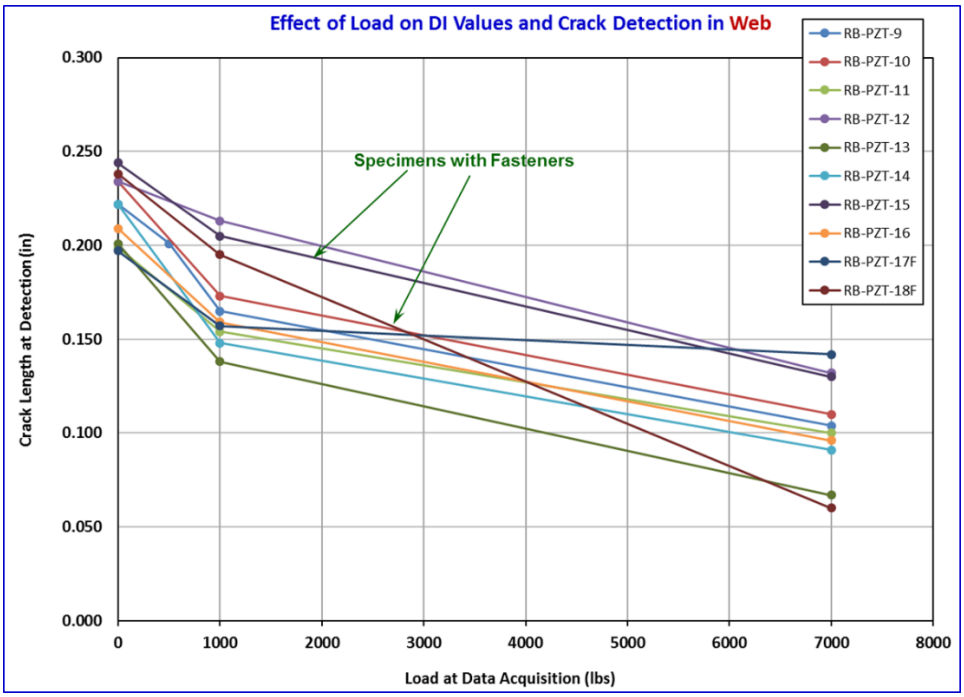

Figure 6-66. Improvement in PZT Web Crack Detection as Specimen Tension Load Increases

Similarly, Table 6-17 provides a summary of PZT crack detection in the Rotorbeam flange region and highlights the specific improvements in crack detection as the tension load is increased. It shows a consistent reduction in crack length at PZT detection as the structural loads increase. DI value comparisons showed that DI levels in the flange region fluctuated between compression and tension as cracks throughout beam propagate and create stress redistribution. In the case of the Rotorbeam component, such fluctuations occurred after initial crack detection in the targeted flange region. The improvement in flange crack detection with increasing tension load is shown graphically in Figure 6-67. Crack detection improvements of up to 82% were observed.

Table 6-18 and Table 6-19 provide another summary of crack detection throughout the Rotorbeam (web and flanges) for multiple specimen and monitoring scenarios at 0, 1,000, and 7,000 lbs tension load. These tables stress the exact data acquisition set-up including the Baseline used for damage detection. The consistency and scatter of the crack detection levels can be clearly observed in the color-coded boxes.

After the data above was acquired, it was used in various POD analyses to make comparisons of POD(90/95) for unloaded structure with POD(90/95) when the same structure is monitored while under load. To compare PZT POD(90/95) levels at different stress levels, the data for PZT crack detection for lightly loaded Rotorbeam webs under 1,000 lbs tension is compiled in Table 6-20. For this data, all monitoring was performed on structure at 1,000 lb loads, however, the Baseline signals for comparison and damage detection were acquired from the structure in unloaded condition.

Table 6-17. Comparison of PZT Crack Detection in Flanges Under Different Loads

PZT Performance in Flange of Rotorbeam - Crack Length and Damage Index at Initial Crack Detection (Comparison of Crack Detection in Loaded & Unloaded Structures)							
Specimen #	Load at Data Acquisition (lbs)	Load Used to Determine Baseline (lbs)	Fatigue Cycles at Detection	Crack Length at Detection (in)	Damage Detection Freq. (KHz)	First Path Detecting Crack	DI Value of First Path
RB-PZT-9	0	0	44,645	0.330	300	9-12	0.10479
RB-PZT-9-500	500	0	44,645	0.330	300	10-12	0.05952
RB-PZT-9-1000	1000	0	18,000	0.150	350	1-4	0.05221
RB-PZT-9-7000	7000	7000	9,000	0.077	300	2-3	0.05274
RB-PZT-10	0	0	48,359	0.330	300	10-12	0.08661
RB-PZT-10-1000	1000	0	24,000	0.195	300	2-4	0.06304
RB-PZT-10-7000	7000	7000	12,000	0.091	300	2-3	0.07921
RB-PZT-11	0	0	39,000	0.330	300	1-4	0.11759
RB-PZT-11-1000	1000	0	39,000	0.330	300	10-12	0.34956
RB-PZT-11-7000	7000	7000	12,000	0.059	300	2-4	0.06588
RB-PZT-12	0	0	42,000	0.330	300	2-4	0.14539
RB-PZT-12-1000	1000	0	42,000	0.330	300	2-4	0.42740
RB-PZT-12-7000	7000	7000	12,000	0.075	300	2-3	0.05201
RB-PZT-15	0	0	45,000	0.330	300	1-3	0.17531
RB-PZT-15-1000	1000	0	45,000	0.330	300	1-3	0.50284
RB-PZT-15-7000	7000	7000	21,000	0.083	350	9-12	0.05622
RB-PZT-16	0	0	33,000	0.330	300	2-4	0.22765
RB-PZT-16-1000	1000	0	21,000	0.177	350	1-4	0.06555
RB-PZT-16-7000	7000	7000	12,000	0.094	300	2-3	0.12480
RB-PZT-17F	0	0	68,076	0.330	300	1-4	0.29948
RB-PZT-17F-1000	1000	0	45,000	0.083	350	1-4	0.06183
RB-PZT-17F-7000	7000	7000	42,000	0.047	350	1-4	0.06380
RB-PZT-18F	0	0	60,000	0.305	350	1-4	0.08509
RB-PZT-18F-1000	1000	0	42,000	0.142	350	1-4	0.07428
RB-PZT-18F-7000	7000	7000	36,000	0.118	350	1-4	0.05894

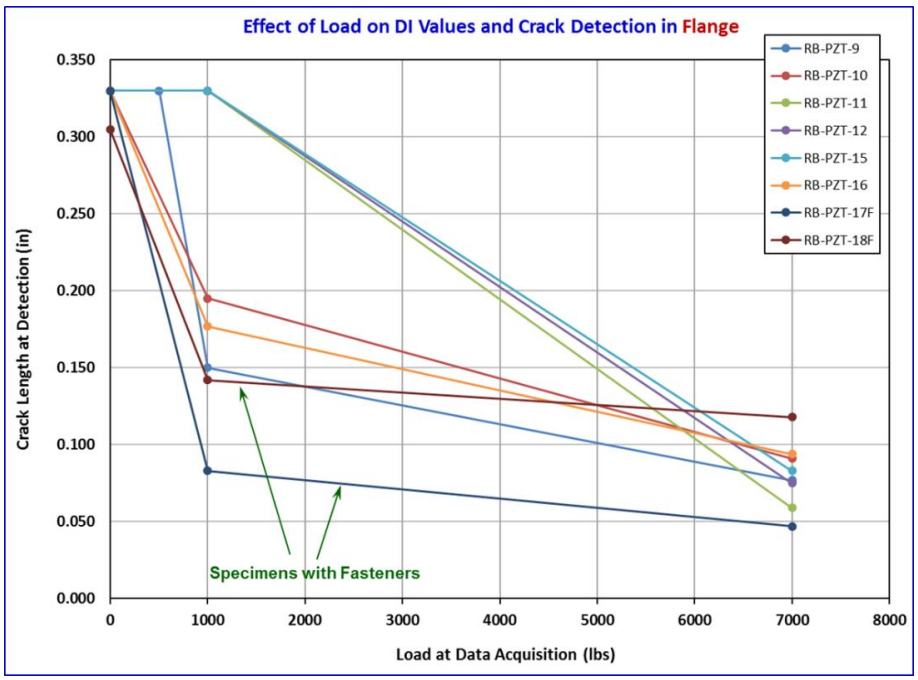

Figure 6-67. Change in PZT Flange Crack Detection as Specimen Tension Load Increases

Table 6-18. Summary of Effect of Load on Web and Flange Crack Detection – RB-PZT-11 & -12

RB-PZT-11 Cycles and Crack Length			
Cycles	EC Crack Length (mm)		
	SS1 (BF)	SS2 (W)	SS3 (TF)
0	0	0	0
5,000	0.1	0.15	0.2
7,000	0.2	0.4	0.5
9,000	0.4	0.75	0.9
12,000	0.7	1.35	1.55
15,000	1.2	2.05	2.4
18,000	2	2.55	3.1
21,000	2.55	3.05	3.8
24,000	2.95	3.55	4.45
27,000	3.5	3.9	5.2
30,000	4.2	4.7	6
33,000	4.65	5.05	6.5
36,000	4.95	5.95	7.1
39,000	5.5	6.55	8.38
42,000	6.1	7.8	8.38
45,000	6.9	8.4	8.38
48,359	8.38	9.45	8.38
37,633	-	-	Thru Flange
48,359	Thru Flange	-	-

RB-PZT-12 Cycles and Crack Length			
Cycles	EC Crack Length (mm)		
	SS1 (BF)	SS2 (W)	SS3 (TF)
0	0	0	0
5,000	0.4	0.2	0.3
7,000	0.7	0.4	0.6
9,000	1.2	0.7	1
12,000	1.9	1.2	1.6
15,000	2.8	1.6	2.25
18,000	3.4	2.1	2.95
21,000	4.05	2.6	3.4
24,000	4.8	3.35	3.8
27,000	5.5	3.65	4.15
30,000	6.4	4.3	4.8
33,000	7.35	5.1	5.4
36,000	8.38	5.4	5.85
39,000	8.38	5.95	7.25
42,000	8.38	6.7	8.38
45,000	8.38	7.55	8.38
48,000	8.38	8.15	8.38
34,978	Thru Flange	-	-
39,841	-	-	Thru Flange

	0 - Load, BL at 0 lbs: Damage Detection @ DI Thr = 0.05 (500KHz for the Web)
	7000 - Load, BL at 7000 lbs: Damage Detection @ DI Thr = 0.05 (300KHz for Flanges and 250KHz for the Web)
	1000 - Load, BL at 0 lbs: Damage Detection @ DI Thr = 0.05 (500KHz for the Web)
	0 - Load, BL at 0 lbs and 1000 - Load, BL at 0 lbs: Damage Detection @ DI Thr = 0.05 (300KHz for the Flanges)

Table 6-19. Summary of Effect of Load on Web Crack Detection – RB-PZT-13 & -14

RB-PZT-13 Cycles and Crack Length	
Cycles	Crack Length (mm)
	Webb
0	0
5,000	0.4
7,000	0.7
9,000	1.1
12,000	1.7
15,000	2.3
18,000	2.8
21,000	3.5
24,000	4.1
27,000	4.75
30,000	5.1
33,000	5.7
36,000	6.55
39,000	7.25
42,000	8.3
45,000	9.3

RB-PZT-14 Cycles and Crack Length	
Cycles	EC Crack Length (mm)
	Webb
0	0
5,000	0.5
7,000	1.2
9,000	1.8
12,000	2.3
15,000	3.05
18,000	3.4
21,000	3.75
24,000	4.25
27,000	4.8
30,000	5.2
33,000	5.65
36,000	6.1
39,000	6.85
42,000	7.6
45,000	8.5
48,000	9.3

	0 - Load, BL at 0 lbs: Damage Detection @ DI Thr = 0.05 (500KHz for the Web)
	1000 - Load, BL at 0 lbs: Damage Detection @ DI Thr = 0.05 (300KHz for the Web)
	7000 - Load, BL at 7000 lbs: Damage Detection @ DI Thr = 0.05 (300KHz for the Web)

Table 6-20. PZT Crack Detection for Lightly Loaded Rotorbeam Web (1,000 lbs tension)

PZT Performance in Web of Rotorbeam - Crack Length and Damage Index at Initial Crack Detection in 1,000 PSI Loaded Specimens (1,000 lb. Load at Data Acquisition & Baseline Determined at 0 Load)							
Specimen #	Fatigue Cycles at Detection	Crack Length at Detection mm (in)	Damage Detection Freq. (KHz)	First Path Detecting Crack	DI Value of First Path	Second Path Detecting Crack (if applicable)	DI Value of Second Path
RB-PZT-6-1000	18,000	4.10 (0.161)	500	5-8	0.06818		
RB-PZT-7-1000	15,000	3.30 (0.130)	500	5-8	0.05714		
RB-PZT-9-1000	24,000	4.20 (0.165)	500	5-8	0.06152		
RB-PZT-10-1000	24,000	4.40 (0.173)	500	5-8	0.06027		
RB-PZT-11-1000	27,000	3.90 (0.154)	500	5-8	0.06443		
RB-PZT-12-1000	36,000	5.40 (0.213)	500	5-8	0.06144		
RB-PZT-13-1000	21,000	3.50 (0.138)	500	5-8	0.06630		
RB-PZT-14-1000	21,000	3.75 (0.148)	300	5-8	0.05493		
RB-PZT-15-1000	39,000	5.20 (0.205)	500	5-8	0.05611		
RB-PZT-16-1000	21,000	4.05 (0.159)	500	5-8	0.06785	6-8	0.06437
RB-PZT-17F-1000	60,000	4.0 (0.157)	500	6-8	0.05300		
RB-PZT-18F-1000	69,000	4.95 (0.195)	500	5-7	0.05084		

One-Sided Tolerance Interval POD Method and Lightly Loaded Rotorbeam Web (1,000 lbs) - The 12 data points listed in Table 6-20 for crack detection in the web of the Rotorbeam were used in the OSTI method described in Section 4.6 to calculate the POD performance. Table 6-21 and Table 6-22 summarizes the results from the OSTI calculations for open hole crack detection and open/riveted hole crack detection, respectively. Average crack detection from the 10 specimens with open holes revealed an average crack length at detection = 0.167" and a low Standard Deviation of 0.026". The resulting $POD_{90/95}$ value for PZT sensors on the Rotorbeam web monitored at 1,000 lbs load was 0.235" (5.97 mm). This can be compared to the PZT performance for an unloaded web region where the $POD_{90/95}$ = 0.274" (6.95 mm). Thus, the light tension load was able to result in a 14% improvement in crack detection POD. There was also a 21% improvement in average length of crack at detection (0.210" at 0 load vs. 0.165" at 1,000 lb. load). Table 6-22 simply shows the same analysis when the additional two data points are added from the holes with rivets present. The average crack length at detection and the $POD_{90/95}$ levels are essentially the same as the open hole results indicating that the presence of fasteners does not affect the crack detection performance of this PZT system for this Rotorbeam configurations. Differences in these values range from just 1-2%.

Table 6-21. POD Calculations Using One-Sided Tolerance Interval from PZT Response Data on Rotorbeam Web (1,000 lb tension load)

PZT Crack Detection Data in Web

Crack Length at PZT Detection a (in)	Log of Crack Length at PZT Detection a (in)
0.161	-0.793174
0.130	-0.886057
0.165	-0.782516
0.173	-0.761954
0.154	-0.812479
0.213	-0.671620
0.138	-0.860121
0.148	-0.829738
0.205	-0.688246
0.159	-0.798603

PZT Crack Detection in Web for Open Holes at 1,000 PSI Stress

Statistic Estimates in Log & Linear Scales

Statistic	Value in Log Scale	Value in Linear Scale
Mean (X)	-0.788451	0.165
Stnd Deviation (S)	0.067904	0.026630

POD Detection Levels (γ = 95%, n = 10)

	POD in inches	POD in mm
Flaw Size: POD = X + K(S) =	0.235	5.97

Web Open Hole at 1,000 PSI Stress: Crack Length at PZT Detection = 5.97 mm

Recall – Web Unloaded Open Hole Data: Crack Length at PZT Detection = 6.95 mm

Table 6-22. POD Calculations Using One-Sided Tolerance Interval from PZT Response Data on Riveted Rotorbeam Web (1,000 lb tension load)

PZT Crack Detection Data in Web

Crack Length at PZT Detection a (in)	Log of Crack Length at PZT Detection a (in)
0.161	-0.793174
0.130	-0.886057
0.165	-0.782516
0.173	-0.761954
0.154	-0.812479
0.213	-0.671620
0.138	-0.860121
0.148	-0.829738
0.205	-0.688246
0.159	-0.798603
0.157	-0.804100
0.195	-0.709965

PZT Crack Detection in Web for Open and Riveted Holes at 1,000 PSI Stress

Statistic Estimates in Log & Linear Scales

Statistic	Value in Log Scale	Value in Linear Scale
Mean (X)	-0.783215	0.167
Stnd Deviation (S)	0.065764	0.025798

POD Detection Levels (γ = 95%, n = 12)

	POD in inches	POD in mm
Flaw Size: POD = X + K(S) =	0.230	5.85

Web Open/Riveted Hole Data at 1,000 PSI Stress: Crack Length at PZT Detection = 5.85 mm

Recall – Web Unloaded Open/Riveted Hole: Crack Length at PZT Detection = 6.85 mm

One-Sided Tolerance Interval POD Method and Medium Loaded Rotorbeam Web (7,000 lbs) - To compare PZT POD(90/95) levels at different stress levels, the data for PZT crack detection for medium loaded Rotorbeam webs under 7,000 lbs tension is compiled in Table 6-23. For this data,

all monitoring was performed on structure at 7,000 lb loads and Baseline data for comparisons was acquired from the structure at also 7,000 PSI loaded condition. The 11 data points listed in Table 6-23 for crack detection in the web of the Rotorbeam at 7,000 lb load were used in the OSTI method described in Section 4.6 to calculate the POD performance. Table 6-24 and Table 6-25 summarize the results from the OSTI calculations for open hole crack detection and open/riveted hole crack detection, respectively. Average crack detection from the 9 specimens with open holes revealed an average crack length at detection = 0.095" and a low Standard Deviation of 0.022". The resulting $POD_{90/95}$ value for PZT sensors on the Rotorbeam web monitored at 7,000 lbs load was 0.169" (4.31 mm). This can be compared to the PZT performance for an unloaded web region where the $POD_{90/95}$ = 0.274" (6.95 mm). Thus, the light tension load was able to result in a 38% improvement in crack detection POD. There was also a 55% improvement in average length of crack at detection (0.210" at 0 load vs. 0.095" at 7,000 lb. load). Table 6-25 simply shows the same analysis when the additional two data points are added from the holes with rivets present. The average crack length at detection and the $POD_{90/95}$ levels are essentially the same as the open hole results indicating that the presence of fasteners does not affect the crack detection performance of this PZT system for this Rotorbeam configurations. Differences in these values range from just 1-5%.

Table 6-23. PZT Crack Detection for Medium Loaded Rotorbeam Web (7,000 lbs tension)

PZT Performance in Web of Rotorbeam - Crack Length and Damage Index at Initial Crack Detection in 7,000 PSI Loaded Specimens (7,000 lb. Load at Data Acquisition & Baseline Determined at 7,000 Load)							
Specimen #	Fatigue Cycles at Detection	Crack Length at Detection mm (in)	Damage Detection Freq. (KHz)	First Path Detecting Crack	DI Value of First Path	Second Path Detecting Crack (if applicable)	DI Value of Second Path
RB-PZT-8-7000	9,000	1.50 (0.059)	500	5-8	0.05165		
RB-PZT-9-7000	15,000	2.65 (0.104)	500	5-8	0.06371		
RB-PZT-10-7000	15,000	2.80 (0.110)	500	5-8	0.06922		
RB-PZT-11-7000	18,000	2.55 (0.100)	250	5-8	0.05453		
RB-PZT-12-7000	24,000	3.35 (0.132)	500	5-8	0.06496		
RB-PZT-13-7000	12,000	1.70 (0.067)	500	5-8	0.05002		
RB-PZT-14-7000	12,000	2.30 (0.091)	300	5-8	0.07720		
RB-PZT-15-7000	30,000	3.30 (0.130)	500	5-8	0.07725		
RB-PZT-16-7000	12,000	2.45 (0.096)	500	5-8	0.06230		
RB-PZT-17F-7000	57,000	3.60 (0.142)	350	5-8	0.05238		
RB-PZT-18F-7000	42,000	1.50 (0.060)	500	5-8	0.05701		

Table 6-24. POD Calculations Using One-Sided Tolerance Interval from PZT Response Data on Rotorbeam Web (7,000 lb tension load)

PZT Crack Detection Data in Web

Crack Length at PZT Detection a (in)	Log of Crack Length at PZT Detection a (in)
0.059	-1.229148
0.104	-0.982967
0.110	-0.958607
0.100	-1.000000
0.132	-0.879426
0.067	-1.173925
0.091	-1.040959
0.096	-1.017729
0.096	-1.017729

PZT Crack Detection in Web for Open Holes at 7,000 PSI Stress

Statistic Estimates in Log & Linear Scales

Statistic	Value in Log Scale	Value in Linear Scale
Mean (X)	-1.033388	0.095
Stnd Deviation (S)	0.106989	0.021789

POD Detection Levels (γ = 95%, n = 9)

	POD in inches	POD in mm
Flaw Size: POD = X + K(S) =	0.169	4.31

Web Open Hole at 7,000 PSI Stress: Crack Length at PZT Detection = 4.31 mm

Recall – Web Unloaded Open Hole Data: Crack Length at PZT Detection = 6.95 mm

Table 6-25. POD Calculations Using One-Sided Tolerance Interval from PZT Response Data on Riveted Rotorbeam Web (7,000 lb tension load)

PZT Crack Detection Data in Web

Crack Length at PZT Detection a (in)	Log of Crack Length at PZT Detection a (in)
0.059	-1.229148
0.104	-0.982967
0.110	-0.958607
0.100	-1.000000
0.132	-0.879426
0.067	-1.173925
0.091	-1.040959
0.096	-1.017729
0.096	-1.017729
0.142	-0.847712
0.060	-1.221849

PZT Crack Detection in Web for Open and Riveted Holes at 7,000 PSI Stress

Statistic Estimates in Log & Linear Scales

Statistic	Value in Log Scale	Value in Linear Scale
Mean (X)	-1.033641	0.096
Stnd Deviation (S)	0.127109	0.026868

POD Detection Levels (γ = 95%, n = 11)

	POD in inches	POD in mm
Flaw Size: POD = X + K(S) =	0.180	4.57

Web Open/Riveted Hole Data at 7,000 PSI Stress: Crack Length at PZT Detection = 4.57 mm

Recall – Web Unloaded Open/Riveted Hole: Crack Length at PZT Detection = 6.85 mm

Table 6-26 provides a concise summary of just the PZT crack detection levels on the web at each of the load levels. Results are for the optimum, first detection obtained using data from all frequencies of interrogation (200, 250, 300, 350, 500 KHz). Improvement in crack detection performance can be easily observed by comparing the crack lengths in each load column.

Table 6-26. Comparison of PZT Crack Detection for Different Loads in Rotorbeam Web

Rotorbeam PZT Testing - Web Results Optimized Using Detection at Any Frequency						
Specimen Number	Crack Length @ Detection Load=0 lb, Baseline=0 lb mm(in)	Detection Freq @ 0 Load (KHz)	Crack Length @ Detection Load=1000 lb, Baseline=0 lb mm(in)	Detection Freq @ 1K Load (KHz)	Crack Length @ Detection Load=7000 lb, Baseline=7000 lb mm(in)	Detection Freq @ 7K Load (KHz)
RB-PZT-6	5.20 (0.205)	500	4.10 (0.161)	500	n/a	n/a
RB-PZT-7	4.35 (0.171)	500	3.30 (0.130)	500	n/a	n/a
RB-PZT-8	4.35 (0.171)	500	n/a	n/a	1.50 (0.059)	500
RB-PZT-9	5.65 (0.222)	500	4.20 (0.165)	500	2.65 (0.104)	500
RB-PZT-10	5.95 (0.234)	500	4.40 (0.173)	500	2.80 (0.110)	500
RB-PZT-11	5.05 (0.199)	500	3.90 (0.154)	500	2.55 (0.100)	250
RB-PZT-12	5.95 (0.234)	500	5.40 (0.213)	500	3.35 (0.132)	500
RB-PZT-13	5.10 (0.201)	500	3.50 (0.138)	500	1.70 (0.067)	500
RB-PZT-14	5.65 (0.222)	500	3.75 (0.148)	300	2.30 (0.091)	300
RB-PZT-15	6.20 (0.244)	500	5.20 (0.205)	500	2.45 (0.096)	500
RB-PZT-16	5.30 (0.209)	500	4.05 (0.159)	500	2.45 (0.096)	500
RB-PZT-17F	5.00 (0.197)	500	4.0 (0.157)	500	3.60 (0.142)	350
RB-PZT-18F	6.05 (0.238)	500	4.95 (0.195)	500	1.5 (0.060)*	500

After the data above was acquired, it was used in various POD analyses to make comparisons of POD(90/95) for unloaded structure with POD(90/95) when the same structure is monitored while under load. To compare PZT POD(90/95) levels at different stress levels, the data for PZT crack detection for lightly loaded Rotorbeam flange under 1,000 lbs tension is compiled in Table 6-27. For this data, all monitoring was performed on the structure at 1,000 lb loads, however, the Baseline signals for comparison and damage detection were acquired from the structure in unloaded condition.

One-Sided Tolerance Interval POD Method and Lightly Loaded Rotorbeam Flange (1,000 lbs) - The 16 data points listed in Table 6-27 for crack detection in the flanges of the Rotorbeam were used in the OSTI method described in Section 4.6 to calculate the POD performance. Table 6-28 and Table 6-29 summarizes the results from the OSTI calculations for open hole crack detection and open/riveted hole crack detection, respectively. Average crack detection from the 16 crack sites with open holes revealed an average crack length at detection = 0.273" and a low Standard Deviation of 0.076". The resulting $POD_{90/95}$ value for PZT sensors on the Rotorbeam flange monitored at 1,000 lbs load was 0.500" (12.70 mm). This can be compared to the PZT performance for an unloaded flange region where the $POD_{90/95}$ = 0.343" (8.72 mm). Thus, the

light tension load actually produced a 46% reduction in crack detection performance. This is because the OSTI calculations include a parameter that amounts to an increase in POD as the Standard Deviation of the data increases. As a result, while all of the crack detection levels were less than those determined for unloaded monitoring, the Standard Deviation of the data increased from 0.007 to 0.076 and this caused the overall $POD_{90/95}$ value for PZT crack detection on the Rotorbeam flange to increase. However, there was a 17% improvement in average length of crack at detection (0.328" at 0 load vs. 0.273" at 1,000 lb. load). Table 6-29 simply shows the same analysis when the additional two data points are added from the holes with rivets present. The average crack length at detection and the $POD_{90/95}$ levels are essentially the same as the open hole results indicating that the presence of fasteners does not affect the crack detection performance of this PZT system for this Rotorbeam configurations. Differences in these values were ~ 6%.

Table 6-27. PZT Crack Detection for Lightly Loaded Rotorbeam Flange (1,000 lbs tension)

PZT Performance in Flange of Rotorbeam - Crack Length and Damage Index at Initial Crack Detection in 1,000 PSI Loaded Specimens (1,000 lb. Load at Data Acquisition & Baseline Determined at 0 Load)									
Specimen #	Fatigue Cycles at Detection	Crack Length at Detection mm (in)	Damage Detection Freq. (KHz)	First Path Detecting Crack	DI Value of First Path	Second Path Detecting Crack (if applicable)	DI Value of Second Path	Third Path Detecting Crack (if applicable)	DI Value of Third Path
RB-PZT-6-1000	24,000	5.90 (0.232)	350	9-12	0.06113				
	38,800	8.38 (0.330)	300	2-4	0.38464	1-3	0.30942	1-4	0.19524
RB-PZT-7-1000	46,288	8.38 (0.330)	300	9-11	0.07052				
	21,000	4.50 (0.177)	300	1-3	0.07699				
RB-PZT-9-1000	44,645	8.38 (0.330)	300	10-12	0.07657	9-12	0.05412	9-11	0.05027
	18,000	3.80 (0.150)	350	1-4	0.05221				
RB-PZT-10-1000	18,000	3.80 (0.150)	350	1-4	0.05661				
	24,000	4.95 (0.195)	300	2-4	0.06304				
RB-PZT-11-1000	48,359	8.38 (0.330)	300	10-12	0.31374	9-11	0.24518	10-11	0.07683
	39,000	8.38 (0.330)	300	10-12	0.34956	9-11	0.29543	9-12	0.11840
RB-PZT-12-1000	36,000	8.38 (0.330)	300	1-3	0.44270	2-4	0.37276	1-4	0.12682
	42,000	8.38 (0.330)	300	2-4	0.42740	1-3	0.23134	1-4	0.11224
RB-PZT-15-1000	48,226	8.38 (0.330)	300	9-11	0.05299	10-12	0.08144		
	45,000	8.38 (0.330)	300	1-3	0.50284	2-4	0.36648	2-3	0.16370
RB-PZT-16-1000	45,000	7.85 (0.309)	350	10-11	0.05426				
	21,000	4.50 (0.177)	350	1-4	0.06555				
RB-PZT-17F-1000	45,000	2.10 (0.083)	350	1-4	0.06183				
RB-PZT-18F-1000	42,000	3.60 (0.142)	350	1-4	0.07428				

Table 6-28. POD Calculations Using One-Sided Tolerance Interval from PZT Response Data on Rotorbeam Flange (1,000 lb tension load)

PZT Crack Detection Data in Flange (all open holes)

Crack Length at PZT Detection a (in)	Log of Crack Length at PZT Detection a (in)
0.232	-0.634512
0.330	-0.481486
0.330	-0.481486
0.195	-0.709965
0.330	-0.481486
0.330	-0.481486
0.330	-0.481486
0.309	-0.510042
0.330	-0.481486
0.177	-0.752027
0.150	-0.823909
0.150	-0.823909
0.330	-0.481486
0.330	-0.481486
0.330	-0.481486
0.177	-0.752027

PZT Crack Detection in Flange for Open Holes at 1,000 PSI Stress

Statistic Estimates in Log & Linear Scales

Statistic	Value in Log Scale	Value in Linear Scale
Mean (X)	-0.583735	0.273
Stnd Deviation (S)	0.139056	0.076152

Note: Stnd Dev @ 0 Load = 0.0075

POD Detection Levels (γ = 95%, n = 16)

	POD in inches	POD in mm
Flaw Size: POD = X + K(S) =	0.500	12.70

Flange Open Hole at 1,000 PSI Stress: Crack Length at PZT Detection = 12.70 mm

Recall – Flange Unloaded Open Hole Data: Crack Length at PZT Detection = 8.72 mm

Table 6-29. POD Calculations Using One-Sided Tolerance Interval from PZT Response Data on Riveted Rotorbeam Flange (1,000 lb tension load)

PZT Crack Detection Data in Flange (open holes & riveted holes)

Crack Length at PZT Detection a (in)	Log of Crack Length at PZT Detection a (in)
0.232	-0.634512
0.330	-0.481486
0.330	-0.481486
0.195	-0.709965
0.330	-0.481486
0.330	-0.481486
0.330	-0.481486
0.309	-0.510042
0.330	-0.481486
0.177	-0.752027
0.150	-0.823909
0.150	-0.823909
0.330	-0.481486
0.330	-0.481486
0.330	-0.481486
0.177	-0.752027
0.083	-1.080922
0.142	-0.847712

PZT Crack Detection in Flange for Open and Riveted Holes at 1,000 PSI Stress

Statistic Estimates in Log & Linear Scales

Statistic	Value in Log Scale	Value in Linear Scale
Mean (X)	-0.626022	0.255
Stnd Deviation (S)	0.183870	0.088862

Note: Stnd Dev @ 0 Load = 0.0086

POD Detection Levels (γ = 95%, n = 18)

	POD in inches	POD in mm
Flaw Size: POD = X + K(S) =	0.546	13.86

Flange Open/Riveted Hole Data at 1,000 PSI Stress: Crack Length at PZT Detection = 13.9 mm

Recall – Flange Unloaded Open/Riveted Hole: Crack Length at PZT Detection = 8.75 mm

One-Sided Tolerance Interval POD Method and Medium Loaded Rotorbeam Flange (7,000 lbs) - To compare PZT POD(90/95) levels at different stress levels, the data for PZT crack detection for medium loaded Rotorbeam flanges under 7,000 lbs tension is compiled in Table 6-30Table 6-20. For this data, all monitoring was performed on the structure at 7,000 lb loads and Baseline data for comparisons was acquired from the structure also at 7,000 lb loaded condition. Optimum detection was obtained using data from all frequencies of interrogation (200, 250, 300, 350, 500 KHz). The 16 data points listed in Table 6-30 for crack detection in the web of the Rotorbeam at 7,000 lb load were used in the OSTI method described in Section 4.6 to calculate the POD performance. Table 6-31 and Table 6-32 summarize the results from the OSTI calculations for open hole crack detection and open/riveted hole crack detection, respectively. Average crack detection from the 14 specimens with open holes revealed an average crack length at detection = 0.083" and a low Standard Deviation of 0.023". The resulting $POD_{90/95}$ value for PZT sensors on the Rotorbeam flange monitored at 7,000 lbs load was 0.138" (3.50 mm). This can be compared to the PZT performance for an unloaded flange region where the $POD_{90/95}$ = 0.274" (6.95 mm). Thus, the light tension load was able to result in a 50% improvement in crack detection POD. There was also a 75% improvement in average length of crack at detection (0.328" at 0 load vs. 0.083" at 7,000 lb. load). Table 6-33 simply shows the same analysis when the additional two data points are added from the holes with rivets present. The average crack length at detection and the $POD_{90/95}$ levels are essentially the same as the open hole results indicating that the presence of fasteners does not affect the crack detection performance of this PZT system for this Rotorbeam configurations. Differences in these values range from just 0-4%.

Table 6-30. PZT Crack Detection for Medium Loaded Rotorbeam Flange (7,000 lbs tension)

PZT Performance in Flange of Rotorbeam - Crack Length and Damage Index at Initial Crack Detection in 7,000 PSI Loaded Specimens (7,000 lb. Load at Data Acquisition & Baseline Determined at 7,000 Load)									
Specimen #	Fatigue Cycles at Detection	Crack Length at Detection mm (in)	Damage Detection Freq. (KHz)	First Path Detecting Crack	DI Value of First Path	Second Path Detecting Crack (if applicable)	DI Value of Second Path	Third Path Detecting Crack (if applicable)	DI Value of Third Path
RB-PZT-8-7000	15,000	2.45 (0.096)	300	10-12	0.05770				
	12,000	3.60 (0.142)	300	2-3	0.09471	1-3	0.06248	2-4	0.05824
RB-PZT-9-7000	15,000	2.70 (0.106)	300	10-12	0.07873	10-11	0.05895		
	9,000	1.95 (0.077)	300	2-3	0.05274				
RB-PZT-10-7000	15,000	1.50 (0.059)	350	9-12	0.05380				
	12,000	2.30 (0.091)	300	2-3	0.07921	2-4	0.07083	1-3	0.05014
RB-PZT-11-7000	21,000	2.55 (0.100)	300	10-12	0.09439	9-11	0.05384		
	12,000	1.50 (0.059)	300	2-4	0.06588				
RB-PZT-12-7000	12,000	1.90 (0.075)	300	2-3	0.05201				
	12,000	1.60 (0.063)	300	9-11	0.06690				
RB-PZT-15-7000	21,000	2.10 (0.083)	350	9-12	0.05622				
	15,000	1.85 (0.073)	300	2-3	0.08072	1-3	0.05435		
RB-PZT-16-7000	9,000	1.55 (0.061)	350	1-4	0.06402				
	12,000	2.00 (0.079)	300	2-3	0.12480	1-3	0.06348	2-4	0.05168
RB-PZT-17F-7000	42,000	1.20 (0.047)	350	1-4	0.06380				
RB-PZT-18F-7000	36,000	3.00 (0.118)	350	1-4	0.05894				

Table 6-33 provides a concise summary of just the PZT crack detection levels on the flange at each of the load levels. Results are for the optimum, first detection obtained using data from all frequencies of interrogation (200, 250, 300, 350, 500 KHz). Improvement in crack detection performance can be easily observed by comparing the crack lengths in each load column. In general, crack detection performance improves with load as higher stress levels produce greater crack openings and positive changes in the stress fields conducting the Lamb Waves. When

attempting to monitor PZT networks under load, users need to simultaneously assess the challenges associated with obtaining proper Baselines at load and comparing that to PZT monitoring at similar load conditions.

Table 6-31. POD Calculations Using One-Sided Tolerance Interval from PZT Response Data on Rotorbeam Flange (7,000 lb tension load)

PZT Crack Detection Data in Flange (all open holes)

Crack Length at PZT Detection a (in)	Log of Crack Length at PZT Detection a (in)
0.096	-1.017729
0.106	-0.974694
0.059	-1.229148
0.100	-1.000000
0.075	-1.124939
0.083	-1.080922
0.079	-1.102373
0.142	-0.847712
0.077	-1.113509
0.091	-1.040959
0.059	-1.229148
0.063	-1.200659
0.073	-1.136677
0.061	-1.214670

PZT Crack Detection in Flange for Open Holes at 7,000 PSI Stress

Statistic Estimates in Log & Linear Scales

Statistic	Value in Log Scale	Value in Linear Scale
Mean (X)	-1.093796	0.083
Stnd Deviation (S)	0.110323	0.022843

POD Detection Levels (γ = 95%, n = 14)

	POD in inches	POD in mm
Flaw Size: POD = X + K(S) =	0.138	3.50

Flange Open Hole at 7,000 PSI Stress: Crack Length at PZT Detection = 3.50 mm

Recall – Flange Unloaded Open Hole Data: Crack Length at PZT Detection = 8.72 mm

Table 6-32. POD Calculations Using One-Sided Tolerance Interval from PZT Response Data on Riveted Rotorbeam Flange (7,000 lb tension load)

PZT Crack Detection Data in Flange (open holes & riveted holes)

Crack Length at PZT Detection a (in)	Log of Crack Length at PZT Detection a (in)
0.096	-1.017729
0.106	-0.974694
0.059	-1.229148
0.100	-1.000000
0.075	-1.124939
0.083	-1.080922
0.079	-1.102373
0.142	-0.847712
0.077	-1.113509
0.091	-1.040959
0.059	-1.229148
0.063	-1.200659
0.073	-1.136677
0.061	-1.214670
0.047	-1.327902
0.118	-0.928118

PZT Crack Detection in Flange for Open and Riveted Holes at 7,000 PSI Stress

Statistic Estimates in Log & Linear Scales

Statistic	Value in Log Scale	Value in Linear Scale
Mean (X)	-1.098072	0.083
Stnd Deviation (S)	0.126541	0.024906

POD Detection Levels (γ = 95%, n = 16)

	POD in inches	POD in mm
Flaw Size: POD = X + K(S) =	0.144	3.66

Flange Open/Riveted Hole Data at 7,000 PSI Stress: Crack Length at PZT Detection = 3.66 mm

Recall – Flange Unloaded Open/Riveted Hole: Crack Length at PZT Detection = 8.75 mm

Table 6-33. Comparison of PZT Crack Detection for Different Loads in Rotorbeam Flange

Rotorbeam PZT Testing - Flange Results Optimized Using Detection at Any Frequency							
Specimen Number	Crack Length @ Detection Load=0 lb, Baseline=0 lb mm (in)	Detection Freq @ 0 Load (KHz)	Crack Length @ Detection Load=1000 lb, Baseline=0 lb mm (in)	Detection Freq @ 1K Load (KHz)	Crack Length @ Detection Load=7000 lb, Baseline=7000 lb mm (in)	Detection Freq @ 7K Load (KHz)	
RB-PZT-3	8.38 (0.330)	300	n/a	n/a	n/a	n/a	Top Flange
RB-PZT-4	8.38 (0.330)	300	n/a	n/a	n/a	n/a	
RB-PZT-5	8.38 (0.330)	300	n/a	n/a	n/a	n/a	
RB-PZT-6	8.38 (0.330)	300	8.38 (0.330)	300	n/a	n/a	
RB-PZT-7	8.38 (0.330)	300	4.50 (0.177)	300	n/a	n/a	
RB-PZT-8	8.38 (0.330)	300	n/a	n/a	3.60 (0.142)	300	
RB-PZT-9	8.38 (0.330)	300	3.80 (0.150)	350	1.95 (0.077)	300	
RB-PZT-10	8.38 (0.330)	300	3.80 (0.150)	350	2.30 (0.091)	300	
RB-PZT-11	8.38 (0.330)	300	8.38 (0.330)	300	1.50 (0.059)	300	
RB-PZT-12	8.38 (0.330)	300	8.38 (0.330)	300	1.60 (0.063)	300	
RB-PZT-15	8.38 (0.330)	300	8.38 (0.330)	300	1.85 (0.073)	300	
RB-PZT-16	8.38 (0.330)	300	4.50 (0.177)	350	1.55 (0.061)	350	
RB-PZT-17F	8.38 (0.330)	300	2.10 (0.083)	350	1.20 (0.047)	350	
RB-PZT-18F	7.75 (0.305)	350	3.60 (0.142)	350	3.00 (0.118)	350	
RB-PZT-3	7.50 (0.295)	300	n/a	n/a	n/a	n/a	Bottom Flange
RB-PZT-4	8.38 (0.330)	300	n/a	n/a	n/a	n/a	
RB-PZT-5	8.38 (0.330)	300	n/a	n/a	n/a	n/a	
RB-PZT-6	8.38 (0.330)	300	5.90 (0.232)	350	n/a	n/a	
RB-PZT-7	8.38 (0.330)	300	8.38 (0.330)	300	n/a	n/a	
RB-PZT-8	8.38 (0.330)	300	n/a	n/a	2.45 (0.096)	300	
RB-PZT-9	8.38 (0.330)	300	8.38 (0.330)	300	2.70 (0.106)	300	
RB-PZT-10	No Detection*	n/a	4.95 (0.195)	n/a	1.50 (0.059)	350	
RB-PZT-11	8.38 (0.330)	300	8.38 (0.330)	300	2.55 (0.100)	300	
RB-PZT-12	8.38 (0.330)	300	8.38 (0.330)	300	1.90 (0.075)	300	
RB-PZT-15	No Detection*	n/a	8.38 (0.330)	300	2.10 (0.083)	350	
RB-PZT-16	8.38 (0.330)	300	7.85 (0.309)	350	2.00 (0.079)	350	

Both the average crack length at detection and the POD(90/95) level provide good metrics for assessing any improvements in crack detection performance and the value of attempting to conduct on-board SHM monitoring when the structure is under load. Table 6-34 compares the average crack length at detection for the PZT sensor networks on both the web and flange of the Rotorbeam. The average crack detection in the flange drops from 0.210" (unloaded) to 0.095" at 7,000 lb load (55% decrease). The average crack detection in the web drops from 0.328" (unloaded) to 0.083" at 7,000 lb load (75% decrease). These numbers are shown pictorially in Figure 6-68. When the change in POD levels associated with increasing tension load are studies, there is one anomaly noted. Figure 6-69 shows histograms for the POD(90/95) levels corresponding to the unloaded,

1,000 lb and 7,000 lb monitoring scenarios. In the web region, the POD (90/95) levels drop uniformly with increasing tension load with an overall improvement from 0.274" (unloaded) to 0.169" (7,000 lbs) for a 38% improvement. In the flange region, the lightly loaded condition of 1,000 lbs produces an increase in the POD(90/95) level. This is produced by the torsional/compressive strains generated in the more complex structure at low loads. This results in a higher variation in test results at low stress levels (joint torsion) which produces a higher Std Deviation and higher POD. Higher stress levels (see 7,000 PSI results) move the structure into uniform tension and show the associated decrease in POD levels. The key take-away is that the stress field in complex structures must be understood and properly simulated in the performance testing.

Table 6-34. Comparison of Average Crack Length at PZT Detection for Specimens Loaded to Different Stress Levels

Crack Detection with PZT Networks			
Average Crack Length at PZT Detection		Average Crack Length in Web at PZT Detection (in)	Average Crack Length in Flange at PZT Detection (in)
Unloaded Rotorbeam	Open Holes	0.210	0.328
	Open and Riveted Holes	0.211	0.328
Rotorbeam at 1,000 PSI Stress	Open Holes	0.165	0.273
	Open and Riveted Holes	0.167	0.253
Rotorbeam at 7,000 PSI Stress	Open Holes	0.095	0.083
	Open and Riveted Holes	0.096	0.083

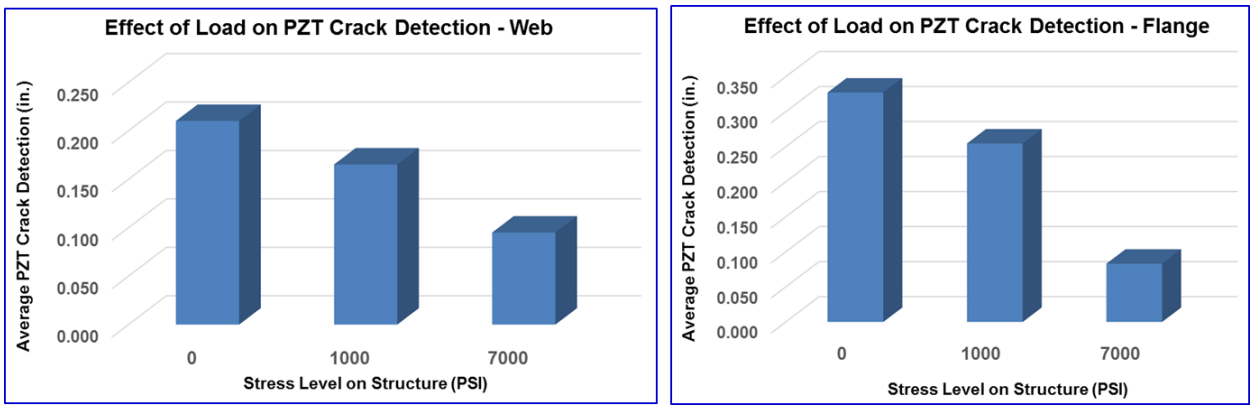

Figure 6-68. Effect of Load on Average PZT Crack Detection in Web and Flange

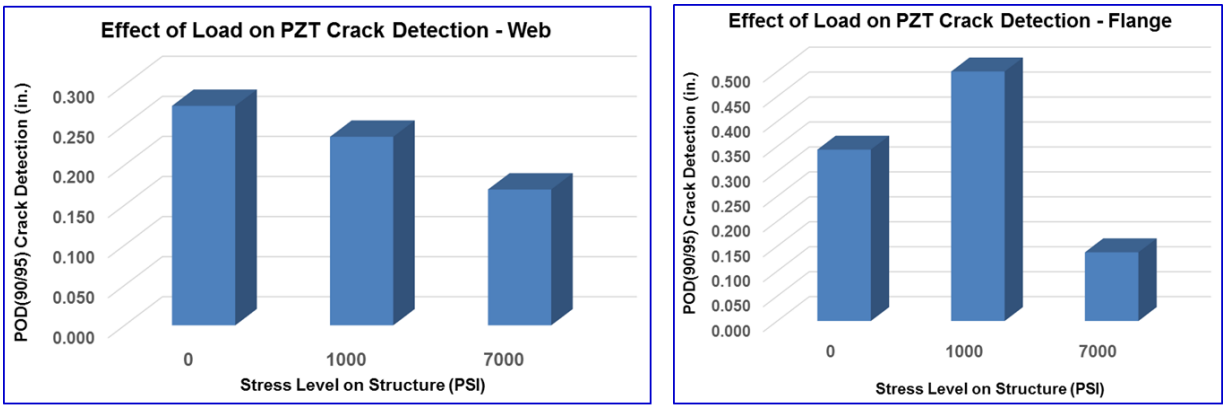

Figure 6-69. Effect of Load on POD(90/95) for PZT Crack Detection in Web and Flange

Finally, the effects of tension loads on the crack detection performance of the PZT network, as summarized in Table 6-34, can be seen in the changes observed in the DI curves of Figure 6-70 through Figure 6-72. Figure 6-70 plots the DI vs cycles curves for the critical Path 5-8 on the web from an unloaded Rotorbeam specimen. It shows the resulting crack detection level for specimens RB-PZT-6 through RB-PZT-16. The range of lengths is 0.171" to 0/234" (average crack length at detection = 0.210"). Figure 6-71 plots the DI vs cycles curves for the critical Path 5-8 on the web from a light 1,000 lb loaded Rotorbeam specimen. It shows the more rapid rise in the DI levels and earlier crack detection in specimens RB-PZT-6 through RB-PZT-16 (average crack length at detection = 0.165"). Figure 6-72 plots the DI vs cycles curves for the critical Path 5-8 on the web from a medium 7,000 lb loaded Rotorbeam specimen. It shows the most rapid rise in the DI levels and earlier crack detection in specimens RB-PZT-6 through RB-PZT-16 (average crack length at detection = 0.095").

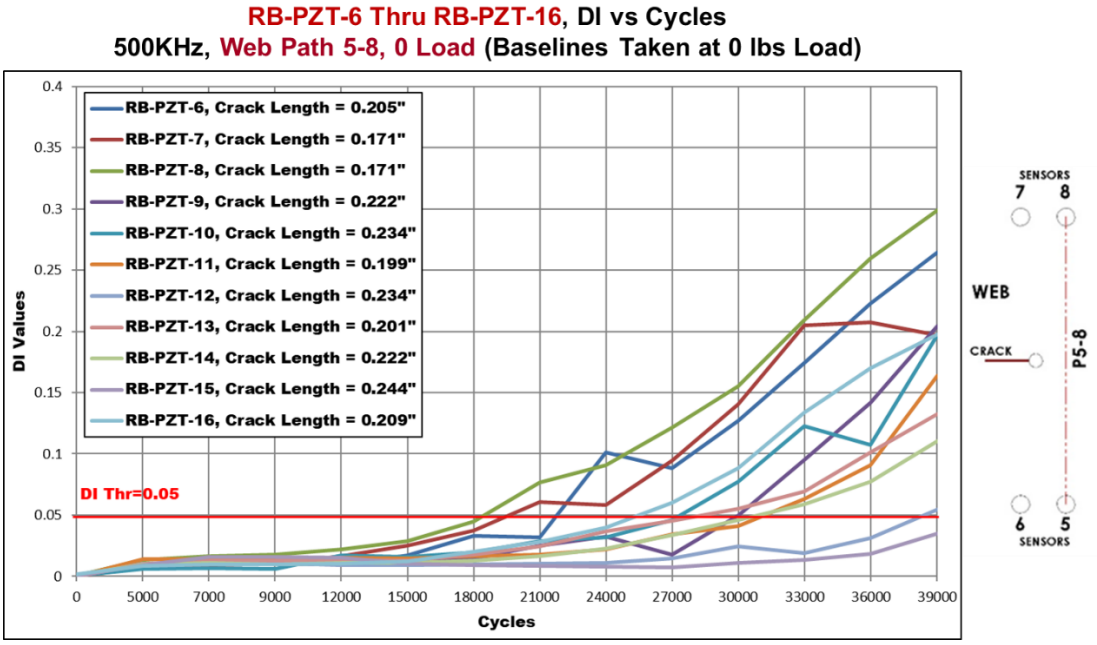

Figure 6-70. Comparison of DI Progression in Web for PZT Crack Detection in Unloaded Specimens

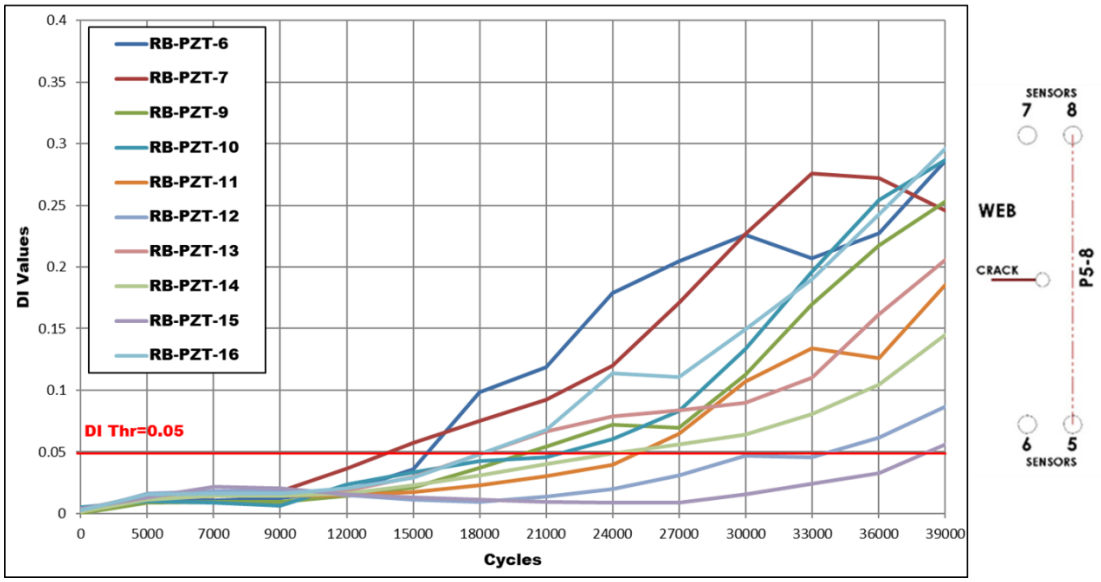

Figure 6-71. Comparison of DI Progression in Web for Crack Detection in Specimens with 1,000 lb Load

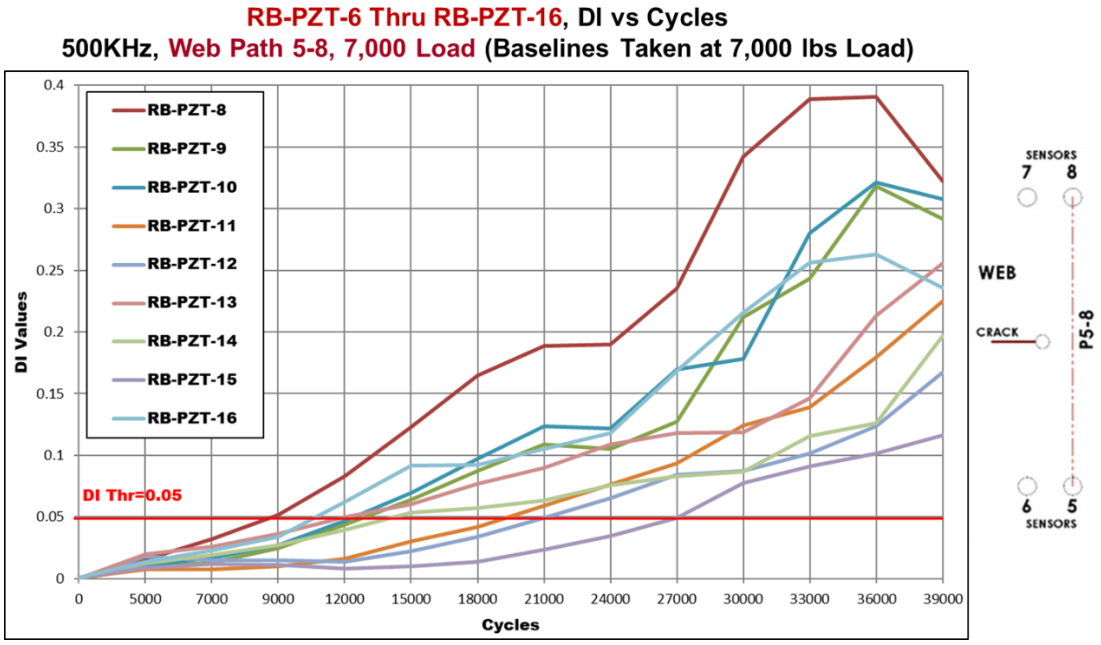

Figure 6-72. Comparison of DI Progression in Web for Crack Detection in Specimens with 7,000 lb Load

6.2.2. Comparison of Results at Extreme Temperature

Changing temperatures can induce changes in the PZT signals in a network. If not properly accounted for in the data acquisition phase, such changes could erroneously produce false calls (DI levels in excess of the threshold when no damage is actually present) or result in a missed damage detection. Thus, it is necessary to utilize software features that can accommodate and account for PZT signal changes that are the result of temperature alone. The Acellent Scan Genie software automatically acquires a series of different Baseline signatures to represent the response of the pristine (undamaged) structure over a range of temperatures. Temperature sensors, placed on board the structure near the PZT network, then determine the current temperature of the structure being monitored and assign the proper Baseline signatures to use for comparison and calculation of DI levels.

To evaluate the accuracy of this temperature compensation approach, a series of tests were conducted to measure the effect of extreme temperatures on PZT function and crack detection. Figure 6-73 and Figure 6-74 show the application of cooling systems and heat lamps to produce high and low temperatures in the test specimens during fatigue tests.

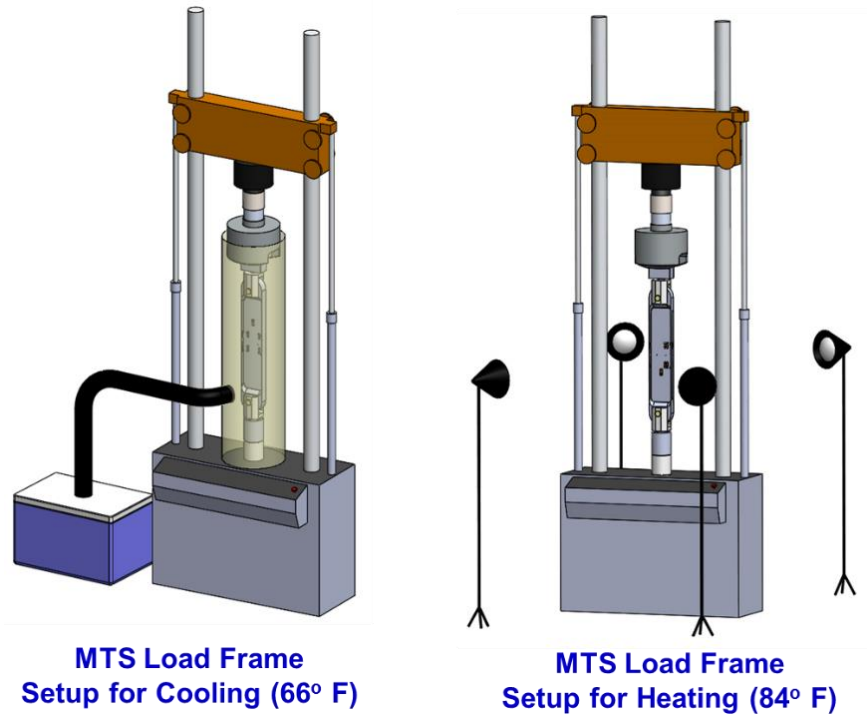

Figure 6-73. Schematic of Test Set-Up to Assess PZT Crack Detection at Hot and Cold Temperature Extremes

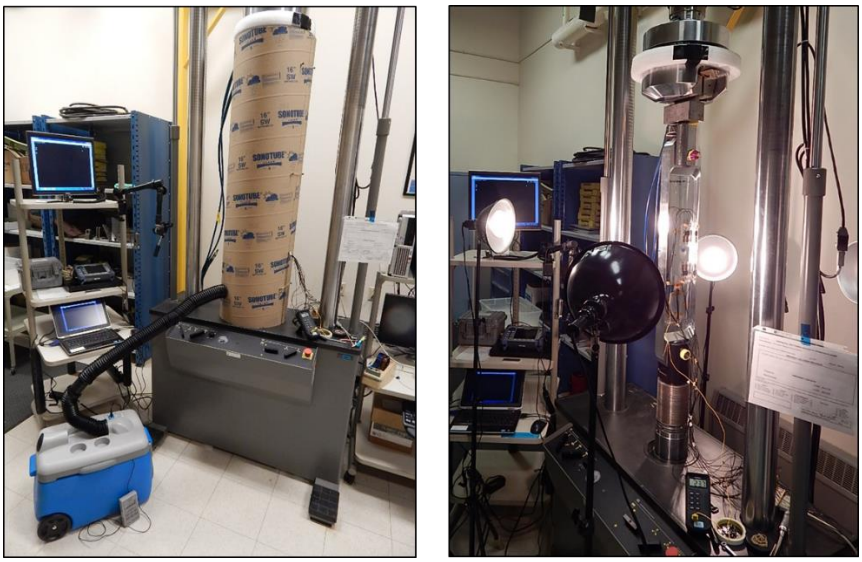

Figure 6-74. Equipment Set-Up Used to Produce Hot and Cold Temperature Extremes

In these tests, each test specimen was exposed to hot and cold conditions so that Baselines were acquired in 2°F increments over a temperature range of 64°F to 84°F. After the application of fatigue cycles and the growth of cracks in the webs and flanges, the Rotorbeam specimens were

exposed to similar temperature cycles. DI levels were calculated by the Scan Genie software using the temperature compensation algorithm to ensure proper comparisons of PZT signals from similar temperatures.

Table 6-35 lists the DI values for multiple paths defined in the web and flanges in specimen RB-PZT-15. It highlights a web crack detection at Room Temperature, a flange crack detection at Room Temperature and lists the variations in DI values as the specimen is exposed to hot, then cold, then returned to RT. With ideal temperature compensation adjustments, the DI values should change very little over the course of the temperature excursions. For the web Path 5-8, which detected the web crack with a DI of 0.074, the DI values dropped as low as 0.046 at 64.5°F (37% change in DI) and rose as high as 0.081 at 82.6°F (9.5%). For the flange Path 2-4, which detected the flange crack with a DI of 0.059, the DI values dropped as low as 0.058 at 73.7°F (1.7%) and rose as high as 0.068 at 68.2°F (15%). Such magnitudes of DI change could potentially effect crack detection if monitoring were to occur outside of DT environments (~ 74°F).

Table 6-36 focuses on the DI values in web Path 5-8 (500 KHz) for specimen RB-PST-15 and lists DI changes over temperature for initial crack detection at 45,000 cycles and later at 51,000 cycles. These DI values at each temperature are plotted in Figure 6-75. These plots show that: 1) for data at initial crack detection (45,000 cycles), DI variations at both hot and cold conditions produced conditions where the crack would be undetected (DI level dropped below the 0.05 threshold), and 2) for data at a slightly higher cycle count and crack length (51,000 cycles), DI variations occurred but the crack was still detected (DI remained above 0.05) at all extreme temperatures. These results indicate that the software temperature compensation is not absolute when applied to the Rotorbeam specimens and that crack detection may occur later if PZT sensors are monitored at extreme temperatures. If such monitoring is envisioned for the PZT application, these temperature effects should be taken into consideration when quantifying the overall crack detection performance. Note that the DI level at detection was at 0.074 which is quite close to the DI(threshold).

Table 6-35. Overall Summary of DI Values at Temperature Extremes – RB-PZT-15

	RB-PZT-15 High and Low Temp. Compensation Table - 500 KHz - 45,000 Cycles											
		Low Temperature Data Taken After Detection			Detection at RT	High Temperature Data Taken After Detection			Data Taken at Room Temperature after Taking Data at High and Low Temps.			
	Temp-F	64.51	66.42	68.16	73.85	79.59	81.16	82.62	73.74	74.08	74.25	74.30
	Temp-C	18.06	19.12	20.09	23.25	26.44	27.31	28.12	23.19	23.38	23.47	23.50
	Cycles	45000	45000	45000	45000	45000	45000	45000	45000	45000	45000	45000
Top Flange DI Values	Path 1-3	0.05000	0.05064	0.04791	0.04755	0.05042	0.04702	0.04897	0.04828	0.04723	0.04622	0.04576
	Path 1-4	0.02430	0.02604	0.02478	0.02524	0.02730	0.02693	0.02633	0.02675	0.02656	0.02682	0.02683
	Path 2-3	0.01293	0.01512	0.01368	0.01663	0.01123	0.01257	0.01234	0.01422	0.01486	0.01465	0.01437
	Path 2-4	0.06042	0.06579	0.06752	0.05862	0.05932	0.05901	0.06056	0.05833	0.05985	0.05901	0.05904
Web DI Values	Path 5-7	0.02498	0.02271	0.02234	0.02808	0.02448	0.02313	0.02380	0.02335	0.02643	0.02829	0.02849
	Path 5-8	0.04623	0.04982	0.04780	0.07385	0.04441	0.08074	0.04918	0.07309	0.06820	0.07054	0.06976
	Path 6-7	0.03057	0.04790	0.04805	0.02807	0.02409	0.04814	0.04808	0.04600	0.02515	0.02546	0.02593
	Path 6-8	0.04662	0.03793	0.03620	0.04369	0.03699	0.03868	0.03794	0.03780	0.04063	0.04265	0.04301
Bottom Flange DI Values	Path 9-11	0.02246	0.02600	0.02208	0.02013	0.02038	0.01745	0.02074	0.01671	0.01773	0.01865	0.01868
	Path 9-12	0.01383	0.01302	0.01871	0.01136	0.01985	0.01196	0.01880	0.00962	0.01109	0.01369	0.01391
	Path 10-11	0.01101	0.00908	0.01174	0.00868	0.00974	0.01063	0.01090	0.00851	0.00825	0.00943	0.00915
	Path 10-12	0.01594	0.01913	0.01589	0.01807	0.01417	0.01766	0.01836	0.01677	0.01592	0.01163	0.01145

Table 6-36. DI Variations in Web Caused by Temperature Changes in Specimen – RB-PZT-15

	RB-PZT-15 High and Low Temp. Compensation Table - Web - 500 KHz - 45K & 51K Cycles										
		Low Temperature Data Taken After Detection			Detection at RT	High Temperature Data Taken After Detection			Data Taken at Room Temperature after Taking Data at High and Low Temps.			
Detection at 45,000 Cycles	Temp °F (°C)	64.51 (18.06)	66.42 (19.12)	68.16 (20.09)	73.85 (23.25)	79.59 (26.44)	81.16 (27.31)	82.62 (28.12)	73.74 (23.19)	74.08 (23.38)	74.25 (23.47)	74.30 (23.50)
	DI - Web Path 5-8	0.04623	0.04982	0.04780	0.07385	0.04441	0.08074	0.04918	0.07309	0.06820	0.07054	0.06976
51,000 Cycles	Temp °F (°C)	65.14 (18.41)	66.88 (19.38)	68.61 (20.34)	73.62 (23.12)	80.04 (26.69)	81.66 (27.59)	83.46 (28.59)	n/a	n/a	n/a	n/a
	DI - Web Path 5-8	0.11402	0.12036	0.11328	0.15512	0.11451	0.15107	0.12194	n/a	n/a	n/a	n/a

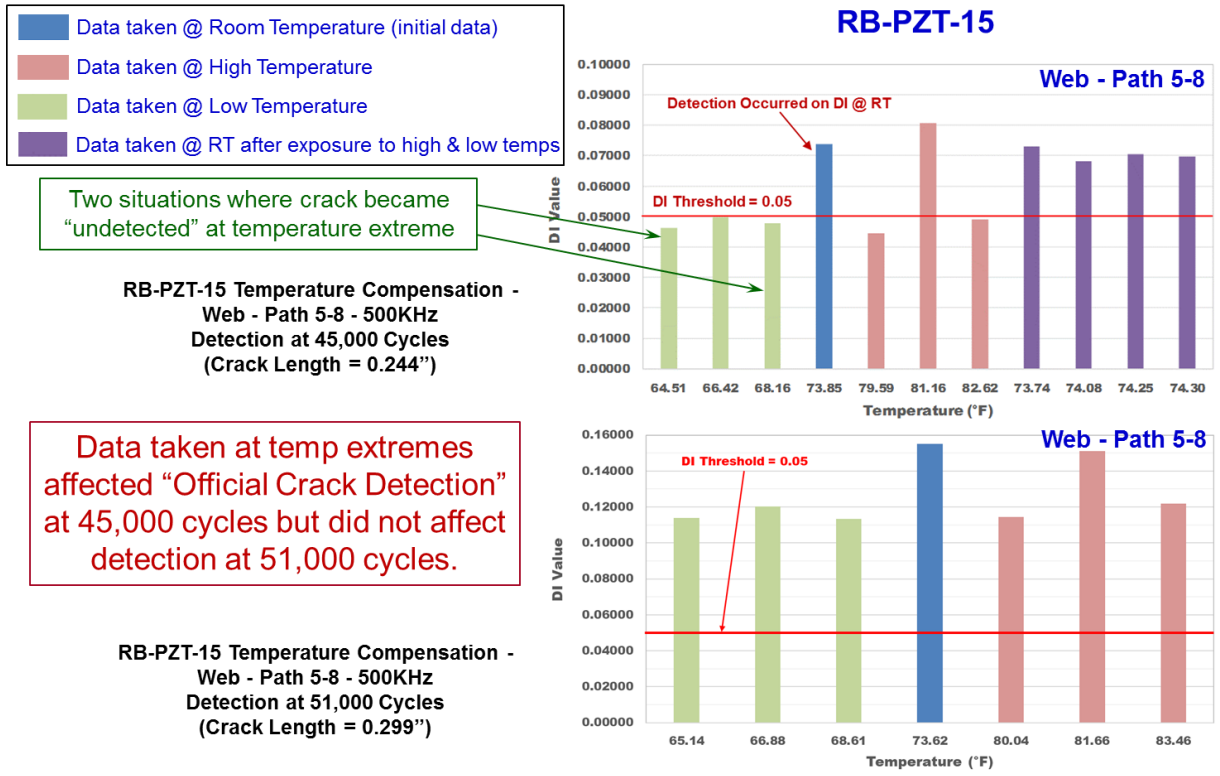

Figure 6-75. Change in Web DI Values for Same Crack at Different Temperatures – RB-PZT-15

Table 6-37 focuses on the DI values in flange Path 1-3 (300 KHz) for specimen RB-PST-15 and lists DI changes over temperature for initial crack detection at 45,000 cycles and later at 51,000 cycles. These DI values at each temperature are plotted in Figure 6-76. In this case, the DI levels remained above the DI(threshold) = 0.05 so crack detection was unaffected by data monitoring at temperature extremes. However, it should be noted that the DI level at initial detection was 0.175 which is significantly above the DI(threshold). DI levels for Path 1-3 dropped as much as 4.6% the (DI values dropped as low as 0.167 at 81.2°F). These results also indicate that caution should be used whenever monitoring PZT networks at temperatures different from RT. It may require an adjustment in the DI(threshold) to account for DI changes at different temperatures.

Table 6-37. DI Variations in Flange Caused by Temperature Changes in Specimen – RB-PZT-15

	RB-PZT-15 High and Low Temp. Compensation Table - Top Flange - 300 KHz - 45K & 51K Cycles											
		Low Temperature Data Taken After Detection			Detection at RT	High Temperature Data Taken After Detection			Data Taken at Room Temperature after Taking Data at High and Low Temps.			
Detection at 45,000 Cycles	Temp °F (°C)	64.51 (18.06)	66.42 (19.12)	68.16 (20.09)	73.85 (23.25)	79.59 (26.44)	81.16 (27.31)	82.62 (28.12)	73.74 (23.19)	74.08 (23.38)	74.25 (23.47)	74.30 (23.50)
	DI - Top Flange Path 1-3	0.20820	0.21632	0.18234	0.17531	0.17119	0.16763	0.17512	0.21314	0.17996	0.22109	0.22430
51,000 Cycles	Temp °F (°C)	65.14 (18.41)	66.88 (19.38)	68.61 (20.34)	73.62 (23.12)	80.04 (26.69)	81.66 (27.59)	83.46 (28.59)	n/a	n/a	n/a	n/a
	DI - Top Flange Path 1-3	0.27430	0.27801	0.27468	0.30728	0.28983	0.28629	0.28062	n/a	n/a	n/a	n/a

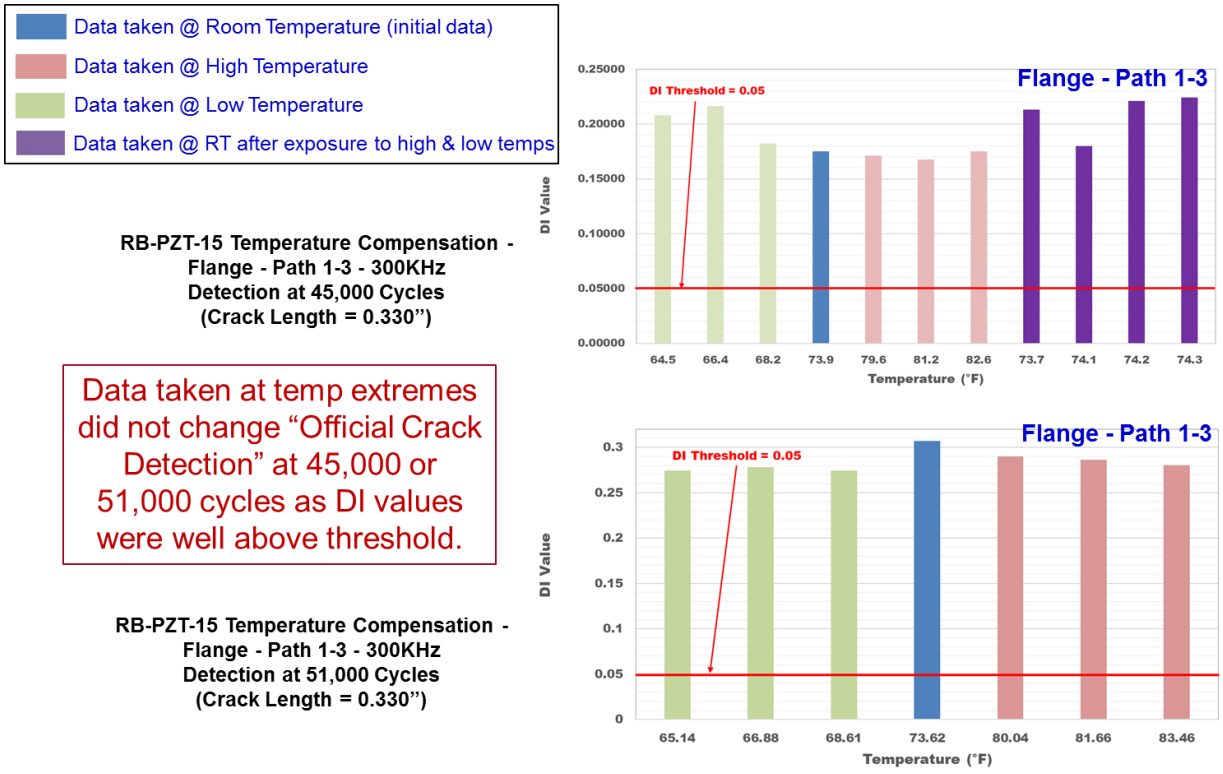

Figure 6-76. Change in Flange DI Values for Same Crack at Different Temperatures – RB-PZT-15

Table 6-38 and Figure 6-77 highlight the effects of temperature on the PZT response, and subsequent changes in DI, for the web region on specimen RB-PZT-16. They focus on the DI values in web Path 5-8 (500 KHz) for specimen RB-PST-16 and show DI changes over temperature for initial crack detection at 27,000 cycles and later at 30,000 and 33,000 cycles. These DI values at each temperature are plotted in Figure 6-77. In this case, there was one single situation where the crack became undetected at low temperature. In this case, the DI value of 0.060 dropped below the DI(threshold) to 0.045 at 66.8°F. So, crack detection was mostly unaffected by data monitoring at temperature extremes. However, this is dependent on the "starting" DI level at initial detection and its magnitude relative to the DI(threshold). DI levels for Path 5-8 dropped as much as 25%. At 30,000 cycles the RT DI was 50% above the DI(threshold) such that any variations in DI caused by temperature extremes were still above the DI(threshold).

Table 6-38. DI Variations in Web Caused by Temperature Changes in Specimen – RB-PZT-16

	RB-PZT-16 High and Low Temp. Compensation Table - 500 KHz - 27K to 33K Cycles - Web							
		Low Temperature Data Taken After Detection			Detection at RT	High Temperature Data Taken After Detection		
Detection at 27,000 Cycles	Temp °F (°C)	65.14 (18.41)	66.81 (19.34)	68.68 (20.38)	75.49 (24.16)	79.30 (26.28)	81.00 (27.22)	82.80 (28.22)
	DI - Web Path 5-8	0.06722	0.04511	0.06397	0.06016	0.05655	0.06653	0.05774
30,000 Cycles	Temp °F (°C)	64.96 (18.31)	66.60 (19.22)	68.50 (20.28)	72.72 (22.62)	79.48 (26.38)	81.34 (27.41)	83.08 (28.38)
	DI - Web Path 5-8	0.07055	0.06635	0.06660	0.08834	0.07617	0.08288	0.07219
33,000 Cycles	Temp °F (°C)	66.49 (19.16)	68.50 (20.28)	70.20 (21.22)	76.15 (24.53)	79.14 (26.19)	80.94 (27.19)	82.74 (28.19)
	DI - Web Path 5-8	0.13409	0.13256	0.12805	0.13364	0.13787	0.12651	0.12075

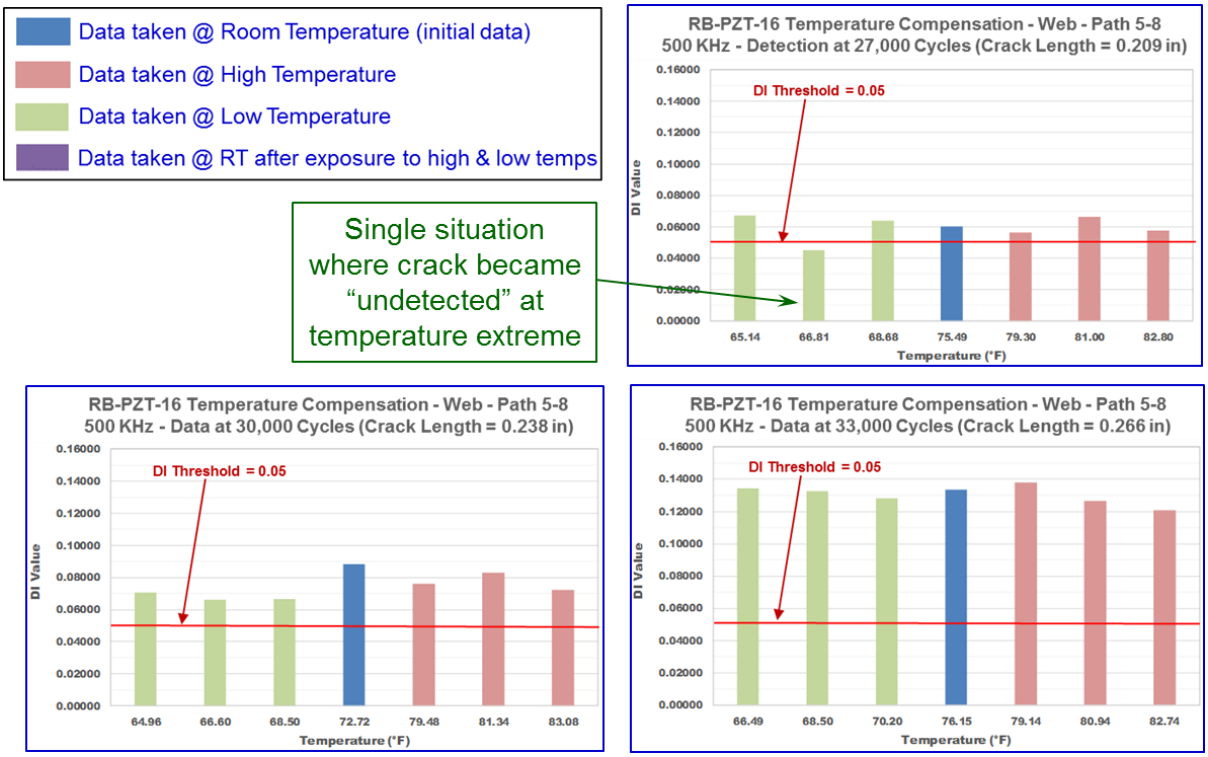

Figure 6-77. Change in Web DI Values for Same Crack at Different Temperatures – RB-PZT-16

Table 6-39 and Figure 6-78 highlight the effects of temperature on the PZT response changes, and subsequent changes in DI, for the flange region on specimen RB-PZT-16. They focus on the DI values in the flange for multiple paths and different RT DI levels; all are above the DI(threshold) level. These DI values at each temperature are plotted in Figure 6-78 showing that DI levels remained above the DI(threshold) = 0.05 so crack detection was unaffected by data monitoring at temperature extremes. However, this example is provided to demonstrate that if DI levels start off

at RT sufficiently above DI(threshold), then any deviation in DIs from those at room temperature will not produce any DI levels that are subsequently below the crack detection threshold for the same crack length monitored at different temperatures (i.e. crack was always "detected" at all temps). Once again, this shows the dependency of crack detection at all temperatures on the "starting" DI level at initial detection and its magnitude relative to the DI(threshold).

Table 6-39. DI Variations in Flange Caused by Temperature Changes in Specimen – RB-PZT-16

RB-PZT-16 High and Low Temp. Compensation Table - 300 KHz - 33K Cycles - Top Flange							
Detection at 33,000 Cycles	Low Temperature Data Taken After Detection			Detection at RT	High Temperature Data Taken After Detection		
Temp °F (°C)	66.49 (19.16)	68.50 (20.28)	70.20 (21.22)	76.15 (24.53)	79.14 (26.19)	80.94 (27.19)	82.74 (28.19)
DI - Flange Path 1-3	0.20084	0.20805	0.19636	0.20327	0.20046	0.17871	0.17704
DI - Flange Path 1-4	0.17036	0.15836	0.16305	0.14762	0.15878	0.16285	0.14428
DI - Flange Path 2-3	0.11168	0.10301	0.07051	0.09580	0.09992	0.10308	0.09837
DI - Flange Path 2-4	0.21445	0.21097	0.21266	0.22765	0.20069	0.19903	0.23218

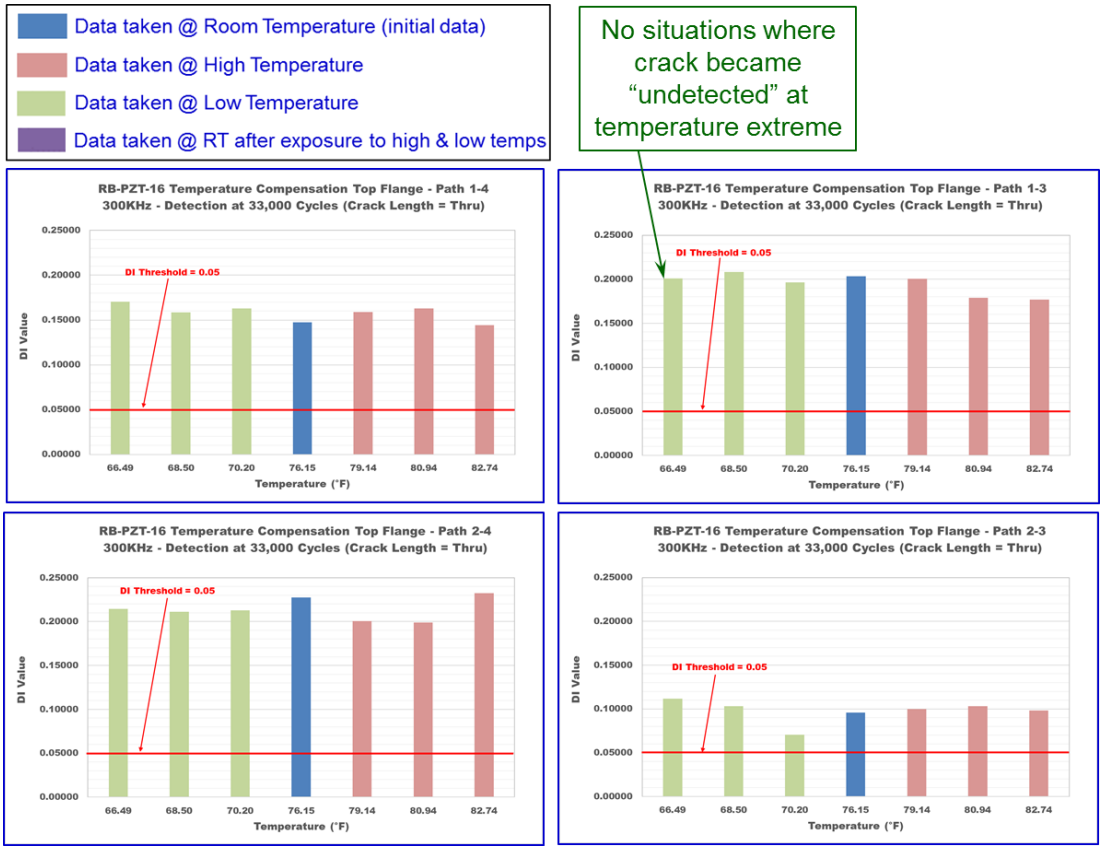

Figure 6-78. Change in Flange DI Values for Same Crack at Different Temperatures – RB-PZT-16

6.2.3. *Cracked Holes with Rivets Installed*

Normally, fatigue cracks will develop in joints and other structural connection regions that contain fasteners. The Rotorbeam test specimens were primarily fatigue tested with open holes acting as the crack initiation points. To determine if the resulting PZT performance would be different if each hole had a fastener installed, several specimens were tested with rivets installed in each hole. The goal was to evaluate the use of rivets to study PZT damage detection under different joint "tightness." PZT performance was quantified and crack detection results from riveted holes were compared with those from open holes.

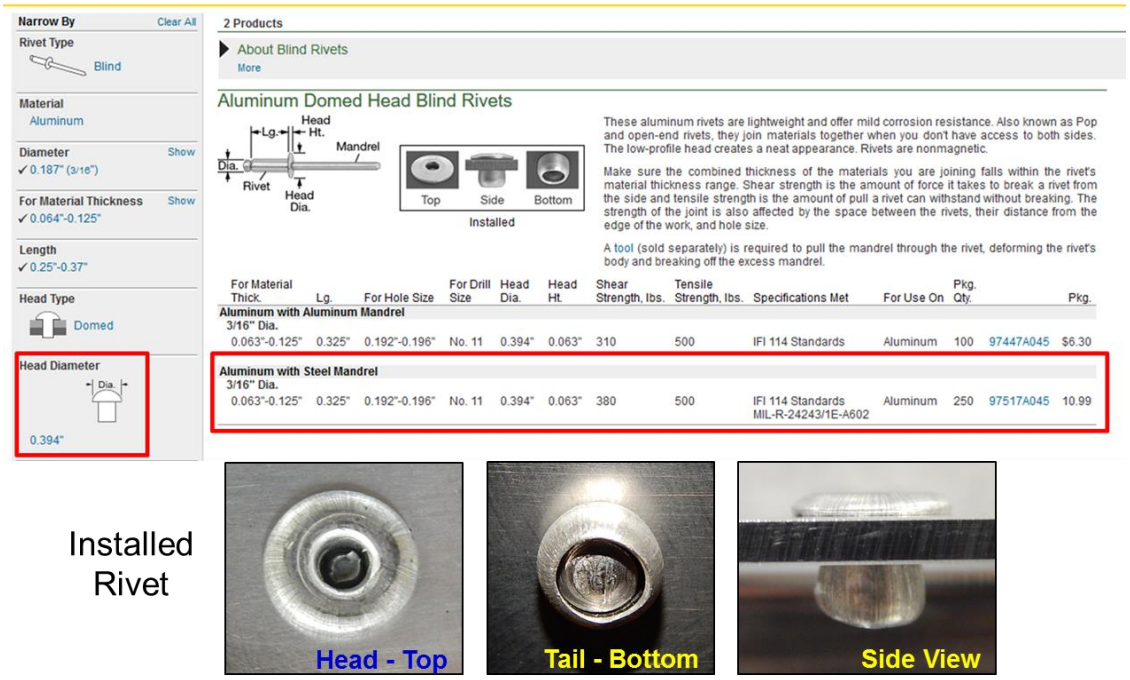

Figure 6-79. Rivet Used to Assess Effect of Joint Tightness on PZT Response

Figure 6-79 shows the blind rivet fastener that was used to study the effect of joint tightness and expanding fastener shaft on PZT response. Figure 6-80 shows the test specimens with rivets installed in both the web and flange regions. An example of crack growth observed at a fastener site is shown Figure 6-81 in along with the crack measurements made at different fatigue cycles. Typical crack growth *da/dN* curves for cracks emanating from riveted holes in the web and the flange are shown in Figure 6-82. The fatigue cycle data also indicates where the PZT network detected the cracks. Data was acquired for unloaded, lightly-loaded (1,000 lbs) and medium-loaded (7,000 lbs) Rotorbeam specimens to determine if the effects of fasteners changes as the structure is loaded

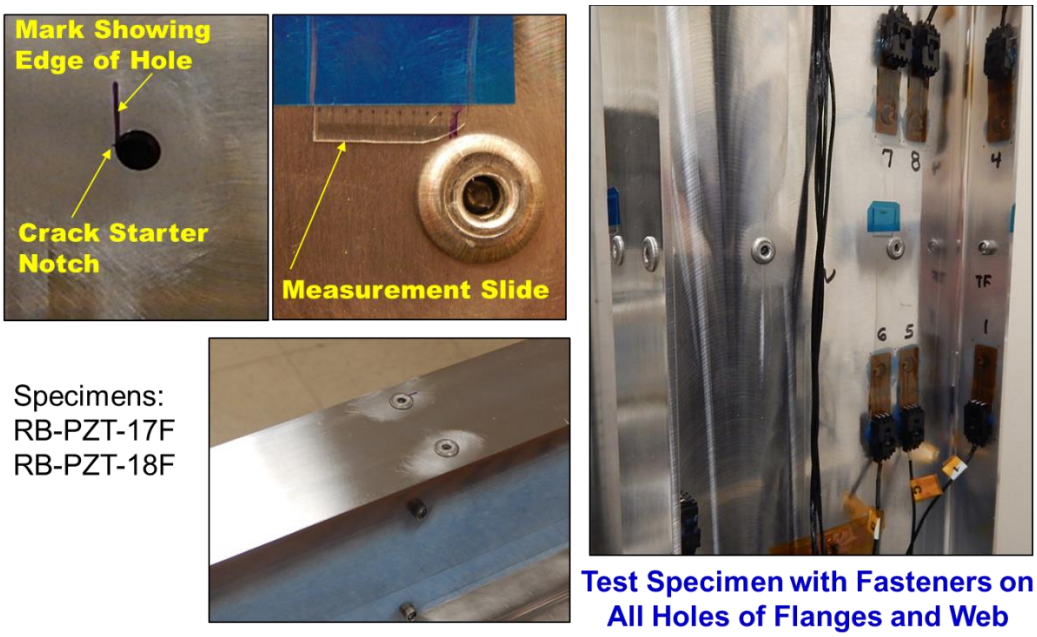

Figure 6-80. Comparison of PZT Network Performance in Open Holes vs Holes with Blind Rivet Fasteners Installed

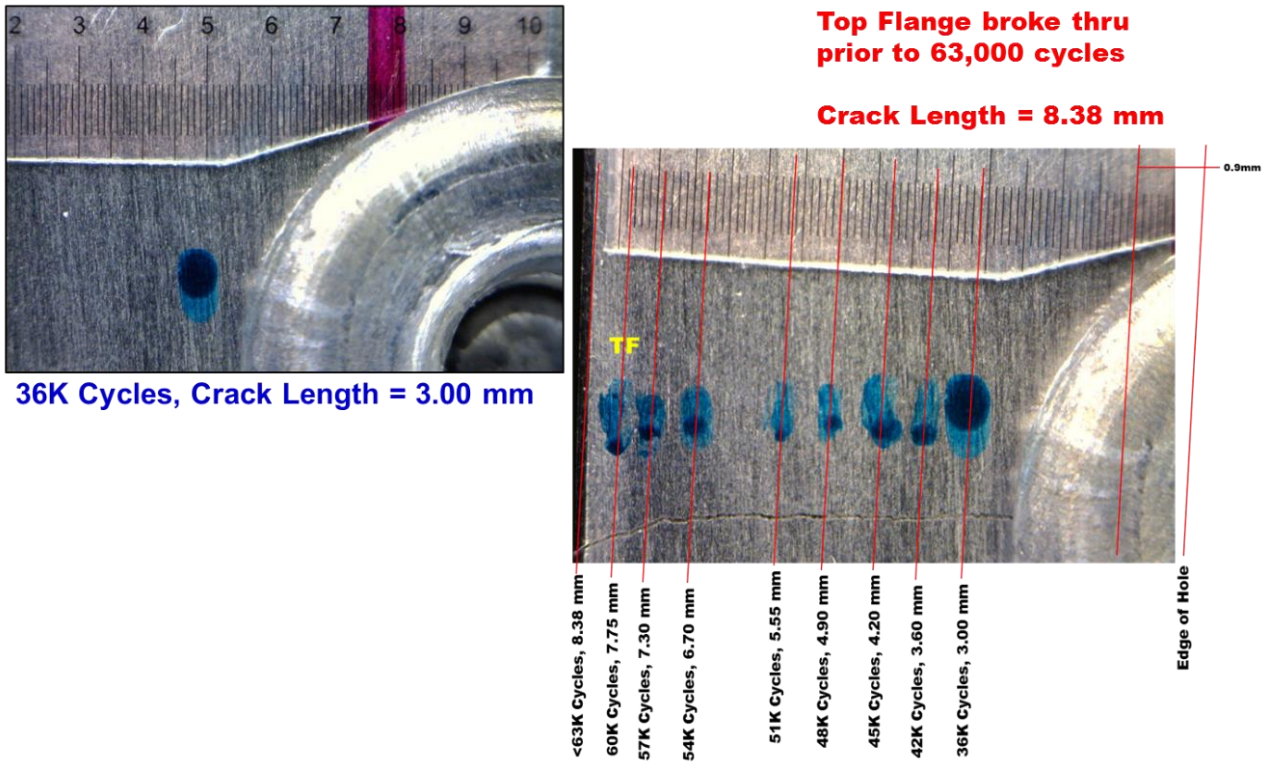

Figure 6-81. Crack Length Measurement in Holes with Blind Rivet Fasteners - RB-PZT-18F

RB-PZT-18F Cycles and Crack Length			
Cycles	EC Crack Length (mm)		
	SS1 (BF)	SS2 (W)	SS3 (TF)
0	0.00	0.00	0.00
5,000	0.00	0.00	0.00
Baseline taken after 5,000 Cycles			
15,000	n/a	n/a	n/a
24,000	n/a	n/a	n/a
30,000	n/a	n/a	n/a
36,000	n/a	n/a	3.00
42,000	n/a	n/a	3.60
45,000	n/a	n/a	4.20
48,000	n/a	n/a	4.90
51,000	n/a	n/a	5.55
54,000	n/a	n/a	6.70
57,000	n/a	n/a	7.30
60,000	n/a	n/a	7.75
63,000	n/a	3.40	8.38
66,000	3.10	4.30	8.38
69,000	4.00	4.95	8.38
72,000	4.90	5.55	8.38
75,000	5.40	6.05	8.38
78,000	5.90	6.70	8.38
81,000	6.20	7.15	8.38
<63,000	-	-	Thru Flange

= crack length at PZT detection

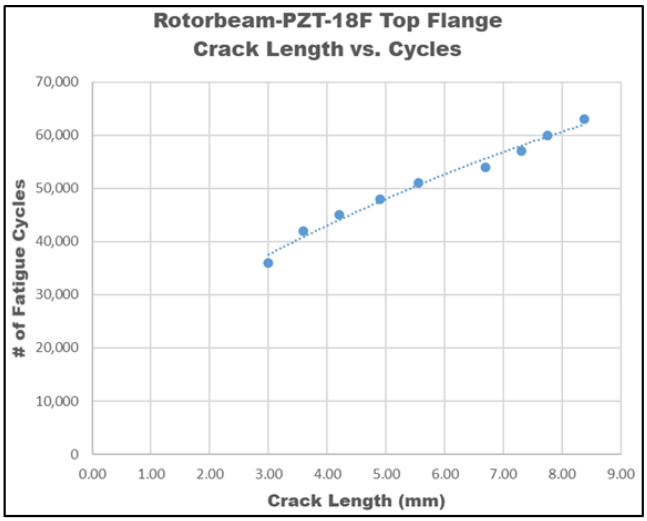

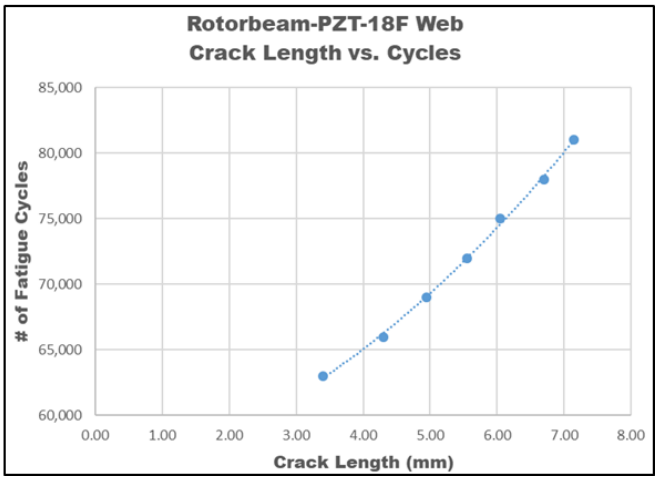

Figure 6-82. Crack Growth and Detection - PZT Network Performance in Web and Flange for Holes with Blind Rivet Fasteners

Figure 6-83 and Figure 6-84 show DI vs fatigue cycles (crack growth) for different paths in the riveted web and flange, respectively. A comparison of the average PZT crack detection for open (blue bar) and riveted (red bar) holes in both unloaded and loaded conditions is shown in Figure 6-85 while the specific crack detection lengths are listed in Table 6-40. These results indicate that the presence of rivets in the structure did not affect crack detection as there was no difference between the crack detection in riveted and open holes. While there may have been some difference in the rate of crack growth (*da/dN* curve), the "DI vs a" plots were still similar. Finally, Figure 6-86 plots the POD curves for PZT crack detection in the web and flange regions and compares the curves with and without rivets in the holes. The POD(90/95) levels were not affected by the presence of rivets as the POD values differed by less than 0.5%.

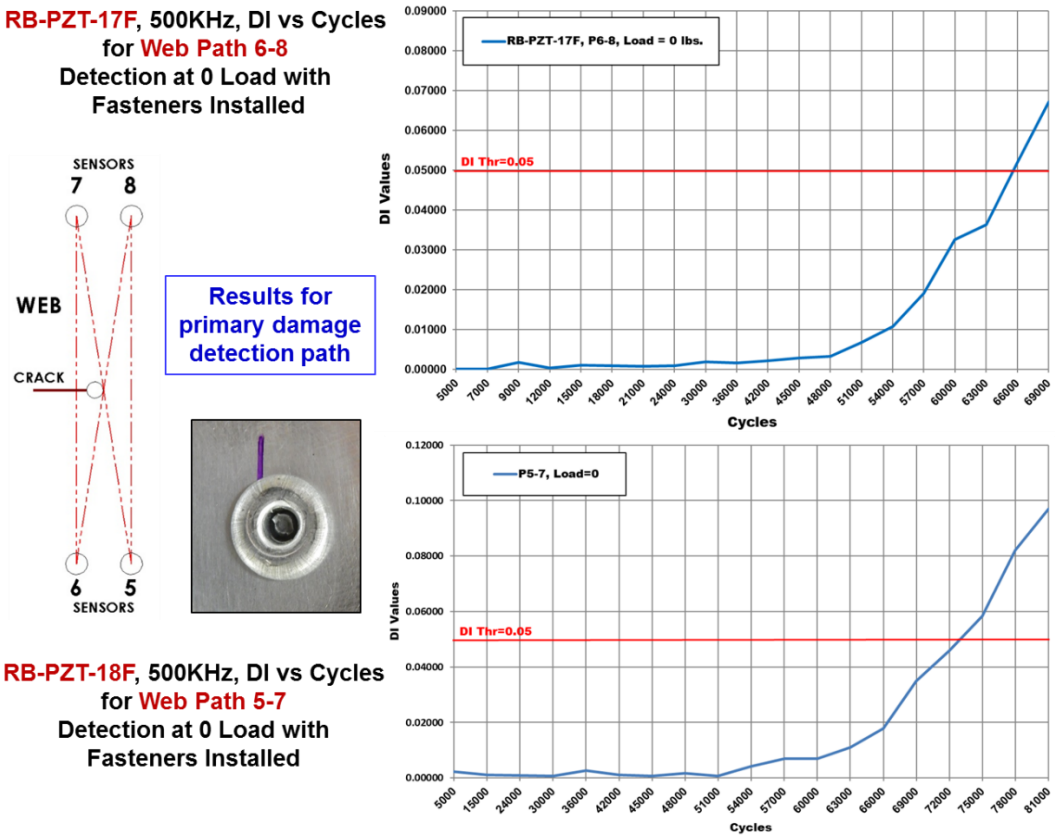

Figure 6-83. Effects of Rivets on PZT Crack Detection in Web - DI Levels

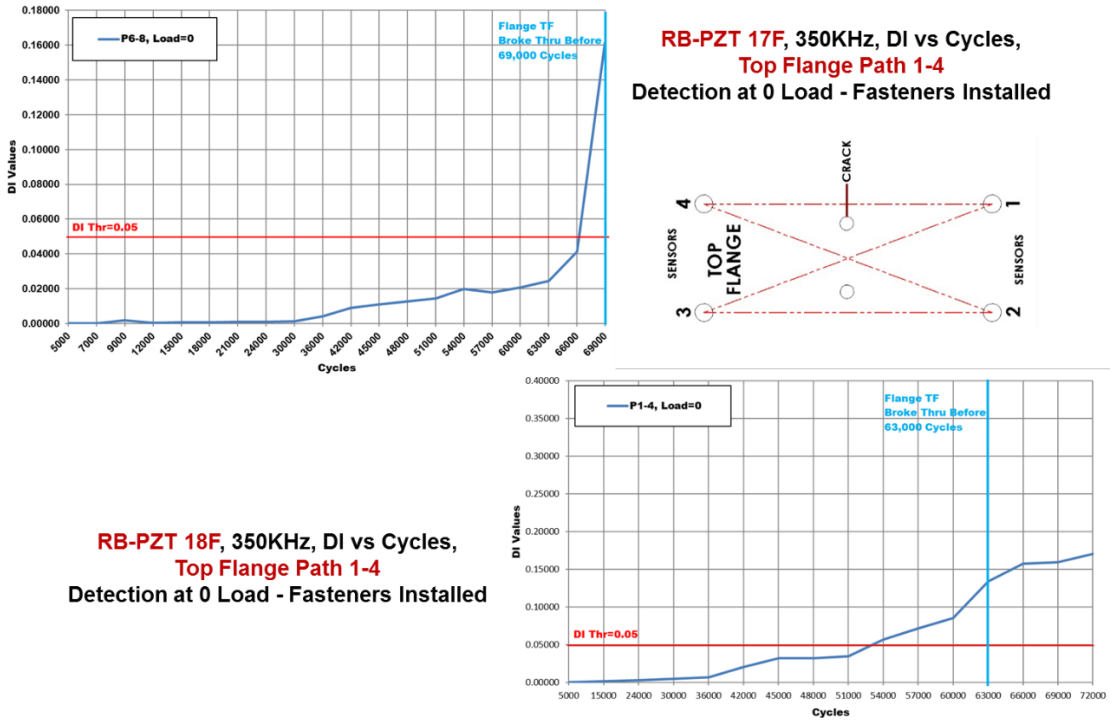

Figure 6-84. Effects of Rivets on PZT Crack Detection in Flange - DI Levels

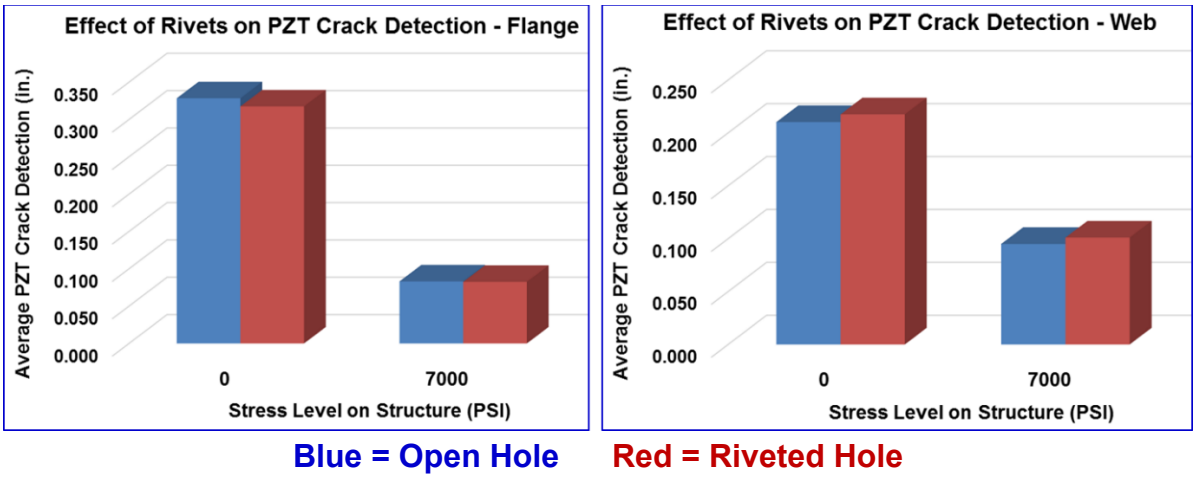

Figure 6-85. Comparison of Crack Detection for Riveted vs Open Holes in Web and Flange

Table 6-40. Comparison of PZT Crack Detection Performance from Riveted and Open Holes at Different Stress Level

PZT Crack Detection in Web at 0 Load	PZT Crack Detection in Flange at 0 Load
Average for Open Hole = 0.210”	Average for Open Hole = 0.327”
Avg Detection with Rivet = 0.218”	Avg Detection with Rivet = 0.318”
PZT Crack Detection in Web at 1,000 Load	**PZT Crack Detection in Flange at 1,000 Load**
Average for Open Hole = 0.165”	Average for Open Hole = 0.278”
Avg Detection with Rivet = 0.176”	Avg Detection with Rivet = 0.113”
PZT Crack Detection in Web at 7,000 Load	**PZT Crack Detection in Flange at 7,000 Load**
Average for Open Hole = 0.095”	Average for Open Hole = 0.083”
Avg Detection with Rivet = 0.101”	Avg Detection with Rivet = 0.083”

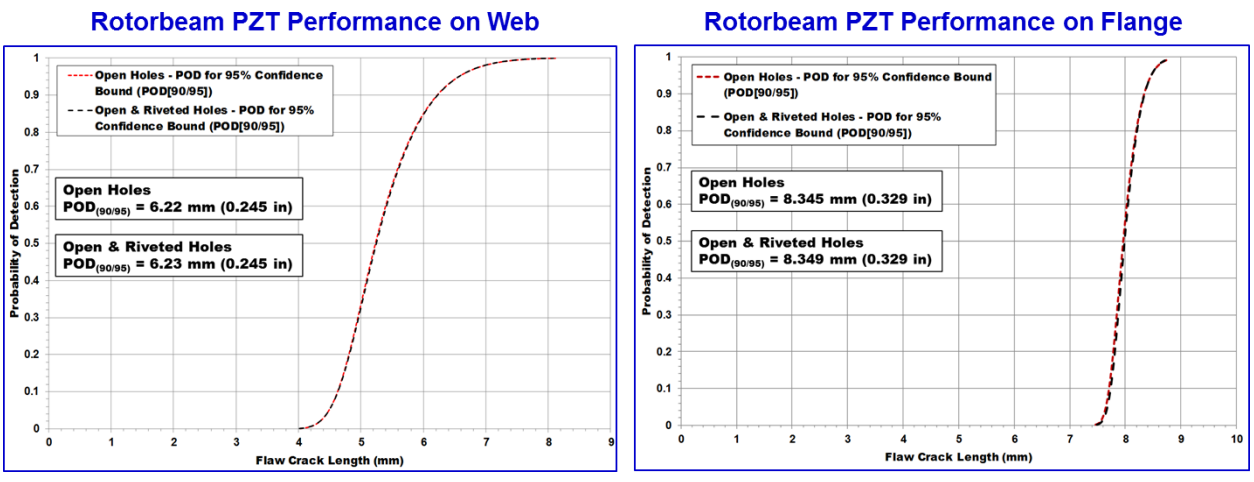

Figure 6-86. POD Curve Comparison for Open and Riveted Holes

6.2.4. *Comparison of Response from Flat Plates with Similar Flange Dimensions*

Crack growth, load shedding and the reapportion of stresses was discussed in Section 6.2.1 as these items can amplify the effects of monitoring the structure while it is under load. This is especially true in the case of the Rotorbeam flange region where a crack can propagate to the edge of the flange (through-crack). Load shedding in extreme non-symmetrical conditions (e.g. through-crack on the upper flange and no cracks on the lower flange can translate tension loads into torsional loads further changing the PZT response levels. Such torsional loads and stress reapportions cause the DI levels to fluctuate during early stages of crack growth; thus, DI(threshold) for crack detection was placed at a level above the observed up-down fluctuations in DI.

To compare results from the complex boundary conditions and load paths in the Rotorbeam with a very simplified structure, PZT fatigue tests were conducted on a "Flat Plate Flange" specimen. The Flat Plate Flange specimen possessed the same dimensions as the flange region on the Rotorbeam (same width and thickness). However, the simple, flat plate, shown in Figure 6-87 and Figure 6-88, does not experience the torsional/bending loads that are produced when crack propagation is non-symmetrical and stresses are redistributed accordingly (i.e. on upper flange but not on lower flange). The Flat Plate Flange specimen was exposed to the same stress levels used in the Rotorbeam fatigue tests:

Stress Level = 14 KSI

Load = Stress * X-Section Area
= 14,000 *0.21 = 2,940 lbs.

MTS Fatigue Settings:

Target Set Point = (2,940 – (2,940*0.1))/2 + (2,940*0.1) = 1,617 lbs.

Amplitude = (2,940 – 1,617) = 1,323 lbs.

Tension-Tension Cycle = 2,940 to 294

Figure 6-89 shows the continuously increasing DI values for the most sensitive Path 1-4 in specimen RB-PZT-T1. Crack detection at a = 1.35 mm can be seen in the tabulated results and where the DI curve rises above the DI(threshold) = 0.05. Note that this data was acquired with the 350 KHz driving frequency. This will be compared with other driving frequencies later. Figure 6-90 is a related data display with the DI histogram and damage imaging indicating crack detection at 1.35 mm. As additional PZT paths exceed the DI(threshold), Figure 6-91 shows that the damage image becomes more pronounced in size and color. There is an increase in the number of red paths indicating damage as the fatigue cycles increase and the crack grows. The final, lower image shows that all four paths(1-4, 1-3, 2-4, 2-3) exceed the DI(threshold) at 19,600 cycles and are, thus, all plotted as red bars in the DI histogram. The full set of DI profiles for all paths on the Flat Plate Flange specimen are shown in Figure 6-92. All DI values are continuously-increasing. This graph is shown to demonstrate that the uniformity of the flat plate structure does not produce any fluctuations or reversals in the DI levels.

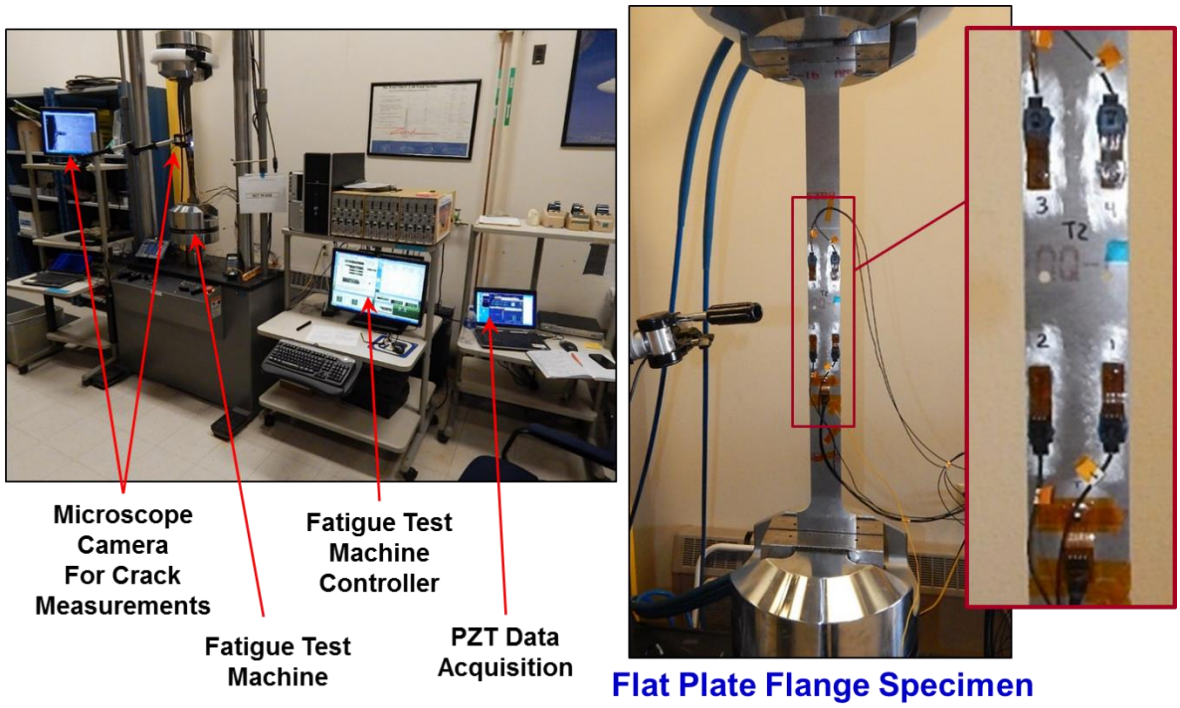

Figure 6-87. Comparison of PZT Crack Detection Response from Flat Plates with Similar Flange Dimensions

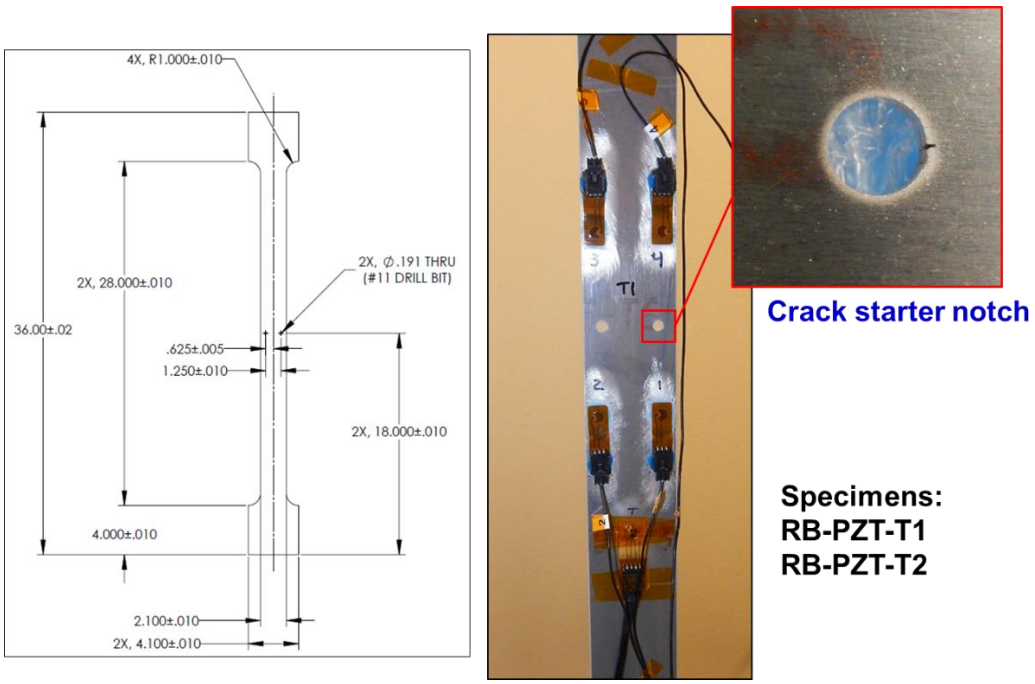

Figure 6-88. PZT Flat Flange Plate Test Specimen

RB-PZT-T1 (Flat Plate)		
Cycles	Crack Length (mm)	DI Value Path 1-4 350 KHz
0	0.00	0.00024
5000	0.00	0.03710
7000	0.00	0.03928
9000	0.50	0.04321
11000	1.35	0.05252
13000	2.40	0.05564
15000	3.25	0.06876
17000	4.20	0.10185
19000	6.30	0.10992
19610	7.55	0.15869

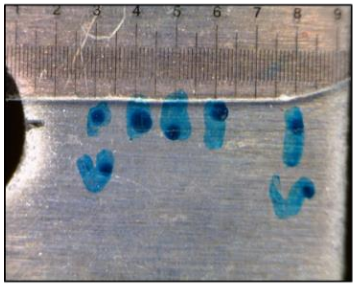

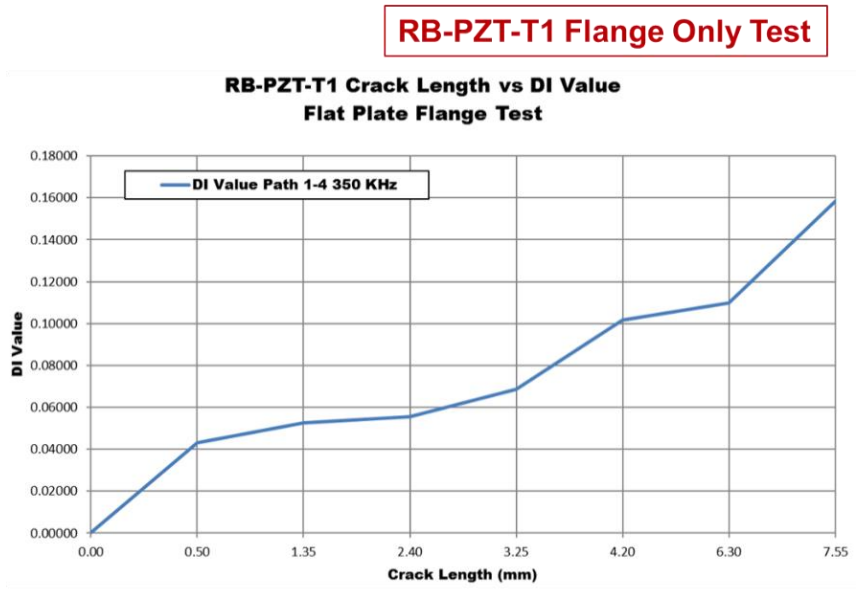

Crack growth determined from
EC inspection & micro-scale

Figure 6-89. Crack Growth and DI Values from PZT Flat Flange Plate – RB-PZT-T1

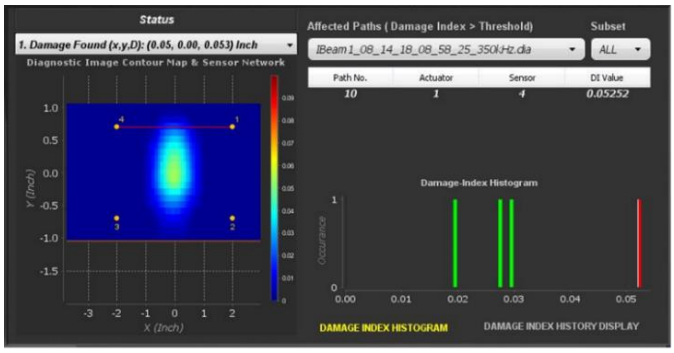

First Damage Detection
350 KHz, 11K Cycles, Path 1-4
DI = 0.0525 (DI Threshold = 0.05)
Crack Length = 1.35 mm

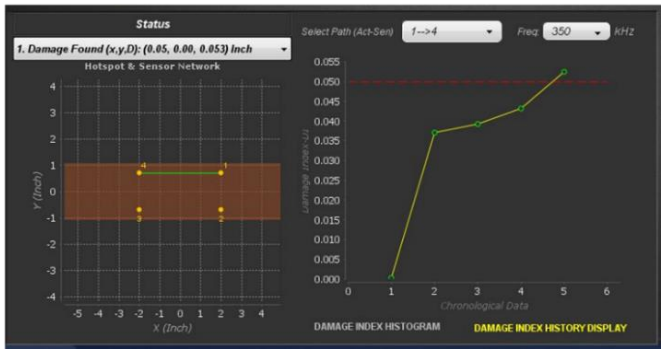

Figure 6-90. Initial Damage Detection – First Path Exceeding Threshold in Flat Flange RB-PZT-T1

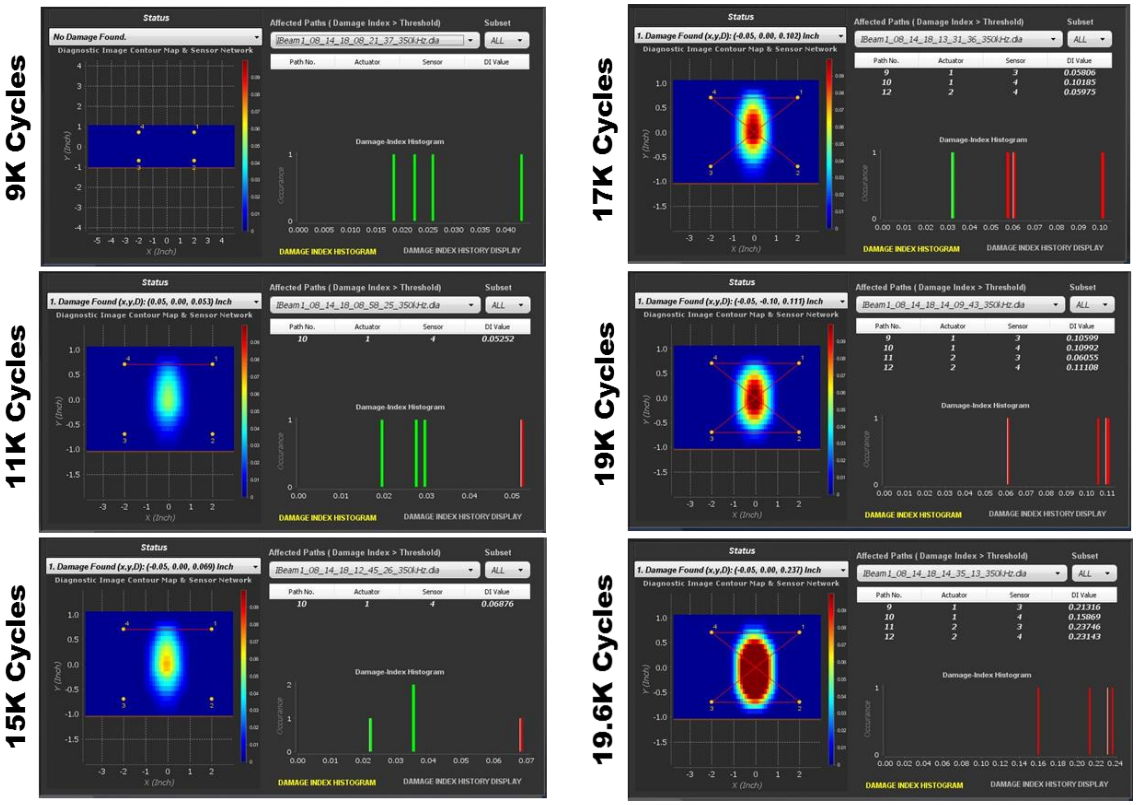

Figure 6-91. Damage Imaging in Flat Flange RB-PZT-T1 as Additional Paths Exceed Threshold

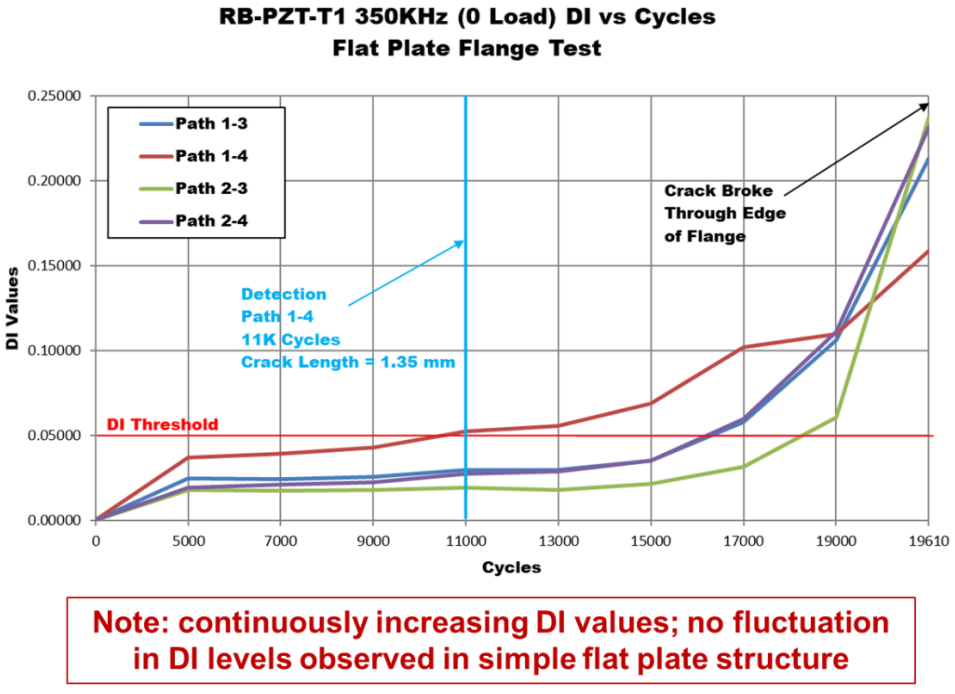

Note: continuously increasing DI values; no fluctuation in DI levels observed in simple flat plate structure

Figure 6-92. DI Profiles from PZT Flat Flange Plate – RB-PZT-T1

Figure 6-93 shows DI profiles for all paths along with the DI histogram for data acquired using 300 KHz as the driving frequency in specimen RB-PZT-T1. This data highlights that 300 KHz is not the optimum frequency for detecting crack growth in the Flat Plate Flange specimen because the crack is not detected until it reaches 6.3 mm in length. Figure 6-94 shows the continuously increasing DI values for the most sensitive Path 1-4 in specimen RB-PZT-T2. Crack detection at a = 4.65 mm can be seen in the tabulated results and where the DI curve rises above the DI(threshold) = 0.05. Note that this data was acquired with the optimum 350 KHz driving frequency. Figure 6-95 and Figure 6-96 show related data displays with the DI histogram and damage imaging indicating crack detection at 4.65 mm. As additional PZT paths exceed the DI(threshold), it shows that the damage image becomes more pronounced in size and color. There is an increase in the number of red paths indicating damage as the fatigue cycles increase and the crack grows. The final, lower image shows that all four paths(1-4, 1-3, 2-4, 2-3) exceed the DI(threshold) at 16,500 cycles and are, thus, all plotted as red bars in the DI histogram. The full set of DI profiles for all paths on the Flat Plate Flange specimen are shown in Figure 6-97. All DI values are continuously-increasing. This graph is shown to demonstrate that the uniformity of the flat plate structure does not produce any fluctuations or reversals in the DI levels up through crack detection. Figure 6-98 shows DI profiles for all paths along with the DI histogram for data acquired using 250 KHz as the driving frequency in specimen RB-PZT-T2. This data highlights that 250 KHz is less sensitive to crack onset which delays crack detection until it reaches 6.65 mm in length.

Summary discussion comparing PZT damage detection results from complex geometry of rotorbeam structures with simple geometry of flat plate flange structures:

- Flat Plate Flange Specimen – eliminates torsional/bending loads that are produced when crack propagation is non-symmetrical and stresses are redistributed accordingly (i.e. on upper flange but not on lower flange)
- Same fatigue stress levels in both I-Beam and Simple Flange (plate) tests
- Average PZT Crack Detection:
  - Flange Region in I-Beam = 8.33 mm (average crack length at detection)
  - Flange Region in Flat Plate = 3 mm (average crack length at detection)
- Elimination of distortion (including compressive strains) during non-symmetrical crack growth in I-Beam improves crack detection in simple plate (same dimensions as flange) by 64%
- Clearly demonstrates the effects of complex strain fields in complex structures and potential for reapportion of stresses/deformations during damage growth.
- Indicates that the damage detection performance of SHM systems is influenced by the structural geometry, damage growth scenarios and resulting stress distribution in the structure. Thus, validation testing must properly account for all of these features.

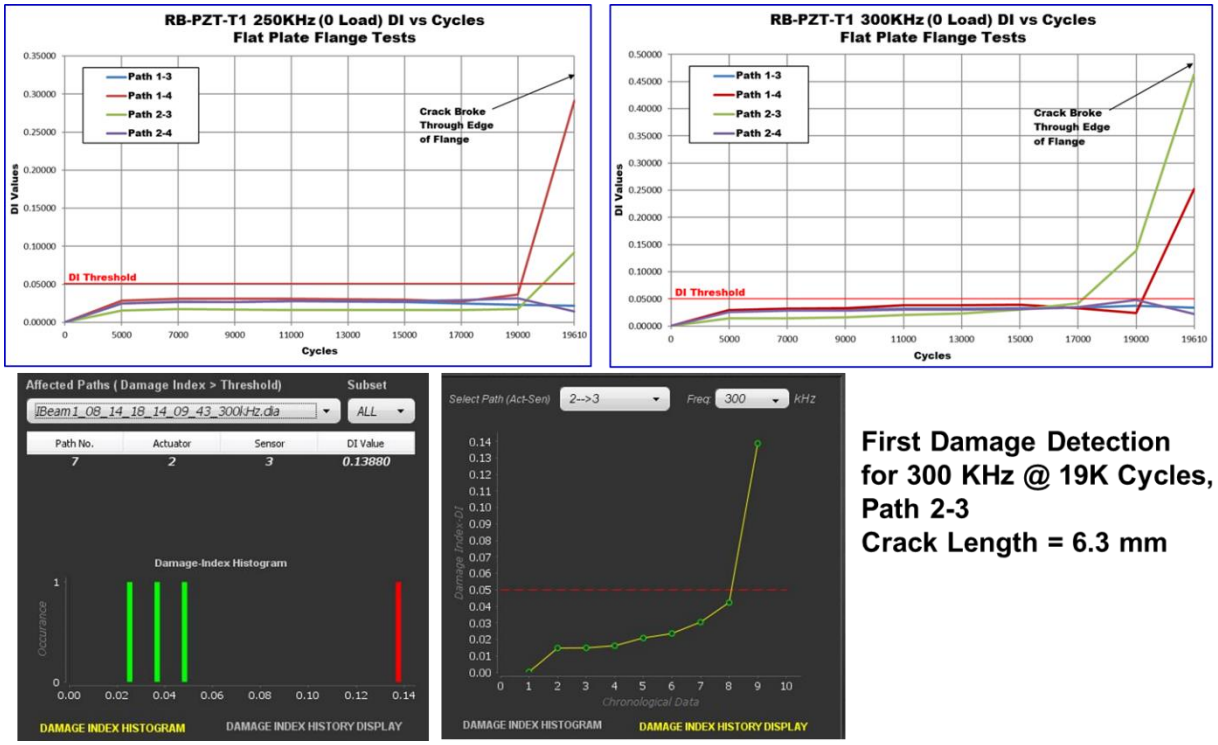

Figure 6-93. Damage Detection is Less Sensitive at Other Frequencies - RB-PZT-T1

RB-PZT-T2 (Flat Plate)		
Cycles	Crack Length (mm)	DI Value Path 1-4 350 KHz
0	0.00	0.00015
5000	0.00	0.01921
7000	1.05	0.02285
9000	2.05	0.02510
11000	2.65	0.03367
13000	3.50	0.04734
15000	4.65	0.06160
16500	6.65	0.04927
16600	7.50	0.14126

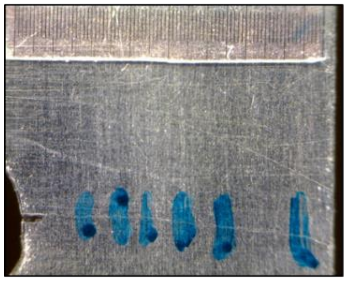

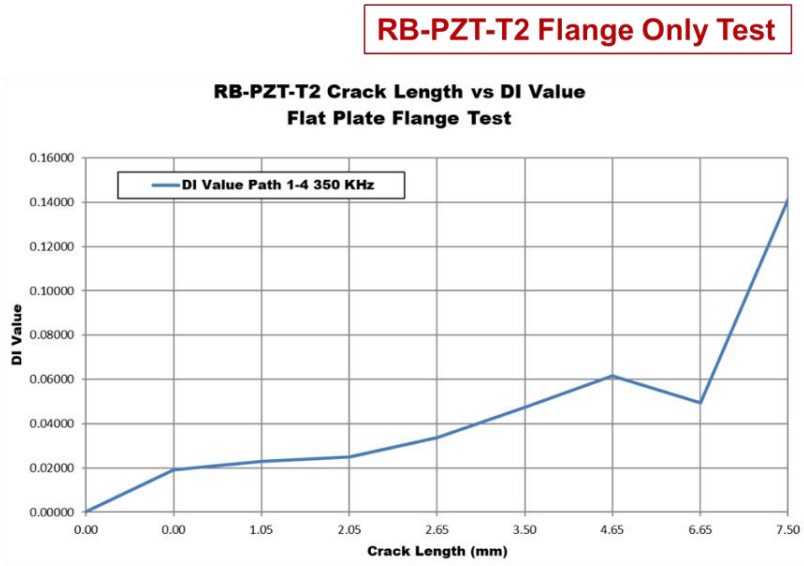

Crack growth determined from EC inspection & micro-scale

Figure 6-94. Crack Growth and DI Values from PZT Flat Flange Plate – RB-PZT-T2

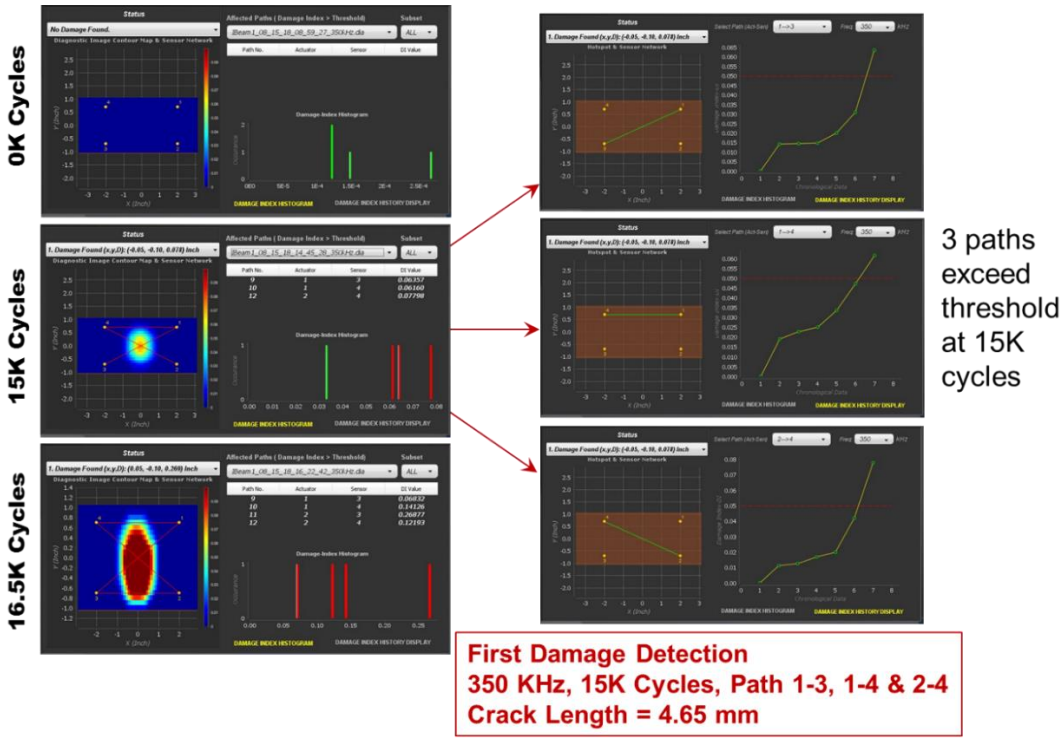

Figure 6-95. Initial Damage Detection – First Path Exceeding Threshold in Flat Flange RB-PZT-T2

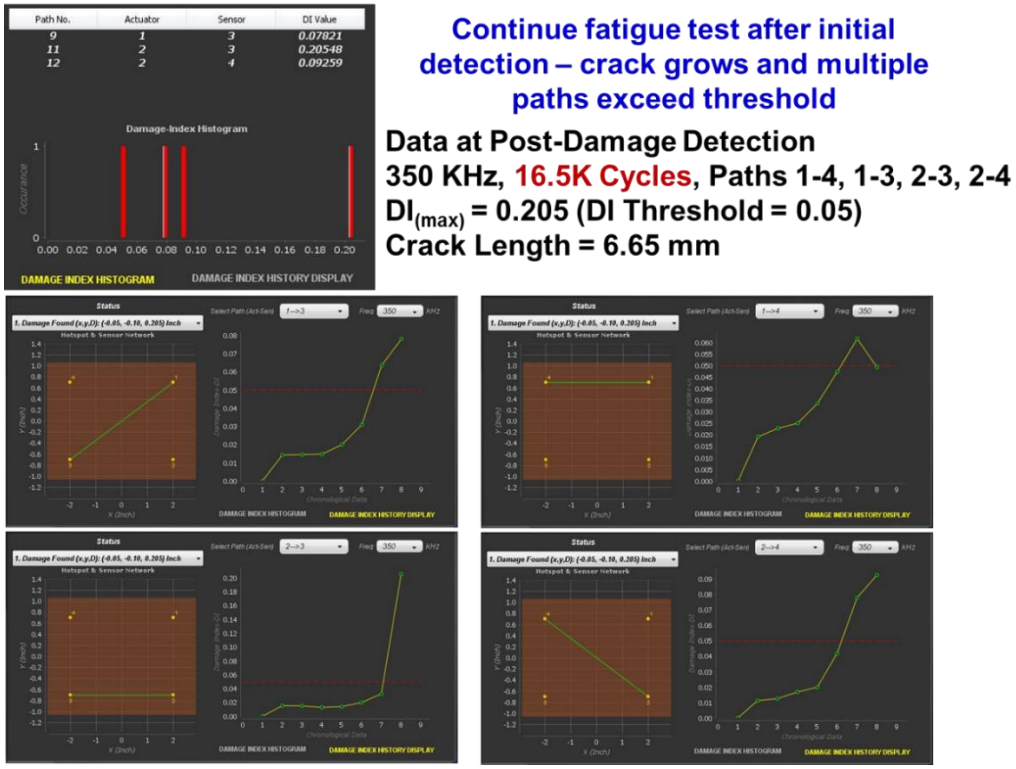

Figure 6-96. Damage Imaging in Flat Flange RB-PZT-T2 as Additional Paths Exceed Threshold

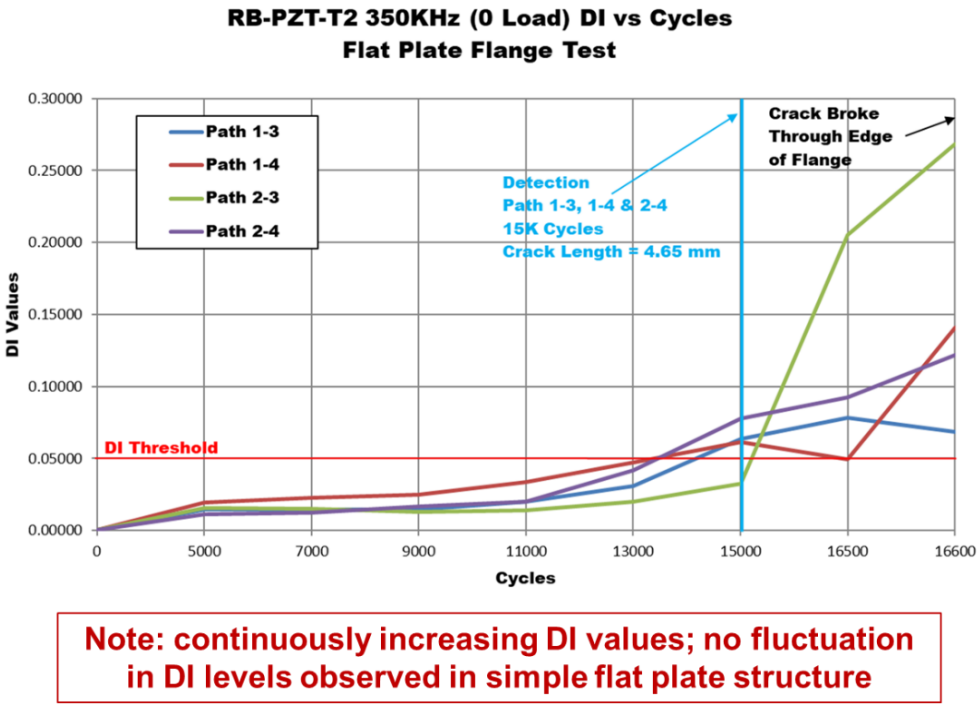

Figure 6-97. DI Profiles from PZT Flat Flange Plate – RB-PZT-T2

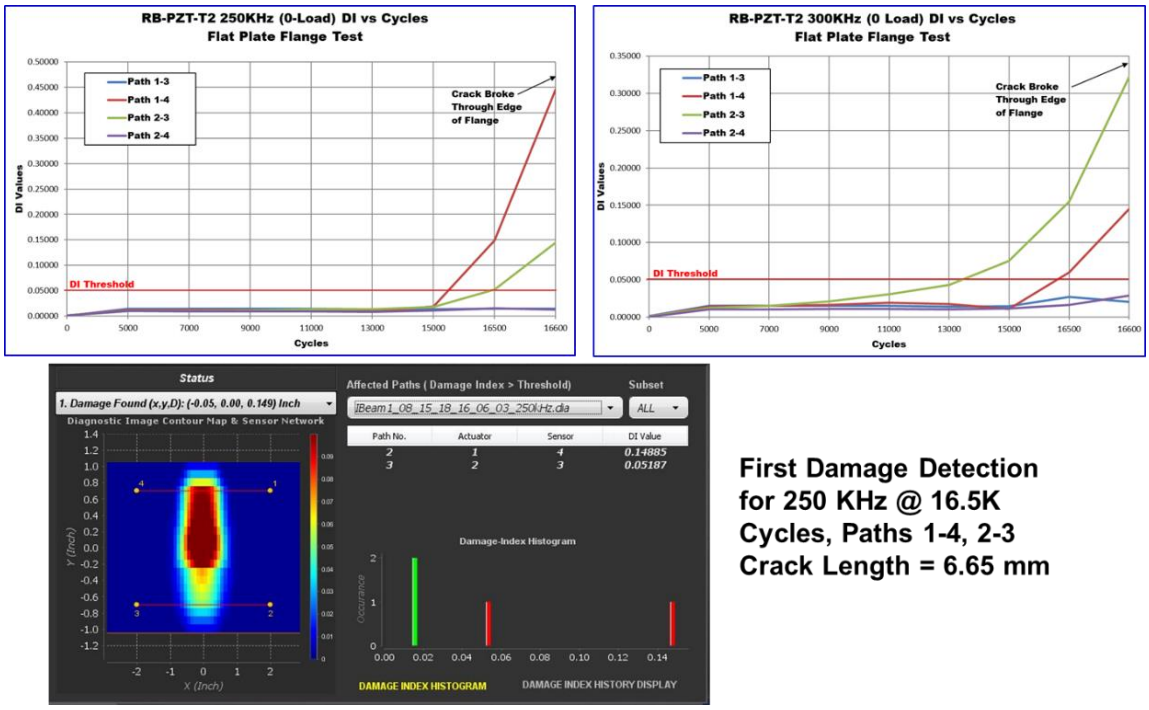

Figure 6-98. Damage Detection is Less Sensitive at Other Frequencies - RB-PZT-T2

As discussed above, the PZT data acquisition software uses baseline response data at different temperatures and includes embedded subroutines to minimize the effects of temperature change on the overall PZT performance. The Flat Plate Flange specimens were used to further study the effect of temperature change on PZT performance. Figure 6-99 and Figure 6-100 show some slight changes in damage detection performance that were observed during temperature conditioning of these specimens. After crack growth and initial damage detection at room temperature in the flat plate (flange only) tests, specimen RB-PZT-T2 was subjected to -18°F and then allowed to return to room temperature. Figure 6-99 and Figure 6-100 show the effects observed when the flat flange plate specimens were subjected to cold temperatures. The post-freeze data shows slight changes to DI levels after cold exposure:

- DI changes at 350 KHz = 13.8%, 12.6%, 15.6%
- Average DI change = 10%
- Indicates that adjustment in the damage detection threshold may be warranted to accommodate for DI level drop after temperature cycling.
- Variation in DI levels are probably dependent on structure geometry.

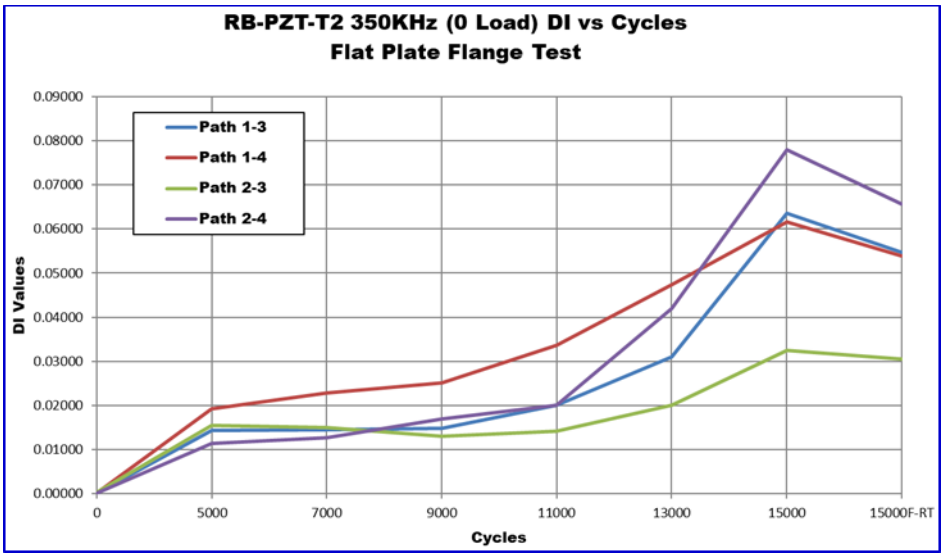

Figure 6-99. Use of Flat Plate Specimens to Assess PZT Response After Exposure to Freezing Temperature Exposure – Considerations for Damage Detection Threshold

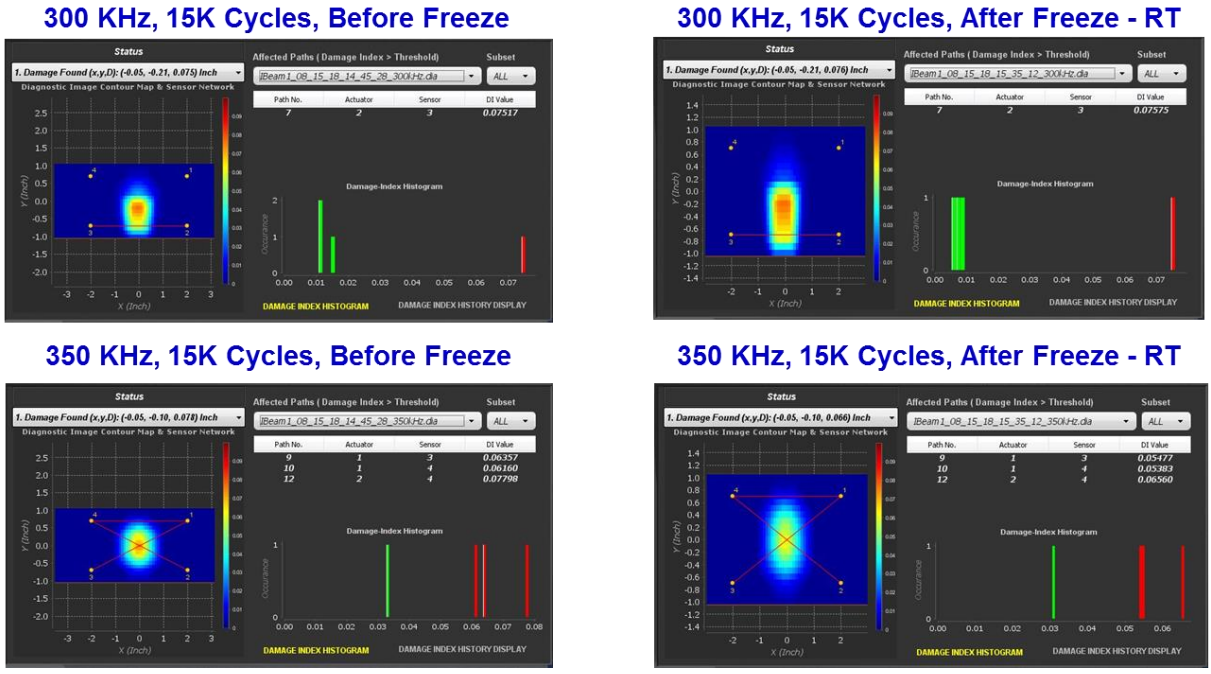

Figure 6-100. Effect of Temperature on PZT Paths Exceeding Damage Threshold

6.3. Comparison of Pitch-Catch with Pulse-Echo PZT Data Analysis Methods

Thus far, all results presented in this report have come from data acquired using a Pitch-Catch (PC) mode of sensor operation. The Pitch-Catch mode is where one PZT sensor acts as the wave transmitter and a different PZT sensor acts as the receiver of the wave. This sets up the various sensor-to-sensor paths referenced above. Interpretation of the subsequent signal changes in the path between the two sensors is used to detect damage or other changes within the structure. Another data acquisition mode can be used to interrogate the structure with the PZT sensor network. This other mode is called the Pulse-Echo (PE) mode as it uses a single PZT sensor to act as both the transmitter and receiver of the wave. The PE mode uses changes in the set reflected signals coming back to the PZT sensor to detect damage or other changes within the structure.

This is very analogous to traditional ultrasonic inspections which utilizes high-frequency sound waves as a means of detecting anomalies in parts. In Pulse-Echo Ultrasonic (PE-UT) inspections, shown in Figure 6-101 short bursts of high frequency sound waves are introduced into materials for the detection of surface and subsurface flaws in the material. The sound waves travel through the material with some attendant loss of energy (attenuation) and are reflected at interfaces. The reflected beam is displayed and then analyzed to define the presence and location of flaws. Sound is transmitted into the test item by means of a transducer. The reflected waves are then received by a transducer, often the same transducer for pulse-echo ultrasonics, and converted back into electrical signals for display. Ultrasonic testing involves one or more of the following measurements: time of wave transit (or delay), path length, frequency, phase angle, amplitude, impedance, and angle of wave deflection (reflection and refraction). The interaction of the

ultrasonic waves with defects and the resulting time vs. amplitude signal produced on the computer screen depends on the wave mode, its frequency and the material properties of the structure. Flaw size can be estimated by comparing the amplitude of a discontinuity signal with that of a signal from a discontinuity of known size and shape. Flaw location (depth) is determined from the position of the flaw echo along a calibrated time base. In the pitch-catch UT method, one transducer introduces a pressure wave into the specimen and a second transducer detects the transmitted wave. A complex wave front is generated internally in the material as a result of velocity characteristics, acoustical impedance, and thickness. The time and amount of energy is affected by the changes in material properties, such as thickness, disbonds, and discontinuities. Complete reflection, partial reflection, scattering, or other detectable effects on the ultrasonic waves can be used as the basis of flaw detection. Data analyses for PZT uses similar physics, along with comparisons between baseline (pristine structure) signals and signals acquired at a later time to detect damage.

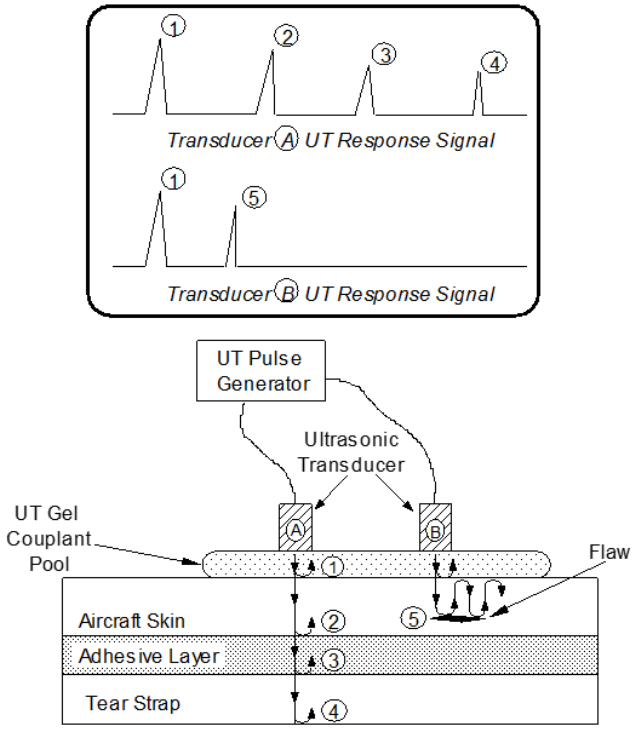

Figure 6-101. Schematic of Pulse-Echo Ultrasonic Inspection and A-Scan Signal Showing Reflection of UT Waves at Assorted Interfaces

In most pulse-echo systems, a single transducer acts alternately as the sending and receiving transducer. Figure 6-101 shows the interaction of UT waves with various interfaces within a structure and the corresponding A-scan waveforms that are displayed on an ultrasonic inspection instrument. Sometimes it is advantageous to use separate sending and receiving transducers for UT inspections. The term pitch-catch is often used in connection with separate sending and receiving transducers. Both PE and PC modes of structural interrogation with PZT sensors are shown in Figure 6-102. The PZT data form and a schematic showing DI estimation in PE Mode is depicted in Figure 6-103.

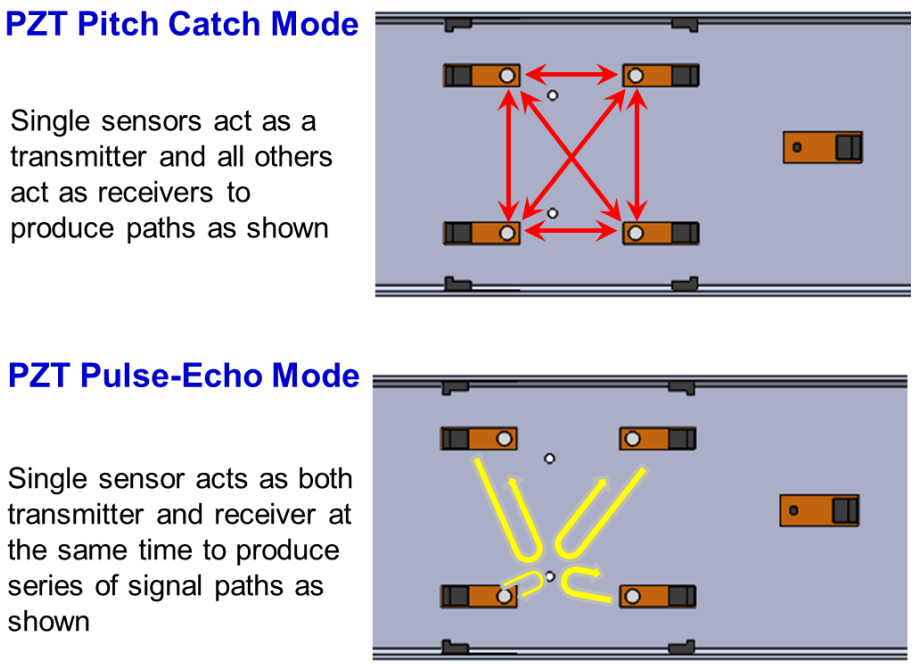

Figure 6-102. Different PZT Interrogation Modes for Damage Detection

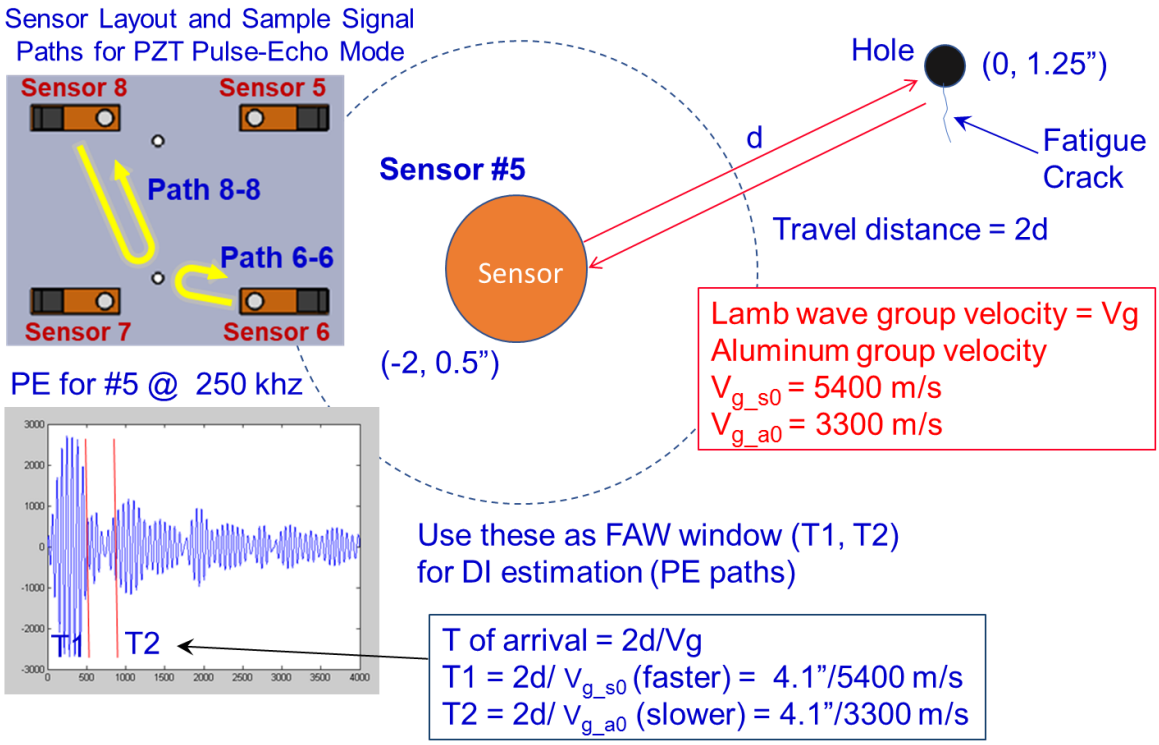

Figure 6-103. Data Form and Schematic Showing DI Estimation in Pulse-Echo Mode

The tests to evaluate PE mode were conducted on the web and flange portion of the Rotorbeam specimens RB-PZT-11 through RB-PZT-14. Sensor placement on the flanges remained the same as those used in the PC mode described above. For the web region, sensors were placed non-symmetrically around the center holes in the web to better evaluate PE mode and compare different PZT responses on either side of the hole. PE mode was assessed using the two different sensor layouts shown in Figure 6-104. Configuration "E" was called a Distributed Sensor Arrangement (specimens RB-PZT-11 & RB-PZT-12) and Configuration "F" was called a Clustered Sensor Arrangement (specimens RB-PZT-13 & RB-PZT-14). In the example of the linear "Clustered Sensor" arrangement ("Configuration F"), the crack growth toward sensor 5, 6 or 3, 4 can be captured by PE sensor data. However, if the crack grows straight down toward sensor 2 then neither of 5, 6 or 3, 4 could show much sensitivity. In that case, we do need the sensors in positions 1 and 2. A summary of the evaluation of PZT crack detection using the PE mode of interrogation is as follows:

- For analogous ultrasonic inspections, we associate PE mode with ONE single sensor. Each sensor in the network is used to independently to acquire data.
- Pulse Echo mode is truly signal out and back from the same sensor (e.g. Paths 3-3, 4-4, 7-7). When PE data is collected at sensor 6, for example, then sensor 6 is actuated and the reflected (returned) signal is received (acquired) at 6 but no data is collected at other web sensors 5, 7, 8 at that time. This process is repeated for PE acquisition for sensors 5, 7, 8.
- Damage detection is determined from information from each single sensor path alone to arrive at the final DI and damage determination (each DI is calculated from the single path back and forth to the same PZT sensor).
- Results are plotted as DI vs. fatigue cycle for each of the individual sensors.
- The reason for different sensor layouts was to study the best angle from crack to sensor that will change the response path and, thus, increase the Damage Index level.
- Sensor placement relative to the crack influences the resulting damage detection. Thus, the Distributed Sensor Arrangement could have different results from the Clustered Sensor Arrangement

Figure 6-105 shows the Configuration E PZT network set-up on the ScanGenie software for detecting cracks in RB-PZT-11 and RB-PZT-12 specimens using PE interrogation mode. All of the PE results are for Rotorbeam specimens in an unloaded state. Crack length measurements and associated fatigue cycle information for specimen RB-PZT-11 are shown in Figure 6-106 (web), Figure 6-107 (top flange), and Figure 6-108 (bottom flange). The *da/dN* crack growth curves and associated DI values for PE data are shown in Figure 6-109. The summary of PE results for all paths is shown in Figure 6-110. The earliest crack detection in the web occurred in Path 8-8 at a = 0.185" (4.7 mm). The associated DI vs crack growth curves are shown in Figure 6-111 where the DI exceeds the DI(threshold) = 0.05 when the crack length is 0.185". The PE results for all flange paths are provided in Figure 6-112. This reveals crack detection on both flanges at the same crack length. Crack detection occurred on the top flange of specimen RB-PZT-11 at 37,633 cycles when the crack length was 0.33" (8.38 mm). Crack detection occurred on the bottom flange of specimen RB-PZT-11 at 48,359 cycles when the crack length was also 0.33" (8.38 mm).

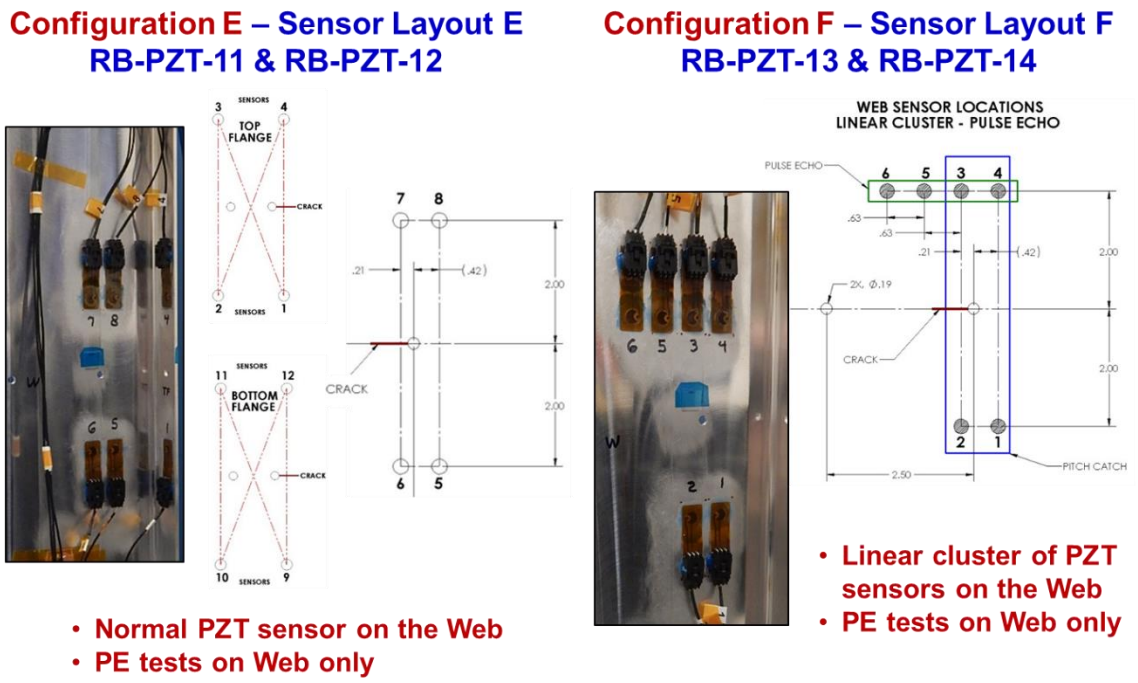

Figure 6-104. Two Different Sensor Layouts Used for PZT Performance Assessment on Rotorcraft I-Beam in Pulse-Echo Mode

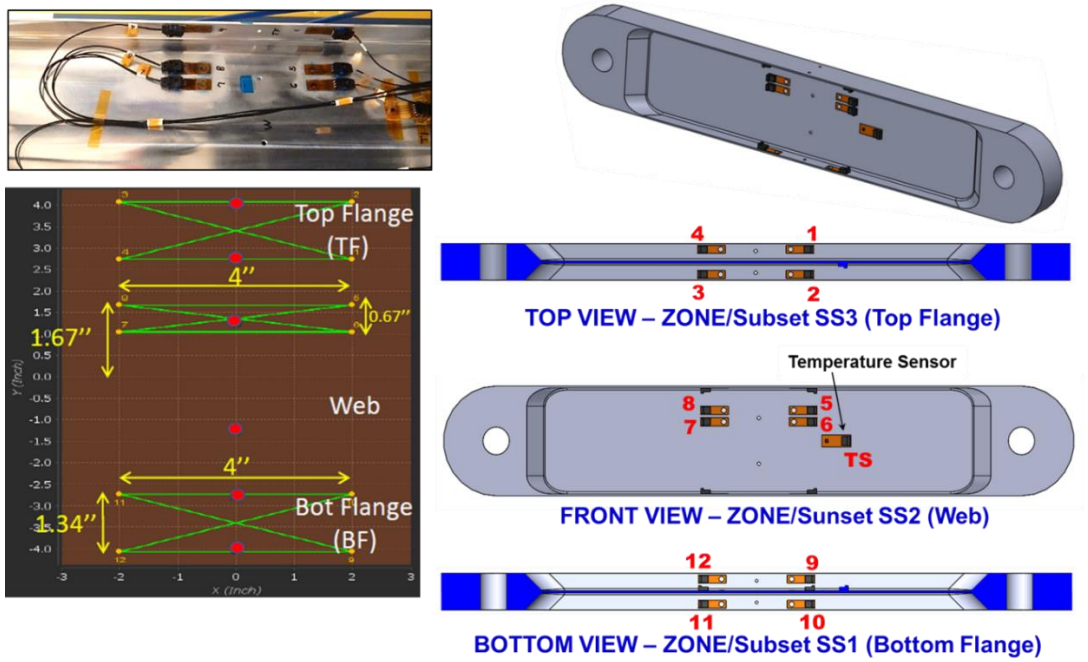

Figure 6-105. Set-up for Sensor Configuration E in Acellent Data Acquisition System for Pulse-Echo Data Analysis Approach in RB-PZT-11, -12

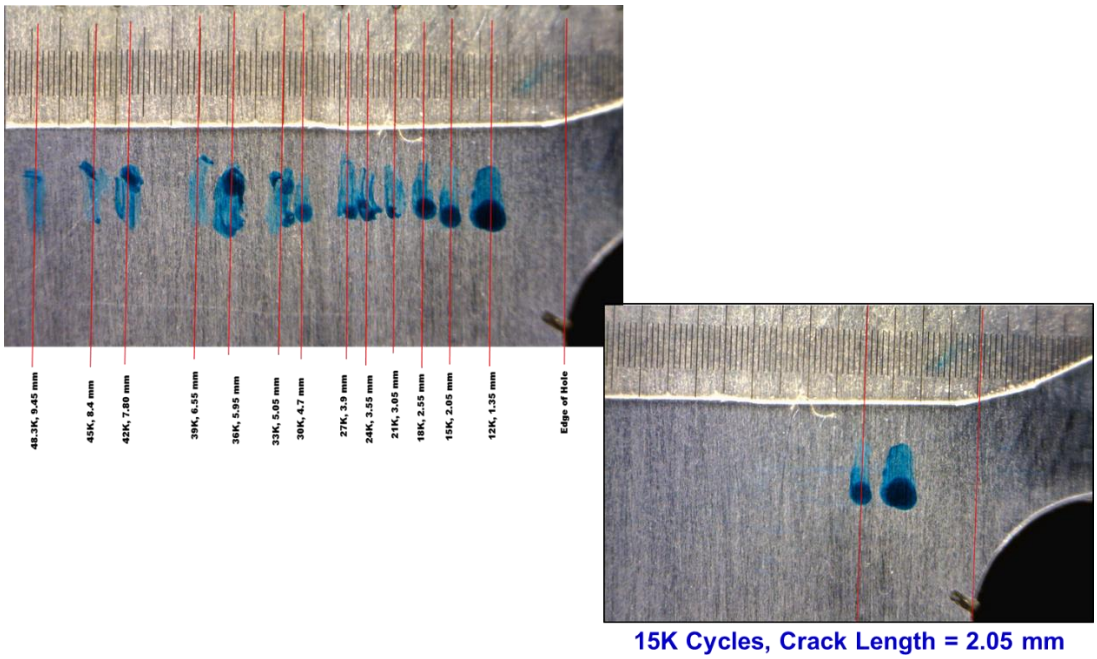

Figure 6-106. Web Crack Length Measurements for PZT Pulse-Echo Results –RB-PZT-11

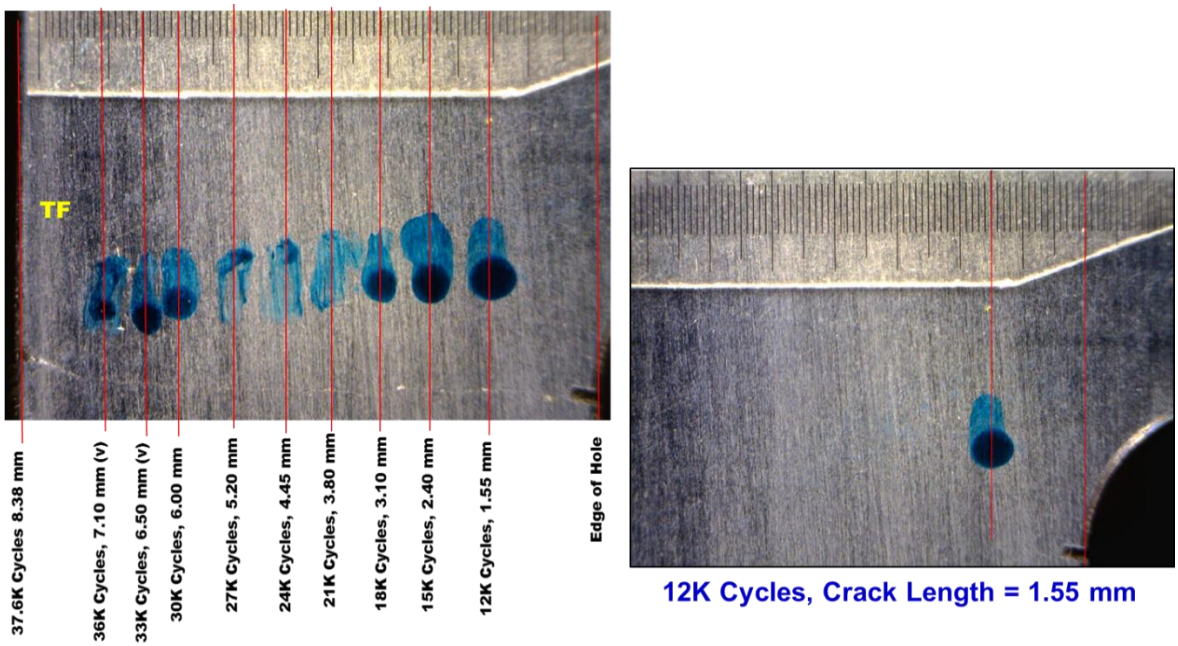

Figure 6-107. Top Flange Crack Length Measurements for PZT Pulse-Echo Results –RB-PZT-11

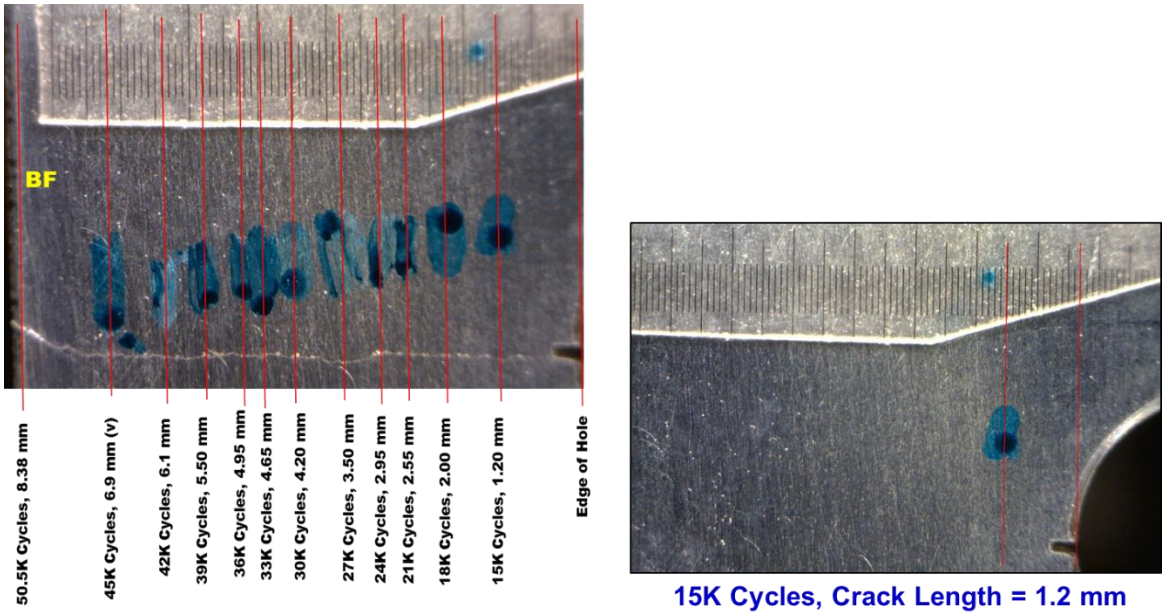

Figure 6-108. Bottom Flange Crack Length Measurements for PZT Pulse-Echo Results –RB-PZT-11

RB-PZT-11 Cycles and Crack Length			
Cycles	EC Crack Length (mm)		
	SS1 (BF)	SS2 (W)	SS3 (TF)
0	0	0	0
5,000	0.1	0.15	0.2
7,000	0.2	0.4	0.5
9,000	0.4	0.75	0.9
12,000	0.7	1.35	1.55
15,000	1.2	2.05	2.4
18,000	2	2.55	3.1
21,000	2.55	3.05	3.8
24,000	2.95	3.55	4.45
27,000	3.5	3.9	5.2
30,000	4.2	4.7	6
33,000	4.65	5.05	6.5
36,000	4.95	5.95	7.1
39,000	5.5	6.55	8.38
42,000	6.1	7.8	8.38
45,000	6.9	8.4	8.38
48,359	8.38	9.45	8.38
37,633	-	-	Thru Flange
48,359	Thru Flange	-	-

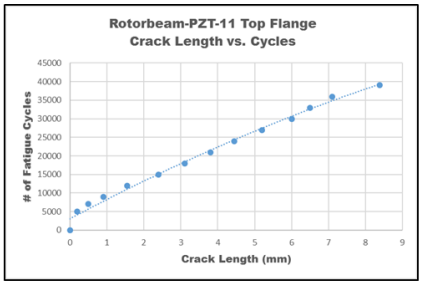

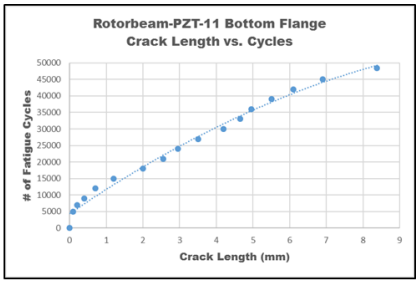

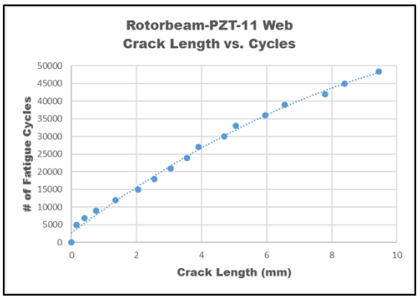

0 - Load: Damage Detection using Pitch-Catch Mode @ DI Threshold = 0.05 (Data for 300KHz = Flanges & 500KHz = Web)

Figure 6-109. PZT Damage Detection Using Pulse-Echo Mode –RB-PZT-11

Pulse-Echo Mode for Distributed Sensor Configuration E
Data for Threshold at Damage Index > 0.05

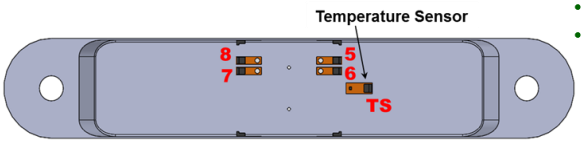

FRONT VIEW – ZONE/Sunset SS2 (Web)

- Earliest web crack detection at 0.185" length
- Crack propagation results in detection from path 8-8 first (250 KHz) and path 6-6 second (350 KHz)

= crack detection at frequency indicated

X = DI was less than 0.05 threshold for that PE path

	Freq	PE 5-5			PE 6-6			PE 7-7			PE 8-8		
		PE paths detected(DI>0.05)	DI	Cycle (k)	Crack Len (inch)	DI	Cycle (k)	Crack Len (inch)	DI	Cycle (k)	Crack Len (inch)	DI	Cycle (k)	Crack Len (inch)
Web area	250	5-5, 8-8	0.05119	39	0.258	x	x	x	x	x	x	0.16079	30	0.185
	300	5-5,6-6,7-7,8-8	0.05803	42	0.307	0.05545	42	0.307	0.05602	39	0.258	0.10711	30	0.185
	350	5-5,6-6,7-7,8-9	0.0592	42	0.307	0.05988	33	0.199	0.06558	42	0.307	0.06505	36	0.234
	500	No-data	x	x	x	x	x	x	x	x	x	x	x	x

Figure 6-110. PZT Pulse-Echo Results for Web of Specimen RB-PZT-11

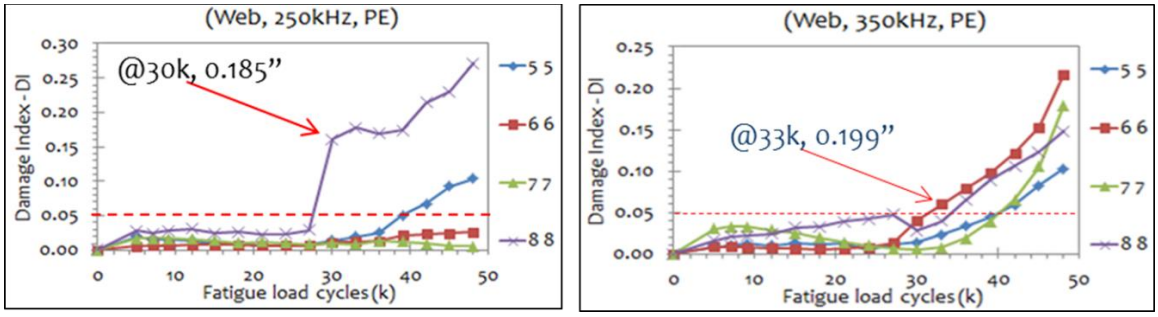

Figure 6-111. DI Progression for Pulse-Echo Interrogation of Web - RB-PZT-11

Pulse-Echo Mode for Distributed Sensor Configuration E
Data for Threshold at Damage Index > 0.05

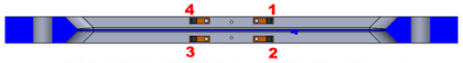

TOP VIEW – ZONE/Subset SS3 (Top Flange)

- All flange cracks detected at 0.33" length
- Crack propagation results in detection from paths 1-1/4-4 in top flange and 9-9/12-12 in bottom flange

	Freq	PE 1-1			PE 4-4		
		PE paths detected(DI>0.05)	DI	Cycle (k)	Crack Len (inch)	DI	Cycle (k)	Crack Len (inch)
Top flange	250	1-1, 4-4	0.12704	39	0.33	0.06928	39	0.33
	300	x	x	x	x	x	x	x
	350	1-1,	0.05779	48	0.33	x	x	x
	500	No-data	x	x	x	x	x	x

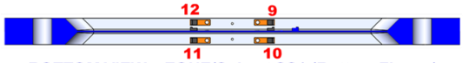

BOTTOM VIEW – ZONE/Subset SS1 (Bottom Flange)

= crack detection at frequency indicated

X = DI was less than 0.05 threshold for that PE path

	Freq	PE 9-9			PE 12-12		
		PE paths detected(DI>0.05)	DI	Cycle (k)	Crack Len (inch)	DI	Cycle (k)	Crack Len (inch)
Bot flange	250	9-9, 12-12	0.08427	48	0.33	0.19268	48	0.33
	300	9-9,	0.05123	48	0.33	x	x	x
	350	x	x	x	x	x	x	x
	500	No-data	x	x	x	x	x	x

Figure 6-112. PZT Pulse-Echo Results for Flanges of Specimen RB-PZT-11

Crack length measurements and associated fatigue cycle information for the web region of specimen RB-PZT-12 is shown in Figure 6-113 (web). The *da/dN* crack growth curves and associated DI values for PE data are shown in Figure 6-114. The summary of PE results for all paths is shown in Figure 6-115. The earliest crack detection in the web occurred in Path 8-8 at *a* = 0.047" (1.2 mm). The associated DI vs crack growth curves are shown in Figure 6-116 where the DI exceeds the DI(threshold) = 0.05 when the crack length is 0.047". The PE results for all flange paths are provided in Figure 6-117. This reveals the earliest crack detection in the top flanges at when the crack length was 0.15" (3.81 mm). Crack detection occurred on the bottom flange of specimen RB-PZT-12 when the crack length was 0.33" (8.38 mm).

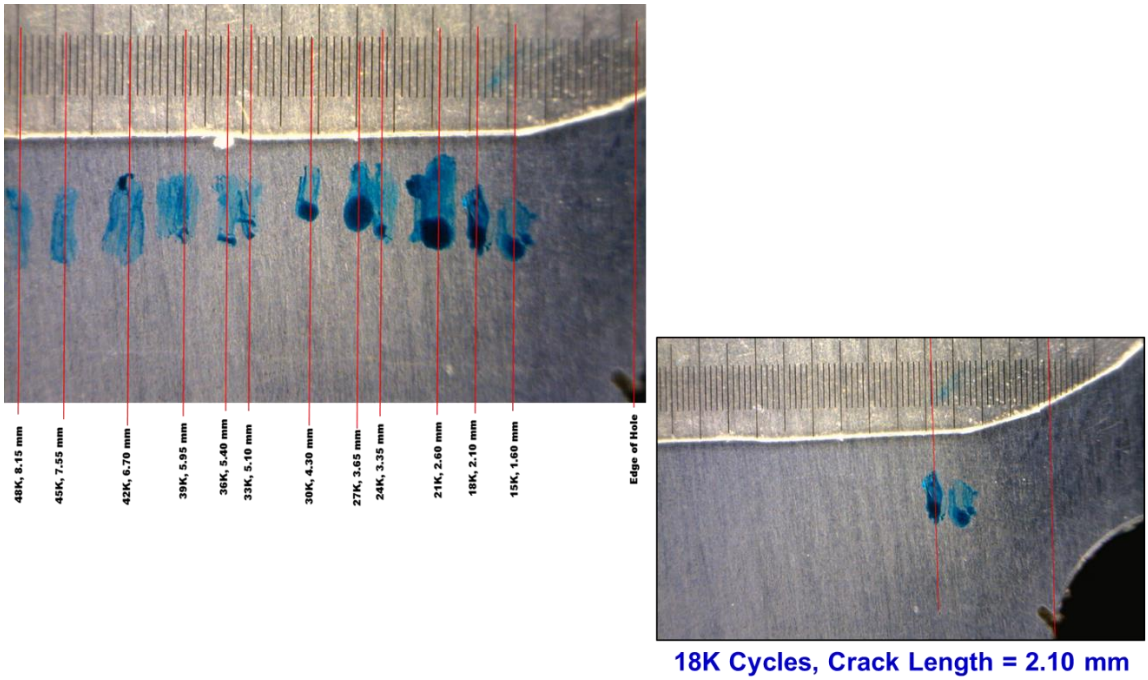

Figure 6-113. Web Crack Length Measurements for PZT Pulse-Echo Results –RB-PZT-12

RB-PZT-12 Cycles and Crack Length			
Cycles	EC Crack Length (mm)		
	SS1 (BF)	SS2 (W)	SS3 (TF)
0	0	0	0
5,000	0.4	0.2	0.3
7,000	0.7	0.4	0.6
9,000	1.2	0.7	1
12,000	1.9	1.2	1.6
15,000	2.8	1.6	2.25
18,000	3.4	2.1	2.95
21,000	4.05	2.6	3.4
24,000	4.8	3.35	3.8
27,000	5.5	3.65	4.15
30,000	6.4	4.3	4.8
33,000	7.35	5.1	5.4
36,000	8.38	5.4	5.85
39,000	8.38	5.95	7.25
42,000	8.38	6.7	8.38
45,000	8.38	7.55	8.38
48,000	8.38	8.15	8.38
34,978	Thru Flange	-	-
39,841	-	-	Thru Flange

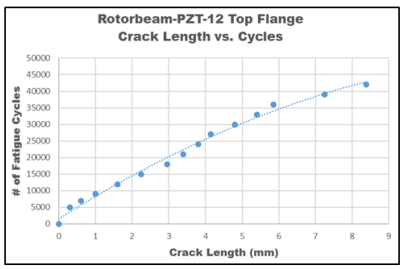

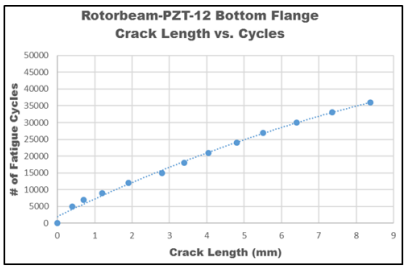

0 - Load: Damage Detection using Pitch-Catch Mode @ DI Threshold = 0.05 (Data for 300KHz = Flanges & 500KHz = Web)

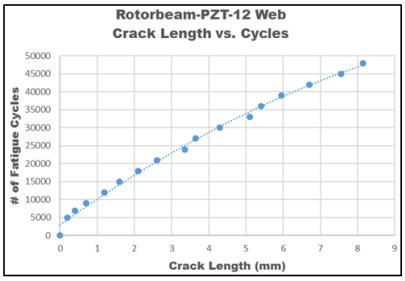

Figure 6-114. PZT Damage Detection Using Pulse-Echo Mode –RB-PZT-12

Pulse-Echo Mode for Distributed Sensor Configuration E
Data for Threshold at Damage Index > 0.05

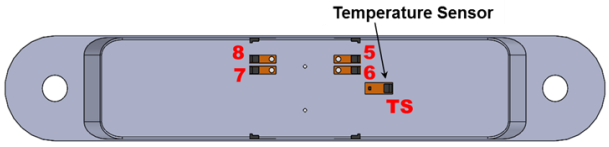

FRONT VIEW – ZONE/Sunset SS2 (Web)

- Earliest web crack detection at 0.047" length
- Crack propagation results in detection from path 8-8 first (300 KHz) and path 5-5 second (300 KHz)

= crack detection at frequency indicated

X = DI was less than 0.05 threshold for that PE path

	Freq	PE 5-5			PE 6-6			PE 7-7			PE 8-8		
		PE paths detected(DI>0.05)	DI	Cycle (k)	Crack Len (inch)	DI	Cycle (k)	Crack Len (inch)	DI	Cycle (k)	Crack Len (inch)	DI	Cycle (k)	Crack Len (inch)
Web area	250	5-5, 8-8	0.06671	45	0.297	x	x	x	x	x	x	0.06859	30	0.169
	300	5-5, 6-6, 7-7, 8-8	0.05086	27	0.144	0.05652	45	0.297	0.05347	48	0.321	0.05996	12	0.047
	350	5-5, 6-6, 7-7, 8-9	0.06712	39	0.234	0.07372	39	0.234	0.06557	42	0.264	0.0561	45	0.297
	500	No-data	x	x	x	x	x	x	x	x	x	x	x	x

Figure 6-115. PZT Pulse-Echo Results for Web of Specimen RB-PZT-12

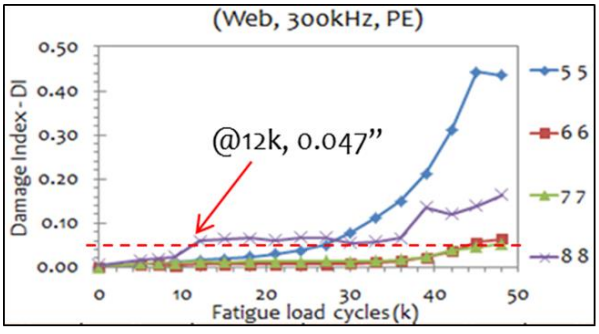

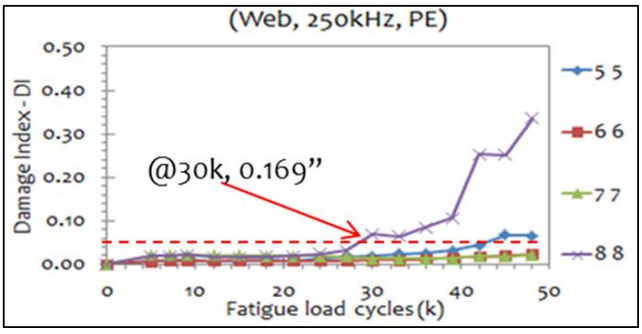

Figure 6-116. DI Progression for Pulse-Echo Interrogation of Web - RB-PZT-12

Pulse-Echo Mode for Distributed Sensor Configuration E
Data for Threshold at Damage Index > 0.05

- **Earliest flange crack detection at 0.15" length in top flange and 0.33" length in bottom flange**
- **Crack propagation results in detection from path 4-4 in top flange and 12-12 in bottom flange**

TOP VIEW – ZONE/Subset SS3 (Top Flange)

	Freq	PE 1-1				PE 2-2			PE 3-3			PE 4-4		
		PE paths detected(DI>0.05)	DI	Cycle (k)	Crack Len (inch)	DI	Cycle (k)	Crack Len (inch)	DI	Cycle (k)	Crack Len (inch)	DI	Cycle (k)	Crack Len (inch)
Top flange	250	1-1, 4-4	0.07454	42	0.33	x	x	x	x	x	x	0.05463	27	0.163
	300	2-2,3-3	x	x	x	0.063	42	0.33	0.0569	48	0.33	x	x	x
	350	4-4,	x	x	x	x	x	x	x	x	x	0.05165	24	0.15
	500	No-data	x	x	x	x	x	x	x	x	x	x	x	x

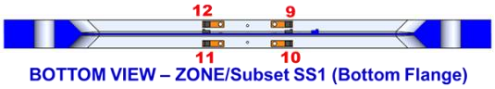

BOTTOM VIEW – ZONE/Subset SS1 (Bottom Flange)

= crack detection at frequency indicated

X = DI was less than 0.05 threshold for that PE path

	Freq	PE 9-9				PE 10-10			PE 11-11			PE 12-12		
		PE paths detected(DI>0.05)	DI	Cycle (k)	Crack Len (inch)	DI	Cycle (k)	Crack Len (inch)	DI	Cycle (k)	Crack Len (inch)	DI	Cycle (k)	Crack Len (inch)
Bot flange	250	12-12,	x	x	x	x	x	x	x	x	x	0.4154	36	0.33
	300	9-9, 10-10, 11-11	0.16411	39	0.33	0.05567	36	0.33	0.05495	45	0.33	x	x	x
	350	9-9, 11-11, 12-12	0.12955	36	0.33	x	x	x	0.05085	39	0.33	0.05125	45	0.33
	500	No-data	x	x	x	x	x	x	x	x	x	x	x	x

X = DI was less than 0.05 threshold for that PE path

Figure 6-117. PZT Pulse-Echo Results for Flanges of Specimen RB-PZT-12

The linear Clustered Sensors Arrangement (Configuration F) was used for the PE analysis approach on the web of specimens RB-PZT-13 and RB-PZT-14. These tests studied crack detection in the web region only. Figure 6-118 shows this sensor layout on the Rotorbeam web.

Crack length measurements and associated fatigue cycle information for the web region of specimen RB-PZT-13 is shown in Figure 6-119 (web). The *da/dN* crack growth curves and associated DI values for PE data are shown in Figure 6-120. The summary of PE results for all paths is shown in Figure 6-121. The earliest crack detection in the web occurred in Path 6-6 at *a* = 0.028" (0.7 mm). The associated DI vs crack growth curves are shown in Figure 6-122 where the DI exceeds the DI(threshold) = 0.05 when the crack length is 0.028". In Pulse Echo Mode for the web area:

- Sensor 6-6 path is the most sensitive at 250kHz → for DI threshold of 0.05, detection occurs at 7,000 cycles and crack length = 0.028" (0.71 mm); DI index reverses as cycles increase so use of data must be further scrutinized
- Sensor 5-5 path is the most sensitive at 300kHz → for DI threshold of 0.05, detection occurs at 33,000 cycles and crack length = 0.22" (5.7 mm)
- Sensor 3-3 path is the most sensitive at 350kHz → for DI threshold of 0.05, detection occurs at 30,000 cycles and crack length = 0.22" (5.7 mm)

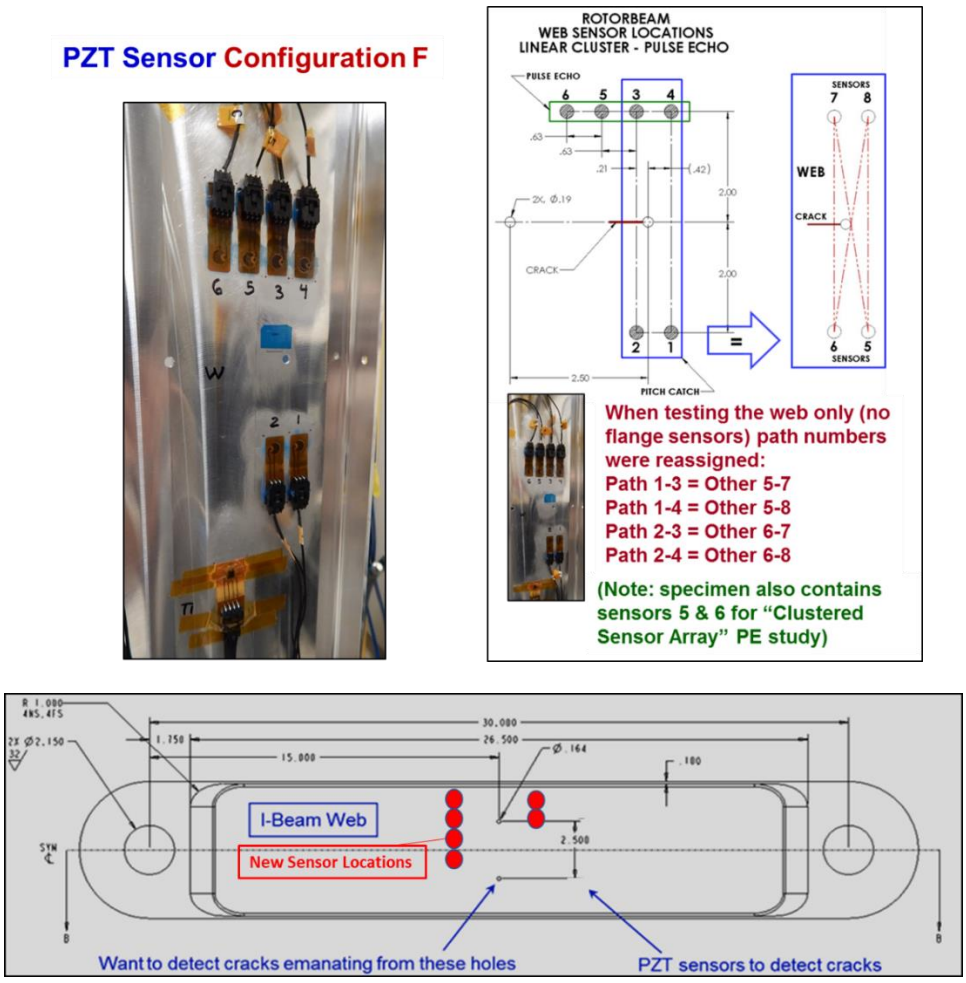

Figure 6-118. PZT Sensor Network for Pulse-Echo Data Analysis Approach in RB-PZT-13, -14

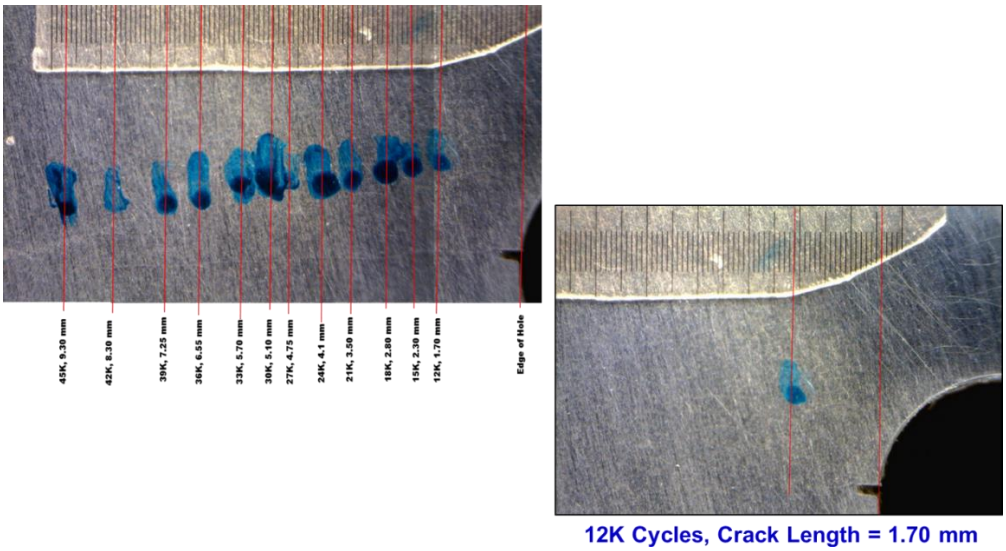

Figure 6-119. Web Crack Length Measurements for PZT Pulse-Echo Results –RB-PZT-13

RB-PZT-13 Cycles and Crack Length	
Cycles	Crack Length (mm)
	Web
0	0
5,000	0.4
7,000	0.7
9,000	1.1
12,000	1.7
15,000	2.3
18,000	2.8
21,000	3.5
24,000	4.1
27,000	4.75
30,000	5.1
33,000	5.7
36,000	6.55
39,000	7.25
42,000	8.3
45,000	9.3

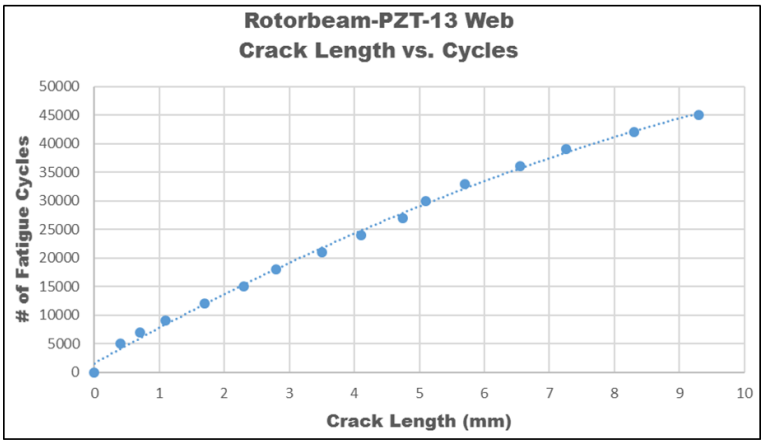

Figure 6-120. PZT Damage Detection in Web Using Pulse-Echo Mode –RB-PZT-13

Pulse-Echo Mode for Clustered Sensor Configuration F
Data for Threshold at Damage Index > 0.05

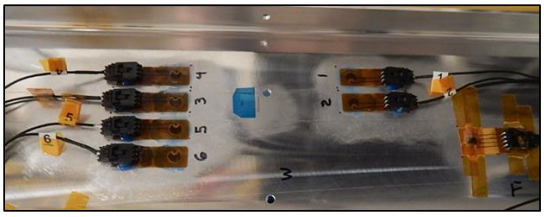

- **Earliest web crack detection at 0.028" length**
- **Crack propagation results in detection from path 6-6 first (250 KHz) and path 5-5 second (300 KHz)**

= crack detection at frequency indicated

X = DI was less than 0.05 threshold for that PE path

	Freq	PE paths detected(DI>0.05)	PE 3-3 DI	PE 3-3 Cycle (k)	PE 3-3 Crack Len (inch)	PE 4-4 DI	PE 4-4 Cycle (k)	PE 4-4 Crack Len (inch)	PE 5-5 DI	PE 5-5 Cycle (k)	PE 5-5 Crack Len (inch)	PE 6-6 DI	PE 6-6 Cycle (k)	PE 6-6 Crack Len (inch)
Web area	250	4-4, 5-5, 6-6	x	x	x	0.05939	39	0.285	0.05205	42	0.327	0.05955	7	0.028
	300	3-3, 4-4, 5-5	0.05622	39	0.285	0.06067	39	0.285	0.06688	33	0.224	x	x	x
	350	3-3, 4-4	0.06135	33	0.224	0.06353	39	0.285	x	x	x	x	x	x
	500	No-data	x	x	x	x	x	x	x	x	x	x	x	x

Figure 6-121. PZT Pulse-Echo Results for Web of Specimen RB-PZT-13

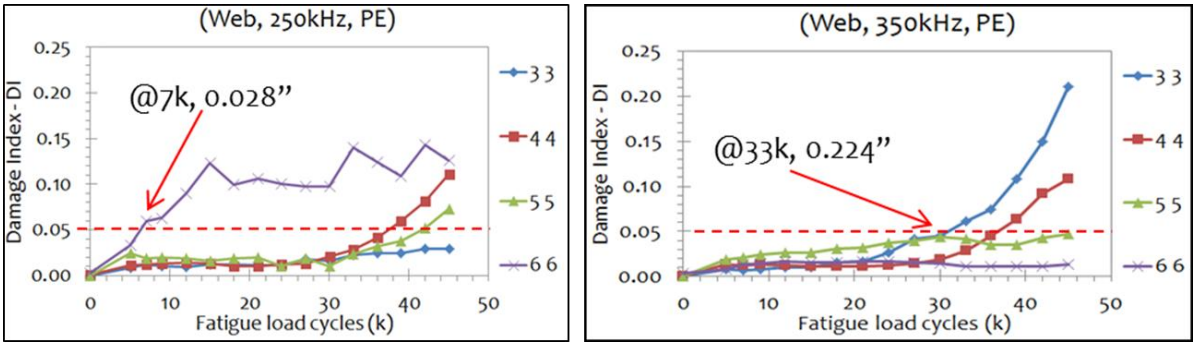

Figure 6-122. DI Progression for Pulse-Echo Interrogation of Web - RB-PZT-13

Crack length measurements and associated fatigue cycle information for the web region of specimen RB-PZT-14 is shown in Figure 6-123 (web). The *da/dN* crack growth curves and associated DI values for PE data are shown in Figure 6-124. The summary of PE results for all paths is shown in Figure 6-125. The earliest crack detection in the web occurred in Path 6-6 at *a* = 0.02" (0.51 mm). The associated DI vs crack growth curves are shown in Figure 6-126 where the DI exceeds the DI(threshold) = 0.05 when the crack length is 0.02". In Pulse Echo Mode for the web area:

- Sensor 6-6 path is the most sensitive at 350kHz → for DI threshold of 0.05, detection occurs at 7,000 cycles and crack length = 0.02" (0.51 mm); DI index at 300 KHz reverses as cycles increase so use of data must be further scrutinized
- Sensor 4-4 path is the most reliable/sensitive at 300kHz → for DI threshold of 0.05, detection occurs at 27,000 cycles and crack length = 0.189" (4.8 mm)
- Sensor 4-4 & 3-3 paths are the most sensitive at 350kHz → for DI threshold of 0.05, detection occurs at 30,000 cycles and crack length = 0.205" (5.2 mm)

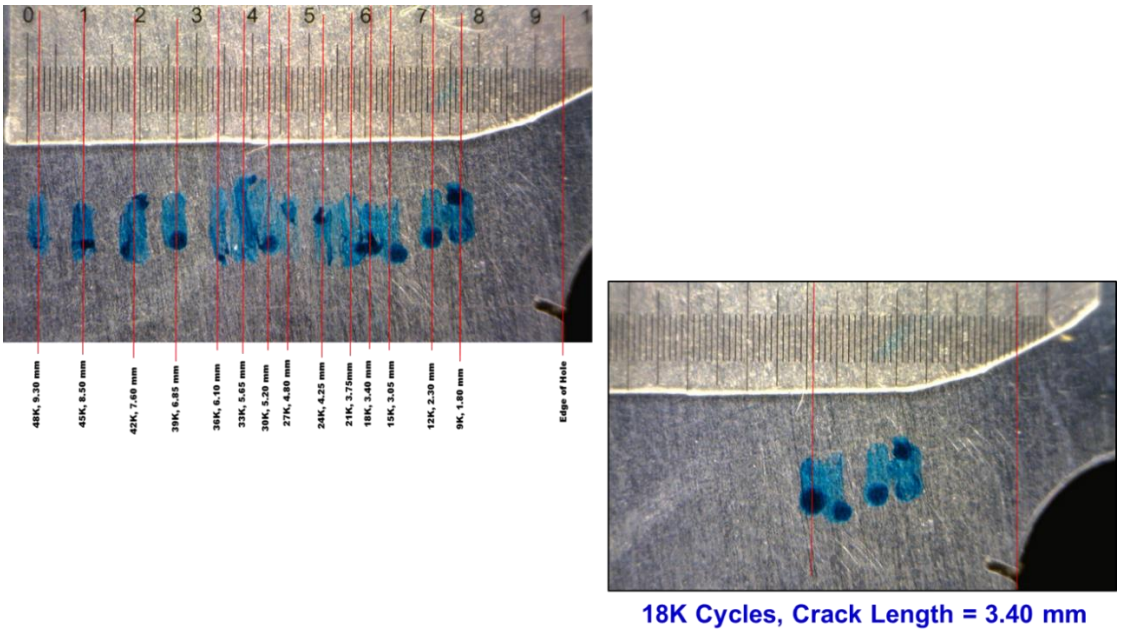

Figure 6-123. Web Crack Length Measurements for PZT Pulse-Echo Results –RB-PZT-14

Following are some general conclusions regarding the Pulse-Echo PZT data analysis method:

- The Clustered Sensor Arrangement (Configuration F) is used to evaluate the sensitivity of PE mode when sensors are positioned directly over the crack growth direction (5-5 and 6-6 are front facing) and when sensors are positioned on the opposite side of the crack direction (3-3 and 4-4 are back facing)
- Configuration F (Clustered) showed slightly better coverage than Configuration E (Distributed) for the crack growth experienced in the I-beam web region.
- Pulse-Echo Mode – Sensitivity is related to orientation between crack growth and sensor. Sensor placement relative to the crack influences the resulting damage detection.

- Multiple sensors are still needed in PE mode since the sensitivity may differ depending on crack growth direction. Also, in cases where crack growth direction is uncertain, more sensors are needed to capture the most sensitive path for various crack orientations.
- Additional data is needed for true statistical conclusions. However, initial results show the potential for high sensitivity and small crack detection in PE mode.
- An overall comparison between PZT crack detection performance in Pulse-Echo and Pitch-Catch modes is provided in Table 6-41.

RB-PZT-14 Cycles and Crack Length	
Cycles	Crack Length (mm)
	Web
0	0
5,000	0.5
7,000	1.2
9,000	1.8
12,000	2.3
15,000	3.05
18,000	3.4
21,000	3.75
24,000	4.25
27,000	4.8
30,000	5.2
33,000	5.65
36,000	6.1
39,000	6.85
42,000	7.6
45,000	8.5
48,000	9.3

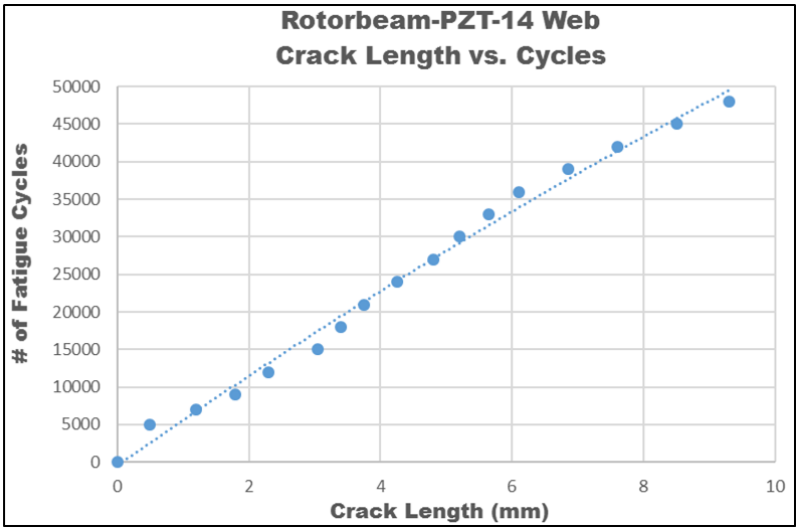

0 - Load: Damage Detection using Pitch-Catch Mode
@ DI Threshold = 0.05
(Data for 500KHz = Web)

Figure 6-124. PZT Damage Detection in Web Using Pulse-Echo Mode –RB-PZT-14

Pulse-Echo Mode for Clustered Sensor Configuration F
Data for Threshold at Damage Index > 0.05

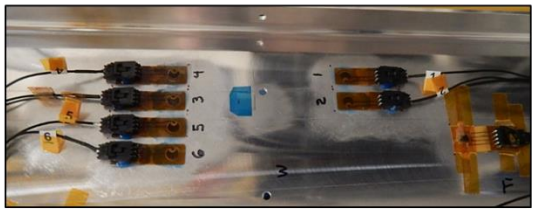

- Earliest web crack detection at 0.02" length
- Crack propagation results in detection from path 6-6 first (250 KHz) and path 4-4 second (250 KHz)

= crack detection at frequency indicated

X = DI was less than 0.05 threshold for that PE path

	Freq	PE paths detected(DI>0.05)	PE 3-3 DI	PE 3-3 Cycle (k)	PE 3-3 Crack Len (inch)	PE 4-4 DI	PE 4-4 Cycle (k)	PE 4-4 Crack Len (inch)	PE 5-5 DI	PE 5-5 Cycle (k)	PE 5-5 Crack Len (inch)	PE 6-6 DI	PE 6-6 Cycle (k)	PE 6-6 Crack Len (inch)
Web area	250	4-4, 5-5	x	x	x	0.07588	27	0.189	0.05108	45	0.335	x	x	x
	300	3-3, 4-4, 5-5, 6-6	0.05538	45	0.335	0.05253	27	0.189	0.05313	33	0.222	0.05918	5	0.02
	350	3-3, 4-4, 5-5, 6-7	0.05753	30	0.205	0.05328	33	0.222	0.05313	42	0.299	0.21025	5	0.02
	500	No-data	x	x	x	x	x	x	x	x	x	x	x	x

Figure 6-125. PZT Pulse-Echo Results for Web of Specimen RB-PZT-14

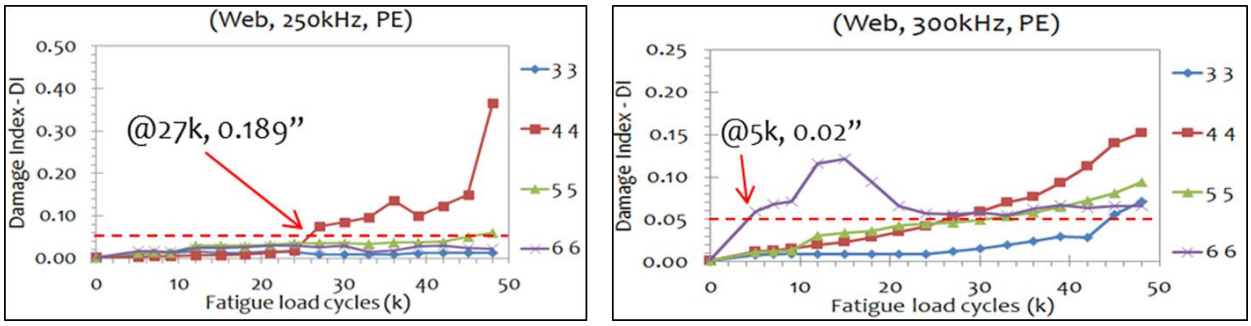

Figure 6-126. DI Progression for Pulse-Echo Interrogation of Web - RB-PZT-14

Table 6-41. PZT Crack Detection Performance in Pulse-Echo and Pitch-Catch Interrogation Modes for Rotorbeam Test Specimens

	Flange Avg Crack Length (in)	Web Avg Crack Length (in)
Distributed Sensors in Pitch-Catch	0.328	0.210
Distributed Sensors in Pulse-Echo	0.240	0.116
Clustered Sensors in Pulse-Echo	N/A	0.024

6.4. Durability Assessments - Environmental Testing of PZT Sensors

Durability assessments of PZT sensors were completed in both laboratory and field environments. For the laboratory tests, the specimen (set of PZT sensors) shown in Figure 4-55 and Figure 6-127 was subjected to the environmental test environment shown in Figure 4-57. Sensor response measurements were made after each of the three environments listed in Figure 4-57 (hot-wet, cold, heat) and this process was repeated for a total of four cycles. Each test specimen included all hardware that remains on the aircraft during operation. The tests evaluated sensor ability to function after severe exposure to humidity, temperature variations, icing/freezing and heat.

Figure 6-128 contains sample plots of impedance levels measured from some of the PZT sensors contained within the four Smart Patches. The consistent and proper impedance levels in the graphic on the left side (Smart Patch 2), reveal that these PZT sensors did not change over the course of the four-cycle environmental tests. This is the desired result as the PZT sensors should produce similar signatures over time if there is no damage growth in the underlying structure. Figure 6-128 also shows sample plots of the Damage Indices calculated from some of the PZT paths present in the Smart Patches. The graphic on the right, produced by Smart Patch 2, shows that the DI levels for these PZT sensors remained within the "undamaged" response levels over the course of the four-cycle environmental tests.

The PZT systems includes a fail-safe feature which is critical to the application of SHM systems in general. This prevents the unknowing acquisition of faulty data that might result in a missed

detection of damage structure. With a fail-safe feature ensured, the durability tests primarily evaluate the nuisance factor that might be inflicted on an airline that uses such SHM systems. It is an undesirable scenario for airlines to revisit SHM sensor network installation sites to address, and possibly replace, failed sensors. Thus, durability of SHM systems is an important consideration related to the value and long-term use of SHM solutions over the life of an aircraft.

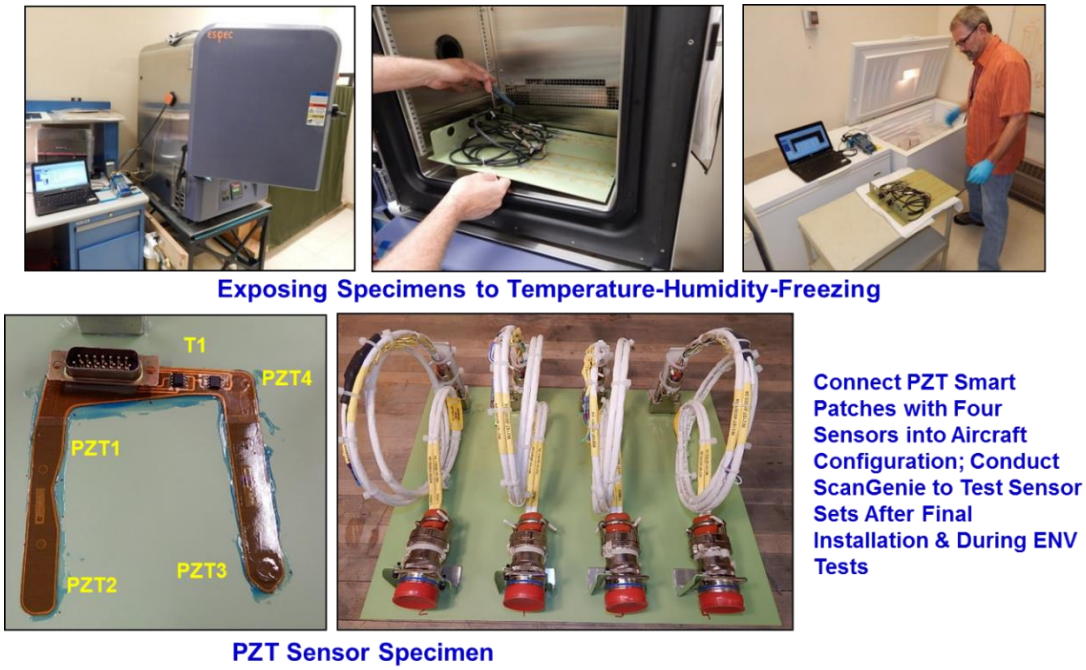

Figure 6-127. PZT Environmental Durability Tests – Hot-Wet-Freeze

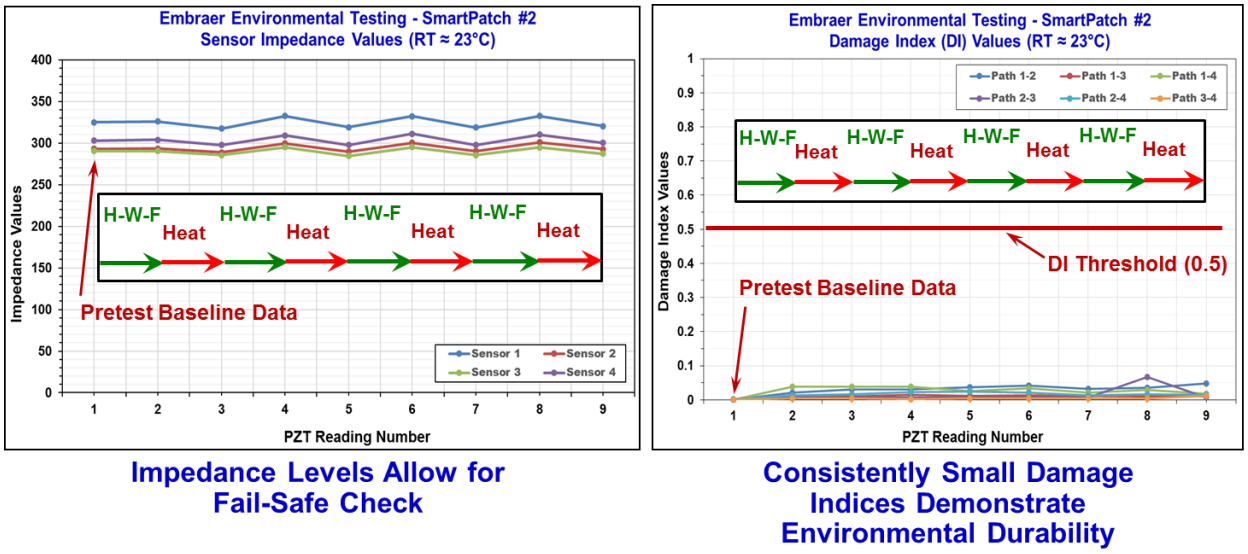

Figure 6-128. PZT Sensor Response During Environmental Tests

Exposure of the PZT system to field environments included various flight testing such as that described in Section 2.3 and References [6.4 – 6.6]. In addition, a series of PZT and CVM sensors were installed on several Embraer test aircraft and several aircraft operating in the Azul Airlines fleet. Some of the PZT sensor installations and subsequent monitoring took place at the Embraer flight test facility in Gavião Peixoto, Brazil. Other sensor installation and monitoring sites included various Azul Airline maintenance depots. Figure 6-129 shows a sample PZT application. Successful flight test data, indicating properly functioning PZT systems, has been acquired for a number of years through this flight test series.

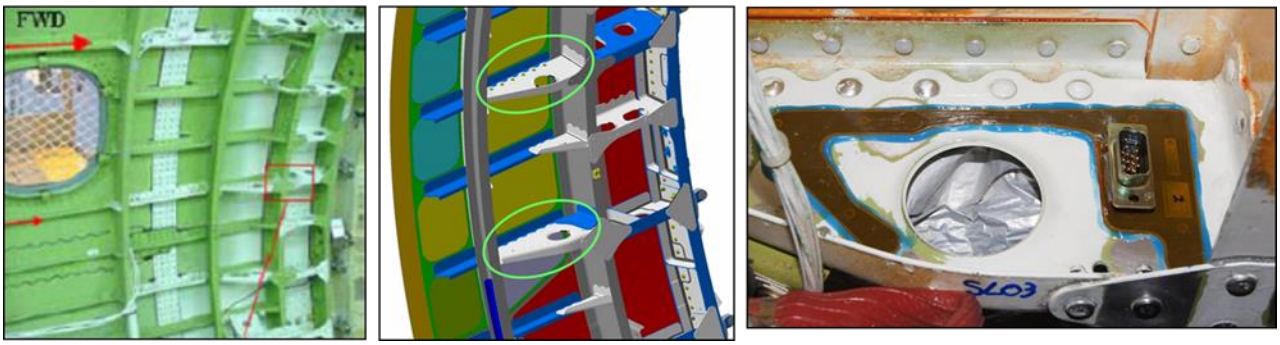

Figure 6-129. Trial Embraer Application of PZT Sensors for Monitoring Door Surround Bracket and Stringers

6.5. Insights into Optimizing PZT Deployment

The extensive PZT validation test series described in this report provided the opportunity to obtain many insights with respect to optimum PZT deployment, data acquisition and data analysis. This section describes the major learning points that can advance the use of PZT senor networks in SHM applications. Specific steps that can be used to optimize overall PZT performance include:

- Setting Proper Damage Index – To avoid False Calls, set DI above the changing/uncertain DI profile and in a region of higher magnitude where the DI increases continuously (no reversals observed).
- Changing Boundary Conditions – Joint fretting and "initial settling" will affect Lamb Wave characteristics. As a result, the Baseline data should be acquired after sufficient, initial fatigue has occurred, especially in more complex structure. This allows for initial settling of components that are critical in the PZT signals, such as joints, bond lines, fasteners, substructure, sealant, and the acquisition of a Baseline that provides a good representation of a stable, pristine structure. If this practice is not observed and a premature Baseline is acquired, subsequent PZT signals may vary greatly even without any damage present. Such variations may be due solely to the component settling described here.
- PZT Monitoring at Temperature – Due to the effect of temperature on PZT signals, a proper series of Baselines must be acquired at the same temperature(s) as the expected monitoring temperatures. This will produce maximum sensitivity while reducing false calls.

- PZT Monitoring at Load – Due to the effect of load on PZT signals, a proper series of Baselines must be acquired at the same load(s) as the expected monitoring load. This will produce maximum sensitivity while reducing false calls.
- Residual Strains and Stress Reapportion – If the PZT networks are monitored while the structure is under load, it may be possible to improve the performance of the SHM system. This depends on the both the magnitude of the load (stress) and the direction of the stress. Tension loads, for example, tend to open a fatigue crack and increase the magnitude of the PZT signals (increase DI). Compression loads, on the other hand, may tighten the fatigue crack opening and decrease the DI levels. Compressive strains reduce crack PZT response so the effects of compressive strains on Lamb Waves must be properly considered. Torsional and bending loads can have either effect depending on the geometry of the component and the resulting direction of the local strain at the fatigue crack. In addition, load reapportionment and load shedding can occur as damage grows in a component. This can change the stress fields in a structure and change how the structure responds to load when it already has some damage. These factors must all be considered whenever deciding to monitor an SHM system while a structure is under load (e.g. monitoring during flight).
- Fretting and Settling of Fasteners – Torqued bolts do not represent realistic aircraft structures. Side studies conducted with joints containing torqued bolts exhibited rapidly-changing PZT signals due to changing torque levels in the bolts as the fatigue tests progressed. Limited testing with the Rotorbeam specimen revealed that the presence of rivets in the cracked hole did not affect PZT performance.

Optimizing Data Driving Frequencies - At almost all fatigue test stopping points, data acquisition was conducted at a number of different PZT sensor driving frequencies. This allowed for optimum crack detection using data from the most sensitive/responsive frequency. Once a "best" frequency is determined, it may be possible to simply acquire data from this frequency. For the web region, 500 KHz provided the best DI response while for the flange region 300 KHz provided the best DI response. Figure 6-130 and Figure 6-131 compare crack detection at these optimum frequencies with crack detection at all other frequencies. Figure 6-130 shows that similar results were obtained in the web from the response frequency of 500 KHz (any path) and data stemming from first detection at any frequency (any path). Figure 6-131 shows that similar results were obtained in the flange from the response frequency of 300 KHz (any path) and data stemming from first detection at any frequency (any path. Figure 6-132 compares PZT response data from four of the different driving frequencies and provides an example of the data used to arrive at 500 KHz as the optimum frequency for monitoring the web region. If the PZT network is monitored while the structure is under load, then a suite of driving frequencies may provide the best data acquisition approach. This is because, as the loads were increased in the "response at load" tests, more detections occurred at different frequencies.

Performance Assessment of PZT Networks for Crack Detection in Complex Structures							
Results from PZT Network on Web		PZT Network Crack Detection in Rotorbeam Web					
		PZT Performance Using Detection at Any Frequency			PZT Performance Using Detection at Selected Best Frequency of 500KHz		
		POD Value (in)	Average Crack Length at Detection (in)	Standard Deviation in Test Series	POD Value (in)	Average Crack Length at Detection (in)	Standard Deviation in Test Series
Unloaded Rotorbeam	Open Holes	0.274	0.210	0.0242	0.274	0.210	0.0242
	Open and Riveted Holes	0.270	0.211	0.0238	0.270	0.211	0.0238
Rotorbeam at 1,000 PSI Stress	Open Holes	0.235	0.165	0.0266	0.243	0.169	0.0270
	Open and Riveted Holes	0.230	0.167	0.0258	0.235	0.170	0.0258
Rotorbeam at 7,000 PSI Stress	Open Holes	0.169	0.095	0.0218	0.190	0.100	0.0243
	Open and Riveted Holes	0.180	0.096	0.0269	0.204	0.102	0.0309

- Comparison of PZT performance when using all frequencies or when using determined best frequency
- Comparison of PZT performance at different loads

Figure 6-130. Comparison of PZT Performance in Web as a Function of DAQ Frequency Selection and Load

Results from PZT Network on Flange		PZT Network Crack Detection in Rotorbeam Flange					
		PZT Performance Using Detection at Any Frequency			PZT Performance Using Detection at Selected Best Frequency of 300KHz		
		POD Value	Average Crack Length at Detection	Standard Deviation in Test Series	POD Value	Average Crack Length at Detection	Standard Deviation in Test Series
Unloaded Rotorbeam	Open Holes	0.343	0.328	0.0075	0.343	0.328	0.0075
	Open and Riveted Holes	0.344	0.328	0.0086	0.343	0.329	0.0071
Rotorbeam at 1,000 PSI Stress	Open Holes	0.517	0.273	0.0759	0.484	0.292	0.0647
	Open and Riveted Holes	0.570	0.253	0.0903	0.465	0.282	0.0674
Rotorbeam at 7,000 PSI Stress	Open Holes	0.138	0.083	0.0228	0.144	0.091	0.0211
	Open and Riveted Holes	0.144	0.083	0.0249	0.149	0.093	0.0236

Figure 6-131. Comparison of PZT Performance in Flange as a Function of DAQ Frequency Selection and Load

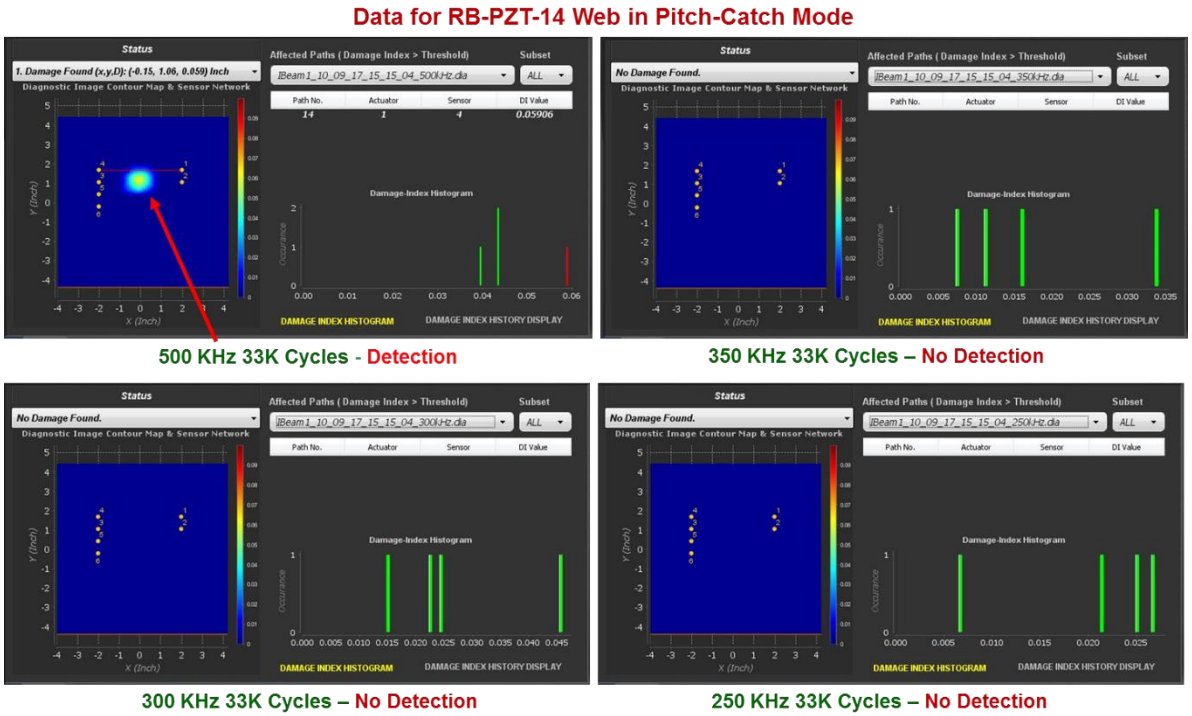

Figure 6-132. Validation of 500 KHz Selection as Best Single Frequency for Crack Detection in the Web

Monitoring PZT Networks at Load - If it is possible to create tension stresses around the crack, the PZT performance can be improved. Figure 6-130 and Figure 6-131 also compare crack detection from the PZT network when the Rotorbeam specimen is subjected to tension loads. The web shows a 21% improvement in the average crack length at detection for a 1,000 lb load and a 55% improvement in the average crack length at detection for a 7,000 lb load. The flange shows a 17% improvement in the average crack length at detection for a 1,000 lb load and a 75% improvement in the average crack length at detection for a 7,000 lb load. Note that compression loads, or torsion loads that lead to localized compression around the cracks, could reverse this trend and lead to a decrease in performance.

Sources of PZT Signal Changes that are Not Associated with Damage - Along those lines, it is important to revisit the effects of strain fields on Lamb Wave travel and overall PZT response. Applied loads, changing boundary conditions and stress reapportion due to damage onset and growth can all affect the Lamb Waves. Stress fields directly affect waves propagating between array elements because of dimensional changes and the acoustoelastic effect. The acoustoelastic effect describes how the sound velocities (both longitudinal and shear wave velocities) of an elastic material change if subjected to an initial static stress field. This is a non-linear effect of the constitutive relation between mechanical stress and finite strain in a material of continuous mass. In classical linear elasticity theory small deformations of most elastic materials can be described by a linear relation between the applied stress and the resulting strain. This relationship is commonly known as the generalized Hooke's law. The linear elastic theory involves second order

elastic constants and yields constant longitudinal and shear sound velocities in an elastic material that are not affected by an applied stress.

The acoustoelastic effect, on the other hand, includes higher order expansion of the constitutive relation (non-linear elasticity theory) between the applied stress and resulting strain, which yields longitudinal and shear sound velocities that are dependent of the stress state of the material. When applied loads change wave propagation, this results in changes in phase velocity that depend on the Lamb Wave mode and frequency. It is possible to determine this acoustoelastic response of a specific mode and frequency. Thus, specific PZT response data can be used to estimate the biaxial stress field [6.4]. Once this is understood, it is possible to compensate for the stress field and minimize their interference on the focused task of damage detection. In this manner opening fatigue cracks can disrupt with Lamb Wave travel much more than the stress field and damage detection can be emphasized in the PZT network.

Effects of Overall Structure Response on Setting Proper DI Thresholds – Loads and associated stress fields are important issues in PZT testing and one must perform baseline data acquisition under the same temperature and loading conditions as those that will exist during actual PZT interrogation (unloaded or loaded, in-flight monitoring). It may not be possible to simulate all aspects of changes in the stress fields that occur in a complex structure. This fact should be taken into consideration such that appropriate DI levels can be chosen to avoid a high number of false calls. This data suggests that using PZT technology for onboard SHM testing during flight would be extremely challenging due to the changing loading conditions during flight. The data acquisition must be repeatable and correlated to accurate temperature and load/stress conditions such that suitable PZT baselines can be used for DI calculations.

The wise approach to selecting a suitable DI(threshold) is to conservatively place it above any effects from non-damage parameters such as the loads discussed above or the DI fluctuations that may arise, especially in complex structures. Figure 6-133 provides an example where the DI progression increases, then decreases in the web data during fatigue cycling. Note this occurrence in the DI levels around 0.03 to 0.04. This data suggests that the selected DI(threshold) should be greater than 0.04 for best crack detection with minimum possibility for false calls.

Establishing Temperature and Load Compensation - Some of the major points above describe how temperature and load at monitoring must be taken into account when obtaining baseline PZT signals. Use of proper baseline data and associated compensation algorithms can help reduce the deleterious effects of changing PZT signals caused by temperature and loads alone (i.e. not caused by damage). Temperature compensation algorithms already exist within the ScanGenie PZT software. However, it is possible to add load compensation algorithms such that Lamb Wave and associated PZT response changes associated with loads in a pristine structure, not damage, are properly considered and properly filtered from the DI calculations. The resulting series of temperature and load compensation curves would produce an overall, three-dimensional compensation contour map as shown in Figure 6-134. This mapping can be used if both parameters create changes in the baseline signals and the subsequent in-service signals such that changes associated with damage detection can be highlighted.

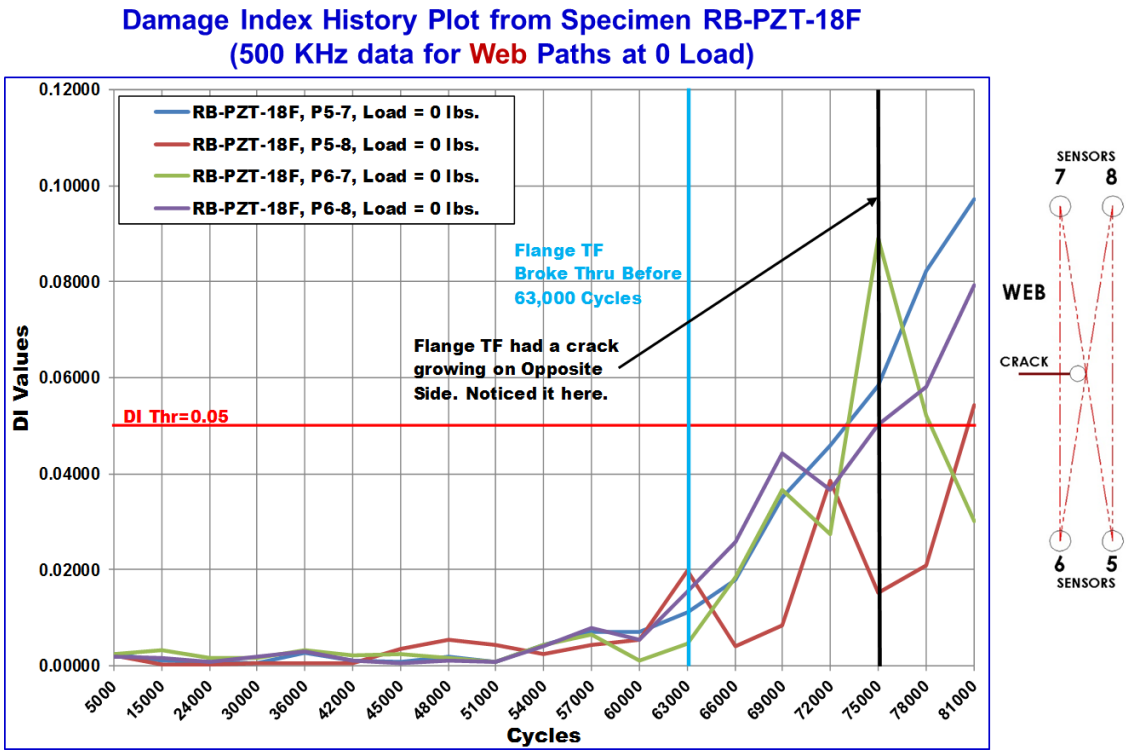

Figure 6-133. Sample Fluctuations in PZT Signals – Key Consideration in Establishing Damage Detection Threshold

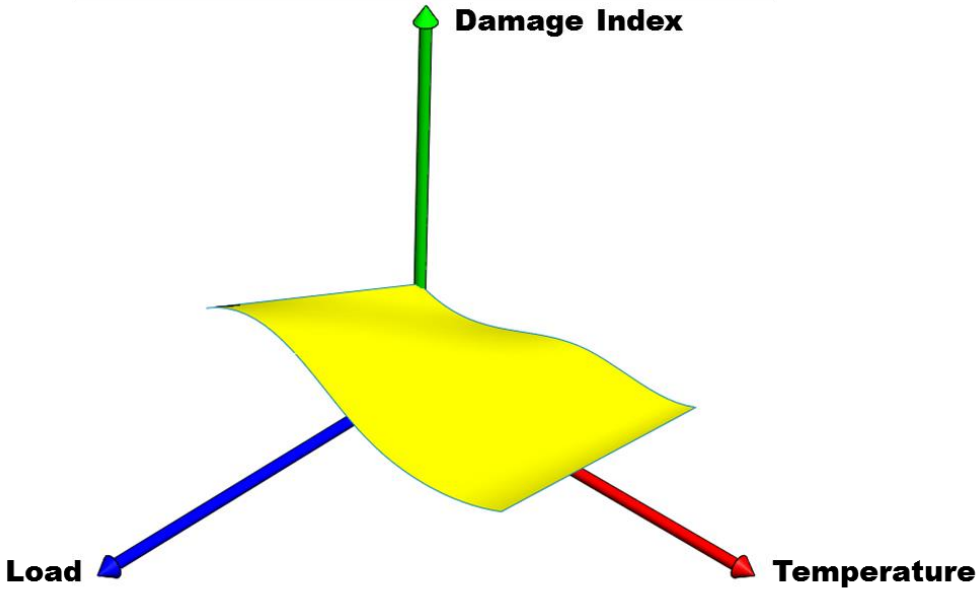

Figure 6-134. Possible PZT Adjustments to Account for Baseline Variations Caused by Temperature and Load

Establishing Proper PZT Baselines – Related to temperature and load compensation is the use of proper baseline data. Table 6-42 lists a comparison of different Baseline approaches where baseline data was acquired at load and in an unloaded condition. These different baselines were then compared to subsequent PZT response data acquired after fatigue and crack growth. It shows that, for lightly loaded structures, similar results can be obtained from baselines at 0 load and baselines at small loads. For 500 lb and 1,000 lb loads, there was no difference between crack detection using a 0 load baseline or a baseline that matched the subsequent monitoring load. Crack length at detection was essentially the same. However, this changed when the loads increased into the medium range of 7,000 lbs. It was observed that a 7,000 lb load structure required comparisons to a baseline acquired also at 7,000 lbs to avoid false calls. The crossover from "lightly loaded" structure where 0 load baselines are acceptable and "medium loaded" structure requiring matching baselines depends on the stress distribution within the structure and the redistribution of stresses as damage grows in the structure.

Table 6-42. Establishing Proper PZT Baselines – Minimal Effect of Lightly Loaded Structures

PZT Performance in Web of Rotorbeam - Crack Length and Damage Index at Initial Crack Detection in Lightly Loaded Specimens (Comparison of Performance from Different Baselines)

Specimen #	Load at Data Acquisition (lbs)	Load Used to Determine Baseline (lbs)	Fatigue Cycles at Detection	Crack Length at Detection mm (in)	Damage Detection Freq. (KHz)	First Path Detecting Crack	DI Value of First Path
RB-PZT-9-500	500	0	27,440	5.10 (0.201)	500	5-8	0.06846
RB-PZT-9-500	500	500	30,000	5.65 (0.222)	500	5-8	0.08024
RB-PZT-9-1000	1000	0	24,000	4.20 (0.165)	500	5-8	0.06152
RB-PZT-9-1000	1000	1000	21,000	3.65 (0.144)	500	5-8	0.05399

PZT Performance in Flange of Rotorbeam - Crack Length and Damage Index at Initial Crack Detection in Lightly Loaded Specimens (Comparison of Performance from Different Baselines)

Specimen #	Flange	Load at Data Acquisition (lbs)	Load Used to Determine Baseline (lbs)	Fatigue Cycles at Detection	Crack Length at Detection mm (in)	Damage Detection Freq. (KHz)
RB-PZT-9-500	Bottom	500	500	44,645	8.38 (0.330)	300
	Bottom	500	0	44,645	8.38 (0.330)	300
RB-PZT-9-500	Top	500	500	30,000	8.38 (0.330)	300
	Top	500	0	30,000	8.38 (0.330)	300
RB-PZT-9-1000	Bottom	1000	1000	44,645	8.38 (0.330)	300
	Bottom	1000	0	44,645	8.38 (0.330)	300
RB-PZT-9-1000	Top	1000	1000	21,000	4.65 (0.183)	300
	Top	1000	0	18,000	3.80 (0.150)	350

Figure 6-135 shows one example of the effects of "significant" load levels. It shows where variations in baselines can produce false alarms if proper baseline comparisons are not used. In this comparison, changes in DI levels were caused by changes in structural loads such that, even without any damage onset (0 fatigue cycles), a false indication of damage was produced. Notice

multiple DI levels above the DI(threshold) of 0.05 even though there was no damage present. Thus, the stress field at monitoring must be properly considered when establishing and acquiring the PZT baseline data.

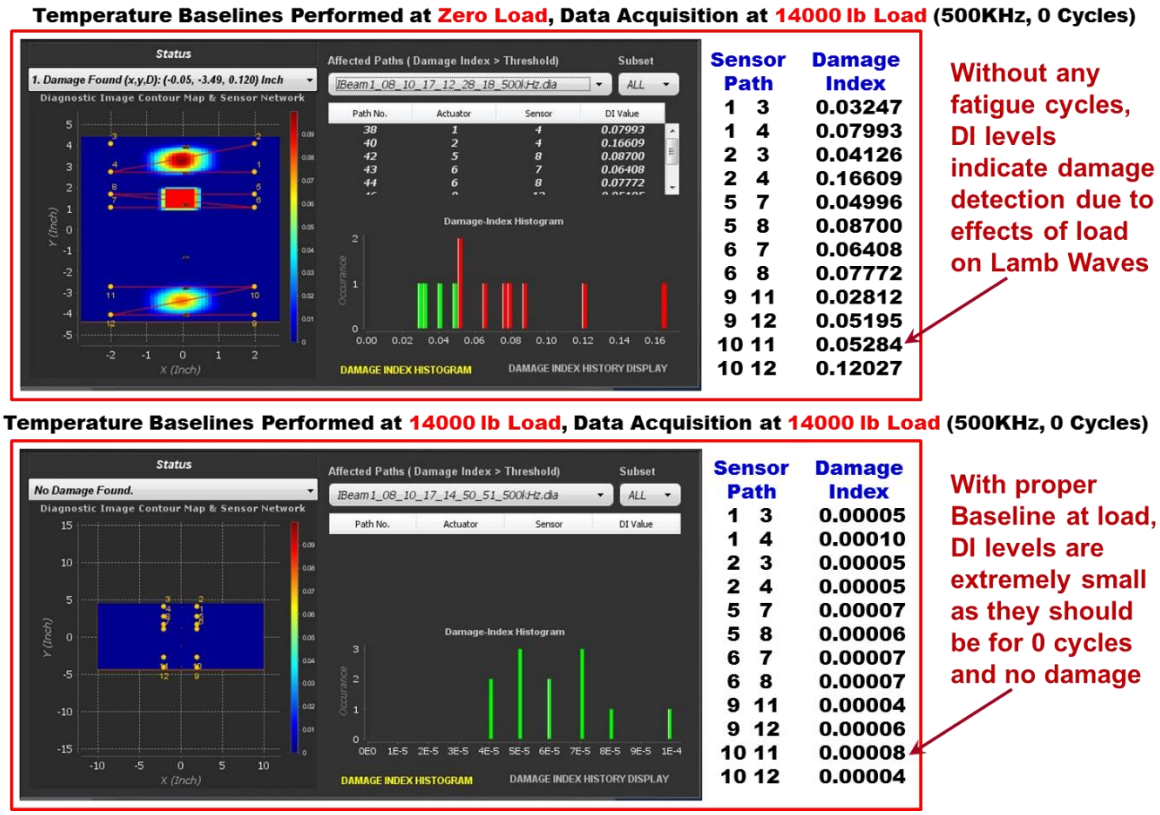

Figure 6-135. Effects of Loading on PZT Response - RB-PZT-8

References

6.1. Roach, D., Rice, T., "Design and Assessment of Comparative Vacuum Monitoring and Piezoelectric Transducer Systems for Certified Use in Aircraft Structural Health Monitoring Solutions," Sandia Dept of Energy Report, SAND2017-6401, July 2017.

6.2. Dotta, F., Rulli, R., Roach, D., "Embraer SHM Qualification Process and the Future of Aircraft Maintenance," Proceedings of the Aircraft Airworthiness & Sustainment Conference, April 2019.

6.3. Rulli, R., Dotta, F., Roach, D., Rice, T., "Advancements on the Adoption of SHM Damage Detection Technologies into Embraer Aircraft Maintenance Procedures," Int'l Workshop on Structural Health Monitoring, September 2017.

6.4. Shi, F., Michaels, J., Sang, J. "In-Situ Estimation of Applied Biaxial Loads with Lamb Waves," Journal of Acoustic Society, February 2013.

THIS PAGE INTENTIONALLY LEFT BLANK

7. CONCLUSIONS AND PATH FORWARD FOR CVM AND PZT USAGE

Background and Motivation for SHM Usage

Recent advances in on-board structural health monitoring sensors have proven that distributed and autonomous health monitoring systems can be applied to reliably detect incipient damage. Such systems have wide use in aerospace, automotive, civil infrastructure and other industrial applications. This report presents data that establishes the viability of the Comparative Vacuum Monitoring (CVM) and Piezoelectric Transducer (PZT) systems for implementation on helicopter structures. Through the use of in-situ CVM and PZT sensors, it is possible to quickly, routinely, and remotely monitor the integrity of a structure in service. On-board sensors, such as the ones described in this report, may be used to directly detect the onset of crack, corrosion, or disbond flaws. Whether the health monitoring approach is local or global, the key element in a SHM system is a calibration of sensor responses so that damage signatures can be clearly delineated from sensor data produced by unflawed structures.

Currently, rotorcraft Health and Usage Monitoring Systems (HUMS) emphasize usage monitoring and associated effects on maintenance programs. Additional benefits from deploying HUMS may be realized when structural assessment data, collected by an SHM system, is used to compliment the operational environment monitoring. Detection of unexpected flaw growth and structural failure can be improved if on-board health monitoring systems are used continuously assess structural integrity and signal the need for human intervention. The application of SHM systems for monitoring the structural integrity of aircraft provides alternatives to invasive inspections. On-board distributed sensor systems can eliminate costly, and potentially damaging, disassembly, and decrease maintenance costs by eliminating more time-consuming manual inspections. The success of SHM solutions and the decision to implement them ultimately hinges on the capability of the system to reduce the risk of structural failure while providing economic benefit in terms of maintenance cost savings and aircraft availability.

Aircraft downtime is one of the largest costs associated with carrier operations. Current escalations in aircraft utilization hasten the arrival of A, B, C, and D-Checks yet imply the need for less downtime for maintenance. This need for more effective maintenance may be partially addressed through the introduction of SHM practices. Rapid inspections in lieu of tedious and slow inspections, elimination of disassembly for access (remote interrogation of sensors), automated data analysis and disposition, and automated record keeping are several of the features that may produce a positive cost-benefit analysis. Carriers may then choose to modify their maintenance manuals in order to use SHM methods for required maintenance tasks. Similarly, revisions in applicable OEM manuals (e.g. NDT Standard Practices Manuals) can provide one level of approval and allow for the safe and uniform utilization of SHM systems. The Supplemental Type Certificate (STC) process must be augmented to include all aspects of SHM equipment manufacturing, installation, and operation to proactively address the desire to apply SHM systems. Towards these ends, the FAA if proactively and carefully addressing SHM applications via the generation of formal guidance documents.

SHM Validation and Verification

This SHM Validation Program used controlled, representative laboratory testing and the results from previous on-aircraft flight tests. Each phase successfully addressed various aspects of the four critical factors: damage detection capability, durability, installation/supportability, and safety. Validation testing used CVM and PZT sensors mounted to representative specimens which were cyclically loaded to generate and grow typical fatigue damage. The loading spectrum used for fatigue crack propagation was based on the anticipated on-aircraft load environment. These tests demonstrated the capability of the CVM and PZT systems to detect and reliably identify relevant damage in the application on representative rotorcraft structures. The validation process considered the numerous factors that affect the reliability of an inspection methodology including the individual inspector/operator, the equipment, the procedures and the environment in which the inspector is working. It also evaluated the viability of the SHM approach within an airline's maintenance program.

All factors that affect SHM sensitivity were included in this program: flaw size, shape, orientation and location relative to the sensors, as well as operational and environmental variables. Testing evaluated the effects of structural complexity, boundary conditions, presence of fasteners, joint settling during fatigue, residual stresses and load shedding, temperature, load, alternate data analyses methods. Statistical methods were applied to performance data to derive Probability of Detection (POD) values for CVM and PZT sensors in a manner that agrees with current nondestructive inspection (NDI) validation requirements and is acceptable to both the aviation industry and regulatory bodies. The result is a series of flaw detection curves that can be used to propose CVM sensors for crack detection.

The validation plan was developed to properly: 1) provide a vehicle in which skills, automation of instrumentation and human error can be evaluated in an objective and quantitative manner, 2) produce a comprehensive, quantitative performance assessment of the SHM system and utilization procedure in a systematic manner, 3) provide an independent comparison between SHM solutions and alternate maintenance and monitoring methodologies, 4) optimize SHM utilization methodologies through a systematic evaluation of results obtained in laboratory and field test beds, 5) produce the necessary teaming between the airlines, aircraft manufacturers, regulators, and related SHM developers.

Overall Damage Detection Performance of CVM and PZT Candidate SHM Technologies

The goal of this project was to produce sufficient data and to conduct the proper interface with regulatory agencies to certify CVM and PZT sensor technology for specific rotorcraft applications. Comprehensive probability of flaw detection assessments were coupled with durability and on-aircraft flight tests to study the performance, deployment, and long-term operation of these SHM sensors on aircraft. Statistical methods using One-Sided Tolerance Intervals and Log Regression Analysis were employed to derive Probability of Detection (POD) levels for SHM sensors. This produced a series of flaw detection curves that can be used to propose SHM sensors for crack detection on Sikorsky S-92 rotorcraft applications.

An overall summary of the crack detection performance of the CVM and PZT sensors is:

- CVM and PZT sensors detect cracks in the component they are monitoring.
- Inspection process and diagnosis is fully automated and can be conducted remotely.
- Early detection = less costly repairs
- Establishing proper Damage Index levels and signal Baselines is essential to the damage detection process. To do this, users must understand the specific structural response and then complete proper system calibration tests.
- PZT useability will likely require engineering support beyond NDI or A&P personnel.
- CVM and PZT systems are fail-safe (inert sensors produce an alarm). This inherent fail-safe property ensures the sensor is attached to the structure and working properly prior to any data acquisition.
- Multiple sets of lab performance and multi-year flight test programs have been completed
- PZT response can provide pre-cursors to crack growth (system changes with no crack length change)
- An Alternate Means of Compliance (AMOC) has been approved for CVM along with a modified Service Bulletin which allows for routine use of CVM sensors in a select application on fixed-wing aircraft/
- Preferred safety driven use of SHM technology is achieved in concert with OEMS and regulatory agencies.

Probability of Detection Using CVM SHM System

Comparative Vacuum Monitoring is a SHM technology that can monitor the onset and growth of structural cracking. These sensors can be attached to a structure in areas where crack growth is known to occur. On a pre-established engineering interval, a reading will be taken from an easily accessible point on the structure. Each time a reading is taken, the system performs a self-test. This inherent fail-safe property ensures the sensor is attached to the structure and working properly prior to any data acquisition. In a number of structural categories studied in previous programs, the CVM sensors provided crack detection well before the crack propagated to the critical length determined by damage tolerance analysis. The sensitivity, reliability, and cost effectiveness of the CVM sensor system was demonstrated in both laboratory and field test environments.

This rotorcraft effort validated the application of CVM monitoring solutions to a gusset frame on a Sikorsky S-92 platform. The test specimens represented the crack origin sites associated with the nutplates on the frame and statistically-valid performance tests were completed to support routine use of CVM sensors for this application. All crack detections are for the most conservative unloaded state. CVM Crack detection lengths produced POD levels that were lower than the required crack detection level. The final CVM POD was determined to produce an acceptable performance to reliably detect cracks in the chosen family of applications on the S-92 frame. Thus, the CVM sensors were deemed as good, or better than, the current inspection requirement. There were no False Calls (CVM sensor indicated the presence of a crack when actually none was present) associated with these tests.

Probability of Detection Using PZT SHM System

A piezoelectric transducer (PZT) diagnostic technique is also available for monitoring, among other damage, fatigue crack growth in metallic structures. PZT sensors can be bonded to existing structures without changing the local and global structural dynamics. These sensors can act as both transmitters and receptors. As transmitters, piezoelectric sensors use electrical excitation to generate elastic waves in the surrounding material. As receptors, they receive elastic waves and transform them into electric signals. It is possible to install arrays of active-sensors in which each element takes, in turn, the role of transmitter and receptor, and thus scan large structural areas using ultrasonic waves pitched across the sensor network.

The PZT SHM technique uses diagnostic signals, generated from a network of PZT sensors bonded to a structure. It consists of three major components: diagnostic signal generation, signal processing and damage interpretation. In diagnostic signal generation, appropriate ultrasonic guided Lamb Waves were selected for actuators to maximize receiving sensor measurements. In signal processing, analysis methods select an individual mode for damage detection and maximize signal to noise ratio in recorded sensor signals. Finally, in damage interpretation, a physics based Damage Index is used to relate sensor measurements to crack onset and size.

In this Sikorsky-based study, a generalized engine and gearbox mount beam was chosen for PZT monitoring. A PZT network was designed to globally monitor the aft beam used to mount the S-92 main gearbox. This structure has a failure history where cracks have been observed emanating from several fastener locations both on the frame element and the adjoining skin. One advantage associated with the selection of this application is that such a beam is a very common structural arrangement for rotorcraft engine and gearbox mounts. Thus, the results from these validation tests could have a broad use.

The final PZT POD was determined to produce an acceptable performance to reliably detect cracks in this S-92 frame. There were no False Calls (PZT sensor indicated the presence of a crack when none was present) associated with these tests, however, extensive guidance was produced to guide the establishment of suitable Damage Indices and Baseline signatures to avoid false calls. Methods were developed to calibrate the PZT network and determine a damage "threshold" with acceptable Signal-to-Noise Ratio. Overall, the performance testing of the PZT SHM system:

- Proved the ability of the PZT system to provide a Green Light/Red Light ("GO" – "NO GO") decision on the presence of damage; showed need to observe DI trending, especially in complex geometries, to ensure unambiguous detection.
- Showed that monitoring PZT signals under load can improve damage detection sensitivity but must be accompanied by careful consideration of ability to establish proper signal Baselines at these same conditions.
- Highlighted how complex geometries, extreme temperature changes and loads can produce changing crack profile and reversal of DI levels as a crack propagates and stress redistribution occurs. These must be considered when setting the DI(threshold) levels.

SHM Path Forward

The replacement of our present-day manual inspections with automatic health monitoring can substantially reduce the associated life-cycle costs. When accessibility issues are considered, distributed sensors systems may also represent significant time savings by eliminating the need for component tear-down. In addition, corrective repairs initiated by early detection of structural damage are more cost effective since they reduce the need for subsequent major repairs and may avert a structural failure. Aerospace structures have one of the highest payoffs for SHM applications since damage can quickly lead to expensive repairs and aircraft routinely undergo regular, costly inspections.

As SHM systems reach further into these more advanced states and are relied upon for a greater portion of maintenance activities and planning, it may be necessary to accommodate separate approvals for the various elements of an SHM system. Such components include sensors, power supplies, signal conditioning and data acquisition electronics, data analysis software, trends assessments and the need for historical data, maintenance disposition algorithms, and automated record keeping functions. Individual approvals for SHM components will allow for building block approaches to SHM integration and possibly improved efficiency in standardized SHM operations where a single power and data bus can serve a number of SHM sensor networks.

The maintenance program instituted by each air carrier must be modified to accommodate the unique operation and use of SHM systems. Modifications to maintenance program must: 1) produce hardware specifications, installation procedures, operation processes, continued airworthiness instructions, 2) complete SHM indoctrination and training for airline personnel, 3) complete the financial, technical and logistical internal signatures necessary to adopt SHM, and 4) determine an operator's ability to adopt SHM and the FAA support needed to ensure airworthiness.

Long-term SHM applications may include flight monitoring tasks which lead to prognostic health monitoring. Flight loads, mechanical functions, and service problems can all be identified and algorithms can be applied to anticipate maintenance needs. Similarly, SHM sensors can be used to predict structural integrity problems or track trends in specific regions, mechanical systems, electrical systems, or pressure systems such that condition-based maintenance can be used. Thus, SHM systems could further improve maintenance programs by allowing for streamlined, advanced planning based on a more complete picture of an aircraft's structural integrity and operational performance.

Looking forward, large databases on sensor response/performance in multiple applications may help to determine if certain assumptions can be made and how to properly apply this data to support SHM approval efforts. The SHM performance databases will continue to expand as new applications are identified. Much like the time when NDI methods evolved into more applications to vastly increase their performance data, similarities in SHM methods and applications will also facilitate streamlined certification of SHM. However, until much larger databases of SHM performance are obtained - and successful flight history is accumulated - near-term testing levels are expected to be high.

For this specific program to enable SHM for rotorcraft applications, several key activities remain. SHM approvals and certification must be acquired through the appropriate FAA regulatory offices. This will include tasks to: 1) exercise regulatory (e.g. ACO, Rotorcraft Directorate) and OEM system for rotorcraft, 2) conduct SHM education initiatives with regulators, 3) identify regulatory information needs to grant approvals, 4) define the process, in concert with FAA and OEMs (Other Designated Authority (ODAs) leading to approval for routine use of SHM solutions in rotorcraft maintenance programs.

In addition, validation activities necessary to prove the performance and viability of SHM for rotorcraft, should be expanded to include field trials with a rotorcraft operator to: 1) assess overall SHM integration into a rotorcraft maintenance program , 2) identify SHM applications and conduct associated cost-benefit analyses, 3) demonstrate customization of SHM systems to the selected application(s), 4) fill in unique data in the SHM validation and certification plan, 5) complete SHM indoctrination and preliminary training for operator personnel (engineering, maintenance, NDI), 6) show operator's ability to produce SHM hardware specifications, installation procedures, operation processes, and continued airworthiness instructions, 7) understand the necessary modifications to an operator's maintenance program as a result of SHM use.

Global health management, achieved through the use of sensor networks, can be used to assess overall performance (or deviations from optimum performance) of large structures such as aircraft. The application of SHM systems using distributed sensor networks can reduce maintenance costs by facilitating rapid and global assessments of structural integrity. The use of in-situ sensors, coupled with remote interrogation, can also be employed to overcome a myriad of inspection impediments stemming from accessibility limitations, complex geometries, the location and depth of hidden damage, and the isolated location of the structure. The ease of monitoring an entire network of distributed sensors means that structural health assessments can occur more often, allowing operators to be even more vigilant with respect to flaw onset. The activities conducted in this program facilitated the evolution of an SHM certification process including the development of regulatory guidelines and advisory materials for the implementation of SHM systems via reliable certification programs. Formal SHM validation is allowing the aviation industry to confidently make informed decisions about the proper utilization of SHM solutions.

DISTRIBUTION

Ralph Abreu
Sikorsky

Kumio Adachi
Japan Airlines

Bernie Adamache
Jazz Airlines

Doug Adams
Vanderbilt Univ

Aydin Akdeniz
Boeing Company

Nestor Alcoba
Diamond Air

Paulo Anchieta da Silva
Embraer

Tammy Anderson
Federal Aviation Administration

Yasuo Asakawa
All Nippon Airways Co Ltd

Cindy Ashforth
Federal Aviation Administration

Mike Augustin
Bell Helicopter

James Ayers
US Army

Paul Ayers
Ryan Air

Hesham Azzam
Hahn Spring Ltd

Martin Bach
Airbus Helicopters Deutschland

Elise Baker
Sikorsky Aircraft

John Bakuckas
Federal Aviation Administration

Shobbo Basu
Boeing

Preston Bates
Sikorsky

John Bell
Sky West Airlines

Jean-Marc Bertrand
Bombardier Aerospace

Christopher Bigwoog
Etihad Airlines

Todd Blackstock
Anodyne Electronics Manuf Corp

Clemens Bockenheimer
Airbus

John Bohler
Delta Air Lines

Christian Boller
Univ of Saarlandes

Marcel Bos
Nationaal Lucht en Ruimtevaart Laboratorium

Andrew Brookhart
Sikorsky

John Brutlag
Delta Air Lines

Matthias Buderath
Airbus

Daniel Burkhard
Sky West Airlines

Alistair Burns
Air New Zealand

Hayley Burton
Virgin Atlantic Airways

Pierre Calmon
CEA

Peter Carini
United Technologies Corp

Sander Carneiro
Agencia Nacional De Aviacao Civil

Stephen Chan
Singapore Air

Toby Chandler
Structural Monitoring Systems Ltd

Fu-Kuo Chang
Stanford

Christopher Chang
Singapore Air

Todd Chapman
Boeing Company

Zaffir Chaudhry
United Technologies Research Center

Carlos Chaves
Embraer

Cas Cheung
Acellent Technologies

Eric Chesmar
United Airlines

Andy Chilcott
Structural Monitoring Systems Ltd

Steven Chisholm
Boeing Company

EngGuan Chua
Singapore Air

Chris Coleman
Delta Air Lines

John Coles
Boeing Company

Antonio Concilio
CIRA Scpa

Vincent Conway
RyanAir

Ron Cook
American Airlines

Vicente Cortes
Airbus

Joshua Cummins
Boeing Company

James Cycon
Sikorsky

Chris Davis
Boeing Company

Marie-Anne De-Smet
Airbus

Mark Derriso
US Air Force

Jacques Desjardins
Bombardier

Leo Dominguez
American Airlines

Nicolas Dominguez
Airbus

John Dominicus
Nationaal Lucht en Ruimtevaart Laboratorium

Fernando Dotta
Embraer

Chris Dragan
Polish Air Force Inst of Technology

Tom Duffy
Republic Airways

David Dyer
Jet Blue

Benjamin Eckstein
Airbus

Charles Farrar
Los Alamos National Laboratory

David Fauerstenau
Delta Air Lines

Jindrich Finda
Honeywell International SRO

Tom Flournoy
Federal Aviation Administration

Rafael Favaro Foltran
Agencia Nacional De Aviacao Civil

Stephen Forman
Structural Monitoring Systems Ltd

Derrick Formosa
Anodyne Electronics Manuf Corp

David Forsyth
TRI Austin

David Fosse
Delta Air Lines

Keith Frable
Federal Aviation Administration

Kanata Fujii
Mitsubishi Heavy Industries Ltd

Hiro Fukuyama
Japan Civil Aviation Bureau

Akira Fukuzo
Japan Airlines

Hiroshi Furukawa
Anritsu Devices

Stephen Galea
DSTO

Dave Galella
Federal Aviation Administration

Sean Gallinat
Republic Airways

Travis Gang
UTC Aerospace Systems

David Garrison
Delta Air Lines

Gary Georgeson
Boeing

Anindya Ghoshal
US Army

Tim Gibson
Republic Airways

Victor Giurgiutiu
Univ of South Carolina

Neil Goldfine
Jentek Sensors Inc

J.B. Gonsalves
Air India

Michael Gorelik
Federal Aviation Administration

Dennis Granger
US Army

Rafik Hadjria
SAFRAN

Matt Hansen
Goodrich

Ulrike Hanskoetter
Airbus

Aswin Haridas
Testia

Sophie Hasbroucq
Airbus

Eric Haugse
Boeing Company

Tim Hayo
Airbus

Daniel Hebért
Transport Canada

Peter Heer
Lufthansa Technik

Nancy Held-Sheehe
Sikorsky

William Heliker
Federal Aviation Administration

Keiji Hirabayashi,
All Nippon Airways Co Ltd

Dave Hoffman
Boeing

Falk Hoffmann
Airbus

Ed Hohman
Bell Helicopter

Andy Holder
Ryan Air

Allan Howell
Transport Canada

Scott Huddleston
US Army

Masato Iehara
Mitsubishi Heavy Indus Ltd

JB Ihn
Boeing Company

Roy Ikegami
Acellent Technologies

Firdausi Irani
Transportation Technology Center Inc.

Ramki Iyer
US Army

Walt Jarecki
Boeing Company

Pav Kalyan
EasyJet

Russell Keller
Boeing Company

Seth Kessler
Metis Design Corp.

Hiroshi Kobayashi
All Nippon Airways Co Ltd

Michael Kolling
Airbus

James Kornberg
Air France-KLM

Andrew Kornecki
Embry Riddle Aeronautical Univ

Henry Kroker
Anodyne Electronics Manuf Corp

Paul Kulowitch
US Navy

Amrita Kumar
Acellent Technologies

Bill Kunik
Goodrich

Akira Kuraishi
Kawasaki Heavy Industries

Yoshiharu Kuze
Mitsubishi Heavy Industries Ltd

Bernard Laskowski
Analatom Unc.

Melinda Laubach-Hock
National Inst of Aviation Research

Dy Le
Texas Tech Univ

Jae Lee
Allegiant Air

James Leslie
American Airlines

Irene Li
Acellent Technologies

Somboon Limwathnapong
Thai Airways

Eric Lindgren
US Air Force

John Linn
Structural Systems Monitoring Ltd

Trevor Lynch-Staunton
Anodyne Electronics Manuf Corp

Ross MacArthur
Southwest Airlines

Shah Mahmood
US Navy

Yokozuka Makoto
SUBARU

Hiroshi Mamizu
Kawasaki Heavy Industries Ltd

Nancy Marsh
Federal Aviation Administration

Marcias Martinez,
Clarkson Univ

Junya Matsuda
Japan Airlines

Kevin McLean
EasyJet

Bill Meeker
Iowa State Univ

Alex Melton
Delta Air Lines

Bruno Mery
Airbus

Will Milan
U.S. Navy

Andy Miller
Air New Zealand

Shu Minakuchi
Unv of Tokyo

Eric Mitchell
American Airlines

John Mitchell
Transport Canada

Mohammadreza Mofakhami
Bombardier Aerospace

Fernando Moreu
University of New Mexico

Toshiya Nakamura
Japan Aerospace Exploration Agency

Takuya Nakano
SUBARU

Shridhar Nath
General Electric

Emily O'Connor,
Boeing Company

Toshimichi Ogisu
Subaru Corporation

Shashank Pant
NRC Canada

Mark Pappakostas
Acellent Technologies

Francis Peloquin
Bombardier Aerospace

Luiz Perin
Embraer

Tristan Perry
Delta Air Lines

David Piotrowski
Delta Air Lines

Vinnie Ploubis
Southwest Airlines

David Polland
Boeing Company

Laurent Pouget
Airbus

Rich Poutier
Structural Monitoring Systems Ltd

Bill Prosser
NASA

Jerry Qi
Georgia Institute of Technology

Piyush Ranade
Honeywell Aerospace

Bernhard Randerath
Etihad Airlines

Mark Rice
Federal Aviation Administration

Ian Read
BAE Systems

Joe Reeves
Delta Air Lines

Michael Reveley
Structural Monitoring Systems Ltd

Jaret Riddick
US Army

Carlos Rios
Sikorsky

Sean Rogers
RyanAir

Richard Ross
NASA

Ricardo Rulli
Embraer

Dave Rusk
US Navy

Caleb Saathoff
National Inst of Aviation Research

Patrick Safarian
Federal Aviation Administration

Keisuke Saito
Kawasaki Heavy Industries

Joao Santos
OGMA

Luis Santos
Embraer

Avi Sarlashkar
Sikorsky

Noriyuki Sawai
Society of Japanese Aerospace Companies

John Scarcello
Lockheed Martin

Eric Schenck
Sikorsky Aircraft

George Schneider
Sikorsky Aircraft

Greg Schneider
Federal Aviation Administration

Brian Shaigec
Anodyne Electronics Manuf Corp

Charles Shepherd
American Airlines

Kelly Shields
Sky West Airlines

Takeda Shinichi
Japan Aerospace Exploration Agency

Walt Sippel
Federal Aviation Administration

Corey Skarren
Republic Airways

Gary Smith
EasyJet

Chuck Smits
Southwest Airlines

Hideki Soejima
Subaru Corp

Holger Speckmann
Testia

Ben Stanford
Delta Engineering

David Stargel
US Air Force

Danielle Stephens
Federal Aviation Administration

Christian Stolz
Airbus

Jun Sugita
All Nippon Airways Co Ltd

Paul Swindell
Federal Aviation Administration

Kohei Takahashi
Subaru Corp

Shin-ichi Takeda
Japan Aerospace Exploration Agency

Nobuo Takeda
Japan Nat'l Transportation Safety Board

Yutaka Terada
Mitsubishi Heavy Industries

Melvin Taylor
Federal Aviation Administration

Chinnaphan Thattiyaphong
Thai Airways

Yves Theriault
Bombardier

Zuhair Tibi
Jet Blue

Mike Todd
UC-San Diego

John Tomblin
National Inst of Aviation Research

Darryl Toni
Sikorsky

Nilesh Tralshawala
General Electric

Doug Tritsch
Sikorsky

Hin Tsang
Transport Canada

Brian Tucker
Bell Helicopter

John Van Doeselaar
Airbus

Paul Vaughan
Delta Air Lines

John Vincent
European Union Aviation Safety Agency

Tony Vissini
US Army

Hal Voges
Honeywell

Simon Waite
European Union Aviation Safety Agency

Kosuke Watanabe
Mitsubishi Heavy Industries Ltd

Alexander Weisser
Airbus

Lorenz Wenk
Airbus

Farid te Winkel
Nationaal Lucht en Ruimtevaart Laboratorium

Sam Wright
Structural Monitoring Systems Ltd

Ion Won
Federal Aviation Administration

Roy Wong
Bombardier Aerospace

Susheel Yadav
Acellent Technologies

Jun Yamanaka
Japan Airlines

Yasushi Yamashita
All Nippon Airways Co Ltd

Phil Yannaccone
American Airlines

Takashi Yari
Mitsubishi Heavy Industries

Rick Young
NASA

Lei Yue
Cathay Pacific

Sandia National Labs:
1353 Paul Clem
1522 Daniel Roettgen
1543 Chandler Smith
1543 Tim Walsh
1554 Adam Brink
1815 Nelson Bell
1815 Bernadette Hernandez-Sanchez
1815 Rico Treadwell
1816 Erik Spoerke
1911 Technical Library
2496 James Nistler
2496 James Thompson
3651 Stephanie Holinka
5219 Eric Langlois
5229 Christian Arrington
6000 Doug Bruder
6600 Gary Laughlin
6610 Matthew Brown
6620 Roberto Mata
6620 Dennis Roach
6621 Adam Brink
6621 Kurtis Ford
6621 Fred Snoy
6622 Garth Kraus
6623 Donovan Gerty
6623 Marc Ahlen
6623 Michael Pacheco
6623 Jason Schneider
6626 Chad Monthan
6626 Michael Bolduc
6626 Stephen Neidigk
6626 Jim Pacheco
6626 Tom Rice
6626 Josh Romano
6630 Lindsay Klennert
6640 Steven Samuels
6650 Jim Redmond
6651 Barry Boughton
6651 Tim Brown
6651 Scott Kuszmaul
6651 Blake Reece
6652 Daniel Wilcox
6652 Jason Berger
8762 Justin Jacobs
8821 Josh Paquette
9532 Recorded Information Management

THIS PAGE INTENTIONALLY LEFT BLANK

Sandia National Laboratories is a multimission laboratory managed and operated by National Technology & Engineering Solutions of Sandia LLC, a wholly owned subsidiary of Honeywell International Inc. for the U.S. Department of Energy's National Nuclear Security Administration under contract DE-NA0003525.